Fission Product Yield Data for the Transmutation of Minor Actinide Nuclear Waste

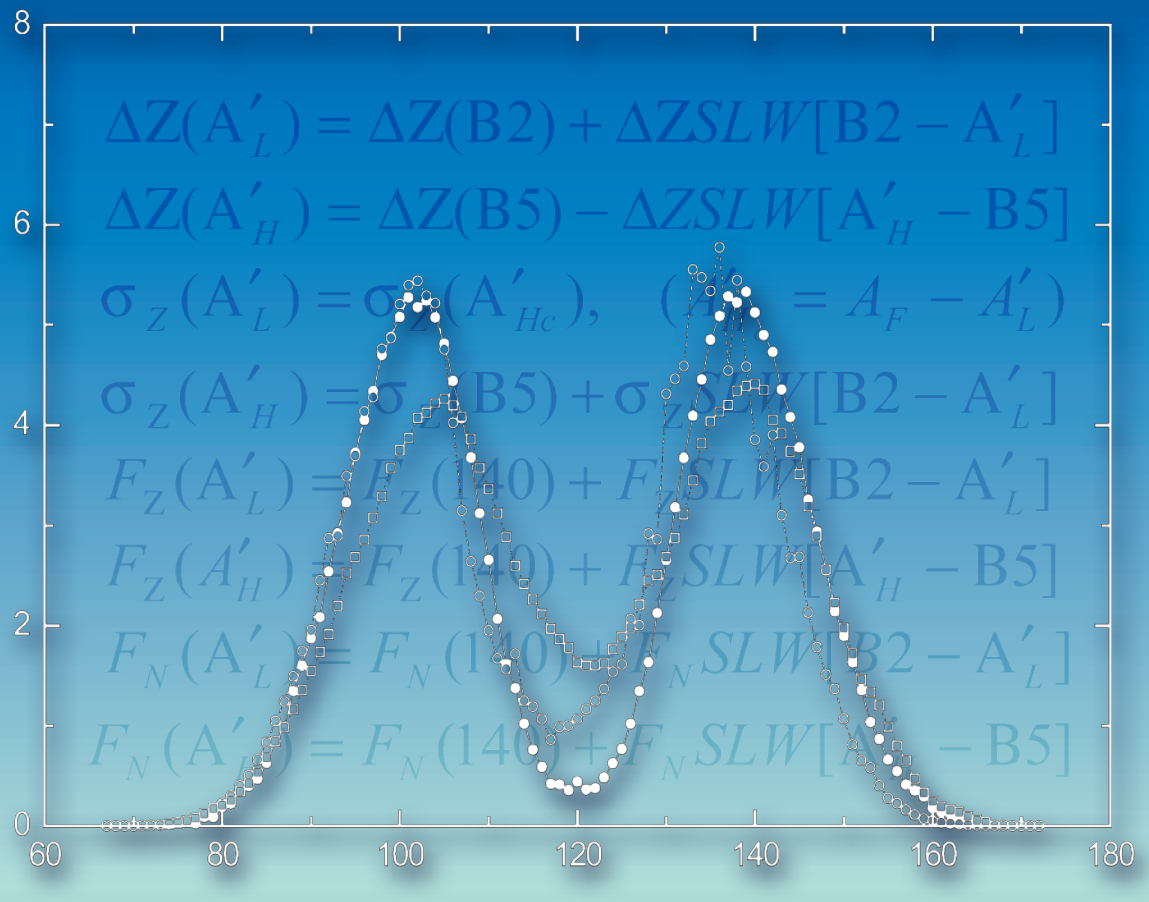

IAEA
International Atomic Energy Agency

FISSION PRODUCT YIELD DATA FOR THE TRANSMUTATION OF MINOR ACTINIDE NUCLEAR WASTE

The following States are Members of the International Atomic Energy Agency:

AFGHANISTAN
ALBANIA
ALGERIA
ANGOLA
ARGENTINA
ARMENIA
AUSTRALIA
AUSTRIA
AZERBAIJAN
BANGLADESH
BELARUS
BELGIUM
BELIZE
BENIN
BOLIVIA
BOSNIA AND HERZEGOVINA
BOTSWANA
BRAZIL
BULGARIA
BURKINA FASO
CAMEROON
CANADA
CENTRAL AFRICAN REPUBLIC
CHAD
CHILE
CHINA
COLOMBIA
COSTA RICA
CÔTE D'IVOIRE
CROATIA
CUBA
CYPRUS
CZECH REPUBLIC
DEMOCRATIC REPUBLIC OF THE CONGO
DENMARK
DOMINICAN REPUBLIC
ECUADOR
EGYPT
EL SALVADOR
ERITREA
ESTONIA
ETHIOPIA
FINLAND
FRANCE
GABON
GEORGIA
GERMANY
GHANA
GREECE
GUATEMALA
HAITI
HOLY SEE
HONDURAS
HUNGARY
ICELAND
INDIA
INDONESIA
IRAN, ISLAMIC REPUBLIC OF
IRAQ
IRELAND
ISRAEL
ITALY
JAMAICA
JAPAN
JORDAN
KAZAKHSTAN
KENYA
KOREA, REPUBLIC OF
KUWAIT
KYRGYZSTAN
LATVIA
LEBANON
LIBERIA
LIBYAN ARAB JAMAHIRIYA
LIECHTENSTEIN
LITHUANIA
LUXEMBOURG
MADAGASCAR
MALAWI
MALAYSIA
MALI
MALTA
MARSHALL ISLANDS
MAURITANIA
MAURITIUS
MEXICO
MONACO
MONGOLIA
MONTENEGRO
MOROCCO
MOZAMBIQUE
MYANMAR
NAMIBIA
NETHERLANDS
NEW ZEALAND
NICARAGUA
NIGER
NIGERIA
NORWAY
PAKISTAN
PALAU
PANAMA
PARAGUAY
PERU
PHILIPPINES
POLAND
PORTUGAL
QATAR
REPUBLIC OF MOLDOVA
ROMANIA
RUSSIAN FEDERATION
SAUDI ARABIA
SENEGAL
SERBIA
SEYCHELLES
SIERRA LEONE
SINGAPORE
SLOVAKIA
SLOVENIA
SOUTH AFRICA
SPAIN
SRI LANKA
SUDAN
SWEDEN
SWITZERLAND
SYRIAN ARAB REPUBLIC
TAJIKISTAN
THAILAND
THE FORMER YUGOSLAV REPUBLIC OF MACEDONIA
TUNISIA
TURKEY
UGANDA
UKRAINE
UNITED ARAB EMIRATES
UNITED KINGDOM OF GREAT BRITAIN AND NORTHERN IRELAND
UNITED REPUBLIC OF TANZANIA
UNITED STATES OF AMERICA
URUGUAY
UZBEKISTAN
VENEZUELA
VIETNAM
YEMEN
ZAMBIA
ZIMBABWE

The Agency's Statute was approved on 23 October 1956 by the Conference on the Statute of the IAEA held at United Nations Headquarters, New York; it entered into force on 29 July 1957. The Headquarters of the Agency are situated in Vienna. Its principal objective is "to accelerate and enlarge the contribution of atomic energy to peace, health and prosperity throughout the world''.

FISSION PRODUCT YIELD DATA FOR THE TRANSMUTATION OF MINOR ACTINIDE NUCLEAR WASTE

INTERNATIONAL ATOMIC ENERGY AGENCY
VIENNA, 2008

COPYRIGHT NOTICE

Sales and Promotion, Publishing Section
International Atomic Energy Agency
Wagramer Strasse 5
P.O. Box 100
1400 Vienna, Austria
fax: +43 1 2600 29302
tel.: +43 1 2600 22417
email: sales.publications@iaea.org
http://www.iaea.org/books

Printed by the IAEA in Austria
April 2008
STI/PUB/1286

IAEA Library Cataloguing in Publication Data

Fission product yield data for the transmutation of minor actinide nuclear waste. – Vienna : International Atomic Energy Agency, 2008.
p. ; 24 cm.
STI/PUB/1286
ISBN 92–0–115306–6
Includes bibliographical references.

1. Fission products — Measurement. 2. Radioactive wastes. 3. Transmutation (Chemistry). 4. Neutron cross-sections. 5. Fission cross-sections — Measurement. I. International Atomic Energy Agency.

IAEAL 08–00504

FOREWORD

A report issued by an international study group for the transmutation of nuclear waste using accelerator driven systems has highlighted the need for specific sets of nuclear data. These authoritative requirements include fission product yields at an intermediate incident neutron energy of up to 150 MeV.

Before the start of the present CRP on fission product yield data for the transmutation of nuclear waste, only four types of evaluated fission yield data sets existed, namely for spontaneous fission, and for fission induced by thermal, fast (or fission) spectrum, and by 'high energy' (14–15 MeV) neutrons. A new type of evaluation for energy dependent neutron induced fission yields was required for this project. In view of the scarcity of experimental data, such an evaluation has to be based on systematics and theoretical model calculations. Unlike fission cross-sections, where nuclear models are being used successfully for the calculation of unmeasured cross-section ranges, such models or theories existed only for low energy fission yields. Hence the CRP participants entered a completely new field of research for which the progress and outcome were unpredictable. Clearly the ultimate goal of such an effort, namely an evaluation of energy dependent fission yields, could not be realized within the perceived lifetime of a CRP.

The main emphasis of the CRP was on the development of adequate systematics and models for the calculation of energy dependent fission yields up to 150 MeV incident neutron energy. Several problems had to be solved, such as the correct choice of model parameters and multiplicity distributions of emitted neutrons, and the effect of multi-chance fission. Models and systematics have been tested for lower energy yields, but they failed to reproduce recent experimental data, particularly at higher energies, and the parameters had to be modified. Other models have been developed from the analysis of experimental data in order to derive systematic dependences and they were adapted in the course of the CRP to predict fission product yields. The valuable role of the CRP in such work became evident during the meetings, at which the discussions formed a fruitful basis for improvements to the models. The benchmark exercise revealed the true worth and predictive capabilities of the systematics and theoretical models developed during the course of the CRP. Necessary improvements and the direction of future studies were also revealed. These models have the potential to give reliable predictions after implementation of the improvements suggested in this report.

A brief introduction and the various studies undertaken by individual participants are given at the beginning of this publication, followed by a detailed description of the resulting overall achievements, conclusions and recommendations of the CRP and a summary of the benchmark exercise and results. Additional material is included on the enclosed CD-ROM, including compilations of the fission product yields, unedited papers and all details of the benchmark exercise.

The IAEA wishes to thank all CRP participants for their contributions to the project. The IAEA responsible officers were M. Lammer and A.L. Nichols of the Division of Physical and Chemical Sciences.

CONTRIBUTING AUTHORS

Denschlag, J.-O.	Johannes-Gutenberg-Universität Mainz, Germany
Duijvestijn, M.C.	Nuclear Research and Consultancy Group, Netherlands
Ethvignot, Th.	Service de Physique Nucléaire, Commissariat à l'Énergie Atomique, France
Hambsch, F.-J.	EC Joint Research Centre, Institute for Reference Materials and Measurements, Belgium
Katakura, J.	Japan Atomic Energy Agency, Japan
Kibkalo, Yu.V.	SC Institute for Nuclear Research, Ukraine
Lammer, M.	International Atomic Energy Agency
Tingjin, Liu	China Institute of Atomic Energy, China
Maslov, V.M.	Belarus Academy of Sciences, Belarus
Mills, R.W.	Nexia Solutions, British Nuclear Fuels plc, United Kingdom
Wahl, A.C.	Los Alamos National Laboratory, United States of America
Zhdanov, S.V.	National Nuclear Centre, Kazakhstan

TECHNICAL ASSISTANCE

Nichols, A.L.	International Atomic Energy Agency

CONTENTS

1. FISSION PRODUCT YIELDS: MINOR ACTINIDES UP TO 150 MeV

M. Lammer
International Atomic Energy Agency

A multinational team with the appropriate expertise participated in a work programme aimed at the development of systematics and nuclear models to assist in the evaluation of energy dependent fission yields for incident neutron energies of up to 150 MeV. New concepts for both systematics and theoretical models were developed, as described in later sections of this report. Various predictions of the fission product mass distributions were compared in a benchmark exercise that gave remarkably good results below 50 MeV. Reasons for the discrepancies at higher energies and some failures of the model predictions are discussed in Sections 5 and 6, pointing the way towards future investigations and fission yield evaluations.

1.1. INTRODUCTION

1.1.1. Transmutation of nuclear waste

The problem of the disposal of nuclear waste is an important feature of the utilization of nuclear power. Thus, during the course of the 1980s and 1990s international efforts concentrated on new concepts of waste removal through transmutation. Several proposals were made, using classical thermal or fast reactors as incinerators, or accelerator driven systems. These highly technical proposals are being studied with regard to their feasibility, neutron economics and environmental safety, and nuclear data (including fission yields) are required for assessments and for the design and operational requirements of such facilities.

While adequate nuclear data exist for thermal and fast reactor incineration, this satisfactory situation is not the case for accelerator driven systems. An international working group has studied the overall problem and recommended the assembly of the required nuclear data at intermediate incident neutron energies of up to at least 150 MeV [1.1]. The staff at the IAEA have also assessed this situation in conjunction with appropriate external expertise and decided to contribute to this effort by the initiation of a coordinated research project (CRP) on fission yields up to 150 MeV.

1.1.2. New approach to fission yield evaluations

Evaluated fission yields as a function of incident neutron energy have to be presented in a way that any fission yield from any target nuclide can be obtained for any desired energy up to 150 MeV (as a first step). Previous evaluations have focused on thermal, fast and 'high' (14–15 MeV) neutrons, as individual data sets. New concepts are required for the presentation of energy dependent fission yields, such as:

(a) Functions for the description of energy dependent yields;
(b) Yield sets at energy intervals with interpolation formulae;
(c) Computer programs using systematics and/or theoretical models, with the desired fission yields as output.

Any evaluation method will also require new procedures, and previous methods of analysis will not be feasible because experimental data are so scarce. Fission yield measurements are impossible for certain targets, while measurements at higher incident neutron energies are extremely difficult for other targets. Therefore, sufficient coverage of the desired neutron energy range by experimental data cannot be expected. Thus nuclear models and systematics need to be developed from the available experimental data to allow the calculation of fission yields and assist in future evaluations of energy dependent fission yields.

1.1.3. Objectives

The primary objectives of the CRP were to study all the problems involved in the development of nuclear models and systematics and to derive a method for fission yield evaluation as a function of incident neutron energy. Hopefully such efforts will result in a new evaluation of the energy dependent neutron induced fission yields up to 150 MeV.

However, this CRP entered an entirely new field of research, as usable models and systematics do not exist over such an energy range and the outcome of the work was deemed to be unpredictable. Therefore, the goals of the CRP were subsequently limited to the development of appropriate nuclear models and systematics for the prediction of fission yields as tools for the evaluation of energy dependent fission yields up to 150 MeV.

1.2. MODELLING OF FISSION FRAGMENT MASS DISTRIBUTIONS

This brief introduction should help in better understanding the problems to be addressed, along with the results of the benchmark exercise (Section 6). More detailed descriptions can be found in Sections 3.1, 4.1 and 4.6.

1.2.1. Fission process

Fission is a slow process on a nuclear timescale, involving deformation of the whole nucleus, and is always a compound process. A captured low energy neutron leads directly to an equilibrated compound system (first chance fission). For sufficiently high incident neutron energies (E_n) of a few MeV, the emission of a pre-equilibrium neutron becomes possible (second chance fission) at an about 100-fold faster timescale than fission. Still higher E_n can lead to the emission of two (third chance fission) or more (multi-chance fission) pre-equilibrium neutrons before fission. This behaviour is also applicable to other projectiles except that there is always a threshold for fission. At such high energies, a 'composite nucleus' (target nucleus plus projectile) is formed that emits fast particles and gradually loses excitation energy and memory of the incident particle by many nucleon–nucleon interactions before reaching an equilibrated compound stage of the reaction, where fission may occur (multi-chance or emissive fission). Thus the fissioning nucleus has a mass lower than the composite nucleus by the number of pre-equilibrium particles emitted.

Fission occurs when the saddle point deformation of the nucleus is reached. On the descent from saddle to scission, neutrons may be emitted and reduce the excitation energy. The highly excited primary fission fragments are de-excited by the emission of prompt neutrons, resulting in secondary fission fragments, followed by prompt γ rays to form the primary fission products. The latter are generally neutron rich and reach stability by the emission of delayed neutrons and/or by radioactive β decay. We distinguish between the 'pre-neutron emission mass distribution' of primary fission fragments and the 'post-neutron emission mass distribution' of secondary fission fragments.

1.2.2. Fission fragment mass distributions

Mass distributions from low energy neutron induced actinide fission are predominantly asymmetric, and such an effect is reflected by the light and heavy mass peaks corresponding to complementary fission fragments. These mass distributions have successfully been represented by five Gaussians, accounting for the observed fine structure in the asymmetric peak regions, whereas seven Gaussians gave a better fit for spontaneous fission and less than five Gaussians were adequate for the pre-actinides and higher actinides where increased symmetric fission is observed [1.2].

Brosa et al. [1.3] have developed a model that relates the above representations of fission fragment mass distributions to different fission modes (corresponding to separate fission channels) through which an excited nucleus in the actinide region can undergo fission: a symmetric 'super long' mode and two asymmetric modes, 'standard 1' (ST-1) and 'standard 2' (ST-2). The super long mode corresponds to the symmetric peak; both the ST-1 and ST-2 modes correspond to two Gaussians, each mode being composed of a light and a heavy mass peak in asymmetric fission. ST-1 and ST-2 are responsible for the observed fine structure in the asymmetric peaks.

The positions of the asymmetric mass peaks are determined by shell effects: the ST-1 contribution to the heavy mass peak at about A = 134 is attributed to the formation of spherical heavy fragments close to Z = 50 and N = 82; that of ST-2 at about A = 142 is identified with the deformed shell closure at N ≅ 88. As a consequence, these positions have been observed to be stable with respect to the change in mass of the fissioning nuclide, as is also confirmed by the Brosa model [1.3] that predicts a change of the mean heavy fragment mass for ST-2 from 142 in ^{238}U to 140 in ^{226}U fission. Thus, only the position of the light mass peak shifts with a change of the mass of the fissioning nuclide.

The symmetric fission contribution has been observed to increase for lower mass actinides

(e.g. ^{232}Th), and is the only fission mode for pre-actinides ($A \leq 227$). A similar trend can be observed for the higher actinides, with only symmetric fission for $A \geq 257$. This systematic behaviour is correctly predicted by the Brosa model [1.3]. However, whereas the symmetric fission of pre-actinides and the smaller symmetric fission contribution in the case of actinides are due to the super long mode, a super short mode is responsible for the symmetric fission of the heavy actinides.

The preferred fission mode also changes with increasing excitation energy due to the disappearance of shell effects, so that fission mechanisms are described solely by the liquid drop model: first the ST-1 contribution disappears, followed by ST-2, to leave only the super long mode and a symmetric mass distribution.

1.2.3. Prediction of fission yields: Systematics and theoretical models

The development of systematics is based on experimental data and represents an empirical approach to understanding the fission process. Measured fission yield distributions are fitted by suitable functions. Mass distributions are normally (but not necessarily) represented by a model consisting of Gaussians, as described above. Model parameters are obtained for different composite nuclides and excitation energies, and the functional dependences of these parameters on the masses and charges of the composite nuclides and on the excitation energies are generally derived through least squares analysis. The systematics can be restricted to neutron induced fission of a certain target nuclide or include different target nuclides and projectiles to derive global systematics.

Emissive fission contributions to the total reaction cross-section for a given target–projectile combination are calculated in the theoretical approach to obtain the fissioning nuclides contributing to the observed mass distribution. Fission fragment mass distributions are then derived with the aid of a suitable nuclear model that calculates the formation of given pairs of complementary fission fragments from the probabilities for the different fission modes and the neck rupture. This approach does not use any fitting procedure. Only the model parameters are adjusted by comparing the predictions with measured yield distributions and can be used to calculate mass distributions correctly from any target–projectile combination.

1.3. PROBLEMS TO BE ADDRESSED

1.3.1. Experimental data

Available experimental data for energy dependent neutron induced fission yields are insufficient for the development of systematics, whereas the theoretical model approach is not affected. One possibility would be to extend the studies to yield data from photon and light charged particle induced fission. Detailed studies are required to quantify the differences between neutron induced and other fission reactions and assess the feasibility of their combined use in systematics. Measurements can also be recommended that are important for the development of systematics and theoretical models.

1.3.2. Collection of experimental data

Clearly, for the development of systematics and for the intercomparison of model predictions the proposed studies cannot be restricted to minor actinides. Models and systematics have to be extensively applicable, and as many data as possible need to be used in their development. However, fairly complete and up to date collections of experimental data (bibliographies and data compilations) exist only for neutron induced fission yields.

1.3.3. Treatment of measured data

Measurement methods can be subdivided into two basic types:

(1) Physical measurements, in which prompt fission fragments are recorded simultaneously and directly to be identified by their mass and charge and/or kinetic energy — this method covers practically the complete range of the mass distribution.
(2) Measurements of the characteristic radiation from fission product decay (mass spectrometry is not possible at higher neutron energies because of the extremely small amounts of fission products available).

The second method can only be applied to specific fission products, and the mass range covered is incomplete. On the other hand, the results of radiation studies are more accurate and enable the determination of fine structure in mass distributions and charge dispersions in mass chains.

'Provisional masses' are determined in physical measurements that lie between the pre- and post-neutron emission mass distributions. The raw data have to be adjusted for neutron emission by fragments to obtain pre- or post-neutron emission mass distributions. This adjustment is a rather complicated procedure that depends on the experimental arrangements and requires assumptions concerning the neutron multiplicity distribution as a function of fragment mass (for the incident neutron energy range under consideration there are practically no experimental or evaluated data). Furthermore, each recorded mass has a Gaussian distribution due to the nature of the experimental set-up. Formulae to correct for this incomplete mass resolution have been proposed and used in data analysis, but there is no evidence that a particular method of adjustment is reliable and universally applicable. Finally, in the analysis of raw data, measurers often assume that mass distributions are symmetric in shape (complementary fission fragments), and the point of symmetry is determined from the composite nucleus mass and nu-bar, which is incorrect because of multi-chance fission (see below).

1.3.4. Multi-chance fission

Fissioning nuclei differ from the original composite nuclei in emissive fission. Thus, several problems have to be taken into account and addressed.

1.3.4.1. Formation of the compound nucleus

The formation process of the compound nucleus prior to disintegration has been established to be unimportant. Therefore, the mass distribution from a given fissioning nuclide at a given excitation energy is expected to be independent of the original target and projectile. However, global systematics of fission product mass distributions are developed as a function of the composite nuclei resulting from different target–projectile combinations. Studies are required to determine the possible differences in the pre-equilibrium particle emission characteristics for different target–projectile combinations leading to the same composite nuclei.

1.3.4.2. Shape of the mass distribution

Effects due to multi-chance fission that influence the final observed mass distribution can be subdivided into three main categories:

(1) Change of fission mode contribution:

Multi-chance fission results in a reduction of the mass (towards neutron deficient isotopes) and the excitation energy of the fissioning nuclides, which changes the preferred fission mode. The resulting total mass distribution is composed of contributions from different preferred fission modes with a shift to lower masses, and therefore a loss in symmetry of shape.

(2) Change of mass peak position and point of mass symmetry:

With the reduction of the mass of the fissioning nuclides the light, heavy and symmetric mass peaks in the mass distribution can also be expected to suffer a shift towards lower masses, leading to a broadening of the mass peaks as several fissioning isotopes contribute to the distribution. Moreover, the composite mass distribution loses symmetry because of the stable position of the heavy fragment mass peak (due to shell effects) that is independent of the mass of the fissioning nuclide. Thus, the position of the light mass peak in emissive fission is shifted towards lower masses, and the composite light mass peak is broadened.

(3) Change in neutron emission by fragments (see Section 1.3.5).

1.3.5. Neutron emission data

Extensive compilations and evaluations of the average number of neutrons emitted in zero and low energy fission are available. Some evaluated data also exist for neutron multiplicity distributions (all neutrons or neutrons emitted by fission fragments) in this energy range. However, prior to the CRP no such data existed as a function of incident neutron energy. Nu-bar values are required for the calculation of the point of reflection symmetry in the shape of the fission fragment mass distribution; multiplicity distributions of neutrons emitted by fission fragments are needed for the calculation of post-neutron mass distributions from pre-neutron mass distributions.

Neutron emission by fragments causes a shift of the post-neutron emission mass distribution to lower masses by an amount determined by the multiplicity distribution of neutrons as a function of fragment mass. Emissive fission results in a change of the mass and excitation energy of the fissioning

nucleus, which in turn leads to a change in the mass distribution and excitation energy of the fragments and hence in the multiplicity distribution of neutrons emitted by fragments. This phenomenon has to be taken into account when assumptions are made about neutron emission distributions for adjustments applied to raw data (provisional masses) in experiments, and in the modelling of fission yield predictions.

1.3.6. Development of systematics and models

At the beginning of the CRP, existing systematics and models for mass and charge distributions were only designed and valid for low energy fission up to 14 MeV. Therefore, studies were undertaken to assess the applicability and adaptability of these techniques to intermediate energy fission and determine whether new models and systematics need to be developed. These investigations entered a new field of research, and the outcome and degree of success were unpredictable.

1.3.7. Nuclear charge distribution

Measurements of charge distributions are even far more scarce in the intermediate energy range than those of mass distributions or cumulative (CU) fission yields. Furthermore, charge distribution data derived by measurers from their experimental results depend on assumptions made about the charge distribution functions and absolute mass yield data. At the beginning of the CRP the decision was taken to solve the problem of reliable mass distribution predictions first (required for adjustment of measured data and derivation of charge distribution functions), before investigating the feasibility of modelling charge distributions as functions of the fissioning nuclide and excitation energy.

1.4. CRP PARTICIPANTS AND TASKS

1.4.1. Participants

The selection of participants was guided by the following criteria:

(a) Compilers and evaluators of fission yield data who are familiar with evaluation methods can advise on the requirements for future evaluations of energy dependent fission yields and perform auxiliary evaluations;
(b) Experts in fission yield measurements;
(c) Specialists in the theory, models and systematics needed for fission yield predictions;
(d) Scientists who are familiar with nuclear data requirements for transmutation studies.

Representatives of two of the major fission yield libraries agreed to participate:

R.W. Mills (UK) has evaluated and prepared the UK fission yield library (versions UKFY2 and UKFY3) — the latter has been adopted for the official OECD nuclear data library JEFF (Joint Evaluated Fission and Fusion file).

Liu Tingjin (China) is the main evaluator of the fission yield file for CENDL, the Chinese Evaluated Nuclear Data Library.

J.-O. Denschlag (Germany) and A.A. Goverdovskii (Russian Federation) are experts in experimental methods and their limitations, and are also familiar with fission theory and the modelling of fission yield distributions.

V.M. Maslov (Belarus) is an expert in fission theory and fission cross-section evaluations.

J. Katakura (Japan) is a member of a Japanese group performing transmutation studies and uses systematics developed in Japan to calculate the required fission yields [1.4].

A.C. Wahl (USA) has performed several specialized fission yield evaluations and model fits, and has developed systematics for mass distributions and the commonly used charged distribution models [1.2], all for low energy fission up to 15 MeV.

M.C. Duijvestijn (Netherlands) is involved in various types of fission yield measurements and the development of theoretical models for intercomparison and a better understanding of nuclear fission (together with A.J. Koning).

Yu.V. Kibkalo (Ukraine) and S.V. Zhdanov (Kazakhstan) were invited to participate because of their development of new models for systematic fission yield studies.

Three scientists were invited to participate as observers at the CRP meetings, because of their valuable contributions to the discussions and presentation of papers that added to the success of the CRP: F. Storrer (France) presented data requirements for transmutation studies, Th. Ethvignot (France) performed measurements, and F.-J. Hambsch (Belgium) performed model calculations for the prediction of fission yields.

1.4.2. Tasks

The following tasks were defined by CRP participants at the first research coordination meeting, and later modified or adapted in accord with the needs and progress:

(1) Experimental data for yields from neutron, light charged particle and photon induced fission:
- Assemble all available bibliographic references;
- Compile the numerical experimental data;
- Recommend and, if possible, perform selected key measurements required to further the work of the CRP.

(2) Evaluation of fission yields:
- Assess the accuracy of transmutation calculations and define the requirements for evaluations;
- Examine possible evaluation methods for future energy dependent fission yield data sets;
- Study experimental methods and their sources of errors and uncertainties, and how to account for them in evaluations;
- Evaluate sets of reference fission yields used as standards in fission yield experiments and as monitors in applied measurements;
- Perform evaluations of selected fission yield measurements for an intercomparison to check the prediction capabilities of systematics and models developed during the CRP.

(3) Multi-chance fission:
- Evaluate the neutron induced fission cross-sections of actinides and the individual emissive fission contributions up to 150 MeV as input to systematics and model calculations;
- Study the problems described in Sections 1.3.4 and 1.3.5 and find solutions for adoption in systematics and calculated yields.

(4) Study the differences between photon, neutron and charged particle induced fission reactions and the possibility of their combined use in systematics.

(5) Prediction of fission yields:
- Study existing systematics and models for the calculation of fission yields with respect to their possible use at neutron energies of up to 150 MeV;
- Elaborate on the necessary adaptation of models and parameters;
- From the results of these studies, develop systematics and models that allow the calculation of fission yields as a function of fissioning nuclides and neutron energies of up to 150 MeV;
- Perform benchmark calculations to check the validity of predictions from systematics and models in an intercomparison, and also with experimental data;
- If feasible, recommend a specific computer program and parameter database for use in fission yield evaluations.

REFERENCES TO SECTION 1

[1.1] KONING, A.J., FUKAHORI, T., HASEGAWA, A., International Evaluation Cooperation: Intermediate Energy Data, Rep. NEA/WPEC-13, ECN-RX-98-014 13 (1998).

[1.2] INTERNATIONAL ATOMIC ENERGY AGENCY, Compilation and Evaluation of Fission Yield Nuclear Data, IAEA-TECDOC-1168, IAEA, Vienna (2000) 45–75.

[1.3] BROSA, U., et al., Nuclear scission, Phys. Rep. **197** (1990) 167–262.

[1.4] MORIYAMA, H., OHNISHI, T., Systematics of Fission Fragment Mass Yield Curves, Rep. 166, Kyoto University, Kyoto (1974).

2. EXPERIMENTAL DATA

2.1. MEASUREMENTS OF PRODUCT YIELDS FROM FISSION REACTIONS INDUCED BY HIGH ENERGY NEUTRONS, PROTONS, DEUTERONS, ALPHA PARTICLES, OTHER CHARGED PARTICLES AND PHOTONS — COLLECTION OF REFERENCES

J.-O. Denschlag
Johannes Gutenberg-Universität Mainz, Germany

A compilation of references is presented for fission reactions induced by neutrons, protons, deuterons, alpha particles, ^{3}He ions, some heavier charged particles and photons. The energy ranges for the collected references are for neutrons from essentially 14 MeV up to 1 GeV. For charged particles the energy range is from the coulomb barrier up to a few hundred MeV. For photon induced fission the energy range (endpoint of Bremsstrahlung) is from the fission barrier up to about 100 MeV. In addition to the printed version, the compilation is also provided as a Microsoft Word file on the attached CD-ROM to permit electronic processing.

References are given for fission reactions induced by neutrons, protons, deuterons, alpha particles, ^{3}He ions, some heavier charged particles and photons. The energy ranges for these references are for neutrons from essentially 14 MeV up to 1 GeV (a few cases of mono-energetic neutrons below 14 MeV are also included). For charged particles the energy range is from the energy required to overcome the coulomb barrier to a few hundred MeV. For photon induced fission the energy range (endpoint of Bremsstrahlung) is from the fission barrier up to about 100 MeV. In addition, some references are given that are concerned with the new technique of fission in inverse kinematics. It should be stressed that the present listing concentrates on the exotic high energy reactions mentioned, and does not cover the well studied fission reactions induced, for example, by neutrons (thermal, reactor spectrum, 14 MeV), spontaneous fission, etc. Ample information on the product yields from these classical fission reactions may be found on web page http://ie.lbl.gov/fission.html

In order to facilitate the use of this listing, a grouping has been made according to the species that induces fission. Furthermore, within each type of fission reaction a differentiation is made according to the type of fission yields obtained (mass yields or independent yields of single nuclides, yields of single isomeric states, yields of neutrons (prompt and delayed), and yields of light charged particles (ternary fission)).

The listing is based on a small databank that will be made available to interested users on request to the author. This databank contains a collection of the original publications, along with more information than the present listing; for instance, in many cases the database contains the abstracts of the respective papers. Interrogation of the databank is based on a program available commercially and access can only be achieved after installation of this program (EndNote 2 by Niles & Associates, USA, internet address info@niles.com). An electronic search for desired references, author names and titles of articles can also be undertaken through provision of the list of references contained on the CD-ROM attached to this publication.

Citations:

(1) Neutron induced fission (14 MeV to 1 GeV):
  (a) Mass distribution: [2.1.1–2.1.13];
  (b) Nuclear charge distribution: [2.1.1, 2.1.7, 2.1.9, 2.1.14];
  (c) Isomeric yields: [2.1.15, 2.1.16];
  (d) Prompt or delayed neutron emission: (no references found);
  (e) Emission of light charged particles: (no references found).

(2) Proton induced fission:
  (a) Mass distribution: [2.1.12, 2.1.17–2.1.79];
  (b) Nuclear charge distribution: [2.1.18, 2.1.24, 2.1.26, 2.1.28, 2.1.29, 2.1.32–2.1.34, 2.1.45–2.1.47, 2.1.49, 2.1.51–2.1.54, 2.1.62, 2.1.67, 2.1.75, 2.1.79–2.1.102];
  (c) Isomeric yields: [2.1.103–2.1.109];

(d) Prompt or delayed neutron emission: [2.1.24, 2.1.32, 2.1.48, 2.1.75, 2.1.79, 2.1.82, 2.1.85, 2.1.110, 2.1.111];
(e) Emission of light charged particles: [2.1.112–2.1.114].

(3) Deuteron induced fission:
(a) Mass distribution: [2.1.23, 2.1.45, 2.1.68, 2.1.115–2.1.117];
(b) Nuclear charge distribution: [2.1.45, 2.1.118, 2.1.119];
(c) Isomeric yields: [2.1.16];
(d) Prompt or delayed neutron emission: [2.1.116];
(e) Emission of light charged particles: (no references found).

(4) Helium-3 induced fission:
(a) Mass distribution: [2.1.20, 2.1.23, 2.1.38, 2.1.78, 2.1.120–2.1.122];
(b) Nuclear charge distribution: [2.1.123];
(c) Isomeric yields: (no references found);
(d) Prompt or delayed neutron emission: (no references found);
(e) Emission of light charged particles: (no references found).

(5) Alpha particle induced fission:
(a) Mass distribution: [2.1.2, 2.1.35–2.1.38, 2.1.45, 2.1.78, 2.1.122, 2.1.124–2.1.142];
(b) Nuclear charge distribution: [2.1.45, 2.1.123, 2.1.136, 2.1.143, 2.1.144];
(c) Isomeric yields: [2.1.15, 2.1.145–2.1.150];
(d) Prompt or delayed neutron emission: [2.1.145];
(e) Emission of light charged particles: [2.1.137].

(6) Fission induced by some other charged particles:
(a) Mass distribution: [2.1.18, 2.1.23, 2.1.26, 2.1.39–2.1.42, 2.1.48, 2.1.49, 2.1.51–2.1.54, 2.1.63, 2.1.66, 2.1.79];
(b) Nuclear charge distribution: [2.1.18, 2.1.26, 2.1.49, 2.1.51–2.1.54, 2.1.79, 2.1.97, 2.1.100, 2.1.102];
(c) Isomeric yields: [2.1.108];
(d) Prompt or delayed neutron emission: [2.1.48, 2.1.79];
(e) Emission of light charged particles: [2.1.112, 2.1.113].

(7) Photon induced fission:
(a) Mass distribution: [2.1.151–2.1.161];
(b) Nuclear charge distribution: [2.1.151, 2.1.153–2.1.157, 2.1.162–2.1.168];
(c) Isomeric yields: [2.1.151, 2.1.152, 2.1.169–2.1.171];
(d) Prompt or delayed neutron emission: [2.1.159, 2.1.172];
(e) Emission of light charged particles: [2.1.173, 2.1.174].

(8) Fission in inverse kinematics: [2.1.175–2.1.185]

REFERENCES TO SECTION 2.1

[2.1.1] ETHVIGNOT, T., et al., Intermediate energy neutron-induced fission of uranium: Product yields and isomer studies, personal communication, 2001.

[2.1.2] FORD, G.P., LEACHMAN, R.B., Fission mass yield dependence on angular momentum, Phys. Rev. **137** (1965) B826–B836.

[2.1.3] GINDLER, J.E., et al., Mass distributions in monoenergetic-neutron-induced fission of ^{239}Pu, Phys. Rev. C **27** (1983) 2058–2062.

[2.1.4] GLENDENIN, L.E., et al., Mass distributions in monoenergetic-neutron-induced fission of ^{232}Th, Phys. Rev. C **22** (1980) 152–159.

[2.1.5] GLENDENIN, L.E., et al., Mass distributions for monoenergetic-neutron-induced fission of ^{235}U, Phys. Rev. C **24** (1981) 2600–2605.

[2.1.6] GOVERDOVSKII, A.A., et al., Temperature effects in pre-scission-deformation spectra of ^{238}Np fission fragments, Phys. At. Nucl. **60** (1997) 1441–1447.

[2.1.7] HAMELIN, C., Etude des Distributions en Masse et en Charge Nucléaire dans la Fission Induite par Neutrons de 3 MeV pour quelques Noyeaux fissiles, PhD thesis, Université scientifique et médicale de Grenoble, France (1983).

[2.1.8] NAGY, S., et al., Mass distribution in monoenergetic-neutron-induced fission of ^{238}U, Phys. Rev. C **17** (1978) 163–171.

[2.1.9] YOUNES, W., et al., Transition from asymmetric to symmetric fission in the ^{235}U(n,f) reaction, Phys. Rev. C **64** (2001) 054613–054635.

[2.1.10] ZÖLLER, C.M., Untersuchung der neutronen-induzierten Spaltung von ^{238}U im Energiebereich von 1 MeV bis 500 MeV, PhD thesis, Technische Hochschule Darmstadt, Germany (1995).

[2.1.11] ZÖLLER, C.M., "Fission fragment properties in the ^{238}U(n,f) reaction at incident neutron energies from 1 MeV to 500 MeV", Pont d'Oye III (Proc. Sem. Habay-la-Neuve, Belgium, 1995), Rep. IKDA-95/25, Technische Hochschule Darmstadt (1995).

[2.1.12] DUIJVESTIJN, M.C., et al., "Experimental and theoretical high energy fission studies", Fission, Pont d'Oye IV (Proc. Sem. Habay-la-Neuve, Belgium) (WAGEMANS, C., et al., Eds), World Scientific, Singapore (1999) 247–255.

[2.1.13] GOVERDOVSKII, A.A., MITROFANOV, V.F., Symmetric and asymmetric fission of ^{236}U, ^{238}U, ^{237}Np, and ^{243}Am by neutrons with energy 16.5 MeV, Phys. At. Nucl. **56** (1993) 24–28.

[2.1.14] WAHL, A.C., Fission of ^{235}U by 14-MeV neutrons: Nuclear charge distribution and yield fine structure, Phys. Rev. **99** (1955) 730–739.

[2.1.15] AUMANN, D.C., et al., Independent isomeric yield ratio of ^{148}Pm in fission of the moderately excited ^{236}U compound nucleus as a measure of fragment angular momentum, Phys. Rev. C **16** (1977) 254–265.

[2.1.16] VISHNEVSKY, I.N., et al., Mean angular momenta of fragments from ^{232}Th fission, Phys. At. Nucl. **61** (1998) 1452–1458.

[2.1.17] BABA, S., et al., Mass distribution and the total fission cross section in the fission of ^{238}U with protons of energies ranging between 13 and 55 MeV, Nucl. Phys. A **175** (1971) 177–198.

[2.1.18] BABA, H., et al., Radiochemical study of fast fission mechanism, J. Radioanal. Nucl. Chem. **239** (1999) 103–108.

[2.1.19] BECCHETTI, F.D., et al., 190 MeV proton-induced symmetric and asymmetric fission, Phys. Rev. C **28** (1983) 276–279.

[2.1.20] BECCHETTI, F.D., et al., "Unusual fission-mass distributions, A < 200, studied using 200 MeV proton and ^{3}He induced fission", Fifty Years with Nuclear Fission (Proc. Conf. Gaithersburg, MD, 1989) (BEHRENS, J.W., CARLSON, A.D., Eds), American Nuclear Society, La Grange Park, IL (1989) 688–693.

[2.1.21] BEIZIN, S.D., et al., Study of the trimodal structure of the mass and energy distributions of fission fragments of transactinide nuclei, Sov. J. Nucl. Phys. **53** (1991) 411–414.

[2.1.22] BEIZIN, S.D., et al., Measurement and three-component analysis of mass-energetic distributions of fragments in fission of ^{232}Th and ^{233,235}U nuclei by protons, Yad. Fiz. **50** (1989) 626–638.

[2.1.23] BRITT, H.C., et al., Fission of ^{255,256}Es, ^{255,257}Fm, and ^{258}Md at moderate excitation energies, Phys. Rev. C **30** (1984) 559–565.

[2.1.24] CHUNG, C., HOGAN, J.J., Fission of ^{232}Th at energies up to 90 MeV, Phys. Rev. C **24** (1981) 180–191.

[2.1.25] CROALL, I.F., CUNINGHAME, J.G., Fragment distributions in the fission of ^{232}Th by protons of energies 13 to 53 MeV, Nucl. Phys. A **125** (1969) 402–416.

[2.1.26] DUH, M.C., et al., Charge and mass characteristics of the fragments in the fission of uranium isotopes induced by ^{12}C ions, Nucl. Phys. A **550** (1992) 281–305.

[2.1.27] DUIJVESTIJN, M.C., et al., Proton-induced fission at 190 MeV of ^{nat}W, ^{197}Au, ^{nat}Pb, ^{208}Pb, and ^{232}Th, Phys. Rev. C **59** (1999) 776–788.

[2.1.28] DUIJVESTIJN, M.C., Nucleon induced fission at intermediate energies, PhD thesis, University of Groningen, Netherlands (2000).

[2.1.29] EAKER, R.W., CHOPPIN, G.R., Mass and charge distribution in the fission of ^{232}Th, J. Inorg. Nucl. Chem. **38** (1976) 31–36.

[2.1.30] EAKER, R., et al., Symmetric-to-asymmetric mass ratios for proton-induced fission of ^{232}Th and ^{238}U, Phys. Rev. C **20** (1979) 1055–1058.

[2.1.31] FERGUSON, R.L., et al., Systematics of fragment mass and energy distributions for proton-induced fission of ^{233}U, ^{235}U, and ^{238}U. 7 to 12 MeV, Phys. Rev. C **7** (1973) 2510–2522.

[2.1.32] GALINIER, J.L., YAFFE, L., Nuclear charge distribution in the region of asymmetric fission of ^{238}U by protons of energy 20–75 MeV, J. Inorg. Nucl. Chem. **39** (1977) 1497–1508.

[2.1.33] HAGEBØ, E., et al., Radiochemical studies of charge and mass distribution in the light fragment region in fission of uranium induced by 170 MeV protons, J. Inorg. Nucl. Chem. **26** (1964) 1639–1652.

[2.1.34] HAGEBØ, E., LUND, T., Fission of lead induced by 600 MeV protons, J. Inorg. Nucl. Chem. **37** (1975) 1569–1582.

[2.1.35] ITKIS, M.G., et al., Asymmetric fission of pre-actinide nuclei, Z. Phys. A Hadrons Nucl. **320** (1985) 433–441.

[2.1.36] ITKIS, M.G., et al., Experimental investigation of the region of asymmetric fission in light nuclei, Sov. J. Nucl. Phys. **41** (1985) 544–553.

[2.1.37] ITKIS, M.G., et al., Low-energy fission of gold nuclei by protons and alpha-particles, Sov. J. Nucl. Phys. **47** (1988) 4–8.

[2.1.38] ITKIS, M.G., et al., Low-energy fission of nuclei lighter than Hg, Sov. J. Nucl. Phys. **53** (1991) 757–763.

[2.1.39] ITKIS, M.G., et al., "Multimodal fission of neutron-deficient nuclides of Th and Ac", Nuclear Fission and Fission Product Spectroscopy (Proc. Workshop Grenoble, 1994) (FAUST, H., FIONI, G., Eds), American Institute of Physics, Woodbury, NY (1994) 77–85.

[2.1.40] ITKIS, M.G., OGANESSIAN, Y.T., CHUBARIAN, G.G., et al., "Studies of fission modes in the neutron-deficient nuclides of Th and Ac", LEND-95 (Proc. XV Nuclear Physics Divisional Conf. on Low Energy Nuclear Dynamics, St. Petersburg, Russian Federation, 1995) (OGANESSIAN, Y.T., et al., Eds), World Scientific, Singapore (1996) 177–186.

[2.1.41] ITKIS, M.G., et al., "Nature and properties of the fission modes of the neutron deficient ^{220,224,226}Th nuclides", Large-scale Collective Motion of Atomic Nuclei (Proc. Conf. Brolo, Messina, Italy, 1996) (GIARDINA, G., et al., Eds), World Scientific, Singapore (1996) 270–281.

[2.1.42] ITKIS, M.G., "Observation of fission modes in heavy ion induced reactions", Nuclear Physics III (Proc. Symp. Tours, France, 1997) (ARNOULD, M., et al., Eds), AIP Conf. Proc. 425/1 (1998) 189–201.

[2.1.43] ÄYSTÖ, J., et al., "New results on superasymmetric fission at intermediate energy", Fission and Properties of Neutron Rich Nuclei (Proc. Conf. Sanibel Island, FL, 1997) (HAMILTON, J.H., RAMAYYA, A.V., Eds), World Scientific, Singapore (1998) 457–466.

[2.1.44] JACOBS, E., et al., Fragment mass and kinetic energy distributions for the photofission of sup ^{238}U with 12-, 15-, 20-, 30-, and 70-MeV Bremsstrahlung, Phys. Rev. C **20** (1979) 2249–2256.

[2.1.45] JAUHO, P.P., et al., "Isotopic A- and isobaric Z-distributions in charged particle induced fission", Nuclear Physics (Proc. 1st European Biennial Workshop Megève, France, 1991) (GUINET, D., PIZZI, J.R., Eds), Inst. Phys. Nucl., Lyon, France (1991) 236–241.

[2.1.46] KANDIL, A.T., Proton induced fission of ^{238}U, J. Inorg. Nucl. Chem. **38** (1976) 37–39.

[2.1.47] KARTTUNEN, E., et al., Cross sections for formation of fission products in the ^{238}U(p,f) reaction at proton energies between 12 and 30 MeV, Nucl. Sci. Eng. **109** (1991) 350–359.

[2.1.48] KELIC, A., et al., Prefission neutron multiplicities and the fission modes of ^{226}Th, Europhys. Lett. **47** (1999) 552–555.

[2.1.49] KRATZ, J.V., et al., Charge and mass distributions in the reaction of ^{40}Ar ions with ^{238}U, Phys. Rev. C **13** (1976) 2347–2365.

[2.1.50] KUDO, H., et al., Fission fragment yields in the fission of ^{232}Th by protons of energies 8 to 22 MeV, Phys. Rev. C **25** (1982) 3011–3023.

[2.1.51] LEE, C.H., et al., Charge and mass distributions from the reaction of 240 MeV ^{12}C ions with ^{238}U, Phys. Rev. C **38** (1988) 1757–1766.

[2.1.52] MACHNER, H., et al., Fission fragment distribution following antiproton absorption, Z. Phys. A Hadrons Nucl. **343** (1992) 73–77.

[2.1.53] MANOHAR, S.B., et al., Mass distribution in ^{12}C induced fission of ^{232}Th, Radiochim. Acta **56** (1992) 69–71.

[2.1.54] NISHINAKA, I., et al., Nuclear fission of neutron-deficient protactinium nuclides, Phys. Rev. C **56** (1997) 891–899.

[2.1.55] OHTSUKI, T., et al., Systematic analysis of mass yield curves in low-energy fission of actinides, Phys. Rev. C **40** (1989) 2144–2153.

[2.1.56] OHTSUKI, T., et al., "A systematic study of mass yield curves in proton-induced fission of actinides", Advanced Nuclear Energy Research — Near Future Chemistry in Nuclear Energy Field (Proc. Int. Symp. Oarai, Ibaraki, Japan, 1989), Japan Atomic Energy Research Institute, Tokai, Ibaraki-ken, Japan (1989) 189–193.

[2.1.57] OHTSUKI, T., et al., "A systematic study of mass yield curves in low energy fission of actinides", Fifty Years with Nuclear Fission (Proc. Conf. Gaithersburg, MD, 1989) (BEHRENS, J.W., CARLSON, A.D., Eds), American Nuclear Society, La Grange Park, IL (1989) 750–757.

[2.1.58] OHTSUKI, T., et al., Mass yield curves in low-energy proton-induced fission of ^{233}U, ^{235}U, ^{236}U, ^{237}Np, ^{239}Pu, ^{242}Pu, ^{244}Pu, ^{241}Am, and ^{243}Am, Phys. Rev. C **44** (1991) 1405–1423.

[2.1.59] OHTSUKI, T., et al., Binary structure in time distributions of fission fragments in 13-MeV proton-induced fission of ^{232}Th, Phys. Rev. Lett. **66** (1991) 17–20.

[2.1.60] OHTSUKI, T., et al., Bimodal nature of actinide fission, J. Alloy Comp. **214** (1994) 423–425.

[2.1.61] OHTSUKI, T., et al., "Binary scission configurations in fission of light actinides", Nuclear Fusion and Fission of Heavy Elements (Proc. Symp. Tokai, Ibaraki, 1997) (MISUOKA, S.-I., et al., Eds), JAERI-Conf 97-009 (1997) 70–75.

[2.1.62] PAPPAS, A.C., HAGEBØ, E., The charge and mass distributions in fission of uranium induced by 170 MeV protons, J. Inorg. Nucl. Chem. **28** (1966) 1769–1785.

[2.1.63] POKROVSKY, I.V., et al., Three fission modes of ^{220}Ra, Phys. Rev. C **60** (1999) 041304–041308.

[2.1.64] POLAK, P., Fission of Neptunium-237 by Medium Energy Protons, PhD thesis, University of Amsterdam, Netherlands (1976).

[2.1.65] QIN, Z., et al., Mass yield distributions in proton-induced fission of ^{248}Cm, Radiochim. Acta **84** (1999) 115–120.

[2.1.66] RAMASWAMI, A., et al., Mass distribution in ^{12}C induced fission of ^{232}Th, J. Radioanal. Nucl. Chem. **246** (2000) 225–228.

[2.1.67] RUBCHENYA, V.A., et al., "Fission product yields at intermediate energy", Nuclear Fission and Fission-Product Spectroscopy (Proc. Conf. Seyssins, France, 1998) (FIONI, G., et al., Eds), American Institute of Physics, Woodbury, NY (1998) 453–461.

[2.1.68] STEVENSON, P.C., et al., Further radiochemical studies of the high-energy fission products, Phys. Rev. **111** (1958) 886–891.

[2.1.69] TEWES, H.A., JAMES, R.A., Proton induced reactions of thorium–fission yield curves, Phys. Rev. **88** (1952) 860–867.

[2.1.70] TITARENKO, Y.E., et al., Experimental and computer simulation study of the radionuclides produced in thin ^{209}Bi targets by 130 MeV and 1.5 GeV proton-induced reactions, Nucl. Instrum. Methods Phys. Res. A **414** (1998) 73–99.

[2.1.71] TRZASKA, W.H., et al., Fragment mass distribution in superasymmetric region in proton-induced fission of U and Th, Nuovo Cimento **111A** (1998) 1055–1060.

[2.1.72] TSUKADA, K.Y., et al., Mass yield and angular distribution of rare earth elements produced in proton-induced fission of ^{244}Pu, J. Alloys Comp. **214** (1994) 414–416.

[2.1.73] TSUKADA, K., et al., Highly asymmetric mass division in low-energy proton-induced fission of ^{232}Th and ^{244}Pu, Radiochim. Acta **76** (1997) 173–180.

[2.1.74] WAGNER, B.J., et al., Radiochemical measurements of 200-MeV proton-induced fission of ^{133}Cs, Phys. Rev. C **31** (1985) 1934–1936.

[2.1.75] YOKOYAMA, A., et al., Precision determination of charge dispersion and distribution in the proton-induced fission of ^{238}U at 13.9 MeV excitation, Z. Phys. A Hadrons Nucl. **356** (1996) 55–60.

[2.1.76] ZHAO, Y.L., et al., Characteristics of binary scission configurations in proton-induced fission of actinides, J. Radioanal. Nucl. Chem. **239** (1999) 113–116.

[2.1.77] ZHDANOV, S.V., et al., Study of the shape of the energy distributions of fission fragments, Sov. J. Nucl. Phys. **50** (1989) 569–573.

[2.1.78] ZHDANOV, S.V., et al., Higher moments of energy distributions of fragments of symmetric fission, Sov. J. Nucl. Phys. **55** (1992) 1766–1771.

[2.1.79] ITKIS, M.G., et al., Fission of heavy and superheavy nuclei at low excitation energies, Nucl. Phys. A **654** (1999) 870c–877c.

[2.1.80] AAGAARD, P., et al., Measurements on electromagnetically separated radioactive isotopes of iodine, J. Inorg. Nucl. Chem. **5** (1957) 105–111.

[2.1.81] BABA, H., et al., Changes of the characteristics of the proton-induced fission of ^{238}U around 14 MeV excitation, Z. Phys. A Hadrons Nucl. **356** (1996) 61–70.

[2.1.82] BEELEY, P.A., et al., Isotopic and neutron yields of products from the asymmetric and near-symmetric proton-induced fission of ^{233}U and ^{235}U, Phys. Rev. C **28** (1983) 1188–1205.

[2.1.83] BENJAMIN, P.P., et al., Nuclear charge dispersion in the fission of ^{232}Th by protons of energy 20–85 MeV, Can. J. Chem. **47** (1969) 301–312.

[2.1.84] BIRGUEL, O., YAFFE, L., The fission of ^{197}Au by protons of energies of 52–85 MeV, J. Radioanal. Nucl. Chem. Lett. **103** (1986) 153–158.

[2.1.85] CHAN, K.C., et al., Independent yields of indium and gallium in the proton induced fission of natural uranium, J. Inorg. Nucl. Chem. **39** (1977) 1915–1919.

[2.1.86] DIKSIC, M., et al., Nuclear charge dispersion in mass chains 130–135 from the fission of ^{238}U by medium-energy protons, J. Inorg. Nucl. Chem. **36** (1974) 7–16.

[2.1.87] DIKSIC, M., et al., Charge dispersion studies of light-mass nuclides in the fission of ^{232}Th by protons of energies 35–75 MeV, J. Inorg. Nucl. Chem. **41** (1979) 795–800.

[2.1.88] GALINIER, J.L., et al., Nuclear charge dispersion studies in the light-mass region formed in the fission of ^{238}U by protons of energy 35–85 MeV, Can. J. Chem. **55** (1977) 3609–3615.

[2.1.89] KUDO, H., et al., Most probable charge of fission products in 24 MeV proton induced fission of ^{238}U, Phys. Rev. C **57** (1998) 178–188.

[2.1.90] HOLUB, R., YAFFE, L., Charge dispersion studies of heavy-mass elements in the fission of ^{232}Th by protons of medium energy, J. Inorg. Nucl. Chem. **35** (1973) 3991–4000.

[2.1.91] LEE, J.K.P., et al., Independent yields of Rb and Cs isotopes from the fission of natural uranium induced by protons of energy 80 and 100 MeV, J. Inorg. Nucl. Chem. **37** (1975) 2035–2038.

[2.1.92] MARSHALL, H., YAFFE, L., Nuclear charge dispersion of products in the light-mass region formed in the fission of ^{233}U by protons of energy 20–85 MeV, J. Inorg. Nucl. Chem. **35** (1973) 1797–1804.

[2.1.93] McGEE, T., et al., Nuclear charge dispersion in the fission of ^{237}Np by protons of medium energy, J. Inorg. Nucl. Chem. **34** (1972) 3323–3333.

[2.1.94] MILLER, L.D., YAFFE, L., Charge dispersion in the fission of ^{238}U by protons of energies 30–160 MeV, J. Inorg. Nucl. Chem. **35** (1973) 1805–1819.

[2.1.95] NIKKINEN, L., et al., Independent yields of Rb, In, and Cs isotopes in the proton-induced fission of ^{232}Th, Phys. Rev. C **22** (1980) 617–626.

[2.1.96] PATE, B.D., et al., Distribution of nuclear charge in the proton-induced fission of ^{232}Th, Can. J. Chem. **36** (1958) 1691–1706.

[2.1.97] REDDY, A.V.R., et al., Charge distribution on 96 MeV ^{16}O induced fission of ^{238}U, Radiochim. Acta **64** (1994) 149–154.

[2.1.98] SAHA, G.B., YAFFE, L., Charge dispersion studies in the fission of ^{239}Pu by protons of medium energy, J. Inorg. Nucl. Chem. **32** (1970) 745–767.

[2.1.99] SARKAR, S., YAFFE, L., Nuclear charge distribution in the region of symmetric fission of ^{238}U by protons of energy 20–85 MeV, Can. J. Chem. **54** (1976) 2349–2358.

[2.1.100] SHINOHARA, N., et al., Cumulative yields of short-lived Ru isotopes in the ^{12}C- and ^{19}F-induced fission of ^{233}U, ^{235}U, ^{238}U and ^{237}Np, Radiochim. Acta **68** (1995) 21–26.

[2.1.101] TRACY, B.L., et al., Rb and Cs isotopic cross sections from 40–60 MeV proton fission of ^{238}U, ^{232}Th, and ^{235}U, Phys. Rev. C **5** (1972) 222–234.

[2.1.102] YOKOYAMA, A., et al., Charge degree of freedom as a sensitive probe for fission mechanism, J. Radioanal. Nucl. Chem. **223** (1999) 99–119.

[2.1.103] FORSTER, J.H., YAFFE, L., Isomeric yield ratios of ^{133}Xe in fission of ^{232}Th, ^{233}U, ^{235}U, and ^{238}U with protons of energies 20–85 MeV, Can. J. Chem. **46** (1968) 1743–1772.

[2.1.104] GOTO, S., et al., Isomeric yield ratios of fission products in proton-induced fission of ^{232}Th, J. Radioanal. Nucl. Chem. **239** (1999) 109–112.

[2.1.105] KHAN, A.H., et al., Isomer ratios of ^{90}Y and ^{91}Y in the fission of ^{235}U and ^{238}U by protons of energies 20–85 MeV, Can. J. Chem. **47** (1969) 3817–3822.

[2.1.106] SAHA, G.B., et al., Isomer ratios of ^{134}Cs formed in the fission of ^{233}U and ^{235}U by protons of energies 20–85 MeV, J. Inorg. Nucl. Chem. **31** (1969) 3731–3737.

[2.1.107] SAHA, G.B., YAFFE, L., An energy-dependent calculation of the isomer ratios of ^{134}Cs produced in the fission of ^{239}Pu by medium-energy protons, J. Inorg. Nucl. Chem. **31** (1969) 1891–1905.

[2.1.108] SHINOHARA, N., et al., Isomeric yield ratios of ^{134}I and ^{136}I in the proton-, ^{12}C- and ^{19}F-induced fission of ^{235}U, ^{237}Np and ^{238}U, Radiochim. Acta **88** (2000) 1–5.

[2.1.109] TANIKAWA, M., et al., Isomeric yield ratios of fission products in the system of 24 MeV proton-induced fusion of ^{238}U, Z. Phys. A Hadrons Nucl. **347** (1993) 53–62.

[2.1.110] FRAENKEL, Z., et al., Measurement of the neutrons emitted in the proton-induced fission of ^{209}Bi and ^{238}U at 475 MeV, Phys. Rev. C **41** (1990) 1050–1061.

[2.1.111] STRECKER, M., et al., Pre-scission and post-scission neutrons from the reactions p+^{235,236,238}U with $E_p \leq 25.6$ MeV, Phys. Rev. C **41** (1990) 2172–2187.

[2.1.112] IKEZOE, H., et al., "Light charged particle emission in fission", Fifty Years with Nuclear Fission (Proc. Conf. Gaithersburg, MD, 1989) (BEHRENS, J.W., CARLSON, A.D., Eds), American Nuclear Society, La Grange Park, IL (1989) 721–726.

[2.1.113] IKEZOE, H., et al., Charged particle multiplicities in heavy-ion-induced fission, Phys. Rev. C **46** (1992) 1922–1933.

[2.1.114] THOMAS, T.D., WHETSTONE, S.L., Jr., Emission of alpha particles in the fission of ^{238}U by 11 to 21 MeV protons, Phys. Rev. **144** (1966) 1060–1070.

[2.1.115] RUBCHENYA, V.A., et al., "Fission modes in ^{238}U+d reaction at intermediate energy", Fission and Neutron Rich Nuclei (Proc. 2nd Int. Conf. St. Andrews, UK, 1999) (HAMILTON, J.H., et al., Eds), World Scientific, Singapore (1999).

[2.1.116] SUGIHARA, T.T., et al., Fission yields of natural uranium with deuterons of 5, 10, and 13.6 MeV: Deuteron capture and competition with stripping, Phys. Rev. **108** (1957) 1264–1273.

[2.1.117] TRZASKA, W.H., et al., "Deuteron induced fission of ^{238}U", Fission, Pont d'Oye IV (Proc. Sem. Habay-la-Neuve, Belgium, 1999) (WAGEMANS, C., et al., Eds), World Scientific, Singapore (2000) 257–266.

[2.1.118] ALEXANDER, J.M., CORYELL, C.D., Nuclear charge distribution in the fission of uranium and thorium with 13.6-MeV deuterons, Phys. Rev. **108** (1957) 1274–1279.

[2.1.119] HICKS, H.G., et al., Fission product yields of uranium bombarded with deuterons of various energies (20–190 MeV), Phys. Rev. **100** (1955) 1284–1286.

[2.1.120] BEIZIN, S.D., et al., Fission of actinides by ^{3}He ions with energy 60 MeV, Sov. J. Nucl. Phys. **50** (1989) 201–206.

[2.1.121] BEIZIN, S.D., et al., Fission of actinides by 60 MeV ^{3}He ions ^{232}Th, ^{233,235,236,238}U, ^{238,239,240,242}Pu, ^{244}Cm nuclei, Yad. Fiz. **50** (1989) 320–329.

[2.1.122] GRUZINTSEV, E.N., et al., Fission of mercury nuclei in reactions induced by protons, ^{3}He ions, and alpha particles, Sov. J. Nucl. Phys. **45** (1987) 959–964.

[2.1.123] REEDER, P.L., Mass spectrometric determination of Rb fission yields from ^{3}He and ^{4}He induced fission of ^{238}U and ^{232}Th, Can. J. Chem. **61** (1983) 786–794.

[2.1.124] ASTIER, A., Experimental Research of Isospin and Spin Exotic Nuclei with an Ion Guide and Gamma Multidetectors, PhD thesis, University of Lyon, Villeurbanne, France (1992) (in French).

[2.1.125] CHOUDHURY, R.K., et al., Variation of kinetic energy distributions of fission fragments with bombarding energy in ^{4}He induced fission of ^{238}U at medium energies, Nucl. Phys. A **463** (1987) 597–604.

[2.1.126] DMITRIEV, V.D., et al., Study on certain characteristics of trans-uranium nuclei fission induced by alpha-particles, Yad. Fiz. **30** (1979) 915–922.

[2.1.127] DMITRIEV, V.D., et al., Mass distribution of fission fragments of ^{249}Cf, ^{237}Np and ^{238}U nuclei induced by alpha particles, Yad. Fiz. **35** (1982) 1112–1118.

[2.1.128] GUIN, R., et al., "Mass distribution at moderate excitation energies: 28.5 MeV helium ion induced fission of ^{232}Th", Radiochemistry and Radiation Chemistry (Proc. Symp. Pune, India, 1982), Department of Atomic Energy, Mumbai (1982).

[2.1.129] GUIN, R., et al., "Mass distribution at moderate energy: 38.5 MeV helium ion induced fission of ^{232}Th", Radiochemistry and Radiation Chemistry (Proc. Symp. Kanpur, India, 1985), Bhabha Atomic Research Centre, Mumbai (1985) 242–245.

[2.1.130] GUIN, R., et al., Mass distribution of fission products in the 28.5 MeV alpha particle induced fission of ^{232}Th, Radiochim. Acta **48** (1989) 7–9.

[2.1.131] GUIN, R., et al., Mass distribution of fission products from moderately excited ^{236}U compound nucleus, Radiochim. Acta **51** (1990) 97–100.

[2.1.132] LUEBKE, F., Investigation of the Fission Fragment Mass and Energy Distribution in Dependence from Excitation Energy for the Alpha Induced Fission of ^{238}U, PhD thesis, Universität Bonn, Germany (1975).

[2.1.133] NEUZIL, E.F., APT, K., The 65 MeV helium ion-induced fission of ^{107}Pb, J. Inorg. Nucl. Chem. **30** (1968) 1151–1154.

[2.1.134] RAO, B.V.N., et al., "Alpha induced fission in ^{238}U", Nuclear Physics and Solid State Physics (Proc. Symp. Kolkata, 1975), 144–146.

[2.1.135] RATTAN, S.S., SINGH, R.J., Alpha induced fission of ^{209}Bi, Radiochim. Acta **38** (1985) 69–71.

[2.1.136] RATTAN, S.S., et al., Alpha particle induced fission of ^{209}Bi at 55.7 and 58.6 MeV, Radiochim. Acta **55** (1991) 169–172.

[2.1.137] ROGINSKI, T.C., et al., Fission of ^{232}Th induced by intermediate-energy ^{4}He ion, Phys. Rev. C **4** (1971) 1361–1366.

[2.1.138] TAKAHASHI, N., et al., Two mode fission: existence of two independent path in the fission of actinide elements, Z. Phys. A Hadrons Nucl. **353** (1995) 35–42.

[2.1.139] UNIK, J.P., HUIZENGA, J.R., Binary fission studies of helium-ion-induced fission of ^{209}Bi, ^{226}Ra, and ^{238}U, Phys. Rev. **134** (1964) B90–B99.

[2.1.140] VARMA, R., et al., "Fragment mass and kinetic energy correlation studies in alpha induced fission of ^{235}U", Nuclear Physics (Proc. Symp. Jaipur, 1985), Bhabha Atomic Research Center, Mumbai (1986) 30–31.

[2.1.141] ZAIKA, N.I., et al., Osobennosty massovych i energetichieskych raspredelenii oskolkov delenii yader ^{235}U i ^{236}U alpha-chastitsami crednych energii (≤80 MeV), Yad. Phys./J. Nucl. Phys. **42** (1985) 304–311.

[2.1.142] ZAIKA, N.I., et al., Massovie i energetichieskie raspredelenia oskolkov delenia yadra ^{232}Th alpha-chastitsami c energyami 21–26,4 MeV, Ukr. Phys. J. **34** (1989) 493–498.

[2.1.143] RAMASWAMI, A., et al., Charge distribution study in the alpha-particle induced fission of ^{232}Th. Effect of excitation energy, J. Radioanal. Nucl. Chem. **102** (1986) 499–506.

[2.1.144] RAMASWAMI, A., et al., "Charge distribution study in the alpha particle induced fission of ^{238}U", Radiochemistry and Radiation Chemistry (Proc. Symp. Kalpakkam, 1989), Bhabha Atomic Research Centre, Mumbai (1989) 2.

[2.1.145] AUMANN, D.C., et al., Independent formation cross-section of ^{148m}Pm and ^{148g}Pm in the fission of ^{232}Th induced by 26- to 42-MeV ^{4}He-ions, J. Inorg. Nucl. Chem. **40** (1978) 1–4.

[2.1.146] IMANISHI, N., et al., Mean angular momenta of primary fragments formed in alpha-particle induced fission of ^{232}Th, Rep. 207, Kyoto University, Uji, Japan (1987).

[2.1.147] NAIK, H., et al., Effect of entrance channel parameters on fission fragment angular momentum in medium energy fission, Z. Phys. A Hadrons Nucl. **342** (1992) 95–100.

[2.1.148] TOMAR, B.S., et al., Fragment angular momenta in low and medium energy fission of ^{242}Pu, Z. Phys. A Hadrons Nucl. **327** (1987) 225–229.

[2.1.149] TOMAR, B.S., et al., Fragment angular momenta in alpha-induced fission of ^{238}U, Phys. Rev. C **38** (1988) 1787–1791.

[2.1.150] TOMAR, B.S., et al., Independent isomeric yield ratios of ^{132}Sb in ^{241}Pu(n_{th},f) and ^{238}U(α,f), Radiochim. Acta **55** (1991) 173–176.

[2.1.151] JACOBS, E., et al., Product yields for the photofission of ^{238}U with 12, 15, 20, 30 and 70 MeV Bremsstrahlung, Phys. Rev. C **19** (1979) 422–432.

[2.1.152] JACOBS, E., et al., Product yields for the photofission of ^{235}U with 12, 15, 20, 30 and 70 MeV Bremsstrahlung, Phys. Rev. C **21** (1980) 237–245.

[2.1.153] KONDRAT'KO, M.Y., et al., Fission fragment yields in Np-237 photofission, At. Energ. **35** (1973) 211–213.

[2.1.154] PERSYN, K., et al., "Mass, charge and total kinetic energy distributions for the photon induced fission of ^{232}Th, ^{235}U and ^{238}U", Dynamic Aspects of Nuclear Fission (Proc. 2nd Int. Conf. Smolenice, Slovakia, 1993) (KRISTIAK, J., PUSTYLNIK, B.I., Eds), Rep. E7-94-19 (1994) 59–63.

[2.1.155] PERSYN, K., et al., "Mass and charge distribution for photon-induced fission of ^{232}Th", Nuclear Fission and Fission Product Spectroscopy (Proc. Conf. Seyssins, France, 1994) (FAUST, H., FIONI, G., Eds), American Institute of Physics, Woodbury, NY (1994) 86–90.

[2.1.156] PERSYN, K., et al., Excitation energy dependence of fragment characteristics for the photofission of ^{232}Th, Nucl. Phys. A **620 (**1997) 171–190.

[2.1.157] PERSYN, K., et al., Influence of the odd neutron on the fragment characteristics in the photofission of ^{235}U, Nucl. Phys. A **615** (1997) 198–206.

[2.1.158] PIESSENS, M., et al., Mass and kinetic energy distributions for the photofission of ^{232}Th with 6.44 to 13.15 MeV Bremsstrahlung, Nucl. Phys. A **556** (1993) 88–106.

[2.1.159] POMME, S., et al., Fragment characteristics for the photofission of ^{238}U with 6.1–13.1 MeV Bremsstrahlung, Nucl. Phys. A **572** (1994) 237–266.

[2.1.160] THIERENS, H., et al., Kinetic energy and fragment mass distributions for ^{240}Pu(sf), ^{239}Pu(n_{th},f), and ^{240}Pu(γ,f), Phys. Rev. C **23** (1981) 2104–2113.

[2.1.161] THIERENS, H., et al., Fragment mass and kinetic energy distributions for ^{242}Pu(sf), ^{241}Pu(n_{th},f), and ^{242}Pu(γ,f), Phys. Rev. C **29** (1984) 498–507.

[2.1.162] DE FRENNE, D., et al., Charge distribution for the photofission of ^{238}U with 20-MeV Bremsstrahlung, Phys. Rev. C **21** (1980) 629–636.

[2.1.163] DE FRENNE, D., et al., Charge distributions for the photofission of ^{235}U and ^{238}U with 12–30 MeV Bremsstrahlung, Phys. Rev. C **26** (1982) 1356–1368.

[2.1.164] DE FRENNE, D., et al., Isotopic distributions and elemental yields for the photofission of ^{235,238}U with 12–30 MeV Bremsstrahlung, Phys. Rev. C **29** (1984) 1908–1911.

[2.1.165] GÄGGELER, H., VON GUNTEN, H.R., Charge distribution in the photofission of ^{238}U with Bremsstrahlung of E_{max} 20–50 MeV, J. Inorg. Nucl. Chem. **40** (1978) 1859–1863.

[2.1.166] PETRZHAK, K.A., et al., Relative yields of xenon isotopes in ^{238}U photofission, Yad. Fiz. **14** (1971) 950–952.

[2.1.167] POMME, S., et al., Excitation energy dependence of charge odd–even effects in the fission of ^{238}U close to the fission barrier, Nucl. Phys. A **560** (1993) 689–714.

[2.1.168] SMITH, J.R., RICHARDSON, A.E., Independent yields from the photofission of ^{232}Th, and the Zp and statistical-dynamic models, Phys. Rev. C **44** (1991) 1118–1127.

[2.1.169] DE FRENNE, D., et al., Independent isomeric yield ratios and primary angular momenta in the photofission of ^{235,238}U with 12–30-MeV Bremsstrahlung, Phys. Rev. C **29** (1984) 1777–1783.

[2.1.170] THIERENS, H., et al., Independent isomeric yield ratio of ^{134}I in the photofission of ^{235}U and ^{238}U, Phys. Rev. C **25** (1982) 1546–1550.

[2.1.171] TONCHEV, A.P., et al., Isomeric yield ratio of ^{134}I in photofission of ^{232}Th and ^{238}U, J. Radioanal. Nucl. Chem. Lett. **155** (1991) 299–309.

[2.1.172] CALDWELL, J.T., et al., "Prompt and delayed neutron yields from low-energy photofission of ^{232}Th, ^{235}U, ^{238}U and ^{239}Pu", Physics and Chemistry of Fission (Proc. Conf. Rochester, NY, 1973), IAEA, Vienna (1973) 431–444.

[2.1.173] D'HONDT, P., et al., Emission of long-range alpha particles in the photofission of ^{235}U with 20 MeV Bremsstrahlung, Phys. Rev. C **21** (1980) 963–965.

[2.1.174] VERBOVEN, M., et al., Emission of light charged particles in photon induced fission, Phys. Rev. C **49** (1994) 991–1000.

[2.1.175] ARMBRUSTER, P., et al., Low-energy fission investigated in reactions of 750 A MeV ^{238}U-ions with Pb and Be targets. Part 1. Nuclear charge distributions, Z. Phys. A Hadrons Nucl. **355** (1996) 191–201.

[2.1.176] BENLLIURE, J.H., et al., Production of medium-weight isotopes by fragmentation in 750 A MeV ^{238}U on ^{208}Pb collisions, Eur. Phys. J. A **2** (1998) 193–198.

[2.1.177] BÖCKSTIEGEL, C., et al., Total kinetic energies and nuclear-charge yields in the fission of relativistic ^{233}U secondary projectiles, Phys. Lett. **398B** (1997) 259–263.

[2.1.178] DONZAUD, C., et al., Low-energy fission investigated in reactions of 750 A MeV ^{238}U-ions on ^{208}Pb, II: Isotopic Distributions, Eur. Phys. J. A **1** (1998) 407–426.

[2.1.179] ENQUIST, T., et al., "Systematic experimental survey on projectile fission induced in collisions of ^{238}U at 1 GeV with lead", Nuclear Fission and Fission Product Spectroscopy (Proc. Conf. Seyssins, France, 1998) (FIONI, G., et al., Eds), American Institute of Physics, Woodbury, NY (1998) 427–434.

[2.1.180] SCHMIDT, K.-H., et al., Low-energy fission studies of neutron-deficient projectile fragments of ^{238}U, Phys. Lett. **325B** (1994) 313–316.

[2.1.181] SCHMIDT, K.-H., et al., "Fission experiments with secondary beams", Nuclear Fission and Fission Product Spectroscopy (Proc. Conf. Seyssins, France, 1998) (FIONI, G., et al., Eds), American Institute of Physics, Woodbury, NY (1998) 407–419.

[2.1.182] SCHMIDT, K.-H., et al., Influence of shell effects on fission probabilities and on fission-fragment properties of ^{238}U projectile fragments, Nucl. Phys. A **630** (1998) 208c–214c.

[2.1.183] SCHMIDT, K.-H., et al., Relativistic radioactive beams: A new access to nuclear fission studies, Nucl. Phys. A **665** (2000) 221–267.

[2.1.184] SCHWAB, W., et al., Fission of highly excited fragments from collisions of 750 A MeV ^{238}U-ions on ^{208}Pb, Eur. Phys. J. A **2** (1998) 179–191.

[2.1.185] STEINHÄUSER, S., et al., Odd-even effects observed in the fission of nuclei with unpaired protons, Nucl. Phys. A **634** (1998) 89–111.

2.2. MEASUREMENTS OF THE ENERGY DEPENDENCE OF FISSION YIELDS FOR ^{238}U(n,f) FROM THRESHOLD TO 200 MeV

Th. Ethvignot
Commissariat à l'Énergie Atomique, France

An experimental programme to study the properties of fission induced by intermediate energy neutrons (i.e. several hundreds of keV to several hundreds of MeV) is in progress at the Los Alamos Neutron Science Center, USA. Experiments using the germanium array for neutron induced excitations (GEANIE) high resolution gamma and X ray spectrometer have been performed with ^{238}U targets. Information on the fragment yields (i.e. excitation functions and isotopic distributions) were extracted from the germanium array for neutron induced excitations inclusive gamma and gamma–gamma data. Charge yields were extracted by measuring prompt X rays using a specially designed thin fission sensitive target. The experimental results are presented and compared with the systematics of Wahl.

2.2.1. Introduction

A collaborative experimental programme is being carried out by CEA Bruyères-le-Châtel and Los Alamos National Laboratory. This programme takes advantage of the WNR facility at the Los Alamos Neutron Science Center, a spallation neutron source that provides a relatively large flux of fast neutrons in a broad energy range extending up to more than 400 MeV. Experiments utilizing the existing GEANIE detector system have provided new data on X and gamma ray emissions. Fission is accompanied by the prompt emission of neutrons and photons that originate from several stages of the phenomenon. Depending on the incident neutron energy, neutrons and photons may be emitted by the fissioning nucleus. After scission, the prompt de-excitation of the fission fragments occurs through evaporation of neutrons and electromagnetic processes that may be coupled to the atomic system. Most of the prompt electromagnetic de-excitation occurs mainly after neutron evaporation is exhausted. Two processes are involved in electromagnetic de-excitation: gamma ray emission and internal conversion. The latter is accompanied by the emission of K X rays characteristic of the atomic number of the primary fragment.

2.2.2. Experiments

GEANIE is an array of 26 high resolution germanium (Ge) gamma ray detectors with 20 BGO (bismuth germinate) background suppression shields. Eleven of the Ge detectors are dedicated to low energy photon spectroscopy from 10 to 300 keV. The other 15 detectors are more adapted to higher energy gamma rays, typically from 300 to 2000 keV. GEANIE is located 20 m from the WNR neutron production target at the end of a collimated flight path [2.2.1]. Two types of experiment were undertaken at GEANIE with ^{238}U targets and the time of flight technique was used in both cases to measure the energy of the incident neutrons. The first class of experiments consisted of inclusive gamma ray measurements performed with a ~400 mg/cm^2 target of ^{238}U. The large array of detectors gave the opportunity for an analysis of the recorded gamma rays in both single gamma and double gamma coincidence modes. The relative thickness of the target provided high gamma counting rates. However, the recorded gamma rays originate not only from the de-exciting post-neutron fragments, but also from other neutron induced reactions occurring in the target, such as (n,xn) and (n,n') on uranium. This problem of separating fission product gamma rays from those of other reactions is minimized in the second class of experiments, with a thin fission sensitive target of ^{238}U. This target consists of 8×1 mg/cm^2 layers deposited on photovoltaic cells used as fission fragment detectors [2.2.2]. A coincidence with the detection of a fission fragment in the target was required in the gamma ray recording. Moreover, both the uranium samples and the photovoltaic cells were thin enough for the measurement of prompt fission K X rays. This is the first time fission X rays have been measured at a broad spectrum neutron source.

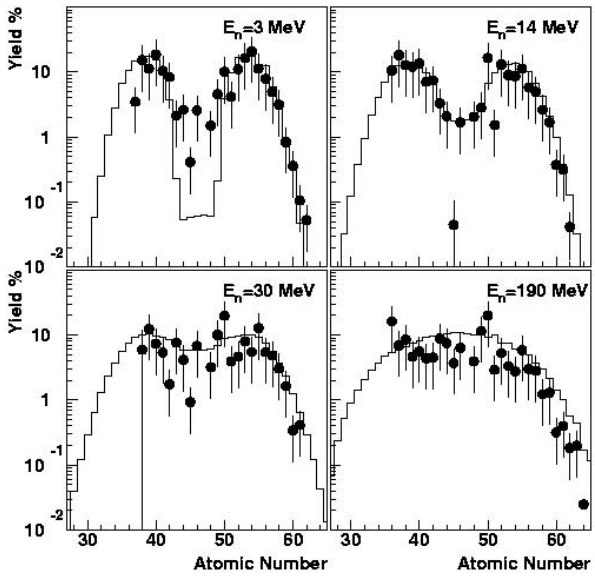

FIG. 2.2.1. Independent charge yields per 100 fissions determined from the X ray yield measurements for $^{238}U(n,f)$ involving four incident neutron energy bins (black dots): threshold-6 MeV, 11–20 MeV, 20–50 MeV, 50 MeV and above. Average energies are labelled: 3 MeV, 14 MeV, 30 MeV, 190 MeV, and the histograms correspond to calculations obtained at the average energies with Wahl systematics [2.2.7].

2.2.3. Results

2.2.3.1. Charge yields

Coincidence between photon and fission fragment detection in the active target experiment permitted prompt K X ray measurements [2.2.3]. Due to the large number of K X ray lines (five per element), the X ray energy spectrum is quite complex. Nevertheless, the energies and relative intensities of these lines are known to a high precision [2.2.4]. Within the limits of the recorded statistics, the contributions of the different elements produced for different groups of incident neutron energy can be de-convolted by fitting the data with a parametric function of one free parameter per element. In the 1970s, Reisdorf and collaborators measured the X ray yields per fission fragment Y(Z) in spontaneous and low energy neutron induced fission [2.2.5]. Y(Z) would appear to depend only weakly on the nature of the fissioning system. By applying Reisdorf's prescription to our X ray yields it is possible to extract an elemental distribution of the primary fission fragments, as shown in Fig. 2.2.1. The X ray data have been corrected for self-absorption and detection efficiency with point source calibrations and a Monte Carlo N Particle Transport Code (MCNP) simulation [2.2.6]. The preliminary results exhibit the expected increase in the probability for symmetric fission as one goes towards high incident neutron energies. Moreover, they agree quite well with the systematics from Wahl for 14 MeV neutrons [2.2.7], particularly at 14 MeV. At 50 MeV and above, the symmetric region gap fills up. These results agree with the mass distribution measurements of Zöller et al. [2.2.8] for the same system.

2.2.3.2. Fragment excitation functions

From the inclusive gamma ray measurements, more than one hundred post-neutron fission fragments were identified from Ge to Nd. Among them the even–even nuclei are particularly interesting. Indeed, the 2^+ to 0^+ (G.S.) transition of the ground state rotational band of an even–even fragment is usually fed at 100% in the de-excitation process [2.2.9]. Measuring the corresponding gamma ray intensities gives a measurement of the fragment production for 23 bins of incident neutron energies. In some cases, because of pollution or conversion of the 2^+ to 0^+ (G.S.) transition, higher transitions in the G.S. band are used. In cases where no singles data are usable, coincidence data best describe the production cross-section, but with much lower statistics (only three bins of incident neutron energies). In this way the fragment production cross-section has been extracted for about thirty even–even post-neutron emission fragments as a function of incident neutron energy. The fragment production excitation functions are extracted from Ref. [2.2.10] and shown in Figs 2.2.2–2.2.31 for ^{92}Sr to ^{150}Ce. Up to three experimental

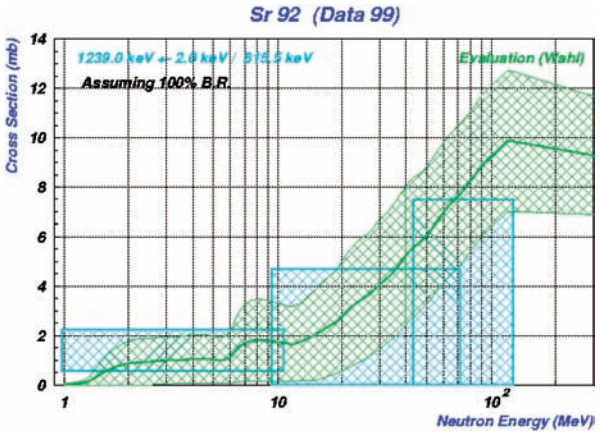

FIG. 2.2.2. ^{92}Sr: best experimental data from the cyan points divided by 1 × 1 (BR from adopted levels of the evaluated nuclear structure data file (ENSDF)).

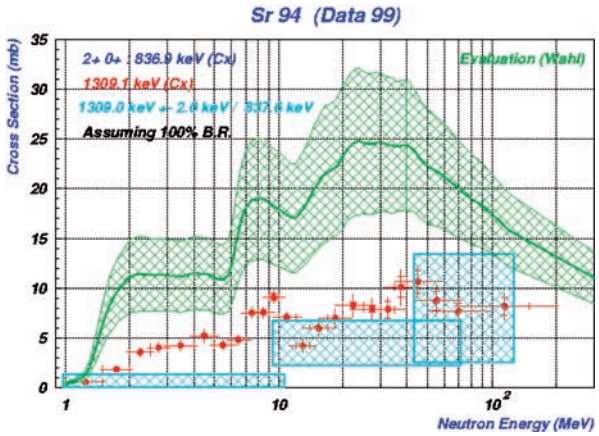

FIG. 2.2.3. ^{94}Sr: best experimental data from the cyan points divided by 1 × 1 (BR from adopted levels of the evaluated nuclear structure data file (ENSDF)).

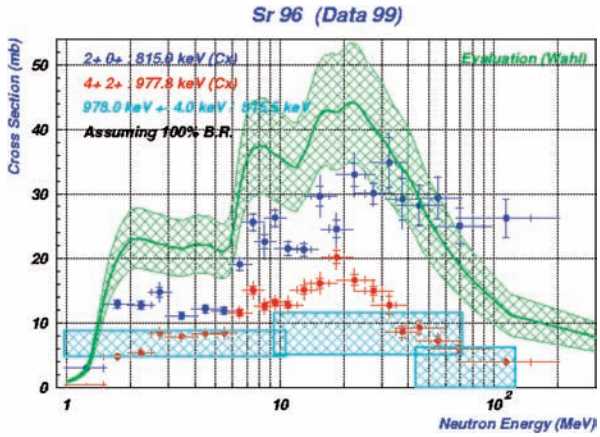

FIG. 2.2.4. ^{96}Sr: best experimental data from the blue points divided by 1 (BR from SF in experimental unevaluated nuclear data list (XUNDL)).

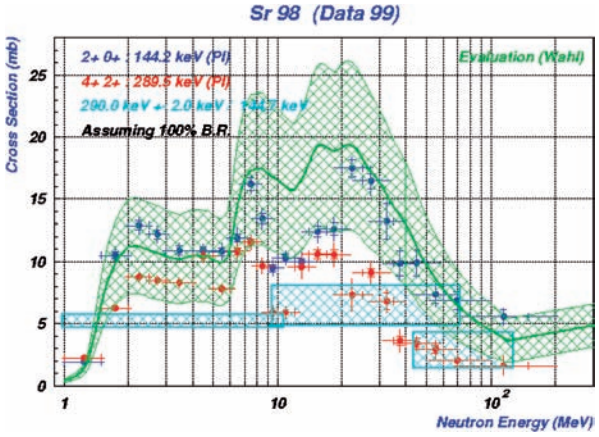

FIG. 2.2.5. ^{98}Sr: best experimental data from the blue points divided by 1 (BR from SF in experimental unevaluated nuclear data list (XUNDL)).

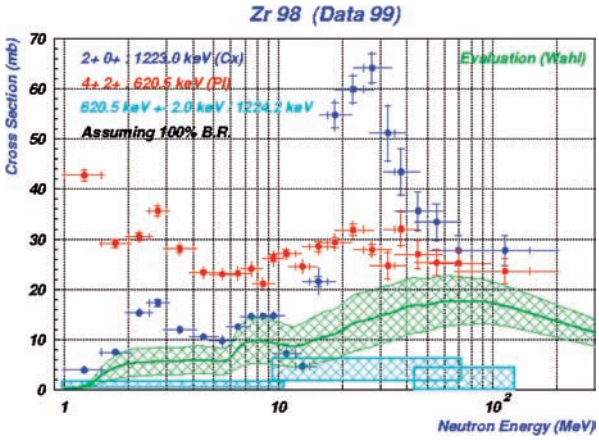

FIG. 2.2.6. ^{98}Zr: best experimental data from the cyan points divided by 1.0 × 0.63 (BR from SF in evaluated nuclear structure data file (ENSDF)).

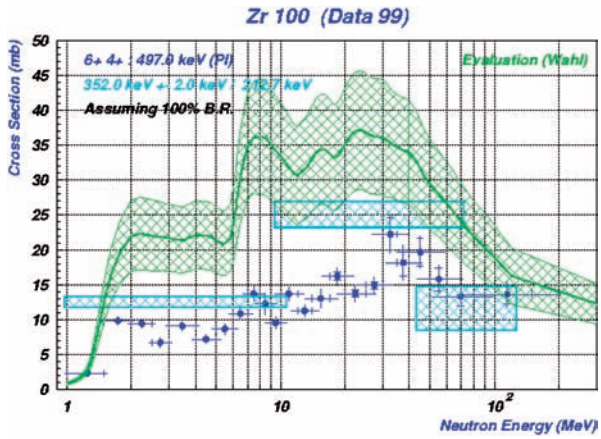

FIG. 2.2.7. ^{100}Zr: best experimental data from the cyan points divided by 1.0 × 0.84 (BR from SF in evaluated nuclear structure data file (ENSDF)).

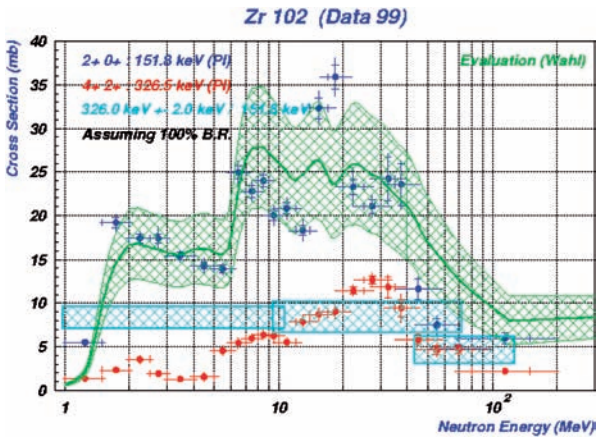

FIG. 2.2.8. ^{102}Zr: best experimental data from the blue points divided by 1 (BR from SF in evaluated nuclear structure data file (ENSDF)).

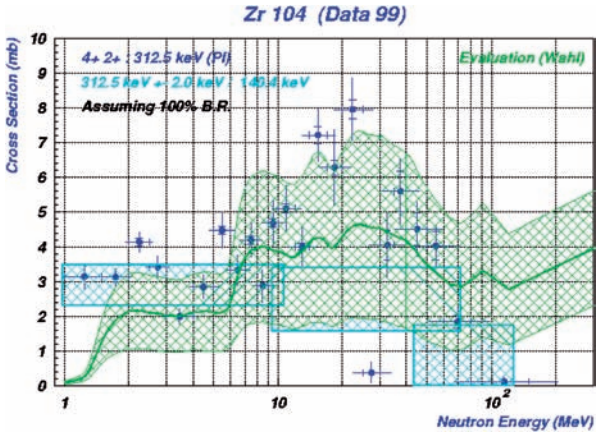

FIG. 2.2.9. ^{104}Zr: best experimental data from the blue points divided by 1 (BR from SF in evaluated nuclear structure data file (ENSDF)).

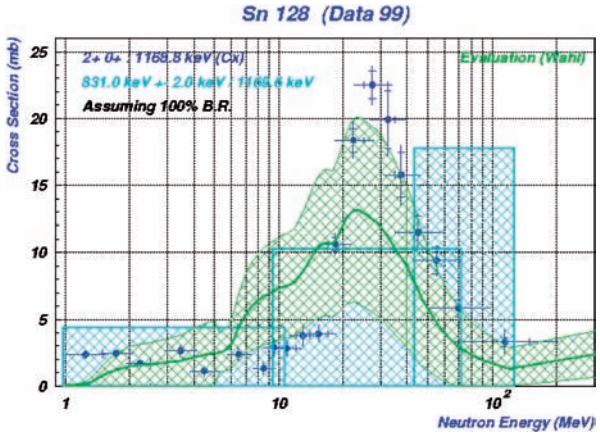

FIG. 2.2.10. ^{128}Sn: best experimental data from the blue points divided by 1 (BR from adopted levels of the evaluated nuclear structure data file (ENSDF)).

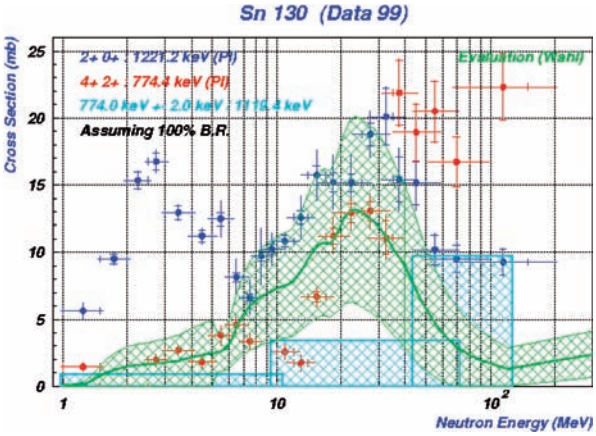

FIG. 2.2.11. ^{130}Sn: best experimental data from the red points divided by 1 (BR from adopted levels of the evaluated nuclear structure data file (ENSDF)).

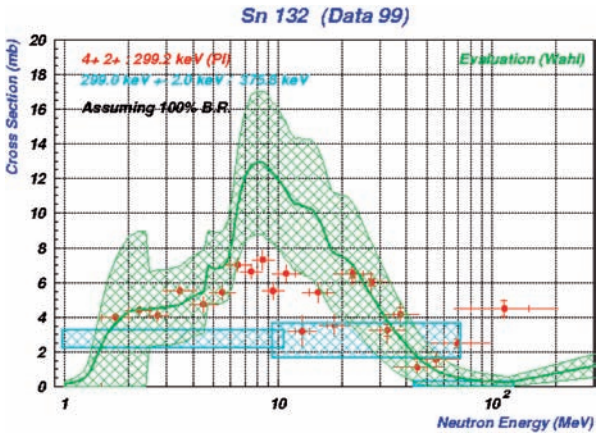

FIG. 2.2.12. ^{132}Sn: best experimental data from the red points divided by 1 (BR from adopted levels of the evaluated nuclear structure data file (ENSDF)).

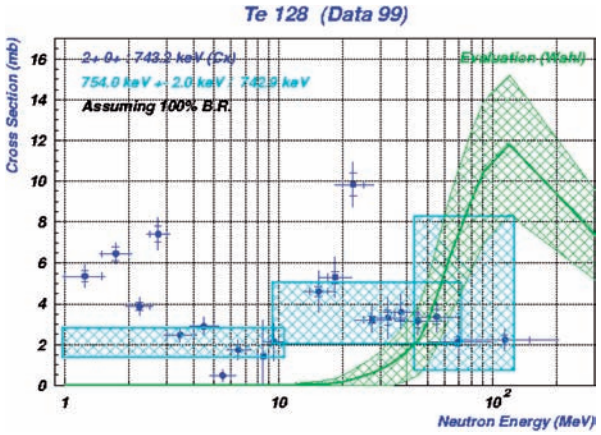

FIG. 2.2.13. ^{128}Te: best experimental data from the cyan points divided by 1.0 × 0.64 (BR from heavy ion induced fission in evaluated nuclear structure data file (ENSDF)).

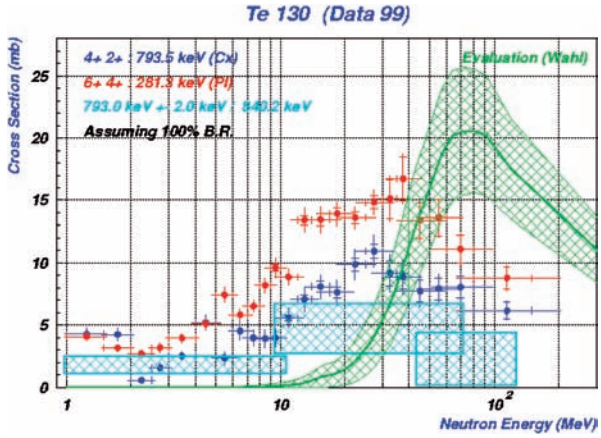

FIG. 2.2.14. ^{130}Te: best experimental data from the blue points divided by 0.25 (BR from (n,n') in evaluated nuclear structure data file (ENSDF)).

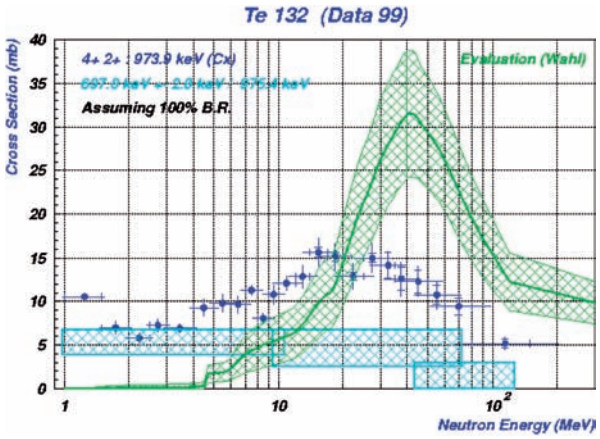

FIG. 2.2.15. ^{132}Te: best experimental data from the cyan points divided by 0.14 × 0.87 (BR from beta decay in evaluated nuclear structure data file (ENSDF)).

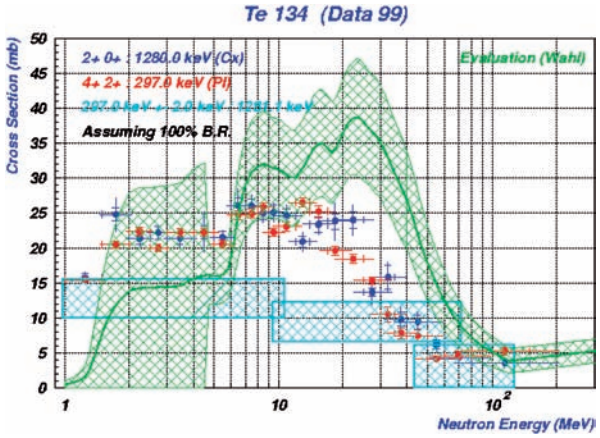

FIG.2.2.16. ^{134}Te: best experimental data from the blue points divided by 1 (BR from SF in experimental unevaluated nuclear data list (XUNDL)).

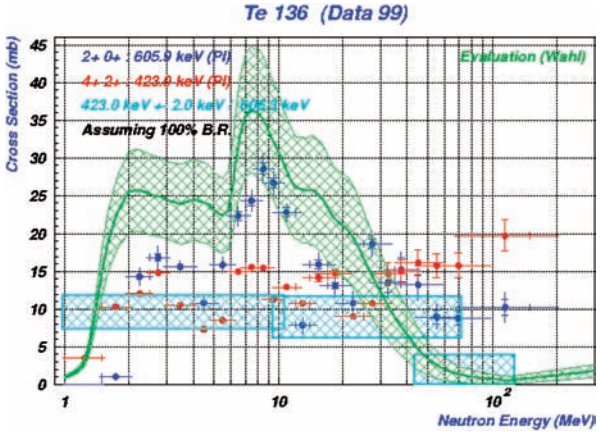

FIG. 2.2.17. ^{136}Te: best experimental data from the blue points divided by 1 (BR from SF in evaluated nuclear structure data file (ENSDF)).

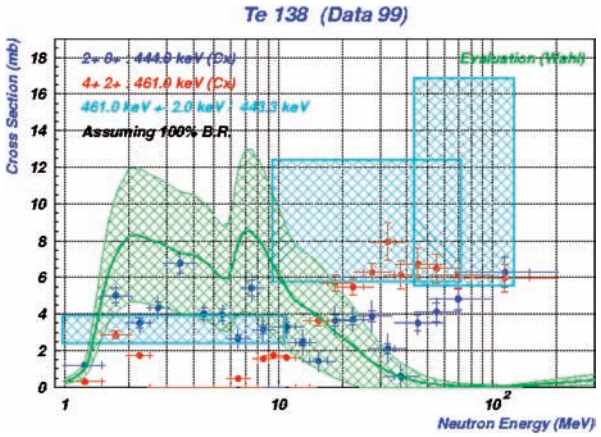

FIG. 2.2.18. ^{138}Te: best experimental data from the blue points divided by 1 (BR from SF in experimental unevaluated nuclear data list (XUNDL)).

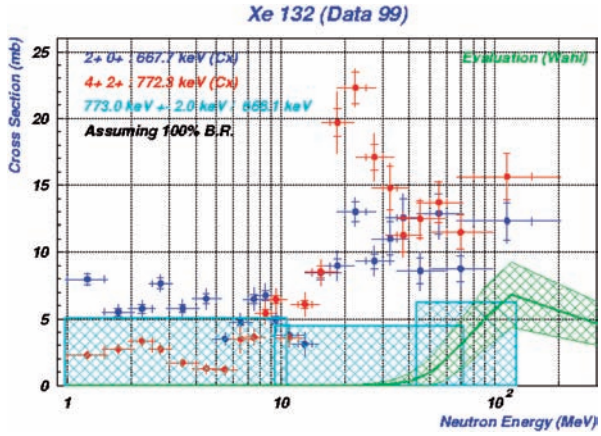

FIG. 2.2.19. ^{132}Xe: best experimental data from the cyan points divided by 1.0 × 0.77 (BR from beta decay in evaluated nuclear structure data file (ENSDF)).

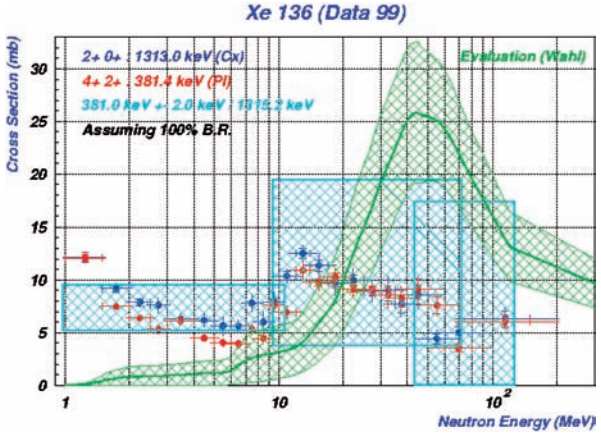

FIG. 2.2.20. ^{136}Xe: best experimental data from the blue points divided by 1 (BR from SF in evaluated nuclear structure data file (ENSDF)).

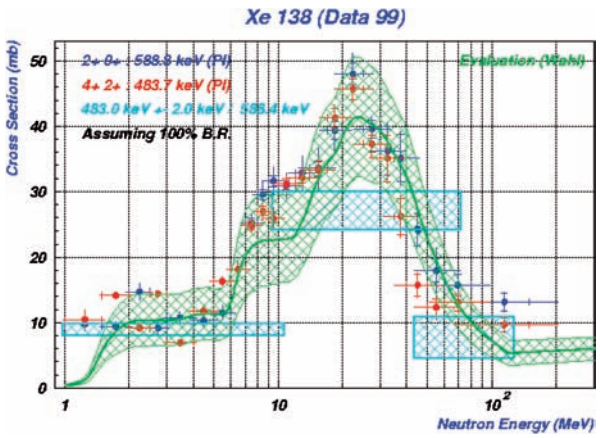

FIG. 2.2.21. ^{138}Xe: best experimental data from the blue points divided by 1 (BR from SF in evaluated nuclear structure data file (ENSDF)).

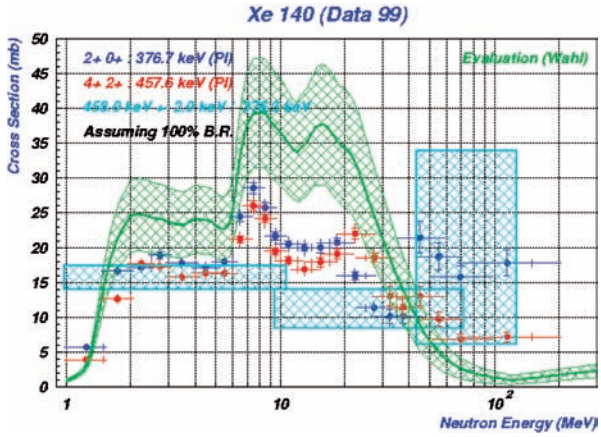

FIG. 2.2.22. ^{140}Xe: best experimental data from the blue points divided by 1 (BR from SF in evaluated nuclear structure data file (ENSDF)).

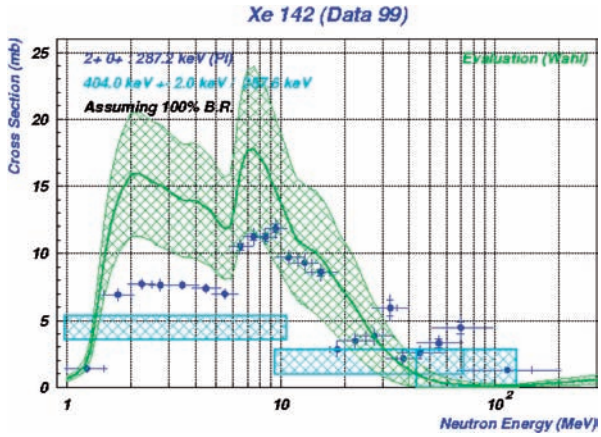

FIG. 2.2.23. ^{142}Xe: best experimental data from the blue points divided by 1 (BR from SF in evaluated nuclear structure data file (ENSDF)).

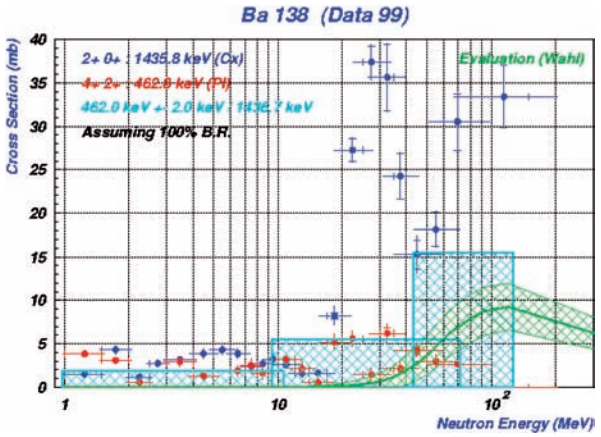

FIG. 2.2.24. ^{138}Ba: best experimental data from the cyan points divided by 0.31 × 1.0 (BR from (n,n') in evaluated nuclear structure data file (ENSDF)).

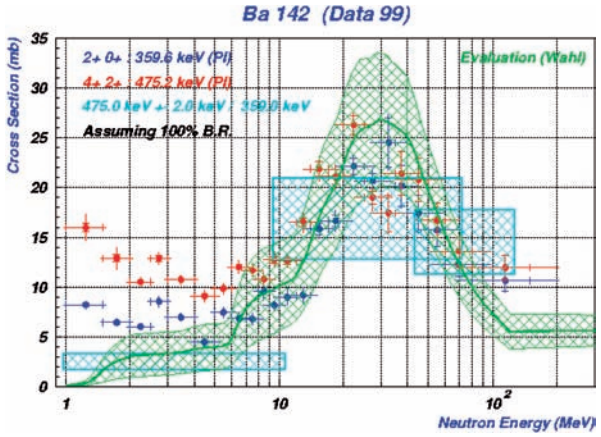

FIG. 2.2.25. ^{142}Ba: best experimental data from the blue points divided by 1 (BR from SF in evaluated nuclear structure data file (ENSDF)).

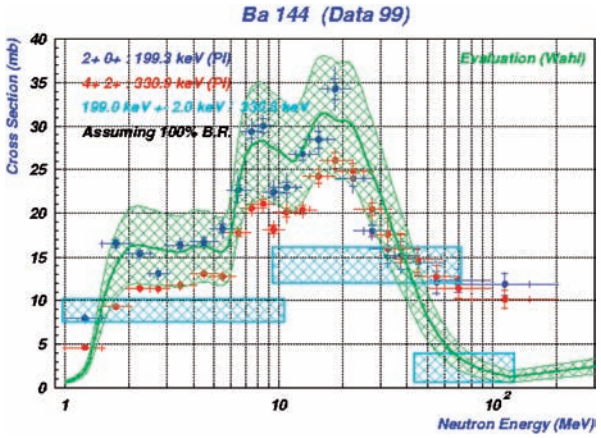

FIG. 2.2.26. ^{144}Ba: best experimental data from the blue points divided by 1 (BR from SF in evaluated nuclear structure data file (ENSDF)).

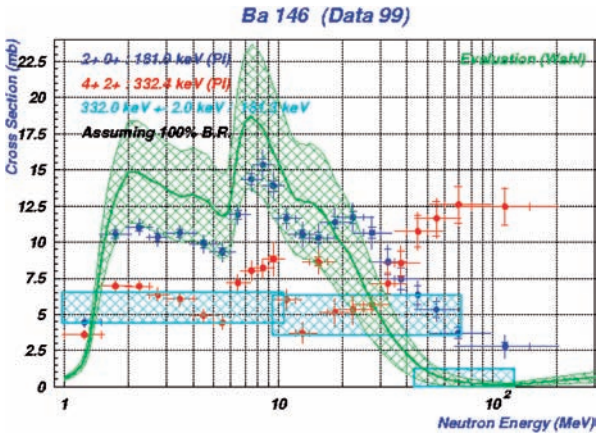

FIG. 2.2.27. ^{146}Ba: best experimental data from the blue points divided by 1 (BR from SF in evaluated nuclear structure data file (ENSDF)).

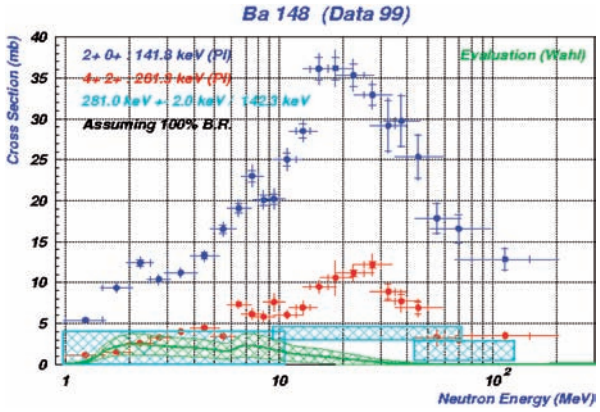

FIG. 2.2.28. ^{148}Ba: best experimental data from the cyan points divided by 1.0 × 0.86 (BR from SF in evaluated nuclear structure data file (ENSDF)).

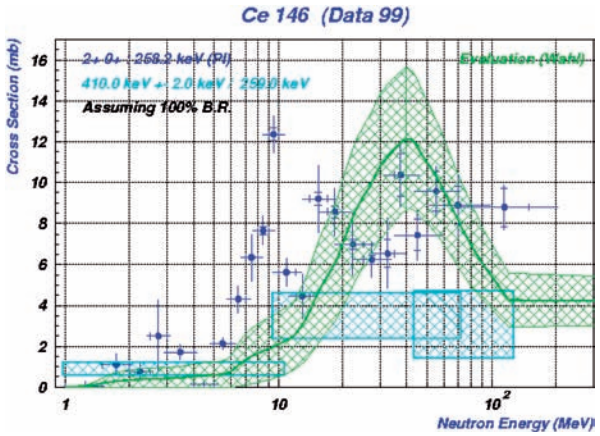

FIG. 2.2.29. ^{146}Ce: best experimental data from the blue points divided by 1 (BR from SF in evaluated nuclear structure data file (ENSDF)).

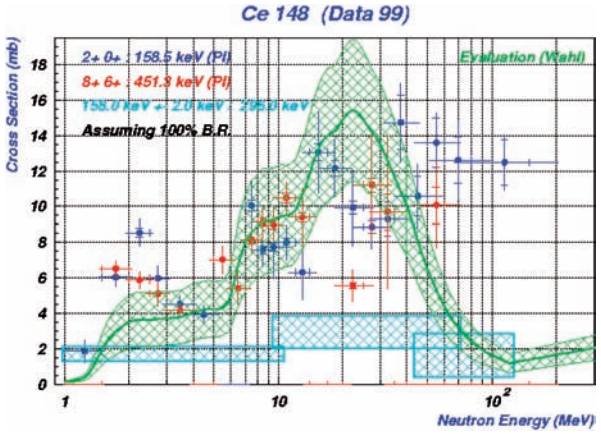

FIG. 2.2.30. ^{148}Ce: best experimental data from the blue points divided by 1 (BR from SF in experimental unevaluated nuclear data list (XUNDL)).

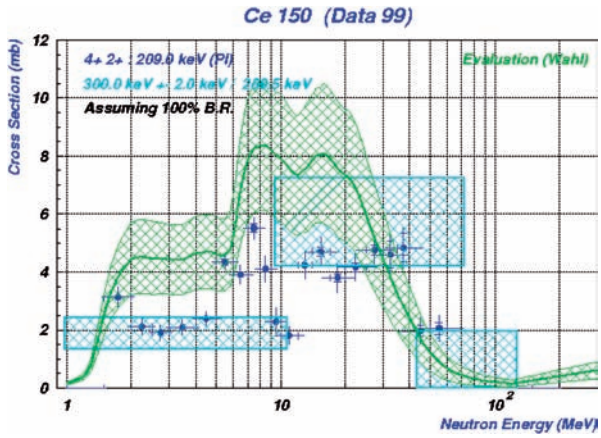

FIG. 2.2.31. ^{150}Ce: best experimental data from the blue points divided by 1 (no BR available in evaluated nuclear structure data file or experimental unevaluated nuclear data list (XUNDL)).

data sets are given. For singles gamma ray data, excitation functions are given with blue and red dots. For coincidence data only three points are plotted in cyan, corresponding to neutron energy bins of 1–10, 10–50 and 50–100 MeV. The data are corrected for conversion, with the internal conversion coefficients taken from the evaluated nuclear structure data file. The branching ratios for singles and coincidences have been assumed to be 100% for the plots. One needs to correct with known branching ratios from the evaluated nuclear structure data file or experimental unevaluated nuclear data list fission data (given in the captions) to determine the actual cross-section. For example, determining the experimental cross-section for the production of ^{100}Zr at 30 MeV requires the following actions:

(1) Read the value plotted in Fig. 2.2.7, i.e. 25 ± 2 mb from the 10–50 MeV bin;
(2) Apply the branching ratio correction to give $25 \pm 2 \times 1/(1 \times 0.84) = 29.8 \pm 2.4$ mb.

The data are compared to the systematics by Wahl [2.2.7] in green. At energies above 14 MeV, Wahl uses data from ^{238}U(p,f) and ^{232}Th(p,f). The evolution of the fragment production cross-section as a function of neutron energy (excitation function) exhibits correlations with the thresholds of fission chances. However, for a given element, the behaviour differs strongly from one isotope to another.

2.2.4. Conclusions

New data on prompt photon emission during the intermediate energy neutron induced fission of ^{238}U have been obtained. Gamma ray measurements have enabled the extraction of individual post-neutron emission fragment production excitation functions. From X ray measurements, the primary fragment Z distribution has been extracted for different incident neutron energies. Although these last results have to be finalized, they agree quite well with calculations and other measurements.

REFERENCES TO SECTION 2.2

[2.2.1] NELSON, R., et al., Nuclear Data for Science and Technology, Italian Physics Society (1997) 445.

[2.2.2] ETHVIGNOT, Th., et al., A fission-fragment-sensitive target for X-ray spectroscopy in neutron-induced fission, Nucl. Instrum. Methods Phys. Res. A **490** (2002) 559–565.

[2.2.3] GRANIER, Th., et al., CEA Bruyères-le-Chatel, personal communication, 2003.

[2.2.4] BEARDEN, J.A., X-ray wavelengths, Rev. Mod. Phys. **39** (1967) 78–124.

[2.2.5] REISDORF, W., et al., Fission fragment K X-ray emission and nuclear charge distribution for thermal neutron fission of ^{233}U, ^{235}U, ^{239}Pu and spontaneous fission of ^{252} Cf, Nucl. Phys. A **177** (1971) 337–378.

[2.2.6] BREISMEISTER, J., Ed., MCNP — A Monte-Carlo N-particle Transport Code, Rep. LA-12625-M, Los Alamos National Laboratory, NM (1997).

[2.2.7] WAHL, A.C., Contribution to Compilation and Evaluation of Fission Yields Nuclear Data, Rep. LA-13928, Los Alamos National Laboratory, NM (2002).

[2.2.8] ZÖLLER, C.M., Fission Fragment Properties in the ^{238}U(n,f) Reaction at Incident Neutron Energies from 1 MeV to 500 MeV, Rep. IKDA-95/25, Technische Hochschule Darmstadt (1995).

[2.2.9] CHEIFETZ, E., et al., Determination of the charge and mass distribution in the fission of ^{252}Cf, Phys. Rev. C **4** (1971) 1913–1926.

[2.2.10] CASOLI, P., Étude de la Production de Fragments dans la Fission Induite par Neutrons sur l'Uranium-238, PhD thesis, Université de Bordeaux (2003).

3. EVALUATIONS

3.1. ACTINIDE NUCLEON INDUCED FISSION CROSS-SECTIONS UP TO 200 MeV

V.M. Maslov
Belarus Academy of Sciences, Belarus

Neutron induced fission cross-sections of U, Np and Th target nuclides have been analysed in terms of a fission/evaporation approximation up to 200 MeV incident neutron energy. The contribution of the damping of collective modes to the level density at excitation energies higher than about 20 MeV for saddle and equilibrium deformations is shown to be essential for the description of the observed fission cross-section. Effective estimates of intrinsic level densities are obtained. Differences of measured proton and neutron induced fission cross-sections of ^{238}U are attributed to the influence of the iso-vector term of the nucleon–nucleus optical potential. The ratio of symmetric (super long mode) and asymmetric (S1 + S2) fission cross-sections of ^{238}U(n,f) is described up to 200 MeV in terms of the Hauser–Feshbach statistical model. For actinide nuclei emerging in multiple chance fission reactions, a separate outer fission barrier is assumed for the super long mode, while the inner fission barrier is assumed to be the same for super long, S1 and S2 modes. super long mode multiple chance fission cross-sections seem to be controlled by a rather high outer fission barrier with significant transparency. Axial asymmetry as assumed for the super long mode outer saddle (as distinct from S1 and S2 modes, which are axially symmetric and mass asymmetric) is found to be essential to reproduce the ratio of symmetric and asymmetric fission of the ^{238}U(n,f) reaction up to 200 MeV. Partitioning of the observed fission cross-sections of ^{238}U(n,f), ^{238}U(p,f), ^{235}U(n,f), ^{233}U(n,f), ^{237}Np(n,f) and ^{232}Th(n,f) into symmetric and asymmetric fission is provided.

3.1.1. Introduction

Traditionally, fission product yield data are fitted with a set of up to five Gaussian functions. Neutron induced fission of major actinides at thermal energies is comprehensively described by Wahl [3.1.1]. However, at higher energies, when emissive fission occurs, a physical modelling of fission yield distributions is of value since many fissioning nuclides at different excitation energies contribute to fission observables. A multichannel random neck rupture model by Brosa et al. [3.1.2–3.1.5] seems to provide a flexible tool for fission yield data analysis in a wide range of mass and charge numbers and excitation energies of fissioning nuclides. Up to the emissive fission threshold, the important model parameters are mass channel probabilities and their energy dependence. The relative contributions of channels could be quite different for different fissioning nuclei. It is well known that fission is predominantly symmetric for pre-actinides with $A \leq 227$ and for heavy actinides with $A \geq 257$. However, for actinides $227 < A < 257$, fission is a mixture of two global channels (asymmetric and symmetric) and there is a further splitting of the standard channel into standard I and standard II channels. Symmetric channels for light pre-actinides ($A \leq 227$) and heavy actinides ($A \geq 257$) are also different, as derived from the analysis of the mass dependence of the kinetic energy [3.1.2–3.1.5]. The conclusion was that there is a super long symmetric channel for pre-actinides and actinides with mass numbers $A < 257$, and a super short symmetric channel for heavy actinides. Different channel contributions lead to the assumption that there are different fission barriers relevant for super long, standard and super short channels. The proposals were demonstrated in studies of the proton induced fission of U, Pu and Am target nuclei by Ohtsuki et al. [3.1.6] and the fission of ^{227,228}Ac and ^{228}Ra nuclides excited by transfer reactions and studied by Konecny et al. [3.1.7] and Weber et al. [3.1.8]. All these features would come into play simultaneously in high energy particle induced fission (or photofission) of actinides via emissive fission contribution, when a significant number of neutrons and protons could be emitted.

The super long mode fission yields in the ^{235}U(n,f) and ^{238}U(n,f) reactions for incident neutron energies up to the emissive fission threshold (related to symmetric scission of the

compound nucleus) was analysed recently within the Hauser–Feshbach statistical model [3.1.9]. Individual contributions of the super long fission mode to the observed fission cross-sections were reproduced up to the emissive fission threshold [3.1.10, 3.1.11]. A separate outer fission barrier was assumed for the super long mode, while a common inner barrier was assumed for the symmetric super long and asymmetric S1 and S2 modes. This assumption is supported by fission mode calculations [3.1.12, 3.1.13] that use the multimodal random neck rupture model [3.1.2–3.1.5], and reveal that the final bifurcation point is close to the second minimum of the actinide double humped fission barrier. The super long mode ^{235}U(n,f) and ^{238}U(n,f) fission cross-sections were shown to be controlled by a rather high outer fission barrier with significant transparency. A steeply rising shape of the super long mode contribution was found to be compatible with outer saddle point axial asymmetry that accompanied mass symmetry. Outer saddle shapes for S1 and S2 modes were assumed to be axially symmetric and mass asymmetric.

Above the emissive fission threshold, a number of nuclei contribute to the fission observables: the ^{238}U(n,f) reaction at E_n ~ 200 MeV may involve an appreciable contribution from about 20 nuclides. The ratio of symmetric to the sum of symmetric and asymmetric fission events was obtained in the reaction ^{238}U(n,f) by Zöller et al. [3.1.14] for incident neutron energies of up to E_n ~ 500 MeV. They deduced the ratio of symmetric to all fission events from the fission fragment total kinetic energy distribution as well as from the mass total kinetic energy distributions. A simultaneous analysis of this ratio and the observed neutron induced fission cross-section for a ^{238}U target [3.1.15, 3.1.16] up to E_n ~ 200 MeV might be attempted within statistical theory. The observed ^{238}U neutron induced fission cross-section data [3.1.15, 3.1.16] were analysed recently in a fission/neutron evaporation approximation up to E_n ~ 200 MeV, in which first chance pre-equilibrium neutron emission was taken into account [3.1.17]. Fission probabilities of U nuclei in the domain of the emissive fission reaction ^{238}U(n,xnf) were estimated without making any distinction regarding symmetric or asymmetric fission (i.e. super long, S1 or S2 modes). These fission probabilities provide correct estimates of lumped fission competition against neutron emission. Damping of the collective modes' contribution to the level density at excitation energies higher than ~20 MeV for axial symmetric saddle and equilibrium deformations was shown to be essential for the description of the observed fission cross-section. Effective estimates of intrinsic level densities were obtained, which define the competition between fission and neutron emission at high excitation energies when rotational collective modes are completely damped.

Competition of the symmetric and asymmetric fission of U nuclei would depend essentially on the excitation energies of the U nuclei emerging after the emission of pre-fission (n,xnf) neutrons. Level densities can be anticipated to play a key role in the relevant saddle deformation. We can probe the sensitivity of the calculated super long mode and lumped asymmetric (S1 + S2) mode yields to the damping of triaxial deformations at the outer saddles of U nuclei. The range of mass numbers of U nuclei that make an appreciable contribution to the fission observables depends on fission barriers and intrinsic level densities at saddle and equilibrium deformation. We anticipate that the ratio of symmetric to all fission events will strongly depend on the relative contributions to the observed cross-section of fission chances with different numbers of pre-fission neutrons. The analysis of the ratio of symmetric to all fission events might be a sensitive tool for the partitioning of the fission (n,xnf) chance contribution to the fission observables.

With an increase of the target nuclide fissility, the number of nuclei that make an appreciable contribution to the fission observables will tend to be lower. We have developed an approach to describe the ^{238}U(n,f) cross-section and branching ratio of symmetric/asymmetric fission up to 200 MeV incident neutron energy. This model will be applied to the observed ^{235}U(n,f), ^{233}U(n,f), ^{232}Th(n,f), ^{237}Np(n,f) and ^{238}U(p,f) fission cross-section data.

We will predict ^{235}U(n,f)^{sym}, ^{233}U(n,f)^{sym}, ^{232}Th(n,f)^{sym}, ^{237}Np(n,f)^{sym} and ^{235}U(n,f)^{asym}, ^{233}U(n,f)^{asym}, ^{232}Th(n,f)^{asym} and ^{237}Np(n,f)^{asym} fission cross-sections, which represent a wide range of target nuclide fissilities. Analyses of observed neutron and proton induced fission cross-sections would provide valuable information about the relative contributions of emissive fission. The possibility of using proton induced fission yields can then be defined to estimate the neutron induced fission yields at high excitation energies.

3.1.2. Statistical model

At least two stages can be distinguished in the interaction of high energy neutrons with heavy actinide nuclei. The fast emission of secondary nucleons might take place via direct, semi-direct or pre-equilibrium mechanisms in the first stage. Fission is a relatively slow process of collective deformations of the entire nucleus and could only compete with light particle emission in an equilibrated nucleus when excitation in the composite nucleus is thermalized (i.e. at the second, slow stage of interaction). At incident neutron energies of several hundred MeV, the first fast stage might be treated via a series of pair-like interactions of incident neutrons with nucleons of a target nucleus [3.1.18]. A hierarchy of models was developed for lower incident neutron energies that predict emitted nucleon spectra and reaction cross-sections [3.1.19, 3.1.20]. The relative importance of the fast and slow stages depends significantly on the incident neutron energy. We assume that for neutron energies up to E_n ~ 200 MeV the first stage of the n + ^{238}U interaction might be modelled with the pre-equilibrium emission of neutrons. As shown in Ref. [3.1.21], such an approach reproduces pre-fission neutron spectra as well as ^{238}U(n,f) and ^{238}U(n,xn) reaction cross-sections up to 20 MeV. The present statistical model of the fission reaction assumes fission/neutron evaporation competition during the decay of an excited compound nucleus (formed after first chance emission of pre-equilibrium neutrons [3.1.22] and treated with a simple version of the exciton model [3.1.23, 3.1.24]). Equilibration is treated with a set of master equations that describe the evolution of the excited nucleus states, classified by the number of particles plus holes [3.1.22]. The pre-equilibrium emission is modelled via different nucleon emission rates that are higher when incident and emitted nucleons are the same type, and lower when they are the opposite type [3.1.24]. Transition rates during equilibration of excited composite nuclei through a series of two body collisions are also different, being higher in the case of the (n,p) and (p,n) reactions [3.1.25] when compared with the (n,n) and (p,p) reactions.

We assume that the emissive fission contribution comes only from a chain of U nuclei. Fission of other nuclei, for example ^{238}Pa and ^{237}Pa, might contribute to the observed fission reaction via emissive fission reactions if first chance pre-equilibrium emission of protons can be taken into account. The probability of pre-equilibrium emission of protons or other light charged particles is much lower than that of neutrons. The contribution of pre-equilibrium emission of protons to the n + ^{238}U interaction could be estimated on the basis of a consistent analysis of ^{238}U(p,f), ^{238}U(p,n) and ^{238}U(p,3n) data up to E_p ~ 30 MeV [3.1.25]. Proton induced fission preceded by the emission of a pre-equilibrium proton (i.e. ^{238}U(p,pxnf)) at the fission/evaporation stage gives a very small contribution to the observed ^{238}U(p,f) fission cross-section, compared with the ^{238}U(p,xnf) reaction that leads to fission of Np nuclei [3.1.17]. The fissilities of relevant Np nuclei are generally higher than those of U nuclei. The same behaviour occurs in the case of the ^{238}U(n,pxnf) and ^{238}U(n,xnf) reactions, and the contributions of ^{238}U(n,pxnf) reactions are much lower (about three to four orders of magnitude) than in the ^{238}U(n,xnf) chain, another factor that contributes to the fissilities of the relevant Pa nuclei while being generally lower than those of the U nuclei.

3.1.2.1. Fission cross-section

A calculated fission cross-section is a complex function of compound nucleus formation cross-section, fission barrier parameters, intrinsic and collective mode contributions to the level density at equilibrium, and saddle point deformations for nuclei emerging in the decay chain. A coupled channel model has been adopted for the calculation of the neutron reaction cross-section. Reasonable estimates of the reaction cross-section up to E_n ~ 200 MeV can be determined by obtaining optical potential parameters with the 0^+–2^+–4^+–6^+–8^+ coupling scheme within a rigid rotator model from fitting ^{238}U total data up to E_n ~ 200 MeV [3.1.26].

The first chance fission cross-section for the super long mode could be defined as:

$$\sigma_{\mathrm{nfSL}}(\mathrm{E_n}) = \mathrm{q}(E_n)\frac{\pi\lambda^2}{2(2I+1)} \times \sum_{\mathrm{lJ}\pi}(2\mathrm{J}+1)\mathrm{T_l}(\mathrm{E_n})\mathrm{P}_{\mathrm{fSL}}^{\mathrm{J}\pi}(E_n) \quad (3.1.1)$$

where $q(E_n)$ is the fraction of first composite ^{239}U nuclides that survive the pre-equilibrium emission of first neutrons, $T_1(E_n)$ are neutron transmission coefficients, and $P_{\mathrm{fSL}}^{\mathrm{J}\pi}(\mathrm{E_n})$ is the super long mode fission probability. The cross-section for the asymmetric (S1 + S2) mode fission can be defined in

a similar way, and we will concentrate below on the analysis of super long mode fission. Contributions of super long mode fission to the observed fission cross-section are defined by the following equation:

$$\sigma_{\mathrm{nFSL}}(E_n) = \sigma_{\mathrm{nfSL}}(E_n) + \sum_{x=1}^{X} \sigma_{\mathrm{n,xnffSL}}(E_n) \qquad (3.1.2)$$

coming from (n,xnf), x = 1, 2, 3...X fission reactions of relevant equilibrated uranium nuclei, and can be calculated using fission probability estimates $\mathrm{P}^{\mathrm{J}\pi}_{\mathrm{fSL}}(\mathrm{E_n})$:

$$\sigma_{\mathrm{n,xnfSL}}(E_n) = \sum_{J\pi} \int_0^{U_{\max}} W^{J\pi}_{x+1}(U) P^{J\pi}_{fSL(x+1)}(U)\, dU \qquad (3.1.3)$$

where $W^{J\pi}_{x+1}(U)$ is the population of the (x + 1)th nucleus at excitation energy U after emission of x neutrons. The excitation energy $\mathrm{U_{max}}$ is defined by the incident neutron energy (E_n) and energy removed from the composite system by ^{238}U(n,xnf) reaction neutrons. The fission probability $P^{J\pi}_{fSL(x+1)}(U)$ is related to the symmetric scission of the xth fissioning nucleus, and can be approximated as:

$$\mathrm{P}^{\mathrm{J}\pi}_{\mathrm{fSL(x+1)}}(U) = \frac{\mathrm{T}^{\mathrm{J}\pi}_{\mathrm{fSLx}}(U)}{\mathrm{T}^{\mathrm{J}\pi}_{\mathrm{fSLx}}(U) + \mathrm{T}^{\mathrm{J}\pi}_{\mathrm{fSIx}}(U) + \mathrm{T}^{\mathrm{J}\pi}_{\mathrm{fSIIx}}(U) + \mathrm{T}^{\mathrm{J}\pi}_{\mathrm{nx}}(U) + \mathrm{T}^{\mathrm{J}\pi}_{\gamma x}(U)} \qquad (3.1.4)$$

where the super long mode fission probability ($P^{J\pi}_{fSL(x+1)}(U)$) depends on $\mathrm{T}^{\mathrm{J}\pi}_{\mathrm{fSLx}}(U)$, $\mathrm{T}^{\mathrm{J}\pi}_{\mathrm{fSIx}}(U)$, $\mathrm{T}^{\mathrm{J}\pi}_{\mathrm{fSIIx}}(U)$, $\mathrm{T}^{\mathrm{J}\pi}_{\mathrm{nx}}(U)$ and $\mathrm{T}^{\mathrm{J}\pi}_{\gamma x}(U)$, the transmission coefficients of the super long (SL), S1, S2 mode fission, neutron emission and radiative decay channels, respectively. The index 'x' refers to the nuclides fissioning in the (n,xnf) reaction, and will be omitted from the equations developed below for simplicity.

Consider a double humped fission barrier model [3.1.27] in which the neutron induced super long mode fission process can be viewed as a two step process (i.e. successive crossing over the inner hump A and outer hump BSL), while separate outer barrier humps BS1 and BS2 are assumed for S1 and S2 modes. Hence, the transmission coefficient of the super long mode fission channel $\mathrm{T}^{\mathrm{J}\pi}_{\mathrm{fSL}}(U)$ can be approximated by the equation [3.1.28, 3.1.29]:

$$\mathrm{T}^{\mathrm{J}\pi}_{\mathrm{fSL}}(U) = \frac{\mathrm{T}^{\mathrm{J}\pi}_{\mathrm{fA}}(U)\,\mathrm{T}^{\mathrm{J}\pi}_{\mathrm{fB}}(U)}{\mathrm{T}^{\mathrm{J}\pi}_{\mathrm{fA}}(U) + \mathrm{T}^{\mathrm{J}\pi}_{\mathrm{fB}}(U)}. \qquad (3.1.5)$$

The fission transmission coefficients $\mathrm{T}^{\mathrm{J}\pi}_{\mathrm{fi}}(U)$ are defined by the discrete transition states and level density $\rho_{fi}(\varepsilon, J, \pi)$ of the fissioning nucleus at the inner and outer saddles (i = A, BSL, BS1, BS2):

$$\mathrm{T}^{\mathrm{J}\pi}_{fi}(U) = \sum_{K=-J}^{J} \mathrm{T}^{\mathrm{JK}\pi}_{\mathrm{fi}}(U) + \int_0^U \frac{\rho_{fi}(\varepsilon, J, \pi)\, d\varepsilon}{1 + \exp\left(2\pi\left(E_{fi} + \varepsilon - U\right)/\hbar\omega_i\right)}. \qquad (3.1.6)$$

The outer fission barrier height (E_{fBSL}) and width ($\hbar\omega_{BSL}$) are correlated with the axial asymmetry of the outer saddle point, which increases the level density $\rho_{fBSL}(\varepsilon, J, \pi)$ at outer saddle point deformations while the width should also influence the energy dependence of the super long mode yield.

3.1.2.2. Level density

The total nuclear level density $\rho(U, J, \pi)$ is represented as the factorised contribution of quasi-particle and collective states [3.1.30]. Quasi-particle level densities $\rho_{\mathrm{qp}}(U, J, \pi)$ were calculated with a phenomenological generalized super fluid model by Ignatyuk et al. [3.1.31], taking into account shell, pairing and collective effects:

$$\rho(U, J, \pi) = K_{rot}(U, J) K_{vib}(U) \rho_{qp}(U, J, \pi) \qquad (3.1.7)$$

where $K_{rot}(U, J)$ and $K_{vib}(U, J)$ are the factors of rotational and vibrational enhancement. At low intrinsic excitation energies of a few MeV, few-quasi-particle effects are essential, and their treatment is described in Ref. [3.1.9]. At saddle and ground state deformations, $K^{sym}_{rot}(U, J)$ is defined by the deformation order of symmetry adopted from shell correction model calculations by Howard and Möller [3.1.32]. Consider axially symmetric deformations (U nuclei at equilibrium deformation, neutron deficient U nuclei (N ≤ 144) at inner saddle deformations and S1(S2) modes at outer saddle deformations):

$$K_{rot}^{sym}(U,J)=\sum_{K=-J}^{J}\exp\left(-K^2/K_o^2\right)\approx\sigma_{\perp}^2 \qquad (3.1.8)$$

while for axially asymmetric deformations (U nuclei at inner saddle deformations for N > 144 and super long mode outer saddle):

$$K_{rot}^{asym}(U)\cong 2\sqrt{2\pi}\,\sigma_{\perp}^2\sigma_{|} \qquad (3.1.9)$$

where K is the projection of the spin J on the nuclear symmetry axis, $K_0^2=\left(\sigma_{|}^{-2}-\sigma_{\perp}^{-2}\right)^{-1}$; $\sigma_{|}^{-2}=F_{|}t$ is the spin distribution parameter, and t is the thermodynamic temperature $F_{|}=(6/\pi^2\langle m^2\rangle(1-2/3\varepsilon)$ in which $\langle m^2\rangle$ is the average value of the squared projection of the angular momentum of the single particle states and ε is the quadrupole deformation parameter. The other spin cut-off parameter $\sigma_{\perp}^2$ is given by the equation:

$$\sigma_{\perp}^2=F_{\perp}t=0.4mr_0^2\hbar^{-2}\left(1+1/3\varepsilon\right) \qquad (3.1.10)$$

where $F_{\perp}$ is the nuclear momentum of inertia perpendicular to the symmetry axis (equals the rigid body value at high excitation energies (pairing correlations are completely destroyed), and there are experimental values at zero temperature so that interpolations can be made using the generalized super fluid model equations [3.1.31]. The mass asymmetry for S1(S2) modes at outer saddles doubles the rotational enhancement factors, as defined by Eqs (3.1.8, 3.1.9).

Adiabatic approximation might be valid up to a critical energy (U_r), with damping of rotational modes being anticipated by Hansen and Jensen [3.1.33] at higher excitation energies. The damping of rotational modes as a function of excitation energy might differ for axially symmetric and triaxial nuclei:

$$K_{rot}^{ax}(U)=\left(\sigma_{\perp}^2-1\right)F(U)+1 \qquad (3.1.11)$$

$$K_{rot}^{tax}(U)=K_{rot}^{ax}(U)\left(\left(2\sqrt{2\pi}\sigma-1\right)F(U)+1\right) \qquad (3.1.12)$$

$$F(U)=(1+\exp(U-U_r)/\mathrm{d}_r)^{-1}. \qquad (3.1.13)$$

Shell effects in level density are modelled with the shell correction dependence of the '*a*' parameter, as recommended by Ignatyuk et al. [3.1.31]. The value of the main *a* parameter is defined by fitting neutron resonance spacing $\langle D_{obs}\rangle$ or systematics [3.1.34], while the shell correction dependence of the *a* parameter is defined using the following equation [3.1.30]:

$$a(U)=\begin{cases}\tilde{a}\left(1+\delta Wf(U-E_{cond})/\left(U-E_{cond}\right)\right),\\ U>U_{cr}=0.47a_{cr}\Delta^2-m\Delta\\ a(U_{cr})=a_{cr},U\le U_{cr}=0.47a_{cr}\Delta^2-m\Delta\end{cases} \qquad (3.1.14)$$

where m = 0, 1, 2 for even–even, odd-A and odd–odd nuclei, respectively; f(x) = 1 – exp(–0.064x) is the dimensionless function defining the damping of shell effects; condensation energy is $E_{cond}=0.152a_{cr}\Delta^2$, where Δ is the correlation function, ã is the value of the asymptotic *a* parameter at high excitation energies, and a_{cr} is the *a* parameter value at the excitation energy $U=U_{cr}$. When $\tilde{a}$ parameter values for equilibrium $\tilde{a}_n$ and saddle $\tilde{a}_f$ deformations are identical, the a_f/a_n ratio of fissioning and residual nuclei depends solely upon the respective shell correction values of $\delta W_{f(n)}$ taken from Ref. [3.1.35] (δW_n) and Ref. [3.1.28] (δW_f). See Ref. [3.1.9] for more details.

3.1.3. Analysis of fission cross-sections

The observed fission cross-section (σ_{nF}(Em)) can be calculated as follows:

$$\begin{aligned}\sigma_{nF}(\mathrm{E_n})&=\sigma_{nF}^{sym}+\sigma_{nF}^{asym}\\&=\sigma_{nFSL}(\mathrm{E_n})+\sigma_{nF(S1+S2)}(\mathrm{E_n})\\&=\sigma_{nfSL}(\mathrm{E_n})+\sum_{x=1}^{X}\sigma_{n,xnfSL}(\mathrm{E_n})\\&\quad+\sigma_{nf(S1+S2)}(\mathrm{E_n})+\sum_{x=1}^{X}\sigma_{n,xnf(S1+S2)}(\mathrm{E_n})\end{aligned} \qquad (3.1.15)$$

These equations depend on symmetric $\sigma_{nFSL}(E_n)$ and asymmetric $\sigma_{nF(S1+S2)}(E_n)$ fission cross-sections, and contributions of emissive fission to both terms. We will show that the contributions of emissive fission chances are strongly dependent on the asymptotic value of the a_f parameter, while the branching ratio of symmetric/asymmetric fission depends on both the contributions of fission chances and the damping of collective modes at saddle deformations.

3.1.3.1. Fission barrier parameters

Shell correction model calculations by Howard and Möller [3.1.32] for actinide nuclei predicted axial asymmetry of the inner fission barrier A for neutron numbers N > 144 and axial symmetry for N ≤ 144, whereas the outer barrier B was predicted to be mass asymmetric. Uranium inner and outer fission barrier parameters are relevant for these asymmetries, and were defined in Refs [3.1.36, 3.1.37]. These fission barrier parameters fit neutron induced fission cross-section data for actinide target nuclides up to emissive fission thresholds, and reproduce available neutron induced fission cross-sections up to E_n of 20 MeV [3.1.38]. Inner E_{fA}, $\hbar\omega_{fA}$ and outer E_{fB}, $\hbar\omega_{fB}$ barrier heights and widths correspond to lumped (S1 + S2) mode asymmetric fission, that will be employed to calculate the combined yield of lumped (S1 + S2) mode fission. Fission barrier parameters for light U nuclei (A < 230) were defined by maintaining the difference $(E_{fA(B)} - B_n)$, where B_n is the neutron binding energy (depends on the odd/even type of the number of neutrons). Axial symmetry is assumed at the inner saddle A for neutron deficient U nuclei ($E_{fAB} < E_{fB}$).

Outer barrier parameters for the super long mode (E_{fBSL}) and width ($\hbar\omega_{BSL}$) depend on the saddle symmetry. However, symmetry of the outer saddle shape for the super long mode fission of U nuclei has not been defined unambiguously. A rather strong symmetric fission yield was observed below the emissive fission threshold in the fission reactions of lower mass nuclides ^{227}Ac, ^{228}Ac and ^{228}Ra formed in reactions ^{226}Ra(^{3}He,p)^{228}Ac, ^{226}Ra(^{3}He,d)^{227}Ac [3.1.7] and ^{226}Ra(t,p)^{228}Ra [3.1.8], respectively. The double humped fission barrier model was used to fit the data, assuming arbitrarily that symmetric fission "involves a separate outer barrier that is axially asymmetric" [3.1.7, 3.1.8]. The potential energy surface was investigated with the shell correction model as a function of axial and mass degrees of freedom in the vicinity of the second saddle point for ^{228}Ra and ^{238}U [3.1.39]. Two distinct saddle points were separated by ~1 MeV, and were distinguishable for ^{228}Ra: the normal mass asymmetric saddle (i.e. S1 or S2), which is stable with respect to triaxial deformation; and the mass symmetric saddle point with axially asymmetric deformations (i.e. super long). As regards the threshold energy and excitation energy dependence, these conclusions are consistent with measured fission probability data [3.1.7, 3.1.8]. However, the situation is less certain in the case of the ^{238}U fissioning nuclide. The mass asymmetric saddle and mass symmetric outer saddle were found to be separated by ~700 keV, but the ridge that separates the two saddles of ^{238}U was lower than in the case of ^{228}Ra. The lower ridge separating the symmetric and asymmetric mode valleys was discovered recently by Möller et al. [3.1.40] through extensive shell correction model calculations in the case of ^{234}U. Möller et al. [3.1.40] have shown that mass symmetric saddle and mass asymmetric saddle modes are well separated in the case of ^{228}Ra until scission, while for U nuclei the situation is less certain. Thus, the symmetric outer saddle point for ^{234}U is ~1 to 2 MeV higher than the asymmetric saddle point, but splitting of the asymmetric valley into S1 and S2 modes was not predicted. Since S1 and S2 saddle point asymmetries would be similar, we have assumed one symmetric and one asymmetric mode for fission probability calculations. This assumption provides a means of interpreting the super long mode fission yield in the ^{238}U(n,f) and ^{235}U(n,f) reactions up to E_n ~ 6 MeV. Partial S1 and S2 mode fission yields could be easily fitted with adopted values of the $E_{fA(B)}$ and $\hbar\omega_{fA(B)}$ parameters by varying $E_{fBS1(S2)}$ and $\hbar\omega_{BS1(S2)}$.

Statistical Hauser–Feshbach model calculations have shown that level density modelling at the equilibrium ground state of ^{238}U and saddle deformations of ^{239}U represent a key tool in fitting neutron induced super long mode fission cross-section data [3.1.9] for ^{238}U(n,f) up to E_n ~ 6 MeV. Super long mode fission barrier parameters for the ^{239}U and ^{236}U fissioning nuclei were found to be higher than those of asymmetric modes by ~3.5 MeV, and a barrier width $\hbar\omega_{BSL}$ = 2.25 MeV was obtained. The contributions of lower mass U nuclides via (n,xnf) reaction to the observed ^{239}U symmetric fission might be obtained by assuming the same difference of the outer barriers for the symmetric super long and asymmetric S1(S2) fission modes $(E_{fBSL} - E_{fBS1(S2)})$ ~ 3.5 MeV. Shell correction values are defined as $(\delta W_{fBSL} - \delta W_{fBS1(S2)})$ ~ 3.5 MeV, assuming $\delta W_{fS1(S2)}$ ~ 0.6 MeV [3.1.28] (i.e. for the higher height of the outer saddle, the higher shell correction value is assumed). Asymmetric fission of ^{239}U will dominate for excitation energies up to the emissive fission threshold, because a fission barrier leading to the asymmetric valley is much lower than one leading to the symmetric valley. We assumed that ^{239}U and ^{236}U nuclei at the outer mass symmetric saddles might be unstable with respect to triaxial deformations. The same instability was assumed for the inner saddle of U

nuclei with N > 144. However, for higher excitation energies, symmetric fission may dominate asymmetric fission since fission transmission coefficients for symmetric $T^{J\pi}_{fSLx}$ fission could possibly increase faster than those for asymmetric $T^{J\pi}_{fS1x}$, $T^{J\pi}_{fS2x}$ fission. Two factors might contribute to this behaviour: super long mode outer saddle triaxiality, and the higher value of the relevant shell correction, δW_{fBSL}.

3.1.3.2. Triaxial damping and a_f energy dependence

Damping of the contribution of the collective modes to the level density at the saddles is an important factor in describing fission. When damping of the axial collective contribution to the level density at the inner and the outer saddle occurs and equilibrium deformation is assumed, the major contribution to the observed ^{238}U(n,f) fission cross-section comes from neutron deficient U fissioning nuclei [3.1.17]. We assume rather strong damping of the contribution of the axial symmetric rotational mode, both at equilibrium and saddle deformation (i.e. parameter values $U_r = 20$ MeV and $d_r = 5$ MeV of Eq. (3.1.13) are assumed). However, damping of axial collective modes leads to a reduction of contributions from predecessors (lower chance fission) and to an increase of those contributions from successors (higher chance fission), so that the net effect is only a slight decrease in the observed ^{238}U(n,f) cross-section. Consequently, the calculated fission cross-section overestimates the measured data for $E_n > 20$ MeV and approaches asymptotically the neutron absorption cross-section, which is appreciably higher than the observed ^{238}U neutron induced fission cross-section. Damping of triaxial deformations at high excitations for the inner saddle (U nuclei with N > 144) could not be studied in detail, since only the fissioning nuclides ^{239}U, ^{238}U and ^{237}U are assumed to have triaxial inner saddles [3.1.32].

The calculated $\sigma_{nF} = \sigma^{sym}_{nF} + \sigma^{asym}_{nF}$ fission cross-section can be reduced by decreasing the contribution of fission chances, both with low and high numbers of pre-fission neutrons. This reduction can be achieved by decreasing the asymptotic value of the a_f parameter:

$$\tilde{a}_f(U,A) = \tilde{a}_f(A)\left(1 - 0.1\left((U-20)/U\right)^{1/4}\right) \quad (3.1.16)$$

where U is the intrinsic excitation energy of $^{239\text{-}x}$U nuclides, x = 0, 1, 2,... X. The term $\tilde{a}_f$(U, A) decreases by ~10% at the highest excitations, and therefore we could reproduce the observed trend of the ^{238}U(n,f) data to $E_n \sim 200$ MeV. Decrease of the asymptotic value of the a_f parameter leads to a major redistribution of the contributions of multiple chance fission reactions to the observed fission reaction. This behaviour seems to be important in the description of the observed fission cross-section for target nuclei with low fissility, such as that of ^{232}Th. Competition between symmetric and asymmetric fission for the higher fissility target ^{238}U nuclide appears to be very sensitive to the relative contributions of multiple chance fission reactions. Other factors may be important (e.g. the influence of fission barriers of neutron deficient nuclides on σ_{nF}(En) in the vicinity of the neutron shell N = 126). The influence of changing the shape of nuclei in the vicinity of the N = 126 shell from deformed to spherical may also be important [3.1.41]. We anticipate that the lowering of a_f at U = 20 MeV might be perceived as a lumped effect of these factors.

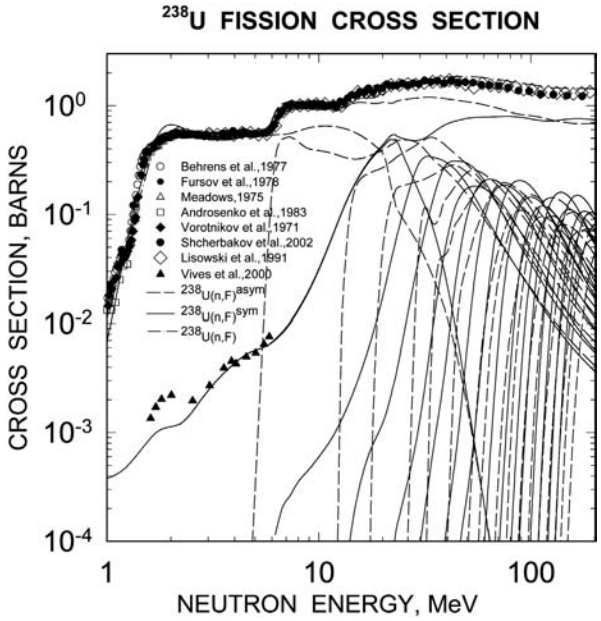

FIG. 3.1.1. ^{238}U(n,f) cross-section: super long fission mode cross-section data of Vivès et al. [3.1.10] for ^{238}U(n,f) are shown as black triangles — short dashed lines show asymmetric fission cross-sections; solid lines show symmetric fission cross-sections for triaxial outer saddles; the dot–dashed line shows the sum of symmetric and asymmetric fission cross-sections. An asymptotic value $\tilde{a}_f$(U, A) of the a_f parameter is employed (Eq. (3.1.16)), and triaxial damping at the outer super long mode saddle is assumed (Eqs (3.1.12, 3.1.13)).

3.1.3.2.1. Fission cross-section and branching ratio

Figure 3.1.1 shows the calculated symmetric ($^{238}U^{sym}_{n,F}$), asymmetric ($^{238}U^{asym}_{n,F}$) and symmetric + asymmetric ^{238}U(n,f) fission cross-sections up to E_n ~ 200 MeV for different assumptions concerning the contributions of fission chances (n,xnf) and the damping of triaxial deformations at outer symmetric saddles. The curves in Fig. 3.1.1 correspond to the energy dependent asymptotic value $\tilde{a}_f(U, A)$ of the a_f parameter, assuming damping of triaxial collective modes at the outer saddle. Calculations show that emissive fission chance contributions for either symmetric or asymmetric fission do not depend significantly on triaxial damping. Distributions of fission chances for symmetric and asymmetric fission are also rather similar, as demonstrated more explicitly in Fig. 3.1.2 — asymmetric relative contributions of multiple chance fission, ^{238}U(n,xnf)^{asym}/^{238}U(n,f)^{asym}, for E_n = 50, 100 and 200 MeV are compared with the symmetric data, ^{238}U(n,xnf)^{sym}/^{238}U(n,f)^{sym}. The cross-sections corresponding to the symmetric and asymmetric fission chance distributions are shown in Fig. 3.1.1. Distributions for the E_n = 50 MeV peak around pre-fission neutron number x = 3. At higher energies E_n = 100 and 200 MeV, the peak of the distribution of fission chances shifts to higher numbers of pre-fission neutrons and becomes skewed. The situation is quite different when distributions of fission chances in Fig. 3.1.1 are compared with those corresponding to the asymptotic value $\tilde{a}_f(U, A)$ of the a_f parameter independent of the energy.

Figure 3.1.2 shows the relative symmetric ^{238}U(n,xnf)^{sym}/^{238}U(n,f)^{sym} contributions of fission chances for E_n = 50, 100 and 200 MeV. The solid lines represent the energy dependent asymptotic value $\tilde{a}_f(U, A)$ of the a_f parameter (corresponding to the fission cross-sections shown in Fig. 3.1.1), while the dashed lines show the contributions of relative fission chances for a_f independent of the excitation energy. When a_f is independent of the excitation energy, the distribution for E_n = 50 MeV peaks around the pre-fission neutron number x = 1. At higher energies of E_n = 100 and 200 MeV, the peak of the fission chance distribution shifts towards x = 3 pre-fission neutrons; for E_n = 200 MeV, the peak becomes skewed, with a higher right wing. When energy dependence of the asymptotic value $a_f(U, A)$ of the a_f parameter is assumed, the distributions change drastically: at E_n = 50 MeV the distribution is still peaked around x = 3; for E_n = 100, the peak of the fission chance distribution shifts towards x = 7; for E_n = 200 MeV the distribution is rather wide and skewed, and centres around x = 15 (see Fig. 3.1.3). The odd–even effect is evident in the distribution at E_n = 200 MeV, which means that the fissioning U nuclei are relatively cold due to the high pre-fission

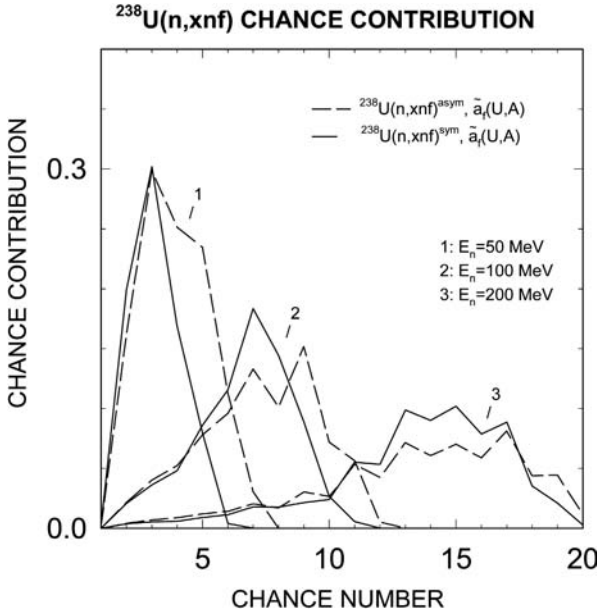

FIG. 3.1.2. Distribution of fission chances for $^{238}U(n,xnf)^{sym}$ (solid lines) and $^{238}U(n,xnf)^{asym}$ (dashed lines) reactions for the energy dependent asymptotic value $\tilde{a}_f(U, A)$ of the a_f parameter (see Eq. (3.1.16)).

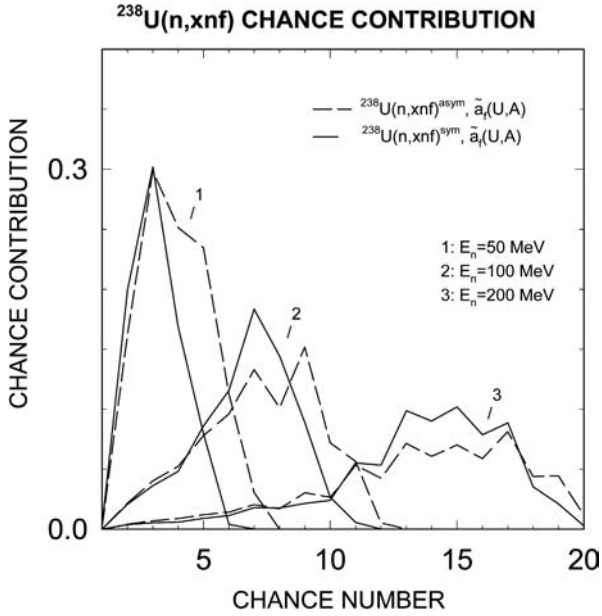

FIG. 3.1.3. Distribution of fission chances for the $^{238}U(n,xnf)^{sym}$ reaction for energy dependent $\tilde{a}_f(U, A)$ (solid lines), and energy independent $\tilde{a}_f(A)$ (dashed lines).

neutron number. The observed fission cross-section ^{238}U(n,f) is reproduced in both cases, but symmetric/asymmetric branching ratios are different. As described below for this particular fission chance distribution, we can reproduce the branching ratio of symmetric/asymmetric fission. Another important point for the low fissility target nuclide ^{232}Th is that the observed fission cross-section could only be reproduced with a fission chance distribution favouring fission of neutron deficient Th nuclei.

3.1.3.2.2. Branching ratio for a_f(U, A)

When triaxial damping is assumed, the symmetric fission cross-section (σ_{nF}^{sym}) is higher than the asymmetric fission cross-section (σ_{nF}^{asym}) at $E_n \geq$ 150 MeV (see Fig. 3.1.1), which happens at $E_n \geq$ 80 MeV in the absence of triaxial damping. Relative contributions of σ_{nF}^{sym} and σ_{nF}^{asym} to the observed fission cross-section can be checked by comparing the calculated branching ratio ($r^{sym} = \sigma_{nF}^{sym} / \left(\sigma_{nF}^{sym} + \sigma_{nF}^{asym}\right)$) with the measured data of Zöller et al. [3.1.14], as shown in Fig. 3.1.4. The calculated ratio of the symmetric mode contribution to the observed fission cross-section is compared with the corresponding measured data that were deduced from the fission fragment total kinetic energy distribution (full circles) and mass total kinetic energy distributions (open circles) [3.1.14]. Assuming triaxial damping (see Fig. 3.1.1) with U_r = 30 MeV and d_r = 10 MeV (Eq. (3.1.13)), the experimental r^{sym} data in the energy range E_n ~ 10 to 200 MeV can be well reproduced by our calculations (solid line in Fig. 3.1.4). Damping of triaxial deformations at the outer saddle for the symmetric fission mode seems to be compatible with the data of Zöller et al. [3.1.14]. The dashed curve corresponds to 'no triaxial damping', which exceeds the experimental r^{sym} data for $E_n \geq$ 25 MeV. Symmetric and asymmetric fission cross-sections for both 'triaxial damping' and 'no triaxial damping' give a similar energy dependence of the branching ratio r^{sym}, but the contribution of symmetric fission seems to be rather high for $E_n \geq$ 40 MeV. There is a step-like structure in the measured r^{sym} data (open circles) in the energy range E_n of 20 to 40 MeV. Full black circles also predict the change in shape of the r^{sym} energy dependence — this step-like irregularity and further increase of the ratio r^{sym} above E_n ~ 30 MeV is due to the contribution of the symmetric fission of ^{238}U after emission of the first pre-fission neutron. Over the energy range E_n ~ 20 to 40 MeV, the symmetric fission of ^{238}U gives an appreciable

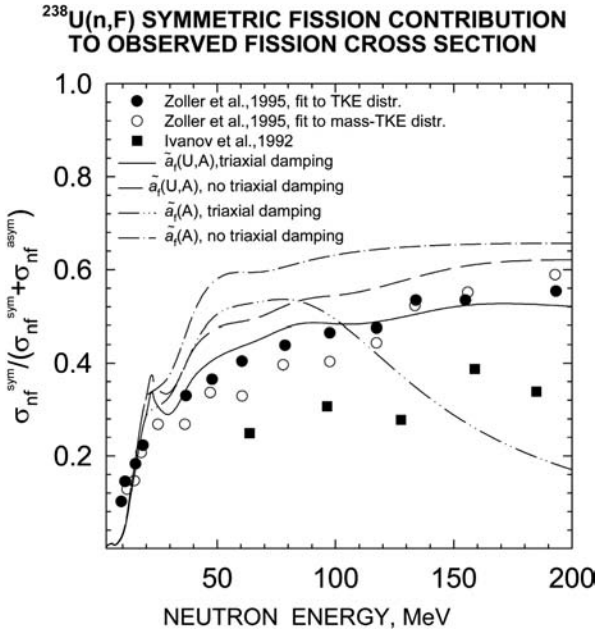

FIG. 3.1.4. Branching ratio r^{sym} of the symmetric to symmetric plus asymmetric fission events for the ^{238}U(n,f reaction. Symbols show measured data of Zöller et al. [3.1.14] and Ivanov et al. [3.1.42]. Solid and dashed lines correspond to the energy dependent asymptotic value $\tilde{a}_f$(U, A) of the a_f parameter, defined by Eq. (3.1.16). Damping of triaxial deformations (Eqs (3.1.12, 3.1.13)) is represented by the solid line, while the dashed line corresponds to the case of 'no triaxial damping'. Dot–dashed and double-dot–dashed lines correspond to the asymptotic value $\tilde{a}_f$(A) of the a_f parameter (which is independent of the excitation energy), where 'no triaxial damping' is represented by the dot–dashed line, and damping of triaxial deformations (Eqs (3.1.12, 3.1.13)) by the double dot–dashed line.

contribution to the observed total symmetric fission cross-section, which is higher than that of ^{239}U compound nuclide fission (see Fig. 3.1.1). Over the energy range E_n ~ 40 to 60 MeV (Fig. 3.1.1), the major contribution originates from symmetric fission of ^{237}U (via the ^{238}U(n,xnf) reaction).

3.1.3.2.3. Branching ratio for $\tilde{a}_f$(A)

Relative contributions of fission chances with low and high numbers of pre-fission neutrons have a major influence on the energy dependence of r^{sym} at incident neutron energies $E_n \geq$ 25 MeV. When an energy independent asymptotic value $\tilde{a}_f$(A) of the a_f parameter is employed, lower chances make predominant contributions to the observed fission cross-section (see Fig. 3.1.3). Consider no triaxial damping in which the calculated branching ratio r^{sym} is much higher than the data of Zöller et al. [3.1.14]

(dot–dashed curve in Fig. 3.1.4) — the calculated contribution of σ_{nF}^{sym} increases rapidly; and at $E_n \geq$ 40 MeV, the σ_{nF}^{sym} contribution is higher than that of σ_{nF}^{asym}. The assumption of rather weak damping of the triaxial collective contributions at the outer saddle deformations with U_r = 30 MeV and d_r = 10 MeV (Eq. (3.1.13)) is not helpful: calculated r^{sym} overestimates data in the energy range 30 to 100 MeV, but underestimates severely the data at E_n ~ 100 to 200 MeV (double dot–dashed curve in Fig. 3.1.4). The contribution of σ_{nF}^{sym} reaches that of σ_{nF}^{asym} at E_n ~ 45 MeV, but decreases sharply at $E_n \geq$ 100 MeV (see Fig. 3.1.4).

The r^{sym} data measured with a tagged photon beam in the range E_γ= 60–240 MeV give a much lower contribution of symmetric fission to the observed photo-fission cross-section [3.1.42]. This low level for the r^{sym} data can only be reproduced if a much higher contribution of fissions from very neutron deficient U nuclides can be adopted, and this requirement can only be achieved by introducing a much stronger and unrealistic energy dependence of the asymptotic value of the a_f parameter.

The observed r^{sym} ratio corresponds to different masses of fissioning U nuclei due to pre-fission neutron emission. As a consequence of the higher symmetric fission barrier, the number of nuclides that make an appreciable contribution to the 'observed' symmetric fission cross-section is lower than in the case of asymmetric fission events. Partial branching ratios $r_x^{sym} = \sigma_{n,xnf}^{sym} / (\sigma_{n,xnf}^{sym} + \sigma_{n,xnf}^{asym})$ for ^{238}U(n,nf), ^{238}U(n,3nf), ^{238}U(n,8nf) and ^{238}U(n,17nf) are shown in Fig. 3.1.5. Partial contributions to the ^{238}U(n,xnf)^{sym} and ^{238}U(n,xnf)^{asym} reactions correspond to the fission cross-sections shown in Fig. 3.1.1. r_x^{sym} for lower fission chances reaches higher values at lower incident neutron energies; and for the ^{238}U(n,nf) reaction, the maximum of $r_1^{sym} = \sigma_{n,nf}^{sym} / (\sigma_{n,nf}^{sym} + \sigma_{n,nf}^{asym})$ is reached at E_n ~ 40 MeV. The ratio r_x^{sym} for higher chances x = 3 or x = 8 has a similar shape, while r_x^{sym} at x = 17 never reaches the maximum value in the excitation energy range under consideration.

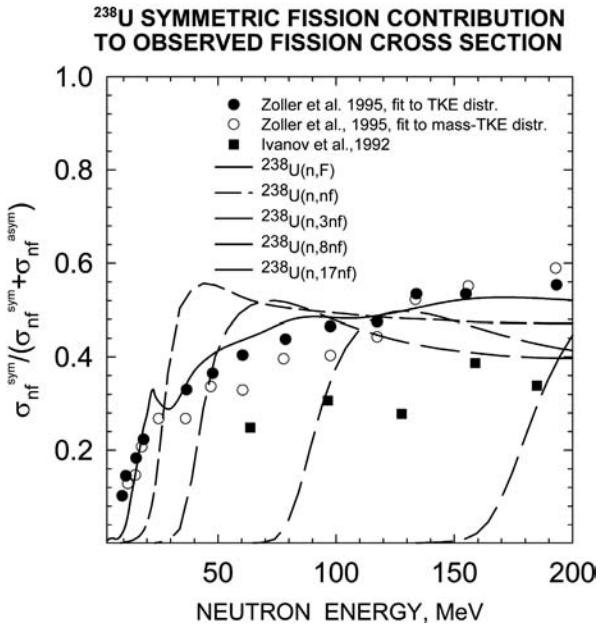

FIG. 3.1.5. Ratio r^{sym} of symmetric to symmetric plus asymmetric fission events for ^{238}U(n,f). The solid line is the same as in Fig. 3.1.4; dashed lines correspond to the respective ratios r_x^{sym} for partial ^{238}U(n,xnf) reactions with x = 1, 3, 8, 17.

3.1.3.3. Other actinides

3.1.3.3.1. ^{235}U(n,f)

Simple systematics of the level density parameters (($\delta W_{fBSL} - \delta W_{fBS1(S2)}$) ~ 3.5 MeV, $\delta W_{fS1(S2)}$ ~ 0.6 MeV) and the fission barrier ((E_{fBSL}-$E_{fBS1(S2)}$) ~ 3.5 MeV, $\hbar\omega_{BSL}$ ~ 2.25 MeV) for U nuclides reproduces the observed ^{235}U(n,f) [3.1.15] and ^{233}U(n,f) [3.1.16] fission cross-sections.

Figure 3.1.6 shows calculated symmetric ^{235}U(n,f)^{sym}, asymmetric ^{235}U(n,f)^{asym} and symmetric + asymmetric ^{235}U(n,f) fission cross-sections for the damping of axial and triaxial deformations at outer super long mode saddles. The energy dependent asymptotic value $\tilde{a}_f$(A, U) of the a_f parameter (see Eq. (3.1.16)) is employed. Data by Lisowski et al. [3.1.15] for the ^{235}U(n,f) reaction below 20 MeV are compatible with earlier data by Poenitz [3.1.44], Czirr and Sidhu [3.1.45] and Leugers et al. [3.1.46]. Solid lines show the symmetric cross-sections (^{235}U(n,f)^{sym}), and dashed lines show the asymmetric cross-sections (^{235}U(n,f)^{asym}) for the neutron induced fission of ^{235}U. The sum of ^{235}U(n,f)^{sym} and ^{235}U(n,f)^{asym} (dash–dotted line) agrees reasonably well with the observed ^{235}U(n,f)^{sym} up to E_n < 200 MeV.

3.1.3.3.2. ^{233}U(n,f)

The fissility of ^{233}U is much higher that that of ^{235}U. Figure 3.1.7 shows symmetric ^{233}U(n,f)^{sym}, asymmetric ^{233}U(n,f)^{asym} and symmetric plus asymmetric ^{233}U(n,xnf) fission cross-sections. The lines in Fig. 3.1.7 have the same meanings as in Fig. 3.1.6. There is a fair number of measured data for the ^{233}U(n,f) reaction cross-section at incident

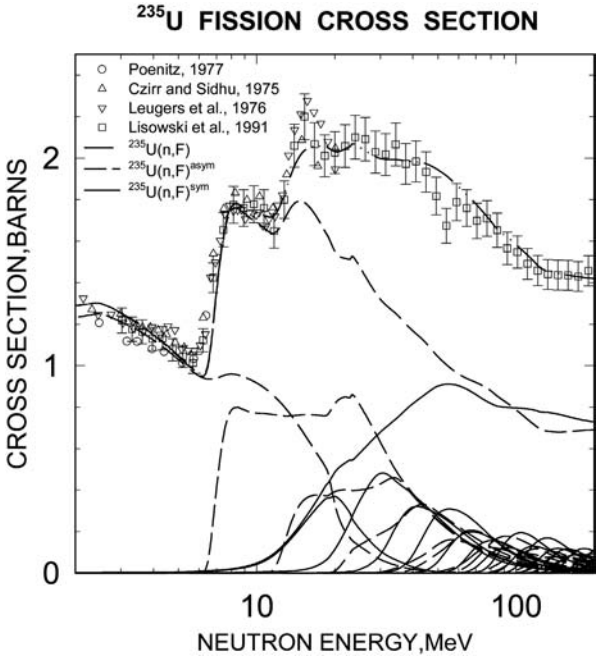

FIG. 3.1.6. $^{235}U(n,f)$ fission cross-section (dot–dashed line) and partial cross-sections for the $^{235}U(n,f)^{sym}$ and $^{235}U(n,xnf)^{sym}$ (solid lines), $^{235}U(n,f)^{asym}$ and $^{235}U(n,xnf)^{asym}$ (dashed lines) reactions, with the energy dependent asymptotic value $\tilde{a}_f(U, A)$ of the a_f parameter (see Eq. (3.1.16)).

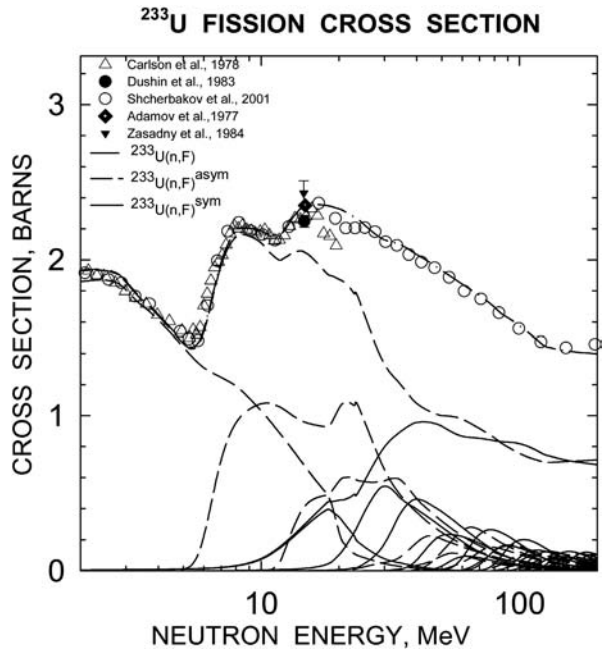

FIG. 3.1.7. $^{233}U(n,f)$ fission cross-section (dot–dashed line) and partial cross-sections for the $^{233}U(n,f)^{sym}$ and $^{233}U(n,xnf)^{sym}$ (solid lines), $^{233}U(n,f)^{asym}$ and $^{233}U(n,xnf)^{asym}$ (dashed lines) reactions, with the energy dependent asymptotic value $\tilde{a}_f(U, A)$ of the a_f parameter (see Eq. (3.1.16)).

neutron energies below 20 MeV, except for the recent data by Shcherbakov et al. [3.1.16] that were measured relative to the $^{235}U(n,f)$ cross-section (original data by Shcherbakov et al. [3.1.16] are systematically higher than most of the available data for $E_n < 20$ MeV). A limited set of published relative data are included in Fig. 3.1.7 for clarity — Carlson and Behrens [3.1.47] measured relative to the $^{235}U(n,f)$ cross-section, together with the absolute data by Dushin et al. [3.1.48], Adamov et al. [3.1.49] and Zasadny et al. [3.1.50] at E_n ~ 15 MeV. The data of Shcherbakov et al. [3.1.16] have been normalized to the absolute $^{233}U(n,f)$ fission data at E_n ~ 1.9 MeV by Kalinin [3.1.51]. Note that the sum of the calculated $^{233}U(n,f)^{sym}$ and $^{233}U(n,f)^{asym}$ reaction cross-sections (dash–dotted line) agrees reasonably well with the observed fission cross-section of the $^{233}U(n,f)$ reaction up to E_n ~ 20 MeV, and with the normalized data by Shcherbakov et al. [3.1.16] up to E_n ~ 200 MeV.

3.1.3.3.3. Branching ratio r^{sym}

Relative contributions of σ_{nF}^{sym} and σ_{nF}^{asym} to the observed fission cross-section can be checked by comparing the calculated branching ratio r^{sym} with the measured data of Zöller et al. [3.1.14] for $^{238}U(n,f)$, and the measured data below the emissive fission threshold of Hambsch [3.1.11] for $^{235}U(n,f)$ and Vives et al. [3.1.10] for $^{238}U(n,f)$ (see Fig. 3.1.8). Relative contributions of fission chances with low and high numbers of pre-fission neutrons have a major influence on the energy dependence of r^{sym} at $E_n \geq 25$ MeV. When the energy dependent asymptotic value $\tilde{a}_f(A)$ of the a_f parameter is employed, the higher chances make predominant contributions to the observed fission cross-section. 'Triaxial damping' reproduces the measured data of Zöller et al. [3.1.14] for $^{238}U(n,f)$ at $E_n \geq 10$ MeV. However, the data of Zöller et al. [3.1.14] for $^{238}U(n,f)$ at $E_n \leq 10$ MeV are judged to be too high by the authors themselves. Below the emissive fission threshold there is a systematic difference between the branching ratios determined by Hambsch [3.1.11] for $^{235}U(n,f)$ and those by Vivès et al. [3.1.10] for $^{238}U(n,f)$. The branching ratio for the $^{233}U(n,f)$ reaction can be calculated from fission barrier and level density parameter systematics, and falls between the two data sets.

Calculated branching ratios r^{sym} for the $^{233}U(n,f)$, $^{235}U(n,f)$ and $^{238}U(n,f)$ reactions exhibit different shapes around the $^{233,235,238}U(n,nf)$ reaction thresholds. A significant dip is observed for the

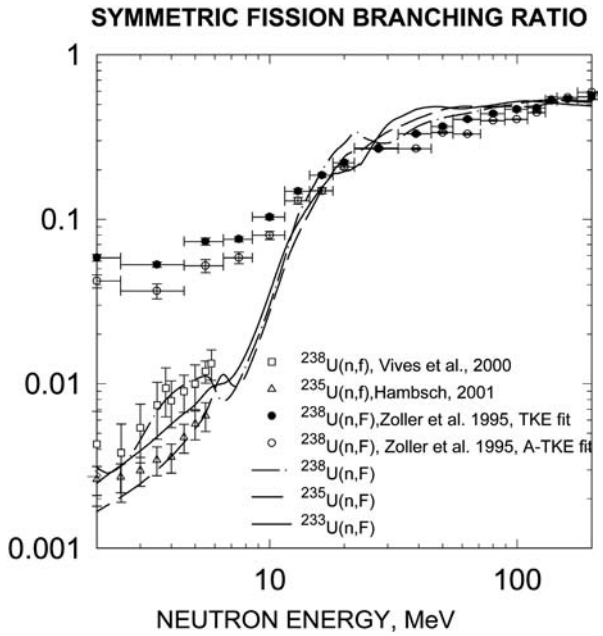

FIG. 3.1.8. Calculated branching ratio r_{sym} of symmetric to symmetric plus asymmetric fission events of $^{233}U(n,f)$ (solid line), $^{235}U(n,f)$ (dashed line) and $^{238}U(n,f)$ reaction (dot–dashed line). Symbols show measured data of Zöller et al. [3.1.14] for $^{238}U(n,f)$, Vivès et al. [3.1.10] for $^{238}U(n,f)$, and Hambsch [3.1.11] for $^{235}U(n,f)$. Solid and dashed lines correspond to the energy dependent asymptotic value $\tilde{a}_f(U, A)$ of the a_f parameter defined by Eq. (3.1.16), assuming damping of triaxial deformations.

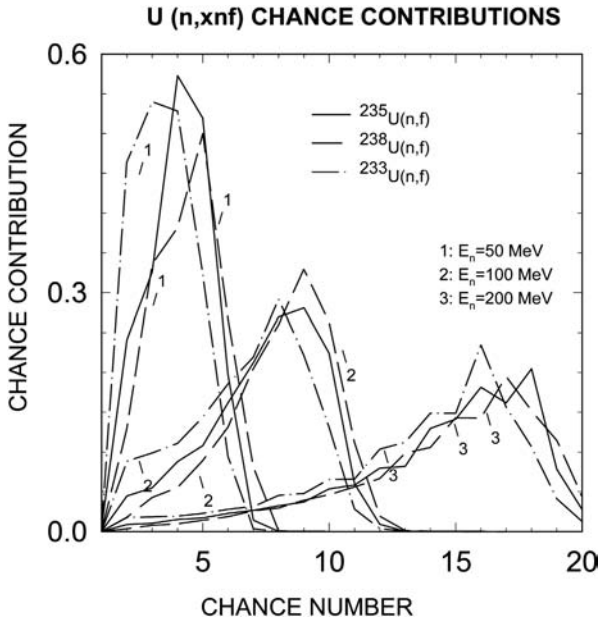

FIG. 3.1.9. Distribution of fission chances for $^{233}U(n,xnf)^{sym+asym}$ (dot–dashed line), $^{235}U(n,xnf)^{sym+asym}$ (solid lines) and $^{238}U(n,xnf)^{sym+asym}$ (dashed lines) for the energy dependent asymptotic value $\tilde{a}_f(U, A)$ of the a_f parameter (see Eq.(3.1.16)), assuming triaxial damping at the outer saddle of the super long mode.

^{238}U(n,f) reaction, and similar behaviour is predicted of lower amplitude for the ^{235}U(n,f) reaction, while this effect almost disappears in the case of the ^{233}U(n,f) reaction. These peculiarities are due to different emphases of the competitive processes within the U(n,f)^{sym} and U(n,f)^{asym} reactions because of the higher fission thresholds of symmetric fission modes compared with those of asymmetric fission. At incident neutron energies of $25 \leq E_n \leq 60$ MeV, symmetric fission makes the highest contribution to the observed fission cross-section in the ^{233}U(n,f) reaction, but the lowest in the ^{238}U(n,f) reaction. This behaviour can be explained in terms of different emissive fission contributions to the (n,f)^{asym} and (n,f)^{sym} reactions for the ^{233}U(n,f), ^{235}U(n,f) and ^{238}U(n,f) reactions. Figure 3.1.9 shows that the contributions of lower fission chances (i.e. chances with a lower number of pre-saddle neutrons) at incident neutron energies E_n = 50, 100 and 200 MeV are highest in the case of ^{233}U, and lowest in the case of ^{238}U. Thus, different shapes of the branching ratios r^{sym} for the ^{233}U(n,f), ^{235}U(n,f) and ^{238}U(n,f) reactions at $E_n \leq 60$ MeV may be attributed to the higher contributions of lower fission chances for higher target nuclide fissility, whereas they do not significantly differ at higher neutron energies.

3.1.3.3.4. ^{237}Np(n,f)

Figure 3.1.10 shows symmetric ^{237}Np(n,f)^{sym}, asymmetric ^{237}Np(n,f)^{asym} and symmetric + asymmetric ^{237}Np(n,f) fission cross-sections (lines in Fig. 3.1.10 have the same meaning as in Fig. 3.1.6). The sum of the calculated ^{237}Np(n,f)^{sym} and ^{237}Np(n,f)^{asym} reaction cross-sections (dash–dotted line) agrees well with the measured fission cross-section up to E_n = 200 MeV [3.1.16]. Data of Hambsch et al. [3.1.13] for the symmetric fission yield are also shown.

3.1.3.3.5. ^{238}U(p,f)

The ^{238}U(p,f) reaction can be calculated by means of the fission barrier and level density parameters of Np nuclei, as obtained by fitting the ^{237}Np(n,f) fission cross-section. ^{238}U(p,xnf) reactions should give an overwhelming contribution to the observed fission cross-section. The sum of the ^{238}U(p,f)^{asym} and ^{238}U(p,f)^{sym} cross-sections is compared with measured data in Fig. 3.1.11.

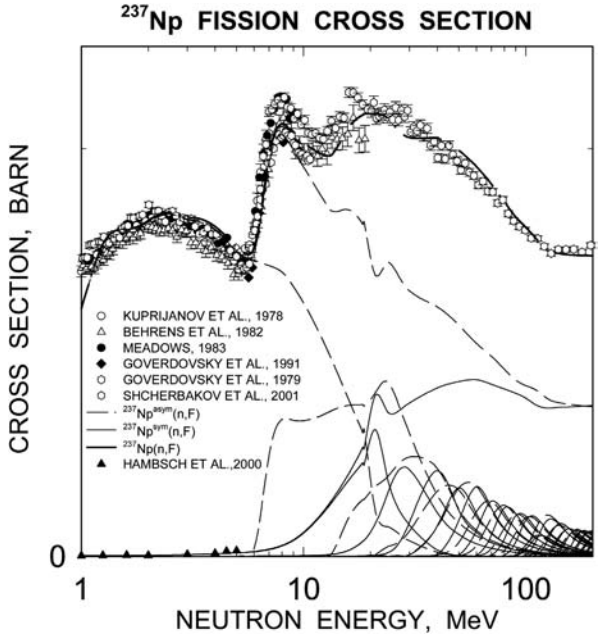

FIG. 3.1.10. $^{237}Np(n,f)$ fission cross-section (dot–dashed line) and partial cross-sections for the $^{237}Np(n,f)^{sym}$ and $^{237}Np(n,xnf)^{sym}$ (solid lines), $^{237}Np(n,f)^{asym}$ and $^{237}Np(n,xnf)^{asym}$ (dashed lines) reactions with the energy dependent asymptotic value $\tilde{a}_f(U, A)$ of the a_f parameter (see Eq. (3.1.16)).

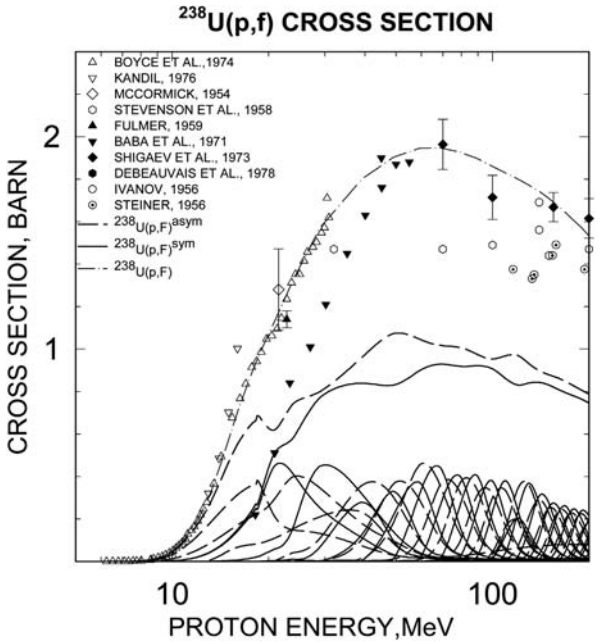

FIG. 3.1.11. $^{238}U(p,f)$ fission cross–section (dot–dashed line) and partial cross-sections for the $^{238}U(p,xnf)^{sym}$ and $^{238}U(p,f)^{sym}$ (solid lines), $^{238}U(p,xnf)^{asym}$ and $^{238}U(p,f)^{asym}$ (dashed lines) reactions with the energy dependent asymptotic value $\tilde{a}_f(U, A)$ of the a_f parameter (see Eq. (3.1.16)).

The branching ratio for the $^{238}U(p,f)$ reaction is not much different from that of the $^{238}U(n,f)$ reaction at incident nucleon energies $E_{n(p)} \geq 50$ MeV (see Fig. 3.1.12). At lower energies of $15 \leq E_{n(p)} \leq 50$ MeV, the difference is caused by different contributions of the emissive fission reactions to the observed proton and neutron induced fission cross-sections. Different shapes of branching ratios r^{sym} for the $^{237}Np(n,f)$, $^{235}U(n,f)$, $^{238}U(n,f)$ and $^{238}U(p,f)$ reactions at $E_n \leq 90$ MeV can be attributed to higher contributions of lower fission chances for higher target nuclide fissility, whereas they do not differ much at higher neutron energies.

3.1.3.3.6. $^{232}Th(n,f)$

The other extreme of a low fissility target is represented by ^{232}Th, for which measurements of the (n,f) reaction are presented in Ref. [3.1.16]. The measured fission cross-section could only be reproduced for larger contributions of higher fission chances (i.e. fissions from neutron deficient Th nuclei). Otherwise the calculated fission cross-section would be systematically higher than the measured data [3.1.17] (see Fig. 3.1.12). Figure 3.1.13 shows the

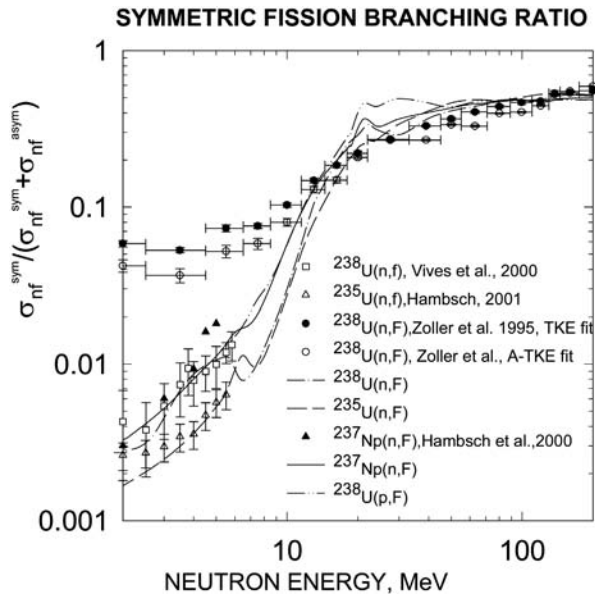

FIG. 3.1.12. Branching ratio r^{sym} of symmetric to total (symmetric + asymmetric) fission events for $^{237}Np(n,f)$ (solid line), $^{238}U(n,f)$ (dot–dashed line), $^{235}U(n,f)$ (dashed line) and $^{238}U(p,f)$ (double dot–dashed line) reactions. Symbols show measured data of Zöller et al. [3.1.14] and Vivès et al. [3.1.10] for $^{238}U(n,f)$, Hambsch [3.1.11] for $^{235}U(n,f)$, and Hambsch et al. [3.1.13] for $^{237}Np(n,f)$.

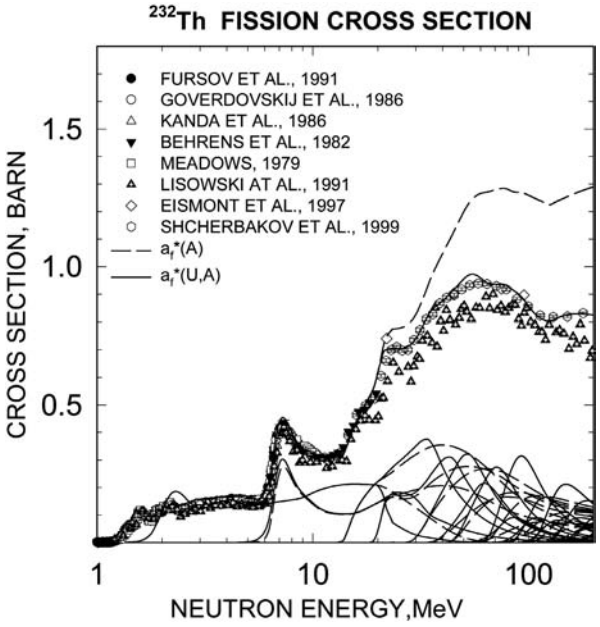

FIG. 3.1.13. $^{232}Th(n,f)$ fission cross-section for the energy dependent $\tilde{a}_f(U, A)$ (solid lines), and the energy independent $\tilde{a}_f(A)$ (dashed lines) asymptotic value of the a_f parameter (see Eq. (3.1.16)).

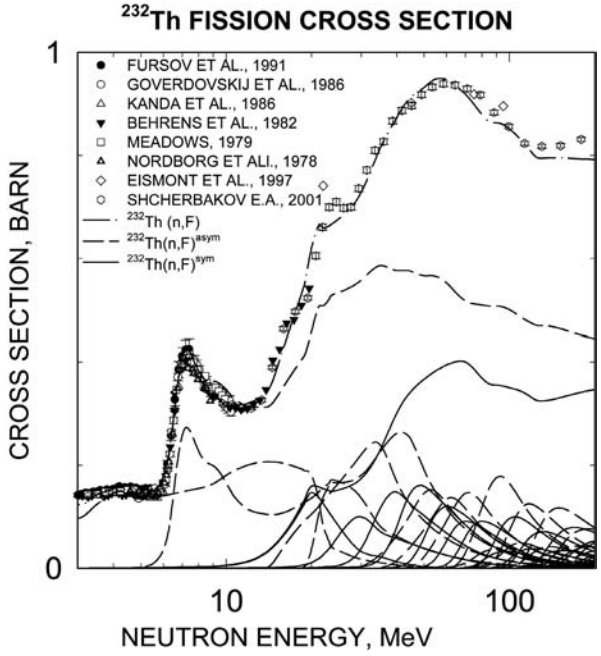

FIG. 3.1.14. $^{232}Th(n,f)$ fission cross-section (dot-dashed line) and partial cross-sections for the $^{232}Th(n,f)^{sym}$ and $^{232}Th(n,xnf)^{sym}$ (solid lines), $^{232}Th(n,f)^{asym}$ and $^{232}Th(n,xnf)^{asym}$ (dashed lines) reactions with the energy dependent asymptotic value $\tilde{a}_f(U, A)$ of the a_f parameter (see Eq. (3.1.16)).

$^{232}Th(n,f)^{asym}$ and $^{232}Th(n,f)^{sym}$ contributions to the observed fission cross-section.

3.1.4. Concluding remarks

Statistical theory describes adequately the observed actinide neutron induced fission cross-sections and symmetric branching ratios for all fission events identified with the neutron induced fission cross-section of ^{238}U, ^{235}U, ^{233}U, ^{237}Np, ^{232}Th and the proton induced fission cross-section of ^{238}U up to $E_{n(p)}$ ~ 200 MeV. Collective damping modes for both the inner and outer saddle and equilibrium deformations produce a reasonable partitioning of the observed fission cross-sections into emissive symmetric and asymmetric fission chances. An effective estimate of intrinsic fission level densities is obtained. This situation corresponds to a decrease of the contributions of fission chances with the lower number of pre-fission (n,xnf) neutrons and an increase of the contribution of fission chances with higher numbers of (n,xnf) neutrons at $E_n \geq 20$ MeV. Such behaviour is equivalent to more fission events at lower intrinsic excitation energies, or more fission events from neutron deficient U nuclei (i.e. from higher fission chances).

Damping of triaxial deformations at the outer saddle for the symmetric fission mode has been shown to be essential for the description of the ratio of symmetric to all fission events, as obtained by Zöller [3.1.14]. The outer saddle shape and height for the symmetric fission cross-section define the shape of the fission cross-section. Damping of triaxial mode contributions to the level density at the outer symmetric saddle corresponds to a relative preference of asymmetric fission over symmetric fission, compared with the case of 'no triaxial damping'. This observation is equivalent to less symmetric fission events at higher excitation energies and more symmetric fission contribution from neutron deficient isotopes, compared with the case of 'no triaxial damping'.

Duijvestijn et al. [3.1.43] have concluded that the description of the observed fission cross-section and fission fragment mass distribution of the $^{238}U(n,f)$ reaction can be achieved by different contributions of higher and lower chances to the fission observables. Specifically, the description of the $^{238}U(n,f)$ fission fragment mass distribution needs stronger contributions of lower chances, or less fission contributions from very neutron deficient U nuclei. On the other hand, the description of the observed $^{238}U(n,f)$ fission cross-section was concluded to need more contributions

from higher fission chances [3.1.43] (i.e. from very neutron deficient U nuclei). We have demonstrated that a more detailed treatment of the observed fission cross-section as a sum of the symmetric and asymmetric fission cross-sections needs stronger contributions from higher chances, or more fissions from very neutron deficient isotopes. This situation is described by the energy dependence of the asymptotic value $\tilde{a}_f(U, A)$ for the a_f parameter at saddle deformations. The description of the branching ratio of symmetric to all fission events needs a relative increase of the contribution of symmetric fission from neutron deficient isotopes, which is achieved by the damping of triaxial rotational mode contributions at outer saddle deformations. Further refinements of the model (such as inclusion of the temperature and angular momentum dependence of fission barriers, the influence of neutron shell N = 126 on the collective enhancement in the neutron channel [3.1.41], and calculation of fission barriers for symmetric and asymmetric fission modes of U nuclei with the shell correction model method [3.1.40]) would not change our main conclusions. Lowering of the asymptotic value $\tilde{a}_f$ of the a_f parameter at saddle deformations can be considered as reproducing the lumped effect of all these factors. We also expect that the possible vanishing of the distinction between symmetric and asymmetric valleys in the energy surface at high excitation of fissioning nuclei [3.1.43] would not have much influence on the calculated values because of the strong emissive fission nature of the ^{238}U(n,f) reaction for $E_n \leq$ 200 MeV.

Damping of the contribution of the axial collective modes to the level density for both inner and outer saddle and for equilibrium deformations, as well as triaxial damping at super long mode outer saddle deformations, were assumed. A consistent description of the observed fission cross-sections and the symmetric fission branching ratio for the ^{238}U(n,f) reaction was obtained on the basis of this assumption. Symmetric/asymmetric emissive fission partitioning of the ^{235}U(n,f), ^{233}U(n,f), ^{237}Np(n,f), ^{232}Th(n,f) and ^{238}U(p,f) reaction cross-sections have been predicted. The dependence of the symmetric fission branching ratio on the target nuclide fissility is interpreted as being due to a higher contribution of lower fission chances in the case of higher target nuclide fissilities.

REFERENCES TO SECTION 3.1

[3.1.1] WAHL, A.C., Nuclear-charge distribution and delayed-neutron yields for thermal-neutron-induced fission of ^{235}U, ^{233}U, and ^{239}Pu and for spontaneous fission of ^{252}Cf, At. Data Nucl. Data Tables **39** (1988) 1–156.

[3.1.2] BROSA, U., et al., Nuclear scission, Phys. Rep. **197** (1990) 167–262.

[3.1.3] BROSA, U., et al., Nuclear scission, Nucl. Phys. A **502** (1989) 423–442.

[3.1.4] BROSA, U., et al., Fission channels in ^{258}Fm, Z. Phys. A **325** (1986) 241–242.

[3.1.5] BROSA, U., Sawtooth curve of neutron multiplicity, Phys. Rev. C **32** (1985) 1438–1441.

[3.1.6] OHTSUKI, T., et al., Systematic variations of fission barrier heights for symmetric and asymmetric mass divisions, Phys. Rev. C **48** (1993) 1667–1676.

[3.1.7] KONECNY, E., et al., Symmetric and asymmetric fission of Ac isotopes near the fission threshold, Phys. Lett. **45B** (1973) 329–331.

[3.1.8] WEBER, J., et al., Fission of ^{228}Ra, Phys. Rev. C **13** (1976) 2413–2420.

[3.1.9] MASLOV, V.M., HAMBSCH, F.-J., Symmetric uranium neutron-induced fission, Nucl. Phys. A **705** (2002) 352–363.

[3.1.10] VIVÈS, F., et al., Investigation of the fission fragment properties of the reaction ^{238}U(n,f) at incident neutron energies up to 5.8 MeV, Nucl. Phys. A **662** (2000) 63–92.

[3.1.11] HAMBSCH, F.-J., EC Joint Research Centre, Institute of Reference Materials and Measurements, Geel, Belgium, personal communication, 2001.

[3.1.12] OBERSTEDT, S., et al., Fission-mode calculations for ^{239}U, a revision of the multi-modal random neck-rupture model, Nucl. Phys. A **644** (1998) 289–305.

[3.1.13] HAMBSCH, F.-J., et al., Study of the ^{237}Np(n,f) reaction at MeV neutron energies, Nucl. Phys. A **679** (2000) 3–24.

[3.1.14] ZÖLLER, C.M., Fission Fragment Properties in the ^{238}U(n,f) Reaction at Incident Neutron Energies from 1 MeV to 500 MeV, Rep. IKDA-95/25, Technische Hochschule Darmstadt (1995).

[3.1.15] LISOWSKI, P., et al., "Neutron cross-section standards for the energy region above 20 MeV", in Proc. Specialists Mtg Uppsala, Sweden, 1991, OECD, Paris (1991) 177.

[3.1.16] SHCHERBAKOV, O.A., et al., "Neutron-induced fission of ^{233}U, ^{238}U, ^{232}Th, ^{239}Pu, ^{237}Np, ^{nat}Pb, and ^{209}Bi relative to ^{235}U in the energy range 1–200 MeV", Nuclear Data Science Technology (Proc. Int. Conf. Tsukuba, Japan, 2001), J. Nucl. Sci. Technol. **1** Suppl. 2 (2002) 230–233.

[3.1.17] MASLOV, V.M., et al., "Actinide neutron-induced fission up to 200 MeV", Nuclear Data Science Technology (Proc. Int. Conf. Tsukuba, Japan, 2001), J. Nucl. Sci. Technol. **1** Suppl. 2 (2002) 80–83.

[3.1.18] BARASHENKOV, V.S., TONEEV, V.D., Interaction of High Energy Particle and Nuclei with Atomic Nuclei, Atomizdat, Moscow (1972).

[3.1.19] FESHBACH, H., et al., The statistical theory of multi-step compound and direct reactions, Ann. Phys. **125** (1980) 429–476.

[3.1.20] KONING, A.J., CHADWICK, M.B., Microscopic two-component multistep direct theory for continuum nuclear reactions, Phys. Rev. C **56** (1997) 970–994.

[3.1.21] MASLOV, V.M., et al., Neutron Data Evaluation of ^{238}U, INDC(BLR)-014, IAEA, Vienna (2003).

[3.1.22] STROHMAIER, B., UHL, M., STAPRE — A statistical model code with consideration of pre-equilibrium decay, Rep. IAEA-SMR–43, International Atomic Energy Agency (1980) 313–326.

[3.1.23] CLINE, C.K., The Pauli exclusion principle in pre-equilibrium decay, Nucl. Phys. A **195** (1972) 353–360.

[3.1.24] GADIOLI, E., et al., Intermediate-state decay rates in the exciton model, Nucl. Phys. A **217** (1973) 589–610.

[3.1.25] MASLOV, V.M., Isomeric ratio and cross-section of ^{238}U(p, 3n), Sov. J. At. Energy **69** (1991) 878–880.

[3.1.26] ABFALTERER, W.P., et al., Measurement of neutron total cross sections up to 560 MeV, Phys. Rev. C **63** (2001) 044608–044627.

[3.1.27] STRUTINSKY, V.M., Shell effects in nuclear masses and deformation energies, Nucl. Phys. A **95** (1967) 420–442.

[3.1.28] BJØRNHOLM, S., LYNN, J.E., The double-humped fission barrier, Rev. Mod. Phys. **52** (1980) 725–931.

[3.1.29] WEIGMANN, H., Fission Barriers in the Fission Process (WAGEMANS, C., Ed.), CRC Press, Boca Raton, FL (1991) 22.

[3.1.30] BOHR, A., MOTTELSON, B., Nuclear Structure, Volume 2 — Nuclear Deformations Book, Benjamin, New York (1975).

[3.1.31] IGNATYUK, A.V., et al., The role of collective effects in the systematics of nuclear level densities, Sov. J. Nucl. Phys. **29** (1979) 450–454.

[3.1.32] HOWARD, W.M., MÖLLER, P., Calculated fission barriers, ground-state masses, and particle separation energies for nuclei with $76 \leq Z \leq 100$ and $140 \leq N \leq 184$, At. Data Nucl. Data Tables **25** (1980) 219–285.

[3.1.33] HANSEN, G., JENSEN, A.S., Energy dependence of the rotational enhancement factor in the level density, Nucl. Phys. A **406** (1983) 236–256.

[3.1.34] MASLOV, V.M., PORODZINSKIJ, Yu.V., Actinide Level Density Parameter Systematics, Rep. 98-038, Japan Atomic Energy Research Institute (1998).

[3.1.35] MYERS, W.O., SWIATECKY, W.J., Anomalies in nuclear masses, Ark. Fyzik **36** (1967) 343–352.

[3.1.36] INTERNATIONAL ATOMIC ENERGY AGENCY, Handbook for Calculations of Nuclear Reaction Data: Reference Input Parameter Library, IAEA-TECDOC-1034, IAEA, Vienna (1998) 81.

[3.1.37] INTERNATIONAL ATOMIC ENERGY AGENCY, Fission Level Density and Barrier Parameters for Actinide Neutron-Induced Cross-Section Calculations, INDC(BLR)-013, IAEA, Vienna (1998).

[3.1.38] MASLOV, V.M., "Actinide neutron-induced fission up to 20 MeV", Nuclear Reaction Data and Nuclear Reactors: Physics, Design and Safety (Proc. Workshop Trieste, 2000) (PAVER, N., et al., Eds), Abdus Salam International Centre for Theoretical Physics, Trieste (2001) 231–268.

[3.1.39] GAVRON, A., et al., Complexity of the potential energy surface for fission of ^{238}U, Phys. Rev. Lett. **38** (1977) 1457–1460.

[3.1.40] MÖLLER, P., et al., Nuclear fission modes and fragment mass asymmetries in a five-dimensional deformation space, Nature **409** (2001) 785–790.

[3.1.41] JUNGHANS A.R., et al., Projectile-fragment yields as a probe for the collective enhancement in the nuclear level density, Nucl. Phys. A **629** (1998) 635–655.

[3.1.42] IVANOV, D.I., et al., Symmetric and asymmetric fission of ^{238}U and ^{237}Np induced by tagged γ rays of energy 60–240 MeV, Sov. J. Nucl. Phys. **55** (1992) 506–513.

[3.1.43] DUIJVESTIJN, M.C., et al., Mass distributions in nucleon-induced fission at intermediate energies, Phys. Rev. C **64** (2001) 014607–014643.

[3.1.44] POENITZ, W.P., Additional measurements of the ^{235}U(n,f) cross section in the 0.2- to 8.2-MeV range, Nucl. Sci. Eng. **64** (1977) 894–901.

[3.1.45] CZIRR, J.B., SIDHU, J.B., Fission cross section of uranium-235 from 3-20 MeV, Nucl. Sci. Eng. **57** (1975) 18–27.

[3.1.46] LEUGER, S.B., et al., in Proc NEANDC/NEACRP Specialists Mtg on Fast neutron fission cross sections ^{233}U, ^{235}U, ^{238}U and ^{239}Pu, Rep. ANL-79–90, Argonne National Laboratory, IL (1976) 183.

[3.1.47] CARLSON, G.W., BEHRENS, J.W., Measurement of the fission cross sections of uranium-233 and plutonium-239 relative to uranium-235 from 1 keV to 30 MeV, Nucl. Sci. Eng. **66** (1978) 205–216.

[3.1.48] DUSHIN, V.N., et al., Statistical analysis of experimential data on the cross sections of ^{233,235,238}U, ^{237}Np, ^{239,242}Pu fission by neutrons of energy 2.6, 8.5, and 14.5 MeV, At. Energ. **55** (1983) 218–222.

[3.1.49] ADAMOV, V.M., et al., Absolute measurements of fission cross-sections of heavy elements for fast neutrons, Yad. Konstanty **24** (1977) 8–15.

[3.1.50] ZASADNY, K.R., et al., Nuclear data/reactor instrumentation, Trans. Am. Nucl. Soc. **47** (1984) 425–438.

[3.1.51] KALININ, V.A., et al., Absolute measurements of the ^{237}Np and ^{233}U fission cross-sections at the neutron energy of 1.9 MeV using the TCAP method with magnetic analysis, Vopr. At. Nauki Tekh. (Ser. Yad. Konstanty) **4** (1987) 3–10.

3.2. EVALUATED REFERENCE FISSION YIELD DATA FILE

Liu Tingjin, Liang Qichang
China Institute of Atomic Energy, China

The Chinese reference fission yield file has been established, in which all experimental data available at the time of evaluation were considered. The data were processed using the AVERAG codes for calculating weighted averages, and ZOTT for the simultaneous evaluation of experimental input data. Our evaluated data were compared with those from ENDF/B-VI, JEF-2, JENDL-3 and CENDL/FY. The data were updated and improved, and uncertainties were considerably reduced in comparison with JEF-2 and CENDL/FY.

3.2.1. Introduction

Fission yield data used as standards in fission yield measurements and evaluations or as monitors in the nuclear industry for decay heat calculations, burnup studies, etc., are referred to as 'reference fission yields'. These reference fission products and their yields were selected and recommended by an earlier IAEA CRP [3.2.1].

The uncertainties of relative yield measurements depend directly on the accuracy of the standard data, and the same situation applies to yield data derived from measured ratios and R values. Applied calculations, such as decay heat and burnup, etc., also depend on the accuracy of the monitor fission yield.

A summary is given of the formulation of this file, including the evaluation method and the system of supporting activities, the result of this evaluation, and the comparison with yield data from other evaluated libraries. Details of the evaluation can be found in Refs [3.2.2–3.2.8], which describe the evaluation of ^{235}U and ^{238}U reference fission yields from 1997 to 2001.

3.2.2. Evaluation method

3.2.2.1. Data collection and selection

Experimental data were retrieved from the EXFOR master data library and evaluated by using the fission yield data evaluation system FYDES [3.2.9]. Relevant data were also collected from the open literature. All of the data collected are listed in the tables of Refs [3.2.2–3.2.8]. The EXFOR BIB information and papers were carefully studied and the method and physics background were analysed. The adoption or rejection of the data was based on the date of the original study, the measurement method and discrepancies compared with other data. In general, the following data were discarded:

(a) The parameter(s) measured are not relevant to this evaluation.
(b) There is something wrong with the measurement or data analysis.
(c) Compared with other data, the discrepancy is large and the measurement method is not reliable, or no detailed information is given concerning the experiment and/or analysis.
(d) The values or the reliability of the adopted standard data in measurements of relative data are not given in the paper. Such information is indispensable in the evaluation of 'reference yield data', and data cannot be used that are based on standards of unknown value or reliability.

As a result, about half of the data were discarded, and half were used (for details, see Refs [3.2.2–3.2.8]).

3.2.2.2. Data correction

If necessary, the measured data were corrected for the values used for the standards, γ ray intensities and fission cross-sections (in absolute measurements). As mentioned above, the relative data were generally not used as published. Such data were only selected when the standard yields used by the authors correspond to, or agree with, the recently evaluated values, or if they can be corrected using our reference yields.

These corrections were made by using the equation:

$$Y = Y_0 \frac{Y_8}{Y_{SO}} \qquad (3.2.1)$$

where Y_S is our new standard, and Y_{S0} is the standard originally used.

If the gamma ray intensity adopted by the author is given, the data can be corrected by introducing the following new intensity data (in order of priority):

(1) Decay data evaluated at CNDC [3.2.10];
(2) 'Table of Isotopes', 8th edition [3.2.13];
(3) ENSDF (evaluated nuclear structure data file).

If only one gamma ray emission (intensity I_0) was used in the data processing, the correction is simply:

$$Y = Y_0 \frac{I_8}{I_{SO}} \tag{3.2.2}$$

where *I* is the corrected intensity.

If several gamma ray emissions were used in the analysis and there is a gamma ray with an intensity that significantly exceeds all others, the data were corrected as above for one gamma ray emission (weighted average assumed). If several gamma ray emissions with comparable intensity were used, the data were corrected on the basis of the following formula (arithmetical average assumed):

$$Y = Y \frac{1}{N} \sum \frac{I_{0i}}{I_I} \tag{3.2.3}$$

where *N* is the number of gamma ray emissions incorporated into the calculation.

The data were also corrected for outdated fission cross-sections by using a formula similar to Eq. (3.2.2). New fission cross-sections were taken from ENDF/B-VI.

3.2.2.3. Processing uncertainties

The uncertainties given in the EXFOR entries are of a different type to those required in the file, and often of a complicated composite nature. They must be adjusted if values are judged to be unreasonable, or assigned by the evaluator if no uncertainties are given. Overall uncertainties are required, and their magnitude should be identical for the same measurement method over the same period of time. The uncertainty ranges assigned by the evaluator are listed in Table 3.2.1 for different measurement methods and periods of time. Generally, if the uncertainties given by the author are in the adopted range, these values were not changed. Otherwise they were adjusted or assigned by the evaluator according to the adopted range (Table 3.2.1). In some cases, the author-assigned uncertainty could be adjusted within the adopted range for a given method and period of time, depending on the value of the yield (e.g. low yields are assigned higher uncertainties), measured energy point, experimental equipment and/or laboratory. When no uncertainties are given by the authors, an overall uncertainty was assigned according to the measurement conditions, and the upper limit of ranges given in Table 3.2.1 was adopted. However, apart from the general conditions described above, there can be special cases where the adopted uncertainties may lie outside the given ranges.

TABLE 3.2.1. ASSIGNED RELATIVE UNCERTAINTY (%) OF MEASURED FISSION YIELD DATA FOR DIFFERENT METHODS

Method		Fission yield		Ratio
		Before 1965	After 1965	
RC	GeLi	7–15	4–8	3–4
	NaI	8–16	6–9	3–5
	Geiger	15–25		5–6
γ spectrum		6–10	3–6	2–3
Mass spectrometry		2–3	1–2	1–2

The uncertainty was processed as follows:

(a) Adjustment for standard fission yield:

$$\Delta Y' = \left(\Delta Y_0'^2 + \Delta Y_S'^2 - \Delta Y_{S0}'^2\right)^{1/2} \quad (3.2.4)$$

or for fission cross-section:

$$\Delta Y' = \left(\Delta Y_0'^2 + \Delta \sigma_S'^2 - \Delta \sigma_{S0}'^2\right)^{1/2} \quad (3.2.5)$$

where $\Delta Y'$ is the relative uncertainty of the data Y: $\Delta Y' = \Delta Y/Y$. However, $\Delta Y'_{S0}$ (uncertainty of the old standard) may not be included in Y_0 (total uncertainty of the data given by the author); under such circumstances, $\Delta Y'_{S0}$ should be taken to be zero.

(b) Gamma ray intensity adjustment: The ΔY uncertainty was not changed, because this adjustment is usually not large and the uncertainty of the gamma ray intensity is not given.

(c) Calculate the yield from ratio $\mathbf{R_0}$

$$\Delta Y' = \left(\Delta R_0'^2 + \Delta Y_S'^2\right)^{1/2} \quad (3.2.6)$$

(d) Calculate the ratio R_0 from R value $\boldsymbol{R_v}$:

$$\Delta R_0' = \left(\Delta R_v'^2 + \Delta Y'^2_{mxw} + \Delta Y'^2_{Smxw}\right)^{1/2} \quad (3.2.7)$$

where $\Delta Y'_{mxw}$ and $\Delta Y'_{Smxww}$ are the uncertainties of the measured and standard nuclides, respectively.

(e) Calculate ratio R_0 from fission yield: since this evaluation is for reference fission yield data, only ratios for measured relative data were used, if the details of the standards are given (otherwise the data were discarded). Under these circumstances:

$$\Delta R_0' = \left(\Delta Y'^2 + \Delta Y_S'^2\right)^{1/2} \quad (3.2.8)$$

If $\Delta Y'_s$ is not included in the total ΔY given by the author, $\Delta Y'_s$ is assigned a value of 0.

The processing of the data and their uncertainties for each sub-entry in a paper are given in the corresponding tables of Refs [3.2.2–3.2.8].

3.2.2.4. Data processing

The collected and adjusted data with their (re-)evaluated uncertainties were processed with weighted averages, and simultaneously evaluated.

(a) Data average: Data measured at the same energy points for the same fissioning nuclide were averaged using the AVERAG code. The recommended weighted mean and external uncertainty were calculated. Tables 3.2.2 and 3.2.3: Data for which averages have been calculated are marked 'A' in the column headed 'PROC', and the number of data points is given in the column headed 'POINT'; averages have been taken in most cases.

(b) Simultaneous evaluation: Data for which absolute yields and their ratios had been measured were simultaneously evaluated by using the ZOTT code [3.2.11]. Simultaneously evaluated data are marked 'S' in Tables 3.2.2 and 3.2.3. There are two kinds of correlated measurements: different energy points for the same nuclide, and different nuclides at the same energy point.

3.2.2.5. Evaluation system FYDES

All data retrievals, adjustments, modifications to quoted uncertainties and data processing were performed with the fission yield data evaluation system FYDES which has been developed to assist in the evaluation of fission yield data. The following specific characteristics of these data and the FYDES system make them distinct from other data types (like cross-section data) and corresponding evaluation systems:

(a) Data in the EXFOR file can also be given under the heading 'ELEM/MASS' (see below);

(b) More fission yield data are measured on a relative basis as ratios or R values;

(c) Many data need to be adjusted for the standard yield, gamma ray intensity and fission cross-section and have to be recalculated from ratios or R values;

(d) The dependence of yields on neutron energy appears to be linear for most cases.

The fission yield data can be retrieved from the EXFOR database by target, or by incident neutron energy, or by product (if given in REACTION), using the EXFOR retrieval system. But when in an EXFOR entry the 'variable product' formalism is used, 'ELEM/MASS' is given in REACTION, and the product occurs under the heading 'ELEM/MASS' of the DATA table and cannot be retrieved this way. Some supplementary programs were developed to solve this problem,

TABLE 3.2.2. EVALUATED REFERENCE FISSION YIELD FROM ^{235}U FISSION

Z-Sy-A	E	FY	FYUNCERTAINTY	POINT	PROC.	RECOMM.	YEAR
33-As-85	T	3.4494E-01	1.8974E-02	1(1)	A	N	1998
34-Se-79	T	4.3900E-02	3.0000E-03	1	N	R	2001
35-Br-88	T	1.6358E+00	8.0621E-02	3	AS	R	1998
35-Br-89	T	1.0988E+00	5.5885E-02	2+1	AS	R	1998
35-Br-90	T	4.2893E-01	7.6576E-02	3	A	R	1998
35-Br-91	T	3.4000E-01	9.0000E-02	1	N	N	1998
36-Kr-83	T	5.3937E-01	2.6115E-03	4+(2)	AS	R	1999
36-Kr-83	F	5.8132E-01	1.4759E-02	2	A	R	1999
36-Kr-86	T	1.9689E+00	7.3392E-03	6+2	AS	R	1999
36-Kr-86	F	1.9900E+00	2.0000E-02	1	N	(R)	1999
36-Kr-87	T	2.6445E+00	8.7407E-02	3	A	R	1999
36-Kr-87	F	2.4332E+00	7.1561E-02	2	A	R	1999
37-Rb-93	T	3.3914E+00	1.1804E-01	1+1	S	R	2001
37-Rb-94	T	1.6726E+00	4.2809E-02	+1(B6)	S	R	2001
37-Rb-95	T	7.2229E-01	2.1583E-02	1+(2)	S	R	2001
38-Sr-89	T	4.7855E+00	4.3800E-02	7+1+(3)	AS	R	1999
38-Sr-89	F	4.2200E+00	2.1000E-01	1	N	(R)	1999
38-Sr-89	H	4.1084E+00	1.1607E-01	1+3	AS	R	1999
38-Sr-90	T	5.8499E+00	2.8991E-02	7+(1)	AS	R	1999
38-Sr-90	F	5.4873E+00	4.5042E-02	3	A	R	1999
38-Sr-90	H	4.6072E+00	2.7311E-01	2	A	R	1999
38-Sr-92	T	(6.0000E+00	1.7000E-01)	1	N	(R)	1997
39-Y-91	T	5.8974E+00	4.7033E-02	6+(1+1)	AS	R	1999
39-Y-91	F	5.8307E+00	7.7762E-02	1+1	AS	R	1999
39-Y-91	H	4.9312E+00	2.4815E-01	1+1	AS	R	1999
39-Y-99	T	2.0482E+00	6.1049E-02	+1(B6)	S	R	2001
40-Zr-91	T	5.9288E+00	4.3812E-02	5+1	AS	R	2001
40-Zr-91	F	5.6600E+00	5.1089E-02	3	A	R	2001
40-Zr-91	H	4.9100E+00	2.4513E-01	2	A	R	2001
40-Zr-93	T	6.3470E+00	4.6309E-02	5+(1)	AS	R	2001
40-Zr-93	F	6.1579E+00	5.3653E-02	3	A	R	2001
40-Zr-93	H	5.0863E+00	2.7621E-01	2	A	R	2001
40-Zr-96	T	6.2615E+00	8.0721E-02	4	A	R	1999
40-Zr-96	F	6.1205E+00	5.3841E-02	2	A	R	1999
41-Nb-95	T	6.5780E+00	3.2600E-02	5+(1)	AS	R	1999
41-Nb-95	F	6.4531E+00	1.5442E-01	1+1	AS	R	1999
42-Mo-95	T	6.5035E+00	3.6541E-02	6	A	R	1999
42-Mo-95	F	6.3837E+00	4.2355E-02	3	A	R	1999
42-Mo-97	T	5.9163E+00	3.6324E-02	6+1	AS	R	1999
42-Mo-97	F	5.9471E+00	3.9022E-02	4	A	R	1999
42-Mo-100	T	6.2135E+00	3.2212E-02	5+(1)	AS	R	1999
42-Mo-100	F	6.2425E+00	1.4085E-01	2	A	R	1999
43-Tc-99	T	6.0756E+00	6.1049E-02	3+(1)	AS	R	2001

TABLE 3.2.2. EVALUATED REFERENCE FISSION YIELD FROM ^{235}U FISSION (cont.)

Z-Sy-A	E	FY	FYUNCERTAINTY	POINT	PROC.	RECOMM.	YEAR
44-Ru-101	T	5.1895E+00	3.6259E-02	5+(1+1)	AS	R	1999
44-Ru-101	F	5.3019E+00	1.1431E-01	2	A	R	1999
44-Ru-102	T	4.2954E+00	4.6497E-02	5+1	AS	R	1999
44-Ru-102	F	4.4100E+00	2.0000E-01	1	N	(R)	1999
44-Ru-103	T	3.0405E+00	2.9504E-02	7+2+(2)	AS	R	1997
44-Ru-103	F	3.5525E+00	5.9455E-02	3+2	AS	R	1997
44-Ru-103	H	3.4127E+00	1.0228E-01	1+1	S	R	1997
44-Ru-104	T	1.8914E+00	1.4203E-02	6+1	AS	R	1999
44-Ru-104	F	1.9905E+00	1.0950E-01	2	A	R	1999
44-Ru-106	T	3.9134E-01	3.4295E-03	5+(1)	AS	R	1997
44-Ru-106	F	1.6691E+00	6.5418E-02	1	N	N	1997
44-Ru-106	H	1.6691E+00	6.5418E-02	1+1	S	R	1997
45-Rh-103	T	2.9667E+00	3.2215E-02	4	A	R	2001
45-Rh-103	F	3.2100E+00	1.2840E-01	1	N	R	2001
45-Rh-103	H	3.4930E+00	2.0960E-01	1	N	R	2001
45-Rh-106	T	4.0167E-01	1.4203E-02	3+1	AS	R	1999
46-Pd-105	T	9.4645E-01	8.8925E-03	4+(1)	AS	R	2001
46-Pd-105	F	1.1700E+00	1.3000E-01	1	N	R	2001
46-Pd-105	H	1.7010E+00	1.0210E-01	1	N	N	2001
46-Pd-107	T	1.4574E-01	1.3758E-03	2+1	AS	R	2001
47-Ag-109	T	3.1000E-02	7.0000E-03	2	A	R	1999
47-Ag-111	T	1.5789E-02	5.3149E-04	3+(2+3)	AS	R	1999
47-Ag-111	F	3.1492E-02	8.9783E-04	1+2	AS	R	1999
47-Ag-111	H	1.0272E+00	1.5797E-02	1+3	AS	R	1999
48-Cd-115	T	1.7587E-02	7.5623E-04	3+(5)	AS	R	1998
48-Cd-115	F	3.7075E-02	4.4833E-03	+2	S	R	1998
48-Cd-115	H	6.7990E-01	3.2034E-02	1+3	S	R	1998
48-Cd-115M	T	8.2810E-04	6.4324E-05	2+(1)	AS	R	1998
48-Cd-115M	F	1.9000E-02	4.0000E-03	1	N	N	1998
48-Cd-115M	H	7.1261E-02	5.4627E-03	1+1	S	(R)	1998
50-Sn-126	T	5.7213E-02	2.6396E-03	2	A	R	2001
50-Sn-126	F	1.0000E-01	5.0000E-03	1	N	R	2001
51-Sb-125	T	2.8095E-02	1.3388E-03	5	A	R	1999
51-Sb-125	F	6.5502E-02	6.8783E-03	2	A	R	1999
51-Sb-135	T	1.5040E-01	7.5200E-03	1	N	R	1998
52-Te-132	T	4.2339E+00	2.7238E-02	9	AS	R	2000
52-Te-132	F	4.8215E+00	4.5799E-02	9	AS	R	2000
52-Te-132	H	4.1098E+00	7.4305E-02	1	S	R	2000
53-I-129	T	7.5145E-01	3.7840E-02	6	A	R	2001
53-I-129	F	1.0900E+00	5.5000E-02	1	N	R	2001
53-I-129	H	3.2630E+00	1.9580E-01	1	N	R	2001
53-I-131	T	2.8787E+00	1.7314E-02	14	AS	R	2000
53-I-131	F	3.3518E+00	3.5906E-02	12	AS	R	2000

TABLE 3.2.2. EVALUATED REFERENCE FISSION YIELD FROM ^{235}U FISSION (cont.)

Z-Sy-A	E	FY	FYUNCERTAINTY	POINT	PROC.	RECOMM.	YEAR
53-I-131	H	4.2232E+00	1.1298E-01	1	S	R	2000
53-I-135	T	6.2543E+00	2.9860E-01	5	A	R	1998
53-I-135	F	6.7447E+00	1.7049E-01	3	A	R	1998
53-I-135	H	4.3150E+00	2.4200E-01	+1	N	R	1998
53-I-137	T	2.7757E+00	2.8616E-01	4	A	R	1998
53-I-137	F	3.0000E+00	6.0000E-01	1	N	R	1998
53-I-138	T	1.5356E+00	1.3112E-01	2	A	R	2001
53-I-139	T	6.3139E-01	1.0900E-01	2	A	R	2001
54-Xe-131	T	2.9997E+00	4.6787E-02	B6+2	S	N	1997
54-Xe-131	F	3.2620E+00	4.6180E-02	2	A	R	1997
54-Xe-132	T	4.3004E+00	3.7756E-02	8	A	R	2000
54-Xe-132	F	4.6167E+00	2.7318E-02	6	AS	R	2000
54-Xe-134	T	7.5175E+00	1.0897E-01	1	S	(R)	1997
54-Xe-134	F	7.6946E+00	1.0827E-01	2	A	R	1997
54-Xe-135	T	(6.7770E+00	1.8000E-01)	1	N	N	1997
54-Xe-136	T	6.3213E+00	7.1535E-02	6	A	R	2000
54-Xe-136	F	6.2763E+00	4.8396E-02	4	AS	R	2000
54-Xe-137	T	6.3361E+00	6.5122E-02	4	A	R	2000
54-Xe-137	F	5.8200E+00	2.9100E-01	1	N	R	2000
54-Xe-138	T	6.3810E+00	1.5087E-01	2	A	R	2000
54-Xe-138	F	6.1200E+00	3.0600E-01	1	N	R	2000
55-Cs-133	T	6.7996E+00	4.8287E-02	3+1+(3)	AS	R	1997
55-Cs-133	F	6.7457E+00	6.0255E-02	2	A	R	1997
55-Cs-135	T	6.5311E+00	4.3430E-02	6	A	R	2001
55-Cs-135	F	6.5240E+00	4.2048E-02	6	A	R	2001
55-Cs-135	H	5.6990E+00	3.4190E-01	1	N	R	2001
55-Cs-136	T	5.4965E-03	3.6828E-04	1+(1)	A	R	1998
55-Cs-137	T	6.2052E+00	5.1090E-02	4+2	AS	R	1997
55-Cs-137	F	6.2008E+00	5.3101E-02	4+1+(1)	AS	R	1997
56-Ba-140	T	6.2059E+00	6.1693E-02	9+(2)	AS	R	1997
56-Ba-140	F	6.1514E+00	9.8714E-02	3+1	AS	R	1997
56-Ba-140	H	4.5963E+00	1.1617E-01	2+1	AS	R	1997
57-La-140	T	6.4070E+00	1.1000E-01	1	N	N	1997
58-Ce-141	T	5.9823E+00	5.0693E-02	9	AS	R	2000
58-Ce-141	F	5.6817E+00	8.8476E-02	5	A	R	2000
58-Ce-141	H	4.5883E+00	1.4147E-01	2	AS	R	2000
58-Ce-143	T	5.9993E+00	4.5942E-02	9	AS	R	2000
58-Ce-143	F	5.6022E+00	5.6617E-02	11	AS	R	2000
58-Ce-143	H	3.7919E+00	1.0107E-01	2	AS	R	2000
59-Pr-141	T	5.9929E+00	5.6213E-02	4	A	R	2000
59-Pr-141	F	5.6184E+00	1.7269E-01	3	A	R	2000
59-Pr-141	H	4.5600E+00	5.0000E-01	1	N	R	2000
59-Pr-144	T	5.5523E+00	3.8875E-02	4	A	R	2000

TABLE 3.2.2. EVALUATED REFERENCE FISSION YIELD FROM ^{235}U FISSION (cont.)

Z-Sy-A	E	FY	FYUNCERTAINTY	POINT	PROC.	RECOMM.	YEAR
59-Pr-144	F	5.1470E+00	1.2950E-01	2	A	R	2000
60-Nd-143	T	5.9603E+00	4.1624E-02	3+3+(2)	AS	R	1997
60-Nd-143	F	5.6920E+00	4.9160E-02	4+2	AS	R	1997
60-Nd-144	T	5.4571E+00	2.5820E-02	10	A	R	2000
60-Nd-144	F	5.1929E+00	5.0361E-02	5	A	R	2000
60-Nd-145	T	3.9403E+00	2.8346E-02	2+8	AS	R	1997
60-Nd-145	F	3.7641E+00	3.9075E-02	4+1	AS	R	1997
60-Nd-146	T	2.9654E+00	1.1300E-02	11	A	R	2000
60-Nd-146	F	2.9102E+00	1.8337E-02	9	A	R	2000
60-Nd-148	T	1.6747E+00	1.1279E-02	3+5+(4)	AS	R	1997
60-Nd-148	F	1.6980E+00	1.1222E-02	4+2+(5)	AS	R	1997
61-Pm-147	T	2.2440E+00	1.8227E-02	5	A	R	2001
61-Pm-147	F	2.1807E+00	8.2012E-02	2	A	R	2001
61-Pm-147	H	2.0220E+00	1.2130E-01	1	N	N	2001
61-Pm-149	T	1.0000E+00	1.6767E-02	5	A	R	2000
61-Pm-149	F	1.0280E+00	3.4222E-02	2	A	R	2000
61-Pm-151	T	4.0693E-01	4.5482E-03	5	A	R	2000
61-Pm-151	F	4.0077E-01	1.5855E-02	3	A	R	2000
61-Pm-151	H	2.6400E-01	4.0000E-03	1	N	R	2000
62-Sm-147	T	2.1184E+00	2.2587E-02	2+1	AS	R	1998
62-Sm-147	F	2.1650E+00	2.2000E-02	1	N	(R)	1998
62-Sm-149	T	1.0101E+00	1.3172E-02	2+(3)	AS	R	1997
62-Sm-149	F	1.0457E+00	2.2794E-02	2	A	R	1997
62-Sm-151	T	4.0348E-01	4.3027E-03	2+1	AS	R	1997
62-Sm-151	F	4.1735E-01	9.4766E-03	2	A	R	1997
62-Sm-152	T	2.5316E-01	4.4089E-03	2+1	AS	R	1997
62-Sm-152	F	2.9522E-01	6.6607E-03	2	A	R	1997
62-Sm-153	T	1.4789E-01	3.9498E-03	6	A	R	2000
62-Sm-153	F	1.5400E-01	2.0000E-02	1	N	(R)	2000
62-Sm-153	H	2.3900E-01	2.2000E-02	1	N	(R)	2000
63-Eu-153	T	1.4840E-01	4.1331E-03	3	A	R	2000

Number: data sets adopted in the evaluation — for the simultaneous evaluation case, this is the absolutely measured data sets, with the ratio number in parentheses. A: average with weight; S: simultaneous evaluation; R: recommended; (R): recommended only as reference; N: not processed or not recommended; T: thermal energy spectrum average; F: fission spectrum average; H: high energy (around 14 MeV).

TABLE 3.2.3. EVALUATED REFERENCE YIELDS FOR ^{238}U FISSION

Nuclide	E	FY	FYUNCERTAINTY	POINT	PROC.	RECOMM.	YEAR
35-Br-88	H	1.9000E+00	3.7000E-01	1	N	N	1998
35-Br-89	H	1.1900E+00	2.0000E-01	1	N	N	1998
36-Kr-83	F	3.8640E-01	3.1000E-03	1(1)	S	R	1999
36-Kr-83	H	7.4110E-01	2.9700E-02	2(1)	AS	R	1999
36-Kr-85	F	1.6600E-01	1.2000E-02	1	N	(R)	1998
36-Kr-85	H	2.5290E-01	2.1000E-02	2	A	R	1998
36-Kr-85M	F	7.4250E-01	2.8100E-02	2	A	R	1998
36-Kr-85M	H	1.0820E+00	2.9000E-02	7	A	R	1998
36-Kr-86	F	1.2969E+00	8.9000E-03	1(1)	S	R	1999
36-Kr-86	H	1.7519E+00	7.0300E-02	1(1)	S	R	1999
36-Kr-87	F	1.6030E+00	4.7400E-02	2	A	R	1998
36-Kr-87	H	1.7325E+00	6.4400E-02	4	A	R	1998
36-Kr-88	F	2.0180E+00	9.6300E-02	3	A	R	1998
36-Kr-88	H	2.0253E+00	6.8000E-02	7	A	R	1998
38-Sr-89	F	3.0664E+00	1.0710E-01	5	A	R	1999
38-Sr-89	H	2.9195E+00	1.2500E-01	4	A	R	1999
38-Sr-90	F	3.1861E+00	1.5970E-01	2	A	R	1999
38-Sr-90	H	3.1282E+00	1.8180E-01	2	A	R	1999
38-Sr-92	F	4.4403E+00	1.0979E-01	2(2)	AS	R	1997
38-Sr-92	H	3.9440E+00	8.2076E-02	4(3)	AS	R	1997
39-Y-91	F	3.9594E+00	7.8941E-02	2(2)	AS	R	1998
39-Y-91	H	3.7723E+00	8.6100E-02	7	A	R	1998
40-Zr-91	F	3.9594E+00	7.8941E-02	2(2)	AS	R	1999
40-Zr-91	H	3.7723E+00	8.1600E-02	7	A	R	1999
40-Zr-93	F	5.0492E+00	2.1195E-01	1(1)	S	R	1999
40-Zr-93	H	4.3144E+00	4.4860E-01	2	A	R	1999
40-Zr-95	F	5.1438E+00	5.6800E-02	9	A	R	1998
40-Zr-95	H	4.9197E+00	6.7100E-02	13	A	R	1998
41-Nb-95	F	5.1425E+00	5.6786E-02	10	A	R	1999
41-Nb-95	H	4.9185E+00	6.7084E-02	13	A	R	1999
42-Mo-95	F	5.1438E+00	5.6800E-02	10	A	R	1999
42-Mo-95	H	4.9197E+00	6.7100E-02	13	A	R	1999
42-Mo-97	F	5.6021E+00	3.8838E-02	3(2)	AS	R	1997
42-Mo-97	H	5.4470E+00	9.7386E-02	3(1)	AS	R	1997
42-Mo-99	F	6.1403E+00	1.9020E-01	4	A	R	1998
42-Mo-99	H	5.6423E+00	7.2800E-02	14	A	R	1998
43-Tc-99	F	6.1403E+00	1.9020E-01	4	A	R	1999
43-Tc-99	H	5.6423E+00	7.2800E-02	14	A	R	1999
44-Ru-101	F	6.3298E+00	3.7430E-01	2	A	R	1999
44-Ru-101	H	5.7600E+00	2.2000E-01	1	N	R	1999
44-Ru-103	F	6.0778E+00	5.8911E-02	8(4)	AS	R	1997
44-Ru-103	H	4.6604E+00	9.0389E-02	6(4)	AS	R	1997
44-Ru-104	F	5.0200E+00	3.0000E-01	1	N	R	1999

TABLE 3.2.3. EVALUATED REFERENCE YIELDS FOR ^{238}U FISSION (cont.)

Nuclide	E	FY	FYUNCERTAINTY	POINT	PROC.	RECOMM.	YEAR
44-Ru-104	H	3.5900E+00	1.5000E-01	1	N	R	1999
44-Ru-106	F	2.4676E+00	1.2240E-01	2(1)	AS	R	1998
44-Ru-106	H	2.5478E+00	1.1710E-01	2	A	R	1998
45-Rh-103	F	6.0778E+00	5.8911E-02	8(4)	AS	R	1999
45-Rh-103	H	4.6604E+00	9.0389E-02	6(4)	AS	R	1999
45-Rh-105	F	3.9059E+00	8.1867E-02	1(3)	AS	R	1998
45-Rh-105	H	3.2895E+00	5.4200E-02	8	A	R	1998
45-Rh-106	F	2.4676E+00	1.2240E-01	2	A	R	1999
45-Rh-106	H	2.5299E+00	9.8200E-02	2	A	R	1999
46-Pd-105	F	3.9059E+00	8.1867E-02	1(3)	S	R	1999
46-Pd-105	H	3.2895E+00	5.4200E-02	8	A	R	1999
47-Ag-109	F	2.5200E-01	1.3000E-02	1	N	R	1999
47-Ag-109	H	1.5496E+00	1.2000E-01	1	N	(R)	1999
47-Ag-111	F	6.9142E-02	3.0296E-03	3(1)	AS	R	1998
47-Ag-111	H	1.0477E+00	2.2800E-02	7	A	R	1998
48-Cd-115	F	3.2700E-02	3.8000E-03	2	A	R	1999
48-Cd-115	H	7.9890E-01	2.7700E-02	5	A	R	1999
48-Cd-115M	F	2.5790E-03	3.1000E-04	1	N	R	1998
48-Cd-115M	H	6.7700E-02	9.7000E-03	2	A	R	1998
51-Sb-125	F	4.9220E-02	2.0310E-02	2	A	R	1998
51-Sb-125	H	1.2771E+00	7.1800E-02	2	A	R	1998
52-Te-132	F	5.1359E+00	1.2740E-01	4	A	R	2000
52-Te-132	H	4.5748E+00	9.2900E-02	5	A	R	2000
53-I-129	F	5.8820E-01	5.9500E-02	3	A	R	2000
53-I-129	H	1.6850E+00	9.5800E-02	2	A	R	2000
53-I-131	F	3.2193E+00	3.4200E-02	12	A	R	1998
53-I-131	H	3.8538E+00	6.7381E-02	5(2)	AS	R	1998
53-I-133	H	5.9714E+00	9.6900E-02	6(3)	AS	R	1997
53-I-137	F	6.0000E+00	1.0000E+00	1	N	N	1998
53-I-137	H	3.2800E+00	6.6000E-01	1	N	R	1998
54-Xe-131	F	3.2330E+00	6.9613E-02	4(2)	AS	R	1997
54-Xe-131	H	3.8143E+00	1.4630E-01	3	A	R	1997
54-Xe-132	F	5.1360E+00	4.5000E-02	5	A	R	2000
54-Xe-132	H	4.8843E+00	5.8500E-02	4	A	R	2000
54-Xe-133	F	6.5664E+00	1.8590E-01	3	A	R	1998
54-Xe-133	H	6.0094E+00	1.1490E-01	6	A	R	1998
54-Xe-134	F	7.5977E+00	3.2390E-01	3	A	R	1998
54-Xe-134	H	6.4616E+00	1.0870E-01	4	A	R	1998
54-Xe-135	F	6.7282E+00	1.5930E-01	6	A	R	1997
54-Xe-135	H	5.8049E+00	1.2020E-01	6	A	R	1997
54-Xe-136	F	7.0095E+00	1.0750E-01	4	A	R	2000
54-Xe-136	H	5.7228E+00	9.1900E-02	2	A	R	2000
54-Xe-137	F	6.0500E+00	3.0000E-01	1	N	R	2000

TABLE 3.2.3. EVALUATED REFERENCE YIELDS FOR ^{238}U FISSION (cont.)

Nuclide	E	FY	FYUNCERTAINTY	POINT	PROC.	RECOMM.	YEAR
54-Xe-137	H	4.6300E+00	2.3000E-01	1	N	R	2000
54-Xe-138	F	5.9900E+00	3.0000E-01	1	N	R	2000
54-Xe-138	H	4.2559E+00	1.1150E-01	4	A	R	2000
55-Cs-133	F	6.7631E+00	7.1388E-02	2(2)	AS	R	1997
55-Cs-133	H	6.0174E+00	1.6800E-01	2	A	R	1997
55-Cs-135	F	6.8688E+00	9.3600E-02	6	A	R	2000
55-Cs-135	H	5.8508E+00	1.0100E-01	6	A	R	2000
55-Cs-137	F	5.9376E+00	5.0172E-02	4	AS	R	1997
55-Cs-137	H	5.1737E+00	1.8120E-01	4	A	R	1997
56-Ba-140	F	5.8798E+00	3.5758E-02	12(1)	AS	R	1998
56-Ba-140	H	4.5693E+00	5.3390E-02	7	AS	R	1998
57-La-140	F	5.8948E+00	8.8467E-02	3(2)	AS	R	1997
57-La-140	H	4.6529E+00	1.3010E-01	3	A	R	1997
58-Ce-141	F	5.3879E+00	2.0400E-01	3	A	R	2000
58-Ce-141	H	4.3583E+00	7.3600E-02	7(1)	AS	R	2000
58-Ce-143	F	4.6420E+00	7.7000E-02	7	A	R	2000
58-Ce-143	H	3.9123E+00	6.4300E-02	9(1)	AS	R	2000
58-Ce-144	F	4.5493E+00	8.4700E-02	7	A	R	1998
58-Ce-144	H	3.7165E+00	8.6800E-02	9	A	R	1998
59-Pr-141	F	5.3879E+00	2.0400E-01	3	A	R	2000
59-Pr-141	H	4.3583E+00	7.3600E-02	7(1)	AS	R	2000
59-Pr-144	F	4.5493E+00	8.4700E-02	7	A	R	2000
59-Pr-144	H	3.7165E+00	8.6800E-02	9	A	R	2000
60-Nd-143	F	4.5338E+00	3.2080E-02	4(3)	AS	R	1997
60-Nd-143	H	4.1917E+00	1.1580E-01	4	A	R	1997
60-Nd-144	F	4.5493E+00	8.4700E-02	7	A	R	2000
60-Nd-144	H	3.7165E+00	8.6800E-02	9	A	R	2000
60-Nd-145	F	3.7548E+00	3.2806E-02	2(1)	AS	R	1997
60-Nd-145	H	3.0894E+00	1.6000E-01	1	N	R	1997
60-Nd-146	F	3.3848E+00	3.3100E-02	5	A	R	2000
60-Nd-146	H	1.9250E+00	2.3500E-01	1	N	N	2000
60-Nd-147	F	2.5867E+00	5.7200E-02	5	A	R	1998
60-Nd-147	H	2.0878E+00	3.3800E-02	12	A	R	1998
60-Nd-148	F	2.1015E+00	1.8580E-02	3(1)	AS	R	1998
60-Nd-148	H	1.6000E+00	9.0000E-02	1	N	R	1998
61-Pm-147	F	2.5867E+00	5.7200E-02	5	A	R	2000
61-Pm-147	H	2.0878E+00	3.3800E-02	12	A	R	2000
61-Pm-149	F	1.6279E+00	4.6800E-02	4	A	R	2000
61-Pm-149	H	1.4189E+00	1.5840E-01	3	A	R	2000
61-Pm-151	F	7.9970E-01	1.6300E-02	5	A	R	2000
61-Pm-151	H	8.0120E-01	3.3400E-02	4	A	R	2000
62-Sm-147	F	2.5266E+00	3.0405E-02	2(2)	AS	R	1997
62-Sm-147	H	2.0365E+00	5.3261E-02	3	AS	R	1997

TABLE 3.2.3. EVALUATED REFERENCE YIELDS FOR ^{238}U FISSION (cont.)

Nuclide	E	FY	FYUNCERTAINTY	POINT	PROC.	RECOMM.	YEAR
62-Sm-149	F	1.5850E+00	1.9000E-02	2	A	R	1997
62-Sm-149	H	1.2038E+00	3.4174E-02	1(1)	S	(R)	1997
62-Sm-151	F	7.8691E-01	2.4570E-02	2(2)	AS	R	1998
62-Sm-151	H	6.5409E-01	1.7017E-02	1(1)	S	N	1998
62-Sm-152	F	5.2168E-01	5.7700E-03	2	A	N	1997
63-Eu-156	F	6.7100E-02	2.1000E-03	3	A	R	1998
63-Eu-156	H	1.0900E-01	2.9000E-03	8	A	R	1998
65-Tb-161	F	1.1436E-03	9.0000E-05	3	A	R	1998
65-Tb-161	H	8.2450E-03	5.0500E-04	2	A	R	1998

Note: Symbols are the same as in Table 3.2.2.

including FORM to exchange the column position and standardizing the data table, FYRET to extract the data table from each sub-entry in the EXFOR file, and FYRET1 to retrieve yield data according to Z and A.

Data can be adjusted through implementation of the FYCRECT and FYCRECT1 codes that include the calculation of absolute fission yields from given ratios, the calculation of ratios from given R values, or absolute yields, and the performance of various adjustments and uncertainty processing as noted above.

Data measured at the same energy point can be averaged with the AVERAG code. The weighted mean and external uncertainty are calculated, taking into account the uncertainties given by authors for each set of data and the discrepancies between data sets. In general, the weighted mean and external uncertainty are recommended. The reduced χ^2 and internal uncertainty, as well as the arithmetic (unweighted) mean of the measured data and associated uncertainty, are also calculated for reference.

Data can be simultaneously evaluated with the ZOTT code [3.2.11], which takes into account measured absolute fission yields, their ratios and the measurement uncertainties as well as their correlations, and ensures consistency. This code can be used to adjust fission yields and their ratios, and calculates a covariance matrix. The data can be fitted with a linear function by using LIFIT, with options for

$$Y = aE + b \text{ or } ln\ Y = aE + b$$

The least squares method is used to determine the optimum fit coefficients a and b and their uncertainties, as well as the reduced χ^2 (goodness of fit). If the data cannot be fitted well by LIFIT (for example $\chi^2 > 2.0$), the SPF code [3.2.12] can be substituted that adopts a spline fitting procedure for multi-sets of data with knot optimization and spline order selection. SPF can be used for any shape of curves.

3.2.3. Results and recommendations

The evaluated results are shown in Tables 3.2.2 and 3.2.3. Uncertainties are about 1–2% for most of the product nuclides, about 3–5% for some, and larger than 5% for one fifth of the data. An uncertainty of 1–2% for an evaluated yield stems from the fact that data measured by the mass spectrometric method have an uncertainty of 1–2% (after 1965) or 2–3% (before 1965), and a large number of measurements result in a reduced average uncertainty (assuming the data are statistically consistent). Uncertainties of 3–5% occur with later measurements that use direct gamma ray spectrometry or radiochemical methods, while uncertainties larger than 5% arise from earlier measurements employing direct gamma ray spectrometry and radiochemistry. An additional increase of the overall uncertainty of the average is caused by discrepancies between the data sets measured at different laboratories.

If the evaluated data are based on more than three measured data sets, they are generally considered reliable and are recommended, irrespective of whether they are in agreement with other evaluated data or not. Evaluated yields based on only one measurement are recommended, but only if they agree with other evaluated data. When yields are in disagreement with other evaluated data, no data are recommended.

The comparisons of our evaluated data with ENDF/B-VI, JENDL-3, JEF-2.2 and CENDL/FY are given in Tables 3.2.4–3.2.7 and Figs 3.2.1–3.2.5, and show the following:

(a) General agreement with other libraries:

For most cases, differences between our present evaluated data and others are not large. Defining 'discrepant' as those data in which the difference of our evaluated data to others exceeds 10%, or is larger than the uncertainty given by the corresponding library, the number of such cases is about 11% for ^{235}U and ^{238}U fission. Moreover, the number of such cases for ^{235}U is approximately the same for different libraries and different energy points for thermal (T) and fission spectrum (F) yields; however, this number is considerably smaller for 14 MeV (H) in CENDL/FY than in ENDF/B-VI and JENDL-3. The number of such 'discrepancies' for ^{238}U fission with JEF-2 and CENDL/FY is larger than with ENDF/B-VI for fission spectrum neutrons (but the opposite for 14 MeV neutrons (H)). According to the above definition, the number of discrepant cases is influenced by the magnitude of the uncertainties assigned in the different libraries. For example, the uncertainties in ENDF/B-VI are reasonably small, whereas the uncertainties in CENDL/FY are larger (see Tables 3.2.8 and 3.2.9). So when the number of discrepant cases is the same for both libraries, the differences in the yields when compared with CENDL/FY are attributed to the larger uncertainties; if this number is smaller for CENDL/FY this does not mean that the differences in yield values are smaller. Certainly the differences between the present evaluated values and those in ENDF/B-VI are smaller than with JEF-2 and CENDL/FY for ^{235}U fission by thermal and fission spectrum neutrons, and for ^{238}U fission by fission spectrum neutrons.

(b) Discrepant ^{235}U yields:

When compared with data in the other four libraries, our recommended yields are larger by 27–62% for ^{91}Br(T), by 65–70% for ^{106}Ru(F), by 34–44% for ^{115}Cd(T), by 16–35% for ^{115}Cd(F), by 85–95% for ^{115m}Cd(F) and by 19–20% for ^{147}Pm(H); and smaller by 25–60% for ^{90}Br(T), by 10–26% for ^{137}I(T) and by 33–80% for ^{151}Pm(H). Our evaluated yields for ^{91}Br(T), ^{106}Ru(F), ^{115m}Cd(F), ^{147}Pm(H) and ^{151}Pm(H) are not recommended because they are based on only one set of measurements; whereas those for ^{90}Br(T), ^{115}Cd(T, F), ^{137}I(T) are recommended — they are based on more than one set of measurements, but the existing discrepancies should be borne in mind. Furthermore, our values for ^{111}Ag(T, F, H) are also recommended, although only some of them are in agreement with one or two of the four libraries — they are mainly 10–30% smaller than the equivalent data from all other libraries. Care should be taken when using these data because some systematic uncertainties may exist.

(c) Discrepant ^{238}U yields:

Our recommended yields are larger by 20–27% for ^{88}Br(H), and smaller by 9–26% for ^{89}Br(H), by 8–28% ^{146}Nd(H), by 11–21% for ^{149}Sm(H) and by 20–25% for ^{151}Sm(H) when compared with the other four libraries. Except for ^{149}Sm(H) our evaluated data are not recommended because they are based on only one set of measurements. There are only two sets of measured data available for ^{149}Sm(H), and our evaluated data are only recommended as reference.

The recommended yield for ^{85}Kr(F) is 10–15% larger than the equivalent data in ENDF/B-VI, JENDL-3 and CENDL/FY, but is 18% smaller than in JEF-2, while our value for ^{109}Ag(H) is about 20% larger than the data in ENDF/B-VI, JENDL-3 and CENDL/FY, but agrees with JEF-2; our ^{129}I(F) value is about 70% smaller than the data in ENDF/B-VI, JENDL-3 and CENDL/FY, but agrees with JEF-2. Our evaluation for ^{85}Kr(F) and ^{109}Ag(H) is based on only one set of measured data and is recommended only as reference. However, the evaluated yield for ^{129}I(F) is recommended, since the data are based on three sets of measured data (although the existing discrepancies should be borne in mind).

Compared with CENDL/FY, our recommended yield is 39% smaller for ^{93}Zr(H), 26% smaller for ^{144}Pr(F) and 19% smaller for ^{147,149}Pm(H), although in agreement with all other evaluations.

TABLE 3.2.4. COMPARISON OF RECOMMENDED YIELDS FROM ^{235}U FISSION WITH THOSE FROM OTHER LIBRARIES

Nuclide	Library	Thermal spectrum			Fission spectrum			14 MeV		
		YIELD Y	UNCERT (%)	DIFF (%)	YIELD Y	UNCERT (%)	DIFF (%)	YIELD Y	UNCERT (%)	DIFF (%)
33-As-85	THIS WORK	3.4494E–01	5.50	0						
33-As-85	ENDF/B-VI	2.1880E–01	64.00	36.57						
33-As-85	JEF-2	1.6059E–01	31.55	53.44						
33-As-85	JENDL-3	1.5604E–01	0.00	54.76						
33-As-85	CENDL/FY	6.8792E–01	76.66	–99.43						
34-Se-79	THIS WORK	4.3900E–02	6.83	0						
34-Se-79	ENDF/B-VI	4.4729E–02	8.00	–1.89						
34-Se-79	JEF-2	4.7360E–02	10.09	–07.88						
34-Se-79	JENDL-3	4.5321E–02	0.00	–3.24						
34-Se-79	CENDL/FY	4.4457E–02	13.62	–1.27						
35-Br-88	THIS WORK	1.6358E+00	4.93	0						
35-Br-88	ENDF/B-VI	1.7796E+00	2.80	–8.79						
35-Br-88	JEF-2	1.8206E+00	16.42	–11.30						
35-Br-88	JENDL-3	2.0344E+00	0.00	–24.37						
35-Br-88	CENDL/FY	1.5556E+00	11.60	4.90						
35-Br-89	THIS WORK	1.0988E+00	5.09	0						
35-Br-89	ENDF/B-VI	1.0854E+00	2.80	1.22						
35-Br-89	JEF-2	1.4539E+00	23.69	–32.32						
35-Br-89	JENDL-3	1.3190E+00	0.00	–20.04						
35-Br-89	CENDL/FY	1.2293E+00	8.90	–11.88						
35-Br-90	THIS WORK	4.2893E–01	17.85	0						
35-Br-90	ENDF/B-VI	5.6426E–01	4.00	–31.55						
35-Br-90	JEF-2	5.3798E–01	33.83	–25.42						
35-Br-90	JENDL-3	6.8412E–01	0.00	–59.49						
35-Br-90	CENDL/FY	6.2023E–01	9.11	–44.60						
35-Br-91	THIS WORK	3.4000E–01	26.47	0						
35-Br-91	ENDF/B-VI	2.2421E–01	11.00	34.06						
35-Br-91	JEF-2	1.7014E–01	34.99	49.96						

TABLE 3.2.4. COMPARISON OF RECOMMENDED YIELDS FROM ^{235}U FISSION WITH THOSE FROM OTHER LIBRARIES (cont.)

Nuclide	Library	Thermal spectrum			Fission spectrum			14 MeV		
		YIELD Y	UNCERT (%)	DIFF (%)	YIELD Y	UNCERT (%)	DIFF (%)	YIELD Y	UNCERT (%)	DIFF (%)
35-Br-91	JENDL-3	2.4583E–01	0.00	27.70						
35-Br-91	CENDL/FY	1.3018E–01	90.37	61.71						
36-Kr-83	THIS WORK	5.3937E–01	0.48	0	5.8132E–01	2.54	0			
36-Kr-83	ENDF/B-VI	5.3620E–01	0.50	0.59	5.7653E–01	1.00	0.82			
36-Kr-83	JEF-2	5.4950E–01	1.59	–1.88	5.8135E–01	7.00	–0.01			
36-Kr-83	JENDL-3	5.3805E–01	0.00	0.24	5.7053E–01	0.00	1.86			
36-Kr-83	CENDL/FY	5.3593E–01	4.09	0.64	6.0121E–01	1.34	–3.42			
36-Kr-86	THIS WORK	1.9689E+00	0.37	0	1.9900E+00	1.01	0			
36-Kr-86	ENDF/B-VI	1.9650E+00	0.50	0.20	1.9468E+00	1.00	2.17			
36-Kr-86	JEF-2	1.9644E+00	0.93	0.23	1.9965E+00	6.55	–0.33			
36-Kr-86	JENDL-3	1.9725E+00	0.00	–0.18	1.9359E+00	0.00	2.72			
36-Kr-86	CENDL/FY	1.9653E+00	13.09	0.18	1.9609E+00	3.26	1.46			
36-Kr-87	THIS WORK	2.6445E+00	3.31	0	2.4332E+00	2.94	0			
36-Kr-87	ENDF/B-VI	2.5576E+00	1.00	3.29	2.5425E+00	1.40	–4.49			
36-Kr-87	JEF-2	2.5416E+00	4.85	3.89	2.5741E+00	5.85	–5.79			
36-Kr-87	JENDL-3	2.5147E+00	0.00	4.91	2.4682E+00	0.00	–1.44			
36-Kr-87	CENDL/FY	2.6243E+00	4.68	0.76	2.3692E+00	6.40	2.63			
37-Rb-93	THIS WORK	3.3914E+00	3.48	0						
37-Rb-93	ENDF/B-VI	3.5508E+00	1.00	–4.70						
37-Rb-93	JEF-2	3.5294E+00	14.74	–4.07						
37-Rb-93	JENDL-3	3.6134E+00	0.00	–6.55						
37-Rb-93	CENDL/FY	3.9050E+00	4.43	–15.14						
37-Rb-94	THIS WORK	1.6726E+00	2.56	0						
37-Rb-94	ENDF/B-VI	1.6487E+00	2.80	1.43						
37-Rb-94	JEF-2	1.5884E+00	27.73	5.03						
37-Rb-94	JENDL-3	1.7808E+00	0.00	–6.47						
37-Rb-94	CENDL/FY	1.6737E+00	11.80	–0.07						
37-Rb-95	THIS WORK	7.2229E–01	2.99	0						

TABLE 3.2.4. COMPARISON OF RECOMMENDED YIELDS FROM ^{235}U FISSION WITH THOSE FROM OTHER LIBRARIES (cont.)

Nuclide	Library	Thermal spectrum			Fission spectrum			14 MeV		
		YIELD Y	UNCERT (%)	DIFF (%)	YIELD Y	UNCERT (%)	DIFF (%)	YIELD Y	UNCERT (%)	DIFF (%)
37-Rb-95	ENDF/B-VI	7.7034E–01	4.00	–6.65						
37-Rb-95	JEF-2	7.1945E–01	33.30	0.39						
37-Rb-95	JENDL-3	8.1829E–01	0.00	–13.29						
37-Rb-95	CENDL/FY	8.5965E–01	9.09	–19.02						
38-Sr-89	THIS WORK	4.7855E+00	0.92	0	4.2200E+00	4.98	0	4.1084E+00	2.83	0
38-Sr-89	ENDF/B-VI	4.7327E+00	1.00	1.10	4.3737E+00	1.40	–3.64	4.1226E+00	2.80	–0.34
38-Sr-89	JEF-2	4.7726E+00	7.32	0.27	4.3961E+00	13.08	–4.17	4.1218E+00	6.37	–0.33
38-Sr-89	JENDL-3	4.8850E+00	0.00	–2.08	4.5347E+00	0.00	–7.46	4.2150E+00	0.00	–2.59
38-Sr-89	CENDL/FY	4.7903E+00	6.71	–0.10	4.5441E+00	2.24	–7.68	4.1861E+00	3.70	–1.89
38-Sr-90	THIS WORK	5.8499E+00	0.50	0	5.4873E+00	0.82	0	4.6072E+00	5.93	0
38-Sr-90	ENDF/B-VI	5.7819E+00	1.00	1.16	5.4650E+00	0.70	0.41	4.5926E+00	4.00	0.32
38-Sr-90	JEF-2	5.8472E+00	3.22	0.05	5.2471E+00	7.63	4.38	4.5862E+00	2.60	0.46
38-Sr-90	JENDL-3	5.9045E+00	0.00	–0.93	5.4341E+00	0.00	0.97	4.6607E+00	0.00	–1.16
38-Sr-90	CENDL/FY	5.7251E+00	1.08	2.13	5.1847E+00	2.63	5.51	4.5253E+00	4.47	1.78
38-Sr-92	THIS WORK	6.0000E+00	2.83	0						
38-Sr-92	ENDF/B-VI	5.9379E+00	1.40	1.04						
38-Sr-92	JEF-2	5.9863E+00	5.42	0.23						
38-Sr-92	JENDL-3	5.9080E+00	0.00	1.53						
38-Sr-92	CENDL/FY	5.9218E+00	3.38	1.30						
39-Y-91	THIS WORK	5.8974E+00	0.80	0	5.8307E+00	1.33	0	4.9312E+00	5.03	0
39-Y-91	ENDF/B-VI	5.8278E+00	64.00	1.18	5.7334E+00	64.00	1.67	4.8227E+00	64.00	2.20
39-Y-91	JEF-2	5.8800E+00	1.33	0.30	5.3922E+00	1.06	7.52	4.6336E+00	4.74	6.04
39-Y-91	JENDL-3	5.9187E+00	0.00	–0.36	5.6549E+00	0.00	3.02	4.8924E+00	0.00	0.79
39-Y-91	CENDL/FY	6.0346E+00	1.84	–2.33	5.2569E+00	4.14	9.84	4.8765E+00	9.90	1.11
39-Y-99	THIS WORK	2.0482E+00	2.98	0						
39-Y-99	ENDF/B-VI	2.0824E+00	6.00	–1.67						
39-Y-99	JEF-2	1.9960E+00	24.43	2.55						
39-Y-99	JENDL-3	2.3703E+00	0.00	–15.73						

TABLE 3.2.4. COMPARISON OF RECOMMENDED YIELDS FROM ^{235}U FISSION WITH THOSE FROM OTHER LIBRARIES (cont.)

Nuclide	Library	Thermal spectrum			Fission spectrum			14 MeV		
		YIELD Y	UNCERT (%)	DIFF (%)	YIELD Y	UNCERT (%)	DIFF (%)	YIELD Y	UNCERT (%)	DIFF (%)
39-Y-99	CENDL/FY	2.4372E+00	15.18	–18.99						
40-Zr-91	THIS WORK	5.9288E+00	0.74	0	5.6600E+00	0.90	0	4.9100E+00	4.99	0
40-Zr-91	ENDF/B-VI	5.8278E+00	0.70	1.70	5.7334E+00	0.70	–1.30	4.8227E+00	4.00	1.78
40-Zr-91	JEF-2	5.8800E+00	8.46	0.82	5.3922E+00	13.37	4.73	4.6336E+00	8.81	5.63
40-Zr-91	JENDL-3	5.9187E+00	0.00	0.17	5.6549E+00	0.00	0.09	4.8924E+00	0.00	0.36
40-Zr-91	CENDL/FY	5.8762E+00	2.04	0.89	5.6500E+00	1.33	0.18	5.0083E+00	69.51	–2.00
40-Zr-93	THIS WORK	6.3470E+00	0.73	0	6.1579E+00	0.87	0	5.0863E+00	5.43	0
40-Zr-93	ENDF/B-VI	6.3463E+00	0.70	0.01	6.2540E+00	0.70	–1.56	5.1932E+00	6.00	–2.10
40-Zr-93	JEF-2	6.3206E+00	2.90	0.42	5.8791E+00	5.85	4.53	5.1759E+00	11.62	–1.76
40-Zr-93	JENDL-3	6.3902E+00	0.00	–0.68	6.1394E+00	0.00	0.30	5.2958E+00	0.00	–4.12
40-Zr-93	CENDL/FY	6.3548E+00	2.42	–0.12	6.1358E+00	0.89	0.36	5.6994E+00	93.82	–12.05
40-Zr-96	THIS WORK	6.2615E+00	1.29	0	6.1205E+00	0.88	0			
40-Zr-96	ENDF/B-VI	6.3392E+00	1.00	–1.24	6.2023E+00	0.70	–1.34			
40-Zr-96	JEF-2	6.2920E+00	1.27	–0.49	6.3421E+00	7.13	–3.62			
40-Zr-96	JENDL-3	6.2641E+00	0.00	–0.04	6.0815E+00	0.00	0.64			
40-Zr-96	CENDL/FY	6.2368E+00	1.80	0.39	6.1010E+00	2.98	0.32			
41-Nb-95	THIS WORK	6.5780E+00	0.50	0	6.4531E+00	2.39	0			
41-Nb-95	ENDF/B-VI	6.5029E+00	1.40	1.14	6.4320E+00	0.70	0.33			
41-Nb-95	JEF-2	6.5563E+00	3.72	0.33	6.3307E+00	8.31	1.90			
41-Nb-95	JENDL-3	6.4947E+00	0.00	1.27	6.3629E+00	0.00	1.40			
41-Nb-95	CENDL/FY	6.6721E+00	6.57	–1.43	6.3692E+00	3.64	1.30			
42-Mo-95	THIS WORK	6.5035E+00	0.56	0	6.3837E+00	0.66	0			
42-Mo-95	ENDF/B-VI	6.5029E+00	0.70	0.01	6.4320E+00	0.50	–0.76			
42-Mo-95	JEF-2	6.5604E+00	0.85	–0.87	6.3346E+00	1.77	0.77			
42-Mo-95	JENDL-3	6.4962E+00	0.00	0.11	6.3643E+00	0.00	0.30			
42-Mo-95	CENDL/FY	6.5199E+00	1.38	–0.25	6.3806E+00	0.89	0.05			
42-Mo-97	THIS WORK	5.9163E+00	0.61	0	5.9471E+00	0.66	0			
42-Mo-97	ENDF/B-VI	5.9968E+00	0.70	–1.36	6.0029E+00	0.50	–0.94			

TABLE 3.2.4. COMPARISON OF RECOMMENDED YIELDS FROM ^{235}U FISSION WITH THOSE FROM OTHER LIBRARIES (cont.)

Nuclide	Library	Thermal spectrum			Fission spectrum			14 MeV		
		YIELD Y	UNCERT (%)	DIFF (%)	YIELD Y	UNCERT (%)	DIFF (%)	YIELD Y	UNCERT (%)	DIFF (%)
42-Mo-97	JEF-2	5.9835E+00	7.29	–1.14	5.8512E+00	13.11	1.61			
42-Mo-97	JENDL-3	6.0082E+00	0.00	–1.55	5.9905E+00	0.00	–0.73			
42-Mo-97	CENDL/FY	5.9336E+00	0.92	–0.29	5.8733E+00	4.21	1.24			
42-Mo–100	THIS WORK	6.2135E+00	0.52	0	6.2425E+00	2.26	0			
42-Mo-100	ENDF/B-VI	6.2923E+00	0.70	–1.27	6.2983E+00	1.00	–0.89			
42-Mo-100	JEF-2	6.2237E+00	0.94	–0.16	6.4781E+00	6.37	–3.77			
42-Mo-100	JENDL-3	6.2323E+00	0.00	–0.30	6.3286E+00	0.00	–1.38			
42-Mo-100	CENDL/FY	6.2871E+00	1.00	–1.18	6.0930E+00	3.24	2.39			
43-Tc-99	THIS WORK	6.0756E+00	1.00	0						
43-Tc-99	ENDF/B-VI	6.1087E+00	1.00	–0.55						
43-Tc-99	JEF-2	6.1770E+00	7.91	–1.67						
43-Tc-99	JENDL-3	6.1105E+00	0.00	–0.57						
43-Tc-99	CENDL/FY	6.0367E+00	1.97	0.64						
44-Ru-101	THIS WORK	5.1895E+00	0.70	0	5.3019E+00	2.16	0			
44-Ru-101	ENDF/B-VI	5.1726E+00	1.00	0.33	5.1242E+00	1.40	3.35			
44-Ru-101	JEF-2	5.1368E+00	1.03	1.02	5.2315E+00	5.01	1.33			
44-Ru-101	JENDL-3	5.0814E+00	0.00	2.08	5.3498E+00	0.00	–0.90			
44-Ru-101	CENDL/FY	5.2210E+00	1.14	–0.61	5.2217E+00	1.83	1.51			
44-Ru-102	THIS WORK	4.2954E+00	1.08	0	4.4100E+00	4.54	0			
44-Ru-102	ENDF/B-VI	4.2985E+00	1.00	–0.07	4.3590E+00	1.00	1.16			
44-Ru-102	JEF-2	4.2806E+00	0.87	0.34	4.4766E+00	6.69	–1.51			
44-Ru-102	JENDL-3	4.2331E+00	0.00	1.45	4.5295E+00	0.00	–2.71			
44-Ru-102	CENDL/FY	4.3290E+00	1.41	–0.78	4.4388E+00	1.98	–0.65			
44-Ru-103	THIS WORK	3.0405E+00	0.97	0	3.5525E+00	1.67	0	3.4127E+00	3.00	0
44-Ru-103	ENDF/B-VI	3.0309E+00	1.40	0.31	3.2439E+00	1.40	8.69	3.2048E+00	2.80	6.09
44-Ru-103	JEF-2	3.0237E+00	7.58	0.55	3.2851E+00	7.99	7.53	3.3855E+00	11.12	0.80
44-Ru-103	JENDL-3	3.0274E+00	0.00	0.43	3.2749E+00	0.00	7.81	3.2180E+00	0.00	5.71
44-Ru-103	CENDL/FY	3.0689E+00	2.49	–0.93	3.2885E+00	1.55	7.43	3.5039E+00	4.57	–2.67

TABLE 3.2.4. COMPARISON OF RECOMMENDED YIELDS FROM ^{235}U FISSION WITH THOSE FROM OTHER LIBRARIES (cont.)

Nuclide	Library	Thermal spectrum			Fission spectrum			14 MeV		
		YIELD Y	UNCERT (%)	DIFF (%)	YIELD Y	UNCERT (%)	DIFF (%)	YIELD Y	UNCERT (%)	DIFF (%)
44-Ru-104	THIS WORK	1.8914E+00	0.75	0	1.9905E+00	5.50	0			
44-Ru-104	ENDF/B-VI	1.8807E+00	1.00	0.57	2.0724E+00	1.00	–4.11			
44-Ru-104	JEF-2	1.8721E+00	1.37	1.02	2.2655E+00	13.31	–13.82			
44-Ru-104	JENDL-3	1.8397E+00	0.00	2.73	2.2820E+00	0.00	–14.64			
44-Ru-104	CENDL/FY	1.8744E+00	1.30	0.90	2.1401E+00	1.47	–7.52			
44-Ru-106	THIS WORK	3.9134E–01	0.88	0	1.6691E+00	3.92	0	1.6691E+00	3.92	0
44-Ru-106	ENDF/B-VI	4.0155E–01	1.40	–2.61	5.3239E–01	1.00	68.10	1.6093E+00	6.00	3.59
44-Ru-106	JEF-2	4.0673E–01	3.75	–3.93	4.9058E–01	13.23	70.61	1.6952E+00	9.89	–1.56
44-Ru-106	JENDL-3	4.0231E–01	0.00	–2.80	5.5937E–01	0.00	66.49	1.5715E+00	0.00	5.85
44-Ru-106	CENDL/FY	3.9097E–01	11.51	0.09	5.4877E–01	4.18	67.12	1.6375E+00	4.47	1.89
45-Rh-103	THIS WORK	2.9667E+00	1.09	0	3.2100E+00	4.00	0	3.4930E+00	6.00	0
45-Rh-103	ENDF/B-VI	3.0309E+00	1.00	–2.17	3.2439E+00	1.40	–1.06	3.2048E+00	2.80	8.25
45-Rh-103	JEF-2	3.0237E+00	4.07	–1.92	3.2851E+00	10.10	–2.34	3.3855E+00	3.04	3.08
45-Rh-103	JENDL-3	3.0274E+00	0.00	–2.05	3.2749E+00	0.00	–2.02	3.2180E+00	0.00	7.87
45-Rh-103	CENDL/FY	3.2209E+00	16.36	–8.57	3.1865E+00	102.17	0.73	3.1847E+00	100.36	8.83
45-Rh-106	THIS WORK	4.0167E–01	3.54	0						
45-Rh-106	ENDF/B-VI	4.0155E–01	1.40	0.03						
45-Rh-106	JEF-2	4.0673E–01	3.75	–1.26						
45-Rh-106	JENDL-3	4.0231E–01	0.00	–0.16						
45-Rh-106	CENDL/FY	4.8049E–01	29.73	–19.62						
46-Pd-105	THIS WORK	9.4645E–01	0.94	0	1.1700E+00	11.11	0	1.7010E+00	6.00	0
46-Pd-105	ENDF/B-VI	9.6416E–01	1.40	–1.87	1.1963E+00	2.80	–2.25	1.8721E+00	4.00	–10.06
46-Pd-105	JEF-2	9.5770E–01	6.82	–1.19	1.2810E+00	14.13	–9.49	1.8310E+00	6.76	–7.64
46-Pd-105	JENDL-3	9.6384E–01	0.00	–1.84	1.2048E+00	0.00	–2.98	1.8861E+00	0.00	–10.88
46-Pd-105	CENDL/FY	9.6888E–01	2.05	–2.37	1.4404E+00	91.23	–23.11	1.8683E+00	100.37	–9.84
46-Pd-107	THIS WORK	1.4574E–01	0.94	0						
46-Pd-107	ENDF/B-VI	1.4619E–01	2.80	–0.31						
46-Pd-107	JEF-2	1.3884E–01	3.93	4.73						

TABLE 3.2.4. COMPARISON OF RECOMMENDED YIELDS FROM ^{235}U FISSION WITH THOSE FROM OTHER LIBRARIES (cont.)

Nuclide	Library	Thermal spectrum			Fission spectrum			14 MeV		
		YIELD Y	UNCERT (%)	DIFF (%)	YIELD Y	UNCERT (%)	DIFF (%)	YIELD Y	UNCERT (%)	DIFF (%)
46-Pd-107	JENDL-3	1.4028E–01	0.00	3.75						
46-Pd-107	CENDL/FY	1.4951E–01	2.30	–2.59						
47-Ag-109	THIS WORK	3.1000E–02	22.58	0						
47-Ag-109	ENDF/B-VI	3.1221E–02	64.00	–0.71						
47-Ag-109	JEF-2	2.6001E–02	21.12	16.13						
47-Ag-109	JENDL-3	3.4482E–02	0.00	–11.23						
47-Ag-109	CENDL/FY	3.2332E–02	96.68	–4.30						
47-Ag-111	THIS WORK	1.5789E–02	3.37	0	3.1492E–02	2.85	0	1.0272E+00	1.54	0
47-Ag-111	ENDF/B-VI	1.7379E–02	4.00	–10.07	4.2450E–02	2.80	–34.79	1.0760E+00	2.80	–4.76
47-Ag-111	JEF-2	2.8212E–02	17.61	–78.68	3.3122E–02	16.35	–5.18	1.2117E+00	3.05	–17.96
47-Ag-111	JENDL-3	1.9963E–02	0.00	–26.43	4.2930E–02	0.00	–36.32	1.2006E+00	0.00	–16.88
47-Ag-111	CENDL/FY	1.7732E–02	40.66	–12.31	3.9334E–02	12.46	–24.90	1.2327E+00	7.05	–20.01
48-Cd-115	THIS WORK	1.7587E–02	4.30	0	3.7075E–02	12.09	0	6.7990E–01	4.71	0
48-Cd-115	ENDF/B-VI	1.1578E–02	6.00	34.17	3.1077E–02	2.80	16.18	6.3547E–01	4.00	6.53
48-Cd-115	JEF-2	1.0605E–02	10.40	39.70	2.4047E–02	19.67	35.14	9.3446E–01	12.61	–37.44
48-Cd-115	JENDL-3	1.0248E–02	0.00	41.73	2.7946E–02	0.00	24.62	9.0056E–01	0.00	–32.45
48-Cd-115	CENDL/FY	9.8007E–03	7.53	44.27	2.5074E–02	5.31	32.37	8.3272E–01	5.10	–22.48
48-Cd-115	THIS WORK	8.2810E–04	7.77	0	1.9000E–02	21.05	0	7.1261E–02	7.67	0
48-Cd-115	ENDF/B-VI	1.0049E–03	6.00	–21.35	2.8010E–03	23.00	85.26	4.5607E–01	1.40	–540.0
48-Cd-115	JEF-2	4.4288E–04	10.85	46.52	1.0091E–03	20.16	94.69	3.8719E–02	13.28	45.67
48-Cd-115	JENDL-3	8.9398E–04	0.00	–7.96	2.4118E–03	0.00	87.31	9.3034E–02	0.00	–30.55
48-Cd-115	CENDL/FY	9.0722E–04	18.25	–9.55	2.3233E–03	54.31	87.77	5.4799E–02	33.85	23.10
50-Sn-126	THIS WORK	5.7213E–02	4.61	0	1.0000E–01	5.00	0			
50-Sn-126	ENDF/B-VI	5.6143E–02	8.00	1.87	9.7355E–02	16.00	2.64			
50-Sn-126	JEF-2	5.9717E–02	9.25	–4.38	9.6017E–02	32.31	3.98			
50-Sn-126	JENDL-3	5.4932E–02	0.00	3.99	1.3794E–01	0.00	–37.94			
50-Sn-126	CENDL/FY	5.8456E–02	98.49	–2.17	9.9509E–02	98.80	0.49			
51-Sb-125	THIS WORK	2.8095E–02	4.77	0	6.5502E–02	10.50	0			

TABLE 3.2.4. COMPARISON OF RECOMMENDED YIELDS FROM ^{235}U FISSION WITH THOSE FROM OTHER LIBRARIES (cont.)

Nuclide	Library	Thermal spectrum			Fission spectrum			14 MeV		
		YIELD Y	UNCERT (%)	DIFF (%)	YIELD Y	UNCERT (%)	DIFF (%)	YIELD Y	UNCERT (%)	DIFF (%)
51-Sb-125	ENDF/B-VI	3.4020E–02	2.80	–21.09	6.8029E–02	8.00	–3.86			
51-Sb-125	JEF-2	2.7754E–02	5.97	1.21	6.6917E–02	22.76	–2.16			
51-Sb-125	JENDL-3	2.9378E–02	0.00	–4.57	7.0912E–02	0.00	–8.26			
51-Sb-125	CENDL/FY	2.5943E–02	9.05	7.66	6.3426E–02	77.54	3.17			
51-Sb-135	THIS WORK	1.5040E–01	5.00	0						
51-Sb-135	ENDF/B-VI	1.4576E–01	6.00	3.08						
51-Sb-135	JEF-2	1.8025E–01	35.01	–19.85						
51-Sb-135	JENDL-3	1.4628E–01	0.00	2.74						
51-Sb-135	CENDL/FY	1.4742E–01	6.86	1.98						
52-Te-132	THIS WORK	4.2339E+00	0.64	0	4.8215E+00	0.95	0	4.1098E+00	1.81	0
52-Te-132	ENDF/B-VI	4.2948E+00	1.40	–1.44	4.6608E+00	2.00	3.33	4.0897E+00	4.00	0.49
52-Te-132	JEF-2	4.2481E+00	1.00	–0.34	4.5988E+00	2.24	4.62	4.3046E+00	3.87	–4.74
52-Te-132	JENDL-3	4.2830E+00	0.00	–1.16	4.5645E+00	0.00	5.33	4.0024E+00	0.00	2.61
52-Te-132	CENDL/FY	4.3954E+00	2.61	–3.81	4.9137E+00	6.72	–1.91	4.0711E+00	4.47	0.94
53-I-129	THIS WORK	7.5145E–01	5.04	0	1.0900E+00	5.05	0	3.2630E+00	6.00	0
53-I-129	ENDF/B-VI	5.4335E–01	1.00	27.69	8.3516E–01	4.00	23.38	3.3746E+00	8.00	–3.42
53-I-129	JEF-2	7.8234E–01	4.01	–4.11	1.1739E+00	26.79	–7.70	2.4260E+00	33.16	25.65
53-I-129	JENDL-3	7.1785E–01	0.00	4.47	8.2731E–01	0.00	24.10	3.3557E+00	0.00	–2.84
53-I-129	CENDL/FY	8.7909E–01	15.94	–16.99	1.1598E+00	12.30	–6.40	3.5533E+00	100.37	–8.90
53-I-131	THIS WORK	2.8787E+00	0.60	0	3.3518E+00	1.07	0	4.2232E+00	2.68	0
53-I-131	ENDF/B-VI	2.8907E+00	1.00	–0.42	3.2195E+00	1.40	3.95	4.1015E+00	4.00	2.88
53-I-131	JEF-2	2.8871E+00	1.12	–0.29	3.3340E+00	1.89	0.53	3.9306E+00	3.39	6.93
53-I-131	JENDL-3	2.8843E+00	0.00	–0.20	3.1801E+00	0.00	5.12	3.9947E+00	0.00	5.41
53-I-131	CENDL/FY	2.8234E+00	5.08	1.92	3.2456E+00	1.60	3.17	4.0238E+00	3.57	4.72
53-I-135	THIS WORK	6.2543E+00	4.77	0	6.7447E+00	2.53	0	4.3150E+00	5.61	0
53-I-135	ENDF/B-VI	6.2819E+00	1.40	–0.44	6.2959E+00	4.00	6.65	4.2183E+00	8.00	2.24
53-I-135	JEF-2	6.3158E+00	2.93	–0.98	5.9170E+00	5.61	12.27	5.0958E+00	11.31	–18.10
53-I-135	JENDL-3	6.2897E+00	0.00	–0.57	6.2271E+00	0.00	7.67	4.1868E+00	0.00	2.97

TABLE 3.2.4. COMPARISON OF RECOMMENDED YIELDS FROM ^{235}U FISSION WITH THOSE FROM OTHER LIBRARIES (cont.)

Nuclide	Library	Thermal spectrum			Fission spectrum			14 MeV		
		YIELD Y	UNCERT (%)	DIFF (%)	YIELD Y	UNCERT (%)	DIFF (%)	YIELD Y	UNCERT (%)	DIFF (%)
53-I-135	CENDL/FY	6.3108E+00	7.44	–0.90	6.1451E+00	3.57	8.89	4.3285E+00	10.15	–0.31
53-I-137	THIS WORK	2.7757E+00	10.31	0	3.0000E+00	20.00	0			
53-I-137	ENDF/B-VI	3.0680E+00	2.80	–10.53	2.5661E+00	6.00	14.46			
53-I-137	JEF-2	3.5050E+00	15.37	–26.27	2.7737E+00	30.37	7.54			
53-I-137	JENDL-3	3.2222E+00	0.00	–16.09	3.3775E+00	0.00	–12.58			
53-I-137	CENDL/FY	3.4859E+00	4.94	–25.59	3.4174E+00	100.46	–13.91			
53-I-138	THIS WORK	1.5356E+00	8.54	0						
53-I-138	ENDF/B-VI	1.4864E+00	2.80	3.21						
53-I-138	JEF-2	1.4968E+00	28.99	2.53						
53-I-138	JENDL-3	1.5928E+00	0.00	–3.72						
53-I-138	CENDL/FY	1.5350E+00	9.37	0.04						
53-I-139	THIS WORK	6.3139E–01	17.26	0						
53-I-139	ENDF/B-VI	7.7756E–01	8.00	–23.15						
53-I-139	JEF-2	6.2688E–01	34.03	0.71						
53-I-139	JENDL-3	9.8141E–01	0.00	–55.44						
53-I-139	CENDL/FY	8.4390E–01	30.88	–33.66						
54-Xe-131	THIS WORK	2.9997E+00	1.56	0	3.2620E+00	1.42	0			
54-Xe-131	ENDF/B-VI	2.8907E+00	0.50	3.63	3.2195E+00	0.70	1.30			
54-Xe-131	JEF-2	2.8868E+00	1.09	3.76	3.3337E+00	1.89	–2.20			
54-Xe-131	JENDL-3	2.8843E+00	0.00	3.85	3.1801E+00	0.00	2.51			
54-Xe-131	CENDL/FY	2.9074E+00	3.48	3.08	3.1808E+00	0.59	2.49			
54-Xe-132	THIS WORK	4.3004E+00	0.88	0	4.6167E+00	0.59	0			
54-Xe-132	ENDF/B-VI	4.3131E+00	0.35	–0.30	4.6710E+00	0.50	–1.18			
54-Xe-132	JEF-2	4.2731E+00	0.98	0.63	4.6735E+00	2.05	–1.23			
54-Xe-132	JENDL-3	4.2999E+00	0.00	0.01	4.6019E+00	0.00	0.32			
54-Xe-132	CENDL/FY	4.3142E+00	1.31	–0.32	4.6053E+00	3.42	0.25			
54-Xe-134	THIS WORK	7.5175E+00	1.45	0	7.6946E+00	1.41	0			
54-Xe-134	ENDF/B-VI	7.8721E+00	0.50	–4.72	7.6667E+00	0.50	0.36			

TABLE 3.2.4. COMPARISON OF RECOMMENDED YIELDS FROM ^{235}U FISSION WITH THOSE FROM OTHER LIBRARIES (cont.)

Nuclide	Library	Thermal spectrum			Fission spectrum			14 MeV		
		YIELD Y	UNCERT (%)	DIFF (%)	YIELD Y	UNCERT (%)	DIFF (%)	YIELD Y	UNCERT (%)	DIFF (%)
54-Xe-134	JEF-2	7.7486E+00	1.14	–3.07	7.7783E+00	4.76	–1.09			
54-Xe-134	JENDL-3	7.8258E+00	0.00	–4.10	7.5739E+00	0.00	1.57			
54-Xe-134	CENDL/FY	7.9319E+00	0.52	–5.51	7.6109E+00	7.54	1.09			
54-Xe-135	THIS WORK	6.7770E+00	2.66	0						
54-Xe-135	ENDF/B-VI	6.5385E+00	0.70	3.52						
54-Xe-135	JEF-2	6.5792E+00	2.38	2.92						
54-Xe-135	JENDL-3	6.5315E+00	0.00	3.62						
54-Xe-135	CENDL/FY	6.4191E+00	2.57	5.28						
54-Xe-136	THIS WORK	6.3213E+00	1.13	0	6.2763E+00	0.77	0			
54-Xe-136	ENDF/B-VI	6.3127E+00	0.35	0.14	6.2153E+00	0.50	0.97			
54-Xe-136	JEF-2	6.2704E+00	1.66	0.81	6.1953E+00	6.18	1.29			
54-Xe-136	JENDL-3	6.3059E+00	0.00	0.24	6.1429E+00	0.00	2.13			
54-Xe-136	CENDL/FY	6.3162E+00	2.10	0.08	6.1756E+00	4.13	1.60			
54-Xe-137	THIS WORK	6.3361E+00	1.03	0	5.8200E+00	5.00	0			
54-Xe-137	ENDF/B-VI	6.1283E+00	1.00	3.28	5.9931E+00	1.40	–2.97			
54-Xe-137	JEF-2	6.1571E+00	8.77	2.83	5.8449E+00	14.57	–0.43			
54-Xe-137	JENDL-3	6.1109E+00	0.00	3.55	5.9044E+00	0.00	–1.45			
54-Xe-137	CENDL/FY	6.2011E+00	4.16	2.13	5.7848E+00	4.03	0.60			
54-Xe-138	THIS WORK	6.3810E+00	2.36	0	6.1200E+00	5.00	0			
54-Xe-138	ENDF/B-VI	6.2969E+00	1.40	1.32	6.0093E+00	1.40	1.81			
54-Xe-138	JEF-2	6.4079E+00	7.56	–0.42	5.9138E+00	13.45	3.37			
54-Xe-138	JENDL-3	6.3731E+00	0.00	0.12	6.0324E+00	0.00	1.43			
54-Xe-138	CENDL/FY	6.3356E+00	4.17	0.71	5.9612E+00	3.82	2.59			
55-Cs-133	THIS WORK	6.7996E+00	0.71	0	6.7457E+00	0.89	0			
55-Cs-133	ENDF/B-VI	6.6991E+00	0.35	1.48	6.7236E+00	0.50	0.33			
55-Cs-133	JEF-2	6.6149E+00	1.05	2.72	6.6100E+00	2.64	2.01			
55-Cs-133	JENDL-3	6.7019E+00	0.00	1.44	6.7299E+00	0.00	0.23			
55-Cs-133	CENDL/FY	6.6467E+00	0.46	2.25	6.6037E+00	2.87	2.11			

TABLE 3.2.4. COMPARISON OF RECOMMENDED YIELDS FROM ^{235}U FISSION WITH THOSE FROM OTHER LIBRARIES (cont.)

Nuclide	Library	Thermal spectrum			Fission spectrum			14 MeV		
		YIELD Y	UNCERT (%)	DIFF (%)	YIELD Y	UNCERT (%)	DIFF (%)	YIELD Y	UNCERT (%)	DIFF (%)
55-Cs-135	THIS WORK	6.5311E+00	0.66	0	6.5240E+00	0.64	0	5.6990E+00	6.00	0
55-Cs-135	ENDF/B-VI	6.5390E+00	64.00	–0.12	6.6013E+00	64.00	–1.18	5.7288E+00	64.00	–0.52
55-Cs-135	JEF-2	6.5803E+00	2.23	–0.75	6.3696E+00	3.68	2.37	5.7721E+00	10.41	–1.28
55-Cs-135	JENDL-3	6.5337E+00	0.00	–0.04	6.5711E+00	0.00	–0.72	5.9116E+00	0.00	–3.73
55-Cs-135	CENDL/FY	6.5300E+00	0.35	0.02	6.3696E+00	1.73	2.37	5.4936E+00	79.67	3.60
55-Cs-136	THIS WORK	5.4965E–03	6.70	0						
55-Cs-136	ENDF/B-VI	5.5376E–03	64.00	–0.75						
55-Cs-136	JEF-2	8.7521E–03	34.94	–59.23						
55-Cs-136	JENDL-3	5.4718E–03	0.00	0.45						
55-Cs-136	CENDL/FY	6.1531E–03	125.87	–11.95						
55-Cs-137	THIS WORK	6.2052E+00	0.82	0	6.2008E+00	0.86	0			
55-Cs-137	ENDF/B-VI	6.1883E+00	0.50	0.27	6.2214E+00	0.50	–0.33			
55-Cs-137	JEF-2	6.2444E+00	8.64	–0.63	5.9962E+00	14.07	3.30			
55-Cs-137	JENDL-3	6.2686E+00	0.00	–1.02	6.2032E+00	0.00	–0.04			
55-Cs-137	CENDL/FY	6.1844E+00	2.86	0.34	6.1237E+00	0.87	1.24			
56-Ba-140	THIS WORK	6.2059E+00	0.99	0	6.1514E+00	1.60	0	4.5963E+00	2.53	0
56-Ba-140	ENDF/B-VI	6.2145E+00	1.00	–0.14	5.9777E+00	1.00	2.82	4.4949E+00	2.80	2.21
56-Ba-140	JEF-2	6.2760E+00	1.19	–1.13	5.7817E+00	0.99	6.01	4.3034E+00	1.48	6.37
56-Ba-140	JENDL-3	6.2946E+00	0.00	–1.43	6.1187E+00	0.00	0.53	4.4477E+00	0.00	3.23
56-Ba-140	CENDL/FY	6.2801E+00	1.38	–1.20	5.9274E+00	9.02	3.64	4.4743E+00	8.07	2.65
57-La-140	THIS WORK	6.4070E+00	1.72	0						
57-La-140	ENDF/B-VI	6.2197E+00	1.00	2.92						
57-La-140	JEF-2	6.2767E+00	1.19	2.03						
57-La-140	JENDL-3	6.3000E+00	0.00	1.67						
57-La-140	CENDL/FY	6.1538E+00	14.62	3.95						
58-Ce-141	THIS WORK	5.9823E+00	0.85	0	5.6817E+00	1.56	0	4.5883E+00	3.08	0
58-Ce-141	ENDF/B-VI	5.8470E+00	1.00	2.26	5.9491E+00	2.80	–4.71	4.4855E+00	6.00	2.24
58-Ce-141	JEF-2	5.8527E+00	5.28	2.17	5.6784E+00	10.12	0.06	4.4280E+00	10.57	3.49

TABLE 3.2.4. COMPARISON OF RECOMMENDED YIELDS FROM ^{235}U FISSION WITH THOSE FROM OTHER LIBRARIES (cont.)

Nuclide	Library	Thermal spectrum			Fission spectrum			14 MeV		
		YIELD Y	UNCERT (%)	DIFF (%)	YIELD Y	UNCERT (%)	DIFF (%)	YIELD Y	UNCERT (%)	DIFF (%)
58-Ce-141	JENDL-3	5.7967E+00	0.00	3.10	5.9536E+00	0.00	–4.79	4.3742E+00	0.00	4.67
58-Ce-141	CENDL/FY	5.7555E+00	2.22	3.79	5.9961E+00	4.72	–5.53	4.6061E+00	9.94	–0.39
58-Ce-143	THIS WORK	5.9993E+00	0.77	0	5.6022E+00	1.01	0	3.7919E+00	2.67	0
58-Ce-143	ENDF/B-VI	5.9558E+00	1.40	0.73	5.7312E+00	1.40	–2.30	3.8147E+00	2.80	–0.60
58-Ce-143	JEF-2	5.9447E+00	7.31	0.91	5.6893E+00	10.36	–1.55	3.8712E+00	4.89	–2.09
58-Ce-143	JENDL-3	5.9388E+00	0.00	1.01	5.6886E+00	0.00	–1.54	3.8061E+00	0.00	–0.38
58-Ce-143	CENDL/FY	5.7861E+00	4.28	3.55	5.5847E+00	1.74	0.31	3.8820E+00	3.16	–2.38
59-Pr-141	THIS WORK	5.9929E+00	0.94	0	5.6184E+00	3.07	0	4.5600E+00	10.96	0
59-Pr-141	ENDF/B-VI	5.8470E+00	1.00	2.43	5.9491E+00	1.40	–5.89	4.4855E+00	4.00	1.63
59-Pr-141	JEF-2	5.8527E+00	6.96	2.34	5.6784E+00	8.13	–1.07	4.4280E+00	7.25	2.89
59-Pr-141	JENDL-3	5.7967E+00	0.00	3.27	5.9536E+00	0.00	–5.97	4.3742E+00	0.00	4.07
59-Pr-141	CENDL/FY	5.4907E+00	5.37	8.38	5.9747E+00	4.91	–6.34	4.6537E+00	92.35	–2.05
59-Pr-144	THIS WORK	5.5523E+00	0.70	0	5.1470E+00	2.52	0			
59-Pr-144	ENDF/B-VI	5.4996E+00	0.50	0.95	5.2686E+00	1.00	–2.36			
59-Pr-144	JEF-2	5.4629E+00	2.89	1.61	4.8849E+00	4.29	5.09			
59-Pr-144	JENDL-3	5.4725E+00	0.00	1.44	5.2580E+00	0.00	–2.16			
59-Pr-144	CENDL/FY	6.0148E+00	80.71	–8.33	5.3180E+00	99.71	–3.32			
60-Nd-143	THIS WORK	5.9603E+00	0.70	0	5.6920E+00	0.86	0			
60-Nd-143	ENDF/B-VI	5.9558E+00	0.35	0.08	5.7312E+00	0.50	–0.69			
60-Nd-143	JEF-2	5.9447E+00	0.94	0.26	5.6893E+00	1.03	0.05			
60-Nd-143	JENDL-3	5.9388E+00	0.00	0.36	5.6887E+00	0.00	0.06			
60-Nd-143	CENDL/FY	5.9643E+00	0.97	–0.07	5.6870E+00	0.81	0.09			
60-Nd-144	THIS WORK	5.4571E+00	0.47	0	5.1929E+00	0.97	0			
60-Nd-144	ENDF/B-VI	5.4996E+00	0.35	–0.78	5.2687E+00	0.70	–1.46			
60-Nd-144	JEF-2	5.4630E+00	0.70	–0.11	4.8850E+00	2.04	5.93			
60-Nd-144	JENDL-3	5.4725E+00	0.00	–0.28	5.2580E+00	0.00	–1.25			
60-Nd-144	CENDL/FY	5.4904E+00	4.78	–0.61	5.1500E+00	1.86	0.83			
60-Nd-145	THIS WORK	3.9403E+00	0.72	0	3.7641E+00	1.04	0			

TABLE 3.2.4. COMPARISON OF RECOMMENDED YIELDS FROM ^{235}U FISSION WITH THOSE FROM OTHER LIBRARIES (cont.)

Nuclide	Library	Thermal spectrum			Fission spectrum			14 MeV		
		YIELD Y	UNCERT (%)	DIFF (%)	YIELD Y	UNCERT (%)	DIFF (%)	YIELD Y	UNCERT (%)	DIFF (%)
60-Nd-145	ENDF/B-VI	3.9334E+00	0.35	0.18	3.7757E+00	0.50	–0.31			
60-Nd-145	JEF-2	3.9318E+00	0.79	0.22	3.8044E+00	2.66	–1.07			
60-Nd-145	JENDL-3	3.9175E+00	0.00	0.58	3.7429E+00	0.00	0.56			
60-Nd-145	CENDL/FY	3.9495E+00	4.90	–0.23	3.7434E+00	0.40	0.55			
60-Nd-146	THIS WORK	2.9654E+00	0.38	0	2.9102E+00	0.63	0			
60-Nd-146	ENDF/B-VI	2.9969E+00	0.35	–1.06	2.9213E+00	0.50	–0.38			
60-Nd-146	JEF-2	2.9816E+00	0.79	–0.55	2.9268E+00	2.67	–0.57			
60-Nd-146	JENDL-3	2.9755E+00	0.00	–0.34	2.9027E+00	0.00	0.26			
60-Nd-146	CENDL/FY	2.9939E+00	4.52	–0.96	2.9020E+00	0.39	0.28			
60-Nd-148	THIS WORK	1.6747E+00	0.67	0	1.6980E+00	0.66	0			
60-Nd-148	ENDF/B-VI	1.6735E+00	0.35	0.07	1.6834E+00	0.50	0.86			
60-Nd-148	JEF-2	1.6746E+00	1.03	0.01	1.6979E+00	1.93	0.01			
60-Nd-148	JENDL-3	1.6695E+00	0.00	0.31	1.6716E+00	0.00	1.55			
60-Nd-148	CENDL/FY	1.6765E+00	1.80	–0.11	1.6709E+00	1.06	1.60			
61-Pm-147	THIS WORK	2.2440E+00	0.81	0	2.1807E+00	3.76	0	2.0220E+00	6.00	0
61-Pm-147	ENDF/B-VI	2.2467E+00	1.00	–0.12	2.1389E+00	1.00	1.92	1.6232E+00	2.80	19.72
61-Pm-147	JEF-2	2.2665E+00	8.36	–1.00	2.1367E+00	13.88	2.02	1.6392E+00	9.62	18.93
61-Pm-147	JENDL-3	2.2534E+00	0.00	–0.42	2.0961E+00	0.00	3.88	1.6266E+00	0.00	19.56
61-Pm-147	CENDL/FY	2.3606E+00	5.99	–5.20	1.9044E+00	111.88	12.67	1.6302E+00	100.34	19.38
61-Pm-149	THIS WORK	1.0000E+00	1.68	0	1.0280E+00	3.33	0			
61-Pm-149	ENDF/B-VI	1.0816E+00	2.00	–8.16	1.0370E+00	1.40	–0.87			
61-Pm-149	JEF-2	1.0478E+00	3.58	–4.78	1.0660E+00	5.77	–3.70			
61-Pm-149	JENDL-3	1.0663E+00	0.00	–6.63	1.0259E+00	0.00	0.20			
61-Pm-149	CENDL/FY	1.0402E+00	5.19	–4.02	1.0464E+00	16.58	–1.79			
61-Pm-151	THIS WORK	4.0693E–01	1.12	0	4.0077E–01	3.96	0	2.6400E–01	1.52	0
61-Pm-151	ENDF/B-VI	4.1877E–01	2.00	–2.91	4.1199E–01	0.70	–2.80	3.5748E–01	16.00	–35.41
61-Pm-151	JEF-2	4.1594E–01	1.59	–2.21	4.3284E–01	4.58	–8.00	4.7362E–01	30.87	–79.40
61-Pm-151	JENDL-3	4.1838E–01	0.00	–2.81	4.0761E–01	0.00	–1.71	3.5361E–01	0.00	–33.94

TABLE 3.2.4. COMPARISON OF RECOMMENDED YIELDS FROM ^{235}U FISSION WITH THOSE FROM OTHER LIBRARIES (cont.)

Nuclide	Library	Thermal spectrum			Fission spectrum			14 MeV		
		YIELD Y	UNCERT (%)	DIFF (%)	YIELD Y	UNCERT (%)	DIFF (%)	YIELD Y	UNCERT (%)	DIFF (%)
61-Pm-151	CENDL/FY	3.6947E–01	8.07	9.21	4.2426E–01	13.05	–5.86	3.6019E–01	100.36	–36.44
62-Sm-147	THIS WORK	2.1184E+00	1.07	0	2.1650E+00	1.02	0			
62-Sm-147	ENDF/B-VI	2.2467E+00	0.70	–6.06	2.1389E+00	0.70	1.21			
62-Sm-147	JEF-2	2.2665E+00	8.36	–6.99	2.1367E+00	13.88	1.31			
62-Sm-147	JENDL-3	2.2534E+00	0.00	–6.37	2.0961E+00	0.00	3.18			
62-Sm-147	CENDL/FY	2.2135E+00	2.31	–4.49	2.1143E+00	4.97	2.34			
62-Sm-149	THIS WORK	1.0101E+00	1.30	0	1.0457E+00	2.18	0			
62-Sm-149	ENDF/B-VI	1.0816E+00	1.00	–7.08	1.0370E+00	0.70	0.83			
62-Sm-149	JEF-2	1.0478E+00	1.58	–3.73	1.0660E+00	3.94	–1.94			
62-Sm-149	JENDL-3	1.0663E+00	0.00	–5.57	1.0259E+00	0.00	1.89			
62-Sm-149	CENDL/FY	1.0870E+00	5.59	–7.61	1.0301E+00	17.36	1.49			
62-Sm-151	THIS WORK	4.0348E–01	1.07	0	4.1735E–01	2.27	0			
62-Sm-151	ENDF/B-VI	4.1877E–01	1.00	–3.79	4.1199E–01	0.50	1.29			
62-Sm-151	JEF-2	4.1594E–01	1.59	–3.09	4.3284E–01	4.58	–3.71			
62-Sm-151	JENDL-3	4.1838E–01	0.00	–3.69	4.0761E–01	0.00	2.33			
62-Sm-151	CENDL/FY	4.1712E–01	1.23	–3.38	4.1599E–01	6.11	0.33			
62-Sm-152	THIS WORK	2.5316E–01	1.74	0	2.9522E–01	2.26	0			
62-Sm-152	ENDF/B-VI	2.6691E–01	1.00	–5.43	2.7085E–01	1.40	8.25			
62-Sm-152	JEF-2	2.5860E–01	2.39	–2.15	3.0816E–01	5.54	–4.38			
62-Sm-152	JENDL-3	2.6783E–01	0.00	–5.80	2.7972E–01	0.00	5.25			
62-Sm-152	CENDL/FY	2.6826E–01	2.53	–5.96	2.9451E–01	1.41	0.24			
62-Sm-153	THIS WORK	1.4789E–01	2.67	0	1.5400E–01	12.99	0	2.3900E–01	9.21	0
62-Sm-153	ENDF/B-VI	1.5828E–01	4.00	–7.02	1.6706E–01	4.00	–8.48	2.0354E–01	16.00	14.84
62-Sm-153	JEF-2	1.5080E–01	3.91	–1.97	1.3720E–01	6.21	10.91	2.1948E–01	12.21	8.17
62-Sm-153	JENDL-3	1.6135E–01	0.00	–9.10	1.7519E–01	0.00	–13.76	2.0178E–01	0.00	15.57
62-Sm-153	CENDL/FY	1.5150E–01	39.06	–2.44	1.7533E–01	4.89	–13.85	2.1879E–01	14.84	8.46
63-Eu-153	THIS WORK	1.4840E–01	2.79	0						
63-Eu-153	ENDF/B-VI	1.5828E–01	2.80	–6.66						

TABLE 3.2.4. COMPARISON OF RECOMMENDED YIELDS FROM ^{235}U FISSION WITH THOSE FROM OTHER LIBRARIES (cont.)

Nuclide	Library	Thermal spectrum			Fission spectrum			14 MeV		
		YIELD Y	UNCERT (%)	DIFF (%)	YIELD Y	UNCERT (%)	DIFF (%)	YIELD Y	UNCERT (%)	DIFF (%)
63-Eu-153	JEF-2	1.5080E–01	3.91	–1.62						
63-Eu-153	JENDL-3	1.6135E–01	0.00	–8.73						
63-Eu-153	CENDL/FY	1.6385E–01	2.90	–10.41						

TABLE 3.2.5. COMPARISON OF RECOMMENDED YIELDS FROM ^{238}U FISSION WITH THOSE FROM OTHER LIBRARIES

Nuclide	Library	Fission spectrum			14 MeV		
		YIELD Y	UNCERT (%)	DIFF (%)	YIELD Y	UNCERT (%)	DIFF (%)
35-Br-88	THIS WORK				1.9000E+00	19.47	0
35-Br-88	ENDF/B-VI				1.4865E+00	11.00	21.76
35-Br-88	JEF-2				1.3923E+00	18.78	26.72
35-Br-88	JENDL-3				1.5258E+00	0.00	19.69
35-Br-88	CENDL/FY				1.4169E+00	129.06	25.43
35-Br-89	THIS WORK				1.1900E+00	16.81	0
35-Br-89	ENDF/B-VI				1.4993E+00	23.00	–26.00
35-Br-89	JEF-2				1.2975E+00	29.66	–9.03
35-Br-89	JENDL-3				1.4669E+00	0.00	–23.27
35-Br-89	CENDL/FY				1.4164E+00	118.86	–19.03
36-Kr-83	THIS WORK	3.8640E–01	0.80	0	7.4110E–01	4.01	0
36-Kr-83	ENDF/B-VI	3.9586E–01	1.40	–2.45	6.6752E–01	2.80	9.93
36-Kr-83	JEF-2	3.9918E–01	6.07	–3.31	7.2852E–01	6.50	1.70
36-Kr-83	JENDL-3	3.8660E–01	0.00	–0.05	6.3017E–01	0.00	14.97
36-Kr-83	CENDL/FY	3.9505E–01	3.00	–2.24	6.5499E–01	3.00	11.62
36-Kr-85	THIS WORK	1.6600E–01	7.23	0	2.5290E–01	8.30	0
36-Kr-85	ENDF/B-VI	1.4861E–01	2.00	10.47	2.0357E–01	2.00	19.50
36-Kr-85	JEF-2	1.9599E–01	15.89	–18.07	2.2915E–01	11.56	9.39
36-Kr-85	JENDL-3	1.4011E–01	0.00	15.60	1.8720E–01	0.00	25.98
36-Kr-85	CENDL/FY	1.4888E–01	9.06	10.31	2.5149E–01	10.11	0.56
36-Kr-85M	THIS WORK	7.4250E–01	3.78	0	1.0820E+00	2.68	0
36-Kr-85M	ENDF/B-VI	7.4286E–01	2.00	–0.05	1.0027E+00	2.00	7.33
36-Kr-85M	JEF-2	9.1323E–01	15.93	–22.99	1.0564E+00	11.82	2.37
36-Kr-85M	JENDL-3	6.5750E–01	0.00	11.45	8.7676E–01	0.00	18.97
36-Kr-85M	CENDL/FY	7.2019E–01	2.16	3.00	9.8375E–01	2.18	9.08
36-Kr-86	THIS WORK	1.2969E+00	0.69	0	1.7519E+00	4.01	0
36-Kr-86	ENDF/B-VI	1.2965E+00	1.00	0.03	1.5710E+00	2.80	10.32
36-Kr-86	JEF-2	1.3018E+00	5.97	–0.38	1.4614E+00	11.15	16.58
36-Kr-86	JENDL-3	1.2785E+00	0.00	1.42	1.5126E+00	0.00	13.66
36-Kr-86	CENDL/FY	1.2797E+00	3.49	1.33	1.6115E+00	99.91	8.01
36-Kr-87	THIS WORK	1.6030E+00	2.96	0	1.7325E+00	3.72	
36-Kr-87	ENDF/B-VI	1.6254E+00	2.00	–1.40	1.6845E+00	2.00	
36-Kr-87	JEF-2	1.5244E+00	2.09	4.90	1.8593E+00	5.63	
36-Kr-87	JENDL-3	1.5878E+00	0.00	0.95	1.6630E+00	0.00	
36-Kr-87	CENDL/FY	1.4542E+00	5.94	9.28	1.6221E+00	3.70	
36-Kr-88	THIS WORK	2.0180E+00	4.77	0	2.0253E+00	3.36	0
36-Kr-88	ENDF/B-VI	2.0260E+00	2.80	–0.40	2.1605E+00	2.00	–6.68
36-Kr-88	JEF-2	2.0820E+00	6.73	–3.17	1.9896E+00	12.71	1.76
36-Kr-88	JENDL-3	2.0838E+00	0.00	–3.26	2.1978E+00	0.00	–8.52
36-Kr-88	CENDL/FY	2.2416E+00	2.76	–11.08	2.2078E+00	4.83	–9.01
38-Sr-89	THIS WORK	3.0664E+00	3.49	0	2.9195E+00	4.28	0

TABLE 3.2.5. COMPARISON OF RECOMMENDED YIELDS FROM ^{238}U FISSION WITH THOSE FROM OTHER LIBRARIES (cont.)

Nuclide	Library	Fission spectrum			14 MeV		
		YIELD Y	UNCERT (%)	DIFF (%)	YIELD Y	UNCERT (%)	DIFF (%)
38-Sr-89	ENDF/B-VI	2.7611E+00	1.40	9.96	2.9212E+00	2.80	–0.06
38-Sr-89	JEF-2	2.7511E+00	11.11	10.28	2.7979E+00	14.22	4.17
38-Sr-89	JENDL-3	2.8485E+00	0.00	7.11	2.9142E+00	0.00	0.18
38-Sr-89	CENDL/FY	2.8383E+00	2.66	7.44	3.1063E+00	7.57	–6.40
38-Sr-90	THIS WORK	3.1861E+00	5.01	0	3.1282E+00	5.81	0
38-Sr-90	ENDF/B-VI	3.2470E+00	1.40	–1.91	3.1896E+00	4.00	–1.96
38-Sr-90	JEF-2	3.3427E+00	9.79	–4.92	3.2941E+00	8.72	–5.30
38-Sr-90	JENDL-3	3.2431E+00	0.00	–1.79	3.1784E+00	0.00	–1.61
38-Sr-90	CENDL/FY	3.2082E+00	1.68	–0.69	3.1693E+00	4.47	–1.31
38-Sr-92	THIS WORK	4.4403E+00	2.47	0	3.9440E+00	2.08	0
38-Sr-92	ENDF/B-VI	4.3122E+00	2.80	2.88	3.8762E+00	2.80	1.72
38-Sr-92	JEF-2	4.2263E+00	1.88	4.82	3.7811E+00	6.31	4.13
38-Sr-92	JENDL-3	4.5092E+00	0.00	–1.55	3.9095E+00	0.00	0.88
38-Sr-92	CENDL/FY	4.2896E+00	4.34	3.39	3.9739E+00	7.40	–0.76
39-Y-91	THIS WORK	3.9594E+00	1.99	0	3.7723E+00	2.28	0
39-Y-91	ENDF/B-VI	4.0395E+00	64.00	–2.02	3.8676E+00	64.00	–2.53
39-Y-91	JEF-2	4.1435E+00	0.33	–4.65	3.7746E+00	1.58	–0.06
39-Y-91	JENDL-3	4.0454E+00	0.00	–2.17	3.7318E+00	0.00	1.07
39-Y-91	CENDL/FY	4.0577E+00	4.29	–2.48	3.7190E+00	8.66	1.41
40-Zr-91	THIS WORK	3.9594E+00	1.99	0	3.7723E+00	2.16	0
40-Zr-91	ENDF/B-VI	4.0395E+00	2.00	–2.02	3.8676E+00	2.00	–2.53
40-Zr-91	JEF-2	4.1435E+00	8.01	–4.65	3.7746E+00	14.24	–0.06
40-Zr-91	JENDL-3	4.0454E+00	0.00	–2.17	3.7318E+00	0.00	1.07
40-Zr-91	CENDL/FY	4.4351E+00	6.08	–12.01	4.3586E+00	47.06	–15.54
40-Zr-93	THIS WORK	5.0492E+00	4.20	0	4.3144E+00	10.40	0
40-Zr-93	ENDF/B-VI	4.9133E+00	2.00	2.69	4.5291E+00	2.80	–4.98
40-Zr-93	JEF-2	5.1688E+00	8.51	–2.37	4.3289E+00	5.89	–0.34
40-Zr-93	JENDL-3	5.0009E+00	0.00	0.96	4.4896E+00	0.00	–4.06
40-Zr-93	CENDL/FY	5.2507E+00	5.87	–3.99	5.9824E+00	77.65	–38.66
40-Zr-95	THIS WORK	5.1438E+00	1.10	0	4.9197E+00	1.36	0
40-Zr-95	ENDF/B-VI	5.1405E+00	1.40	0.06	4.8918E+00	2.00	0.57
40-Zr-95	JEF-2	5.1191E+00	9.89	0.48	4.6828E+00	7.98	4.82
40-Zr-95	JENDL-3	5.1068E+00	0.00	0.72	4.9498E+00	0.00	–0.61
40-Zr-95	CENDL/FY	5.2337E+00	2.04	–1.75	4.9230E+00	2.21	–0.07
41-Nb-95	THIS WORK	5.1425E+00	1.10	0	4.9185E+00	1.36	0
41-Nb-95	ENDF/B-VI	5.1405E+00	1.00	0.04	4.8918E+00	2.00	0.54
41-Nb-95	JEF-2	5.1159E+00	9.89	0.52	4.6799E+00	7.98	4.85
41-Nb-95	JENDL-3	5.1057E+00	0.00	0.72	4.9487E+00	0.00	–0.61
41-Nb-95	CENDL/FY	5.4526E+00	5.19	–6.03	5.0567E+00	9.65	–2.81
42-Mo-95	THIS WORK	5.1438E+00	1.10	0	4.9197E+00	1.36	0
42-Mo-95	ENDF/B-VI	5.1405E+00	1.00	0.06	4.8918E+00	2.00	0.57

TABLE 3.2.5. COMPARISON OF RECOMMENDED YIELDS FROM ^{238}U FISSION WITH THOSE FROM OTHER LIBRARIES (cont.)

Nuclide	Library	Fission spectrum			14 MeV		
		YIELD Y	UNCERT (%)	DIFF (%)	YIELD Y	UNCERT (%)	DIFF (%)
42-Mo-95	JEF-2	5.1191E+00	2.21	0.48	4.6828E+00	2.09	4.82
42-Mo-95	JENDL-3	5.1068E+00	0.00	0.72	4.9498E+00	0.00	–0.61
42-Mo-95	CENDL/FY	4.9406E+00	1.80	3.95	4.9322E+00	99.92	–0.25
42-Mo-97	THIS WORK	5.6021E+00	0.69	0	5.4470E+00	1.79	0
42-Mo-97	ENDF/B-VI	5.5625E+00	0.70	0.71	5.2800E+00	1.40	3.07
42-Mo-97	JEF-2	5.5235E+00	10.62	1.40	5.2497E+00	11.38	3.62
42-Mo-97	JENDL-3	5.5746E+00	0.00	0.49	5.3738E+00	0.00	1.34
42-Mo-97	CENDL/FY	5.4706E+00	1.30	2.35	5.2373E+00	99.93	3.85
42-Mo-99	THIS WORK	6.1403E+00	3.10	0	5.6423E+00	1.29	0
42-Mo-99	ENDF/B-VI	6.1683E+00	1.40	–0.46	5.7054E+00	1.40	–1.12
42-Mo-99	JEF-2	6.2318E+00	9.98	–1.49	5.7858E+00	13.90	–2.54
42-Mo-99	JENDL-3	6.1957E+00	0.00	–0.90	5.5985E+00	0.00	0.78
42-Mo-99	CENDL/FY	6.2295E+00	3.02	–1.45	5.6231E+00	1.82	0.34
43-Tc-99	THIS WORK	6.1403E+00	3.10	0	5.6423E+00	1.29	0
43-Tc-99	ENDF/B-VI	6.1683E+00	1.40	–0.46	5.7054E+00	1.00	–1.12
43-Tc-99	JEF-2	6.2312E+00	9.98	–1.48	5.7853E+00	13.90	–2.53
43-Tc-99	JENDL-3	6.1957E+00	0.00	–0.90	5.5985E+00	0.00	0.78
43-Tc-99	CENDL/FY	5.8530E+00	104.26	4.68	5.6410E+00	99.92	0.02
44-Ru-101	THIS WORK	6.3298E+00	5.91	0	5.7600E+00	3.82	0
44-Ru-101	ENDF/B-VI	6.2091E+00	1.40	1.91	5.6978E+00	2.80	1.08
44-Ru-101	JEF-2	6.5230E+00	6.68	–3.05	5.7188E+00	2.92	0.72
44-Ru-101	JENDL-3	6.0822E+00	0.00	3.91	5.6499E+00	0.00	1.91
44-Ru-101	CENDL/FY	6.1247E+00	5.89	3.24	5.6231E+00	99.92	2.38
44-Ru-103	THIS WORK	6.0778E+00	0.97	0	4.6604E+00	1.94	0
44-Ru-103	ENDF/B-VI	6.2753E+00	1.40	–3.25	4.6158E+00	2.00	0.96
44-Ru-103	JEF-2	6.0728E+00	3.71	0.08	4.4617E+00	10.77	4.26
44-Ru-103	JENDL-3	6.2096E+00	0.00	–2.17	4.6250E+00	0.00	0.76
44-Ru-103	CENDL/FY	6.3122E+00	1.76	–3.86	4.5116E+00	3.60	3.19
44-Ru-104	THIS WORK	5.0200E+00	5.98	0	3.5900E+00	4.18	0
44-Ru-104	ENDF/B-VI	5.0360E+00	1.00	–0.32	4.0261E+00	4.00	–12.15
44-Ru-104	JEF-2	4.7076E+00	8.08	6.22	3.5514E+00	5.11	1.08
44-Ru-104	JENDL-3	5.0233E+00	0.00	–0.07	3.6258E+00	0.00	–1.00
44-Ru-104	CENDL/FY	5.0128E+00	5.99	0.14	3.5925E+00	99.92	–0.07
44-Ru-106	THIS WORK	2.4676E+00	4.96	0	2.5478E+00	4.60	0
44-Ru-106	ENDF/B-VI	2.4897E+00	1.40	–0.90	2.4546E+00	2.80	3.66
44-Ru-106	JEF-2	2.5491E+00	10.70	–3.30	2.5004E+00	7.79	1.86
44-Ru-106	JENDL-3	2.5311E+00	0.00	–2.57	2.4570E+00	0.00	3.56
44-Ru-106	CENDL/FY	2.6260E+00	4.27	–6.42	2.4247E+00	9.03	4.83
45-Rh-103	THIS WORK	6.0778E+00	0.97	0	4.6604E+00	1.94	0
45-Rh-103	ENDF/B-VI	6.2753E+00	1.40	–3.25	4.6158E+00	2.00	0.96
45-Rh-103	JEF-2	6.0728E+00	10.48	0.08	4.4617E+00	7.43	4.26

TABLE 3.2.5. COMPARISON OF RECOMMENDED YIELDS FROM ^{238}U FISSION WITH THOSE FROM OTHER LIBRARIES (cont.)

Nuclide	Library	Fission spectrum			14 MeV		
		YIELD Y	UNCERT (%)	DIFF (%)	YIELD Y	UNCERT (%)	DIFF (%)
45-Rh-103	JENDL-3	6.2096E+00	0.00	–2.17	4.6250E+00	0.00	0.76
45-Rh-103	CENDL/FY	6.0898E+00	103.62	–0.20	4.6622E+00	99.92	–0.04
45-Rh-105	THIS WORK	3.9059E+00	2.10	0	3.2895E+00	1.65	0
45-Rh-105	ENDF/B-VI	4.0513E+00	2.00	–3.72	3.2159E+00	2.00	2.24
45-Rh-105	JEF-2	3.7166E+00	11.86	4.85	3.1582E+00	11.66	3.99
45-Rh-105	JENDL-3	3.9393E+00	0.00	–0.86	3.2009E+00	0.00	2.69
45-Rh-105	CENDL/FY	4.3175E+00	5.23	–10.54	3.2965E+00	3.40	–0.21
45-Rh-106	THIS WORK	2.4676E+00	4.96	0	2.5299E+00	3.88	0
45-Rh-106	ENDF/B-VI	2.4897E+00	1.40	–0.90	2.4546E+00	2.80	2.98
45-Rh-106	JEF-2	2.5491E+00	10.70	–3.30	2.5004E+00	7.79	1.17
45-Rh-106	JENDL-3	2.5311E+00	0.00	–2.57	2.4570E+00	0.00	2.88
45-Rh-106	CENDL/FY	2.5688E+00	98.35	–4.10	2.4376E+00	99.93	3.65
46-Pd-105	THIS WORK	3.9059E+00	2.10	0	3.2895E+00	1.65	0
46-Pd-105	ENDF/B-VI	4.0513E+00	1.40	–3.72	3.2159E+00	1.40	2.24
46-Pd-105	JEF-2	3.7166E+00	4.86	4.85	3.1582E+00	11.66	3.99
46-Pd-105	JENDL-3	3.9393E+00	0.00	–0.86	3.2009E+00	0.00	2.69
46-Pd-105	CENDL/FY	4.0400E+00	101.25	–3.43	3.2398E+00	99.93	1.51
47-Ag-109	THIS WORK	2.5200E–01	5.16	0	1.5496E+00	7.74	0
47-Ag-109	ENDF/B-VI	2.5214E–01	64.00	–0.06	1.1228E+00	64.00	27.54
47-Ag-109	JEF-2	1.1380E–01	0.15	54.84	1.5203E+00	20.69	1.89
47-Ag-109	JENDL-3	2.6844E–01	0.00	–6.52	1.2284E+00	0.00	20.73
47-Ag-109	CENDL/FY	2.5404E–01	98.83	–0.81	1.2219E+00	99.93	21.15
47-Ag-111	THIS WORK	6.9142E–02	4.38	0	1.0477E+00	2.18	0
47-Ag-111	ENDF/B-VI	7.1003E–02	2.00	–2.69	9.8929E–01	2.80	5.57
47-Ag-111	JEF-2	6.3913E–02	10.44	7.56	1.0629E+00	11.75	–1.45
47-Ag-111	JENDL-3	7.9966E–02	0.00	–15.66	1.1058E+00	0.00	–5.54
47-Ag-111	CENDL/FY	7.8050E–02	6.48	–12.88	1.0189E+00	3.11	2.75
48-Cd-115	THIS WORK	3.2700E–02	11.62	0	7.9890E–01	3.47	0
48-Cd-115	ENDF/B-VI	3.4437E–02	2.00	–5.31	7.8611E–01	4.00	1.60
48-Cd-115	JEF-2	3.6216E–02	9.05	–10.75	8.5763E–01	14.50	–7.35
48-Cd-115	JENDL-3	3.2281E–02	0.00	1.28	7.9857E–01	0.00	0.04
48-Cd-115	CENDL/FY	2.7489E–02	89.37	15.94	7.0172E–01	10.35	12.16
48-Cd-115M	THIS WORK	2.5790E–03	12.02	0	6.7700E–02	14.33	0
48-Cd-115M	ENDF/B-VI	3.1100E–03	6.00	–20.59	7.0933E–02	6.00	–4.78
48-Cd-115M	JEF-2	1.5665E–03	9.04	39.26	3.4807E–02	16.22	48.59
48-Cd-115M	JENDL-3	2.6874E–03	0.00	–4.20	6.8003E–02	0.00	–0.45
48-Cd-115M	CENDL/FY	2.6436E–03	70.93	–2.50	7.0321E–02	14.06	–3.87
51-Sb-125	THIS WORK	4.9220E–02	41.26	0	1.2771E+00	5.62	0
51-Sb-125	ENDF/B-VI	4.8524E–02	8.00	1.41	1.1963E+00	6.00	6.32
51-Sb-125	JEF-2	9.6698E–02	18.66	–96.46	1.2785E+00	7.75	–0.11
51-Sb-125	JENDL-3	5.2542E–02	0.00	–6.75	1.2277E+00	0.00	3.87

TABLE 3.2.5. COMPARISON OF RECOMMENDED YIELDS FROM ^{238}U FISSION WITH THOSE FROM OTHER LIBRARIES (cont.)

Nuclide	Library	Fission spectrum			14 MeV		
		YIELD Y	UNCERT (%)	DIFF (%)	YIELD Y	UNCERT (%)	DIFF (%)
51-Sb-125	CENDL/FY	6.5760E–02	14.33	–33.60	1.2172E+00	9.54	4.69
52-Te-132	THIS WORK	5.1359E+00	2.48	0	4.5748E+00	2.03	0
52-Te-132	ENDF/B-VI	5.1276E+00	1.40	0.16	4.6522E+00	1.40	–1.69
52-Te-132	JEF-2	5.0667E+00	1.99	1.35	4.7068E+00	1.35	–2.89
52-Te-132	JENDL-3	5.1450E+00	0.00	–0.18	4.8061E+00	0.00	–5.06
52-Te-132	CENDL/FY	5.2434E+00	7.25	–2.09	4.5974E+00	4.47	–0.49
53-I-129	THIS WORK	5.8820E–01	10.12	0	1.6850E+00	5.69	0
53-I-129	ENDF/B-VI	1.0113E+00	8.00	–71.94	2.0775E+00	6.00	–23.29
53-I-129	JEF-2	6.2303E–01	7.65	–5.92	1.6470E+00	13.45	2.26
53-I-129	JENDL-3	9.9976E–01	0.00	–69.97	1.9491E+00	0.00	–15.67
53-I-129	CENDL/FY	9.7740E–01	98.88	–66.17	2.0691E+00	99.92	–22.80
53-I-131	THIS WORK	3.2193E+00	1.06	0	3.8538E+00	1.75	0
53-I-131	ENDF/B-VI	3.2908E+00	1.40	–2.22	3.9925E+00	2.00	–3.60
53-I-131	JEF-2	3.3045E+00	2.26	–2.65	3.8261E+00	2.61	0.72
53-I-131	JENDL-3	3.2386E+00	0.00	–0.60	4.0449E+00	0.00	–4.96
53-I-131	CENDL/FY	3.1668E+00	1.50	1.63	3.7999E+00	5.33	1.40
53-I-133	THIS WORK				5.9714E+00	1.62	0
53-I-133	ENDF/B-VI				5.9999E+00	64.00	–0.48
53-I-133	JEF-2				5.7440E+00	5.61	3.81
53-I-133	JENDL-3				6.1263E+00	0.00	–2.59
53-I-133	CENDL/FY				6.0199E+00	2.49	–0.81
53-I-137	THIS WORK	6.0000E+00	16.67	0	3.2800E+00	20.12	0
53-I-137	ENDF/B-VI	5.1250E+00	8.00	14.58	3.1214E+00	8.00	4.84
53-I-137	JEF-2	5.5738E+00	4.92	7.10	4.8864E+00	12.57	–48.98
53-I-137	JENDL-3	5.3137E+00	0.00	11.44	3.3321E+00	0.00	–1.59
53-I-137	CENDL/FY	4.3613E+00	15.88	27.31	3.1512E+00	12.79	3.93
54-Xe-131	THIS WORK	3.2330E+00	2.15	0	3.8143E+00	3.84	0
54-Xe-131	ENDF/B-VI	3.2908E+00	1.00	–1.79	3.9925E+00	1.40	–4.67
54-Xe-131	JEF-2	3.3041E+00	2.26	–2.20	3.8257E+00	2.61	–0.30
54-Xe-131	JENDL-3	3.2386E+00	0.00	–0.17	4.0449E+00	0.00	–6.05
54-Xe-131	CENDL/FY	3.2035E+00	1.20	0.91	3.9860E+00	2.75	–4.50
54-Xe-132	THIS WORK	5.1360E+00	0.88	0	4.8843E+00	1.20	0
54-Xe-132	ENDF/B-VI	5.1475E+00	1.40	–0.22	4.8381E+00	1.00	0.95
54-Xe-132	JEF-2	5.0684E+00	1.84	1.32	4.7101E+00	1.14	3.57
54-Xe-132	JENDL-3	5.1465E+00	0.00	–0.20	4.8542E+00	0.00	0.62
54-Xe-132	CENDL/FY	5.0763E+00	5.83	1.16	4.8857E+00	2.05	–0.03
54-Xe-133	THIS WORK	6.5664E+00	2.83	0	6.0094E+00	1.91	0
54-Xe-133	ENDF/B-VI	6.7610E+00	64.00	–2.96	6.0172E+00	64.00	–0.13
54-Xe-133	JEF-2	6.7252E+00	6.66	–2.42	5.7441E+00	5.61	4.41
54-Xe-133	JENDL-3	6.6062E+00	0.00	–0.61	6.1449E+00	0.00	–2.25
54-Xe-133	CENDL/FY	6.5778E+00	6.07	–0.17	6.8114E+00	5.74	–13.35

TABLE 3.2.5. COMPARISON OF RECOMMENDED YIELDS FROM ^{238}U FISSION WITH THOSE FROM OTHER LIBRARIES (cont.)

Nuclide	Library	Fission spectrum			14 MeV		
		YIELD Y	UNCERT (%)	DIFF (%)	YIELD Y	UNCERT (%)	DIFF (%)
54-Xe-134	THIS WORK	7.5977E+00	4.26	0	6.4616E+00	1.68	0
54-Xe-134	ENDF/B-VI	7.6094E+00	2.80	–0.15	6.4531E+00	2.00	0.13
54-Xe-134	JEF-2	7.5447E+00	3.54	0.70	6.1386E+00	3.52	5.00
54-Xe-134	JENDL-3	7.7456E+00	0.00	–1.95	6.5541E+00	0.00	–1.43
54-Xe-134	CENDL/FY	7.6589E+00	8.19	–0.81	6.5986E+00	82.23	–2.12
54-Xe-135	THIS WORK	6.7282E+00	2.37	0	5.8049E+00	2.07	0
54-Xe-135	ENDF/B-VI	6.9676E+00	1.00	–3.56	5.8393E+00	2.00	–0.59
54-Xe-135	JEF-2	6.5680E+00	7.51	2.38	5.4620E+00	6.09	5.91
54-Xe-135	JENDL-3	6.8110E+00	0.00	–1.23	5.8186E+00	0.00	–0.24
54-Xe-135	CENDL/FY	6.6363E+00	7.48	1.37	5.9361E+00	2.45	–2.26
54-Xe-136	THIS WORK	7.0095E+00	1.53	0	5.7228E+00	1.61	0
54-Xe-136	ENDF/B-VI	6.9789E+00	2.00	0.44	5.6244E+00	2.00	1.72
54-Xe-136	JEF-2	6.5497E+00	4.59	6.56	5.9579E+00	5.69	–4.11
54-Xe-136	JENDL-3	6.8506E+00	0.00	2.27	5.6808E+00	0.00	0.73
54-Xe-136	CENDL/FY	7.0627E+00	3.16	–0.76	5.6687E+00	3.22	0.95
54-Xe-137	THIS WORK	6.0500E+00	4.96	0	4.6300E+00	4.97	0
54-Xe-137	ENDF/B-VI	6.0413E+00	2.00	0.14	4.7249E+00	2.80	–2.05
54-Xe-137	JEF-2	6.0002E+00	4.16	0.82	5.6504E+00	9.38	–22.04
54-Xe-137	JENDL-3	6.0839E+00	0.00	–0.56	4.9313E+00	0.00	–6.51
54-Xe-137	CENDL/FY	5.6152E+00	6.80	7.19	4.6823E+00	3.82	–1.13
54-Xe-138	THIS WORK	5.9900E+00	5.01	0	4.2559E+00	2.62	0
54-Xe-138	ENDF/B-VI	5.7020E+00	2.80	4.81	4.5309E+00	2.00	–6.46
54-Xe-138	JEF-2	6.0323E+00	9.22	–0.71	4.5254E+00	14.84	–6.33
54-Xe-138	JENDL-3	5.4990E+00	0.00	8.20	4.2378E+00	0.00	0.42
54-Xe-138	CENDL/FY	5.3324E+00	4.67	10.98	4.3146E+00	3.27	–1.38
55-Cs-133	THIS WORK	6.7631E+00	1.06	0	6.0174E+00	2.79	0
55-Cs-133	ENDF/B-VI	6.7610E+00	0.50	0.03	6.0172E+00	1.40	0.00
55-Cs-133	JEF-2	6.7252E+00	2.53	0.56	5.7441E+00	2.09	4.54
55-Cs-133	JENDL-3	6.6062E+00	0.00	2.32	6.1449E+00	0.00	–2.12
55-Cs-133	CENDL/FY	6.6924E+00	5.10	1.05	6.1495E+00	100.01	–2.20
55-Cs-135	THIS WORK	6.8688E+00	1.36	0	5.8508E+00	1.73	0
55-Cs-135	ENDF/B-VI	6.9676E+00	64.00	–1.44	5.8419E+00	64.00	0.15
55-Cs-135	JEF-2	6.5684E+00	3.31	4.37	5.4624E+00	2.19	6.64
55-Cs-135	JENDL-3	6.8110E+00	0.00	0.84	5.8195E+00	0.00	0.54
55-Cs-135	CENDL/FY	6.8772E+00	8.98	–0.12	5.9000E+00	97.54	–0.84
55-Cs-137	THIS WORK	5.9376E+00	0.84	0	5.1737E+00	3.50	0
55-Cs-137	ENDF/B-VI	6.0525E+00	1.00	–1.94	5.1460E+00	2.80	0.53
55-Cs-137	JEF-2	6.0045E+00	4.16	–1.13	5.6732E+00	9.40	–9.65
55-Cs-137	JENDL-3	6.0907E+00	0.00	–2.58	4.9857E+00	0.00	3.63
55-Cs-137	CENDL/FY	5.9669E+00	3.50	–0.49	5.0688E+00	4.49	2.03
56-Ba-140	THIS WORK	5.8798E+00	0.61	0	4.5693E+00	1.17	0

TABLE 3.2.5. COMPARISON OF RECOMMENDED YIELDS FROM ^{238}U FISSION WITH THOSE FROM OTHER LIBRARIES (cont.)

Nuclide	Library	Fission spectrum			14 MeV		
		YIELD Y	UNCERT (%)	DIFF (%)	YIELD Y	UNCERT (%)	DIFF (%)
56-Ba-140	ENDF/B-VI	5.8152E+00	0.70	1.10	4.6070E+00	1.40	–0.83
56-Ba-140	JEF-2	5.7428E+00	7.17	2.33	4.7048E+00	4.76	–2.97
56-Ba-140	JENDL-3	5.9882E+00	0.00	–1.84	4.6523E+00	0.00	–1.82
56-Ba-140	CENDL/FY	5.9284E+00	1.06	–0.83	4.5684E+00	2.24	0.02
57-La-140	THIS WORK	5.8948E+00	1.50	0	4.6529E+00	2.80	0
57-La-140	ENDF/B-VI	5.8153E+00	0.70	1.35	4.6112E+00	1.40	0.90
57-La-140	JEF-2	5.7428E+00	7.17	2.58	4.7049E+00	4.76	–1.12
57-La-140	JENDL-3	5.9882E+00	0.00	–1.58	4.6525E+00	0.00	0.01
57-La-140	CENDL/FY	6.0336E+00	3.60	–2.35	4.8061E+00	4.69	–3.29
58-Ce-141	THIS WORK	5.3879E+00	3.79	0	4.3583E+00	1.69	0
58-Ce-141	ENDF/B-VI	5.3365E+00	2.80	0.95	4.3815E+00	2.00	–0.53
58-Ce-141	JEF-2	5.8292E+00	0.77	–8.19	4.4044E+00	3.43	–1.06
58-Ce-141	JENDL-3	5.4832E+00	0.00	–1.77	4.3985E+00	0.00	–0.92
58-Ce-141	CENDL/FY	5.7426E+00	5.01	–6.58	4.4578E+00	2.91	–2.28
58-Ce-143	THIS WORK	4.6420E+00	1.66	0	3.9123E+00	1.64	0
58-Ce-143	ENDF/B-VI	4.6221E+00	1.40	0.43	3.9087E+00	2.00	0.09
58-Ce-143	JEF-2	4.8241E+00	8.48	–3.92	3.9586E+00	13.98	–1.18
58-Ce-143	JENDL-3	4.5666E+00	0.00	1.62	3.9229E+00	0.00	–0.27
58-Ce-143	CENDL/FY	4.7059E+00	2.04	–1.38	3.9238E+00	3.18	–0.29
58-Ce-144	THIS WORK	4.5493E+00	1.86	0	3.7165E+00	2.34	0
58-Ce-144	ENDF/B-VI	4.5480E+00	1.40	0.03	3.7228E+00	2.80	–0.17
58-Ce-144	JEF-2	4.3996E+00	10.70	3.29	3.6397E+00	11.60	2.07
58-Ce-144	JENDL-3	4.5372E+00	0.00	0.27	3.6402E+00	0.00	2.05
58-Ce-144	CENDL/FY	4.5835E+00	12.75	–0.75	3.7167E+00	2.88	–0.01
59-Pr-141	THIS WORK	5.3879E+00	3.79	0	4.3583E+00	1.69	0
59-Pr-141	ENDF/B-VI	5.3365E+00	2.00	0.95	4.3815E+00	2.00	–0.53
59-Pr-141	JEF-2	5.8292E+00	0.77	–8.19	4.4044E+00	13.85	–1.06
59-Pr-141	JENDL-3	5.4832E+00	0.00	–1.77	4.3985E+00	0.00	–0.92
59-Pr-141	CENDL/FY	5.6717E+00	71.42	–5.27	4.3451E+00	69.54	0.30
59-Pr-144	THIS WORK	4.5493E+00	1.86	0	3.7165E+00	2.34	0
59-Pr-144	ENDF/B-VI	4.5480E+00	1.00	0.03	3.7228E+00	2.80	–0.17
59-Pr-144	JEF-2	4.3995E+00	10.70	3.29	3.6397E+00	11.60	2.07
59-Pr-144	JENDL-3	4.5372E+00	0.00	0.27	3.6402E+00	0.00	2.05
59-Pr-144	CENDL/FY	5.7516E+00	88.79	–26.43	3.6904E+00	99.92	0.70
60-Nd-143	THIS WORK	4.5338E+00	0.71	0	4.1917E+00	2.76	0
60-Nd-143	ENDF/B-VI	4.6221E+00	0.70	–1.95	3.9087E+00	2.00	6.75
60-Nd-143	JEF-2	4.8241E+00	8.48	–6.40	3.9586E+00	2.88	5.56
60-Nd-143	JENDL-3	4.5666E+00	0.00	–0.72	3.9229E+00	0.00	6.41
60-Nd-143	CENDL/FY	4.5375E+00	3.97	–0.08	3.9333E+00	99.91	6.16
60-Nd-144	THIS WORK	4.5493E+00	1.86	0	3.7165E+00	2.34	0
60-Nd-144	ENDF/B-VI	4.5480E+00	0.70	0.03	3.7228E+00	2.80	–0.17

TABLE 3.2.5. COMPARISON OF RECOMMENDED YIELDS FROM ^{238}U FISSION WITH THOSE FROM OTHER LIBRARIES (cont.)

Nuclide	Library	Fission spectrum			14 MeV		
		YIELD Y	UNCERT (%)	DIFF (%)	YIELD Y	UNCERT (%)	DIFF (%)
60-Nd-144	JEF-2	4.3996E+00	2.39	3.29	3.6397E+00	3.72	2.07
60-Nd-144	JENDL-3	4.5372E+00	0.00	0.27	3.6402E+00	0.00	2.05
60-Nd-144	CENDL/FY	4.6078E+00	12.42	–1.29	3.6904E+00	99.92	0.70
60-Nd-145	THIS WORK	3.7548E+00	0.87	0	3.0894E+00	5.18	0
60-Nd-145	ENDF/B-VI	3.8090E+00	0.70	–1.44	3.0038E+00	4.00	2.77
60-Nd-145	JEF-2	3.8920E+00	4.06	–3.65	2.9195E+00	6.69	5.50
60-Nd-145	JENDL-3	3.7559E+00	0.00	–0.03	3.0060E+00	0.00	2.70
60-Nd-145	CENDL/FY	3.7550E+00	0.94	–0.01	2.9807E+00	99.93	3.52
60-Nd-146	THIS WORK	3.3848E+00	0.98	0	1.9250E+00	12.21	0
60-Nd-146	ENDF/B-VI	3.4457E+00	0.70	–1.80	2.4369E+00	6.00	–26.59
60-Nd-146	JEF-2	3.5263E+00	3.95	–4.18	2.4570E+00	9.04	–27.64
60-Nd-146	JENDL-3	3.3953E+00	0.00	–0.31	2.1679E+00	0.00	–12.62
60-Nd-146	CENDL/FY	3.3948E+00	1.25	–0.30	2.0909E+00	99.93	–8.62
60-Nd-147	THIS WORK	2.5867E+00	2.21	0	2.0878E+00	1.62	0
60-Nd-147	ENDF/B-VI	2.5927E+00	1.40	–0.23	2.0911E+00	2.00	–0.16
60-Nd-147	JEF-2	2.6632E+00	3.14	–2.96	2.1715E+00	10.08	–4.01
60-Nd-147	JENDL-3	2.5298E+00	0.00	2.20	2.0969E+00	0.00	–0.44
60-Nd-147	CENDL/FY	2.6027E+00	1.70	–0.62	2.0835E+00	2.27	0.21
60-Nd-148	THIS WORK	2.1015E+00	0.88	0	1.6000E+00	5.62	0
60-Nd-148	ENDF/B-VI	2.1125E+00	0.70	–0.52	1.7305E+00	16.00	–8.16
60-Nd-148	JEF-2	2.2791E+00	6.67	–8.45	1.6543E+00	10.25	–3.39
60-Nd-148	JENDL-3	2.0816E+00	0.00	0.95	1.7457E+00	0.00	–9.11
60-Nd-148	CENDL/FY	2.0944E+00	1.70	0.34	1.7628E+00	99.92	–10.18
61-Pm-147	THIS WORK	2.5867E+00	2.21	0	2.0878E+00	1.62	0
61-Pm-147	ENDF/B-VI	2.5927E+00	1.00	–0.23	2.0911E+00	2.00	–0.16
61-Pm-147	JEF-2	2.6632E+00	3.14	–2.96	2.1715E+00	10.08	–4.01
61-Pm-147	JENDL-3	2.5298E+00	0.00	2.20	2.0969E+00	0.00	–0.44
61-Pm-147	CENDL/FY	2.5923E+00	99.00	–0.22	2.4764E+00	13.09	–18.61
61-Pm-149	THIS WORK	1.6279E+00	2.87	0	1.4189E+00	11.16	0
61-Pm-149	ENDF/B-VI	1.6253E+00	2.00	0.16	1.4582E+00	6.00	–2.77
61-Pm-149	JEF-2	1.6647E+00	11.19	–2.26	1.3409E+00	12.48	5.50
61-Pm-149	JENDL-3	1.6076E+00	0.00	1.25	1.4227E+00	0.00	–0.27
61-Pm-149	CENDL/FY	1.6897E+00	6.68	–3.80	1.6883E+00	11.53	–18.99
61-Pm-151	THIS WORK	7.9970E–01	2.04	0	8.0120E–01	4.17	0
61-Pm-151	ENDF/B-VI	7.9940E–01	2.00	0.04	8.0147E–01	4.00	–0.03
61-Pm-151	JEF-2	8.0914E–01	3.62	–1.18	7.8719E–01	9.61	1.75
61-Pm-151	JENDL-3	8.0064E–01	0.00	–0.12	8.0144E–01	0.00	–0.03
61-Pm-151	CENDL/FY	8.2127E–01	4.37	–2.70	6.8015E–01	10.11	15.11
62-Sm-147	THIS WORK	2.5266E+00	1.20	0	2.0365E+00	2.62	0
62-Sm-147	ENDF/B-VI	2.5927E+00	0.70	–2.62	2.0911E+00	2.00	–2.68
62-Sm-147	JEF-2	2.6632E+00	3.14	–5.41	2.1715E+00	10.08	–6.63

TABLE 3.2.5. COMPARISON OF RECOMMENDED YIELDS FROM ^{238}U FISSION WITH THOSE FROM OTHER LIBRARIES (cont.)

Nuclide	Library	Fission spectrum			14 MeV		
		YIELD Y	UNCERT (%)	DIFF (%)	YIELD Y	UNCERT (%)	DIFF (%)
62-Sm-147	JENDL-3	2.5298E+00	0.00	–0.13	2.0969E+00	0.00	–2.97
62-Sm-147	CENDL/FY	2.5149E+00	1.54	0.46	2.0617E+00	11.62	–1.24
62-Sm-149	THIS WORK	1.5850E+00	1.20	0	1.2038E+00	2.84	0
62-Sm-149	ENDF/B-VI	1.6253E+00	1.00	–2.54	1.4582E+00	6.00	–21.13
62-Sm-149	JEF-2	1.6647E+00	4.34	–5.03	1.3409E+00	7.96	–11.39
62-Sm-149	JENDL-3	1.6076E+00	0.00	–1.42	1.4227E+00	0.00	–18.18
62-Sm-149	CENDL/FY	1.5866E+00	6.82	–0.10	1.4303E+00	99.92	–18.82
62-Sm-151	THIS WORK	7.8691E–01	3.12	0	6.5409E–01	2.60	0
62-Sm-151	ENDF/B-VI	7.9940E–01	1.40	–1.59	8.0147E–01	4.00	–22.53
62-Sm-151	JEF-2	8.0914E–01	3.62	–2.82	7.8719E–01	9.61	–20.35
62-Sm-151	JENDL-3	8.0064E–01	0.00	–1.74	8.0144E–01	0.00	–22.53
62-Sm-151	CENDL/FY	7.9910E–01	1.70	–1.55	8.1694E–01	99.93	–24.90
62-Sm-152	THIS WORK	5.2168E–01	1.11	0			
62-Sm-152	ENDF/B-VI	5.3023E–01	1.00	–1.64			
62-Sm-152	JEF-2	5.4985E–01	7.17	–5.40			
62-Sm-152	JENDL-3	5.2075E–01	0.00	0.18			
62-Sm-152	CENDL/FY	5.1920E–01	1.80	0.48			
63-Eu-156	THIS WORK	6.7100E–02	3.13	0	1.0900E–01	2.66	0
63-Eu-156	ENDF/B-VI	7.6034E–02	2.00	–13.31	1.1437E–01	2.80	–4.92
63-Eu-156	JEF-2	6.3156E–02	4.92	5.88	1.1232E–01	6.75	–3.05
63-Eu-156	JENDL-3	6.7481E–02	0.00	–0.57	1.0798E–01	0.00	0.93
63-Eu-156	CENDL/FY	7.5269E–02	3.53	–12.17	1.1259E–01	4.47	–3.29
65-Tb-161	THIS WORK	1.1436E–03	7.87	0	8.2450E–03	6.12	0
65-Tb-161	ENDF/B-VI	1.2150E–03	2.80	–6.24	8.4690E–03	4.00	–2.72
65-Tb-161	JEF-2	1.1559E–03	40.50	–1.08	7.8741E–03	31.30	4.50
65-Tb-161	JENDL-3	1.2798E–03	0.00	–11.91	8.4897E–03	0.00	–2.97
65-Tb-161	CENDL/FY	1.1881E–03	18.30	–3.89	8.7347E–03	3.73	–5.94

TABLE 3.2.6. COMPARISON OF RECOMMENDED YIELDS FROM ^{235}U FISSION WITH THOSE FROM OTHER LIBRARIES

Energy →	T				F				H				Total
Nuclide	B-VI	JEF	CFY	Total	B-VI	JEF	CFY	Total	B-VI	JEF	CFY	Total	
33-As- 85		L	L	2				N				N	2
34-Se- 79								N				N	0
35-Br- 88								N				N	0
35-Br- 89		L	L	2				N				N	2
35-Br- 90	L		L	2				N				N	2
35-Br- 91	L	L		2				N				N	2
36-Kr- 83				0				0				N	0
36-Kr- 86				0				0				N	0

TABLE 3.2.6. COMPARISON OF RECOMMENDED YIELDS FROM ^{235}U FISSION WITH THOSE FROM OTHER LIBRARIES (cont.)

Energy →	T				F				H				Total
Nuclide	B-VI	JEF	CFY	Total	B-VI	JEF	CFY	Total	B-VI	JEF	CFY	Total	
36-Kr- 87				0				0				N	0
37-Rb- 93			L	1				N				N	1
37-Rb- 94				0				N				N	0
37-Rb- 95			L	1				N				N	1
38-Sr- 89				0				0				0	0
38-Sr- 90				0				0				0	0
38-Sr- 92				0				N				N	0
39-Y - 91				0				0				0	0
39-Y - 99			L	1				N				N	1
40-Zr- 91				0				0				0	0
40-Zr- 93				0				0				0	0
40-Zr- 96				0				0				N	0
41-Nb- 95				0				0				N	0
42-Mo- 95				0				0				N	0
42-Mo- 97				0				0				N	0
42-Mo-100				0				0				N	0
43-Tc- 99				0				N				N	0
44-Ru-101				0				0				N	0
44-Ru-102				0				0				N	0
44-Ru-103				0				0				0	0
44-Ru-104				0		L		1				N	1
44-Ru-106				0	L	L	L	3				0	3
45-Rh-103				0				0				0	0
45-Rh-106				0				N				N	0
46-Pd-105				0				0	L			1	1
46-Pd-107				0				N				N	0
47-Ag-109				0				N				N	0
47-Ag-111	L	L		2	L		L	2		L	L	2	6
48-Cd-115	L	L	L	3	L	L	L	3		L	L	2	8
48-Cd-115M	L	L		2	L	L	L	3	L	L		2	7
50-Sn-126				0				0				N	0
51-Sb-125	L			1				0				N	1
51-Sb-135				0				N				N	0
52-Te-132				0				0				0	0
53-I -129	L		L	2	L			1				0	3
53-I -131				0				0				0	0
53-I -135				0				0				0	0
53-I -137	L	L	L	3				0				N	3
53-I -138				0				N				N	0
53-I -139	L	L	L	3				N				N	3
54-Xe-131				0				0				N	0

TABLE 3.2.6. COMPARISON OF RECOMMENDED YIELDS FROM ^{235}U FISSION WITH THOSE FROM OTHER LIBRARIES (cont.)

Energy →	T				F				H				Total
Nuclide	B-VI	JEF	CFY	Total	B-VI	JEF	CFY	Total	B-VI	JEF	CFY	Total	
54-Xe-132				0				0				N	0
54-Xe-134				0				0				N	0
54-Xe-135				0				N				N	0
54-Xe-136		L		1				0				N	1
54-Xe-137				0				0				N	0
54-Xe-138				0				0				N	0
55-Cs-133				0				0				N	0
55-Cs-135				0				0				0	0
55-Cs-136				0				N				N	0
55-Cs-137				0				0				N	0
56-Ba-140				0				0				0	0
57-La-140				0				N				N	0
58-Ce-141				0				0				0	0
58-Ce-143				0				0				0	0
59-Pr-141				0				0				0	0
59-Pr-144				0				0				N	0
60-Nd-143				0				0				N	0
60-Nd-144				0				0				N	0
60-Nd-145				0				0				N	0
60-Nd-146				0				0				N	0
60-Nd-148				0				0				N	0
61-Pm-147				0				0	L	L		2	2
61-Pm-149				0				0				N	0
61-Pm-151				0				0	L	L		2	2
62-Sm-147				0				0				N	0
62-Sm-149				0				0				N	0
62-Sm-151				0				0				N	0
62-Sm-152				0				0				N	0
62-Sm-153				0		L	L	2				0	2
63-Eu-153			L	1				N				N	1
Total	9	9	10	28	5	5	5	15	4	5	2	11	54
Total Nuclides	83	83	83	249	61	61	61	183	24	24	24	72	504
Per cent	11	11	12	11	8	8	8	8	17	21	8	15	11

L: Difference between present evaluated data and data from other libraries is larger than 10%, and larger than the uncertainty given by the corresponding library.
N: No data are given in the present evaluation (no experimentally measured data).
Per cent: number of nuclides divided by the total nuclide number.
No uncertainty given in JENDL-3.2, and therefore no comparison given.

TABLE 3.2.7. COMPARISON OF RECOMMENDED REFERENCE YIELDS FOR ^{238}U FISSION WITH OTHER EVALUATED DATA

Energy →	Fission spectrum				Around 14 MeV				Total
Nuclide	B-VI	JEF	CFY	Total	B-VI	JEF	CFY	Total	
35-Br-88				N	L	L	L	3	3
35-Br-89				N	L			1	1
36-Kr-83				0			L	1	1
36-Kr-85	L	L	L	3	L			1	4
36-Kr-85M		L		1				0	1
36-Kr-86				0	L	L		2	2
36-Kr-87				0				0	0
36-Kr-88			L	1				0	1
38-Sr-89				0				0	0
38-Sr-90				0				0	0
38-Sr-92				0				0	0
39-Y- 91			L	1				0	1
40-Zr-91				0				0	0
40-Zr-93				0				0	0
40-Zr-95				0				0	0
41-Nb-95				0				0	0
42-Mo-95				0				0	0
42-Mo-97				0				0	0
42-Mo-99				0				0	0
43-Tc-99				0				0	0
44-Ru-101				0				0	0
44-Ru-103				0				0	0
44-Ru-104				0	L			1	1
44-Ru-106				0				0	0
45-Rh-103				0				0	0
45-Rh-105			L	1				0	1
45-Rh-106				0				0	0
46-Pd-105				0				0	0
47-Ag-109		L		1	L			1	2
47-Ag-111			L	1				0	1
48-Cd-115		L		1			L	1	2
48-Cd-115M	L	L		2		L		1	3
51-Sb-125		L	L	2				0	0
52-Te-132				0				0	0
53-I- 129	L			1	L			1	2
53-I -131				0				0	0
53-I -133				N				0	0
53-I -137	L		L	2		L		1	3
54-Xe-131				0				0	0
54-Xe-132				0				0	0
54-Xe-133				0			L	1	1

TABLE 3.2.7. COMPARISON OF RECOMMENDED REFERENCE YIELDS FOR ^{238}U FISSION WITH OTHER EVALUATED DATA (cont.)

Energy →	Fission spectrum				Around 14 MeV				Total
Nuclide	B-VI	JEF	CFY	Total	B-VI	JEF	CFY	Total	
54-Xe-134				0				0	0
54-Xe-135				0				0	0
54-Xe-136				0				0	0
54-Xe-137				0		L		1	1
54-Xe-138			L	1				0	1
55-Cs-133				0				0	0
55-Cs-135				0				0	0
55-Cs-137				0				0	0
56-Ba-140				0				0	0
57-La-140				0				0	0
58-Ce-141				0				0	0
58-Ce-143				0				0	0
58-Ce-144				0				0	0
59-Pr-141				0				0	0
59-Pr-144				0				0	0
60-Nd-143				0				0	0
60-Nd-144				0				0	0
60-Nd-145				0				0	0
60-Nd-146				0	L	L		2	2
60-Nd-147				0				0	0
60-Nd-148				0				0	0
61-Pm-147				0			L	1	1
61-Pm-149				0			L	1	1
61-Pm-151				0				0	0
62-Sm-147				0				0	0
62-Sm-149				0	L	L		2	2
62-Sm-151				0	L	L		2	2
62-Sm-152				0				0	0
63-Eu-156	L		L	2				0	2
65-Tb-161				0				0	0
Total	5	6	9	20	10	8	6	24	44
Total nuclides	68	68	68	204	71	71	71	213	417
Per cent	7.35	8.82	13.2	9.80	14.1	11.3	8.45	11.3	10.6

Symbols are the same as in Table 3.2.6.

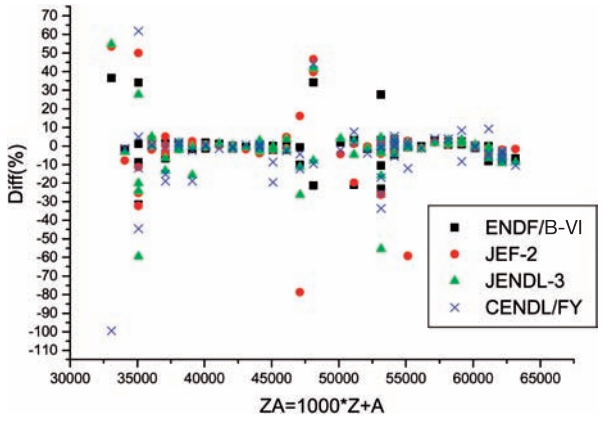

FIG. 3.2.1. Comparison of the present evaluation with others for ^{235}U thermal neutron fission.

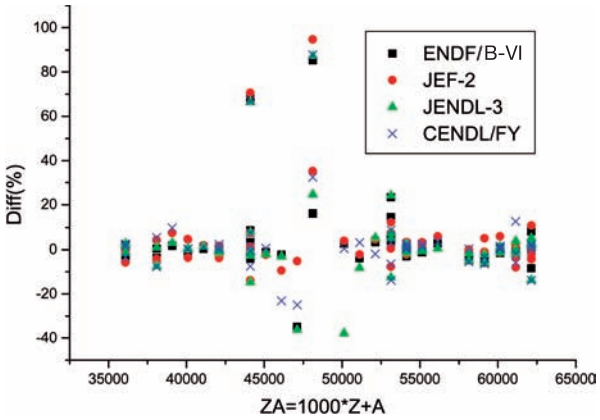

FIG. 3.2.2. Comparison of the present evaluation with others for ^{235}U fission spectrum neutron fission.

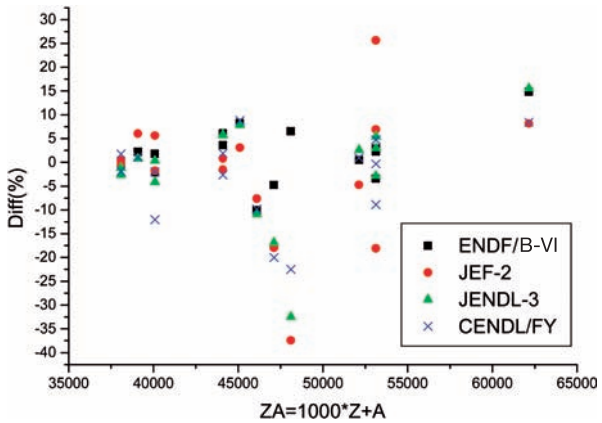

FIG. 3.2.3. Comparison of the present evaluation with others for ^{235}U 14 MeV neutron fission.

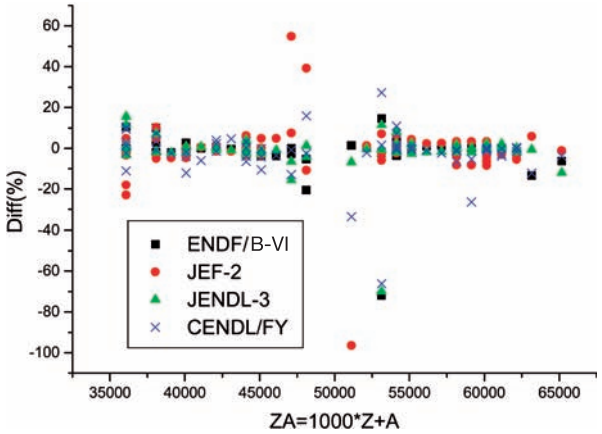

FIG. 3.2.4. Comparison of the present evaluation with others for ^{238}U fission spectrum neutron fission.

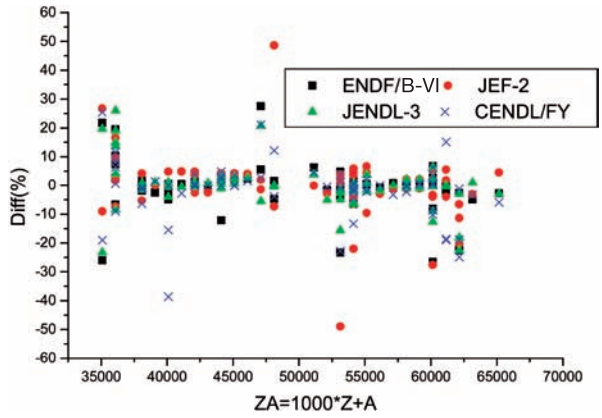

FIG. 3.2.5. Comparison of the present evaluation with others for ^{238}U 14 MeV neutron fission.

Compared with JEF-2, our recommended yield is 23% larger for $^{85m}Kr(H)$, 55% larger for $^{109}Ag(F)$ and 49% larger for $^{115m}Cd(H)$, and 49% smaller for $^{137}I(H)$ and 26% smaller for $^{137}Xe(H)$, although all of these values are in agreement with the equivalent data in the other three libraries.

The uncertainties in the present evaluation have the same magnitude as those in ENDF/B-VI, but are much smaller than those in JEF-2.2 and CENDL/FY (Tables 3.2.8 and 3.2.9 and Figs 3.2.6–3.2.10). Uncertainties in the present evaluation and ENDF/B-VI for ^{235}U are mainly identified with fission products in the range of 0.5–3% for thermal and fission spectrum neutrons, and within 1–9% (our evaluation) and 2–12% (ENDF/B-VI) for neutrons around 14 MeV, while the yield uncertainties in JEF-2.2 and CENDL/FY for most

TABLE 3.2.8. COMPARISON OF THE UNCERTAINTIES OF RECOMMENDED REFERENCE YIELDS FROM ^{235}U FISSION WITH THOSE FROM OTHER LIBRARIES

	Uncertainty range	<1	1–2	2–3	3–4	4–6	6–9	9–12	12–15	15–20	>20
T	THIS WORK	34	15	8	4	9	4	1	0	2	2
	ENDF/B-VI	41	11	10	4	3	4	1	0	0	5
	JEF-2.2	9	17	6	8	6	13	4	1	3	12
	CENDL/FY	6	12	13	2	15	7	7	3	4	10
F	THIS WORK	16	11	11	6	7	0	2	2	1	1
	ENDF/B-VI	35	14	5	5	3	3	1	0	1	12
	JEF-2.2	2	6	6	4	11	12	3	13	4	18
	CENDL/FY	7	12	5	7	11	6	1	3	2	25
H	THIS WORK	0	3	5	2	8	4	2	0	0	0
	ENDF/B-VI	0	1	20	6	9	9	9	0	6	19
	JEF-2.2	0	5	2	6	11	6	13	7	1	28
	CENDL/FY	0	0	0	6	10	3	4	1	1	54

TABLE 3.2.9. COMPARISON OF THE UNCERTAINTIES OF RECOMMENDED REFERENCE YIELDS FROM ^{238}U FISSION WITH THOSE FROM OTHER LIBRARIES

	Uncertainty range	<1	1–2	2–3	3–4	4–6	6–9	9–12	12–15	15–20	>20
F	THIS WORK	12	17	12	8	12	2	2	1	1	1
	ENDF/B-VI	21	30	9	0	1	3	0	0	0	7
	JEF-2.2	4	3	6	9	9	16	19	0	4	1
	CENDL/FY	1	13	5	8	15	10	1	3	2	13
H	THIS WORK	0	23	18	7	12	3	2	2	2	1
	ENDF/B-VI	2	29	17	2	7	5	1	0	2	6
	JEF-2.2	0	3	7	3	8	13	19	12	2	3
	CENDL/FY	0	1	11	9	8	3	8	3	0	28

fission products are within 0.5–9% for thermal neutrons, 1–9% for the fission spectrum and 3–12% for 14 MeV neutrons. There are also a reasonable number of fission yields for which the uncertainties are larger than 20%. Yield uncertainties for most fission products from the ^{238}U fission are within 0.5–3% for fission spectrum neutrons, and 1–6% for neutrons around 14 MeV for the present evaluation and ENDF/B-VI. While the uncertainties of most fission products in JEF-2.2 and CENDL/FY are within 0.5–12% and 1–9% respectively for fission spectrum neutrons, and within 2–12% for 14 MeV neutrons, there are a large number of fission products in CENDL/FY that possess uncertainties larger than 20% for fission spectrum and 14 MeV neutrons.

3.2.4. Concluding remarks

Reference fission yield data were evaluated from the available experimental data by calculating weighted averages with the AVERAG code and using the ZOTT code for simultaneous evaluations. Only measurements of absolute yields and yield ratios were included; thus no standard yields were used (except for our newly evaluated data).

^{235}U fission: 92 CU fission yield data of 47 product nuclides were evaluated — 78 data are recommended, 7 data are not recommended and another 7 are only recommended as references and need to be improved.

^{238}U fission: 74 yield data of 39 product nuclides were evaluated — 65 data are recommended, 6 data

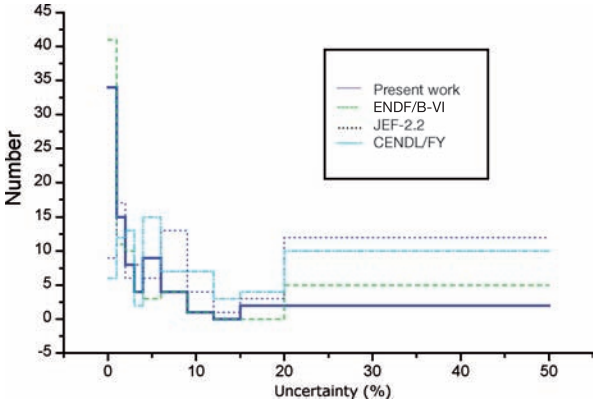

FIG. 3.2.6. Comparison of yield uncertainties in the present evaluation with others for ^{235}U thermal neutron fission.

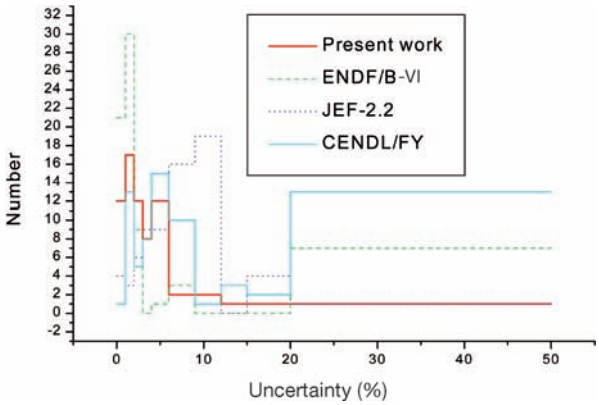

FIG. 3.2.9. Comparison of yield uncertainties in the present evaluation with others for ^{238}U fission spectrum neutron fission.

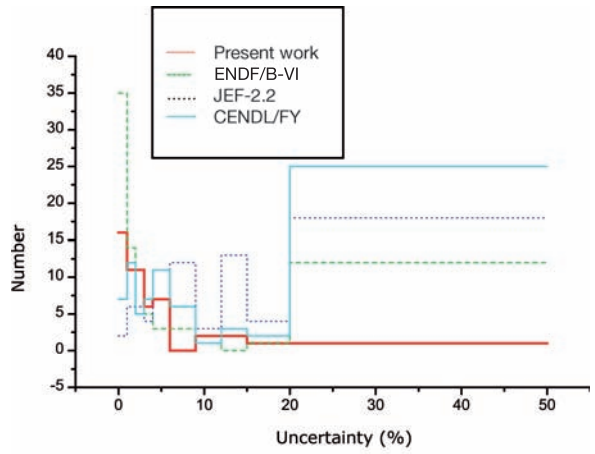

FIG. 3.2.7. Comparison of yield uncertainties in the present evaluation with others for ^{235}U fission spectrum neutron fission.

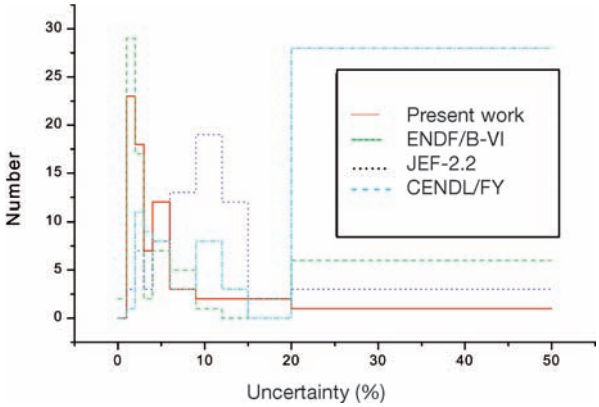

FIG. 3.2.10. Comparison of yield uncertainties in the present evaluation with others for ^{238}U 14 MeV neutron fission.

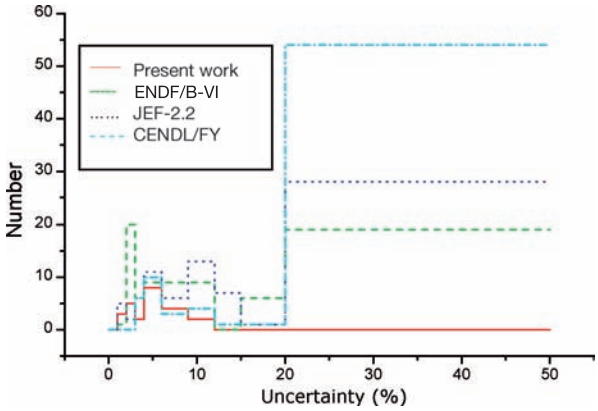

FIG. 3.2.8. Comparison of yield uncertainties in the present evaluation with others for ^{235}U 14 MeV neutron fission.

are not recommended and 3 are recommended only as references.

All the data have been updated. A comparison with ENDF/B-VI, JEF-2.2, JENDL-3.2 and CENDL/FY evaluations revealed that most of the present recommended data are in agreement with other databases. However, there are about 11% of all product nuclides from ^{235}U and ^{238}U fission for which the difference of the yield data in our evaluation to the equivalent data in the other four libraries is larger than 10% and exceeds the uncertainty given in the corresponding library. Uncertainties in the present evaluation are of the same magnitude as the uncertainties in ENDF/B-VI, and much smaller than those in JEF-2.2 and CENDL/FY. Our data are suitable for use as standards in evaluations and measurements or as monitor yields in applied measurements and calculations.

REFERENCES TO SECTION 3.2

[3.2.1] INTERNATIONAL ATOMIC ENERGY AGENCY, Compilation and Evaluation of Fission Yield Nuclear Data, IAEA-TECDOC-1168, IAEA, Vienna (2000).

[3.2.2] LIU TINGJIN, et al., "Some ^{235}U reference fission product yield data evaluation", Communication of Nuclear Data Progress No. 19, INDC(CPR)-0-044/L, IAEA, Vienna (1998) 78–92.

[3.2.3] LIANG QICHANG, et al., "The evaluation for reference fission yield of ^{238}U fission", ibid., pp. 92–102.

[3.2.4] LIANG QICHANG, et al., "The evaluation of fission product yields for ^{238}U fission", Communication of Nuclear Data Progress No. 20, INDC(CPR)-047/L, IAEA, Vienna (1998) 101–109.

[3.2.5] LIU TINGJIN, et al., "The evaluation for ^{85}As etc. 25 reference product yields from ^{235}U fission", Communication of Nuclear Data Progress No. 22, INDC(CPR)-049/L, IAEA, Vienna (1999) 54–64.

[3.2.6] LIU TINGJIN, et al., "The evaluation of some reference fission yield data from ^{235}U fission", Communication of Nuclear Data Progress No. 23, INDC(CPR)-050/L, IAEA, Vienna (2000) 105–119.

[3.2.7] LIANG QICHANG, China Instutute of Atomic Energy, personal communication, 1999.

[3.2.8] LIU TINGJIN, et al., "Reference fission yield data evaluation of ^{79}Se etc. 17 fission product nuclides from ^{235}U fission", Communication of Nuclear Data Progress No. 25, INDC(CPR)-053/L, IAEA, Vienna (2001) 51–55.

[3.2.9] LIU TINGJIN, "Fission yield data evaluation system FYDES", Communication of Nuclear Data Progress No. 19, INDC(CPR)-044/L, IAEA, Vienna (1998) 103–113.

[3.2.10] ZHOU CHUNMEI, personal communication, 1997.

[3.2.11] MUIR, D., Evaluation of correlated data using partitioned least squares: A minimum-variance deviation, Nucl. Sci. Eng. **101** (1989) 88–93.

[3.2.12] LIU TINGJIN, "Spline fitting for multi-set data with knot optimization", Communication of Nuclear Data Progress No. 2 (1989) 58–70.

[3.2.13] FIRESTONE, R.B., Table of Isotopes, 8th Edition (SHIRLEY, V.S., Ed.), Wiley, NY (1996).

3.3. EVALUATION OF MASS DISTRIBUTION DATA FROM ^{252}Cf SPONTANEOUS FISSION

Liu Tingjin
China Institute of Atomic Energy, China

The mass distribution of ^{252}Cf spontaneous fission was evaluated on the basis of seven sets of available experimental data. The measured data were modified on the basis of the authors' adopted standards and γ ray intensities by using our newly evaluated values, and the originally assigned uncertainties were adjusted. The evaluated experimental data were fitted with a spline function. In addition, a symmetric spline function fit of all experimental data was performed by symmetric reflection of the light mass peak into the heavy mass peak. These two sets of fitted data are recommended as reference for the mass distribution of ^{252}Cf spontaneous fission. Uncertainties in the recommended data were considerably reduced compared to the measured values. The light and heavy mass peaks are not completely symmetric. Fine structure has been observed in experimental mass distributions around A = 109–112 and A = 136–139, which is probably real, but could not be reproduced in the evaluation due to inconsistencies in the measurement results. These phenomena and their physical background should be investigated further.

3.3.1. Introduction

The average number and spectrum of neutrons from the spontaneous fission of ^{252}Cf are used as standards in neutron data measurements and evaluations, and internationally recommended data have been published [3.3.1]. The same is true for the mass distribution data of ^{252}Cf spontaneous fission that are used as reference in fission yield data measurements and evaluations. As requested by the CRP, these yield data were evaluated and represent a continuation of our reference fission yield data evaluation following the completion of ^{235}U and ^{238}U yield evaluations in 2001 [3.3.2].

All data were evaluated on the basis of the available experimental data, and the results are summarized in this section. The collection, evaluation and processing of the experimental data are described in Sections 3.3.2 and 3.3.3, the results are given in Section 3.3.4 together with a discussion of some problems encountered, and the conclusions are given in Section 3.3.5.

3.3.2. Collection and evaluation of experimental data

As part of our evaluation effort to derive ^{252}Cf mass distributions, we collected experimental chain yield, CU yield and fragment mass yield data, which we retrieved from the EXFOR data library or collected as publications found in CINDA and elsewhere. Since our goal is to evaluate the mass distribution, we primarily collected and used experiments in which chain yields and fragment mass yields were measured for a wider range of product nuclides. However, chain yields for low yield product nuclides and CU yields were also collected and reviewed in case they were needed (due to the lack of primary data), or to see whether some supplementary information and data could be obtained for the evaluation. As a result of this selection, the following eight sets of data were considered for the evaluation.

3.3.2.1. Schmitt et al. [3.3.3]

The kinetic energy and flight time of fission fragments were measured by means of surface barrier semiconductor detectors. The linear signal of the detector was used to determine the fragment energy E, and the flight time was determined by means of a 'time pickoff' scheme in which transformer coupling was employed. The energy and mass distributions were deduced from these energy and time of flight spectra, in which the energy was calibrated with ^{79,81}Br and ^{127}I ions produced from the ORNL tandem van de Graaff accelerator and the mass resolution was 1.8 amu for ^{79}Br (2.25%) and 3.2 amu for ^{127}I (2.5%). The post-neutron emission mass distribution of the fission fragments was also given. The data were adjusted for mass resolution with the following formula:

$$N_C(A) = N_U(A) - \frac{\sigma^2}{2} \times \frac{d^2 N_C(A)}{dA^2} \qquad (3.3.1)$$

where N_C, N_U are the modified and unmodified mass distributions respectively, and σ is the rms width associated with the mass resolution (full width at half maximum) given above.

These measurements involved the kinetic energy, time of flight correlation method. The yields of all fragments were measured simultaneously and the systematic uncertainty due to the individual measurements of the product nuclides in the radiochemical method was avoided. Compared with the radiochemical and mass spectrometric methods, more nuclides were measured and the mass range was wider. Since this study involved a two dimensional (coincidence) measurement, and the intensity of the source was low (3×10^5 fissions per minute), the counting statistics were poor (only ~350 counts at the peak maximum) and the statistical uncertainty was large. No uncertainty was given by the authors in the paper, nor included in the EXFOR entry. The main uncertainty was statistical and assigned as 5% for the peak yields (Y_0), whereas others were given as $5(Y_0/Y)^{1/2}$%.

3.3.2.2. Thierens et al. [3.3.4]

The chain yields of 43 product nuclides were determined by means of the catcher foil technique and by γ ray spectrometry using a Ge(Li) detector. The intensity of the source was 1.2×10^6 fissions/min, and the efficiency of the detector was calibrated to within an uncertainty of about 5%. The uncertainty from γ peak area statistics was negligible. The chain yield was derived from the measured CU yield by adjusting the measured data using the charge distribution formula, with c = 0.8:

$$p(z) = \frac{1}{\sqrt{\pi c}} \exp\left[-\frac{(z - z_p)^2}{c} \right] \qquad (3.3.2)$$

Gamma decay data were originally taken from Nuclear Data Sheets, Nuclear Physics and other literature published from 1972–1975. Most of these data have been subsequently updated, and therefore they were modified by using the newly recommended data taken primarily from the CNDC evaluation and Table of Isotopes [3.3.16]. Adjustment factors (β) were based on the γ ray measurement technique and were calculated as follows:

(1) Yield was determined by one γ ray, and $\beta = I_0/I_S$, where I_0 is for the γ ray intensity used by the author, and I_S is the new γ ray intensity;

(2) Yield was determined by multi γ rays, and $\beta = \frac{1}{W}\sum w_i \frac{I_{0i}}{I_{Si}}$, where $W = \sum w_i$ and $W_i = \Delta I_{0i}^{-2}$;

(3) Yield was determined by M product nuclides and N_j γ rays for j-th nuclide, $\beta = \frac{1}{M}\sum_j \frac{1}{N_j}\sum_i \frac{I_{0ji}}{I_{Sij}}$, where subscript i is for a γ ray and j is for a nuclide.

3.3.2.3. Blachot et al. [3.3.5]

Chain yields for 27 masses were measured by using aluminium catcher foils for fission fragments. The intensity of the source was 5×10^6 fissions/s and the irradiation time was 1–17 d. Fission products were first separated chemically into fractions containing rare earth, alkali and alkaline earth elements, ruthenium, zirconium and niobium. Thereafter, the γ rays of the individual nuclides were measured with a Ge(Li) detector of energy resolution 2.5 keV at 1.3 MeV. The sum of yields under the heavy mass peak was normalized to a total of 100%, giving a yield of 6.05 for the ^{140}Ba monitor to which the other product yields were normalized. To obtain the total chain yield for each mass, the measured CU yield of a product was adjusted for the independent yields of the nuclides following the measured product in the mass chain, using a charge distribution formula of the form of Eq. (3.3.2).

As one of the two primary monitors, the yield for ^{140}Ba (in fact, for the A = 140 mass chain) was carefully evaluated in this work (see below), and a value of 5.674 ± 0.098 was obtained. Then the data were modified relative to this new monitor value. The data at A = 99, 111, 117, 135, 137 and 149 were discarded, as they were either too large (A = 149) or too small (other A).

3.3.2.4. Nervik [3.3.6]

The R values of 36 fission product nuclides (A = 77–166) were measured by the radiochemical method. Fission products were collected with an aluminium catcher foil, chemically separated, and γ or β radiation was measured with a NaI detector or β counter. The intensity of the ^{252}Cf source was 1×10^6/m, 2×10^7/m or 7×10^7/m. R values were determined relative to the same nuclides measured for ^{235}U thermal neutron fission and the ^{99}Mo yields from ^{235}U thermal neutron fission and ^{252}Cf spontaneous fission. Chain yields were calculated using yield values of 6.14 for ^{99}Mo from ^{235}U

thermal neutron fission and 2.57 ± 0.03 for ^{99}Mo from ^{252}Cf spontaneous fission (the former was obtained from an evaluation, being almost the same as our recently recommended value of 6.15; the latter was determined as the average of three direct measurements).

Data were taken from Table 1 of Ref. [3.3.6] (there is no entry in EXFOR). As the monitor, the yield for ^{99}Mo from ^{252}Cf spontaneous fission was extensively evaluated in this work (see below) to give a recommended value of 2.583 ± 0.062, and all data were adjusted against this value. Measurement uncertainties in the paper are given as average deviations of multiple determinations. However, the measuring time of individual determinations was not very long, and the uncertainties reflect only the reproducibility in multiple determinations and not the real counting statistics. Therefore, the uncertainties given by the author were not used, and we assigned 8% for yields Y ≥ 1%, 15% for 0.05% ≤ Y < 1%, and 25% for Y < 0.05%. The size of the assigned uncertainties arises for these measurements being undertaken with a NaI detector. The measurements for A = 112, 125, 137 were discarded because these data are significantly smaller than other measurements.

3.3.2.5. Flynn et al. [3.3.7]

The CU yields of 39 product nuclides were measured using radiochemical separation, followed by β counting or γ ray spectrometry of unseparated fission products. The absolute measurements involved determination of the fission rates for ^{99}Mo, ^{111}Ag, ^{132}Te and ^{140}Ba. Yields were normalized to a value of 2.60 for the ^{99}Mo monitor, which is the average of three data sets: a value of 2.48 ± 0.13 was measured absolutely by the author, and the other two were taken from the literature. The authors' final data are CU yields and have not been modified to derive total chain yields from the charge distribution function, although the author claimed that calculated differences between CU and total chain yields were smaller than 1% in all cases. The uncertainties given were estimated to be about 10% overall and about 5% for multiple determinations.

The data were checked to see if they could be used as chain yields. Unfortunately, the data for ^{123,125}Sn and ^{127,129}Te are only for ground (former) or metastable (latter) states and therefore have large differences to the corresponding chain yields. The yields of the ^{115}Cd ground and isomeric states were summed to obtain the chain yield. All data were adjusted for the ^{99}Mo monitor yield by using our newly evaluated value of 2.583 ± 0.062 (see below). Finally, when compared with the equivalent data from other sources, the yields at masses A = 121–129 were found to be systematically lower, and were discarded.

3.3.2.6. Li Ze et al. [3.3.8]

Forty-four chain yields from mass number 85–157 were absolutely measured by means of γ ray spectrometry with a Ge(Li) detector. The efficiency of the detector was carefully calibrated and the energy resolution was 1.85 keV at 1.332 MeV. The Al catcher foil technique was used, and the collection efficiency of the catcher foil for fission fragments was determined precisely to obtain the fission rate. A ^{252}Cf source weighing 0.3 μg was used with an intensity of $(1.226 \pm 0.018) \times 10^4$ fissions/s in a solid angle of 0.374π sterad. The areas under the light and heavy mass peaks are 99.76% and 102.08%, respectively. Data were adjusted for product decay during collection, cooling and measurement, along with γ pulse pile-up and cascade effects. Chain yields were determined by adjusting the data by means of the charge distribution equation (3.3.2), with c = 0.8. Uncertainties in the data table include counting statistics, fission rate (1.5%), detector efficiency (2.4% or 4.2%, depending on the fission product measured), adjustment for pulse pile-up (0.5%), and γ ray cascade effects (0.2–2.4%).

Compared with data measured by the radiochemical and γ ray spectrometric method (not kinetic energy method), more product nuclides were measured in this work. Furthermore, these studies represent an absolute measurement, and the integral areas of the light and heavy peaks are consistent with a 100% total within the uncertainty limits of the fission rate. The data were adjusted using new γ decay data taken from the CNDC evaluation or the Table of Isotopes [3.3.16]. However, for ^{117}Cd the yield was not modified because the γ ray intensity given in the publication could be in error (i.e. may be a misprint and not that used by the author to calculate the yield); this yield also remained unadjusted because the effect on the shape of the yield curve is small.

3.3.2.7. Chen et al. [3.3.9]

Chain yields of 35 mass chains were measured absolutely by radiochemical separation, using a source of known intensity. Chemical yields of the separations were measured, and the fission product

activities were recorded with a proportional counter for β emissions and with a NaI scintillator for γ rays. The efficiency of the γ ray detector was determined experimentally. Either the predetermined γ ray efficiency curve was used or the efficiency of the γ ray and β particle detectors was determined directly via the measured fission product. The total uncertainties of the data are 3–15% and include contributions from detector calibration and chemical yield, fission rate and peak area determinations.

The data were taken from Table 1 of the paper (no corresponding EXFOR entry exists) and agree reasonably well with the data of Li Ze et al. [3.3.8], although there are fewer values in the valley range. Chain yields are too large for A = 113, 134 and 135, as deduced from ^{113g}Ag, ^{134}Te and ^{135}I, respectively. These nuclides are far from the stable nuclides of the respective chains (i.e. by 2–3 charges). The adjustment factors from the literature are relatively large (when calculated using ENDF/B-VI data they are even larger), the resulting yields are unreliable, and their uncertainties are increased by 10% for mass chains 113 and 135, and by 13% for mass chain 134. Also, the uncertainty for ^{99}Mo was increased from 3.5% to 5%.

3.3.2.8. Fraser et al. [3.3.10]

Fragment mass distributions of pre- and post-neutron emission were measured by the double time of flight method, with a source intensity of 0.6–3×10^5 fissions/min. The flight paths were 144.3 and 146.2 cm, time resolution was 1.35 ns, and data were adjusted for mass resolution.

The mass yields are given for each mass number in the range 80–168, which represents a reasonably complete coverage of the mass distribution, but the measurement statistics are poor due to the weak source and the long flight distance. Furthermore, there may have been some problems with the energy and mass calibration because the light mass peak is narrower and the heavy mass peak is systematically shifted to the right (Fig. 3.3.1) when compared with other studies (e.g. Li Ze et al., and Schmitt et al.). The data were eventually discarded in the evaluation.

3.3.2.9. Adopted data

All adopted and adjusted experimental data are given in Annex 3.3.1 and shown in Figs 3.3.2–3.3.5. Seven sets of data altogether are in agreement within the assigned uncertainties, except for a few specific data points.

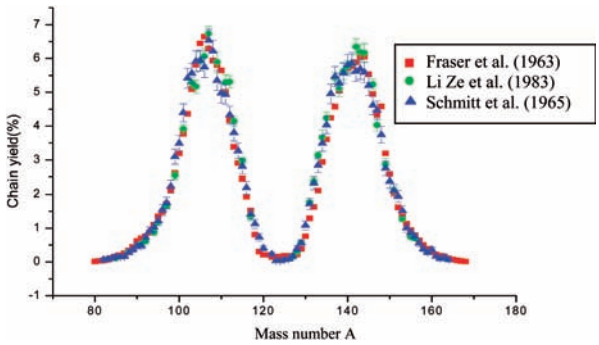

FIG. 3.3.1. Comparison of data of Li Ze, Fraser and Schmitt.

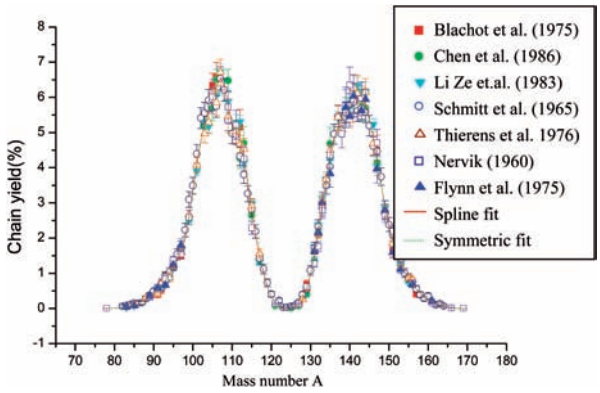

FIG. 3.3.2. Mass distribution from ^{252}Cf spontaneous fission.

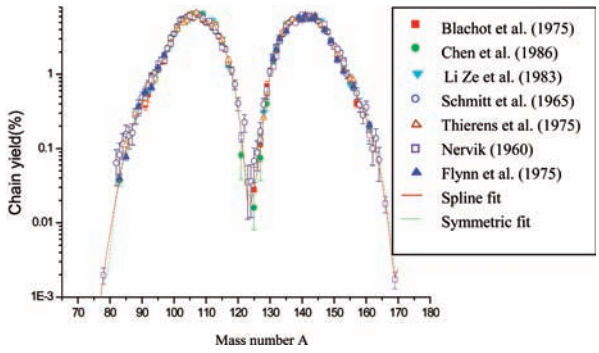

FIG. 3.3.3. Mass distribution from ^{252}Cf spontaneous fission.

3.3.3. Processing of evaluated experimental data

3.3.3.1. Data at mass numbers 99 and 140

The yields for mass numbers 99 (Nervik [3.3.6]) and 140 (Blachot et al. [3.3.5] and Flynn et al. [3.3.7]) were used as monitors in the relative measurements. These data have to be renormalized

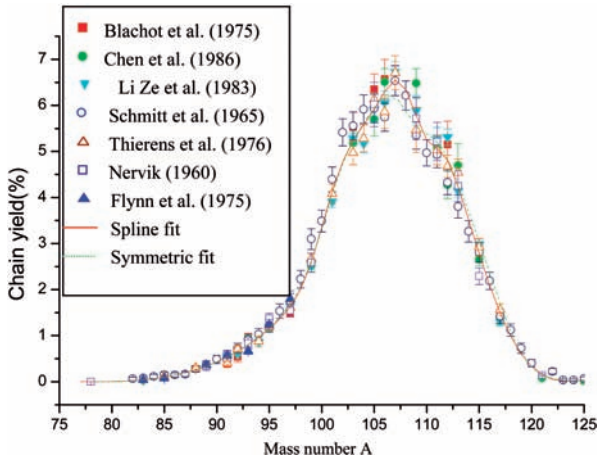

FIG. 3.3.4. ^{252}Cf spontaneous fission: light mass peak.

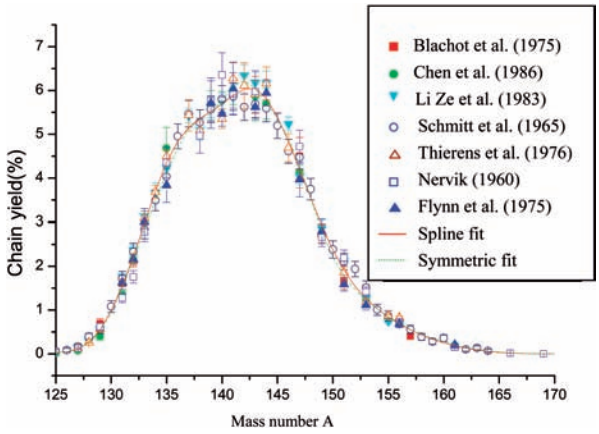

FIG. 3.3.5. ^{252}Cf spontaneous fission: heavy mass peak.

using the monitor yields obtained in our evaluations. Therefore, the yields for masses 99 and 140 were evaluated first, using the absolutely measured yields and uncertainties accepted by us, which are listed in Table 3.3.1. Weighted averages were calculated using the AVERAG code [3.3.11]. The recommended yields are listed as 'mean' in Table 3.3.1, together with their external uncertainties. One point of note is that the reduced χ^2 (1.4) is larger than 1 for A = 99, which is due to the deviation of Schmitt's data from the others.

3.3.3.2. *Spline fitting for evaluated experimental data*

The evaluated data were fitted by means of SPF [3.3.12], a spline fit code for multiple data sets with knot optimization. Primary knots were carefully selected on the basis of the shape of the curve and were automatically optimized by the code. The best result was obtained with 26 knots, and the reduced χ^2 was 1.551.

3.3.3.3. *Symmetric spline fitting*

All models for Gaussian fission fragment mass distributions are based on the assumption that all fissions are binary [3.3.13, 3.3.14]. This means that the primary fragment mass distribution should be symmetric around mass number $\bar{A} = (A_f - \bar{\nu})/2 = 124.1$, where A_f is the mass of the fissioning nucleus and $\bar{\nu} = 3.7661$ is the internationally recommended value of the average number of neutrons emitted per fission [3.3.1]. A symmetric fit of all the data is achieved by fitting the experimental yields at masses A under the light mass peak around $\bar{A}$ to obtain the reflected yields at masses $A' = 252 - \bar{\nu} - A$, which were then combined with the data for the heavy mass peak. The combined data were fitted with a spline function (see Section 3.3.3.2), with a careful selection and adjustment of the knots to obtain the best fit (reduced $\chi^2 = 1.795$). Finally, the fitted data were reflected back to the light mass peak to give a symmetrically fitted mass distribution.

TABLE 3.3.1. FISSION YIELD DATA AT A = 99, 140

Author	A = 99		A = 140	
Chen et al.	2.52	0.13	5.77	0.20
Li Ze et al.	2.55	0.11	5.76	0.18
Flynn et al.	2.48	0.13	5.50	0.28
Nervik	2.57	0.21	6.32	0.51
Schmitt et al.	3.10	0.22	5.81	0.31
Thierens et al.	2.67	0.12	5.35	0.22
Mean	2.583	0.062	5.674	0.098

3.3.4. Results and discussion

The results of the normal spline fit are given in Annex 3.3.2, while the results of the spline fit with symmetric reflection are given in Annex 3.3.3. Both are compared with the evaluated experimental data (Figs 3.3.2–3.3.5).

Total yields under the light and heavy mass peaks, as well as $\bar{\nu}$, were calculated in order to check the correctness of the spline fit curve. The borderline between the light and heavy mass peaks was taken at mass 124, which was calculated from the mass number of ^{252}Cf and $\bar{\nu}$ = 3.7661 (Table 3.3.2). As shown by the normal spline fit, the integral yield under the heavy mass peak is in good agreement with 100%, while the total yield under the light mass peak is in similar agreement within an uncertainty of 1.3%, and $\bar{\nu}$ is in agreement with the internationally recommended value of 3.7661 within an uncertainty of 2.93%. Similarly, for the symmetric fit the integral yield under the light and heavy mass peak is in agreement with 100% within an uncertainty of 1.0%, and $\bar{\nu}$ is in agreement with the internationally recommended value of 3.7661 within an uncertainty of 1.86%.

A comparison between the results of fits with and without symmetric reflection is shown in Fig. 3.3.6. These data are in very good agreement, but there are some differences in the peak regions. The light mass peak without symmetric reflection is narrower than the equivalent peak with symmetric reflection, and the situation is the reverse for the heavy mass peak. Also, the right hand side of the light peak is narrower for the normal fit than for the symmetric fit, but the left hand side of the heavy mass peak is the opposite (see Figs 3.3.1 and 3.3.8). χ^2 is 1.551 for the normal fit and 1.795 for symmetric fit, indicating that the mass distribution is not completely symmetric around the reflection point.

The fits to the results imply that there is a systematic trend towards the light fragment peak being higher and narrower and the area under the peak being slightly smaller. Individual experimental data by different authors also exhibit the same

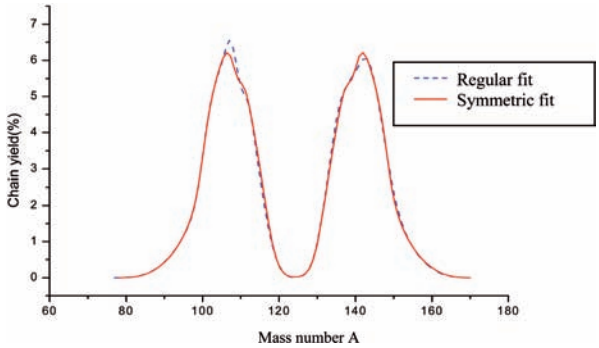

FIG. 3.3.6. Comparison of regular and symmetric spline fit: mass distribution.

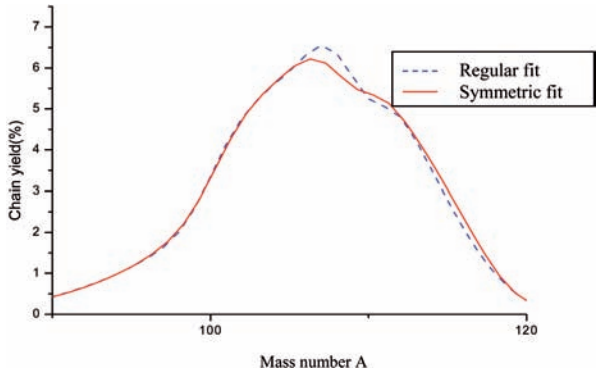

FIG. 3.3.7. Comparison of regular and symmetric spline fit: light mass peak.

trend. Table 3.3.3 shows some of the results from different authors, who measured a wide range of fission products so that integrals of the yields under the peaks can be calculated more reliably. These integral data are given in the papers by Li Ze et al. and Chen et al., and were calculated for Schmitt et al. and Fraser et al. by using their original data without any adjustments. The yields under the light mass peak are smaller than those under the heavy mass peak in all four cases. Comparing the light and heavy mass peak yields of Li Ze et al. and Schmitt et al. (Figs 3.3.9 and 3.3.10), the light peak can be seen to be narrower than the heavy peak — this

TABLE 3.3.2. REDUCED χ^2, TOTAL YIELD AND $\bar{\nu}$ FROM FITTED DATA

Fit mode	Reduced χ^2	Total yield			$\bar{\nu}$
		Light peak	Heavy peak	Total	
Normal	1.551	98.76	99.77	198.52	3.8764
Symmetric	1.795	98.98	98.96	197.95	3.6962

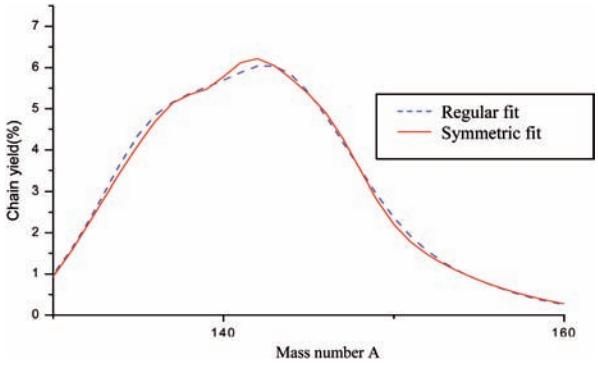

FIG. 3.3.8. Comparison of regular and symmetric spline fit: heavy mass peak.

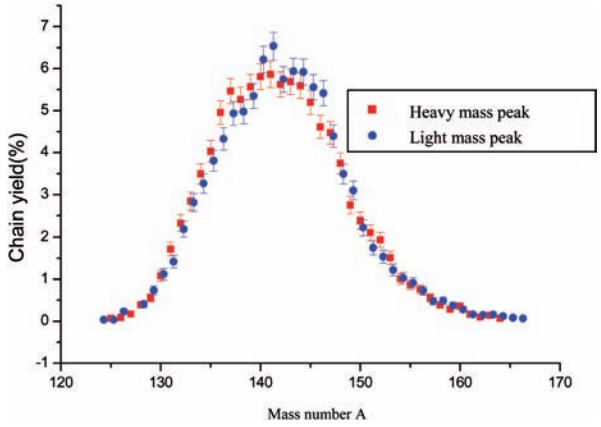

FIG. 3.3.9. Schmitt et al. data: comparison of heavy and reflected light mass peak.

observation is unlikely to be attributed to experimental uncertainties, but can rather be interpreted as a systematic trend.

A more likely explanation involves the small additional contribution of ternary fission or other α or light particle fission processes. Investigations by Mehta et al. [3.3.15] have shown that α particle fission is about 1% of binary fission, and there is a shift to the left in the mass distribution of such processes compared with ordinary binary fission. However, the shift is larger for the light mass peak and smaller for the heavy mass peak. Furthermore, the light mass peak becomes narrower, with the half width at the half maximum changing from about 7.5 to 6.8 amu (see Fig. 4 of Ref. [3.3.15]). α or other light particle fission also increases $\bar{\nu}$, which is reflected in the value derived from the fitted yield data (Table 3.3.2, normal fit), which is larger than the internationally recommended value based on neutron emission measurements.

The experimental and fitted data exhibit a shoulder on the right hand side of the light mass peak (at mass numbers 109–112), and correspondingly on the left hand side of heavy mass peak (at mass numbers 136–139). Discussions in many papers suggest that there is a fine structure in the mass distribution of ^{252}Cf spontaneous fission [3.3.3, 3.3.6, 3.3.10]. However, the observed fine structures extend only over a few (2–4) mass numbers, are very narrow, and differ in their shapes and positions in the different measurements. Therefore, such fine structures could not be confirmed — measured data may not be real but could be the result of statistical fluctuations. Due to the disagreement among measurements, the fine structure was washed out in our evaluation, where seven sets of experimental data were used; shoulders appear in the mass ranges A = 109–112 and 136–139, where there should be structures. These shoulders are systematically consistent with the mass ranges where the experiments exhibit fine structure, and hence this effect may exist in reality. More definite conclusions could be made about the existence and positions of possible fine structure and permit their evaluation if new measurements were made with high accuracy and/or better mass resolution.

Comparing the uncertainties of spline fitted data (without and with symmetric reflection) with the uncertainties of the evaluated experimental data (see Table 3.3.4), the uncertainties of the fitted data are shown to be considerably reduced, especially in the regions of the peaks (from 3–10% to about 1.1–1.5%).

TABLE 3.3.3. INTEGRAL YIELDS UNDER LIGHT AND HEAVY MASS PEAK BY DIFFERENT AUTHORS

	Author			
	Li Ze et al.	Chen et al.	Schmitt et al.	Fraser et al.
Light	99.76	98.43	99.88	97.34
Heavy	102.08	100.97	99.99	97.98

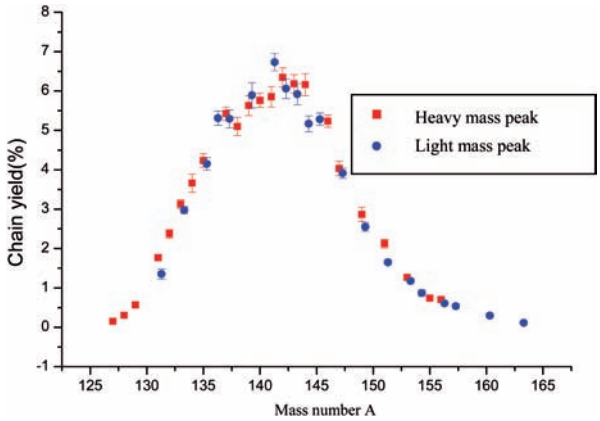

FIG. 3.3.10. Li Ze et al. data: comparison of heavy and reflected light mass peak.

This arises from the well known statistical reason that the weighted average of a consistent data set has an uncertainty reduced by roughly $7.5^{1/2} = 2.6$ times the individual uncertainties of (in our case) seven measurements. Through the curve fitting (spline fit) in our evaluation, the uncertainties are reduced further by including more data points in the fitting procedure. Input data are inconsistent for certain yields in the mass distribution, and the resulting fitted uncertainties are larger than the original measurement uncertainties due to statistical inconsistency.

3.3.5. Concluding remarks

The mass distribution data of ^{252}Cf spontaneous fission were evaluated on the basis of seven sets of available experimental data. Measured data were adjusted against the authors' standards and γ ray intensities by using our newly evaluated values. The originally assigned uncertainties had to be adjusted, and the evaluated experimental data were fitted with a spline function. In addition, a symmetric spline function fit of all experimental data was performed by symmetric reflection of the light mass peak into the heavy mass peak. These two sets of fitted data are recommended as reference for the mass distribution of ^{252}Cf spontaneous fission. The uncertainties of the recommended data were considerably reduced compared to the measured ones.

The evaluated mass distribution has the following features:

(a) Light and heavy mass peaks are not completely symmetric around mass number $A_f - \bar{\nu}$.
(b) The light peak is somewhat narrower than the heavy peak, and the area under the light peak is about 1% smaller than that under the heavy peak.
(c) There is fine structure at A = 109–112 on the right hand side of the light mass peak, and at A = 136–139 on the left hand side of the heavy mass peak.

These observed features need to be explored and should be redetermined experimentally with higher accuracy so that their nuclear physics can be investigated more thoroughly.

TABLE 3.3.4. COMPARISON OF RELATIVE UNCERTAINTIES (%) OF THE FITTED DATA WITH EVALUATED EXPERIMENTAL DATA

Author	Peaks	Valley	Wings	Comments
Blachot et al.	5–7	40–100	10–21	
Chen et al.	3–5	20–50	10–16	
Flynn et al.	5–10		~10	No data in valley region
Li Ze et al.	3–5	~20	10–15	
Nervik	~8	~15	15–25	
Schmitt et al.	~5	10–68	10–50	More nuclides in valley and at wings
Thierens et al.	5–8	~10	10–18	
Regular spline fit	~1.5	10–28	10–25	Except for A = 123, 124, 167, 168
Symmetric spline fit	~1.1	10–28	10–25	Except for A = 124

REFERENCES TO SECTION 3.3

[3.3.1] CONDÉ, H., NEANDC-311-U, Nuclear Data Standards for Nuclear Measurements, INDC(SEC)-101, IAEA, Vienna (1992) 99, 108.

[3.3.2] LIU TINGJIN, et al., The Evaluated Reference Fission Yield Data File, CNIC-01679, CNDC-0033, China Nuclear Information Centre (2002) 163–213.

[3.3.3] SCHMITT, H.W., et al., Precision measurements of correlated energies and velocities of ^{252}Cf fission fragments, Phys. Rev. **137** (1965) B837–B847 (EXFOR 13081002).

[3.3.4] THIERENS, H., et al., Study of the catcherfoil technique with the aid of ^{252}Cf(sf) and ^{235}U(n_{th},f), Nucl. Instrum. Methods **134** (1976) 299–308 (EXFOR 21531003).

[3.3.5] BLACHOT, J., et al., The cumulative decay yield of ^{252}Cf, J. Radioanal. Chem. (1975) 107–125 (EXFOR 21592002).

[3.3.6] NERVIK, W.E., Spontaneous fission yields of ^{252}Cf, Phys. Rev. **119** (1960) 1685–1690.

[3.3.7] FLYNN, K.F., et al., The mass distribution for spontaneous fission of ^{252}Cf, J. Inorg. Nucl. Chem. **37** (1975) 881–885 (EXFOR 13459002).

[3.3.8] LI ZE, et al., The measurement of absolute fission product yield for spontaneous fission of ^{252}Cf, Chin. J. Nucl. Phys. **5** (1983) 221–238 (EXFOR 30691002).

[3.3.9] CHEN QINGJIANG, et al., The absolute determination of the spontaneous fission yield of ^{252}Cf by radiochemical method, At. Energy Sci. Technol. **20** (1986) 161–166 (in Chinese).

[3.3.10] FRASER, J.S., et al., Precise kinetic energy measurements and fine structure in the spontaneous fission of ^{252}Cf, Can. J. Phys. **41** (1963) 2080–2097 (EXFOR 13067002).

[3.3.11] LIU TINGJIN, Fission yield data evaluation system FYDES, Commun. Nucl. Data Progress No. 19 (1998) 103.

[3.3.12] LIU TINGJIN, et al., Spline fitting for multi-set data with knot optimization, Commun. Nucl. Data Progress No. 2 (1989) 58–70.

[3.3.13] WAHL, A.C., "Systematics of fission-product yields", Fission Product Yield Data Required for Transmutation of Minor Actinide Nuclear Waste, IAEA, Vienna (2001).

[3.3.14] KATAKURA, J., A new parameter set of fission product mass yields systematic, personal communication, 2002.

[3.3.15] MEHTA, G.K., et al., Detailed study of alpha emission in ^{252}Cf fission, Phys. Rev. C **7** (1973) 373–387.

[3.3.16] FIRESTONE, R.B., Table of Isotopes, 8th edition (SHIRLEY, V.S., Ed.), Wiley, NY (1996).

Annex 3.3.1

EVALUATED EXPERIMENTAL DATA FOR ^{252}Cf SPONTANEOUS FISSION MASS DISTRIBUTION

	Blachot et al. [3.3.5]				Flynn et al. [3.3.7]		
	Adjusted for yield standard				Adjusted for yield standard		
Mass	Yield (%)	Uncertainty: abs	Rel (%)	Mass	Yield (%)	Uncertainty: abs	Rel (%)
91	3.8500E–01	5.6000E–02	14.55	83	3.9740E–02	3.9740E–03	10.00
92	5.3500E–01	1.1300E–01	21.12	85	7.7490E–02	7.9480E–03	10.26
93	9.3800E–01	1.1300E–01	12.05	89	3.6400E–01	2.0000E–02	5.49
95	1.2000E+00	5.6000E–02	4.67	91	5.7600E–01	6.0000E–02	10.42
97	1.4820E+00	7.5000E–02	5.06	93	6.6600E–01	7.0000E–02	10.51
103	5.5330E+00	3.2400E–01	5.86	95	1.2320E+00	1.1900E–01	9.66
105	6.3490E+00	3.3800E–01	5.32	97	1.7980E+00	1.7900E–01	9.96
106	6.5740E+00	4.2200E–01	6.42	131	1.6290E+00	1.5900E–01	9.76
112	5.1490E+00	5.0600E–01	9.83	132	2.1560E+00	1.0900E–01	5.06
115	2.9260E+00	1.8800E–01	6.43	133	3.0100E+00	2.9800E–01	9.90
125	2.8000E–02	2.8000E–02	100.00	135	3.8350E+00	3.8700E–01	10.09
127	1.1300E–01	4.7000E–02	41.59	139	5.7120E+00	5.7600E–01	10.08
129	6.9400E–01	1.1300E–01	16.28	140	5.4640E+00	2.7800E–01	5.09
131	1.6220E+00	6.6000E–02	4.07	141	6.0400E+00	6.0600E–01	10.03
132	2.1290E+00	1.1300E–01	5.31	143	5.6230E+00	2.7800E–01	4.94
141	5.9370E+00	3.3800E–01	5.69	144	5.9410E+00	2.9800E–01	5.02
143	5.8990E+00	4.2200E–01	7.15	147	3.9640E+00	3.9700E–01	10.02
147	4.5020E+00	4.2200E–01	9.37	149	2.7920E+00	2.7800E–01	9.96
151	1.6600E+00	1.8800E–01	11.33	151	1.5900E+00	1.5900E–01	10.00
153	1.4160E+00	1.6900E–01	11.94	153	1.1130E+00	1.0900E–01	9.79
157	4.0300E–01	4.7000E–02	11.66	156	6.8500E–01	7.0000E–02	10.22
				161	2.0900E–01	2.0000E–02	9.57

	Nervik [3.3.6]				Chen Qingjiang et al. [3.3.9]		
	Adjusted for yield standard				Some uncertainties were increased		
Mass	Yield (%)	Uncertainty: abs	Rel (%)	Mass	Yield (%)	Uncertainty: abs	Rel (%)
78	1.9800E–03	4.9500E–04	25.00	83	3.7000E–02	6.0000E–03	16.22
89	3.2200E–01	4.8000E–02	14.91	89	3.4700E–01	1.6000E–02	4.61
91	5.9300E–01	8.9000E–02	15.01	91	5.8200E–01	2.6000E–02	4.47
93	8.3400E–01	1.2500E–01	14.99	92	7.2500E–01	4.6000E–02	6.34
95	1.3770E+00	1.1000E–01	7.99	93	9.3100E–01	5.8000E–02	6.23
97	1.5480E+00	1.2400E–01	8.01	95	1.1500E+00	4.0000E–02	3.48
99	2.5830E+00	2.0700E–01	8.01	97	1.5700E+00	5.0000E–02	3.18
105	6.0200E+00	4.8200E–01	8.01	99	2.5200E+00	1.3000E–01	5.16
109	5.7190E+00	4.5800E–01	8.01	103	5.1800E+00	2.1000E–01	4.05
111	5.2160E+00	4.1700E–01	7.99	105	5.7000E+00	3.7000E–01	6.49
113	4.2510E+00	3.4000E–01	8.00	106	6.5100E+00	2.9000E–01	4.45
115	2.2920E+00	1.8300E–01	7.98	109	6.4800E+00	3.2000E–01	4.94
121	1.4300E–01	2.1000E–02	14.69	111	5.0800E+00	2.1000E–01	4.13
127	1.3100E–01	2.0000E–02	15.27	112	4.2700E+00	2.9000E–01	6.79
129	6.1800E–01	9.3000E–02	15.05	113	4.7000E+00	4.7000E–01	10.00
131	1.2760E+00	1.0200E–01	7.99	115	2.6600E+00	1.4000E–01	5.26
132	1.7590E+00	1.4100E–01	8.02	117	1.3600E+00	1.2000E–01	8.82
133	2.7840E+00	2.2300E–01	8.01	121	8.1400E–02	4.1000E–02	50.37
135	4.3520E+00	3.4800E–01	8.00	125	1.6000E–02	8.0000E–03	50.00

Nervik [3.3.6]				Chen Qingjiang et al. [3.3.9]			
Adjusted for yield standard				Some uncertainties were increased			
Mass	Yield (%)	Uncertainty: abs	Rel (%)	Mass	Yield (%)	Uncertainty: abs	Rel (%)
138	4.9650E+00	3.9700E–01	8.00	127	7.4800E–02	3.8000E–02	50.80
139	5.7590E+00	4.6100E–01	8.00	129	4.0200E–01	8.0000E–02	19.90
140	6.3520E+00	5.0800E–01	8.00	131	1.3500E+00	9.0000E–02	6.67
141	5.9300E+00	4.7400E–01	7.99	132	2.1500E+00	9.0000E–02	4.19
143	5.9700E+00	4.7800E–01	8.01	133	3.0200E+00	2.9000E–01	9.60
147	4.7140E+00	3.7700E–01	8.00	135	4.6800E+00	4.7000E–01	10.04
149	2.6630E+00	2.1300E–01	8.00	139	5.6600E+00	3.4000E–01	6.01
151	2.1910E+00	1.7500E–01	7.99	140	5.7700E+00	2.0000E–01	3.47
153	1.4170E+00	1.1300E–01	7.97	141	5.9700E+00	2.9000E–01	4.86
156	7.0700E–01	1.0600E–01	14.99	143	5.8600E+00	5.5000E–01	9.39
161	1.5100E–01	2.3000E–02	15.23	144	5.7000E+00	3.5000E–01	6.14
166	1.8090E–02	4.5230E–03	25.00	147	4.1400E+00	1.6000E–01	3.86
169	1.7290E–03	4.3220E–04	25.00	153	1.2300E+00	5.0000E–02	4.07
				156	7.0000E–01	9.0000E–02	12.86
				161	1.9000E–01	2.0000E–02	10.53

Li Ze et al. [3.3.8]				Thierens et al. [3.3.4]			
Adjusted for γray intensity				Adjusted for γray intensity			
Mass	Yield (%)	Uncertainty: abs	Rel (%)	Mass	Yield (%)	Uncertainty: abs	Rel (%)
85	1.1250E–01	7.0000E–03	6.22	85	1.1180E–01	2.0000E–02	17.89
88	2.9600E–01	4.2000E–02	14.19	88	3.0390E–01	3.0000E–02	9.87
91	5.3500E–01	6.0000E–02	11.21	91	4.0800E–01	3.0000E–02	7.35
92	6.0400E–01	2.6000E–02	4.30	92	7.1000E–01	7.0000E–02	9.86
94	8.6920E–01	8.0000E–02	9.20	94	8.7830E–01	1.2000E–01	13.66
95	1.1750E+00	3.5000E–02	2.98	95	1.1900E+00	4.0000E–02	3.36
97	1.6500E+00	5.4000E–02	3.27	97	1.6100E+00	6.0000E–02	3.73
99	2.5500E+00	1.1000E–01	4.31	99	2.6720E+00	1.2000E–01	4.49
101	3.9100E+00	1.3000E–01	3.32	101	4.0800E+00	2.1000E–01	5.15
103	5.2830E+00	1.6000E–01	3.03	103	4.9700E+00	2.6000E–01	5.23
104	5.1680E+00	2.0000E–01	3.87	104	5.2820E+00	2.9000E–01	5.49
105	5.9200E+00	2.7000E–01	4.56	105	6.1300E+00	1.5000E–01	2.45
106	6.0600E+00	2.5000E–01	4.13	106	5.8580E+00	3.6000E–01	6.15
107	6.7300E+00	2.2000E–01	3.27	107	6.7100E+00	3.7000E–01	5.51
109	5.8900E+00	3.2000E–01	5.43	109	5.4680E+00	4.9000E–01	8.96
111	5.2900E+00	2.3000E–01	4.35	111	5.0310E+00	3.2000E–01	6.36
112	5.3100E+00	1.8000E–01	3.39	112	4.6780E+00	2.4000E–01	5.13
113	4.1490E+00	1.6000E–01	3.86	113	4.5380E+00	3.0000E–01	6.61
115	2.9740E+00	9.0000E–02	3.03	115	2.9260E+00	1.8000E–01	6.15
117	1.3500E+00	1.3000E–01	9.63	117	1.5600E+00	1.3000E–01	8.33
127	1.4970E–01	3.0000E–02	20.04	127	1.3980E–01	1.3000E–02	9.30
128	3.0520E–01	3.2000E–02	10.48	128	2.6000E–01	2.7000E–03	1.04
129	5.6990E–01	5.4000E–02	9.48	129	5.7570E–01	7.0000E–02	12.16
131	1.7670E+00	6.0000E–02	3.40	131	1.6270E+00	9.0000E–02	5.53
132	2.3730E+00	1.1000E–01	4.64	132	2.1360E+00	1.6000E–01	7.49
133	3.1310E+00	1.1000E–01	3.51	133	3.0900E+00	1.6000E–01	5.18
134	3.6600E+00	2.3000E–01	6.28	134	3.6790E+00	1.5000E–01	4.08
135	4.2350E+00	1.7000E–01	4.01	135	4.5000E+00	1.4000E–01	3.11
137	5.4240E+00	1.7000E–01	3.13	137	5.4330E+00	3.6000E–01	6.63
138	5.1000E+00	2.3000E–01	4.51	138	5.0870E+00	1.9000E–01	3.74
139	5.6280E+00	2.5000E–01	4.44	140	5.3520E+00	2.2000E–01	4.11

Li Ze et al. [3.3.8] Adjusted for γray intensity				Thierens et al. [3.3.4] Adjusted for γray intensity			
Mass	Yield (%)	Uncertainty: abs	Rel (%)	Mass	Yield (%)	Uncertainty: abs	Rel (%)
140	5.7600E+00	1.8000E–01	3.13	141	6.2700E+00	3.6000E–01	5.74
141	5.8520E+00	2.6000E–01	4.44	142	6.1100E+00	5.2000E–01	8.51
142	6.3450E+00	2.4000E–01	3.78	143	5.9150E+00	3.1000E–01	5.24
143	6.1820E+00	2.3000E–01	3.72	144	6.1600E+00	3.8000E–01	6.17
144	6.1600E+00	2.8000E–01	4.55	146	4.6930E+00	3.2000E–01	6.82
146	5.2340E+00	1.6000E–01	3.06	147	3.9820E+00	2.1000E–01	5.27
147	4.0300E+00	1.8000E–01	4.47	149	2.7360E+00	2.0000E–01	7.31
149	2.8660E+00	1.8000E–01	6.28	151	1.8570E+00	1.3000E–01	7.00
151	2.1220E+00	1.10`00E–01	5.18	153	1.1800E+00	8.0000E–02	6.78
153	1.2650E+00	6.6000E–02	5.22	155	8.6570E–01	3.5000E–02	4.04
155	7.3910E–01	3.9000E–02	5.28	156	8.2940E–01	3.9000E–02	4.70
156	7.0240E–01	4.3000E–02	6.12				

Schmitt et al. [3.3.3], uncertainties assigned by evaluator							
Mass	Yield (%)	Uncertainty: abs	Rel (%)	Mass	Yield (%)	Uncertainty: abs	Rel (%)
82	6.4000E–02	3.2255E–02	50.40	124	3.6000E–02	2.4191E–02	67.20
83	8.2000E–02	3.6510E–02	44.52	125	6.8000E–02	3.3248E–02	48.89
84	1.1500E–01	4.3237E–02	37.60	126	8.8000E–02	3.7823E–02	42.98
85	1.5600E–01	5.0358E–02	32.28	127	1.7100E–01	5.2724E–02	30.83
86	1.4800E–01	4.9050E–02	33.14	128	3.9300E–01	7.9929E–02	20.34
87	1.6300E–01	5.1476E–02	31.58	129	5.5700E–01	9.5156E–02	17.08
88	2.8100E–01	6.7587E–02	24.05	130	1.0810E+00	1.3256E–01	12.26
89	3.7200E–01	7.7765E–02	20.90	131	1.7180E+00	1.6712E–01	9.73
90	4.8700E–01	8.8976E–02	18.27	132	2.3290E+00	1.9458E–01	8.35
91	4.7700E–01	8.8058E–02	18.46	133	2.8430E+00	2.1498E–01	7.56
92	7.2700E–01	1.0871E–01	14.95	134	3.4930E+00	2.3829E–01	6.82
93	9.1100E–01	1.2169E–01	13.36	135	4.0310E+00	2.5599E–01	6.35
94	1.0290E+00	1.2934E–01	12.57	136	4.9530E+00	2.8376E–01	5.73
95	1.2190E+00	1.4077E–01	11.55	137	5.4650E+00	2.9806E–01	5.45
96	1.5350E+00	1.5797E–01	10.29	138	5.2660E+00	2.9258E–01	5.56
97	1.7470E+00	1.6852E–01	9.65	139	5.5640E+00	3.0075E–01	5.41
98	2.2290E+00	1.9036E–01	8.54	140	5.8060E+00	3.0722E–01	5.29
99	3.0980E+00	2.2441E–01	7.24	141	5.8590E+00	3.0862E–01	5.27
100	3.4900E+00	2.3819E–01	6.82	142	5.6210E+00	3.0229E–01	5.38
101	4.3940E+00	2.6726E–01	6.08	143	5.6850E+00	3.0400E–01	5.35
102	5.4140E+00	2.9667E–01	5.48	144	5.5900E+00	3.0145E–01	5.39
103	5.5560E+00	3.0053E–01	5.41	145	5.1960E+00	2.9063E–01	5.59
104	5.9160E+00	3.1012E–01	5.24	146	4.6120E+00	2.7381E–01	5.94
105	5.9350E+00	3.1061E–01	5.23	147	4.4710E+00	2.6960E–01	6.03
106	5.7420E+00	3.0552E–01	5.32	148	3.7440E+00	2.4671E–01	6.59
107	6.5360E+00	3.2596E–01	4.99	149	2.7510E+00	2.1147E–01	7.69
108	6.2150E+00	3.1786E–01	5.11	150	2.3840E+00	1.9686E–01	8.26
109	5.3480E+00	2.9485E–01	5.51	151	2.1070E+00	1.8507E–01	8.78
110	4.9710E+00	2.8427E–01	5.72	152	1.9360E+00	1.7740E–01	9.16
111	4.9310E+00	2.8312E–01	5.74	153	1.5100E+00	1.5667E–01	10.38
112	4.3270E+00	2.6522E–01	6.13	154	1.0070E+00	1.2795E–01	12.71
113	3.8050E+00	2.4871E–01	6.54	155	8.6800E–01	1.1879E–01	13.69
114	3.2650E+00	2.3038E–01	7.06	156	7.5800E–01	1.1101E–01	14.65
115	2.8100E+00	2.1373E–01	7.61	157	5.5900E–01	9.5327E–02	17.05
116	2.1910E+00	1.8873E–01	8.61	158	3.8900E–01	7.9522E–02	20.44
117	1.4190E+00	1.5188E–01	10.70	159	2.8300E–01	6.7827E–02	23.97
118	1.1230E+00	1.3511E-01	12.03	160	3.5900E–01	7.6394E–02	21.28
119	7.3100E–01	1.0901E–01	14.91	161	1.6700E–01	5.2104E–02	31.20
120	4.0400E–01	8.1040E–02	20.06	162	1.0000E–01	4.0319E–02	40.32
122	2.2600E–01	6.0613E–02	26.82	163	1.3700E–01	4.7192E–02	34.45
123	3.5000E–02	2.3853E–02	68.15	164	7.0000E–02	3.3733E–02	48.19

Annex 3.3.2

EVALUATED DATA SET 1 FOR ^{252}Cf SPONTANEOUS FISSION MASS DISTRIBUTION: NORMAL SPLINE FIT WITHOUT ANY RESTRICTION

Mass	Yield (%)	Uncertainty: abs	Rel (%)	Mass	Yield (%)	Uncertainty: abs	Rel (%)
77	9.3000E–04	2.3300E–04	25.05	124	1.7950E–02	7.8425E–03	43.69
78	1.9800E–03	4.9500E–04	25.00	125	2.9604E–02	6.7696E–03	22.87
79	3.9000E–03	9.7500E–04	25.00	126	4.7520E–02	5.7875E–03	12.18
80	7.3000E–03	1.8250E–03	25.00	127	1.1020E–01	3.9306E–03	3.57
81	1.3000E–02	3.2500E–03	25.00	128	2.6211E–01	2.6292E–03	1.00
82	2.2810E–02	3.7225E–03	16.32	129	5.4739E–01	7.0956E–03	1.30
83	4.0575E–02	3.0541E–03	7.53	130	9.8510E–01	1.6211E–02	1.65
84	6.5623E–02	2.7881E–03	4.25	131	1.5519E+00	2.3856E–02	1.54
85	9.9084E–02	3.4590E–03	3.49	132	2.2206E+00	2.6709E–02	1.20
86	1.4208E–01	4.6869E–03	3.30	133	2.9605E+00	3.3827E–02	1.14
87	1.9575E–01	5.9290E–03	3.03	134	3.7045E+00	5.3874E–02	1.45
88	2.6122E–01	6.8764E–03	2.63	135	4.3614E+00	6.6720E–02	1.53
89	3.3960E–01	7.3937E–03	2.18	136	4.8452E+00	6.5753E–02	1.36
90	4.3204E–01	7.5728E–03	1.75	137	5.1560E+00	8.1337E–02	1.58
91	5.3966E–01	7.9633E–03	1.48	138	5.3619E+00	8.8046E–02	1.64
92	6.6363E–01	9.6576E–03	1.46	139	5.5250E+00	6.7787E–02	1.23
93	8.0588E–01	1.2534E–02	1.56	140	5.6889E+00	7.4077E–02	1.30
94	9.6880E–01	1.4637E–02	1.51	141	5.8812E+00	7.3485E–02	1.25
95	1.1548E+00	1.4715E–02	1.27	142	6.0349E+00	6.9389E–02	1.15
96	1.3665E+00	1.5659E–02	1.15	143	6.0440E+00	8.3910E–02	1.39
97	1.6285E+00	2.3876E–02	1.47	144	5.8198E+00	8.2766E–02	1.42
98	2.0100E+00	3.1722E–02	1.58	145	5.3887E+00	6.6945E–02	1.24
99	2.5857E+00	3.9567E–02	1.53	146	4.8221E+00	6.2372E–02	1.29
100	3.3524E+00	6.6332E–02	1.98	147	4.1909E+00	6.4807E–02	1.55
101	4.1404E+00	8.3518E–02	2.02	148	3.5473E+00	5.7319E–02	1.62
102	4.7751E+00	7.4627E–02	1.56	149	2.9289E+00	4.4943E–02	1.53
103	5.2363E+00	8.9065E–02	1.70	150	2.3725E+00	3.7931E–02	1.60
104	5.5888E+00	7.6493E–02	1.37	151	1.9116E+00	3.5662E–02	1.87
105	5.9173E+00	9.0695E–02	1.53	152	1.5468E+00	3.0697E–02	1.98
106	6.3015E+00	8.9912E–02	1.43	153	1.2597E+00	2.2949E–02	1.82
107	6.5546E+00	1.3891E–01	2.12	154	1.0320E+00	1.6515E–02	1.60
108	6.3418E+00	1.4509E–01	2.29	155	8.4511E–01	1.5402E–02	1.82
109	5.7837E+00	1.4591E–01	2.52	156	6.8479E–01	1.6226E–02	2.37
110	5.2496E+00	1.5969E–01	3.04	157	5.4729E–01	1.5669E–02	2.86
111	5.0570E+00	1.0257E–01	2.03	158	4.3061E–01	1.3746E–02	3.19
112	4.8076E+00	8.9389E–02	1.86	159	3.3275E–01	1.1630E–02	3.50
113	4.2337E+00	7.0058E–02	1.65	160	2.5172E–01	1.0625E–02	4.22
114	3.5142E+00	6.1562E–02	1.75	161	1.8550E–01	1.0743E–02	5.79
115	2.7861E+00	5.3401E–02	1.92	162	1.3215E–01	1.0463E–02	7.92
116	2.0970E+00	4.2811E–02	2.04	163	9.0057E–02	8.9804E–03	9.97
117	1.4888E+00	4.9460E–02	3.32	164	5.7935E–02	6.7976E–03	11.73
118	9.9411E–01	5.0357E–02	5.07	165	3.4496E–02	4.9647E–03	14.39
119	6.1188E–01	3.8680E–02	6.32	166	1.8450E–02	4.5000E–03	24.39
120	3.3393E–01	2.3182E–02	6.94	167	8.5093E–03	4.6317E–03	54.43
121	1.5200E–01	1.6078E–02	10.58	168	3.3855E–03	3.5727E–03	105.53
122	5.4264E–02	1.5008E–02	27.66	169	1.7904E–03	4.4009E–04	24.58
123	1.7890E–02	1.1656E–02	65.15				

Annex 3.3.3

EVALUATED DATA SET 2 FOR ^{252}Cf SPONTANEOUS FISSION MASS DISTRIBUTION: SPLINE FIT WITH SYMMETRIC REFLECTION

Mass	Yield (%)	Uncertainty: abs	Rel (%)	Mass	Yield (%)	Uncertainty: abs	Rel (%)
78.3	1.7330E–03	3.9156E–04	22.59	125.0	2.4359E–02	7.0476E–03	28.93
79.3	2.0742E–03	5.1781E–04	24.96	126.0	5.3460E–02	9.1334E–03	17.08
80.3	5.3336E–03	8.0026E–04	15.00	127.0	1.2326E–01	7.9565E–03	6.46
81.3	1.2679E–02	1.0849E–03	8.56	128.0	2.6161E–01	2.6447E–03	1.01
82.3	2.5279E–02	1.4716E–03	5.82	129.0	5.1667E–01	1.0841E–02	2.10
83.3	4.4300E–02	1.9753E–03	4.46	130.0	9.3522E–01	1.5727E–02	1.68
84.3	7.0911E–02	2.5429E–03	3.59	131.0	1.5050E+00	2.0909E–02	1.39
85.3	1.0628E–01	3.1058E–03	2.92	132.0	2.1613E+00	2.5859E–02	1.20
86.3	1.5157E–01	3.6064E–03	2.38	133.0	2.8386E+00	2.7702E–02	0.98
87.3	2.0796E–01	4.0134E–03	1.93	134.0	3.4964E+00	4.1983E–02	1.20
88.3	2.7661E–01	4.3440E–03	1.57	135.0	4.1211E+00	5.1956E–02	1.26
89.3	3.5869E–01	4.7002E–03	1.31	136.0	4.6944E+00	5.0617E–02	1.08
90.3	4.5536E–01	5.3008E–03	1.16	137.0	5.1340E+00	6.7819E–02	1.32
91.3	5.6780E–01	6.4470E–03	1.14	138.0	5.3412E+00	6.1429E–02	1.15
92.3	6.9759E–01	8.2341E–03	1.18	139.0	5.4718E+00	7.5213E–02	1.37
93.3	8.4811E–01	9.8681E–03	1.16	140.0	5.7760E+00	6.4045E–02	1.11
94.3	1.0232E+00	1.0490E–02	1.03	141.0	6.1168E+00	6.8057E–02	1.11
95.3	1.2266E+00	1.0727E–02	0.87	142.0	6.2183E+00	6.9566E–02	1.12
96.3	1.4658E+00	1.4694E–02	1.00	143.0	6.0429E+00	5.3464E–02	0.88
97.3	1.7760E+00	2.2007E–02	1.24	144.0	5.7229E+00	6.3914E–02	1.12
98.3	2.2058E+00	2.6870E–02	1.22	145.0	5.3564E+00	5.5729E–02	1.04
99.3	2.8021E+00	3.0237E–02	1.08	146.0	4.8999E+00	4.9589E–02	1.01
100.3	3.5381E+00	4.2637E–02	1.21	147.0	4.2824E+00	5.3468E–02	1.25
101.3	4.2824E+00	5.3468E–02	1.25	148.0	3.5381E+00	4.2637E–02	1.21
102.3	4.8999E+00	4.9589E–02	1.01	149.0	2.8021E+00	3.0237E–02	1.08
103.3	5.3564E+00	5.5729E–02	1.04	150.0	2.2058E+00	2.6870E–02	1.22
104.3	5.7229E+00	6.3914E–02	1.12	151.0	1.7760E+00	2.2007E–02	1.24
105.3	6.0429E+00	5.3464E–02	0.88	152.0	1.4658E+00	1.4694E–02	1.00
106.3	6.2183E+00	6.9566E–02	1.12	153.0	1.2266E+00	1.0727E–02	0.87
107.3	6.1168E+00	6.8057E–02	1.11	154.0	1.0232E+00	1.0490E–02	1.03
108.3	5.7760E+00	6.4045E–02	1.11	155.0	8.4811E–01	9.8681E–03	1.16
109.3	5.4718E+00	7.5213E–02	1.37	156.0	6.9759E–01	8.2341E–03	1.18
110.3	5.3412E+00	6.1429E–02	1.15	157.0	5.6780E–01	6.4470E–03	1.14
111.3	5.1340E+00	6.7819E–02	1.32	158.0	4.5536E–01	5.3008E–03	1.16
112.3	4.6944E+00	5.0617E–02	1.08	159.0	3.5869E–01	4.7002E–03	1.31
113.3	4.1211E+00	5.1956E–02	1.26	160.0	2.7661E–01	4.3440E–03	1.57
114.3	3.4964E+00	4.1983E–02	1.20	161.0	2.0796E–01	4.0134E–03	1.93
115.3	2.8386E+00	2.7702E–02	0.98	162.0	1.5157E–01	3.6064E–03	2.38
116.3	2.1613E+00	2.5859E–02	1.20	163.0	1.0628E–01	3.1058E–03	2.92
117.3	1.5050E+00	2.0909E–02	1.39	164.0	7.0911E–02	2.5429E–03	3.59
118.3	9.3522E–01	1.5727E–02	1.68	165.0	4.4300E–02	1.9753E–03	4.46
119.3	5.1667E–01	1.0841E–02	2.10	166.0	2.5279E–02	1.4716E–03	5.82
120.3	2.6161E–01	2.6447E–03	1.01	167.0	1.2679E–02	1.0849E–03	8.56
121.3	1.2326E–01	7.9565E–03	6.46	168.0	5.3336E–03	8.0026E–04	15.00
122.3	5.3460E–02	9.1334E–03	17.08	169.0	2.0742E–03	5.1781E–04	24.96
123.3	2.4359E–02	7.0476E–03	28.93	170.0	1.7330E–03	3.9156E–04	22.59
124.0	2.1078E–02	4.1348E–02	196.17				

3.4. EXAMINATION OF POSSIBLE EVALUATION METHODS FOR FUTURE ENERGY DEPENDENT FISSION PRODUCT YIELD DATA SETS REQUIRED FOR MINOR ACTINIDE INCINERATION, AND OTHER CONSIDERATIONS

R.W. Mills
British Nuclear Fuels plc, United Kingdom

Much work has been done on new methods to predict unmeasured fission product yields outside of the traditional thermal, fast and 14 MeV neutron induced fission. The current use of traditional fission product yield data is initially described. Differences required for the evaluation and usage of the new data are considered and possible solutions proposed. Other contributions are noted, and the current status of the UK fission product yield files is briefly summarized.

3.4.1. Introduction

The overall objective of the CRP was to investigate methods for the evaluation of neutron induced fission yields in the energy range 10–150 MeV, as requested for the transmutation of nuclear waste. These investigations include the studies and further development of both empirical and theoretical models for the calculation of energy dependent fission yields, which were benchmarked against the other codes and experimental data.

An examination was initially made of the ways in which the results from other participants could be combined and used in future evaluations to provide the data required to carry out inventory calculations for regulatory required safety assessments. Contributions to the collection of experimental fission yield references and data are described, as well as the adoption of Wahl's CYFP code to produce post-neutron emission data for the benchmark exercise. Finally, related work on the production of a new evaluation file is described (UKFY3.4).

3.4.2. Thoughts on future evaluations utilizing the fission product yield methodologies described by CRP participants

Recent studies have determined that the long term radiotoxicity of nuclear waste could be significantly reduced by transmutation of minor actinides and possibly some long lived fission products (e.g. Refs [3.4.1, 3.4.2]). These technologies need to be quantitatively assessed in terms of the resultant radiation doses to workers and the general public, and the risks from the use of such technologies. Releases to the environment from storage and possible processing are also important in these calculations. The important properties of nuclear waste (activities, toxic potentials, radiation emission and subsequent radiation doses) are all a direct result of the radionuclide inventory of the waste. Thus, as a prerequisite to such calculations, radionuclide inventories resulting from the use of such technologies need to be determined. These inventory calculations require a wide range of nuclear data.

One type of nuclear data required for such calculations that have previously been unavailable in evaluated files are neutron and other particle induced fission product yields as a function of energy, particularly above 10 MeV. Accurate determinations of fission product inventories from accelerator driven minor actinide transmutation scenarios require these yield data to be determined.

The recent empirical and theoretical methodologies reported by other CRP participants have, for the first time, permitted the determination of fission product yields for a wide range of particle induced fission reactions as a function of incident particle energy. The possible use of such predictions is discussed below.

3.4.2.1. Fission product yield libraries and their production

Current fission product yield libraries (e.g. JEF-2.2 [3.4.3]) consist of independent and CU yields for a range of major and minor actinides. Yields are available for a range of neutron induced and spontaneous fission systems. The data are tabulated for a set of standard neutron spectra selected from thermal, fast and 'high' energy (about 14 MeV). The independent and CU yields are given for each product nuclide.

The range of target nuclides available in JEF-2.2 is given in Table 3.4.1. It was felt desirable to base the selection of fission reactions in JEF-2.2 on objective criteria. Consequently, a series of calculations were made with the inventory code FISPIN for both thermal and fast reactors. For the former, initial fuelling by enriched uranium, recycled uranium, mixed plutonium/uranium and thorium/uranium were individually considered. The ratings and irradiations applied to the calculations were greater than actually achieved in practice at present, but these values were regarded as feasible within the near future. Reactions were regarded as important if they contributed more than 0.1% of the fission rate at any time. Thus, it is thought that the derived list is more than adequate for current reactor designs. This list does depend on the initial fuel compositions and on the assumed capture and fission cross-sections for the higher actinides; it is acknowledged that uncertainties in the latter may be considerable. In addition, the JEF-2.2 file includes fission of ^{232}Th, ^{233}U, ^{235}U and ^{238}U by 'high energy' neutrons (about 14 MeV); these reactions were in the earlier UK libraries for calculations involving breeder blankets around fusion devices. The yields from the spontaneous fission of ^{242}Cm and ^{244}Cm were also included, which are important as sources of neutrons in reactors and in fuel handling, and of ^{252}Cf, which is important as a standard.

The reactions considered by the burnup calculations are given as three sub-sets in the three left hand columns of Table 3.4.1. These are distinguished by the value of the maximum fission rate percentage due to the nuclide in question at any time during the irradiation (the range in which the percentage falls is indicated in the column heading). Clearly, the required accuracy of yields is greater if the percentage fission rate is greater; hence the nuclides in the first column need the most careful treatment, followed by those in the second column, and then by those in the third column.

The process by which these files were produced is described in Refs [3.4.4–3.4.6]. The main steps can be summarized as:

(a) Collect as much relevant data as possible;
(b) Analyse data to produce best estimates of measured yields;
(c) Produce parameterizations to allow estimation of unmeasured data;
(d) Produce complete sets of yields for each required nuclide and neutron energy combination;
(e) Adjust results for physical constraints and produce ENDF-6 formatted library.

3.4.2.2. Traditional inventory calculation in reactor fuel

All calculations of the nuclides present in irradiated material, whether from a reactor or accelerator driven system, are governed by a set of coupled linear differential equations. The concentration of an individual nuclide can be calculated by integrating all relevant production and destruction

TABLE 3.4.1. THIRTY-NINE FISSIONING SYSTEMS IN UKFY2

Maximum fraction of fission rate			Spontaneous fission
>10%	1–10%	0.1–1%	
^{233}U TFH	^{240}Pu F	^{232}Th FH	^{252}Cf S
^{235}U TFH	^{245}Cm TF	^{234}U F	^{242}Cm S
^{238}U FH		^{236}U F	^{244}Cm S
^{239}Pu TF		^{237}Np TF	
^{241}Pu TF		^{238}Np TF	
		^{238}Pu TF	
		^{242}Pu F	
		^{241}Am TF	
		^{242m}Am TF	
		^{243}Am TF	
		^{243}Cm TF	
		^{244}Cm TF	

T: Thermal fission; F: Fast fission; H: 14-MeV fission; S: Spontaneous fission.

terms. Destruction terms are only related to the concentration of the nuclide and include both radioactive decay and reactions that transform the nuclide. The production terms are related to the concentrations of the other nuclides present that by radioactive decay processes or induced reactions lead directly to the nuclide of interest.

In traditional inventory calculations the destruction terms considered are the radioactive decay of the nuclide and the main neutron induced reactions of the nuclide (n,γ), (n,f) and (n,2n), and sometimes (n,p), (n,d) and (n,α). The production terms include radioactive decay, fission products from the fission of actinides, and the neutron reactions of all nuclides that generate the nuclide of interest.

There are three ways in which nuclide inventory could be determined. The first and most commonly used is a numerical solution to the complete set of differential equations (e.g. FISPIN [3.4.7], ORIGEN [3.4.8]). An alternative is an analytical solution of simplified nuclide chains (e.g. FISP [3.4.9]). The final alternative used in some special cases, typically where nuclide cross-sections are small and precursor half-lives are short, is direct calculation from the fission rate and the cumulative fission product yield.

In all of these calculations, the neutron induced fission product yields are from a limited set of actinides that significantly contribute to the fission rate during the irradiation. The fission rates are calculated from the neutron flux, spectra and fission cross-sections. The production rate for each fission product is calculated by summing over the product of the independent yield and the fission rate for each significant fissioning nuclide.

3.4.2.3. Requirements for fission product yield data for minor actinide transmutation

There are many scenarios proposed for transmuting minor actinides. Some of these involve accelerated particle beams bombarding a target either inside or on the outer boundary of a reactor core to produce neutrons. Under these circumstances, the traditional yield sets can no longer be assumed to be adequate because the neutron spectra in or near the target may differ significantly from that in traditional fast or thermal reactors. In some other scenarios, the minor actinides are separated and placed in fuel or irradiation assemblies within conventional thermal or fast reactors. The current yield sets for such cases may be adequate, although the higher fission rates in minor actinides may require improved accuracy to predict safety related parameters adequately. Thus the following only considers accelerator driven systems, which require a new evaluation approach.

Fission in the particle beam target can be induced by either the incident particle or a wide range of secondary energetic particles, including neutrons, protons, electrons, photons and heavy ions. The energy range of these particles can extend to several hundred MeV, and even potentially into the GeV region. The range of fission reactions at these energies is much larger than in conventional reactors. For example, natural lead and tungsten isotopes can undergo fission, although in practice their cross-sections will be much lower than typical 'thermal' or 'fast' neutron cross-sections for actinides. A code, such as MCNPX [3.4.10], will be required in this region to calculate the particle fluxes and the resultant fission rates. It will then be necessary to estimate the production rate of fission products to allow the solution of the nuclide concentration equations.

In the fuel or irradiation targets, the fission rate is expected to be dominated by neutron induced reactions as charged particles will not travel far in matter. It will be necessary to estimate the neutron flux in each region and use neutron cross-sections to determine the fission rates from each fissile nuclide, again using codes like MCNPX. As in the target region, it will be necessary to estimate the production rate of fission products to allow the solution of the nuclide concentration equations. Both cases require tabulations of the yields for all significant fissile species for a wide range of neutron or charged particle energies. In practice, the calculations will require three stages.

Firstly, the particle fluxes and the resultant fission rates for all fissionable nuclides need to be determined as a function of energy or within a set of energy groups. These calculations would be carried out by a multi-particle transport code such as MCNPX.

Secondly, the yield tabulations need to be condensed into average product yields per induced fission by weighted averaging of the energy dependent fission product yields with the fission rate for each energy, fissionable nuclide and particle inducing fission. This will require the particle fluxes and fission rates from the transport code. As these parameters may be time dependent, it may be necessary to produce time dependent average fission product yields sets. This is reminiscent of the

condensation of cross-sections by the NJOY [3.4.11] code used to generate cross-sections for radiation transport and reactor physics codes, which may be time or irradiation dependent due to self-shielding.

The final step would involve using the particle fluxes, initial nuclide inventories, decay data, cross-sections and average fission product yield data sets to calculate the inventories during the irradiation and subsequent cooling. This would be very similar to the existing methods of inventory codes, but considering multiple particle fluxes and their associated induced reactions, giving rise to considerably more production and destruction terms than in the traditional differential equations governing nuclide concentration.

3.4.2.4. Generation of fission product yield data for minor actinide transmutation

The required data can be summarized as complete fission product yield sets (independent yields) for all nuclides capable of undergoing fission for all particles that can result in fission and at all appropriate particle energies. Thus, independent yields need to be determined in terms of the mass, charge and isomeric state of each product from both, binary and ternary fission. Complete yield sets can only be generated through combining data from the different methods, such as those described by CRP participants.

The first task for a future evaluator would be to obtain from the various codes or models complete independent fission product yield sets for applicable fissionable nuclides and incident particles at all appropriate energies. This would include collecting the codes and models (or data), and selecting the best models for mass distribution, charge distribution, isomeric splitting and ternary fission by comparing the calculated and experimental data. For neutron induced fission, this exercise could include a traditional evaluation of thermal or threshold yields, as a well characterized starting point.

The individual codes and data will need to be combined into a single code or module to calculate the required independent yield tabulations for all appropriate combinations of incident particles and energies. The easiest method to select the number of tabulations required for an application could be the method used in NJOY. Here the quantities are calculated at many energy values, and then each quantity is independently examined to discover if a simple linear interpolation of the surrounding tabulations can reproduce the value to within a certain tolerance (typically to 1 part in 1000). Those energy tabulations in which all the values can be adequately determined by interpolation of the surrounding energy distributions are removed, and the process is repeated until a minimum number of tabulations remain. Other interpolation methods may allow a smaller data set but could increase processing times. Depending upon the number of data sets required and the speed of calculation of each, either the set of required tabulations could be stored in a data file or the code could be used to regenerate the required tabulations as needed. This file or code package would constitute the evaluated data.

If the evaluated data were stored as tabulations of yields with energy, the existing ENDF-6 format [3.4.12] could be used, although the size of the files would be large and the CU yields would be unnecessary. Alternatively, the parameters of the individual models could be stored in a new format and used by a code to regenerate the required data.

As described above, these tabulations would have to be condensed to a mean set of independent yields per induced fission in an individual region and at each time. This would involve using a weighted averaging of the independent yields, using the fission rates for each inducing particle and energy to conserve product yield per fission. If CU yields were required, they could be generated using the method of James [3.4.4], where the CU yields are generated by a matrix multiplication of the independent yields with a matrix generated from the nuclide decay branching data.

3.4.3. Collation of references and data

Denschlag has prepared a comprehensive list of fission product yield references for all induced fission measurements where the incident photon or particle energy was above 20 MeV [3.4.25]. This list has been reviewed against the UK fission yield database [3.4.16] and a literature search, which lead to a few new references that were passed to Denschlag for consideration:

[1] ALEXANDER, J.M., CORYELL, C.D., Nuclear charge distribution in the fission of uranium and thorium with 13.6 MeV deutrons, Phys. Rev. **108** (1957) 1274–1279.

[2] KARTTUNEN, E., et al., Cross-sections for formation of fission products in the ^{238}U(p,f) reaction at proton energies between 12 and 30 MeV, Nucl. Sci. Eng. **109** (1991) 350–359.
[3] MACHNER, H., et al., Fission fragment distribution following antiproton absorption at rest on ^{238}U, Z. Phys. A, Hadron Nucl. **343** (1992) 73–77.
[4] MANOHAR, S.B., et al., Mass distribution in ^{12}C induced fission of ^{232}Th, Radiochim. Acta **56** (1992) 69–71.
[5] SMITH, J.R., RICHARDSON, A.E., Independent yields from the photo fission of ^{232}Th, and the Z_p and statistical-dynamic models, Phys. Rev. C **44** (1991) 1118–1127.
[6] THOMAS, T.D., WHETSTONE, S.L., Jr., Emission of alpha particles in the fission of ^{238}U by 11–21 MeV protons, Phys. Rev. **144** (1966) 1060–1070.

Duijvestijn [3.4.26] prepared a set of text files containing proton induced fission yield measurements which were placed on a web site to aid those working on theoretical models to predict fission product yields. It was initially envisaged that similar files would be prepared for alpha and photon induced fission. However, discussions at the CRP meetings with those involved with theoretical studies suggested that the data would not add to the understanding of the more important neutron and proton induced fission reactions. Thus no further work was undertaken, although the data collected from the ten relevant references were converted to UKFY3 format [3.4.16] for inclusion in future work. These files are available from the author. The references are in EXFOR style format:

(a)	REFERENCE	(J,PR,133,B724,1964)
	AUTHOR	(J.A. Coleman, A.W. Fairhall, I. Halpern)
	TITLE	Long range particle emission in coincidence with fission at moderate excitation energies.
(b)	REFERENCE	(J,RCA,55,173,1991)
	AUTHOR	(B.S. Tomar, A.Goswami, A.V.R. Reddy, S.K. Das, B. Mar, Satya Prakash)
	TITLE	Independent isomeric yield ratios of Sb-132 in Pu-241 (n'th,f) and U-238(alpha,f).
(c)	REFERENCE	(J,JINC,40,40,1–4,1978)
	AUTHOR	(D.C. Aumann, E. Nirschl, H. Zeising)
	TITLE	Independent formation cross-section of Pm-148m and Pm-148g in the fission of Th-232 induced by 26 to 42 MeV He4 ions.
(d)	REFERENCE	(J,RP/C,44,1118,199109)
	AUTHOR	(J.R. Smith, A.E. Richardson)
	TITLE	Independent yields from the photofission of Th-232, and the Z_p and statistical dynamic model.
(e)	REFERENCE	(J,JIN,40,1859,1978)
	AUTHOR	(H. Gaeggeler, H.R. von Gunten)
	TITLE	Charge distribution in the photofission of U-238 with Bremsstrahlung of E_{max} 20–50 MeV.
(f)	REFERENCE	(J,CNP,10,(3),244,198808) and (C,88MITO,1151,198805)
	AUTHOR	(Jing Kexing, Li Ze, Liu Conggui, Liu Yonghui, Su Shuxin, Huang Shengnian)
	TITLE	Fission yields in 7.64 MeV gamma induced fission of Th-232.
(g)	REFERENCE	(J,JRNL,155,299,1991)
	AUTHOR	(A.P. Tonchev, Ph.G. Kondev, H.G. Hristov, Yu.P. Gangrsky, N.P. Balabnov, V.D. Tcholakov)
	TITLE	Isomeric yield ratio of I-134 in photofission of Th-232 and U-238.

(h) REFERENCE (C,80KIEV,171,1980) in Russian.

AUTHOR (V.F. Teplykh, E.V. Platygina, K.A. Petrzhak)

TITLE Relative cumulative yields of Np-237 xenon isotopes by mass spect.

(i) REFERENCE (J,PR/C,21,3,1988)

AUTHOR (P. d'Hondt, E. Jacobs, A. de Clerq, D. De Frenne, H. Thierens, P. de Gelder, A.J. Deruytter)

TITLE Emission of long range alpha particles in the photofission of U-238 with 20 MeV Bremsstrahlung.

(j) REFERENCE (J,PR/C,49,2,1994)

AUTHOR (M. Verboven, E. Jacobs, D. De Frenne)

TITLE Emission of light charged particles in photon induced fission.

(k) REFERENCE (J,PR/C,114,3,1060,1966)

AUTHOR (T.D. Thomas, S.L. Whetstone Jr.)

TITLE Emission of alpha particles in the fission of U-238 by 11–21 MeV protons.

(l) REFERENCE (J,PR,133,B724,1964)

AUTHOR (J.A. Coleman, A.W. Fairhall, I. Halpern)

TITLE Long range particle emission in coincidence with fission at moderate excitation energies.

3.4.4. Benchmark exercise

3.4.4.1. Installation and testing of the CYFP code

Wahl has prepared a computer code, CYFP, that uses empirically based models to calculate fission product yield distributions for nuclides whose proton number is between 90 and 98 and mass number is between 230 and 252. The code can consider excitation energies (including projectile kinetic and binding energies) between zero and ~200 MeV [3.4.13].

The code was installed from the supplied CD (dated 25 September 2002) on a SUN workstation running the UNIX operating system Solaris (SunOS 5.7). The CYFP code was compiled with the SUN f77 compiler and used to run the 'SOUT' case supplied on the CD. After replacement of a corrupt version of the 'TABLE.DATH' file [3.4.14] the calculated yields were shown to agree with those given on the CD with only small differences in a few of the numbers at the last significant digit. These small differences were attributed to differences in the mathematical routines used on the different computers.

3.4.4.2. Application of the CYFP code to the benchmark

The code was run for the following post-neutron emission cases:

Set A: Studies for comparison with experimental data

U-233	(n,f)	thermal, 1 MeV
Np-237	(n,f)	thermal
Cm-245	(n,f)	thermal
U-238	(n,f)	1.6, 5.5, 8, 10, 13, 14.5, 21, 28, 50, 100, 160 MeV
U-238	(p,f)	20, 60 MeV
Pu-239	(n,f)	0.17, 7.9, 14.5, 15.1 MeV

Set B: Studies of minor actinides

Np-237	(n,f)	13, 28, 50, 100, 160 MeV
Am-241	(n,f)	13, 28, 50, 100, 160 MeV
Cm-244	(n,f)	13, 28, 50, 100, 160 MeV

These results were sent to M. Lammer (IAEA) in November 2002.

An attempt was made to produce data for the pre-neutron emission benchmarks, but these results differed significantly from those of other participants. Wahl [3.4.15] suggested several ways in which improvements could be made, but this work could not be completed for the benchmark deadline.

3.4.5. Progress in the UK fission product yield file

The UKFY3 fission product yield file was initially prepared in 1995 using an extensive experimental database and JEF-2.2 decay data [3.4.16]. This is a development of previous UK work by Cuninghame, Crouch, James and others (see, for example, Refs [3.4.4–3.4.6, 3.4.17]).

The latest version of the UK file is UKFY3.4, which has been submitted to the JEFF project and released for testing. The principle modifications compared with UKFY3 are:

(a) Changes to the experimental database to remove duplicated data and adjust the uncertainties assigned to a single reference which published a collection of early work on fast fission yields. The UKFY3.4 database includes 14 709 experimental measurements.
(b) The use of JEFF3T2 [3.4.18] spins to calculate isomeric splitting using the Madland and England model [3.4.19].
(c) The use of JEFF3T2 decay paths to calculate the CU yields.
(d) Improvement to the method used to calculate uncertainties in the CU yields.
(e) The use of JEFF3T2 MAT and AWR values.

The database and resultant evaluated file are available from the author.

The isomeric splitting of independent yields is an area with little experimental data, but is important for short time decay heat estimates. Table 3.4.2 shows a comparison of experimental data with the isomeric splitting ratios calculated using the Madland and England model, which depends on the spin quantum number of the product. Results from JEF-2.2 and the preliminary version of the JEFF3 decay data (version T2) are shown for nuclides where the spin information is different between the two data sets and experimental results exist. These data show improvement for a few nuclides when the newer library is adopted, but given the range of experimental results and uncertainties significant differences are difficult to specify.

The CU yields were checked both by direct inspection of some mass chains and the calculation of the average delayed neutron emission per fission ($\bar{\nu}_d$) for each fissioning system. The calculated $\bar{\nu}_d$ results are given in Table 3.4.3. These results are highly dependent on the independent yields of nuclides that emit neutrons after beta decay. These nuclides are far from the line of stability, and therefore these calculations are dominated by the extrapolation of the magnitude and shape of the independent yield distributions, as practical considerations make measurements difficult. The UKFY3.4 results show better agreement overall, but the results for the better known systems U235T and Pu-239T are slightly worse, though within the

TABLE 3.4.2. ISOMERIC SPLITTING RATIOS THAT DIFFER BETWEEN JEF-2.2 AND JEFF3T2

Nuclide	Experimental measurements from the UKFY3.4 database	Madland and England model with JEF-2.2 spins	Madland and England model with JEFF3T2 spins
Rb-90	0.897 ± 0.045	0.808	0.899
Sb-130	0.501 ± 0.120	0.576	0.630
Te-131	0.680 ± 0.090	0.517	0.707
Sb-132	0.440 ± 0.090 0.194 ± 0.068	0.576	0.424
I-132	0.386 ± 0.063 0.446 ± 0.045 0.732 ± 0.050	0.643	0.424
I-136	0.803 ± 0.174	0.643	0.701

uncertainties of the calculation. The major differences in delayed neutron emission for these two systems result from changes to the P_n values of As-85, Br-91 and I-137. It is expected that improvements to the P_n values in later versions of JEFF3 will improve these results.

TABLE 3.4.3. COMPARISON OF CALCULATED AND EXPERIMENTAL AVERAGE DELAYED NEUTRONS PER FISSION

Fissioning system[a]	Total delayed neutron yield per 100 fissions				Calculated/Experimental		
	Yields UKFY3.4	UKFY3.4	JEF-2.2	Experimental measurement[b]	UKFY3.4	UKFY3.4	JEF-2.2
	Decay JEFF3T2	JEF-2.2	JEF-2.2		JEFF3T2	JEF-2.2	JEF-2.2
Th-232F	5.601 ± 0.639	6.280	6.046	5.47 ± 0.12	1.02	1.15	1.11
Th-232H	3.226 ± 0.541	3.472	2.939	2.85 ± 0.13	1.13	1.22	1.03
U-233T	0.740 ± 0.072	0.772	0.878	0.664 ± 0.018	1.12	1.16	1.32
U-233F	1.074 ± 0.103	1.131	0.952	0.729 ± 0.019	1.47	1.55	1.31
U-233H	0.576 ± 0.106	0.619	0.344	0.422 ± 0.025	1.36	1.47	0.82
U-234F	1.371 ± 0.169	1.461	1.197	1.06 ± 0.12	1.29	1.38	1.13
U-235T	1.500 ± 0.125	1.572	1.708	1.654 ± 0.042	0.91	0.95	1.03
U-235F	1.772 ± 0.123	1.828	1.910	1.714 ± 0.022	1.03	1.07	1.11
U-235H	0.950 ± 0.086	0.945	0.790	0.927 ± 0.029	1.03	1.02	0.85
U-236F	2.464 ± 0.273	2.652	2.330	2.31 ± 0.26	1.07	1.15	1.01
U-238F	4.191 ± 0.301	4.327	4.266	4.51 ± 0.061	0.93	0.96	0.95
U-238H	2.396 ± 0.244	2.529	2.395	2.73 ± 0.08	0.88	0.93	0.88
Np-237T	1.157 ± 0.174	1.192	1.232	1.07 ± 0.1	1.08	1.11	1.15
Np-237F	1.221 ± 0.103	1.264	1.234	1.22 ± 0.03	1.00	1.04	1.01
Pu-238T	0.314 ± 0.064	0.315	1.472	0.456 ± 0.051	0.69	0.69	3.23
Pu-238F	0.494 ± 0.061	0.502	0.470	0.456 ± 0.051	1.08	1.10	1.03
Pu-239T	0.611 ± 0.080	0.619	0.617	0.624 ± 0.024	0.98	0.99	0.99
Pu-239F	0.708 ± 0.119	0.720	0.690	0.664 ± 0.013	1.07	1.08	1.04
Pu-240F	0.904 ± 0.100	0.912	0.940	0.96 ± 0.11	0.94	0.95	0.98
Pu-241T	1.220 ± 0.135	1.225	1.336	1.56 ± 0.16	0.78	0.79	0.86
Pu-241F	1.325 ± 0.126	1.321	1.452	1.63 ± 0.16	0.81	0.81	0.89
Pu-242F	1.753 ± 0.097	1.725	1.928	2.28 ± 0.25	0.77	0.76	0.85
Am-241T	0.368 ± 0.051	0.371	0.409	0.44 ± 0.05	0.84	0.84	0.93
Am-241F	0.423 ± 0.070	0.429	0.411	0.394 ± 0.024	1.07	1.09	1.04
Am-242^{m}T	0.578 ± 0.105	0.584	0.649	0.69 ± 0.05	0.84	0.85	0.94
Cm-245T	0.432 ± 0.155	0.436	0.507	0.59 ± 0.04	0.73	0.74	0.86
Cf-252S	0.549 ± 0.174	0.542	0.741	0.86 ± 0.1	0.64	0.63	0.86
Sum of deviations squared					1.02	1.33	5.41

[a] S denotes spontaneous fission, T denotes thermal neutron induced fission, F denotes 'fast' neutron induced fission, and H denotes 14 MeV neutron induced fission.

[b] Measured values taken from evaluations of Refs [3.4.20–3.4.24].

REFERENCES TO SECTION 3.4

[3.4.1] BAUDIN, G., et al., "Overview of the French program in chemical separation and transmutation of minor actinides and long lived fission products", Safety and Environmental Aspects of Partitioning and Transmutation of Actinides and Fission Products, IAEA-TECDOC-783, IAEA, Vienna (1994) 37–51.

[3.4.2] EUROPEAN NUCLEAR ENERGY AGENCY, A European Roadmap for Developing Accelerator Driven Systems (ADS) for Nuclear Waste Incineration, NEA, Rome (2001).

[3.4.3] NUCLEAR ENERGY AGENCY, The JEF-2.2 Nuclear Data Library, JEFF Rep. 17, NEA/OECD, Paris (2000).

[3.4.4] JAMES, M.F., et al., A New Evaluation of Fission Product Yields and the Production of a New Library (UKFY2) of Independent and Cumulative Yields, Part I. Methods and Outline of the Evaluation, Rep. AEA-TRS-1015, United Kingdom Atomic Energy Authority (1991).

[3.4.5] JAMES, M.F., et al., A New Evaluation of Fission Product Yields and the Production of a New Library (UKFY2) of Independent and Cumulative Yields, Part II. Tables of Measured and Recommended Fission Yield, Rep. AEA-TRS-1018, United Kingdom Atomic Energy Authority (1991).

[3.4.6] JAMES, M.F., et al., A new evaluation of Fission Product Yields and the Production of a New Library (UKFY2) of Independent and Cumulative Yields, Part III. Tables of Fission Yields with Discrepant or Sparse Data, Rep. AEA-TRS-1019, United Kingdom Atomic Energy Authority (1991).

[3.4.7] BURSTALL, R.F., FISPIN — A Computer Code for Nuclide Inventory Calculations, Rep. ND-R-328(R), United Kingdom Atomic Energy Authority (1979).

[3.4.8] CROFT, A.G., ORIGEN2: A versatile computer code for calculating the nuclide compositions and characteristics of nuclear materials, Nuclear Technol. **62** (1983) 335–352.

[3.4.9] TOBIAS, A., FISP6 — An Enhanced Code for the Evaluation of Fission Products, Rep. TPRD/B/0097/N82, CEGB, UK (1982).

[3.4.10] MASHNIK, S.G., et al., "MCNPX for neutron–proton transport", Mathematics & Computation, Reactor Physics & Environmental. Analysis in Nuclear Applications (Proc. Int. Conf. Madrid, 1999), American Nuclear Society, La Grange Park, IL (1999).

[3.4.11] MacFARLANE, R.F., et al., The NJOY Nuclear Data Processing System, Version 91, Rep. LA-12740-M, Los Alamos National Laboratory, NM (1994).

[3.4.12] McLANE, V., ENDF-102 Data Formats and Procedures for the Evaluated Nuclear Data File ENDF-6, Rep. BNL-NCS-44945-01/04-Rev, Brookhaven National Laboratory, Upton, NY (1990).

[3.4.13] WAHL, A.C., Systematics of Fission-Product Yields, Rep. LA-13928, Los Alamos National Laboratory, NM (2002).

[3.4.14] WAHL, A.C., Los Alamos National Laboratory, personal communication, November 2002.

[3.4.15] WAHL, A.C., Los Alamos National Laboratory, personal communication, December 2002.

[3.4.16] MILLS, R.W., Fission Product Yield Evaluation, PhD thesis, University of Birmingham, UK (1995).

[3.4.17] CROUCH, E.A.C., Fission-product yields from neutron induced fission, At. Data Nucl. Data Tables **19** (1977) 417–532.

[3.4.18] NOURI, A., NEA Data Bank, personal communication.

[3.4.19] MADLAND, D.G., ENGLAND, T.R., The influence of isomeric states on independent fission product yields, Nucl. Sci. Eng. **64** (1977) 859–865.

[3.4.20] MANERO, F., et al., Status of the energy dependent $\bar{\nu}$-values for the heavy isotopes ($Z > 90$) from thermal to 15 MeV and of $\bar{\nu}$-values for spontaneous fission, At. Energy Rev. **10** (1972) 637.

[3.4.21] TUTTLE, R.J., Delayed-neutron data for reactor-physics analysis, Nucl. Sci. Eng. **56** (1975) 37–71.

[3.4.22] TUTTLE, R.J., Delayed Neutron Properties, INDC(NDS)-107, IAEA, Vienna (1979).

[3.4.23] WALDO, R.W., et al., Delayed neutron yields: Time-dependent measurements and a predictive model, Phys. Rev. C **23** (1981) 1113–1127.

[3.4.24] BENEDETTI, G., et al., Delayed neutron yields from fission of Uranium-233, Neptunium-237, Plutonium-238, - 240, - 241, and Americium-241, Nucl. Sci. Eng. **80** (1982) 379–387.

[3.4.25] DENSCHLAG, J.-O., "Measurements of product yields from fission reactions induced by high energy neutrons, protons, deuterons, alpha particles, other charged particles and photons — Collection of references", Section 2.1, this publication.

[3.4.26] DUIJVESTIJN, M.C., KONING, A.J., "Fission yields in nucleon induced reactions at intermediate energies", Section 4.6, this publication.

4. SYSTEMATICS AND MODELS FOR THE PREDICTION OF FISSION YIELDS

4.1. PREDICTION OF FISSION MASS YIELD DISTRIBUTIONS BASED ON CROSS-SECTION EVALUATIONS

F.-J. Hambsch
European Commission Joint Research Centre, IRMM, Belgium

The statistical model for fission cross-section evaluations has been extended by including the concept of multi-modality of the fission process. The three most dominant fission modes, i.e. the two asymmetric standard I (S1) and standard II (S2) modes and the symmetric super long mode, are taken into account. Based on calculations of the nuclear surface within the multi-modal random neck rupture model, separate outer fission barriers are considered for each mode, while the inner barriers and isomeric wells are assumed to be the same. Deconvoluted fission cross-sections for the S1, S2 and super long modes of ^{235,238}U(n,f) and ^{237}Np(n,f), based on experimental branching ratios, were calculated for the first time in the incident neutron energy range from 0.01 to 5.5 MeV, providing good agreement with the experimental fission cross-section data. In this way, branching ratios can also be deduced for incident neutron energies when no experimental data exist, and used for the prediction of the corresponding fragment mass yield distributions.

4.1.1. Introduction

The concept of multi-modality in nuclear fission was introduced theoretically in the 1980s [4.1.1], and the multi-modal random neck rupture model (MM-RNR) has proven to be a good approximation to the fission process. This model pioneered fission research by also giving quantitative predictions for typical observables such as mean mass and mean total kinetic energy of the fission fragments. The first ideas about multi-modal fission date back to as early as 1951 and were introduced in order to interpret the mass distribution of the fissioning compound nucleus ^{233}Th [4.1.2]. In the region of light actinide nuclei, this approach could be applied rather successfully under the assumption of a symmetric and an asymmetric fission mode [4.1.3]. However, for heavier actinides such as ^{236}U this bi-modal approach turned out to be too simple. On the other hand, an MM-RNR model that did not limit the number of possible fission modes could quite successfully explain the characteristic fission fragment properties over the whole actinide range from ^{213}At to ^{258}Fm. A major fraction of this actinide mass range can be satisfactorily covered by assuming three dominant fission modes: the asymmetric standard I (S1) and standard II (S2) modes and the symmetric super long mode. However, in some special cases other modes become important (see, e.g., Ref. [4.1.4]).

Based on potential energy calculations that have been performed for ^{238}Np [4.1.5], ^{239}U [4.1.6] and ^{252}Cf [4.1.4], the bifurcation point of the asymmetric fission modes was found to lie in the second minimum of the double humped fission barrier. This implies the presence of separated outer barriers for each of the modes. This proposal was already established for the symmetric super long mode, since it is a well known experimental fact that the yield of symmetric masses increases with increasing incident neutron energy.

In a collaborative effort to improve on the fission cross-section evaluation by including the multi-modality of the fission process in statistical model codes for cross-section calculations, the codes have been adapted to include the experimentally observed fission modes. For most actinide nuclei, as mentioned above, compound nuclear fission is dominated by three fission modes: the asymmetric S1 and S2 modes and the symmetric super long (SL) mode. The two asymmetric standard modes are generally thought to be linked with the neutron shells in the fission fragments at N = 82 (spherical shell) for S1, and N = 88 (deformed shell) for S2 [4.1.1].

Based on experimental fission mode branching ratios measured at IRMM in the neutron energy range below the second chance fission threshold, and the ENDF/B-VI fission cross-section

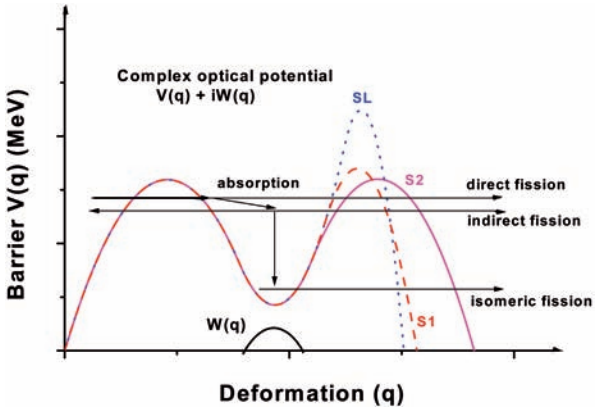

FIG. 4.1.1. Qualitative representation of the double humped fission barrier and the possible fission processes.

[4.1.7], the mode separated fission cross-sections are obtained for the reactions n + ^{235}U, n + ^{238}U and n + ^{237}Np. Over this energy range, the neutron interaction with the target nucleus takes place through direct and compound nuclear mechanisms. For these deformed heavy nuclei, the elastic channel is strongly coupled with the other possible channels in the process, and the direct mechanism has to be treated with the coupled channel method. For the compound nuclear mechanism a statistical treatment is used for fission, neutron elastic and inelastic scattering and radiative capture cross-section calculations.

In order to describe the mode separated fission cross-sections in terms of the statistical model, the statistical STATIS code [4.1.8] was modified to take into account the contribution of each fission mode in competition with the other open channels. Fission mode calculations [4.1.5] based on the MM-RNR model demonstrated that the bifurcation point is close to the second minimum of the double humped fission barrier. Consequently, the inner barriers and the isomeric wells were taken to be the same for all modes, and the outer fission barrier for each fission mode was taken to be different (see Fig. 4.1.1). For each mode, the sub-barrier effects and the direct, indirect and isomeric fission cross-sections are taken into account.

4.1.2. Statistical model

The compound nucleus mechanism is treated in terms of the statistical model with sub-barrier effects, using the statistical STATIS code modified to take into account the multi-modal fission concept. Competitive processes are elastic (n) and inelastic (n_i) scattering, radiative capture (γ) and fission (f) for the neutron induced reactions of actinides in the incident energy range where only one compound nucleus is formed. The three most dominant fission modes S1, S2 and super long are taken into account.

Within the modified statistical model, the compound nucleus formation cross-section and the decay of the compound nucleus are expressed by the following equations [4.1.8]:

$$\sigma_n^{CN}(E) = \sum_{\alpha'} \sigma_{n,\alpha'}^{CN} = \pi \lambda\!\!\!^{-2}_n \sum_{J\Pi} g_n^J \sum_{lj} T_{n,l,j}(E, J\Pi) \tag{4.1.1}$$

$$\sigma_{n,\alpha'}^{CN} = \pi \lambda\!\!\!^{-2}_n \sum_{J\Pi} g_n^J \sum_{lj} V_{n,\,l,j}(E, J\Pi) P_{\alpha'}(E, J\Pi);$$

$$\alpha' = n, n_i, \gamma, f_m; \quad m = S1, S2, SL \tag{4.1.2}$$

E is the incident neutron energy in the laboratory system (LS), J and Π are the spin and parity of the compound nucleus, $V_{n,l,j}$ are the generalized neutron transmission coefficients, and $P_{\alpha'}(E,J\Pi)$ is the compound nucleus decay probability for the exit channel α'. Details of the calculation of these quantities can be found in Ref. [4.1.9].

The coupled channel method (ECIS code [4.1.10]) is used for the direct mechanism, while a statistical model (STATIS code that takes into account sub-barrier effects and the multi-modal fission concept) is used for the compound nucleus mechanism. Direct interaction calculations use the coupled channel ECIS-95 code [4.1.10] that provides the total cross-section, the direct contributions of the neutron elastic and inelastic cross-sections of the rotational levels coupled to the ground state, and the neutron transmission coefficients $T_{n_i,l,j}$ needed in the compound nucleus calculations.

The compound nucleus calculations are carried out with the STATIS statistical code [4.1.8] that provides the fission cross-section, the radiative capture cross-section, and the compound nuclear contributions of the neutron elastic and inelastic cross-sections of the rotational levels coupled to the ground state.

The total cross-section of n + ^{235}U in the incident neutron energy range 0.01–20 MeV as obtained by the coupled channel calculations using the ECIS code is given as an example in Fig. 4.1.2. Such good agreement proves the validity of the

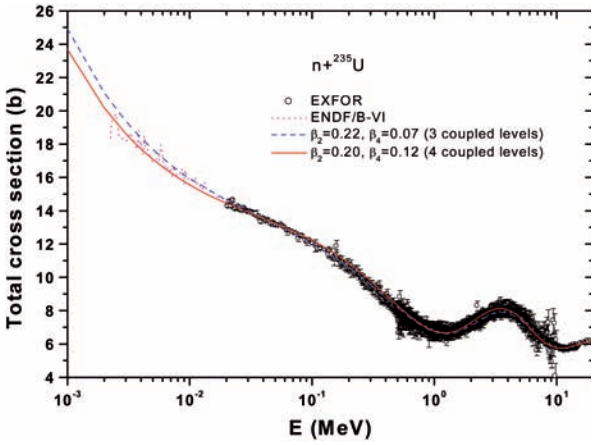

FIG. 4.1.2. ^{235}U total cross-section over the incident neutron energy range 0.01–20 MeV obtained by the coupled channel calculation with ECIS.

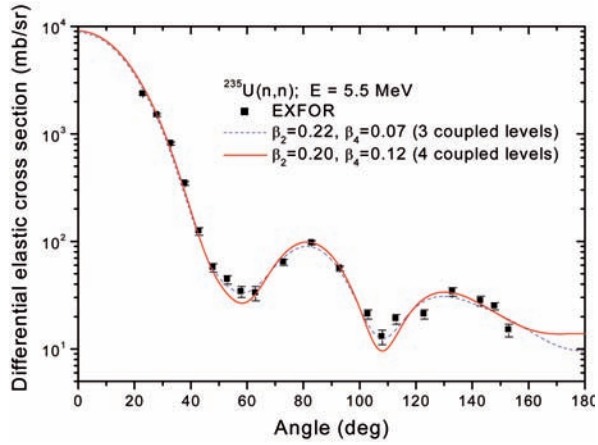

FIG.4.1.3. Differential elastic cross-section for $^{235}U(n,n)$ at E_n = 5.5 MeV.

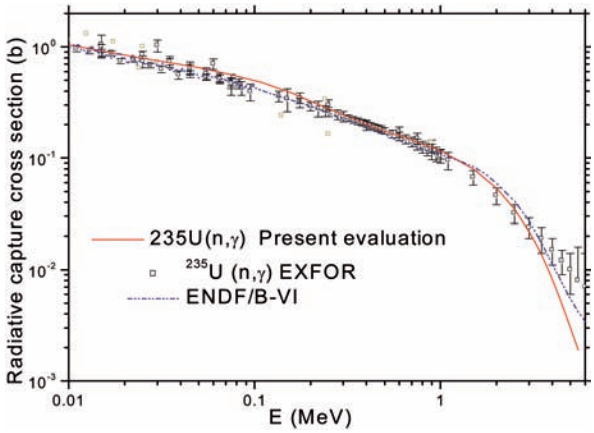

FIG.4.1.4. Radiative capture cross-section for $^{235}U(n,\gamma)$.

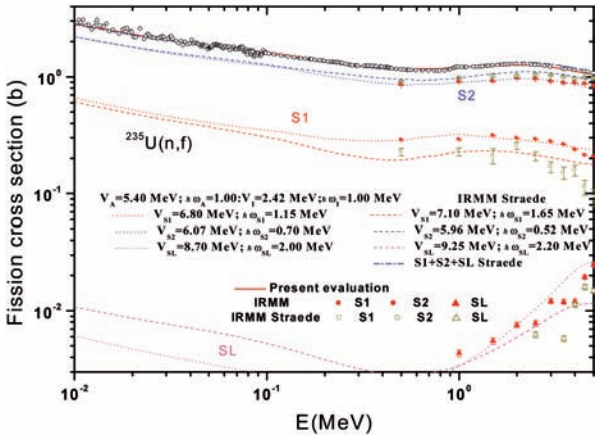

FIG.4.1.5. Total fission cross-section in comparison with mode separated fission cross-sections for $^{235}U(n,f)$.

optical potential used in the calculations. More details of the calculations and corresponding results can be found in Refs [4.1.9, 4.1.11]. Figs 4.1.3 and 4.1.4 show examples of the quality of the calculations for the differential elastic cross-section and the capture cross-section for n + ^{235}U.

4.1.3. Results and discussion

Mode separated fission cross-sections are obtained by multiplying the ENDF/B-VI evaluation for the different compound systems with the IRMM experimentally determined branching ratios. These fission cross-sections are described in terms of the statistical model, as mentioned above. Calculations have been undertaken in the incident energy range between 0.01 (where the statistical model assumptions become valid) and 5.5 MeV (where the first fission chance is dominant).

The calculated fission cross-sections for the S1, S2 and super long modes and the total fission cross-section in comparison with the 'experimental' modal cross-sections (represented by different symbols) and available experimental data from EXFOR [4.1.12] (open circles) are given in Figs 4.1.5 and 4.1.6 for ^{235}U and ^{237}Np, respectively. Agreement of the present calculations with the experimental fission cross-sections for each mode can be appreciated from the data in these figures that compare the calculated branching ratios of each mode with the existing IRMM experimental data.

Two observations can be made. First, for the ^{235}U(n,f) data of Straede et al. [4.1.13] the agreement between the experimental modal and the calculated cross-sections is rather poor, especially at higher incident neutron energies above 2 MeV. We trace this back to the fact that the branching ratios as deduced by Straede et al. were based only on

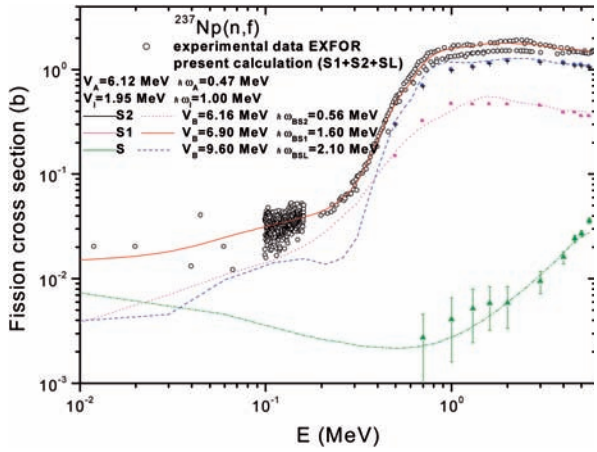

FIG. 4.1.6. Total fission cross-section in comparison with mode separated fission cross-sections for ^{237}Np(n,f).

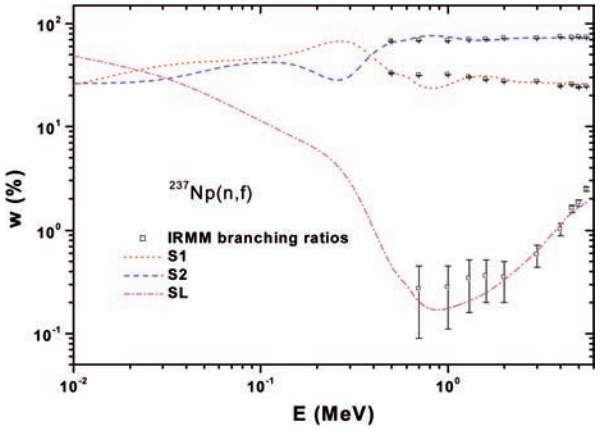

FIG.4.1.8. Branching ratios for ^{237}Np(n,f).

fitting the mass distribution with three Gaussian distributions, and not taking into account the full information contained in the measured Y(A, total kinetic energy) distribution.

The full two dimensional Y(A, total kinetic energy) distribution has been used with the IRMM data set in Fig. 4.1.5 to deduce the branching ratios [4.1.14]. This approach also emphasizes the importance of using the full information on the fission fragments, namely their mass and total kinetic energy dependence, for a reliable deduction of the branching ratios.

Second, in the case of threshold reactions such as ^{237}Np and ^{238}U it is very important for the fission cross-section calculation that experimental modal fission cross-sections are available in the threshold region to make the theoretical calculation and the corresponding barrier parameters more credible.

Although some discrepancies are observed for the S1 mode, especially in the threshold region (0.6–1.3 MeV incident neutron energy), the overall

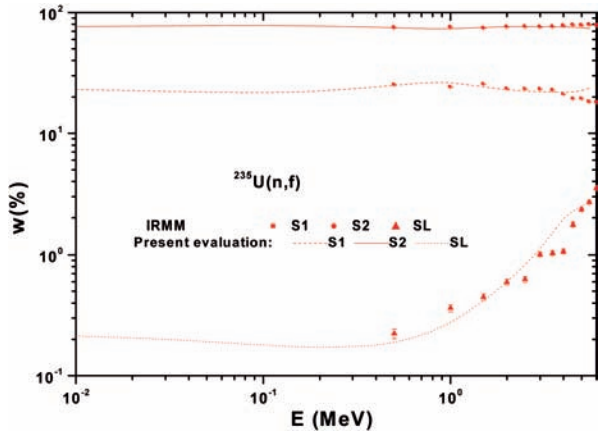

FIG.4.1.7. Branching ratios for ^{235}U(n,f).

agreement is also reasonably convincing for ^{237}Np(n,f). Consequently, we can assume that the calculated branching ratios in the entire incident energy range studied are good. The branching ratios for both ^{235}U(n,f) and ^{237}Np(n,f) as calculated with the model and their comparison to the experimentally deduced branching ratios are given in Figs 4.1.7 and 4.1.8. Using these branching ratios and extrapolating the IRMM modal data for the mass yield, standard deviations and mean masses, the fission fragment mass distribution can be estimated at any incident neutron energy over the energy range studied.

Note should be made of the important contribution of the super long mode in the sub-barrier energy region for ^{237}Np(n,f) at incident neutron energies $E_n \leq 0.02$ MeV. For $E_n \leq 0.1$ MeV, the contributions of the S1 and S2 modes are approximately the same, and the S1 mode dominates in the energy range $0.1 \leq E_n \leq 0.4$ MeV, leading to hitherto unexpected fission fragment mass distributions in this energy range. For ^{235}U(n,f), the branching ratio only changes slightly below 0.5 MeV incident neutron energy (see Fig. 4.1.7).

The results for the modal fission cross-section of ^{238}U(n,f) are also remarkable (see Figs 4.1.9, 4.1.10). First, this isotope has a very small sub-barrier cross-section of only 10^{-4} b, and therefore the calculations are very sensitive to the barrier parameters. Second, the cross-section exhibits structure at the threshold related to the existence of vibrational resonances at incident energies of about 0.9 and 1.2 MeV. Around the second vibrational resonance at about $E_n = 1.2$ MeV, very strong fluctuations in the fission fragment properties such as the mean total kinetic energy and angular distribution have already been observed [4.1.15–4.1.17].

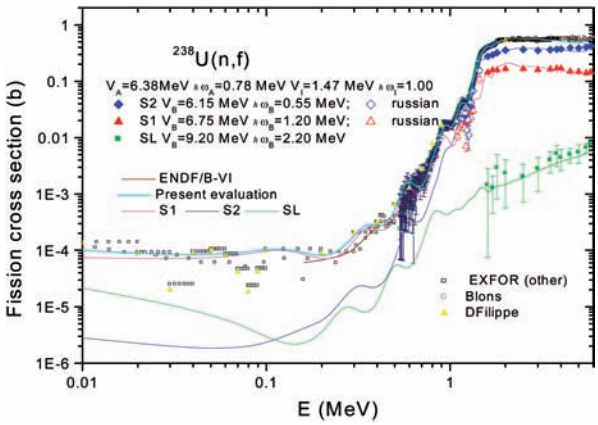

FIG. 4.1.9. Total and mode separated fission cross-section for $^{238}U(n,f)$ together with the corresponding calculated mode separated fission cross-sections.

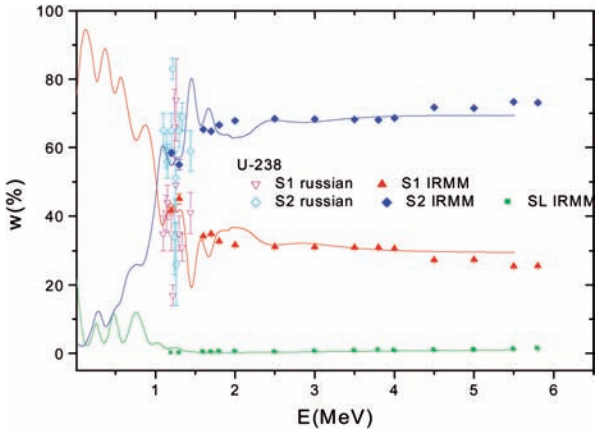

FIG. 4.1.10. Calculated and experimental branching ratios for $^{238}U(n,f)$.

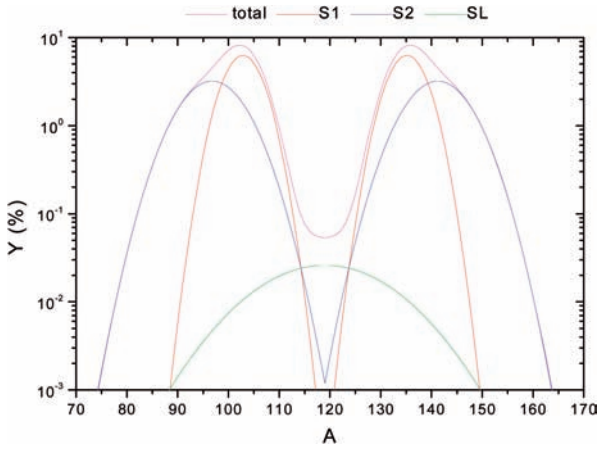

FIG. 4.1.11. Predicted mass distribution for $^{237}Np(n,f)$ at E_n = 0.4 MeV.

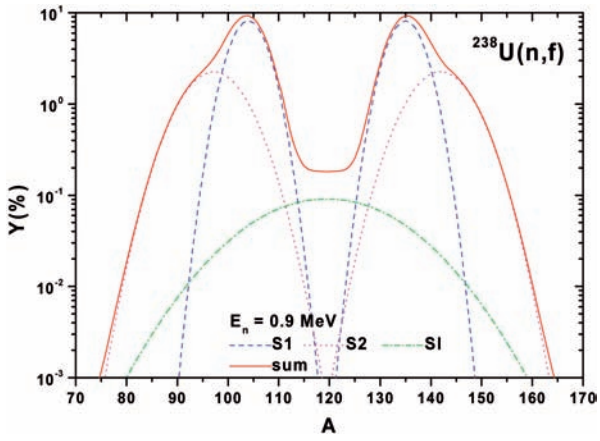

FIG. 4.1.12. Predicted mass distribution for $^{238}U(n,f)$ at E_n = 0.9 MeV.

However, the observed fluctuations in the fission fragment branching ratios from Ref. [4.1.17] are much too strong to be parameterized by the model. The maximum of the observed fluctuations also seems to lie around E_n = 1.25 MeV, whereas the structure in the cross-section is located more towards E_n = 1.2 MeV. More experimental investigations around this vibrational resonance and another at E_n = 0.9 MeV (where no experimental data exist) are necessary to verify the theoretical predictions (experiments are planned for the coming years).

The consequence of the drastic change in the mass distribution is obvious. Two examples of predicted mass distributions are given in Figs 4.1.11 and 4.1.12. The mass distribution for ^{237}Np at E_n = 0.4 MeV is plotted in Fig. 4.1.11 and shows a peak yield towards the position of the S1 mode (calculations predict that this mode is dominant at this incident energy (see Fig. 4.1.8)). This domination should also have a consequence for the mean total kinetic energy, since the S1 mode has a more compact shape and hence a higher total kinetic energy. A similar conclusion can be drawn for ^{238}U. The strength of the S1 mode is also increasing for incident neutron energies smaller than 1.3 MeV, and this behaviour should be observable in state of the art experiments.

4.1.4. Concluding remarks

(a) For the first time, fission mode de-convoluted fission cross-sections based on branching ratios measured at IRMM were calculated for incident neutron energies E_n = 0.01–5.5 MeV. Good agreement with experimental fission

cross-section data has been achieved for three different nuclei, ^{235,238}U and ^{237}Np.

(b) Reasonable values have been derived for the outer barrier heights and the corresponding curvatures of each mode.

(c) Symmetric and asymmetric fission can be explained by penetration through different outer barriers. At sub-barrier neutron incident energies, the least asymmetric mode S1 is dominant, while above the fission threshold the most asymmetric mode S2 becomes dominant in fission. This behaviour has consequences for the observed fission fragment properties, e.g. fragment mass distribution.

(d) Within the concept of multi-modal fission, the calculations of fission fragment mass distributions, the prompt fission neutron multiplicity and neutron energy spectrum for each mode are feasible from the measured fission cross-sections only.

REFERENCES TO SECTION 4.1

[4.1.1] BROSA, U., et al., Nuclear scission, Phys. Rep. **197** (1990) 167–262.

[4.1.2] TURKEVICH, A., NIDAY, J.B., Radiochemical studies on the fission of Th-232 with pile neutrons, Phys. Rev. **84** (1951) 52–60.

[4.1.3] BRITT, H.C., et al., Energetics of charged particle-induced fission reactions, Phys. Rev. **129** (1963) 2239–2252.

[4.1.4] HAMBSCH, F.-J., et al., "^{252}Cf(sf): fission modes and far asymmetric mass yields", Nuclear Data Science Technology (Proc. Int. Conf.. Trieste, 1997) (REFFO, G., et al., Eds), Vol. 59, Part II, SIF, Bologna (1997) 1239–1241.

[4.1.5] SIEGLER, P., et al., et al., Fission modes in the compound nucleus ^{238}Np, Nucl. Phys. A **594** (1995) 45–56.

[4.1.6] OBERSTEDT, S., et al., Fission-mode calculations for ^{239}U, a revision of the multi-modal random neck-rupture model, Nucl. Phys. A **644** (1998) 289–305.

[4.1.7] McLANE et al. (Eds), ENDF/B-VI, ZA93237, MF=3, MT=2, 4, 18, 19, 20, 102; ENDF/B-VI Summary Documentation, Rep. BNL-NCS-17541, 4th Edn, Suppl. 1, Brookhaven National Laboratory (1996).

[4.1.8] VLADUCA, G., et al., Neutron cross-sections of ^{238}U in the energy range 0.01–5.5 MeV, Ann. Nucl. Energy **27** (2000) 995–1010.

[4.1.9] VLADUCA, G., et al., Fission cross-section evaluations in the frame of the multi-modal fission model for ^{237}Np(n,f), Nucl. Phys. A **707** (2002) 32–46.

[4.1.10] RAYNAL, J., Notes on ECIS94, CEA-N-2772 (1994).

[4.1.11] VLADUCA, G., et al., Evaluation of the fission cross-section within the multi-modal fission approach for ^{235}U(n,f), Nucl. Phys. A **720** (2003) 274–292.

[4.1.12] EXFOR Nuclear Data Library (2000), nucleus ZA93237, quantities CS, reactions (n,tot) (n,f) and (n,γ).

[4.1.13] STRAEDE, C., et al., ^{235}U(n,f) fragment mass-, kinetic energy- and angular distributions for incident neutron energies between thermal and 6 MeV, Nucl. Phys. A **462** (1987) 85–108.

[4.1.14] HAMBSCH, F.-J., Institute for Reference Materials and Measurements, EC Joint Research Centre, unpublished studies, 2002.

[4.1.15] VIVÈS, F., et al., Investigation of the fission fragment properties of the reaction ^{238}U(n,f) at incident neutron energies up to 5.8 MeV, Nucl. Phys. A **662** (2000) 63–92.

[4.1.16] SHPAK, D.L., Angular anisotropy of fragments from fission of ^{238}U by 0.85–6.28 MeV neutrons, Sov. J. Nucl. Phys. **50** (1989) 574–577.

[4.1.17] GOVERDOVSKII, A.A., ICTP lecture notes, Nuclear Reaction Data and Nuclear Reactors: Physics, Design and Safety (Proc. Workshop Trieste, 2002), Abdus Salam International Centre for Theoretical Physics, Trieste (2002).

4.2. SYSTEMATICS OF FISSION PRODUCT YIELDS

A.C. Wahl
Los Alamos National Laboratory, United States of America

Empirical equations representing systematics of fission product yields have been derived from experimental data. The systematics give some insight into nuclear structure effects on yields, and the equations allow estimation of yields from fission of any nuclide with atomic number Z_F = 90–98, mass number A_F = 230–252, and precursor excitation energy (projectile kinetic plus binding energies) *PE* = 0 to ~200 MeV, representing the ranges of these quantities for the fissioning nuclei investigated. Calculations can be made with the CYFP computer program. Estimates of uncertainties in the yields were also calculated and range from ~15% for the highest yield values to several orders of magnitude for very small yields. A summation method is used to calculate weighted average parameter values for fast neutron (approximately fission spectrum) induced fission reactions.

4.2.1. Introduction

Systematics of fission product yields were derived in two successive stages:

(1) Gaussian functions were fitted by the least squares method to data (mass yields (*Y*(*A*)), or fractional independent (*FI*) and cumulative (*FC*) yields) for each fission reaction investigated. Frequently, not all parameters could be determined by the least squares method, and some approximate values had to be assumed based on the models. This procedure led to recycling as model values were refined.

(2) Each Gaussian parameter determined for a number of fission reactions was fitted to an equation with terms containing differences between Z_F, A_F and/or *PE* and corresponding values for U-235T [4.2.1–4.2.4], using the least squares method. These equations and the derived term coefficients are listed in Tables 4.2.1, 4.2.2 and 4.2.3 (see below).

Most low and high energy fission reactions were treated separately. Reactions with excitation energies $E^* = PE < 8.0$ MeV were considered low energy, reactions with $PE > 20.0$ MeV were considered high energy, and reactions with *PE* between 8.0 and 20.0 MeV were considered to be of intermediate energy. Gaussian parameters derived from data for the intermediate region (e.g. 14 MeV neutron induced fission reactions) were used with parameters for both low and high energy fission reactions to help achieve smooth model parameter transitions in going from low to high energy.

Data for low energy fission included yields from spontaneous fission and neutron induced fission with neutron energies of 14 MeV or less. Data for high energy fission were for proton induced fission reactions, since no yield data were found for high energy (approximately >14 MeV) neutron induced fission. It was assumed that fission yields are independent of how nuclei were formed. This assumption is supported by the observation that the peak to valley ratio from fission of ^{236}U excited to 11–25 MeV depends only a little (~13%) on whether formation occurs by neutron capture or by alpha particle induced fission of ^{232}Th [4.2.5].

Most yield data for high energy proton induced fission are presented in the literature as formation cross-sections in units of millibarns (mb). Cross-section values were divided by the fission cross-section and multiplied by 100 to give *Y(A)* or independent (IN) or CU yields as per cent in order to use these data with *Y(A)* and *FI–FC* for low energy fission. IN and CU values were subsequently divided by *Y(A)* to give *FI* and *FC* values. Fission cross-sections and chain yields were used from the data source, if available; otherwise values were deduced from their trends with energy. For proton energies above ~25 MeV, cross-sections for proton induced fission of ^{238}U and ^{232}Th are approximately constant at 1.40 ± 0.10 and 0.89 ± 0.06 b, respectively [4.2.6–4.2.8]. Below ~25 MeV there are considerable amounts of data that are useful for interpolation [4.2.8–4.2.10].

For high energy fission reactions, nucleons are lost before fission, and the initial precursor (target + projectile) values of *PA, PZ,* and *PE* are lowered (e.g. Ref. [4.2.11]). The average loss of mass number (*NT*) and atomic number (*NPE*) can be determined from yield calculations, but the loss of excitation energy cannot, and therefore *PE* was used as a parameter.

Preliminary calculations showed that a number of parameters used to represent low energy fission yields (i.e. even–odd proton and neutron factors, F_Z and F_N, slopes of σ_Z and Δ_Z, and special effects near symmetry and on the mass yield wings) could not be determined from high energy data, and the effects described by these parameters were assumed to be negligibly small at high energies.

Most of the equations in Ref. [4.2.4] for yields from low energy fission reactions have been modified to eliminate discontinuities and to enhance smooth transitions of the functions to those for high energy fission reactions. Equations for some Gaussian parameters were derived that can represent both low and high energy values. However, for most parameters, different equations were used for low and high energy, the two functions being connected by a transition function that is linear in *PE* between *PE* = 8 and 20 MeV.

An interesting point of note is that 14 MeV neutron induced fission reactions, treated by low energy systematics in Ref. [4.2.4], are now classified as essentially high energy reactions. However, the current classification seems appropriate because neutrons are often emitted before fission induced by 14 MeV neutrons (as discussed later).

Fission yields from fast neutron induced fission were calculated by a summation method to give weighted average parameter values for those model parameters that are energy dependent [4.2.4]. Equations derived for low energy fission were used (Tables 4.2.1 and 4.2.2) because most of the increments that were summed had E^* values < 8 MeV. Parameters for U-238F were calculated with and without using appropriate values for the intermediate region, and no significant differences in the derived parameter values were observed.

4.2.2. Mass distribution

4.2.2.1. Determination of Gaussian parameters

Parameters for the multi-Gaussian model [4.2.4, 4.2.12, 4.2.13] were determined by the least squares method from experimental chain yield data for 63 fission reactions. Reciprocal variance weighting was used in the calculations, with minimum uncertainties being set at 5% for yields from low energy neutron induced fission and 10% for yields from high energy proton induced fission reactions. Minimum uncertainties were used to prevent data with very small uncertainties from having unduly large weights for the determination of the Gaussian parameters.

The data were obtained from the two comprehensive evaluations of chain yields for spontaneous fission and for thermal and 14 MeV neutron induced fission reactions [4.2.14, 4.2.15], from yields for monoenergetic neutron (0.1–10.0 MeV) induced fission reactions [4.2.16–4.2.19], from yields for light-wing mass numbers from the LOHENGRIN fission product separator [4.2.20–4.2.24], from LOHENGRIN yields for AM242T (^{241}Am(2n,f)) [4.2.25], from monoenergetic proton (10–340 MeV) induced fission of ^{238}U [4.2.7], and from yields for monoenergetic proton (13–53 MeV) induced fission of ^{232}Th [4.2.26]. Mass yield data from fission induced by fast neutrons with a large range of energies can also be represented by Gaussian curves, but the resulting Gaussian parameters were not used in the second stage of the analysis. However, the mass distributions for fast fission reactions can be calculated by a summation method from the model parameters derived from other data, as discussed in a later section.

The total number of nucleons emitted before and after fission *(NT)* is not generally known for high energy fission reactions, and values are needed to determine the midpoint (symmetry point, $\bar{A}$), (*PA* – *NT*)/2, in which *PA* is the sum of the projectile and target mass numbers. Therefore, *NT* was determined as a high energy fission parameter that gave the best representation of complementarity for light and heavy product chain yields in each multi-Gaussian least squares calculation. For low energy fission, the average total number of post-fission neutrons emitted is given by $NT = \nu_F$.

Earlier calculations for low energy fission indicated that the inclusion of an additional pair of Gaussian curves to help represent experimental *Y(A)* on the wings of mass yield curves improved the data representation significantly for some heavier fissioning nuclides (e.g. Figs 4.1–3C, 4C, 5C, 6C of Ref. [4.2.4]). Additional calculations using six or seven curves showed that this effect applied to $Z_F \geq 94$, but not to $Z_F \leq 92$ or high energy fission reactions.

4.2.2.2. Equation for least squares parameter calculations

$$\mathrm{Y}(A) = \sum_{i=1}^{i=7} Y_i e^D / \sigma_i \sqrt{2\pi} \qquad (4.2.1)$$

$$D = -(A - \bar{A} + \Delta_i)^2 / 2\sigma_i^2 \qquad (4.2.1a)$$

$$\bar{A} = (PA - NT)/2 \qquad (4.2.1b)$$

4.2.2.3. Estimated model uncertainties

One helpful approach in efforts to represent measured chain yields by sums of Gaussian curves was to include estimates of uncertainties in model calculated yields. Uncertainties were estimated from the following empirical equation proposed earlier for the per cent uncertainty (PER) [4.2.27]:

$$PER = 25e^{-0.25ln(Y(A))} \qquad (4.2.2)$$

Estimated range of uncertainty: $Y(A)/(1+PER/100)$ to $Y(A)(1+PER/100)$:

Examples:	$Y(A)$, %	PER	$1 + PER/100$
	10	14	1.14
	1	25	1.25
	0.1	44	1.44
	10^{-3}	141	2.41
	10^{-6}	791	8.91
	10^{-10}	7 910	80.10
	10^{-15}	140 600	1 407

Examples of results of multi-Gaussian least squares calculations for individual fission reactions are shown in Figs 4.2.1(a)–4.2.10(a) (Figs 4.2.1(b)–4.2.10(b) show the same experimental points, but the lines are derived from systematic trends (to be discussed later)). Most experimental chain yields (points in the figures) are represented approximately by the sums (solid lines) of several Gaussian curves (broken lines), each sum being normalized to 200%. The dotted lines, between which many data-points fall, represent the estimated uncertainties for the sums of the calculated curves. Reduced χ^2 values in parentheses include estimated model uncertainties as discussed above, and cluster about 1.0; the average of the ten values shown in the figures is 1.0. Thus, the estimated uncertainties for the multi-Gaussian representations behave appropriately for the limited test described. The reduced χ^2 values before the parentheses in the figures are based on experimental or minimum uncertainties and are mostly >1.0, showing that the multi-Gaussian model does not represent the experimental fine structure and other details very well.

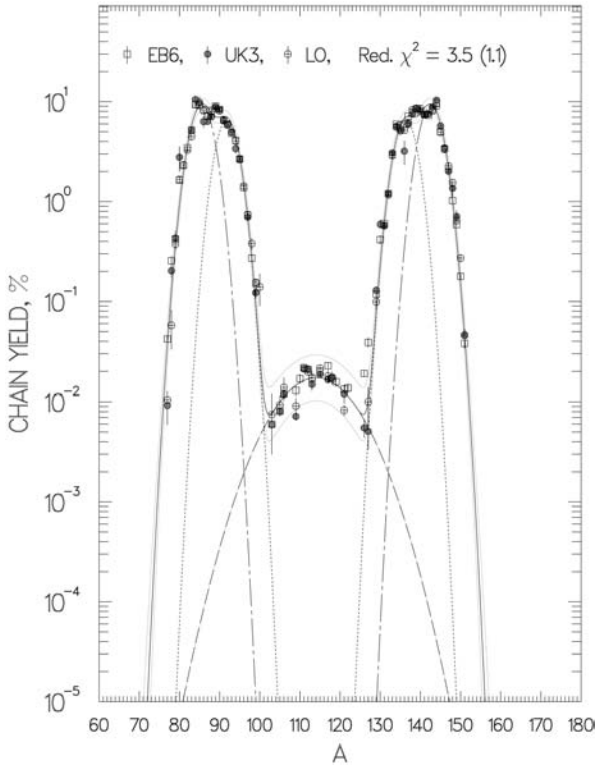

FIG. 4.2.1(a). TH229T, LS Par., 5% min. uncertainty.

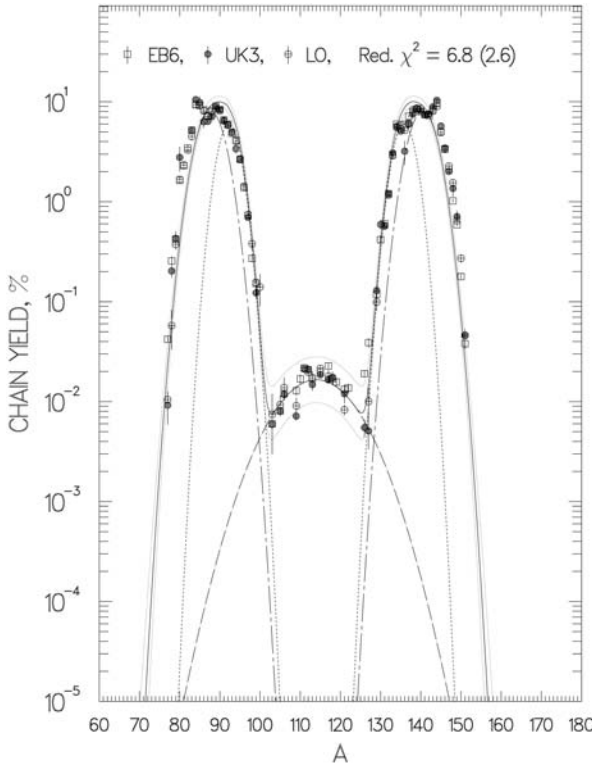

FIG. 4.2.1(b). TH229T, Sys. Par., 5% min. uncertainty.

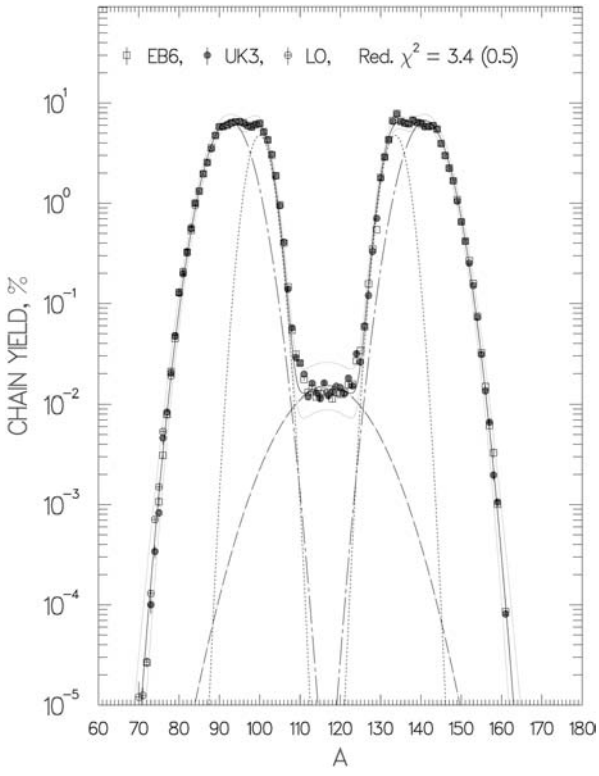

FIG. 4.2.2(a). U235T, LS Par., 5% min. uncertainty.

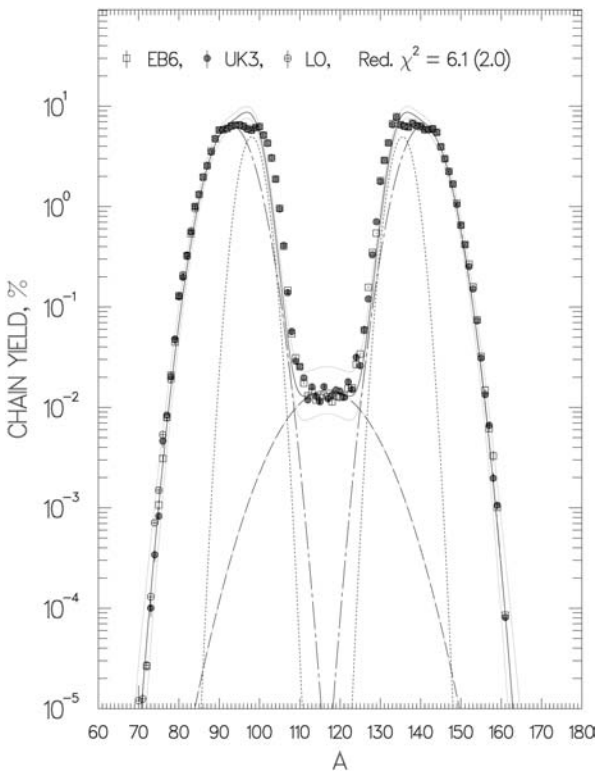

FIG. 4.2.2(b). U235T, Sys. Par., 5% min. uncertainty.

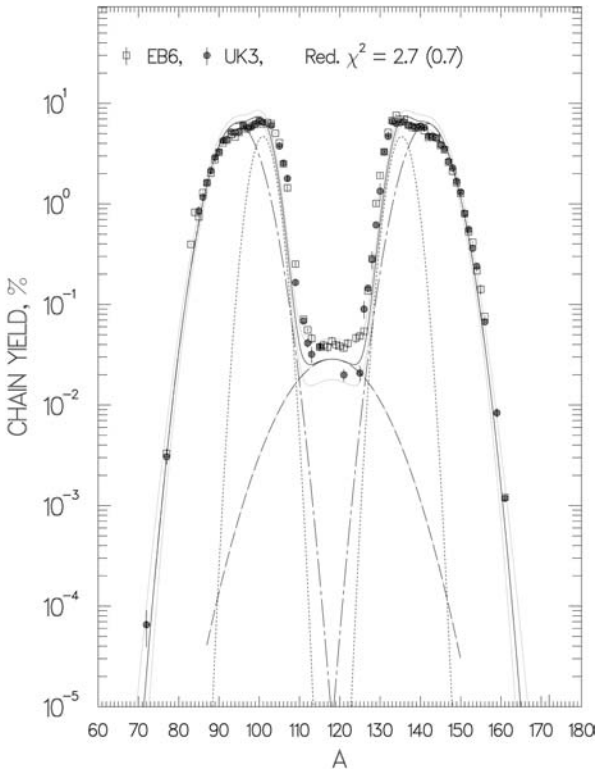

FIG. 4.2.3(a). U238F, LS Par., 5% min. uncertainty.

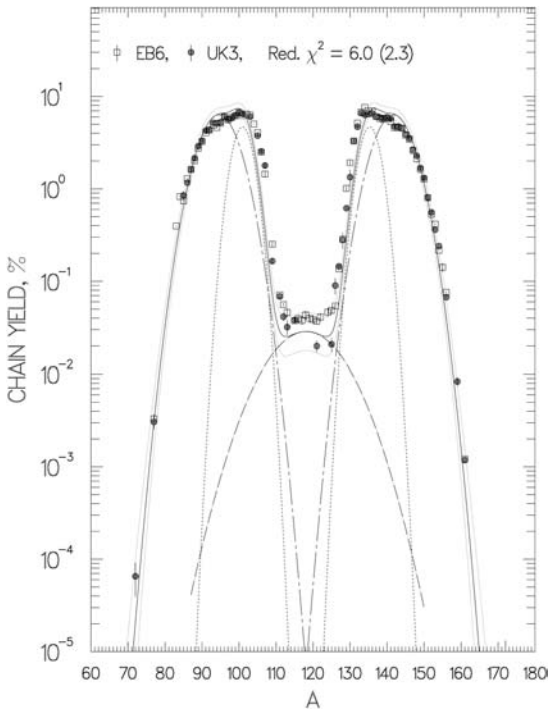

FIG. 4.2.3(b). U238F, Sys. Par., 5% min. uncertainty.

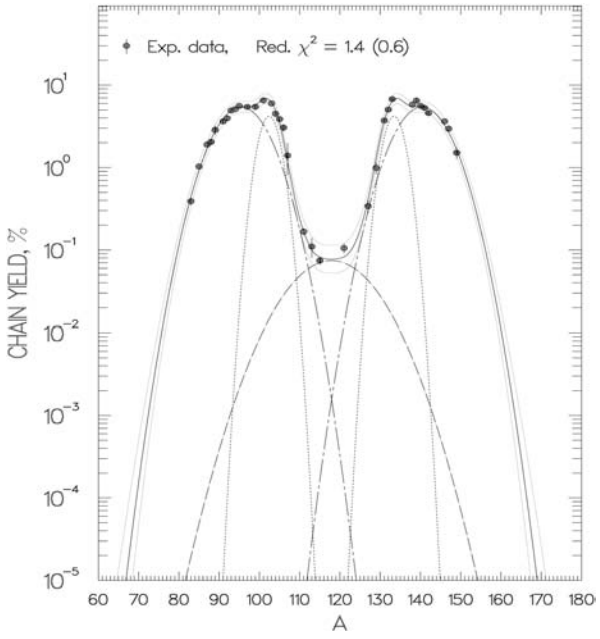

FIG. 4.2.4(a). ^{238}U + 5.5 MeV n, LS Par.

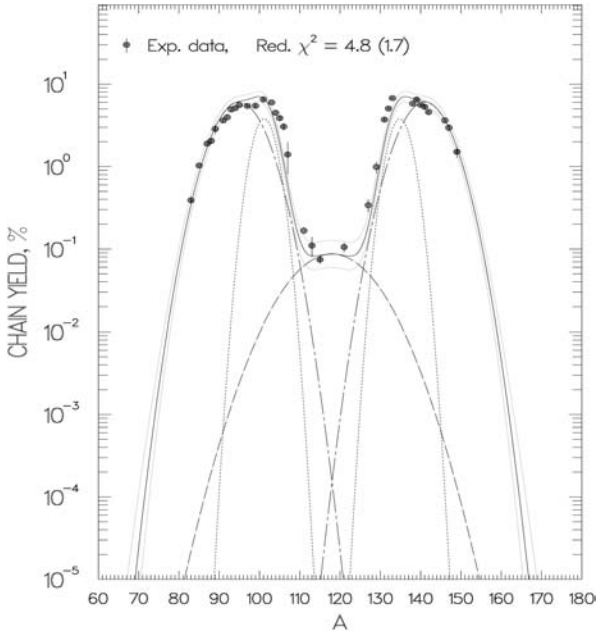

FIG. 4.2.4(b). ^{238}U + 5.5 MeV n, Sys. Par.

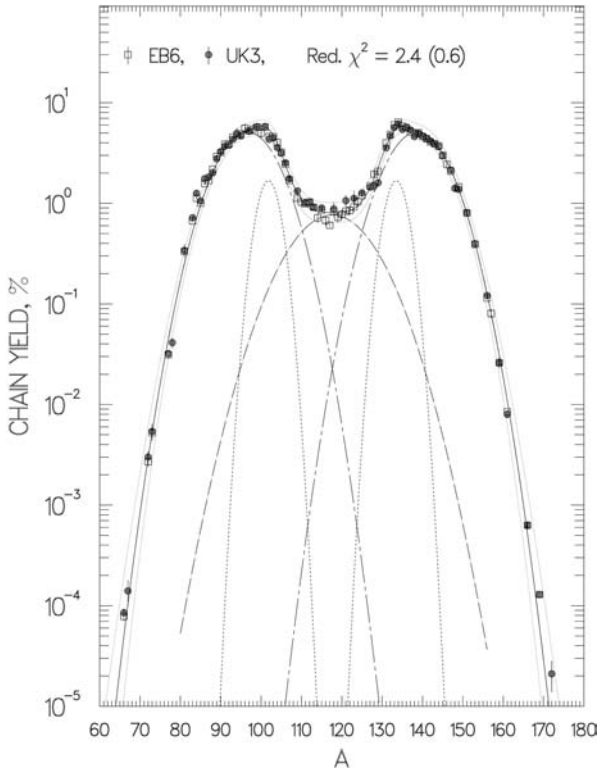

FIG. 4.2.5(a). U238H, LS Par., 5% min. uncertainty.

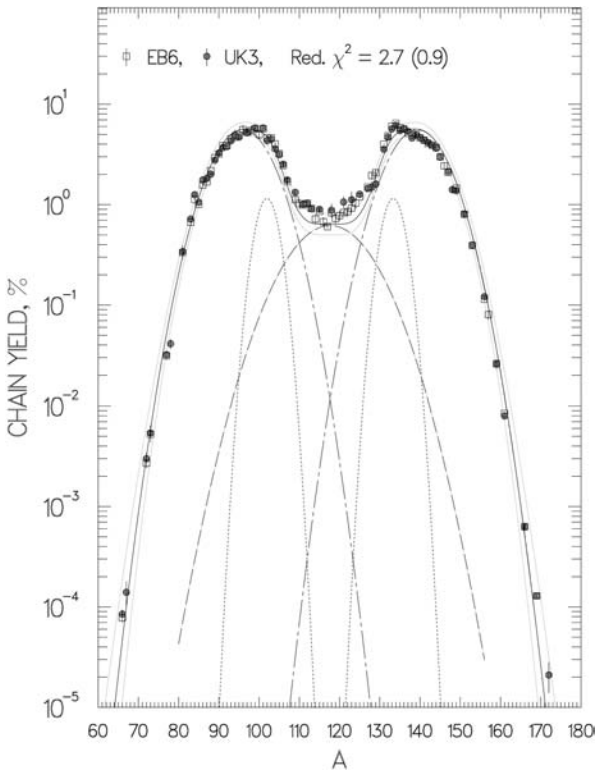

FIG. 4.2.5(b). U238H, Sys. Par., 5% min. uncertainty.

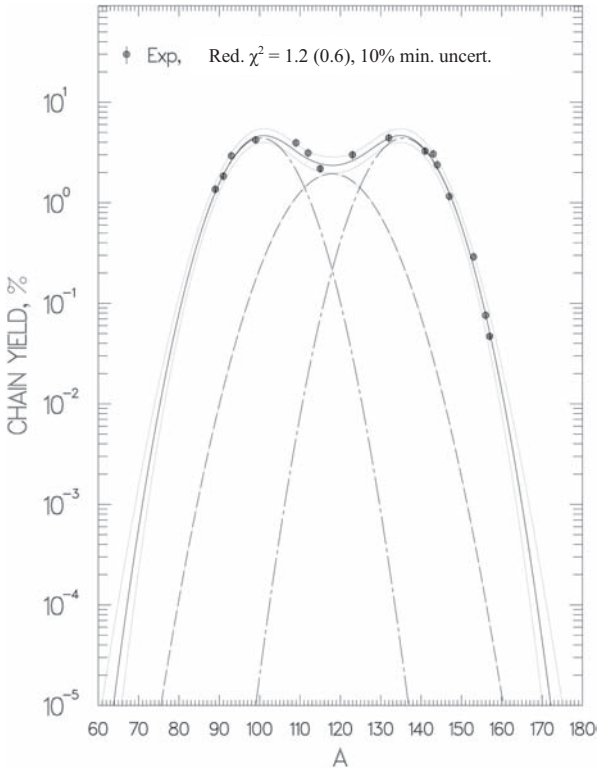

FIG. 4.2.6(a). U238 + 32 MeV p, LS Par.

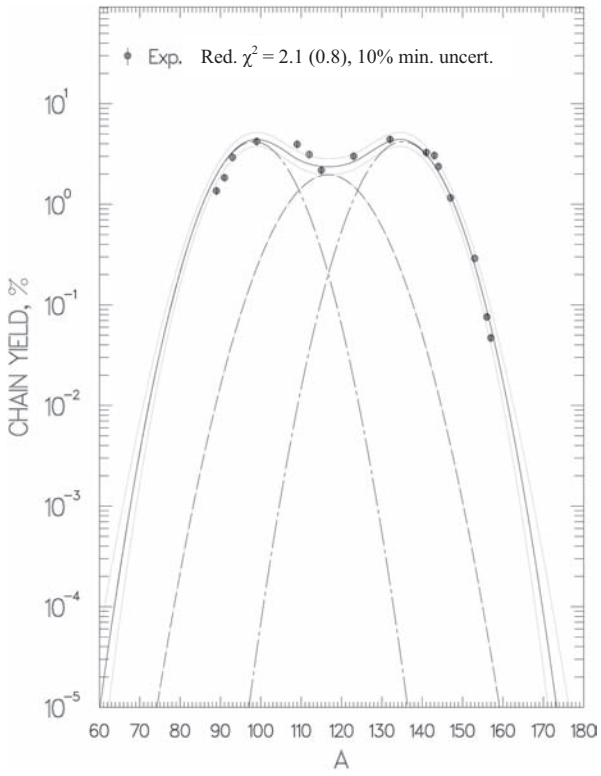

FIG. 4.2.6(b). U238 + 32 MeV p, Sys. Par.

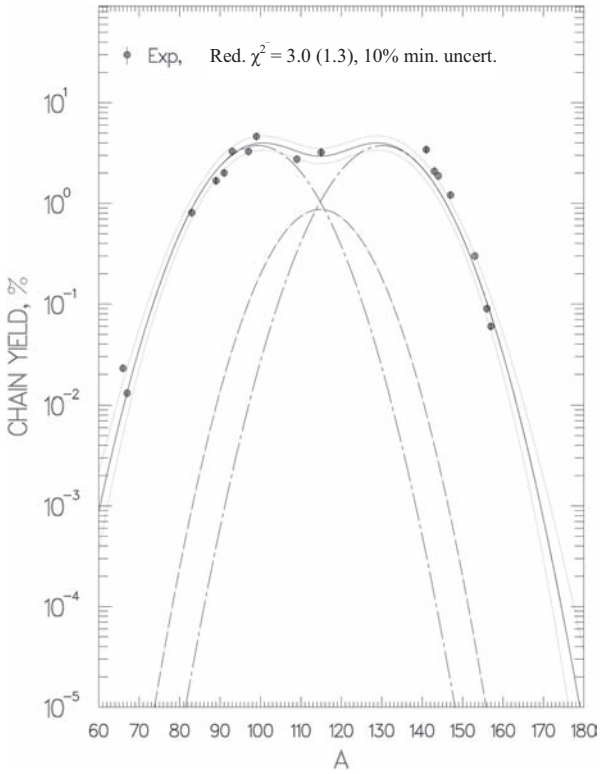

FIG. 4.2.7(a). U238 + 100 MeV p, LS Par.

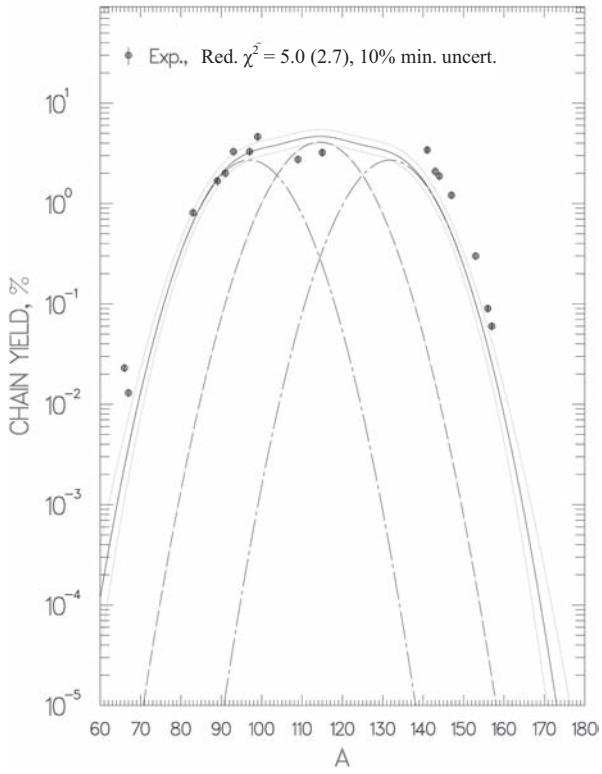

FIG. 4.2.7(b). U238 + 100 MeV p, Sys. Par.

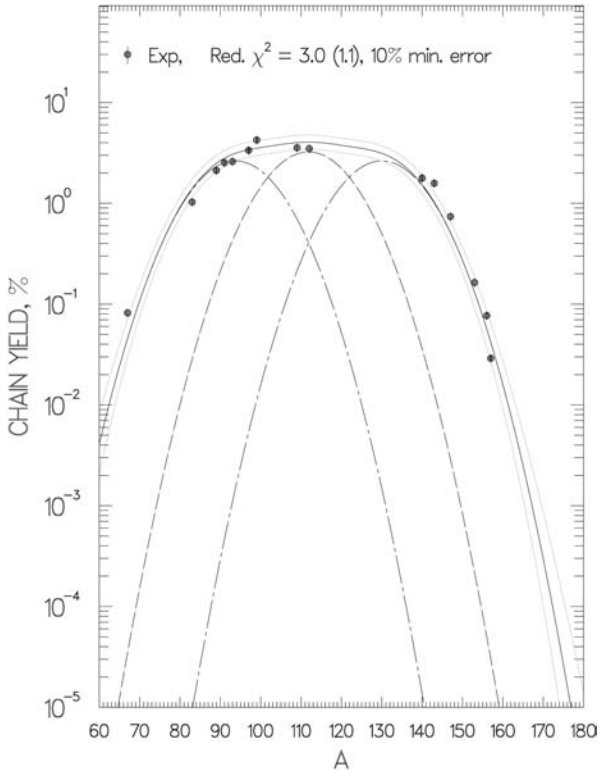

FIG. 4.2.8(a). U238 + 300 MeV p, LS Par.

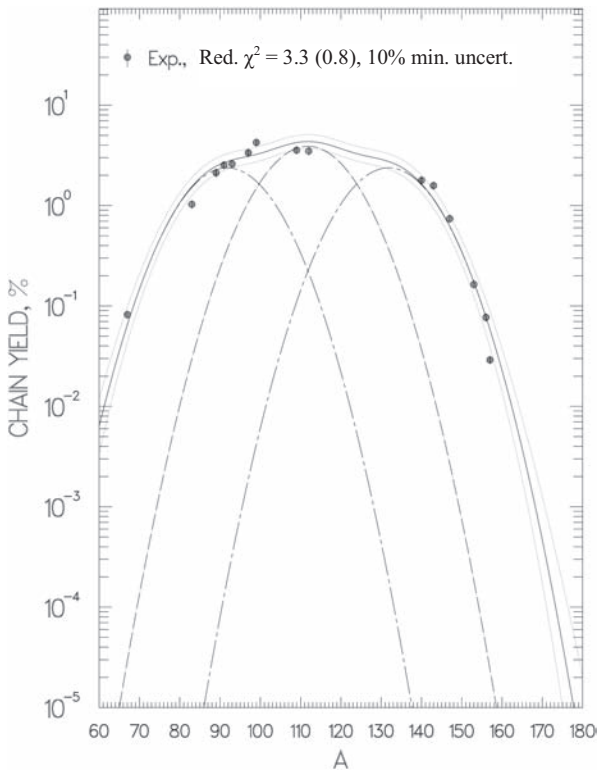

FIG. 4.2.8(b). U238 + 300 MeV p, Sys. Par.

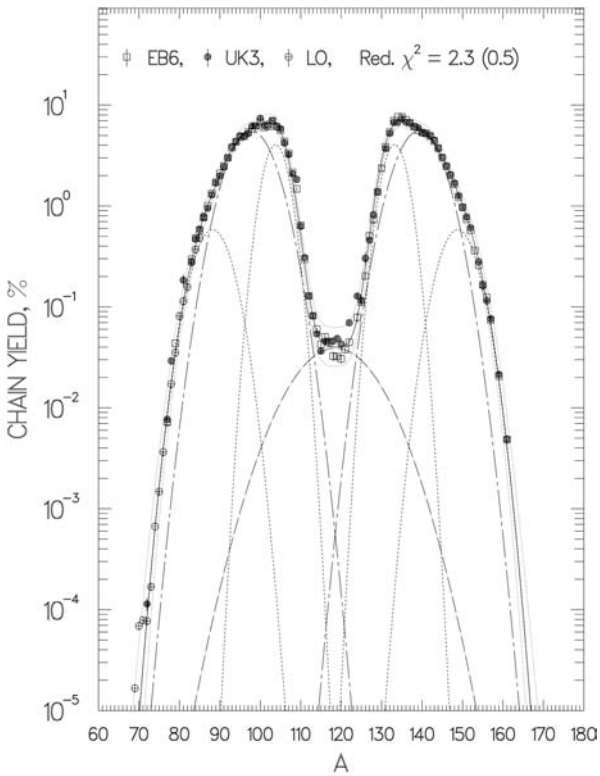

FIG. 4.2.9(a). PU239T, LS Par., 5% min. uncertainty.

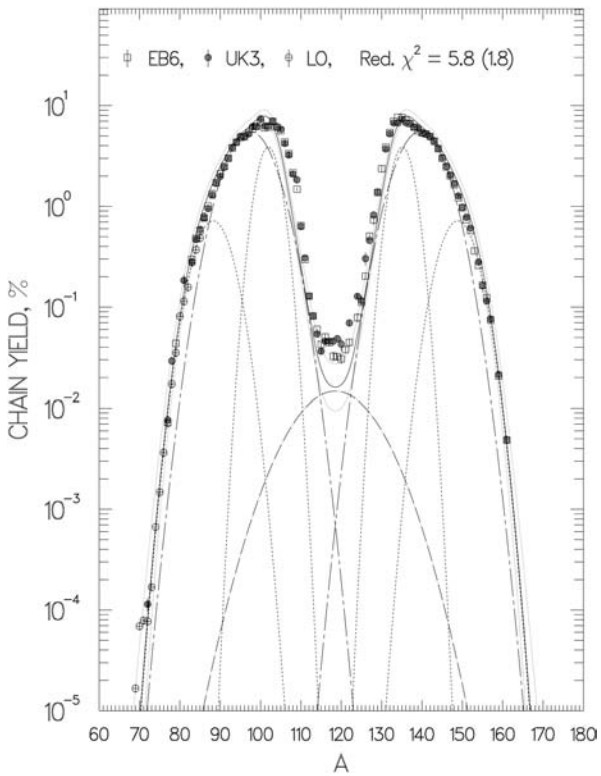

FIG. 4.2. 9(b). PU239T, Sys. Par., 5% min. uncertainty.

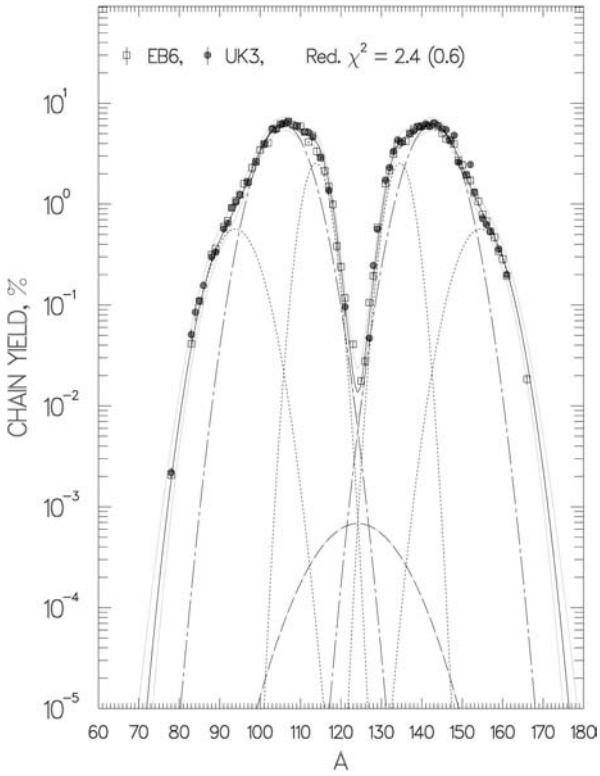

FIG. 4.2.10(a). CF252S, LS Par., 5% min. uncertainty.

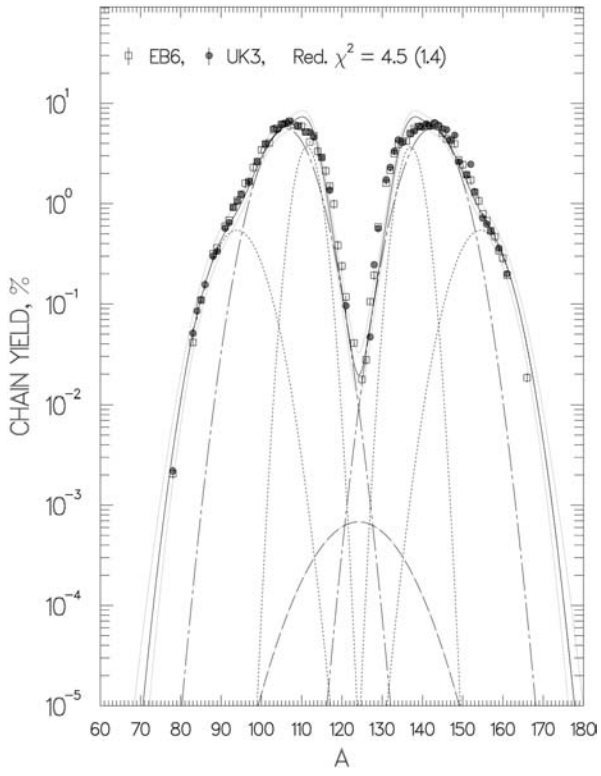

FIG. 4.2.10(b). CF252S, Sys. Par., 5% min. uncertainty.

4.2.2.4. Systematics of Gaussian parameters

The parameters determined to represent the three to seven Gaussian functions for each fission reaction were fitted by mathematical functions of the average Z_F and A_F of fissioning nuclei and *PE* (precursor excitation energy) using the least squares method. Reciprocal variance weighting was used with uncertainties determined earlier for each parameter value or with the minimum uncertainty of 5%. The derived functions are given in Table 4.2.1 and allow the calculation of mass distributions for any fissioning nuclei in the regions investigated.

Chain yield data for proton induced fission of ^{238}U [4.2.7] (nine data sets with monoenergetic protons from 10 to 340 MeV) were used to represent high energy fission reactions, with the assumption that the use of protons instead of neutrons had a negligible effect on model parameters (see Section 3.2.1). Most parameters for the Gaussian curves change fairly rapidly with energy at the lower energies and then level off above $PE \cong 100$ MeV, consistent with the similarity of high energy chain yield curves [4.2.7]. Data and parameters for proton induced fission of ^{232}Th [4.2.26] (seven data sets with monoenergetic protons from 13 to 53 MeV) were included in preliminary calculations. These data consisted of fragment yields before neutron evaporation, as read from mass yield curves without points, and derived from kinetic energy measurements. The resulting Gaussian parameters were of the same magnitude as those from radiochemically determined fission product yields from ^{238}U + p [4.2.7], but the variation of parameters with energy was different (see Figs 4.2.11–4.2.13).

The least squares method was used to identify the more important terms for each model parameter function and to determine the best coefficient values for these terms. Only terms making significant contributions to the reduction of reduced χ^2 from least squares calculations were included in the equation (results are summarized in Table 4.2.1). Some parameters could be represented by the simpler Eq. (4.2.3). The intensity of the central curve (Y_3) that increases with *PE* by several orders of magnitude (see Fig. 4.2.13) required different equations for low and high energies, as shown in the footnotes to Table 4.2.1.

TABLE 4.2.1. EQUATIONS FOR SYSTEMATIC TRENDS IN GAUSSIAN PARAMETERS FOR $Y(A)$

$Par. = P1 + (P2 - P1)(1.0 - e^{P3*PE})$ (4.2.3)

$Par. = P1 + P2 * PE$ (4.2.4)

$P1 = P(1) + P(4)[Z_F - 92]$ (4.2.3a)

$P2 = P(2) + P(5)[Z_F - 92]$ (4.2.3b)

$P3 = P(3) + P(6)[Z_F - 92]$ (4.2.3c)

Par.	Eq.	$P(1)$	$P(2)$	$P(3)$	$P(4)$	$P(5)$	$P(6)$	No.[a]
$\sigma_{1,5}$	4.2.3	2.808	8.685	–0.0454	0.372	–0.620	–0.0122	63
$\sigma_{2,4}$	4.2.4	2.45	0.0	—	0.0	0.0	—	38
σ_3[b]	4.2.4	8.6	0.0	—	0.0	0.0	—	10
$\sigma_{6,7}$	4.2.4	3.17	0.0	—	0.303	0.0	—	6
Δ_5[c]	4.2.3	25.34	18.55	–0.0402	–1.220	–1.732	0.0	63
A_4[d]	4.2.4	136.66	–0.177	—	0.060	–0.038	—	45
Δ_7[c]	4.2.4	30.31	0.0	—	0.0	0.0	—	5
$Y_{2,4}$[e]	4.2.4	43.00	–1.91	—	–3.41	0.0	—	47
$Y_{6,7}$[f]	4.2.4	6.80	0.0	—	0.0	0.0	—	10
NT	4.2.3	1.563	16.66	–0.00804	0.0918	0.0	0.0	45

[a] Number of parameter values used in least squares calculation.

[b] $\sigma_3 = \sigma_{1,5}$ if $\sigma_{1,5} > 8.6$

[c] $\Delta_1 = -\Delta_5$, $\Delta_6 = -\Delta_7$

[d] $\Delta_4 = A_4 - (A_F - NT)/2.0$, $\Delta_2 = -\Delta_4$ (4.2.5)

[e] If $Y_{2,4} < 0.0$, $Y_{2,4} = 0.0$

[f] If $PE > 8$ MeV, $Y_{6,7} = 6.8 - (6.8/12)*(PE - 8.0)$ (4.2.6)

If $Z_F = 93$, $Y_{6,7} = Y_{6,7}/2.0$ (4.2.6a)

If $Z_F < 93$ or $PE > 20$ MeV, $Y_{6,7} = 0.0$ (4.2.6b)

$Y_3 = 4.060e^{[0.470(PE - 11.96)]}$ if $PE < 11.96$ (4.2.7)

$Y_3 = 4.060 + 86.02(1.0 - e^{T(PE - 11.96)})$ if $PE \geq 11.96$ No.[a] = 63 (4.2.8)

$T = -0.030 + 0.0050(A_F - 236.0)$ (4.2.8a)

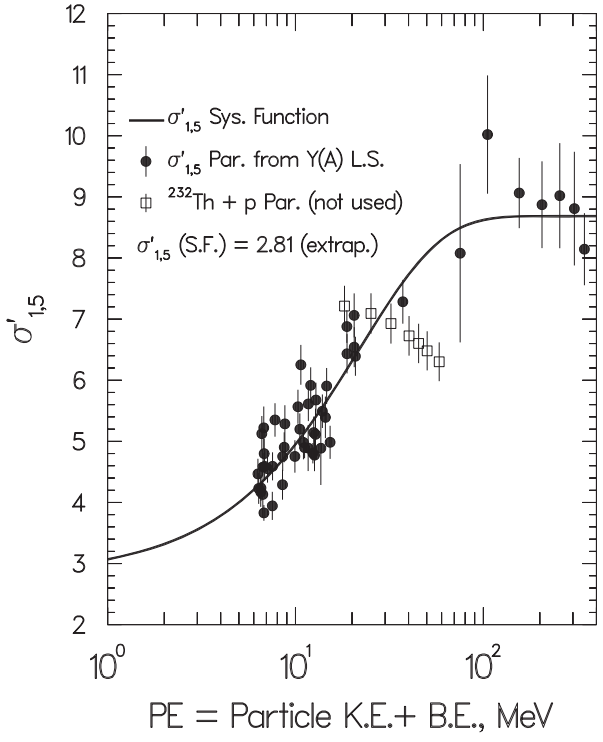

FIG. 4.2.11. $\sigma'_{1,5}$ function, $\sigma'_{1,5} = \sigma_{1,5} - f(Z_F)$.

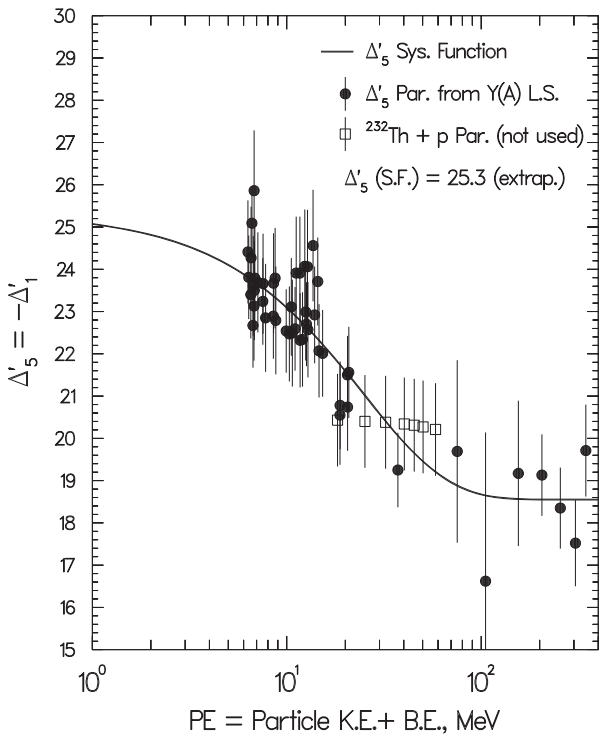

FIG. 4.2.12. Δ'_5 function, $\Delta'_5 = \Delta_5 - f(Z_F)$.

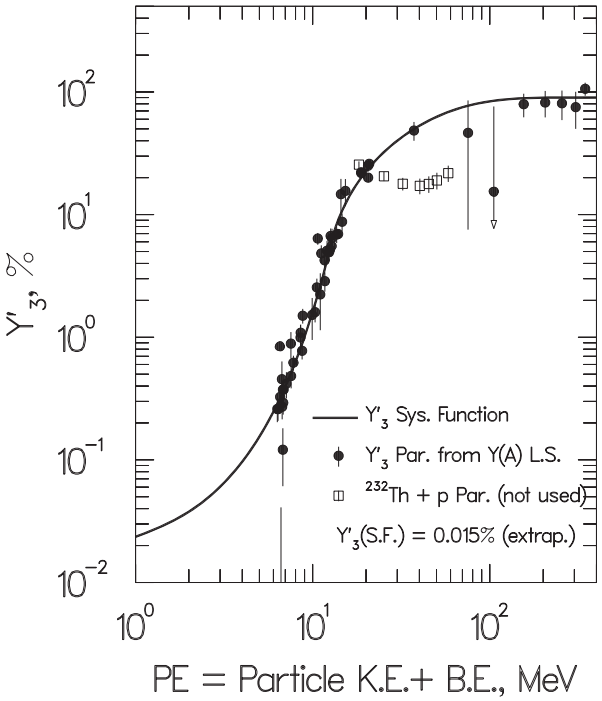

FIG. 4.2.13. Y_3' function, $Y_3' = Y_3 - f(A_f)$.

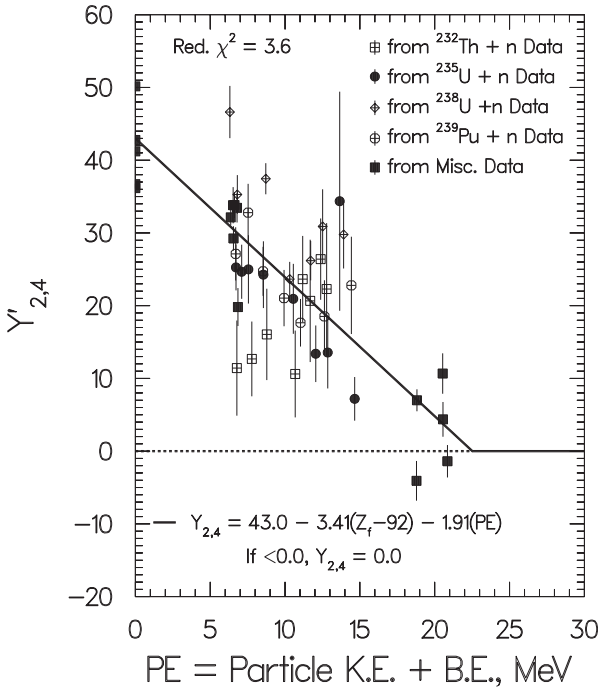

FIG. 4.2.14. $Y_{2,4}' - f(Z_p)$ function.

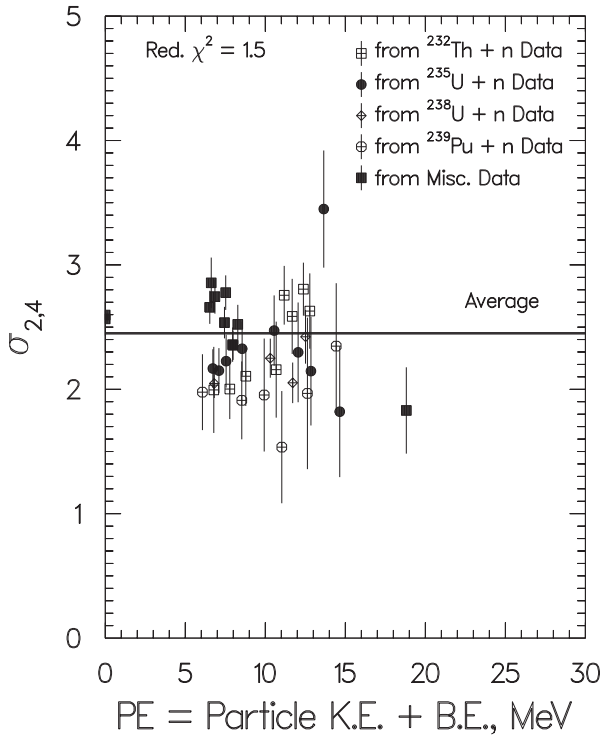

FIG. 4.2.15. Average $\sigma_{2,4}' = 2.45 \pm 0.05$.

4.2.2.5. *Principal peak curves*

The pair of principal peak curves is the main contributor to the mass distribution for both high and low energy fission. Equations for $\sigma_{1,5}$ and $\Delta_{1,5}$ were derived that represent both low and high energy fission reactions. The equations are dependent on both Z_F and *PE*, as shown in Table 4.2.1, Eq. (4.2.3), while the energy dependences are shown in Figs 4.2.11 and 4.2.12. The intensities of these curves ($Y_{1,5}$) were adjusted (normalized) so that the sum of intensities of all curves was 200%.

4.2.2.6. *Inner peak curves*

The yield of the pair of inner peak curves ($Y_{2,4}$) decreases with *PE* and goes to zero when *PE* is approximately >20 MeV, as shown in Fig. 4.2.14. Those inner peak curves are narrow, as shown in Fig. 4.2.15, and represent the sharp change in yields that occurs below the heavy mass number (A_H = 130) and above the light complement (these curves replace the exponential functions used previously [4.2.4]).

Mass numbers (A_4) at the maxima of the heavy inner peak curves were determined, and a function (Eq. (4.2.3), Table 4.2.1) was fitted to the values by the least squares method. The resulting parameter values for the function are given in Table 4.2.1. The displacements (Δ_2 and Δ_4) were then calculated from the function using Eq. (4.2.5) in the footnotes to Table 4.2.1. Figure 4.2.16 shows the

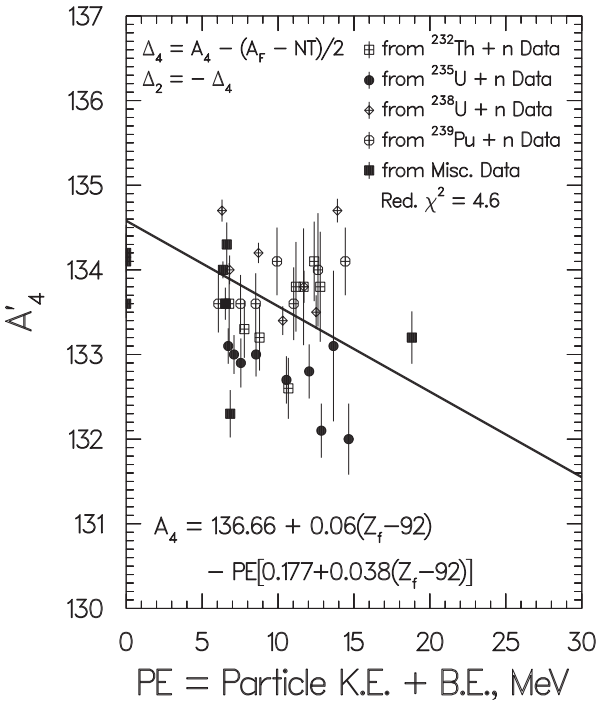

FIG. 4.2.16. $A'_4 = A_4 - f(Z_f)$ function.

values (points) and the derived function (line), both adjusted for the small Z_F dependence to allow comparison of parameter values for a number of fission reactions with the derived function.

The narrowness of the inner peak curves that results from the sharp decrease in yields below $A_H \cong$ 130 and above the light complementary $A_L = PA - 130 - NT$, as well as the large kinetic energies [4.2.28] and small prompt neutron emission near $A = 130$ [4.2.29], may all arise from the proximities of the Z and N of the nascent heavy fragments to the $Z = 50$ and $N = 82$ spherical shells.

4.2.2.7. Central peak curve

The maximum for the central peak is at the midpoint ($\Delta_3 = 0.0$, $AL_3 = (PA - NT)/2$), and the width parameter for the central peak ($\sigma_3 = 8.6 \pm 1.0$) is the average of ten values from the fission of thorium isotopes. Principal peak separations were larger for these fissions than for the other fission reactions investigated, giving optimal information about the properties of the central peak (e.g. see Figs 4.2.1(a) and (b) and compare with Figs 4.2.2(a) and (b) through to 4.2.10(a) and (b)). The value of 8.6 better approximates the nearly flat valleys observed for a number of experimental mass yield data than does the smaller value of 6.0 used previously [4.2.4]. For high energy fission reactions, σ_3 was taken to be 8.6 or σ_1, whichever was the larger.

The curve intensity (Y_3) increases by several orders of magnitude with increasing PE (~0.015% from model calculations for spontaneous fission [4.2.4] and ~90% for high energy fission). This significant change required two functions to be applied in different regions of PE (Eqs (4.2.7) and (4.2.8), Table 4.2.1, and Fig. 4.2.13). The transition between functions is quite smooth (two exponential functions with different slopes were used in Ref. [4.2.4]).

4.2.2.8. Wing curves

Least squares calculations for nuclei with $Z_F \geq$ 94 showed that the wing curve parameters $Y_{6,7}$ and Δ_7 were essentially constant for low PE (<8 MeV), and average values are shown in Table 4.2.1. $Y_{6,7}$ is assumed to be 3.4% for $Z_F = 93$, and to decrease linearly from a value at $E^* = PE = 8.0$ MeV to 0.0 at $PE = 20.0$ MeV. The widths of the curves increase with Z_F, as shown for $\sigma_{6,7}$ in Table 4.2.1.

4.2.2.9. Number of nucleons emitted

Neither the original [4.2.30] nor the revised version [4.2.4] of Howerton's equation for estimating ν_F was intended to be used for extrapolation to high energies, so the total number of nucleons emitted (NT) was determined as a model parameter in order to establish the symmetry point ($(PA\text{-}NT)/2$). Figure 4.2.17 shows NT values determined by least squares from mass yield data for a number of different nuclides and excitation energies PE (points), and the function derived to represent these values (Eq. (4.2.3) in Table 4.2.1 (line)). There is considerable uncertainty and scatter in the values for proton induced fission, possibly because the mass yield data were limited [4.2.7], although they were the best available.

4.2.2.10. Systematic trends represented by parameter equations

The equations and values of parameters listed in Table 4.2.1 represent systematic trends in the multi-Gaussian model parameters that allow estimation of chain yields from both low and high energy fission reactions. Figures 4.2.11–4.2.17 show that the equations give only a moderate representation of most of the parameters derived from the chain yields, with considerable scatter of the points.

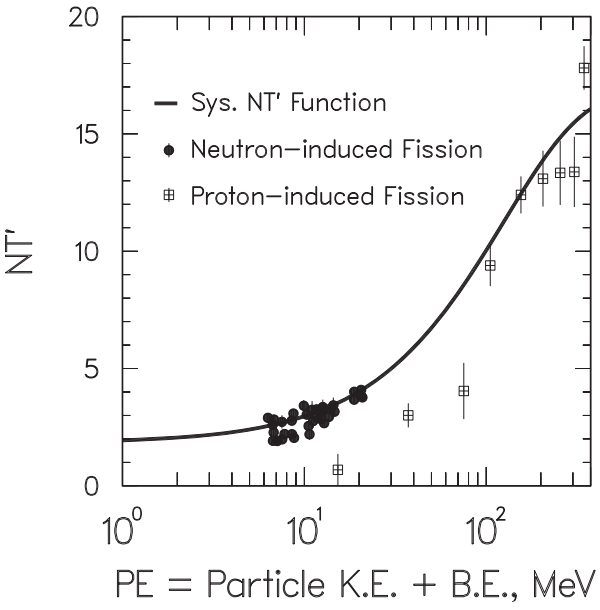

FIG. 4.2.17. NT' = NT – f(Z_P) function.

Most of the reduced χ^2 values shown in Figs 4.2.1(b)–4.2.10(b) are greater than one, showing that the models do not represent a significant amount of the data within a minimal 5–10% or larger experimental uncertainty. Many of the recalculated reduced χ^2 values that include estimated model uncertainties shown in parentheses are >1.0, indicating that the estimated model uncertainties are too small. Perhaps the coefficient of 25 in Eq. (4.2.2) should be increased for yields derived from equations representing the systematics shown in Table 4.2.1.

4.2.3. Nuclear charge distribution

Nuclear charge distribution describes the dispersion of yields with mass and atomic numbers (A and Z) of more than 1000 primary fission products from each of many fission reactions. The yields are for products after prompt neutron emission and before beta decay. Since only a small fraction of the yields have been measured, models are needed to estimate unmeasured yields. Theoretical models are not sufficiently advanced to give reliable yield estimates, so the empirical Z_P model has been used [4.2.4, 4.2.29].

The Z_P model treats dispersion of fractional independent yields (FI) of primary fission products with Z for each A. Gaussian dispersion is assumed after modification for even–odd proton and neutron effects. Model parameters were determined by the least squares method from fractional independent and fractional cumulative (FC) yield values derived from experimental data. Parameter values for 25 fission reactions with excitation energies from 0 MeV (spontaneous fission) to about 170 MeV (proton induced fission) were used.

4.2.3.1. Equations for the Z_P model

The equations for the Z_P model are given below [4.2.29], and involve the error function of x, *erf(x)*. Complementarity of light and heavy fission products is approximated by $A' = A + \nu_P(A)$ and $A'_L + A'_H = A_F$ to allow the same or complementary functions to be used for both light and heavy products. Determination of the $\nu_P(A)$ function (average number of post-fission neutrons emitted to form fission products with A) is discussed in the next section. The parameters σ_Z, Δ_Z, F_Z, F_N and their slopes with respect to A' are determined in contiguous regions of A' for each fission reaction by the least squares method.

$$FI(A,Z) = [0.5][F(A)][N(A)][erf(V) - erf(W)] \quad (4.2.9)$$

$$V = \frac{Z(A) - Z_P(A) + 0.5}{\sigma_Z(A')\sqrt{2}} \quad (4.2.9a)$$

$$W = \frac{Z(A) - Z_P(A) - 0.5}{\sigma_Z(A')\sqrt{2}} \quad (4.2.9b)$$

$$Z_P(A_H) = A'_H[Z_F/A_F] + \Delta Z(A'_H) \quad (4.2.9c)$$

$$Z_P(A_L) = A'_L[Z_F/A_F] - \Delta Z(A'_{Hc}), \quad (A'_{Hc} = A_F - A'_L) \quad (4.2.9d)$$

	for Z	for N
$F(A) = [F_Z(A')][F_N(A')]$	even	even
$F(A) = [F_Z(A')]/[F_N(A')]$	even	odd
$F(A) = [F_N(A')]/[F_Z(A')]$	odd	even
$F(A) = 1/[F_Z(A')][F_N(A')]$	odd	odd

(4.2.9e)

The normalization factor ($N(A)$) is applied to achieve $\Sigma(FI) = 1.00$ for each A, and is required because the even–odd factors ($F(A)$) destroy the inherent normalization properties of Gaussian

distributions. Values of $N(A)$ seldom deviate by more than 10% from unity.

The minimum uncertainty for low energy fission is used for reciprocal variance weighting, and was set to 0.1 to prevent very small *FI* and *FC* values with small absolute uncertainties from being given unduly high weights, but still having weights similar to those of high yield products. For high energy fission, the larger of the experimental uncertainties (0.01 or 10% of a value) was used for weighting. Values of $F_Z(A')$ and $F_N(A')$ for $PE > 20.0$ MeV were set to 1.0, slopes of model parameters were set to 0.0, and neither was varied because preliminary calculations showed that these parameters could not be determined from available data and were assumed not to contribute.

4.2.3.2. Region boundaries

The values determined for $\Delta Z(A')$, $\sigma_Z(A')$, $F_Z(A')$ and $F_N(A')$ from low energy data depend on A' and can be represented by simple functions in each of several regions of A'. Region boundaries are shown as short dotted lines, and labelled B1–6 and Ba, b in Figs 4.2.18(a–d), 4.2.19(a–d) and 4.2.20(a–d), as defined below. The parameters in the functions for each region were calculated by the least squares method if there were sufficient data, or were estimated from derived systematics by using Eq. (4.2.17), Table 4.2.2, with the model parameter values. Several cycles of calculation were sometimes necessary. For fission reactions with *PE* approximately >20 MeV, only average parameter functions and parameter values could be determined for each reaction (Table 4.2.3 and Figs 4.2.21(a)–(d)).

$$\mathrm{B1} = 70 \tag{4.2.10a}$$

$$\mathrm{B2} = 77 + 0.036(A_F - 236) \tag{4.2.10b}$$

$$\mathrm{B3} = A_F - \mathrm{B4} \tag{4.2.10c}$$

$$\mathrm{B4} = \frac{\Delta Z_{\max} - \Delta Z(140) + A'_{\max}[SL50] + 140[\partial\Delta Z/\partial A']}{SL50 + \partial\Delta Z/\partial A'} \tag{4.2.10d}$$

$$\mathrm{B5} = A_F - \mathrm{B2} \tag{4.2.10e}$$

$$\mathrm{B6} = A_F - \mathrm{B1} \tag{4.2.10f}$$

$$\mathrm{Ba} = A'_{\max} \tag{4.2.10g}$$

$$\mathrm{Bb} = A_F - A'_{\max} \tag{4.2.10h}$$

Peak regions (B2–B3, B4–B5):

$$\Delta Z(A'_H) = \Delta Z(140) + \partial\Delta Z/\partial A'[A'_H - 140] \tag{4.2.11a}$$

$$\sigma_Z(A'_H) = \sigma_Z(140) + \partial\sigma_Z/\partial[A'_H - 140] \tag{4.2.11b}$$

$$\sigma_Z(A'_L) = \sigma_Z(A'_{Hc}), \quad (A'_{Hc} = A_F - A'_L) \tag{4.2.11c}$$

$$F_Z(A') = F_Z(140) \tag{4.2.11d}$$

$$F_N(A') = F_N(140) \tag{4.2.11e}$$

Near symmetry region (B3–B4):

$$F(A) = 1.00 \tag{4.2.12a}$$

$$\mathrm{B3 - Ba}: \Delta Z(A') = \Delta Z(\mathrm{B3}) - SL50[A' - \mathrm{B3}] \tag{4.2.12b}$$

$$\sigma_Z(A') = \sigma_{50} \tag{4.2.12c}$$

$$\mathrm{Ba - Bb}: \Delta Z(A') = \Delta Z(\mathrm{Ba}) + A' - \mathrm{Ba}[\Delta Z(\mathrm{Bb}) - \Delta Z(\mathrm{Ba})]/[\mathrm{Ba - Bb}] \tag{4.2.12d}$$

$$\sigma_Z(A') = \sigma_Z(140) - \partial\sigma_Z/\partial A')[140 - \mathrm{Bb}] \tag{4.2.12e}$$

$$\mathrm{Bb - B4}: \Delta Z(A') = \Delta Z(\mathrm{B4}) + SL50[\mathrm{B4} - A'] \tag{4.2.12f}$$

$$\sigma_Z(A') = \sigma_{50} \tag{4.2.12g}$$

$$A'_{\max} = F_1(\mathrm{AK}_1) + F_2(\mathrm{AK}_2)$$

$$F_1 = (250 - A_F)/14 \quad \text{(limits 0.0 and 1.0)}$$

$$F_2 = 1.0 - F_1$$

$$\mathrm{AK}_1 = 50.0(A_F/Z_F) - \partial Z_{\max}/SL50$$

$$\mathrm{AK}_2 = 50.0 - \partial Z_{\max})(A_F/Z_F)$$

Wing regions (B1–B2, B5–B6):

$$\Delta Z(A'_L) = \Delta Z(\mathrm{B2}) + \Delta ZSLW[\mathrm{B2} - A'_L] \tag{4.2.13a}$$

$$\Delta Z(A'_H) = \Delta Z(\mathrm{B5}) - \Delta ZSLW[A'_H - \mathrm{B5}] \tag{4.2.13b}$$

$$\sigma_Z(A'_L) = \sigma_Z(A'_{Hc}), \quad (A'_{Hc} = A_F - A'_L) \tag{4.2.13c}$$

$$\sigma_Z(A'_H) = \sigma_Z(\mathrm{B5}) + \sigma_Z SLW[\mathrm{B2} - A'_L] \tag{4.2.13d}$$

$$F_Z(A'_L) = F_Z(140) + F_Z SLW[\mathrm{B2} - A'_L] \tag{4.2.13e}$$

$$F_Z(A'_H) = F_Z(140) + F_Z SLW[A'_H - \mathrm{B5}] \tag{4.2.13f}$$

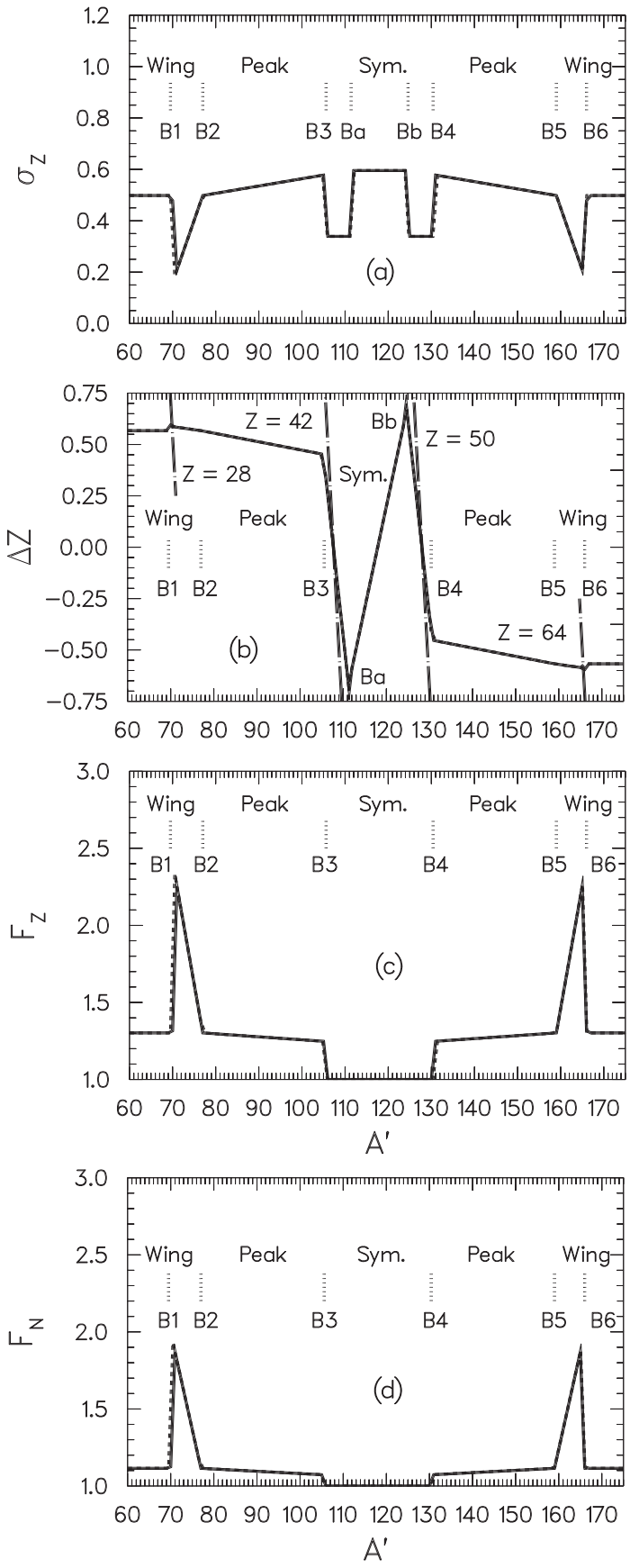

FIG. 4.2.18. Z_P functions for U-235T. Solid lines from CYF systematics, reduced χ^2 = 7.9(0.8).Dashed lines calculated by LS, reduced χ^2 = 2.9(0.8).

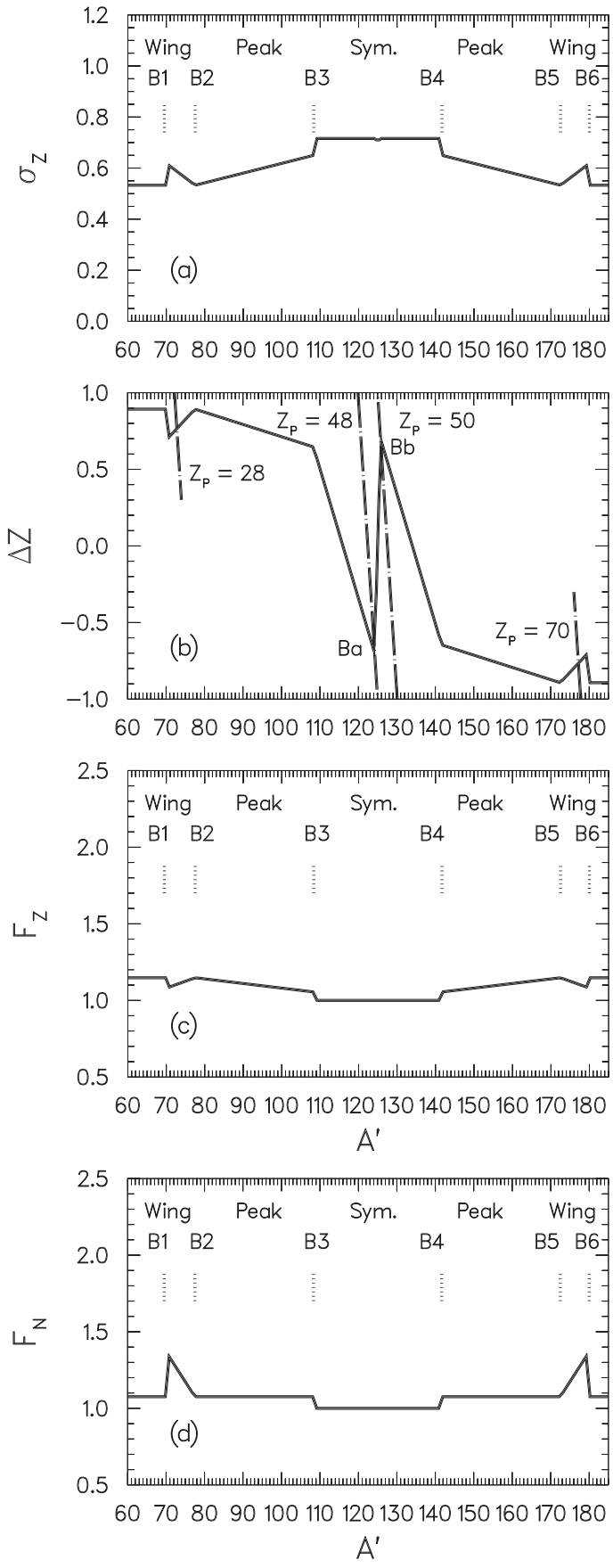

FIG. 4.2.19. Systematic Z_P parameter functions for CF-249T, reduced χ^2 = 2.9(1.0).

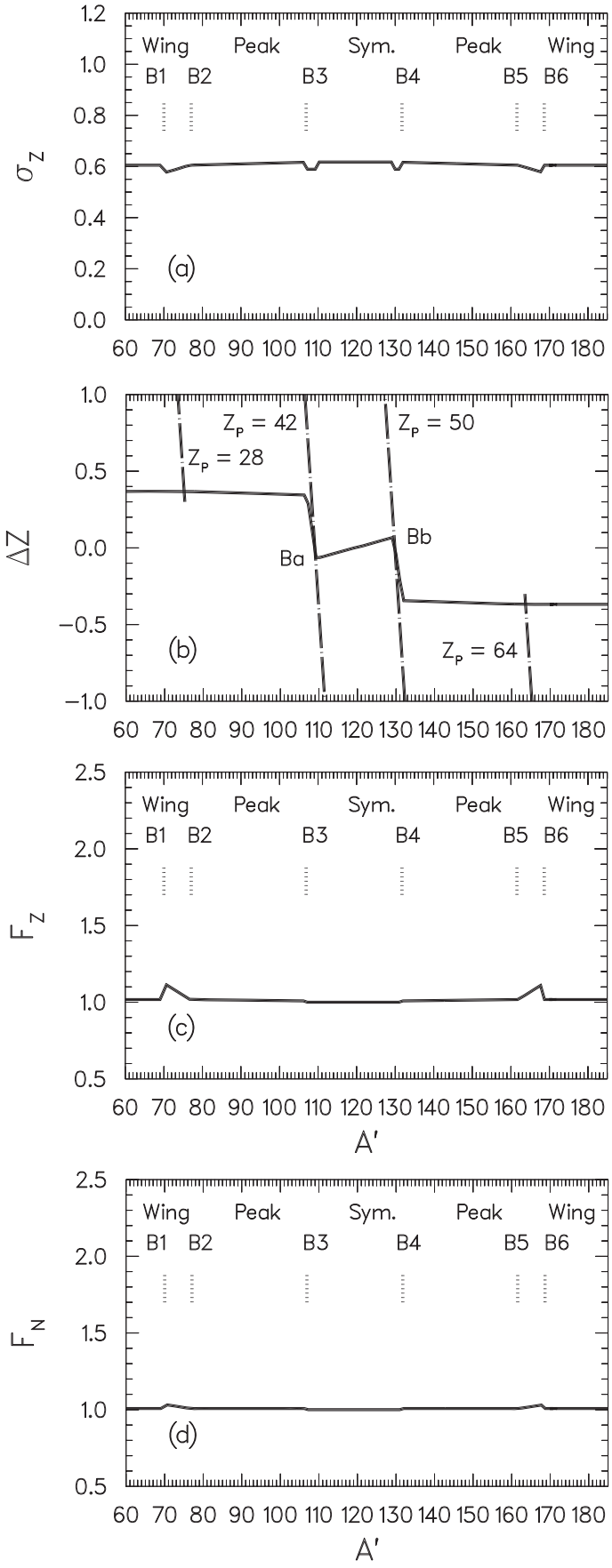

FIG. 4.2.20. Systematic Z_P parameter functions for U-238H, reduced χ^2 = 7.2(1.2).

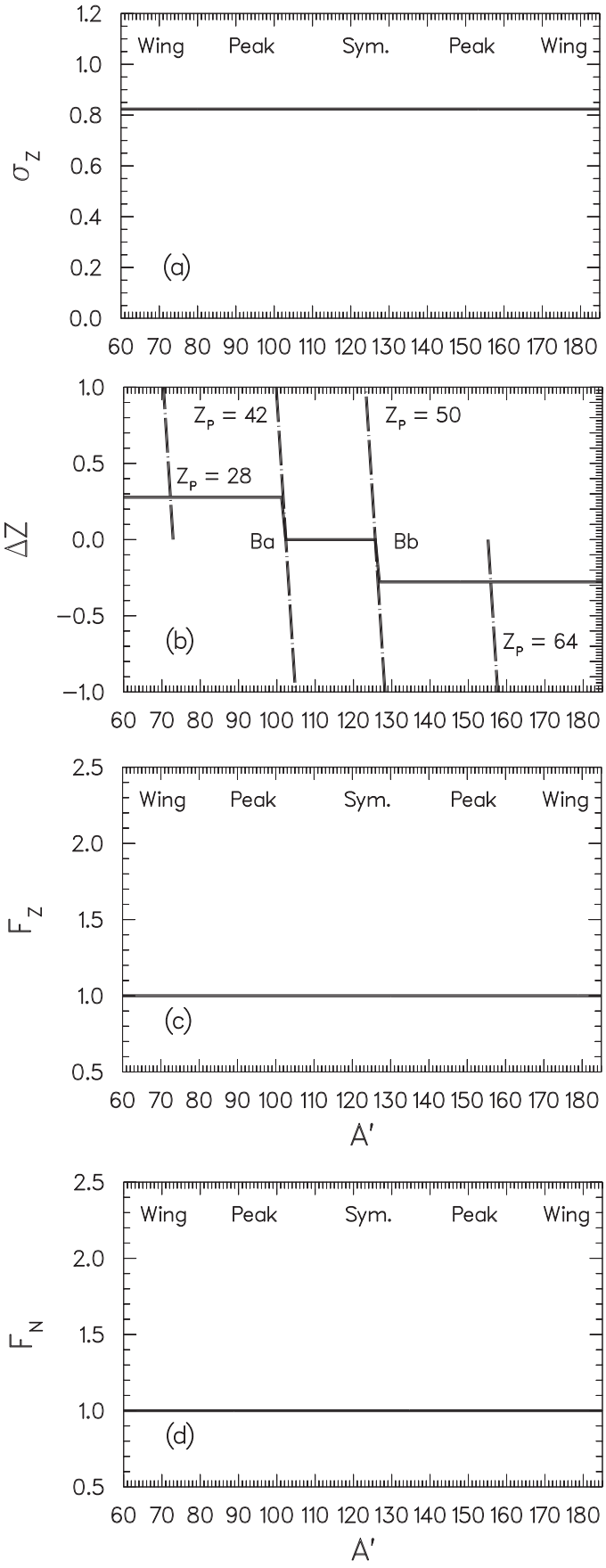

FIG. 4.2.21. Systematic Z_P parameter functions for ^{232}Th + 97 MeV p, reduced χ^2 = 5.2(1.8).

$$F_N(A'_L) = F_N(140) + F_N SLW[\mathrm{B2} - A'_L] \quad (4.2.13g)$$

$$F_N(A'_H) = F_N(140) + F_N SLW[A'_H - \mathrm{B5}] \quad (4.2.13h)$$

Far wing regions (<B1, >B6):

$$\Delta Z(A'_L) = \Delta Z(\mathrm{B2}) \quad (4.2.14a)$$

$$\Delta Z(A'_H) = \Delta Z(\mathrm{B5}) \quad (4.2.14b)$$

$$\sigma_Z(A') = \sigma_Z(\mathrm{B5}) \quad (4.2.14c)$$

$$F_Z(A') = F_Z(140) \quad (4.2.14d)$$

$$F_N(A') = F_N(140) \quad (4.2.14e)$$

4.2.3.3. Z_P near 50

Available data for low energy fission reactions show enhanced yields for $_{50}$Sn fission products with A′ just below 130 [4.2.29]. This effect is represented in the Z_P model for U235T by narrow charge dispersion (small $\sigma_Z = \sigma_{50}$ (see Fig. 4.2.18(a)), and steeply rising ΔZ near $\Delta(Z_P = 50)$ (Fig. 4.2.18(b)). The data for the complementary light products from CF249T do not show a decrease in σ_Z (Fig. 4.2.19(a)), but do show an increase in ΔZ (Fig. 4.2.19(b)) that is less steep than ΔZ for U235T [4.2.31]. The differences were treated by Eq. (4.2.17), Table 4.2.2, for σ_{50} and $SL50$. The average ΔZ_{max} for the two reactions was used for all low energy fission reactions, but intercepts with $\Delta Z_P = 50$ were different. Data for U235T could best be represented by an intercept at $\Delta Z = 0.0$ (Fig. 4.2.18(b)), and those for CF249T could best be represented by an intercept at ΔZ_{max} (Fig. 4.2.19(b)). A linear function in A_F of intercept values from $\Delta Z = 0.0$ to $\Delta Z = \Delta Z_{max}$ was assumed for A_F between 236 and 250. An intercept at $\Delta Z = 0.0$ was assumed for $A_F < 236$, and an intercept at $\Delta Z = \Delta Z_{max}$ was assumed for $A_F > 250$.

4.2.3.4. High energy fission

Data for low energy fission reactions (PE approximately ≤8 MeV) and for high energy fission reactions (PE approximately >20 MeV) were treated separately, with some data being used with both data sets to enhance the smooth transition of parameter values from one energy range to the other (e.g. from fast and 14 MeV neutron induced fission reactions). The equations and parameter values derived by the least squares method are shown in Tables 4.2.2 and 4.2.3. Many parameter values for high energy fission are zero or one (Table 4.2.3) because parameter slopes and even–odd proton and neutron effects could not be determined from the data available and are assumed to be absent. Thus, for high energy ($PE > 20$ MeV) $F(A) = 1.0$, $\sigma_Z(A') = \sigma_Z(140)$ and $\Delta Z(A'_H) = -\Delta Z(A'_L) = \Delta Z(140)$. Near symmetry, $\Delta Z(A'_H) = -\Delta Z(A'_L) = 0.0$, except that the transition to 0.0 near $Z_P = 50$ is assumed to occur with the same slope ($SL50$) as for low energy fission (see Table 4.2.3 and Figs 4.2.21(a)–(d)).

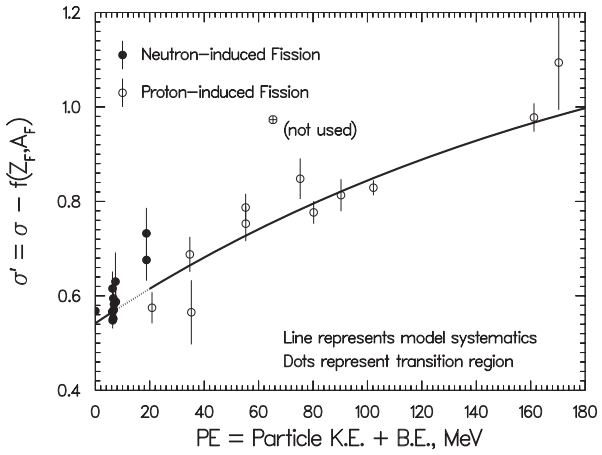

FIG. 4.2.22. Nuclear charge distribution width parameter, σ.

The dependences of $\sigma_Z(140)$ and $\Delta Z(140)$ on PE are shown in Figs 4.2.22 and 4.2.23. Parameter values derived from data for individual fission reactions are shown as points, and the functions derived from these values are shown as lines (Tables 4.2.2 and 4.2.3). For $\sigma_Z(140)$, the transition region (represented by a dotted line) connects the low and high energy functions to give a smooth systematic function; although there are sharp bends for $\Delta Z(140)$, the function is continuous.

4.2.3.5. Pre-fission proton emission

At high excitation energies (PE > 65 MeV), model representation of data can be improved by including a model parameter (NPE) for the number of protons lost before fission, thus reducing Z_F to $PZ - NPE$.

$$NPE = 0.0078(PE - 65) \text{ if } PE > 65 \text{ MeV};$$
$$NPE = 0.0 \text{ if } PE \leq 65 \text{ MeV} \quad (4.2.15)$$

The NPE function and the parameter values used in the derivation are shown in Fig. 4.2.24 as a

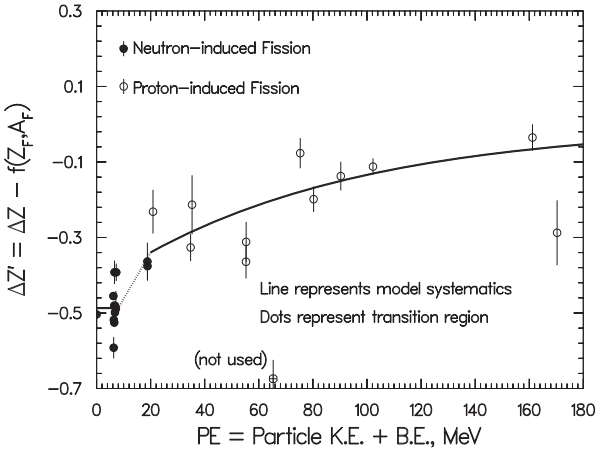

FIG. 4.2.23. Nuclear charge displacement parameter, ΔZ.

line and points, respectively. Values shown as solid points for $PE < 20$ were not used in the analysis; they are consistent with the function to within approximately ±0.5 uncertainty.

4.2.3.6. Estimation of model uncertainties

Measured fractional independent and CU yields can be represented by Gaussian functions, and these functions can be used to estimate unmeasured yields and the uncertainty in the functions. Equation (4.2.16) can be used for this purpose to estimate the per cent uncertainty, *PER* [4.2.27].

$$PER = 6 + 6(e^{(|Z - Z_P|/\sigma_Z)}) \qquad (4.2.16)$$

*FI*PER*/100 can be used for the smaller *PER* as an estimate of the absolute uncertainty. Multiplying and dividing *FI* by 1 + *PER*/100 for the larger *PER* avoids negative lower limit estimates.

Examples:

$FI(\sigma_Z = 0.6)$	$\lvert Z - Z_P\rvert / \sigma_Z$	*PER*	1 + *PER*/100
0.60	0.0	12.0	1.12
0.40	1.0	22.3	1.22
0.12	2.0	50.3	1.50
0.015	3.0	127.0	2.27
$1.5e^{-5}$	5.0	896.0	9.96
$3.5e^{-10}$	7.0	6590.0	66.90

TABLE 4.2.2. EQUATIONS FOR SYSTEMATIC TRENDS IN Z_P PARAMETERS AT LOW ENERGY ($PE \leq 8$ MeV)

$$\text{Par.} = P(1) + P(2)[Z_F - 92] + P(3)[A_F - 236] + P(4)[PE - 6.551] + P(5)[A_F - 236]^2 \qquad (4.2.17)$$

Par.	*P*(1)	*P*(2)	*P*(3)	*P*(4)	*P*(5)	No.[a]
Parameters for regions near peaks (B2–3, B4–5)						
$\sigma_Z(140)$	0.566	0.0	0.0064	0.0109	0.0	13
$\Delta_Z(140)$	–0.487	0.0	0.0180	0.0	–0.00203	13
$F_Z(140)$	1.207	0.0	–0.0420	0.0	0.0022	13
$F_N(140)$	1.076	0.0	0.0	0.0	0.0	12
$\sigma_Z SL$	–0.0038	0.0	0.0	0.0	0.0	6
$\Delta_Z SL$	–0.0080	0.0	0.0	0.0	0.0	6
$F_Z SL$[b]	0.0030	0.0	0.0	0.0	0.0	6
Parameters for regions near symmetry (B3–4)						
*SL*50	0.191	0.0	–0.0076	0.0	0.0	4
$\sigma_Z 50$	0.356	0.060	0.0	0.0	0.0	4
$\Delta_Z max$	0.699	0.0	0.0	0.0	0.0	2

TABLE 4.2.2. EQUATIONS FOR SYSTEMATIC TRENDS IN Z_P PARAMETERS AT LOW ENERGY ($PE \leq 8$ MeV) (cont.)

Par.	$P(1)$	$P(2)$	$P(3)$	$P(4)$	$P(5)$	No.[a]
			Parameters for wing regions (B1–2, B5–6)[c]			
$\sigma_Z SLW$	–0.045	0.0094	0.0	0.0	0.0	3
$\Delta_Z SLW$	0.0	–0.0045	0.0	0.0	0.0	3
$F_Z SLW$	0.159	–0.028	0.0	0.0	0.0	3
$F_N SLW$	0.039	0.0	0.0	0.0	0.0	3

[a] Number of parameter values used as data in least squares calculation.

[b] Weighted averages for the F_Z and F_N slopes are derived from six values each: 0.0030(7) and –0.0006(10), with reduced χ^2 values of 0.85 and 1.59, respectively. For odd-Z fissioning nuclides, F_Z for light products is taken to be 1.032(10), as the average of two values, and the reciprocal of this value is used for heavy products (see discussion).

[c] Wing functions with large slopes are assumed to start at:

$$A'_L = 77.0 + 0.036(A_F - 236) \text{ and } A'_H = A_F - A'_L \qquad (4.2.18)$$

and at the value of each parameter for the peak regions at these A' values. The function was derived empirically by trial and error. Values of A'_L for U235T, PU239T and CF249T are 77.0, 77.1 and 77.5, respectively. The wing slopes for A'_H are the same as for σ, F_Z and F_N for complementary A'_L; magnitude of the adjustment for Δ is the same, but opposite in sign to maintain charge conservation.

TABLE 4.2.3. EQUATIONS FOR SYSTEMATIC TRENDS IN Z_p MODEL PARAMETERS AT HIGH ENERGY ($PE \leq 20$ MeV)

$$\text{Par.} = P1 + (P2 - P1)(1.0 - e^{-P(5)\,(PE)}) \qquad (4.2.19a)$$
$$P1 = P(1) + P(3)[Z_F - 92] \qquad (4.2.19b)$$
$$P2 = P(2) + P(4)[Z_F - 92] \qquad (4.2.19c)$$

Par.	$P(1)$	$P(2)$	$P(3)$	$P(4)$	$P(5)$	No.[a]
			Parameters for regions near peaks (B2–3, B4–5)			
σ_Z	0.542	1.310	0.033	0.0	–0.005	17
Δ_Z	–0.428	0.0	0.0	0.164	–0.0116	17
$F_Z(140)$	1.0	0.0	0.0	0.0	0.0	
$F_N(140)$	1.0	0.0	0.0	0.0	0.0	
$\sigma_Z SL$	0.0	0.0	0.0	0.0	0.0	
$\Delta_Z SL$	0.0	0.0	0.0	0.0	0.0	
$F_Z SL$	0.0	0.0	0.0	0.0	0.0	
			Parameters for regions near symmetry (B3–4)			
$SL50$[b]	0.191	0.0	–0.0076	0.0	0.0	4
$\sigma_Z 50$[c]	0.542	1.310	0.033	0.0	–0.005	17
$\Delta_Z max$	0.0	0.0	0.0	0.0	0.0	
			Parameters for wing regions (B1–2, B5–6)			
$\sigma_Z SLW$	0.0	0.0	0.0	0.0	0.0	
$\Delta_Z SLW$	0.0	0.0	0.0	0.0	0.0	
$F_Z SLW$	0.0	0.0	0.0	0.0	0.0	
$F_N SLW$	0.0	0.0	0.0	0.0	0.0	

$$NPE = 0.0078(PE - 65) \text{ if } PE > 65 \text{ MeV}; \quad NPE = 0.0 \text{ if } PE \leq 65 \text{ MeV} \qquad (4.2.20)$$

[a] Number of parameter values used as data in least squares calculation.

[b] Same as $SL50$, Table 4.2.2 (low energy).

[c] Same as σ_Z.

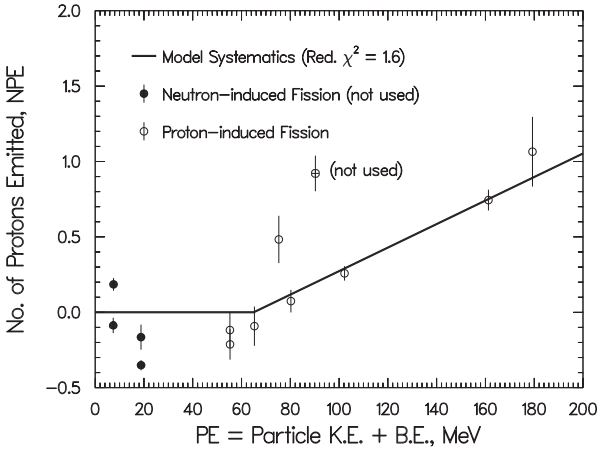

FIG. 4.2.24. Number of protons emitted before fission.

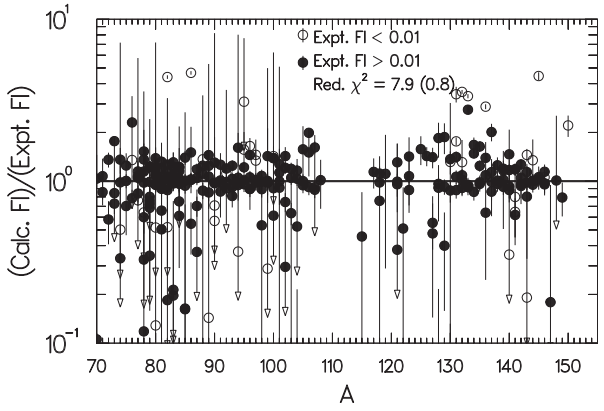

FIG. 4.2.25. Ratios of Sys. F1 to Expt. F1 for U235T.

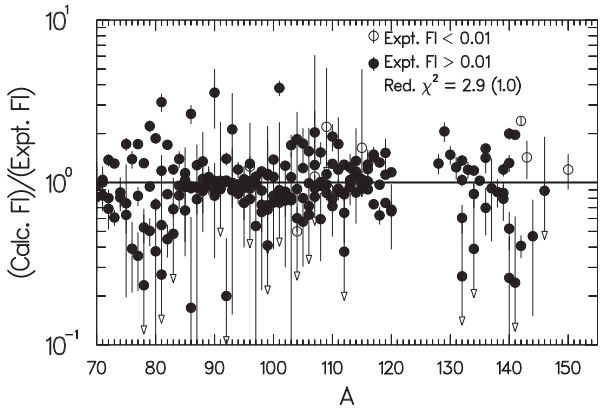

FIG. 4.2.26. Ratios of Sys. F1 to Expt. F1 for CF249T.

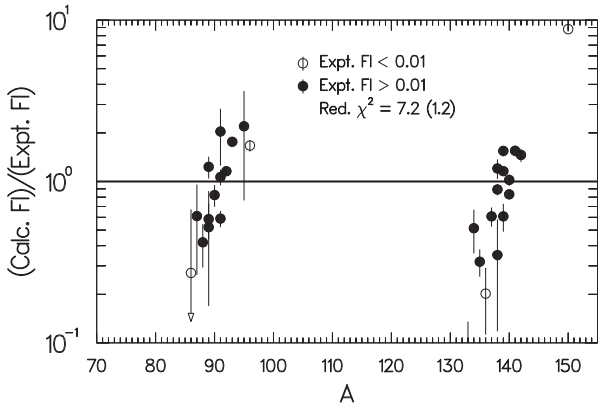

FIG. 4.2.27. Ratios of Sys. F1 to Expt. F1 for U238H.

4.2.3.7. Evaluation of systematic model estimates of yields

FI and *FC* yields were calculated using Gaussian parameters derived from the systematic model functions in Tables 4.2.2 and 4.2.3 and compared to experimental values as ratios of the two for several fission reactions. Some ratios are plotted in Figs 4.2.25–4.2.28. These figures show that the ratios cluster about 1.0, as they should, but that a number deviate considerably from 1.0, especially for the lower experimental *FI, FC* values (<0.01 (open symbols in the figures)). While the reduced χ^2 values obtained when using systematic model functions and experimental values and uncertainties are considerably greater than 1.0, the reduced χ^2 values (shown in parentheses in Figs 4.2.25–4.2.28) are close to 1.0 if estimated model uncertainties (Eq. (4.2.16)) are used in place of experimental uncertainties.

An alternative way of comparing experimental data with Gaussian curves derived from model systematic functions is shown in Figs 4.2.29, 4.2.30(a) and (b). However, this approach can be used only for high energy reactions in which $\sigma_Z(A')$ is assumed constant.

Much of the experimental data for proton induced fission of ^{232}Th is for Rb and Cs fission products measured mass spectrometrically [4.2.32, 4.2.33]. Two problems were encountered with the *FI* values derived from the data for the higher energies (approximately >50 MeV protons):

(1) Many *FI* values fall above the curves as shown in Fig 4.2.30(a), contrary to the requirement that the sum of *FI* at unit intervals of *A′* be 1.0. Compensation for this behaviour can be achieved by normalizing the experimental independent yield data (*IN*, %) so that the sum for each element (Rb or Cs) equals the sum from the model.

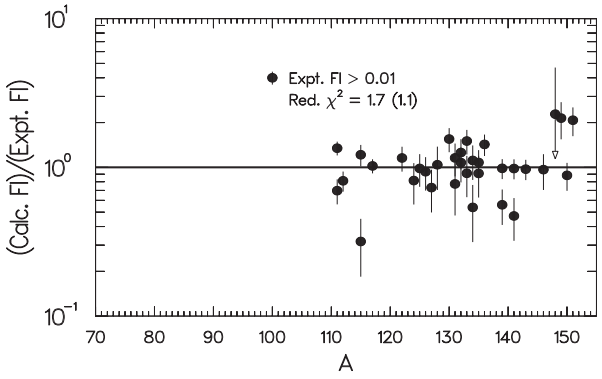

FIG. 4.2.28. Ratios of Sys. FI to Expt. FI for $^{238}U + 85$ MeV p.

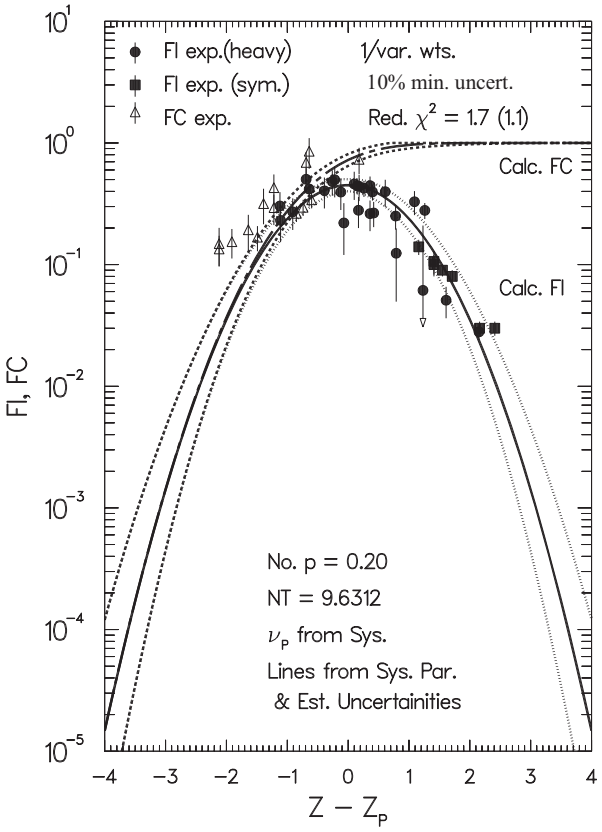

FIG. 4.2.29. Experimental data and systematics curves for $^{238}U + 85$ MeV p.

(2) The renormalized *FI* for Cs isotopes far from stability (large negative $Z - Z_P$) are still well above the same curves in Fig. 4.2.30(b). These *FI* values for Cs were not used to determine the model parameters.

The normalization procedure allowed conversion of published relative indium yields to absolute values [4.2.33]. The indium *FI* values plotted in Fig. 4.2.30(b) are close to the line

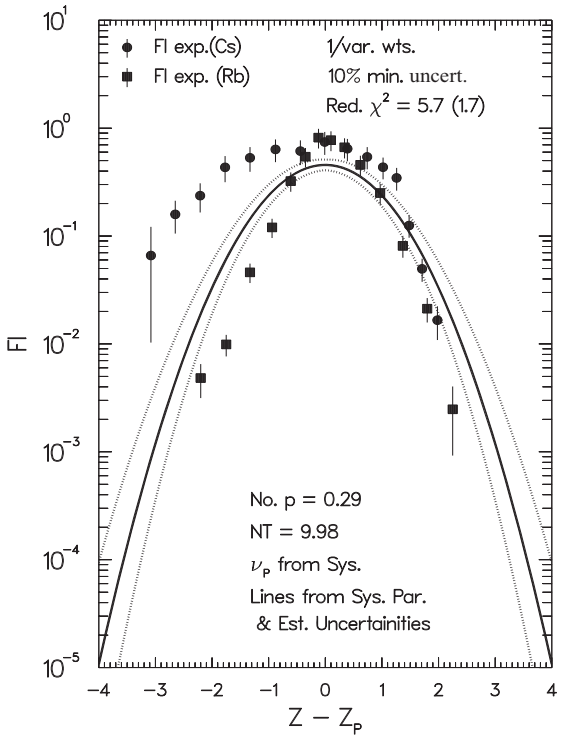

FIG. 4.2.30(a). Experimental MS and systematics curves for $^{232}Th + 97$ MeV p.

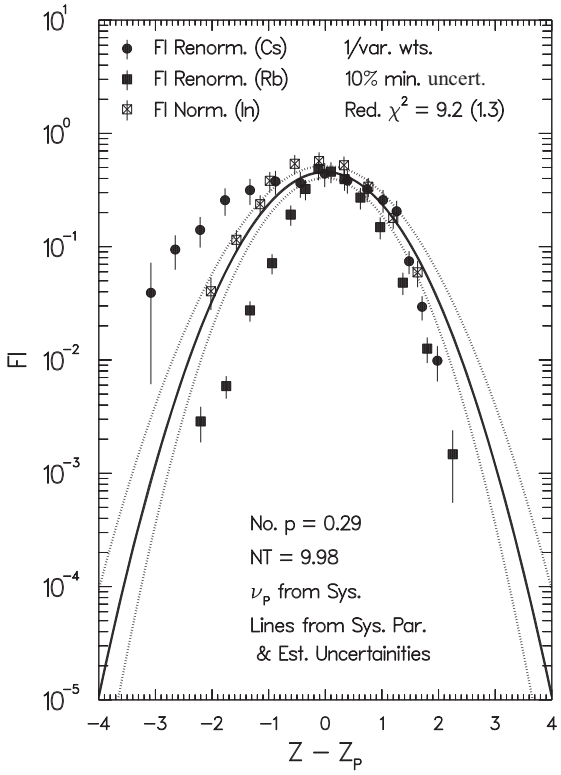

FIG. 4.2.30(b). Renormalized MS and systematics curves for $^{232}Th + 97$ MeV p.

representing model values and thus support model treatments of $\sigma_Z(A')$ and $\Delta Z(A')$ near symmetry.

4.2.4. Models for neutron emission

The average total number (NT) of nucleons emitted before and after scission and the average number of neutrons ($\nu_A(A)$) emitted promptly after scission to form products with mass number A are used in model calculations of mass and nuclear charge distributions, respectively, as described in the preceding two sections. NT is used to determine the central mass number ($A_c = (PA - NT)/2$) in multi-Gaussian mass yield calculations. The quantity $\nu_A(A)$ is used to approximate complementarity in A of light and heavy fission products, $A'_L + A'_H = A_F$, $A' = A + \nu_A(A)$, $\nu_A(A) = \nu_T(A)R(A)$, where $\nu_T(A)$ is the average number of neutrons emitted to form products with mass number A and their complements, and $R(A)$ is the fraction of these neutrons that form products with A [4.2.4, 4.2.29].

The earlier models required a file of $\nu_A(A)$ values for each fission reaction [4.2.3, 4.2.4, 4.2.27, 4.2.29]. Below, a model is proposed that allows calculation of $\nu_A(A)$, and therefore FI, etc., for any fission reaction in the mass, charge and energy regions investigated.

4.2.4.1. Low energy systematics

There are no or very few pre-fission neutrons for PE approximately <8 MeV (E_N approximately <2 MeV), so $NT = \nu_F$ (number of prompt neutrons emitted following scission) is a good approximation. The quantity ν_F is often entitled $\bar{\nu}$, although sometimes in the literature $\bar{\nu}$ refers to NT.

The quantity NT has been determined experimentally for a number of fission reactions with PE approximately <20 MeV [4.2.14, 4.2.15, 4.2.30, 4.2.34–4.2.37]. Estimates of unmeasured or model NT values can be made from Eq. 8 of Howerton [4.2.30], or from a modified Eq. 8 of the same form but with term coefficients re-evaluated by the least squares method. Several hundred (~30%) of the NT values, including values for fission reactions with neutron energies up to ~14 MeV, were selected from the extensive compilation of Manero and Konshin [4.2.34]. Use of experimental NT values from the higher energy neutron induced reactions causes NT values calculated from Eq. (4.2.21) to include pre-fission neutrons, which can amount to about one per fission for 14 MeV neutron induced fission reactions (see below). The last term in Eq. (4.2.21) is omitted for spontaneous fission.

$$NT = 2.286 + 0.147(Z_F - 92) + 0.054(A_F - 236) + 0.040(2 - F_Z - F_N) + (0.145 - 0.0043[A_F - 36]) \times (E_N - TH) \quad (4.2.21)$$

$$F_Z = [-1]^{Z_F},\ F_N = [-1]^{(A_F - Z_F)} \quad (4.2.21a)$$

$$TH = 11.47 - 0.166(Z_F)^2/A_F + 0.093(2 - F_Z - F_N) - BN \quad (4.2.21b)$$

The symbols BN, TH and E_N represent the binding energy, the threshold and the particle kinetic energy, respectively.

The average number of prompt neutrons emitted post-fission (ν_F) and used in the derivation of $\nu_A(A)$ functions can be obtained by subtracting the average numbers of pre-fission neutrons and beta delayed neutrons from NT. Pre-fission neutrons have been neglected for low energy fission reactions with excitation energies approximately <8 MeV. The number of beta delayed neutrons (ν_D) is small, about one per cent or less of NT, and has been neglected.

4.2.4.2. Modified Terrell method

The total number of neutrons emitted to form complementary fission products ($\nu_T(A)$) has been derived [4.2.3, 4.2.4, 4.2.27, 4.2.29] from mass distributions of fission products by a modification of Terrell's summation method [4.2.38]. The mass yield values used recently [4.2.4] are arithmetic average values of evaluated averages of experimental data from ENDF/B-VI [4.2.14], from UKFY-3 [4.2.15] and from recent data not included in the evaluated average values [4.2.20–4.2.25]. Model $Y(A)$ values were used when there were no experimental data [4.2.4]. A value of $\nu_T(A)$ at symmetry must be assumed for the calculation, and a value of 4.0 or ($NT + 1.0$) if a larger value was used. For the fissioning nuclei under study (Z_F = 90–98), a $\nu_T(A)$ value near symmetry and appreciably larger than NT is consistent with the observed low fission fragment kinetic energies near symmetry [4.2.28]. This situation suggests an elongated scission configuration, resulting in highly excited fission fragments that emit more than the average number of neutrons following scission.

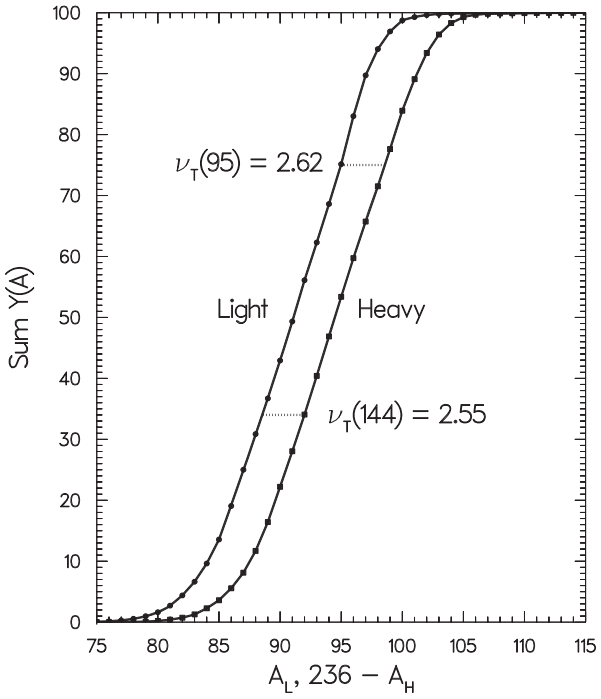

FIG. 4.2.31. Modified Terrell plot for U235T.

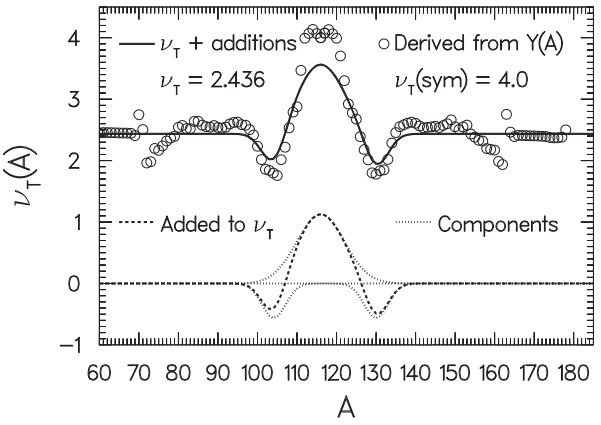

FIG. 4.2.32. $\nu_T(A)$ for U235T.

The modified Terrell summation method is illustrated in Fig. 4.2.31, where the sums of the light and heavy mass number yields starting at the wings are plotted (points) along with smooth functions (solid lines) fitted to the points. Values of $\nu_T(A)$ are taken to be the absolute differences between point values and complementary function values, illustrated in Fig. 4.2.31 by the horizontal dotted lines for A = 95 and 144. The $\nu_T(A)$ values obtained in earlier treatments [4.2.3, 4.2.4, 4.2.27, 4.2.29] and shown as circles in Figs 4.2.32–4.2.37 were used with an $R(A)$ function for each fission reaction to calculate sets of $\nu_A(A)$ values that were smoothed and normalized. Empirical models are proposed below for $\nu_T(A)$ and $R(A)$.

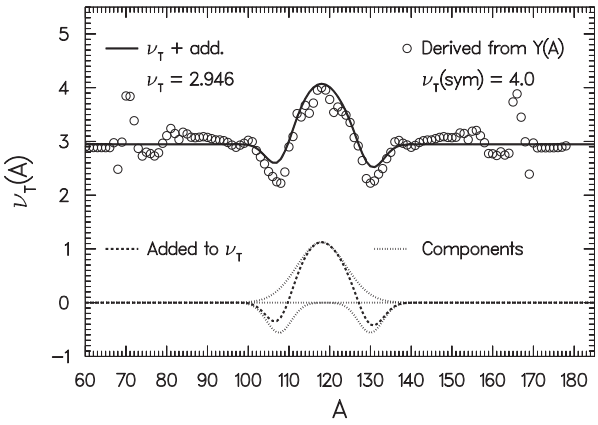

FIG. 4.2.33. $\nu_T(A)$ for PU239T.

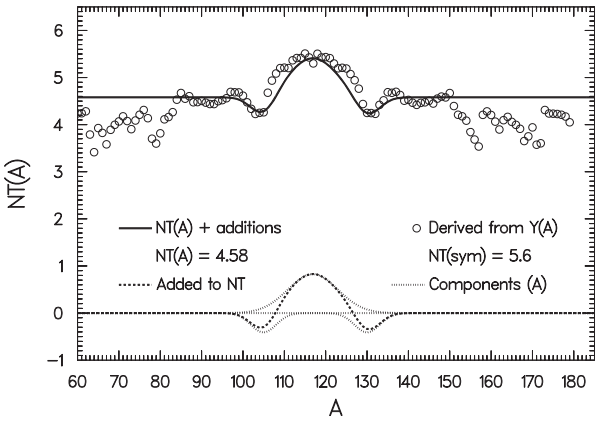

FIG. 4.2.34. NT(A) for U238H.

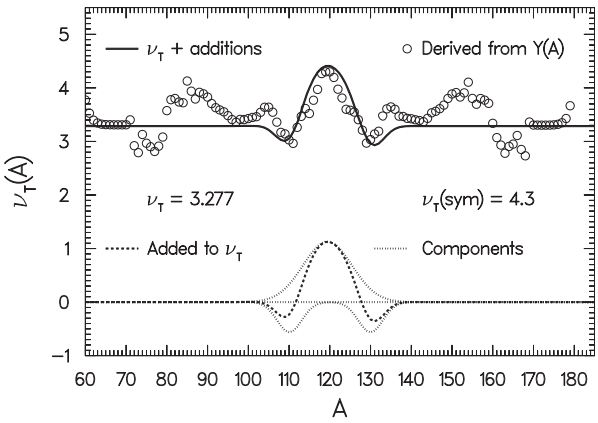

FIG. 4.2.35. $\nu_T(A)$ for AM242MT.

4.2.4.3. Trends in $\nu_T(A)$

The derived values of $\nu_T(A)$ are shown as circles in Figs 4.2.32–4.2.37 and are approximately constant for each of a number of fission reactions, except for some structure near symmetry and for

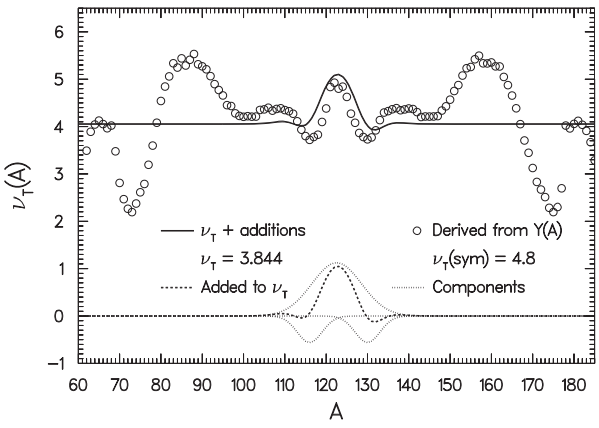

FIG. 4.2.36. $\nu_T(A)$ for CF249T.

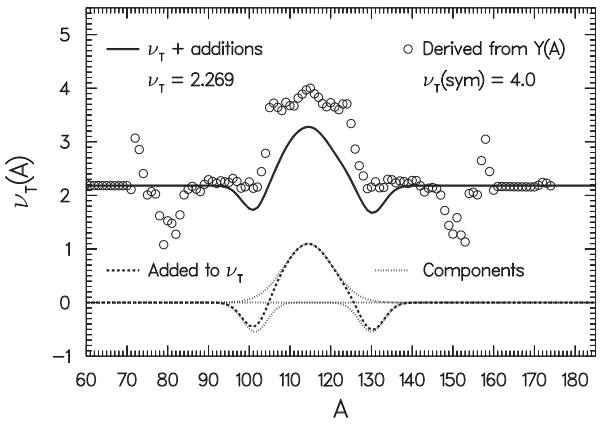

FIG. 4.2.37. $\nu_T(A)$ for TH232F.

very asymmetric mass division. As well as the peak at symmetry that results from the assumption of four or more neutrons being emitted near symmetry, there are small dips on either side of the peak, as can be seen from the circles in Figs 4.2.32–4.2.37. The dips occur near A_H = 130 and in the complementary light product range near A = 104 for U235T, and may be associated with condensed scission configurations, possibly related to the proximity of Z and N of the heavy fragment to the spherical Z = 50 and N = 82 shells. High fragment kinetic energies should result and have been observed [4.2.28], and therefore excitation energies and neutron emission are small.

The dips in the $\nu_T(A)$ function are present for the fission reactions of uranium, plutonium and americium isotopes that were investigated, but are smaller or absent for the fission reactions investigated for the thorium and californium isotopes. This may be due, at least in part, to the somewhat fewer experimental mass yield values for these reactions, since dips are absent when model mass yields calculated from smooth functions are used for U235T (see Fig. 4.2.38).

Other structure appears for very asymmetric mass division (see Figs 4.2.32–4.2.37), but the effects vary in position, magnitude and sign for the various fission reactions investigated, and are attributed to the method applied to low and possibly uncertain fission yield values that form the wings of mass yield curves.

4.2.4.4. Model for $\nu_T(A)$

$\nu_T(A)$ values from the $Y(A)$ summation calculations (circles in Figs 4.2.32–4.2.37) can be approximately represented by the solid lines through the

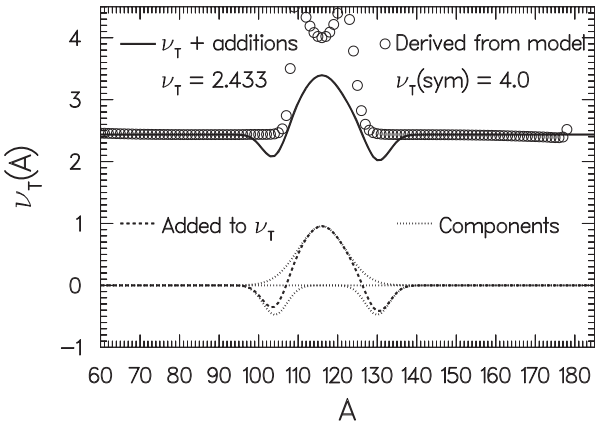

FIG. 4.2.38. $\nu_T(A)$ for U235T, Model Y(A) values.

addition of three Gaussian functions to a constant NT (Eq. (4.2.22)). The ECOR term serves to damp out the peak and dips at high energies (PE), where single particle effects are less important.

$$\nu_T(A) = NT + ECOR[\nu_S(A) + \nu_H(A) + \nu_L(A)] \tag{4.2.22}$$

$$ECOR = e^{-0.05\,PE} \tag{4.2.22a}$$

For the peak at symmetry:

$$\nu_S(A) = I_P[e^{(A-S_P)^2/C_P}]/\sqrt{\pi C_P} \tag{4.2.22b}$$

$$I_P = 20.0, \ = 0.0 \text{ for SF} \tag{4.2.22c}$$

$$C_P = 2.0(6.0^2 + 1/12) = 72.17 \tag{4.2.22d}$$

$$S_P = (A_F - \nu_s)/2.0, \ \nu_s = 4.0 \text{ or } (\text{NYT} + 1.0) \text{ if } >4.0 \tag{4.2.22e}$$

For the dip at $A = 130$:

$$\nu_H(A) = I_D[e^{-(A-130)^2/C_D}]/\sqrt{\pi C_D} \quad (4.2.22f)$$

$$I_D = -5.0 \quad (4.2.22g)$$

$$C_D = 2.0(3.0^2 + 1/12) = 18.17 \quad (4.2.22h)$$

For the light dip complementary to $A = 130$:

$$\nu_L(A) = I_D[e^{-(A-S_C)^2/C_D}]/\sqrt{\pi C_D} \quad (4.2.22i)$$

$$S_C = A_F - 130.0 - (V_F - D_H + S_H) \quad (4.2.22j)$$

$$D_H = I_D/\sqrt{\pi C_D} \quad (4.2.22k)$$

$$S_H = I_D[e^{-(130.0-SYM)^2/C_D}]/\sqrt{\pi C_D} \quad (4.2.22l)$$

$$SYM = (A_F - \nu_s)/2.0 \quad (4.2.22m)$$

4.2.4.5. Model for R(A)

Generalized $R(A)$ functions consist of a number of straight line segments chosen to give sawtooth $\nu_A(A)$ functions with some inflections. Two $R(A)$ functions are shown in Figs 4.2.39 and 4.2.40, and equations for the segments in the various regions designated in Figs (4.2.39) and (4.2.40) are given below. Note that Eqs (4.2.23c) and (4.2.23f) are excitation energy dependent continuous functions that approximate the former discrete values [4.2.4, 4.2.29].

$A < D$: $R(A) = 0.20$ (4.2.23a)

$A = D$ to F: $R(A) = 0.2 + (A - D)(R(F) - 0.2)/(F - D)$ (4.2.23b)

$A = F$ to G: $R(A) = 0.9 - 0.0075(PE)$ (4.2.23c)

$A = G$ to H: $R(A) = 0.5 + (H - A)(R(G) - 0.5)/(H - G)$ (4.2.23d)

$A = H$ to J: $R(A) = 0.5 - (A - H)(0.5 - R(J))/(J - H)$ (4.2.23e)

$A = J$ to K: $R(A) = 0.1 + 0.0075(PE)$ (4.2.23f)

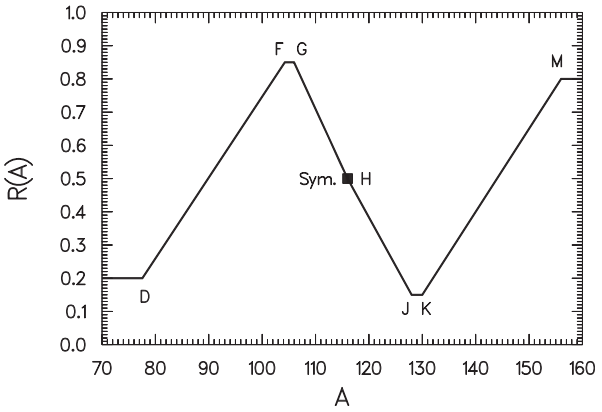

FIG. 4.2.39. Fraction R(A) of $\nu_T(A)$ to A for U235T.

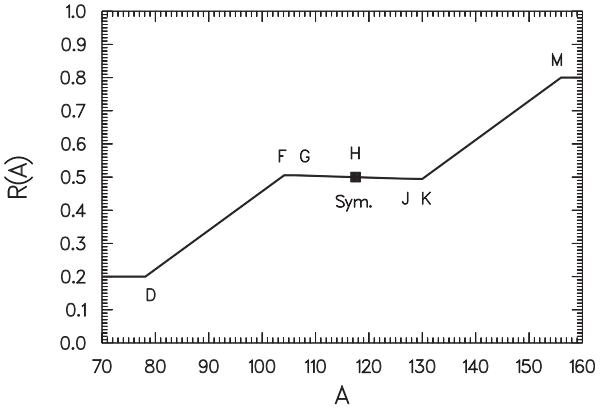

FIG. 4.2.40. Fraction R(A) of $\nu_T(A)$ to A for ^{238}U + 85 MeV p.

$A = K$ to M:
$R(A) = R(K) + (A - K)(0.8 - R(K))/(M - K)$ (4.2.23g)

$A > M$: $R(A) = 0.80$ (4.2.23h)

The $\nu_A(A)$ functions derived from the above equations for two fission reactions are compared with the experimental data in Figs 4.2.41 and 4.2.42 (U235T: Refs [4.2.39-4.2.42]; CF252S: Refs [4.2.43–4.2.47]). As can be seen, the model $\nu_A(A)$ functions represent the data moderately well, and to the same extent as the different data sets for each fission reaction agree with each other. The inflection in the $\nu_A(A)$ model function near $A = 105$ is also exhibited by the data, and is related to the light dip in the $\nu_T(A)$ function. The significant dip in $\nu_T(A)$ is reinforced by the minimum of $R(A)$ at J to K to give the $\nu_A(A)$ minimum just below $A = 130$. The above equations are used in the *CYF* yield calculation program.

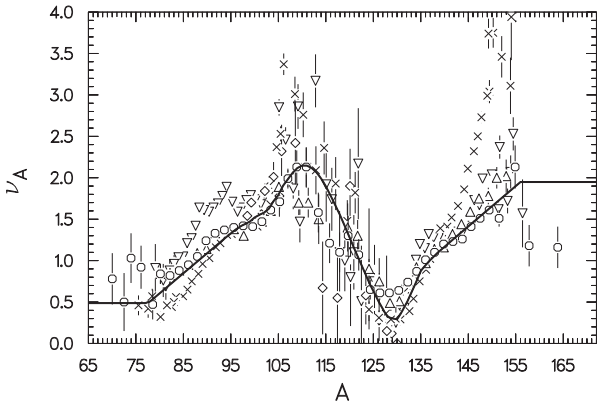

FIG. 4.2.41. U235T, line: model; points: experimental data (see text for references).

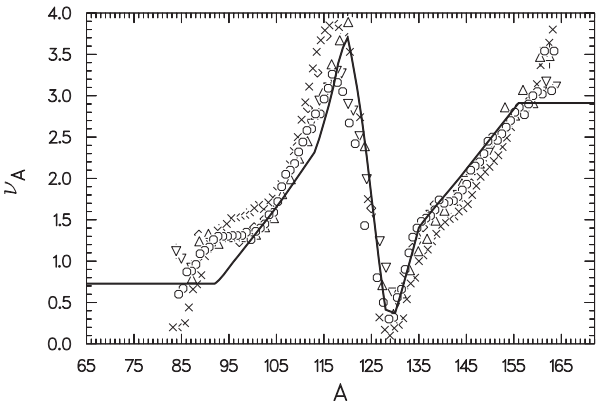

FIG. 4.2.42. CF252S, line: model; points: experimental data (see text for references).

Details of the R(A) function are not believed to be critical because the complementarity of light and heavy fission products as used in both the Z_P and A'_P nuclear charge distribution models is established by $\nu_T(A)$. Although the details of the division of $\nu_T(A)$ between light and heavy products may have a small effect on the values of the model parameters, the changes in these parameter values tend to be compensating for yield calculations; differences in calculated yields are very small when different $R(A)$ functions are used.

4.2.4.6. High energy systematic trends

Nucleons may be emitted before fission during de-excitation of highly excited nuclei. At moderate excitation, only a few neutrons are emitted and then a nucleus may fission if there is sufficient excitation — 'second, third, etc. chance fission'. This process can be inferred from step-wise increases in fission cross-sections with increasing neutron energy about every 6 MeV (approximately

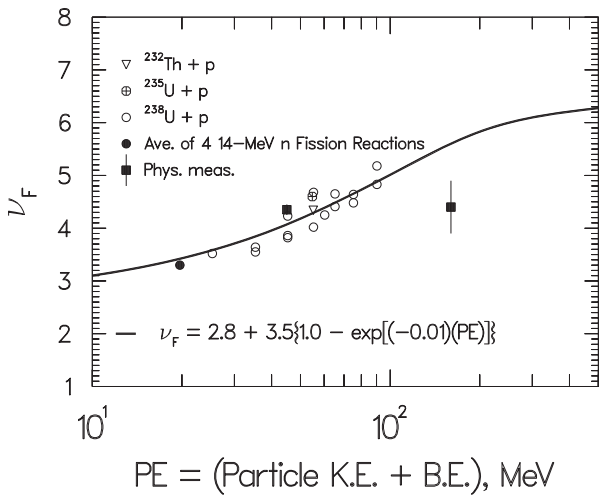

FIG. 4.2.43. High energy ν_F function.

the neutron binding energy [4.2.48, 4.2.49]). Assuming that the nearly flat cross-section between increases can be extrapolated to higher energies, one may estimate from plots of fission cross-section vs. neutron energy [4.2.50] the contributions from 'first, second, etc. chance fission'. For example, this treatment gives the following average per cent contributions for 14 MeV neutron induced fission from four fission reactions (Th-232H, U-235H, U-238H and Pu-239H): 48% 1st, 36% 2nd and 16% 3rd chance fission.

Thus the yields of products from 14 MeV neutron induced fission come from three different fissioning nuclei with different excitation energies. Also, the number of neutrons emitted (NT ~ 4.0). are partly pre-scission neutrons. An estimate of the average number of pre-fission neutrons can be made from the per cent contributions given above: 0.36 + 2(0.16) = 0.68. The average number of post-fission neutrons is obtained by difference to be ν_F ~ 3.3.

There are few experimental data for post-fission neutron emission (ν_F) from high energy fission reactions. Only two references were found [4.2.51, 4.2.52], and give the values plotted in Fig. 4.2.43 as black squares. Also, the average value of ~3.3 deduced above for fission by 14 MeV neutrons is plotted as a black circle.

Other published values are the differences between NT and the number of pre-fission nucleons calculated by Monte Carlo programs. Values of NT were determined from the centroids of relative independent yield distributions of nearly complementary elements, usually Rb and Cs [4.2.32, 4.2.53, 4.2.54]. The ν_F values have been normalized to model NT values, and are plotted as open symbols

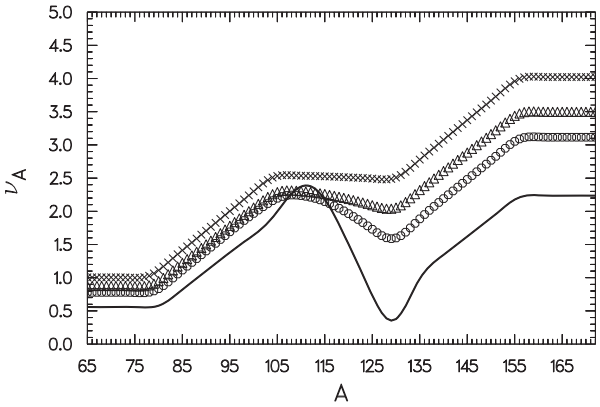

FIG. 4.2.44. ν_A functions, symbols $^{238}U + p$, o = 30 MeV, Δ = 50 MeV, X = 85 MeV; line = U-238F.

in Fig. 4.2.43, which also shows the Eq. (4.2.24) function as a line that approximately represents the various derived values shown as points.

$$\nu_F = 2.8 + 3.5(1.0 - e^{-0.01PE}) \qquad (4.2.24)$$

Functions representing ratio values ($R(A)$) have been developed to give calculated $\nu_A(A)$ values in approximate agreement with experimental $\nu_A(A)$ vs. A plots [4.2.51, 4.2.52, 4.2.55–4.2.57]. All plots of experimental data show that the depth of the dip in $\nu_A(A)$ near A = 130 decreases with increasing energy, while the low $\nu_A(A)$ at low A and the high $\nu_A(A)$ at high A hardly change with energy. These trends were represented by replacing Eqs (4.2.23c) and (4.2.23f) that define $R(A)$ in the *F–G* and *J–K* ranges for low energies by Eqs (4.2.25a) and (4.2.25b) for high energies:

$$A < F \text{ to } G: \qquad R(A) = 0.5 + 0.5e^{-0.05PE} \qquad (4.2.25a)$$

$$A = J \text{ to } K: \qquad R(A) = 0.5 - 0.5e^{-0.05PE} \qquad (4.2.25b)$$

The resulting $R(A)$ function multiplied by ν_F (Eq. (4.2.24)) gives $\nu_A(A)$ values for the high energy fission reactions of interest. The results for 30, 50 and 85 MeV proton induced fission of ^{238}U are shown in Fig. 4.2.44; values of $\nu_A(A)$ for U238F are also shown for comparison.

4.2.5. Fast neutron induced fission

Neutrons from fission (fast neutrons) have a wide range of energies, so a summation calculation was carried out to determine the weighted average value for each energy dependent model parameter. Parameter values for each of 1100 energy increments 0.01 MeV wide were weighted for the relative fission cross-section ($\sigma(E')$) and the relative yields of neutrons ($RY(E')$), at the average neutron energy (E') for each energy increment. The resulting values were summed and normalized to give the weighted average value for each energy dependent parameter.

The relative yield ($RY(E')$) was determined from Eq. (4.2.26) [4.2.58], the constant C = 1.29 for U-235T being multiplied by 3/4 to give C = 0.9675 and allow for energy degradation of fission neutron spectra neutrons in most of the reactor cores used for fast neutron yield measurements.

$$RY(E') = \sqrt{E'}e^{E'/C} \qquad (4.2.26)$$

The value of $C = VX(12)$ in the CYF program can be changed in the IN.PAR file to represent the actual neutron spectra better, if known (see Section 4.2.6).

The relative cross-section ($\sigma(E')$) approximates the experimental curves [4.2.48], and was taken to be 1.00 over much of the energy range. The approach at low energies to $\sigma(E')$ = 1.0 depends on the fission threshold (TH) of fissioning nuclei with Z_F and A_F. The increase of $\sigma(E')$ at $E_N \sim 6$ MeV due to 'second chance fission' depends on the fission threshold ($TH1$) of nuclei with Z_F and $A_F - 1$. The second plateau (σ_2) due to 'first and second chance fission' can be approximated by Eq. (4.2.27), which was derived from experimental curves [4.2.48].

$$\sigma_2 = 1.533 + 0.093(A_F - 236) - 0.431(Z_F - 92) + 0.041(Z_F - 92)^2 \qquad (4.2.27)$$

(limits on σ_2 values: ≥1.0, ≤2.5)

If $TH \le 0.0$, $\sigma(E')$ is assumed to follow the 1/v law to 1.0 at E_N = 0.5 MeV.

$$\sigma(E') = 1.0 + 0.13/\sqrt{E'} - 0.13/\sqrt{0.5} \qquad (4.2.28)$$

If $TH > 0.0$, $\sigma(E')$ is assumed to increase linearly from 0.0 at TH to 1.0 at $TH + 1.0$.

The second change in $\sigma(E')$ is assumed to increase linearly from 1.0 to σ_2 over 1.0 MeV starting at the neutron binding energy (BN) if $TH1 \le 0.0$, or at $BN + TH1$ if $TH1 > 0.0$.

Uncertainties introduced by the approximations made in expressions for $RY(E')$ and $\sigma(E')$ are partially compensated in the treatment because the sum of their products is used for normalization.

The FAST subroutine in the CYFP program has been modified to calculate the weighted average parameter values for all energy dependent model parameters in fast neutron induced fission reactions. Thus, in addition to weighted average values for Y_3, E^* and ν_F as in CYI [4.2.4], weighted average values are also calculated for NT, σ_1, Δ_4, Δ_5, σ_Z, Y_2 and Y_6.

4.2.6. Calculation of fission yields from systematics — CYF program

The previously discussed equations representing fission yield systematics have been incorporated into a new program entitled CYF, which replaces the older CYI program. CYF is written in VAX-FORTRAN (as is CYI), and the formats for the input and output files are the same as those for the CYI program. Parameter and yield values are different, of course. The major difference is that CYF includes equations for systematics at initial excitation energies (*PE*) up to ~200 MeV. Also, most of the equations in CYI [4.2.4] for yields from low energy fission reactions have been modified to eliminate discontinuities and to enhance smooth transitions of the functions to those for high energy fission reactions.

The CYF program has been modified to CYFP, which can be run on a variety of computers, including VAX and personal computers operating under Windows-98. Compilation of CYFP can be accomplished using the VAX-FORTRAN compiler and/or the current version of the G77 compiler from the Internet.

Only four parameters are required to run CYFP (also CFI): *A* and *Z* of the precursor nucleus (target + projectile, *PA* and *PZ*), the type of projectile, and the kinetic energy of the projectile in MeV. Other parameters may be changed to control the calculation; some possibly useful changes are given below.

Most of the parameters needed for a calculation are in a file that is read and usually ends in .PAR (e.g. IN.PAR). Along with a title (line 1) that is not used in the calculation but is printed at the top of most output files, there are three groups of parameters:

Line 2 — integer control parameters (I3);

Line 3 to n = 9999 — real parameters: *XJ, VY(J), VX(J); (J = XJ); (F4.0, 2E13.5);*

Line n + 1 to end — constant model parameters — **WARNING: DO NOT CHANGE!**

Line 2, columns 2–3, NR designates the projectile: 0, neutron; 10, proton; 20, deuteron; 30, triton; 40, 3He; 50, alpha particle;

Line 2, column 39, ISPIN determines if isomeric state yields are calculated: if 0, they are not calculated; if 6, independent yields are distributed equally among isomeric states; if 7, isomer ratios are calculated by the Madland–England method [4.2.59]; if 8, isomer ratios are calculated by the Rudstam method [4.2.60];

Line 3, columns 5–17, $VY(1)$ = precursor *A, PA;* $VY(1) = A_F$ for low energies;

Line 4, columns 5–17, $VY(2)$ = precursor *Z, PZ;* $VY(2) = Z_F$ for low energies;

Line 5, columns 5–17, $VY(4)$ = lowest product *A* treated, default = 60;

Line 6, columns 5–17, $VY(5)$ = highest product *A* treated, default = 180;

Line 8, columns 5–17, $VY(9) = \nu_F$, default = value from systematics; if negative, ν_F determined along with other energy dependent parameters by the fast neutron summation method described in the preceding section;

Line 9, columns 18–30, $VX(10)$ = projectile kinetic energy (MeV); if negative, spontaneous fission is treated ($E^* = PE = 0$).

These and other parameters that could be changed are listed as comments at the beginning of CYFP.FOR.

There are two ways to run the CYFP program on a VAX. A command file may be used, or the file names assigned in CYFP can be used. Only the latter option is available with a PC. The assigned file names are: IN.PAR, TABLE.DATH, IN.SPIN (if ISPIN > 0), and IN.BR (if IBR > 0). The output file names are OUT.PAR, OUT.YNU and OUT.YLD.

ACKNOWLEDGEMENTS

It is a pleasure for the author to thank K. Wright for preparing this manuscript and for much assistance with computer problems during the course of the investigation. Thanks are also due to N. D'Egidio and C. Wilkerson for guidance in modifying CYF to CYFP, and to M. Fowler, W. Inkret and J. Wilhelmy for valuable comments on this report.

REFERENCES TO SECTION 4.2

[4.2.1] CORYELL, C.D., et al., Search for correlations of most probable nuclear charge Z_p of primary fission fragments with composition and excitation energy, Can. J. Chem. **39** (1961) 646–663.

[4.2.2] NETHAWAY, D.R., Variation of Z_p in fission with changes in excitation energy and compound nucleus, Rep. UCRL-51538, University of California Radiation Laboratory (1974).

[4.2.3] WAHL, A.C., "Nuclear-charge and mass distributions from fission", 50 Years with Nuclear Fission (Proc. Conf. Washington, DC, 1989) (BEHRENS, J.W., CARLSON, A.D., Eds), Vol. 2, American Nuclear Society, La Grange Park, IL (1989) 525–532.

[4.2.4] WAHL, A.C., "Compilation and evaluation of fission yield nuclear data", Compilation and Evaluation of Fission Yield Nuclear Data, IAEA-TECDOC-1168, International Atomic Energy Agency, Vienna (2000) 45–75 and 169–170.

[4.2.5] FORD, G.P., LEACHMAN, R.B., Fission mass yield dependence on angular momentum, Phys. Rev. **137** (1965) B826–B836.

[4.2.6] STEINER, H.M., JUNGERMANN, J.A., Proton-induced fission cross sections for ^{238}U, ^{235}U, ^{232}Th, ^{209}Bi and ^{197}Au at 100 to 340 MeV, Phys. Rev. **101** (1956) 807–813.

[4.2.7] STEVENSON, P.C., et al., Further radiochemical studies of the high-energy fission products, Phys. Rev. **111** (1958) 886–891.

[4.2.8] CUMMING, J.B., Monitor reactions for high energy proton beams, Ann. Rev. Nucl. Sci. **13** (1963) 261–286.

[4.2.9] FULMER, C.B., Total reaction and elastic scattering cross sections for 22.8-MeV protons on uranium isotopes, Phys. Rev. **116** (1959) 418–423.

[4.2.10] McCORMICK, G.H., COHEN, B.L., Fission and total reaction cross sections for 22-MeV protons on Th^{232}, U^{235}, and U^{238}, Phys. Rev. **96** (1954) 722–724.

[4.2.11] CHUNG, C., HOGAN, J.J., ^{238}U fission at energies up to 100 MeV, Phys. Rev. C **25** (1982) 899–908.

[4.2.12] MUSGROVE, A.R., et al., "Prediction of unmeasured fission product yields", Fission Product Nuclear Data (Proc. Conf. Bologna, 1973), International Atomic Energy Agency, Vienna (1974) 163–200.

[4.2.13] DICKENS, J.K., Fission product yields for fast neutron fission of $^{243, 244, 246, 248}$Cm, Nucl. Sci. Eng. **96** (1987) 8–16.

[4.2.14] ENGLAND, T.R., RIDER, B.F., Evaluation and Compilation of Fission Product Yields, Rep. LA-UR-94-3106, Los Alamos National Laboratory, NM (1994).

[4.2.15] MILLS, R.W., Fission Product Yield Evaluation, PhD thesis, University of Birmingham, UK (1995).

[4.2.16] NAGY, S., et al., Mass distributions in monoenergetic-neutron-induced fission of ^{238}U, Phys. Rev. C **17** (1978) 163–171.

[4.2.17] GLENDENIN, L.E., et al., Mass distributions in monoenergetic-neutron-induced fission of ^{232}Th, Phys. Rev. C **22** (1980) 152–159.

[4.2.18] GLENDENIN, L.E., et al., Mass distributions for monoenergetic-neutron-induced fission of ^{235}U, Phys. Rev. C **24** (1981) 2600–2605.

[4.2.19] GINDLER, J.E., et al., Mass distributions in monoenergetic-neutron-induced fission of ^{239}Pu, Phys. Rev. C **27** (1983) 2058–2062.

[4.2.20] DENSCHLAG, J.-O., Johannes Gutenberg University Mainz, Germany, personal communication, 1995.

[4.2.21] SIDA, J.L., et al., Mass, charge and energy distributions in very asymmetric thermal fission of ^{235}U, Nucl. Phys. A **502** (1989) 233–242.

[4.2.22] DITZ, W., ^{239}Pu(n_{th},f) Light Wing Fission Yields, PhD Thesis, Johannes Gutenberg University Mainz, Germany (1991).

[4.2.23] HENTZSCHEL, R., et al., Mass, charge and energy distributions in the very asymmetric fission of ^{249}Cf induced by thermal neutrons, Nucl. Phys. A **571** (1994) 427–446.

[4.2.24] STUMPF, R., Concerning ^{241}Am($2n_{th}$,f) Light Wing Fission Yields, PhD Thesis, Johannes Gutenberg University Mainz, Germany (1996).

[4.2.25] MUTTERER, M., SIEGER, P.P., Institut für Kernphysik, Technische Universität Darmstadt, Germany, personal communication, 1996.

[4.2.26] CROALL, I.F., CUNINGHAME, J.G., Fragment distributions in the fission of ^{232}Th by protons of energies 13 to 53 MeV, Nucl. Phys. A **125** (1969) 402–416.

[4.2.27] WAHL, A.C., "Systematic trends in fission yields", Fission Product Nuclear Data (Proc. Specialists Mtg Tokai, Japan, 1992), Rep. NEA/NSC/DOC(92)9, OECD, Paris (1992) 334–345; Rep. LA-UR-92-1425, Los Alamos National Laboratory, NM (1992).

[4.2.28] BELHAFAF, D., et al., Kinetic energy distributions around symmetric thermal fission of U^{234} and U^{236}, Z. Phys. A **309** (1983) 253–259.

[4.2.29] WAHL, A.C., Nuclear-charge distribution and delayed-neutron yields for thermal-neutron-induced fission of ^{235}U, ^{233}U and ^{239}Pu and for spontaneous fission of ^{252}Cf, At. Data Nucl. Data Tables **39** (1988) 1–156.

[4.2.30] HOWERTON, R.J., $\bar{\nu}$ revisited, Nucl. Sci. Eng. **62** (1977) 438–454.

[4.2.31] DJEBARA, M., et al., Mass and nuclear-charge yields for $^{249}Cf(n_{th},f)$ at different fission-product kinetic energies, Nucl. Phys. A **496** (1989) 346–366.

[4.2.32] TRACY, B.L., et al., Rb and Cs isotopic cross sections from 40–60 MeV proton fission of ^{238}U, ^{232}Th and ^{235}U, Phys. Rev. C **5** (1972) 222–234.

[4.2.33] NIKKINEN, L., Independent yields of Rb, In and Cs isotopes in the proton-induced fission of ^{232}Th, Phys. Rev. C **22** (1980) 617–626.

[4.2.34] MANERO, F., KONSHIN, V.A., Status of the energy-dependent $\bar{\nu}$-values for the heavy isotopes (Z > 90) from thermal to 15 MeV and of $\bar{\nu}$-values for spontaneous fission, At. Energy Rev. **10** (1972) 637–756.

[4.2.35] AXTON, E.J., "Evaluation of the thermal neutron constants of ^{233}U, ^{235}U, ^{239}Pu and ^{241}Pu and the fission neutron yield of ^{252}Cf", Nuclear Standard Reference Data (Proc. Advisory Group Mtg Geel, 1984), IAEA-TECDOC-335, IAEA, Vienna (1985) 214–234.

[4.2.36] JAMES, M.F., et al., A New Evaluation of Fission Product Yields and the Production of a New Library (UKFY2) of Independent and Cumulative Yields, Part 1, Methods and Outline of the Evaluation, Rep. AEA-TRS-1015, United Kingdom Atomic Energy Authority (1991).

[4.2.37] DERUYTTER, A.J., et al., "Recent differential low energy cross sections and thermal evaluations", Nuclear Data for the Calculation of Thermal Reactor Reactivity Coefficients (Proc. Advisory Group Mtg Vienna, 1987), IAEA-TECDOC-491, IAEA, Vienna (1989) 115–123 .

[4.2.38] TERRELL, J., Neutron yields from individual fission fragments, Phys. Rev. **127** (1962) 880–904.

[4.2.39] APALIN, V.F., et al., Neutron emission from U^{233}, U^{235} and Pu^{239} fission fragments, Nucl. Phys. **71** (1965) 553–560.

[4.2.40] MASLIN, E.E., et al., Prompt neutron emission from U-235 fission fragments, Phys. Rev. **164** (1967) 1520–1527.

[4.2.41] BOLDEMAN, J.W., et al., Prompt neutrons from ^{236}U fission fragments, Aust. J. Phys. **24** (1971) 821–833.

[4.2.42] MILLER, R., Fragment velocities, energies and masses from fast neutron induced fission of ^{235}U, Phys. Rev. C **29** (1984) 885–905.

[4.2.43] BOWMAN, H.R., et al., Further studies of the prompt neutrons from the spontaneous fission of Cf-252, Phys. Rev. **129** (1963) 2133–2147.

[4.2.44] SIGNARBIEUX, C., et al., "Étude expérimentale de la corrélation entre les nombres de neutrons prompts émis par les deux fragments complémentaires dans la fission spontanée de ^{252}Cf", Physics and Chemistry of Fission 1973 (Proc. 3rd IAEA Symp. Rochester, NY, 1973), Vol. 2, International Atomic Energy Agency, Vienna (1974) 179–188.

[4.2.45] WALSH, R.L., BOLDEMAN, J.W., Fine structure in the neutron emission ν(A) from ^{252}Cf spontaneous fission fragments, Nucl. Phys. A **276** (1977) 189–200.

[4.2.46] GINDLER, J., Dependence of neutron yield on fragment mass for several low-energy fissioning systems, Phys. Rev. C **19** (1979) 1806–1819.

[4.2.47] SCHMIDT, R., HENSCHEL, H., Comparison of the spontaneous fission of ^{244}Cm and ^{252}Cf, Nucl. Phys. A **395** (1983) 29–43.

[4.2.48] HENKEL, R.L., "Fission by fast neutrons", Fast Neutron Physics, Part II (MARION, J.B., FOWLER, J.L., Eds), Interscience (1963) 2006, 2016.

[4.2.49] VANDENBOSCH, R., HUIZENGA, J.R., Nuclear Fission, Academic Press, New York 1973.

[4.2.50] GOLDBERG, M.D., et al., Neutron Cross Sections, Z = 61 to 87, Rep. BNL-325, Vol. IIC, 2nd edn, Supplement 2, Brookhaven National Laboratory, NY (1966).

[4.2.51] BRITT, H.C., WHETSTONE, S.L., Jr., Alpha-particle-induced fission of Th^{230}, Th^{232} and U^{233}, Phys. Rev. **133** (1964) B603–B613.

[4.2.52] CHEIFETZ, E., et al., Measurement of the prompt neutrons emitted in the fission of ^{209}Bi and ^{238}U induced by 155-MeV protons, Phys. Rev. C **2** (1970) 256–288.

[4.2.53] DIKSIC, M., et al., Nuclear charge dispersion in mass chains 130–135 from the fission of ^{238}U by medium energy protons, J. Inorg. Nucl. Chem. **36** (1974) 7–16.

[4.2.54] SARKAR, S., YAFFE, L., Nuclear charge distribution in the region of symmetric fission of ^{238}U by protons of energy 20–85 MeV, Can. J. Chem. **54** (1976) 2349–2358.

[4.2.55] CHEIFETZ, E., FRAENKEL, Z., Prompt neutrons from fission of U-238 induced by 12 MeV protons, Phys. Rev. Lett. **21** (1968) 36–39.

[4.2.56] BURNETT, S.C., et al., Neutron emission and fission energetics in the proton-induced fission of ^{233}U and ^{238}U, Phys. Rev. C **3** (1970) 2034–2048.

[4.2.57] BISHOP, C.J., et al., Excitation energy dependence of neutron yields and fragment kinetic energy release in the proton-induced fission of ^{233}U and ^{238}U, Nucl. Phys. A **150** (1970) 129–142.

[4.2.58] LEACHMAN, R.B., "Determinations of fission quantities of importance to reactors", Peaceful Uses of Atomic Energy (Proc. Int. Conf. Geneva, 1955), Vol. 2, Physics: Research Reactors, United Nations, New York (1956) 193–200.

[4.2.59] MADLAND, D.G., ENGLAND, T.R., The influence of isomeric states on independent fission product yields, Nucl. Sci. Eng. **64** (1977) 859–865.

[4.2.60] RUDSTAM, G., Studsvik Neutron Research Laboratory, Nyköping, Sweden, personal communication, 1992.

4.3. FIVE GAUSSIAN SYSTEMATICS FOR FISSION PRODUCT MASS YIELDS

Jun-ichi Katakura
Japan Atomic Energy Agency, Japan

Systematics of fission product mass distribution with five Gaussian functions is proposed for application to minor actinide fission by neutrons and protons of energies above 100 MeV. This systematics is also applicable to fission by neutrons and protons of lower energy and to spontaneous fission. The mass distributions calculated using the systematics have been compared with various kinds of measured data, and good agreement was found.

4.3.1. Introduction

As part of the agreed programme of work for the IAEA Coordinated Research Project (CRP) on Fission Product Yield Data for the Transmutation of Minor Actinide Nuclear Waste we have developed systematics for fission product mass yields and collected the measured yield data from experiments performed in Japan. The data collected were for ^{243}Am, ^{241}Am, ^{237}Np and ^{248}Cm fission by 25 and 30 MeV protons, and were presented at the Research Coordination Meeting in 2001. The fission yield systematics described in this report were developed in accord with the objectives of the CRP.

Moriyama–Ohnishi [4.3.1] developed systematics in 1974 using five Gaussian functions for the description of fission product mass yields, based on the data available at that time. However, these systematics fail to reproduce recently measured fission product mass distributions from high energy neutron and proton induced fission. The basic structure of the systematics is unique and is still usable when suitable parameters in the systematics are determined from recently measured data. Therefore, the parameters were examined using more recently measured data published after the Moriyama–Ohnishi systematics had been originally developed. The parameters of five Gaussian functions were derived [4.3.2] as described in this section.

4.3.2. Basic structure of present systematics

Mass distribution $\psi(A)$ in the systematics is expressed as follows:

$$\begin{aligned}\psi(A) &= N_s\psi_s(A) + N_a\psi_a(A) \\ &= N_s\psi_s(A) + N_a[\psi_{h1}(A) + \psi_{l1}(A) \\ &\quad + F\{\psi_{h2}(A) + \psi_{l2}(A)\}]\end{aligned} \tag{4.3.1}$$

where $\psi_s(A)$ and $\psi_a(A)$ are symmetric and asymmetric components, respectively. The asymmetric component $\psi_a(A)$ is split up into a heavy $\psi_h(A)$ and a light $\psi_l(A)$ component, each of which consists of two components 1 and 2. Each component is assumed to be of Gaussian shape:

$$\psi_x(A) = \frac{1}{\sqrt{2\pi}\sigma_x}\exp\{-(A - A_x)^2/2\sigma_x^2\} \tag{4.3.2}$$

where subscript x denotes s, $h1$, $h2$, $l1$ and $l2$, representing the five Gaussian functions in this systematics. However, the heavy components $\psi_{h1}(A)$ and $\psi_{h2}(A)$ are related to the light components $\psi_{l1}(A)$ and $\psi_{l2}(A)$ by reflection about the symmetry axis $A_s = (A_f - \bar{\nu})/2$, where A_f is the mass of fissioning nuclide and $\bar{\nu}$ is the average number of emitted neutrons. This relationship reduces the number of independent Gaussian functions to three. As the total mass yield distribution is normalized to a total of 200%, the parameters N_s and N_a are assumed to have the following form:

$$N_s = 200/(1 + 2R) \tag{4.3.3}$$

$$N_a = 200R/\{(1 + F)(1 + 2R)\} \tag{4.3.4}$$

where R is the ratio of the asymmetric to the symmetric component, and F is the ratio of the asymmetric component 1 to the asymmetric component 2. The above expression of the normalization assures the total sum of yields to be 200.

As seen in the above expressions for the mass distribution, there are eight independent parameters to be determined ($\bar{\nu}$, R, F, σ_s, σ_{h1}, σ_{h2}, A_{h1} and A_{h2}). We have to investigate whether these parameters are applicable to the high energy fission of minor actinides.

4.3.3. Examination of parameters

Several measured mass distributions are available. The measured mass distributions were decomposed into five Gaussian functions by least squares fits. A_x and σ_x in Eq. (4.3.2) were obtained from the decomposed Gaussian functions. R and F were calculated using the following relationships:

$$R = \frac{\text{fragment yield given by two asymmetric components}}{\text{fragment yield given by the symmetric component}} = \frac{Y_{h1} + Y_{h2} + Y_{l1} + Y_{l2}}{Y_s}, \quad (4.3.5)$$

$$F = \frac{\text{fragment yield given by component 2}}{\text{fragment yield given by component 1}} = \frac{Y_{h2} + Y_{l2}}{Y_{h1} + Y_{l1}} \quad (4.3.6)$$

where Y_{h1}, Y_{h2}, Y_{l1} and Y_{l2} are the yields of the asymmetric components, and Y_s is the yield of the symmetric component. The resulting parameters were examined by plotting these data against various variables such as the mass of fissioning nuclides, energy of incident particles, etc. Thus the dependence of the parameters on the various variables was determined.

Examples of such dependences are given in Figs 4.3.1 and 4.3.2. Figure 4.3.1 shows the dependence of the R parameter on the incident particle energy. The solid circles represent yields from measured mass distributions of ^{238}U for various incident neutron energies [4.3.3]. The behaviour of the measured data in Fig. 4.3.1 suggests an energy dependence proportional to $1/(E^{C_1} + C_2)$. The values of C_1 and C_2 were determined by least squares fit. Figure 4.3.2 shows the shell factor dependence of the R parameter, which seems to exhibit a sinusoidal dependence on the shell factor. The shell factor mentioned here is that given by Meyers and Swiatecki [4.3.4].

Other examples of the examination are illustrated in Figs 4.3.3 and 4.3.4. Figure 4.3.3 shows the energy dependence of the F parameter. Since a clear energy dependence is not evident, we assume no energy dependence for the F parameter. However, the shell factor dependence is clearly seen in Fig. 4.3.4. The F parameter is assumed to be linearly dependent on the shell factor.

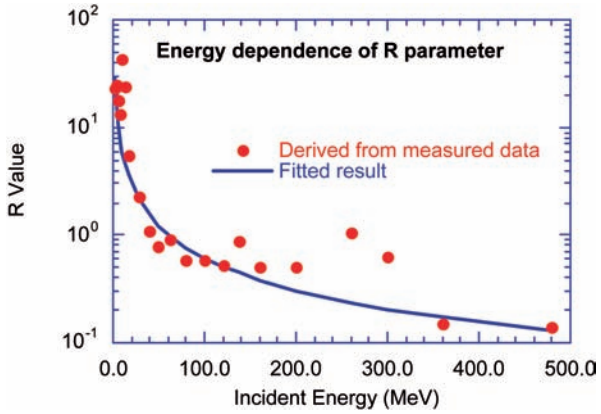

FIG. 4.3.1. Energy dependence of the R parameter.

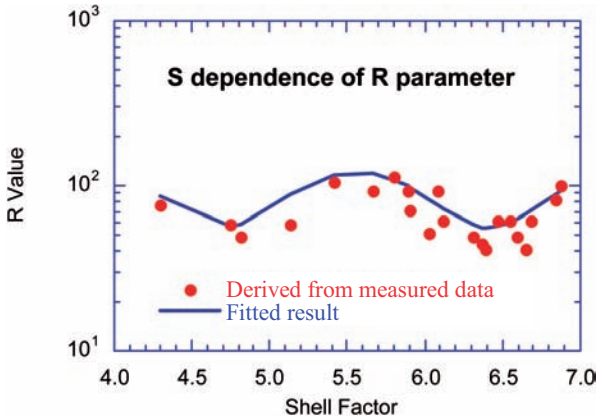

FIG. 4.3.2. Shell factor dependence of the R parameter.

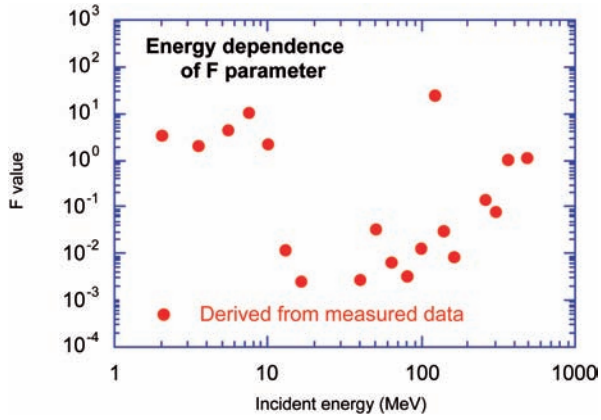

FIG. 4.3.3. Energy dependence of the F parameter.

Similar examinations were performed for other parameters. The resulting parameters for the present systematics are described below.

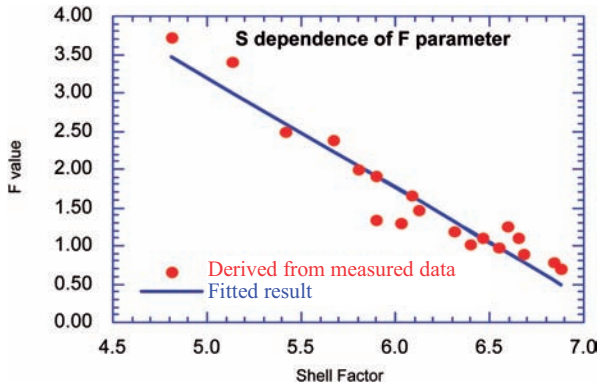

FIG. 4.3.4. Shell factor dependence of the F parameter.

4.3.4. Description of parameters in the systematics

The adopted average number of emitted neutrons $\bar{\nu}$ was that evaluated by Wahl for the CRP [4.3.5], which was not in conflict with the measured data we used. According to Wahl's proposal, $\bar{\nu}$ is expressed as follows:

$$\bar{\nu} = 1.404 + 0.1067(A_f - 236) + [14.986 - 0.1067(A_f - 236)] \times [1.0 - \exp(-0.00858E^*)] \quad (4.3.7)$$

where E^* is the excitation energy of the fissioning nuclide, which is the sum of the kinetic energy E and binding energy B of the incident particle.

Other parameters determined from our examination are listed below:

$$R = [112.0 + 41.24\mathrm{Sin}(3.675S)] \times \frac{1.0}{B^{0.331} + 0.2067} \times \frac{1.0}{E^{0.993} + 0.0951} \quad (4.3.8)$$

$$F = 10.4 - 1.44S \quad (4.3.9)$$

$$\sigma_s = 12.6 \quad (4.3.10)$$

$$\sigma_{h1} = (-25.27 + 0.0345A_f + 0.216Z_f) \times (0.438 + E + 0.333B^{0.333})^{0.0864} \quad (4.3.11)$$

$$\sigma_{h1} = (-30.73 + 0.0394A_f + 0.285Z_f) \times (0.438 + E + 0.333B^{0.333})^{0.0864} \quad (4.3.12)$$

$$A_{h1} = 0.5393(A_f - \bar{\nu}) + 0.01542A_f \times (40.2 - Z_f^2/A_f)^{1/2} \quad (4.3.13)$$

$$A_{h2} = 0.5612(A_f - \bar{\nu}) + 0.01910A_f \times (40.2 - Z_f^2/A_f)^{1/2} \quad (4.3.14)$$

where S in the formula for R and F is the shell factor mentioned in Section 4.3.3. The functional form given by Meyers and Swiatecki [4.3.4] is:

$$S = 5.8s(N, Z) \quad (4.3.15)$$

$$s(N,Z) = \frac{F(N) + F(Z)}{(\frac{1}{2}A)^{2/3}} - 0.26A^{1/3} \quad (4.3.16)$$

$$F(N) = q_i(N - M_{i-1}) - \frac{3}{5}(N^{5/3} - M_{i-1}^{5/3}), \quad (4.3.17)$$

for $M_{i-1} < N < M_i$

$$q_i = \frac{3}{5}\frac{M_i^{5/3} - M_{i-1}^{5/3}}{M_i - M_{i-1}} \quad (4.3.18)$$

where M_i is the magic number: N = 82, 126 and 184 for neutrons, and Z = 50, 82 and 114 for protons.

As seen in the above expressions of our systematics, the mass distribution can be calculated when mass A_f and charge Z_f of the fissioning nuclide, and energy E and binding energy B of the incident particle are given. The energy unit should be MeV. The systematics is applicable not only to neutron induced fission, but also to proton induced fission and even spontaneous fission. In the case of spontaneous fission, both incident energy and binding energy are set to zero. The only restriction for using the systematics is to fulfil the condition $Z_f^2/A_f \leq 40.2$.

4.3.5. Comparisons with measured mass yields

The present systematics was compared to measured mass distributions. Some of the results of the comparison are shown below. For thermal neutron fission, the mass distributions of ^{235}U and ^{245}Cm are shown in Figs 4.3.5 and 4.3.6, and show that the present systematics reproduce the measured mass distributions [4.3.6–4.3.8].

Mass distributions are shown in log scale on the left hand side, and in linear scale on the right hand side. When we calculate the average deviation, the values of 0.664 and 0.208 are obtained for ^{235}U and for ^{245}Cm, respectively. Here the average deviation is defined as:

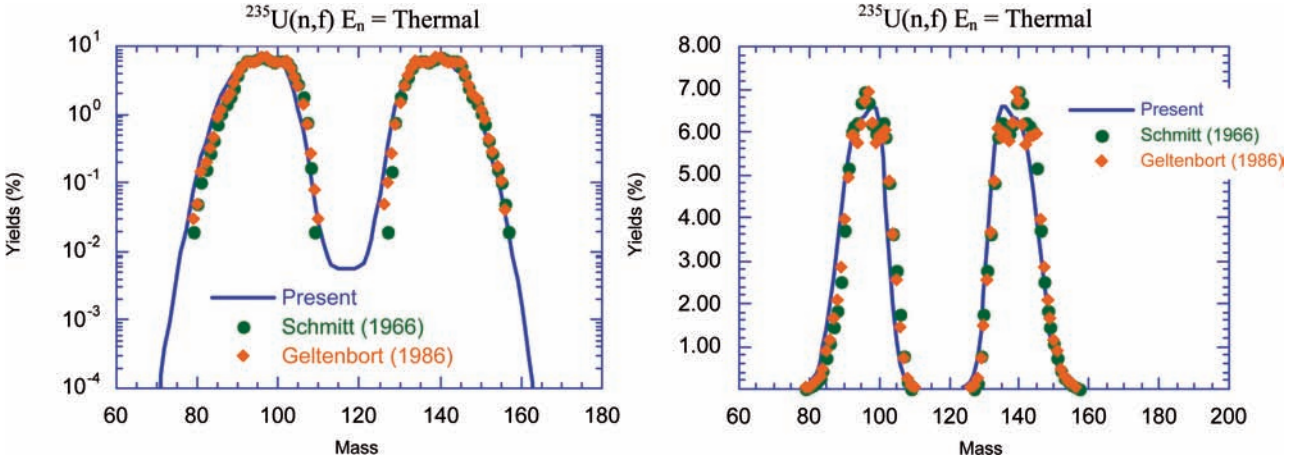

FIG. 4.3.5. Mass distribution of ^{235}U thermal neutron fission.

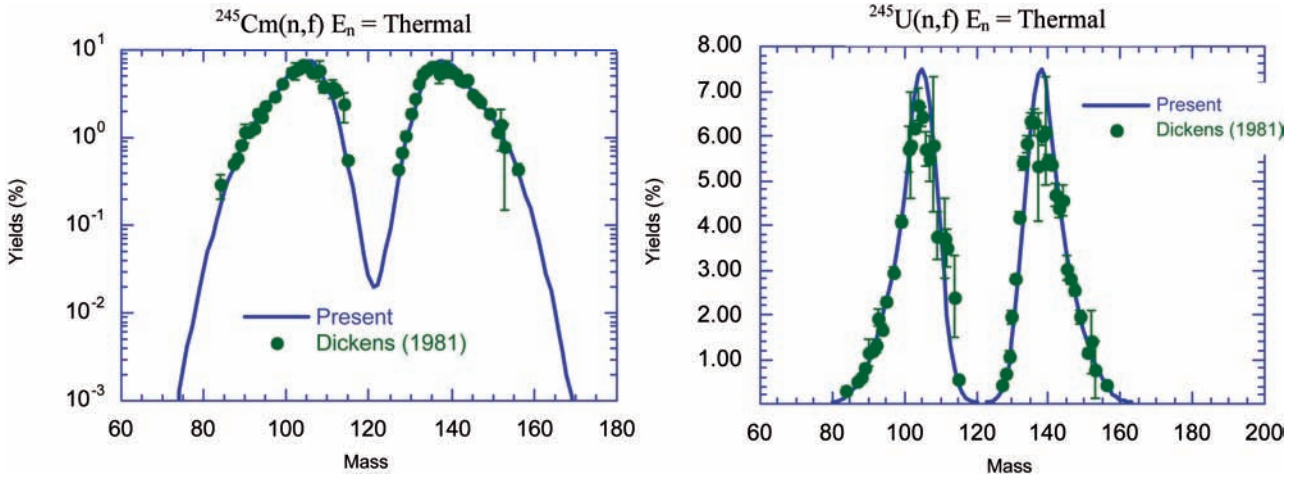

FIG. 4.3.6. Mass distribution of ^{245}Cm thermal neutron fission.

$$\overline{\left|\frac{C-E}{E}\right|} = \sqrt{\frac{1}{N}\sum_{i}^{N}\left(\frac{C_i - E_i}{E_i}\right)^2} \qquad (4.3.19)$$

where C_i and E_i are the calculated and measured values, respectively, and N is the number of data points.

Examples of mass distributions from intermediate energy neutron fission are presented in Figs 4.3.7 and 4.3.8, and show ^{239}Pu fission by 7.9 MeV neutrons and ^{242}Pu fission by 15.1 MeV neutrons.

These comparisons also show rather good agreement between calculations and measurements [4.3.9, 4.3.10]. In these cases the average deviations as defined in Eq. (4.3.19) are 0.484 for ^{239}Pu and 0.230 for ^{242}Pu, respectively.

As examples for high energy neutron induced fission, comparisons for mass distributions of ^{238}U fission by 100 and 160 MeV neutrons are presented in Figs 4.3.9 and 4.3.10. Recognizable deviation between calculation and measurement [4.3.3] is seen in the case of 100 MeV neutron fission. However, the average deviation is 0.436, which is less than the corresponding value for ^{235}U fission by thermal neutrons of 0.664. The comparison for ^{235}U thermal neutron fission seems to be better than for ^{238}U fission at 100 MeV. The reason is that the large average deviation in the case of ^{235}U thermal neutron fission is caused by the large deviation within the valley of the mass distribution where the mass yields are quite small (the deviation cannot be clearly seen in Fig. 4.3.5 where the comparison of the ^{235}U thermal neutron fission is shown). Agreement is better for ^{235}U fission by 160 MeV neutrons (average deviation is 0.145) than for 100 MeV neutron fission.

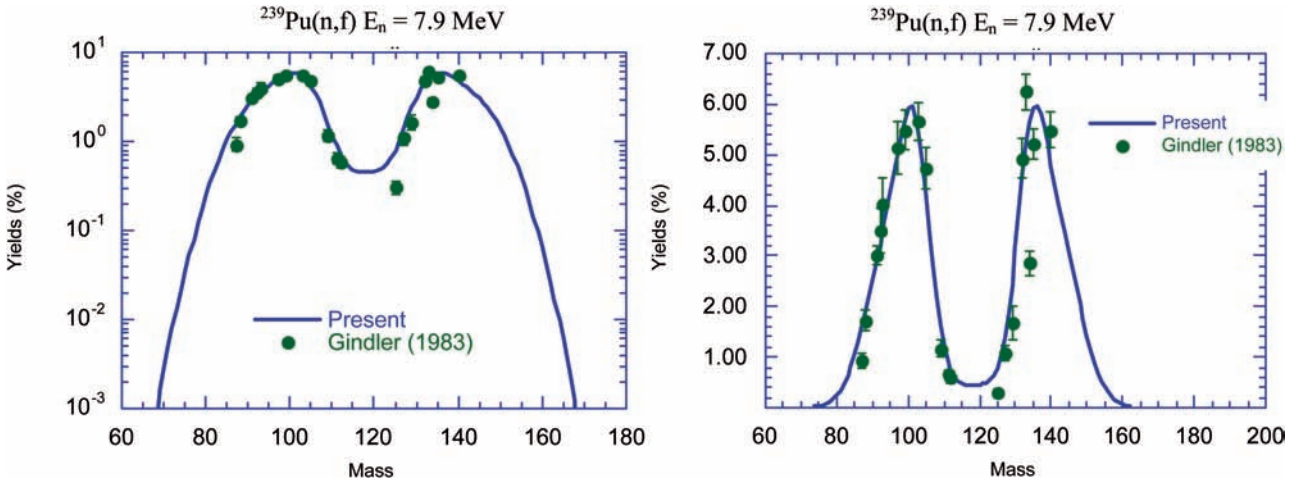

FIG. 4.3.7. Mass distribution of ^{239}Pu fission by 7.9 MeV neutrons.

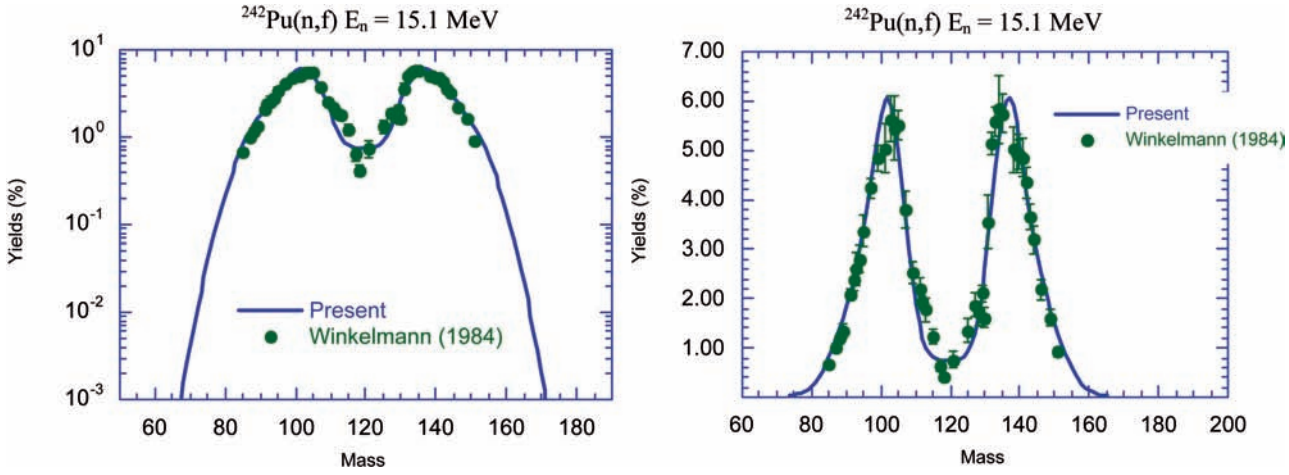

FIG. 4.3.8. Mass distribution of ^{239}Pu fission by 15.1 MeV neutrons.

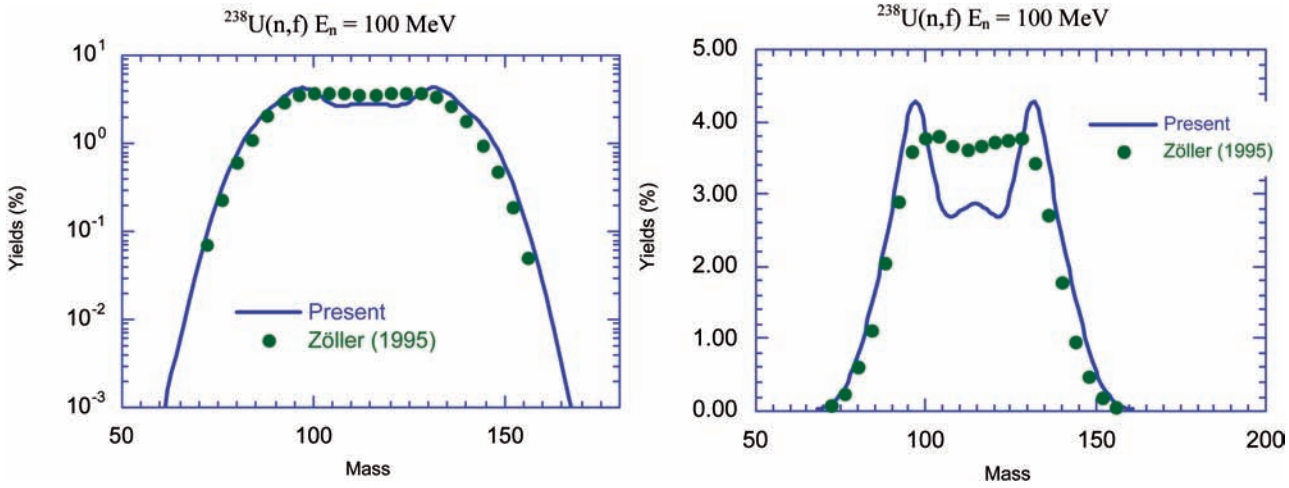

FIG. 4.3.9. Mass distribution of ^{238}U fission by 100 MeV neutrons.

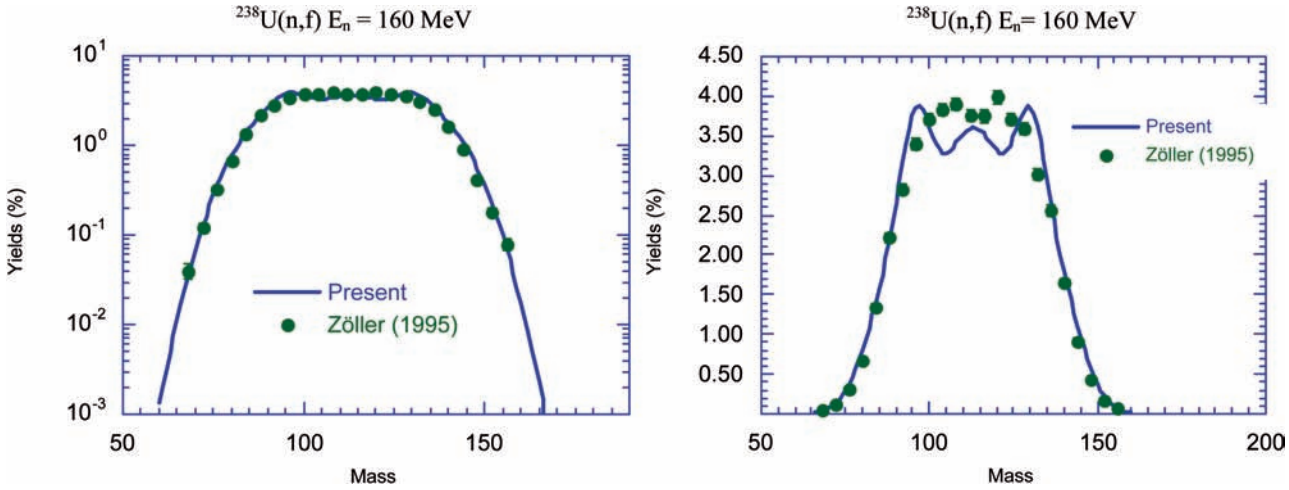

FIG. 4.3.10. Mass distribution of ^{238}U fission by 160 MeV neutrons.

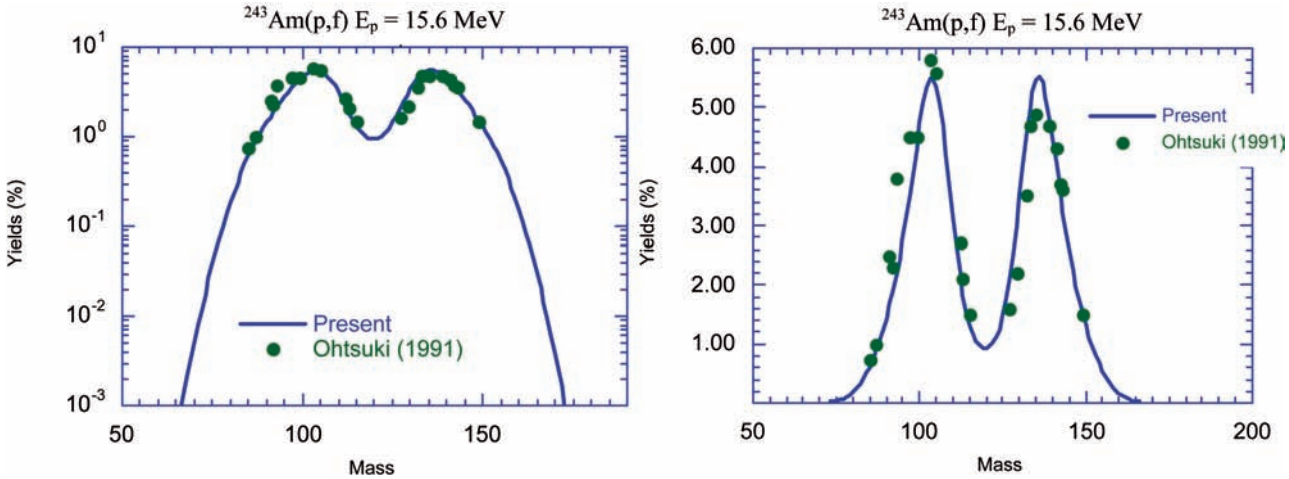

FIG. 4.3.11. Mass distribution of ^{243}Am fission by 15.6 MeV protons.

Comparisons were also performed for proton induced fission. Examples are shown in Figs 4.3.11–4.3.13. As seen in these figures, the present systematics is able to reproduce the measured mass distribution of proton induced fission [4.3.11–4.3.13]. The average deviations are 0.192 for ^{243}Am, 0.836 for ^{248}Cm and 0.338 for ^{238}U. Although the deviation in the case of ^{248}Cm seems to be large, the experimental uncertainties shown in Fig. 4.3.12 are also rather large. As seen in Fig. 4.3.13, the present systematics can also be applied to fission by high energy protons (340 MeV).

The present systematics is even applicable to spontaneous fission. Examples of the comparisons are shown in Figs 4.3.14 and 4.3.15, in which the evaluated data from the ENDF/B-VI file are used [4.3.14]. The present systematics agrees rather well with the evaluated mass yields from the spontaneous fission of minor actinides, even though a slight discrepancy is detectable at the peaks and in the valley region. The comparisons show that the present systematics can predict the gross behaviour of mass distributions from various kinds of fission, from spontaneous fission up to neutron and proton induced fission at energies above 100 MeV.

4.3.6. Summary

As part of the IAEA Coordinated Research Project on Fission Product Yield Data for the Transmutation of Minor Actinide Nuclear Waste, we have developed a systematics for the calculation of fission product mass yields. This systematics uses five Gaussian functions for the description of mass distributions, the parameters of which have a rather simple functional form. We calculated the mass

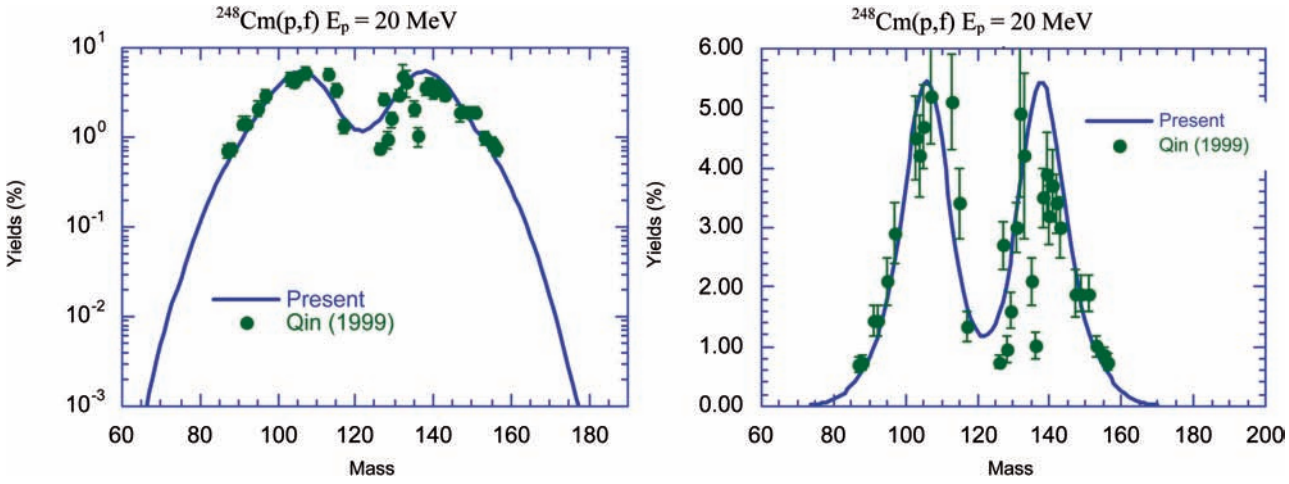

FFIG. 4.3.12. Mass distribution of ^{248}Cm fission by 20 MeV protons.

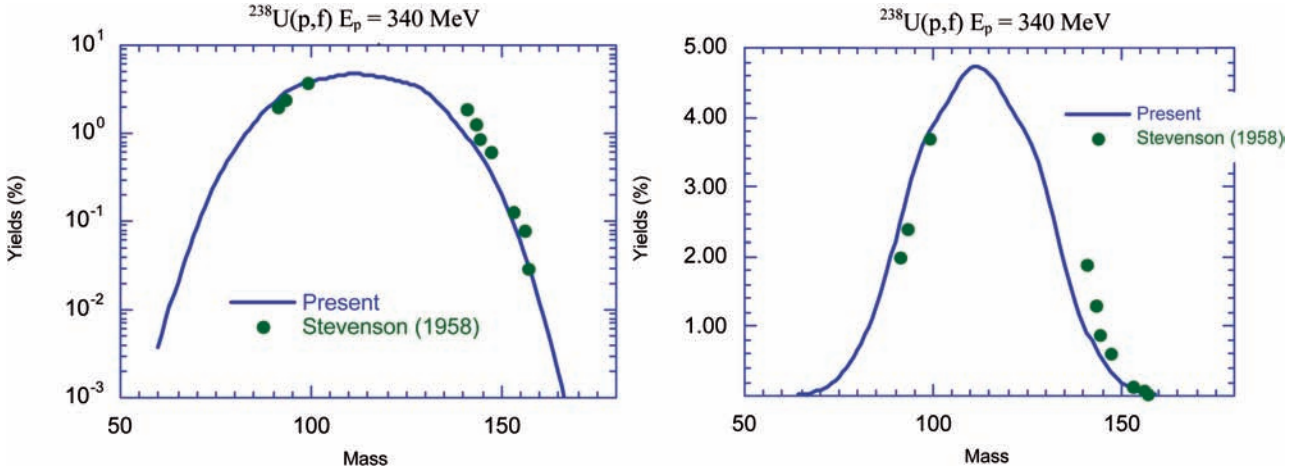

FIG. 4.3.13. Mass distribution of ^{238}U by 340 MeV fission.

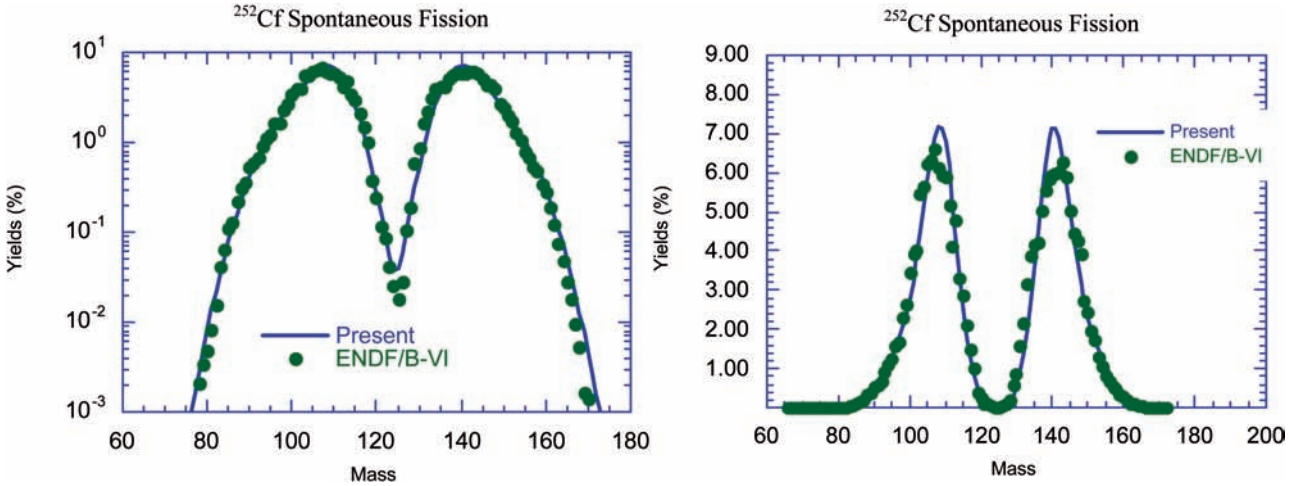

FIG. 4.3.14. Mass distribution of ^{252}Cf spontaneous fission.

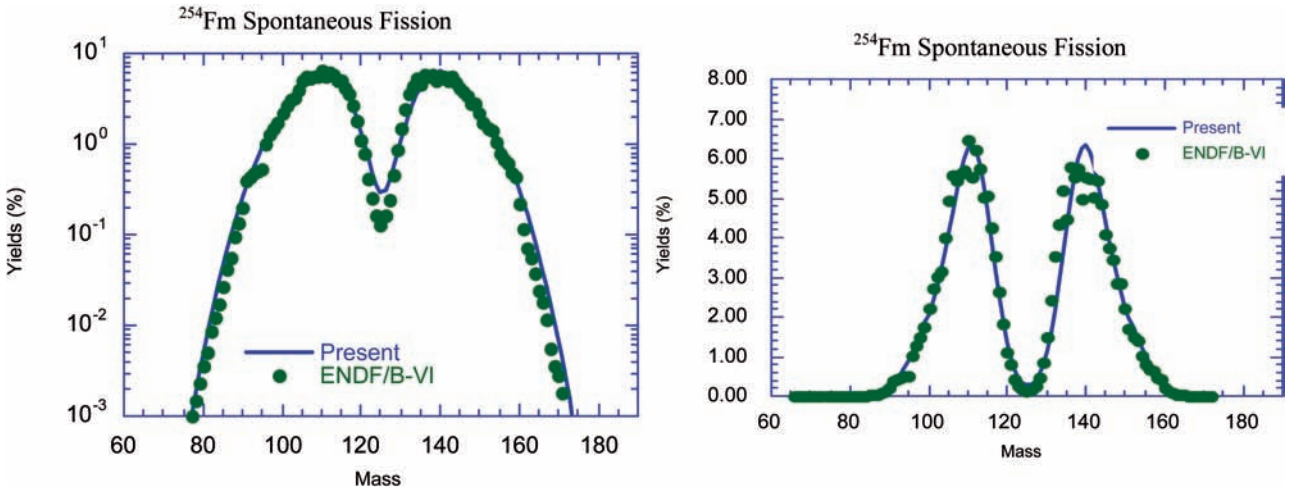

FIG. 4.3.15. Mass distribution of ^{254}Fm spontaneous fission.

distributions of various kinds of fissioning systems and compared them with the measured data. The comparisons show good agreement between the calculations and the measurements, including fission by high energy neutrons and protons.

Benchmark calculations were proposed during the CRP (see Section 5.2 and the attached CD-ROM for details). The present systematics was used to perform the benchmark calculations. As the systematics cannot give the mass distribution for pre-neutron emission, only the mass yields for post-neutron emission were calculated for the benchmark exercise.

REFERENCES TO SECTION 4.3

[4.3.1] MORIYAMA, H., OHNISHI, T., Systematics of Fission Fragment Mass-Yield Curves, Tech. Rep. No. 166, Kyoto University (1974).

[4.3.2] KATAKURA, J., A systematics of fission product mass yields with 5 Gaussian functions, JAERI-Research 2003–004 (2003).

[4.3.3] ZÖLLER, C.M., et al., "Fission fragment properties in the ^{238}U(n,f) reaction at incident neutron energies from 1 MeV to 500 MeV", VII School on Neutron Physics, Vol. I, Ratmino, JINR, Dubna (1995) 130.

[4.3.4] MEYERS, W.D., SWIATECKI, W.J., Nuclear masses and deformations, Nucl. Phys. **81** (1966) 1–60.

[4.3.5] WAHL, A.C., Los Alamos National Laboratory, USA, personal communication, 1999.

[4.3.6] SCHMITT, H.W., et al., Fragment energy correlation measurements for ^{252}Cf spontaneous fission and ^{235}U thermal-neutron fission, Phys. Rev. **141** (1966) 1146–1160.

[4.3.7] GELTENBORT, P., et al., Precision measurements of mean kinetic energy release in thermal-neutron-induced fission of ^{233}U, ^{235}U and ^{239}Pu, Radiat. Eff. **93** (1986) 57.

[4.3.8] DICKENS, J.K., McCONNEL, J.W., Yields of fission products produced by thermal-neutron fission of ^{245}Cm, Phys. Rev. C **23** (1981) 331–350.

[4.3.9] GINDLER, J.E., et al., Mass distributions in monoenergetic-neutron-induced fission of ^{239}Pu, Phys. Rev. C **27** (1983) 2058–2062.

[4.3.10] WINKELMANN, I., AUMANN, D.C., Fission of ^{242}Pu with 15.1-MeV neutrons, Phys. Rev. C **30** (1984) 934–940.

[4.3.11] OHTSUKI, T., et al., Mass yield curves in low-energy proton-induced fission of ^{233}U, ^{235}U, ^{236}U, ^{237}Np, ^{239}Pu, ^{242}Pu, ^{244}Pu, ^{241}Am, and ^{243}Am, Phys. Rev. C **44** (1991) 1405–1423.

[4.3.12] QIN, Z., et al., Mass yield distributions in proton-induced fission of ^{248}Cm, Radiochim. Acta **84** (1999) 115–120.

[4.3.13] STEVENSON, P.C., et al., Further radiochemical studies of the high-energy fission products, Phys. Rev. **111** (1958) 886–891.

[4.3.14] ENGLAND, T.R., RIDER, B.F., Evaluation and compilation of fission product yields 1993, Rep. LA-UR-94-3106, ENDF-349, Los Alamos National Laboratory, NM (1994).

4.4. PHENOMENOLOGICAL MODEL FOR FRAGMENT MASS AND CHARGE DISTRIBUTION IN ACTINIDE NUCLEI FISSION

Yu.V. Kibkalo
SC Institute for Nuclear Research, Ukraine

Detailed analyses of experimental data on nuclear fission show that the process of fragment formation depends not only on the temperature but also on the total angular momentum of the fissioning nucleus. An analysis of the total cross-sections for the fission of ^{232}Th, ^{235}U, ^{236}U and ^{238}U by α particles with energies up to 140 MeV has been carried out to study the dependence of the fissioning nucleus formation cross-section on excitation energy and transferred angular momentum. The energy dependence of the critical value of the angular momentum for fissioning nucleus formation has been obtained for the interaction of α particles with uranium nuclei in this energy range. A new approach is proposed to describe fragment mass distributions from actinide fission that accounts for the influence of the total nuclear angular momentum. The experimental fragment mass distributions for the fission of actinide nuclei formed in spontaneous fission and in reactions with neutrons, γ rays and α particles in the excitation energy range up to 200 MeV have been analysed by this approach. The dependence of fragment mass distribution parameters on the excitation energy and transferred angular momentum of fissioning nuclei was derived. A phenomenological description of fragment mass and charge distributions has been developed that accounts for the quantum-mechanical transmission of real fission barriers.

4.4.1. Introduction

Studies of cross-sections for the interaction of charged particles and heavy ions with nuclei reveal that the reaction mechanism for compound system formation varies with incident particle energy. Nuclei fission should be studied over a wide energy range to ensure that the information obtained from experimental fission data will encompass the full characteristics of the fissioning system. Some progress has been made in explaining the energy dependence of fusion cross-sections for heavy ions with nuclei on the basis of the dynamic model [4.4.1].

Detailed analyses of the dependence of experimental data on actinide nuclei fission at medium excitation energies show that, at the time of formation of the angular, mass and energy distributions of fission fragments, an essential role is played by the spectrum of transition states above the fission barrier. The basic characteristics of transition states are the collective energy and the total angular momentum of the fissioning nucleus. Thus the process of scission and formation of fragments is not only influenced by the temperature, but also by the total angular momentum of the fissioning nucleus. The dependence of the integral and differential fission cross-sections on the total angular momentum is well acknowledged and investigated, while only a few publications are devoted to experimental studies of the influence of the total angular momentum on fission fragment mass and energy distributions. The most complete research of that kind is presented in Ref. [4.4.2]. This work involved an investigation of the ℓ dependence of the fission fragment mass and energy distributions, and the formation of ^{204,206}Po and ^{260}Ku in reactions of heavy ions from ^{12}C up to ^{48}Ti with targets from ^{164}Dy up to ^{244}Cm. The distinctive peculiarity of the work is that heavy ion beams at rather high excitation energies (E* > 40 MeV) and large transferred angular momentum ($\langle\ell\rangle \geq 30\hbar$) were used. Analysis of the experimental data showed a weak dependence of the fragment mass distributions on the average angular momentum of fissioning nucleus, and the total absence of such a dependence for the average total kinetic energy of fission fragments in the case of rather strongly heated fissioning nuclei [4.4.2].

We analysed a large amount of experimental data on the fission of ^{240}Pu formed in reactions with γ quanta, neutrons and α particles in order to study the dependence of the fragment mass distributions from actinide fission on medium excitation energy and small transferred angular momentum [4.4.3, 4.4.4]. Figure 4.4.1 shows the fission fragment mass distributions of ^{240}Pu formed in reactions with γ quanta [4.4.5], neutrons [4.4.6] and α particles [4.4.7] at nearly equal excitation energies (E* = 20,

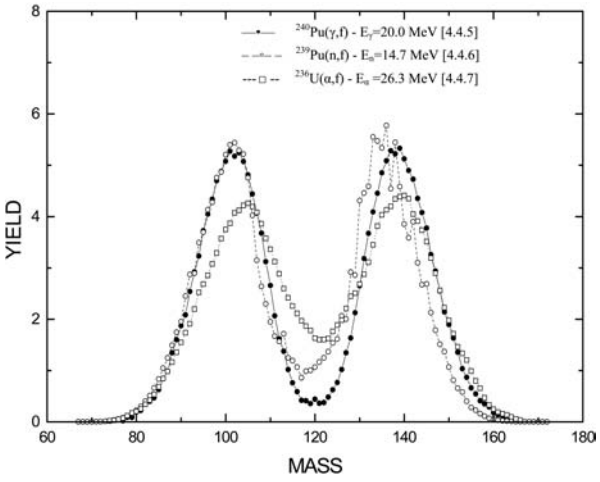

FIG. 4.4.1. Fragment mass distributions from ^{240}Pu fission formed in reactions with γ quanta, neutrons and α particles at nearly equal excitation energies.

21.2 and 21.3 MeV, respectively) but different values of transferred angular momentum ($\langle \ell \rangle = 1\hbar$, $6\hbar$ and $8\hbar$, respectively). One can see that the variance of mass distributions has a minimum for fission induced by γ quanta that increases with increase of particle mass (i.e. with increase of the transferred angular momentum). Thus the fragment mass distribution of fission induced by light particles at low excitation energies depends essentially on the average angular momentum transferred to the fissioning nucleus.

Experimental studies of the fission mechanism in reactions with heavy ions at medium excitation energies [4.4.8, 4.4.9] show that only the interaction of ions with an angular momentum up to some critical value $\ell_{fus} < \ell_{max}$ can lead to complete fusion and compound nucleus formation. If the projectile transfers sufficient energy to the nucleus to exceed the critical energy for fission, the process of fission can take place without an intermediate stage of compound nucleus formation. Such a fission mechanism can be considered to be a result of direct interactions that happen over a nuclear time of ~10^{-21} s. Processes are also possible in which the direct interaction is followed by fission through a compound nucleus. However, the primary particle does not transfer the whole momentum to a target nucleus. Thus the parameters describing fragment distributions at particular excitation energies can only be extracted correctly from the experimental data if the reaction mechanism leading to the formation of a fissioning nucleus is known.

The double humped structure of a fission barrier and the dependence of the transition state shapes of fissioning nuclei on excitation energy complicate the analysis and make the calculation of fragment yields for a particular excitation energy of a fissioning nucleus difficult. For actinide nuclei, the problem is additionally complicated at medium excitation energies where a significant contribution of emissive fission is observed, making more difficult the determination of fragment yields for fission of the target nucleus.

One further interesting peculiarity of actinide nuclei fission at medium excitation energies has been demonstrated in theoretical work [4.4.10–4.4.12]. At some excitation energy, the shell effects are calculated to disappear and the nucleus exhibits averaged properties that are only described by the liquid drop model. Thus the effective transition states of fissioning nuclei are gradually shifted with increasing excitation energy from the shape of the second barrier to the liquid drop saddle shape. The shapes of the fission fragment mass and charge distributions should change from asymmetric (corresponding to the double humped fission barrier) to symmetric (corresponding to the liquid drop barrier). The excitation energy at which the shape of the transition state of a fissioning nucleus coincides with the liquid drop shape is in the range of 40–45 MeV, as shown in Ref. [4.4.13].

4.4.2. Energy dependence of nuclear fission cross-sections

The analysis of the total fission cross-sections for the interaction of 20–140 MeV α particles with ^{232}Th, ^{235}U, ^{236}U and ^{238}U has been carried out in order to study the dependence of the cross-section for fissioning nucleus formation on excitation energy. When analysing the experimental data, two basic processes were assumed to contribute to the total reaction cross-sections as calculated using the optical model:

(a) Complete fusion of a projectile with a target nucleus, leading to the formation of a fissioning nucleus;
(b) Reactions with compound nucleus formation, as well as other non-elastic processes not leading to fissioning nucleus formation.

The total reaction cross-section is described by the following expression:

$$\sigma_R = \pi \lambda\!\!\!^{-2} \sum_{\ell} (2\ell + 1) T_\ell \qquad (4.4.1)$$

where

$\lambda\!\!\!^{-} = \hbar/\sqrt{2\mu E}$ is the wavelength,
E is the projectile energy,
μ is the reduced mass of the system.

The transmission coefficients T_l were calculated by means of the parabolic barrier approximation [4.4.14]:

$$T_\ell = \left[1 + \exp((\ell(\ell+1) - \ell^2_{\max})/D\right]^{-1} \quad (4.4.2)$$

where $\ell_{\max}$ is the maximum value of an orbital angular momentum at the interaction of the projectile with a nucleus and D is the 'transmission diffuseness'.

As mentioned above, there is some critical value of angular momentum ($\ell_{\text{fus}} < \ell_{\max}$) that leads to fissioning nucleus formation. The following quasi-classical expression can be used to calculate ℓ_{fus} [4.4.13]:

$$\ell^2_{fus} = \frac{2\mu}{\hbar^2}\rho(\rho E - Z) \quad (4.4.3)$$

where

$Z = 1.44\ Z_1Z_2$ …, Coulomb parameter,
$\rho = mE+b$ (fm) …, parameterized fusion radius,
E is the projectile energy.

Cross-sections for fissioning system formation in the interaction of α particles with uranium nuclei were calculated from Eqs (4.4.1) and (4.4.2). The limiting value of the angular momentum (ℓ_{fus}) for fissioning nucleus formation was determined from the quasi-classical Eq. (4.4.3), and substituted in Eq. (4.4.2) as the maximum value of an angular orbital momentum ($\ell_{\max}$). Equations given in Ref. [4.4.14] were used for the remaining parameters. Figure 4.4.2 shows the experimental data for the total fission cross-sections of the interaction of α particles with ^{232}Th, ^{235}U, ^{236}U and ^{238}U nuclei [4.4.13, 4.4.15–4.4.18] over the excitation energy range 20–140 MeV compared with theoretical calculations of the cross-sections for fissioning nucleus formation. Over all α particle energy ranges, satisfactory agreement was obtained between the experimental data and calculations with the optimum parameters m = -2.43×10^{-2} (fm/MeV) and b = $1.545(A_1^{1/3} + A_2^{1/3})$ (fm), for the energy

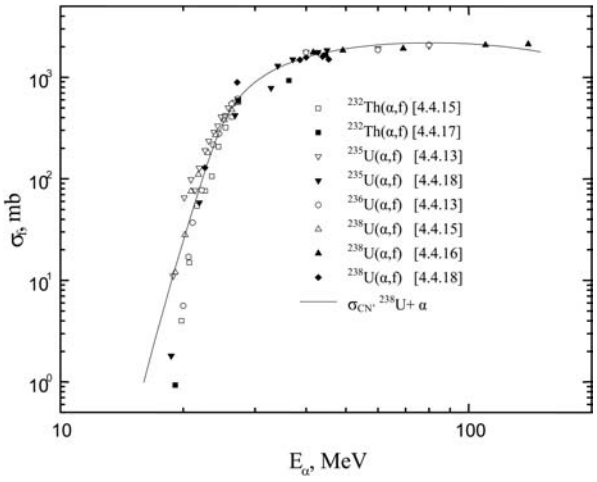

FIG. 4.4.2. Total fission cross-sections of ^{232}Th, ^{235}U, ^{236}U and ^{238}U induced by α particles (line is our calculation).

dependence of the fusion radius as given in Eq. (4.4.3).

4.4.3. Angular momentum dependence of fission fragment mass distributions

During fission fragment formation and as long as the essential role is played by the distribution of l states above the fission barrier, the fragment mass distribution has to be averaged over all l states in the saddle point:

$$Y(A) = \sum_{\ell=0}^{\ell_{\max}} (2\ell+1)T_\ell Y_\ell(A) \Big/ \sum_{\ell=0}^{\ell_{\max}} (2\ell+1)T_\ell \quad (4.4.4)$$

where

$(2\ell + 1)T_\ell$ is the partial cross-section for compound nucleus formation with angular momentum ℓ,
T_ℓ is the transmission coefficient in the input channel of the reaction,
$Y_\ell(A)$ is the partial fragment mass distribution.

Equation 4.4.2 was used to calculate the transmission coefficients T_ℓ. The most suitable values of the parameters for practical calculations of the transmission coefficients of light particles (neutrons, protons, deuterons, tritons, ^{3}He ions and α particles) were obtained from Ref. [4.4.14] for projectile energies from 2 to 50 MeV and for practically all nuclides in the periodic table.

The Brosa model [4.4.19, 4.4.20] was used for the parameterization of $Y_\ell(A)$, which describes well

the fragment mass distributions in fission and has been developed further [4.4.21]:

$$Y_\ell(A) = \sum_i \frac{W_i}{\sqrt{2\pi\sigma_A}} \times \left[\exp\left(-\frac{(A - A_L^i)^2}{2\sigma_{A_i}^2} \right) + \exp\left(-\frac{(A - A_H^i)^2}{2\sigma_{A_i}^2} \right) \right] \quad (4.4.5)$$

where

A_L^i, A_H^i are the most probable masses of the light and heavy fragments,
σ_{A_i} is the variance of the fragment mass distribution,
W_i is the yield probability for a particular fission channel.

We have analysed fission fragment mass distributions from ^{236}U fission with monochromatic neutrons [4.4.22] and α particles [4.4.23] in the excitation energy range up to 30 MeV, in order to define the parameters included in Eq. (4.4.5). These experimental fragment mass distribution data account for the angular momentum in the input channel, and analyses show that there is a critical value of the angular momentum ($\ell_{cr} = 6\hbar$) above which the asymmetric fission channel standard I is converted into the symmetric super long channel over the whole excitation energy range:

$$A_H^\ell = \begin{cases} 134 & \ell \le \ell_{cr} \\ A_f/2 & \ell > \ell_{cr} \end{cases} \quad (4.4.6)$$

where A_f is the mass of the fissioning nucleus.

Fission fragment mass distributions for ^{236}U calculated with the assumptions described above are shown in Figs 4.4.3 and 4.4.4. The analysis of data presented in these figures shows that condition (4.4.6) limits the number of fission channels considered and allows fragment mass distributions from α particle and neutron induced fission of ^{236}U to be described by only two modes (standard I and standard II) for excitation energies up to 30 MeV. These limitations reduce the number of varied parameters significantly — super long mode parameters are not required, and the sum of yields in the two asymmetric channels $W_I + W_{II}$ is equal to 100%.

The dependence of other parameters (A_H^{II}, σ_{A_I}, $\sigma_{A_{II}}$, W_{II}) on the total angular momentum of the fissioning nucleus cannot be derived, although the

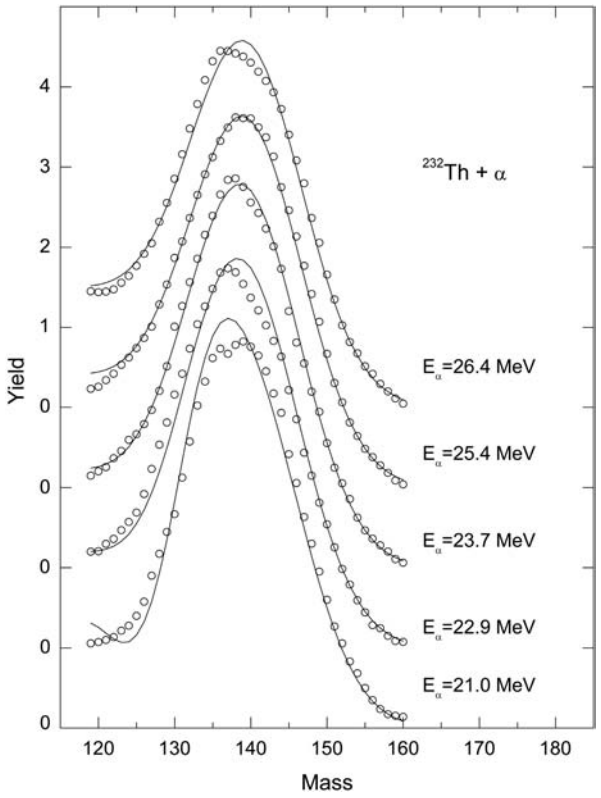

FIG. 4.4.3. Fragment mass distributions from ^{236}U fission induced by ^{232}Th + α reaction (points are experimental data [4.4.23]; lines are our calculations); energies of α particles are shown in the figure.

dependence of these parameters on the excitation energy is shown in Fig. 4.4.5. As a preliminary solution, the dependence of these parameters on the excitation energy can be represented by the following equations:

$$A_H^{II} = 139.4 + 1.4\exp(-0.18(E^* - 8.2)^2) \quad (4.4.7)$$

$$\sigma_{A_I} = 3.02 + \frac{6.96}{1 + \exp((17.95 - E^*)/1.41)} \quad (4.4.8)$$

$$\sigma_{A_{II}} = 5.38 + \frac{2.03}{1 + \exp((12.07 - E^*)/1.1)} \quad (4.4.9)$$

$$W_{II} = 75.48 + 14.38\exp(-0.095(E^* - 11.9)^2) \quad (4.4.10)$$

$$W_I = 100 - W_{II} \quad (4.4.11)$$

We analysed the experimental data for the fragment mass distributions from ^{239}Pu and ^{240}Pu fission by γ quanta [4.4.5, 4.4.24], neutrons [4.4.6, 4.4.25] and α particles [4.4.7] for excitation energies

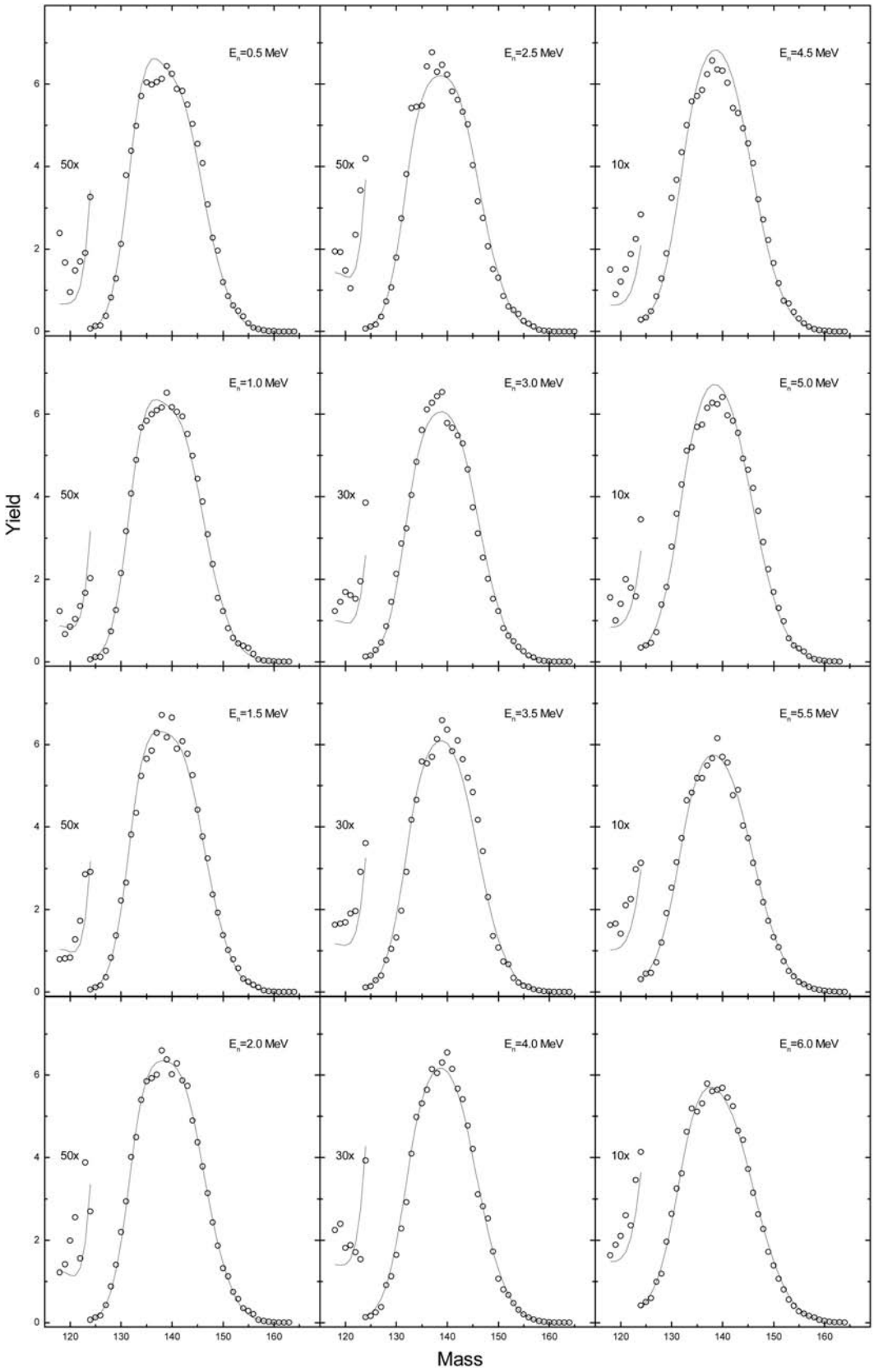

FIG. 4.4.4. Fragment mass distributions from ^{236}U fission induced by ^{235}U+n reaction (points are experimental data [4.4.22]; lines are our calculations); energies of neutrons are shown in the figure.

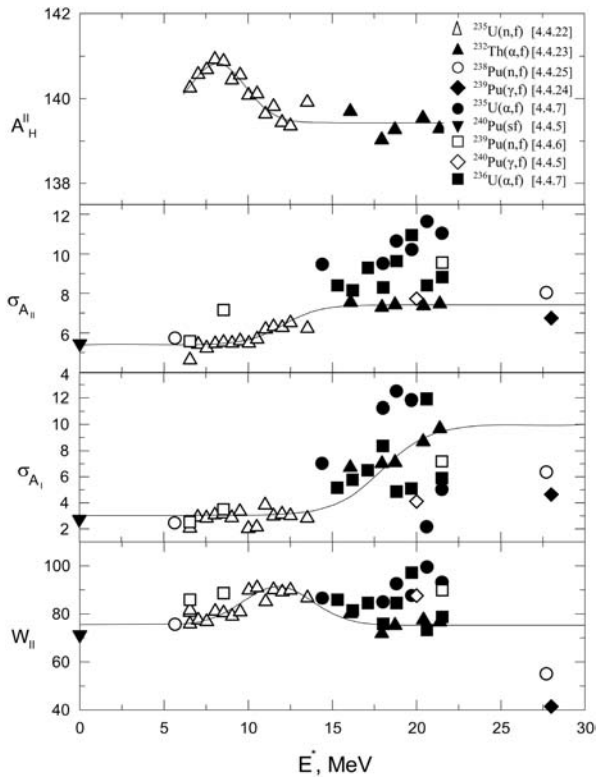

FIG. 4.4.5. Dependence of model parameters on excitation energy for fissioning nuclides ^{236}U, ^{239}Pu and ^{240}Pu formed in reactions with various particles (points are experimental data; lines are our calculations using Eqs ((4.4.6)–(4.4.11)).

up to 30 MeV and from the spontaneous fission of ^{240}Pu [4.4.5]. Results from the analysis show that the most probable mass of heavy fragments for the standard *I* fission mode of ^{239}Pu and ^{240}Pu has a value similar to that for ^{236}U (A^I_H = 134.0). The critical value (ℓ_{cr}) for the angular momentum above which the asymmetric fission channel standard *I* is converted into the symmetric channel (super long mode) is equal to 8$\hbar$. The most probable mass of heavy fragments for the standard *II* fission mode is A^{II}_H = 140.0 for ^{239}Pu and ^{240}Pu fission, up to an excitation energy of 30 MeV. The dependence of the remaining parameters (σ_{A_I}, $\sigma_{A_{II}}$, W_{II}) on the excitation energy is shown in Fig. 4.4.5, where they are compared to similar parameters obtained from fission reactions of monochromatic neutrons [4.4.22] (light triangles) and α particles [4.4.23] (dark triangles) with ^{236}U (solid lines represent calculations using Eqs (4.4.7)–(4.4.11)). At excitation energies above 15 MeV, the calculated energy dependence of the parameters differs significantly from the experimental data for fissioning nuclei ^{239}Pu and ^{240}Pu (Fig. 4.4.5), but shows good agreement with the equivalent data for ^{236}U. Apparently this situation is due to the emissive fission contribution that has to be accounted for more correctly in the case of the fission of actinides by α particles.

Experimental data and the results of calculations are given in Figs 4.4.6 and 4.4.7 for fragment mass distributions from ^{239}Pu and ^{240}Pu fission by neutrons, γ quanta and α particles at excitation energies up to 30 MeV, and also for spontaneous fission of ^{240}Pu. These figures show satisfactory agreement between the experimental data and calculations. Thus an adequate description of the fragment mass distributions is achieved for fissioning nuclei ^{239}Pu and ^{240}Pu formed in reactions with various particles and excitation energies up to 30 MeV by taking into account only two fission modes, namely standard I and standard II.

4.4.4. Fragment mass distributions for photofission

The dependence of the fragment mass distributions on excitation energy at a constant value of the angular momentum transferred to the fissioning nucleus can be studied by analysing the experimental data for the photofission of ^{232}Th, ^{235}U, ^{238}U and ^{239}Pu [4.4.26] at Bremsstrahlung endpoint energies up to 50 MeV. Photofission is one of the most powerful tools for studying the fission process because of the well known spin selectivity of the excitation and the absence of the Coulomb barrier. The main experimental problem in photofission studies is the lack of intense sources of monochromatic photon beams. Therefore, all photofission mass distributions have been measured in bremsstrahlung spectra with a continuous energy distribution, and hence the excitation energy is not well defined.

Symmetric fission components have been observed in all photofission experiments but analysed in different ways so that the results are difficult to compare. The systematic investigations of mass fragment distributions in the photofission of nuclei in the mass region 232 ≤ A ≤ 239 and Bremsstrahlung endpoint energies between 15 and 55 MeV are presented in Ref. [4.4.26]. Due to the exponential increase of the symmetric fission probability with excitation energy, the symmetric to asymmetric fission yield ratio (Y_S/Y_A) is a rather sensitive qualitative measure for the excitation energy of the fissioning nucleus.

At low excitation energies and small transferred angular momentum ($\ell \leq 7\hbar$) the fission

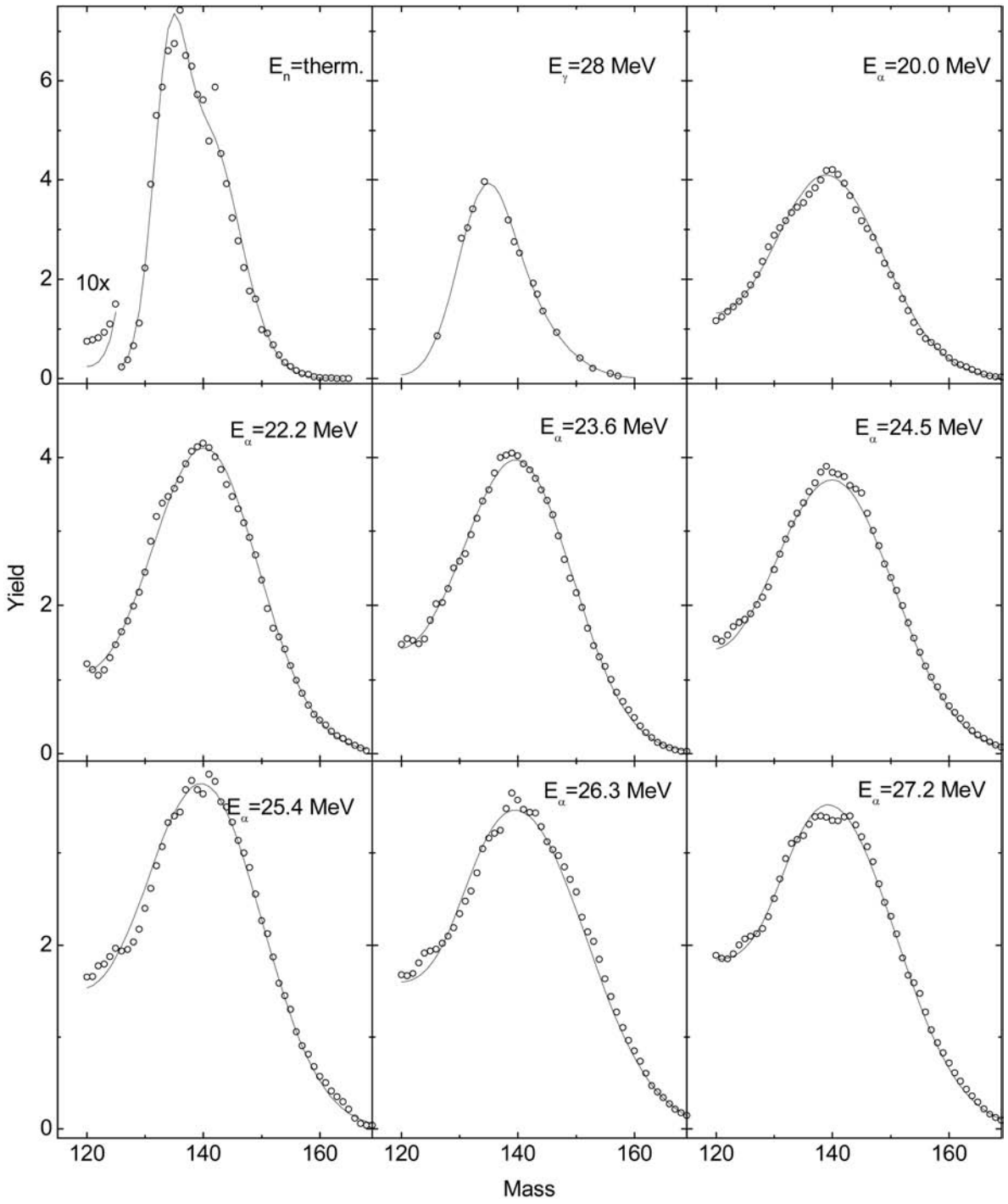

FIG. 4.4.6. Fragment mass distributions from fission of ^{239}Pu by neutrons [4.4.25], γ quanta [4.4.24] and α particles [4.4.7] (points are experimental data; lines are our calculations); energies of projectiles are given in the figure.

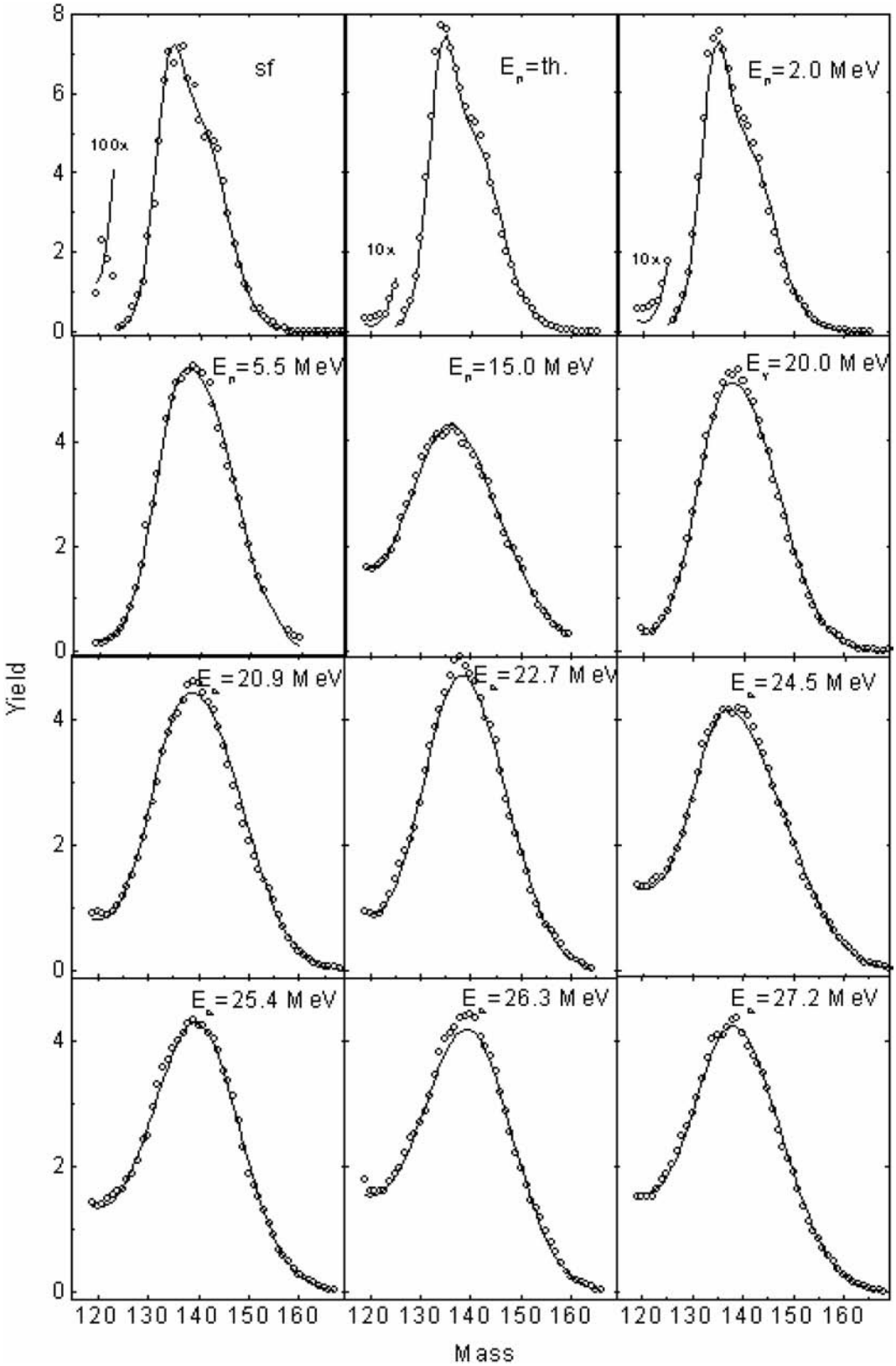

FIG. 4.4.7. Fragment mass distributions from ^{240}Pu spontaneous fission [4.4.5] and from fission induced by neutrons [4.4.6], γ quanta [4.4.5] and α particles [4.4.7] (points are experimental data; lines are our calculations); energies of projectiles are given in the figure.

fragment mass distributions are described by two asymmetric modes only, standard I and standard II [4.4.3, 4.4.4]. Our studies involved the analysis of experimental data published in Ref. [4.4.26], and Figs 4.4.8 and 4.4.9 compare the experimental data (points) for the photofission of ^{232}Th, ^{235}U, ^{238}U and ^{239}Pu nuclei at Bremsstrahlung endpoint energies up to 50 MeV with our calculations (continuous lines). These figures show the good agreement between the experimental data and calculations for all of the nuclei and excitation energy ranges studied. The asymmetric fragment mass distribution is observed in photofission even at a Bremsstrahlung endpoint energy of 50 MeV, which confirms the assumptions made about the absence of the symmetric fission mode for very small angular momenta of the fissioning nucleus.

Referring to the parameters contained in Eq. (4.4.5) the following equations were obtained from an analysis of the experimental data:

$$W_{II} = 96.44 - 0.38\, E_{BS} \tag{4.4.12}$$

$$W_I = 100 - W_{II} \tag{4.4.13}$$

$$\sigma_{A_I} = 9.07 + \frac{9.0}{1+(92-Z_f)^2} \tag{4.4.14}$$

$$\sigma_{A_{II}} = 1.12\frac{N_f Z_f}{A_f} - 55.3 \tag{4.4.15}$$

$$A_H^I = 3.23(Z_f - 50),\ A_L^I = A_f - A_H^I \tag{4.4.16}$$

$$A_L^{II} = 2.84(Z_f - 58),\ A_H^{II} = A_f - A_L^{II} \tag{4.4.17}$$

where

A_f, Z_f and N_f are mass, charge and neutron number of the fissioning nucleus,
E_{BS} is the Bremsstrahlung endpoint energy.

Results of the analysis for the nuclei studied show that no difference can be observed in the description of the fragment mass distributions with or without the inclusion of the symmetric fission mode. However, for a description of mass distributions in terms of five Gaussians, more parameters have to be used, which essentially complicates the derivation of the dependence of the model parameters on mass and charge of a fissioning nucleus and the Bremsstrahlung endpoint energy. As the variance for the symmetric mode of fragment mass distributions in photofission is very large ($\sigma_{SL} > 20$), the noticeable difference in calculations between these two approaches will be seen for fragment masses $A < 70$ and $A > 170$. The contribution of a symmetric mode to the fragment mass distributions for photofission will also be visible at higher energies where shell effects in a fissioning nucleus are decreasing. Thus experimental yields given for broader intervals of fragment masses need to be unambiguously resolved if there is a symmetric contribution for photofission.

4.4.5. Fragment mass distributions from fission by α particles

An analysis was made of the experimental data for the fragment mass distributions of ^{239}Pu and ^{240}Pu fission [4.4.13] formed in reactions with α particles up to 80 MeV. The basic purpose of the work was to find the dependence of the parameters in the Brosa model at higher excitation energies and greater angular momentum of the fissioning nuclei. Results show that the critical value of the angular momentum (ℓ_{cr},) above which the asymmetric standard I fission channel is converted into the symmetric super long channel is defined by the following equation:

$$A_{HI} = \begin{cases} A_{HI} & \ell \le \ell_{cr} \\ A_f/2 & \ell > \ell_{cr} \end{cases} \tag{4.4.18}$$

and is different for ^{239}Pu ($l_{cr} = 7\hbar$) and ^{240}Pu ($l_{cr} = 9\hbar$). As shown in Refs [4.4.10–4.4.13], the influence of the shell effects on the fission process decreases with increasing excitation energy, and therefore the fragment mass distribution should change from asymmetric to the symmetric shape. This change of the fragment mass distribution shape is seen in the parameters of the model used to describe the energy dependence (Eq. (4.4.5)), for which the following equations are derived:

$$W_{II} = W_{II}^0 \times P_{LD} \tag{4.4.19}$$

$$W_I = 100 - W_{II} \tag{4.4.20}$$

$$\sigma_{A_I} = \sigma_{A_I}^0 + \Delta\sigma_{A_I}(1 - P_{LD}) \tag{4.4.21}$$

$$\sigma_{A_{II}} = \sigma_{A_{II}}^0 + \Delta\sigma_{A_{II}}(1 - P_{LD}) \tag{4.4.22}$$

$$A_{L,H}^{II} = A_f/2 \mp \Delta A_{II} \times P_{LD} \tag{4.4.23}$$

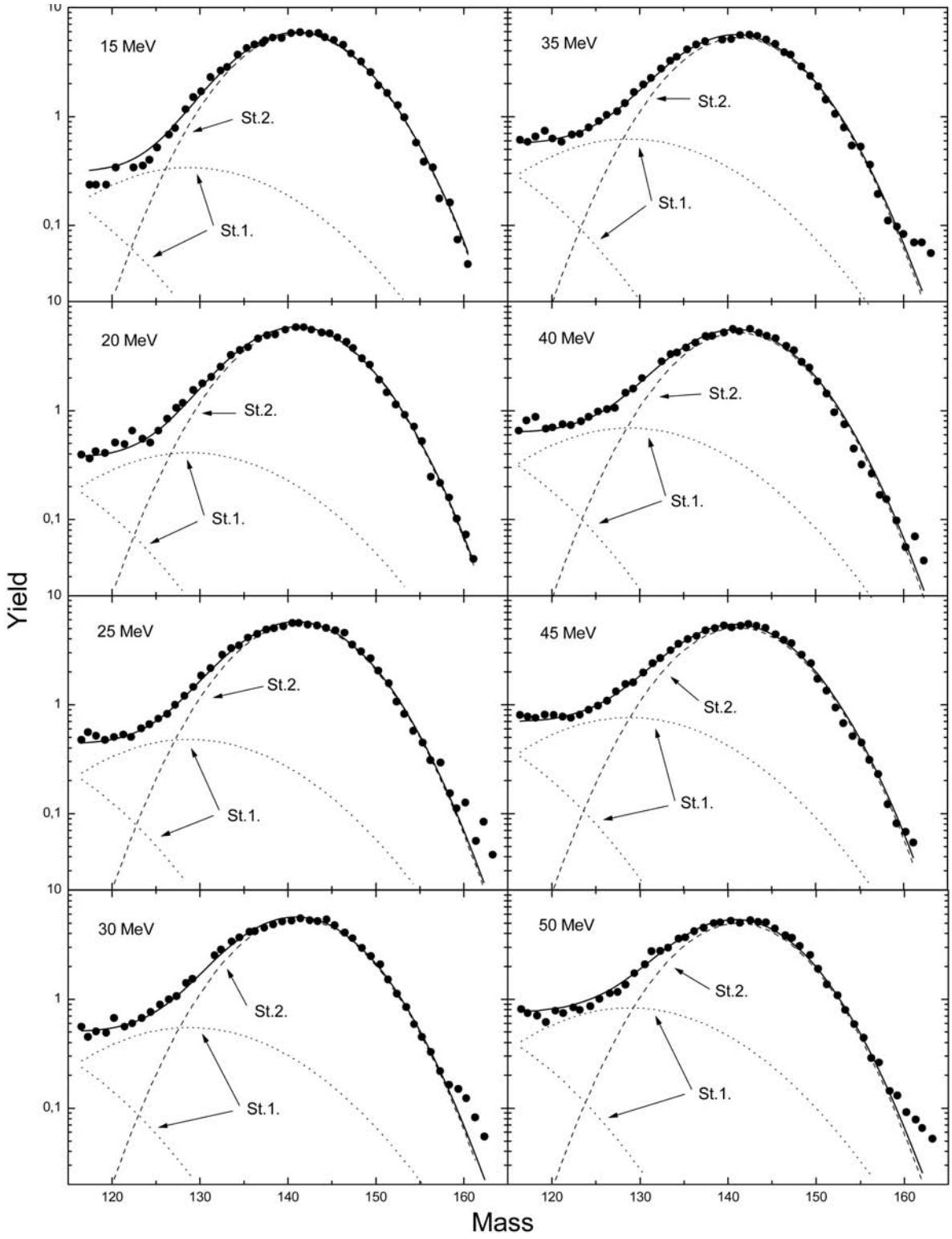

FIG. 4.4.8. Fragment mass distributions from the photofission of ^{232}Th for Bremsstrahlung endpoint energies between 15 and 50 MeV (points are experimental data [4.4.26]; lines are the calculations, as described in the text).

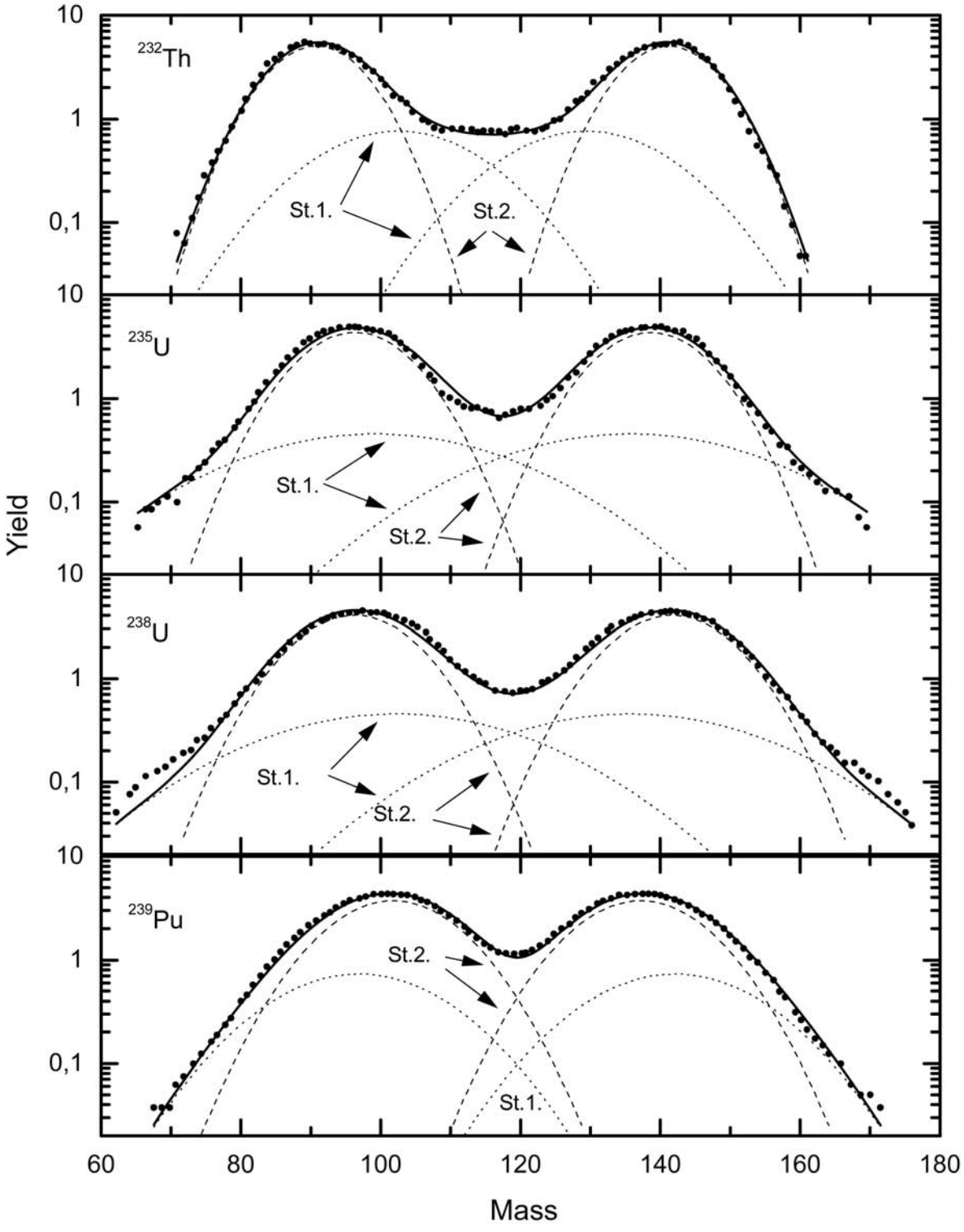

FIG. 4.4.9. Fragment mass distributions from the photofission of ^{232}Th, ^{235}U, ^{238}U and ^{239}Pu (Bremsstrahlung endpoint energy E_{BS} = 45 MeV, points are the experimental data [4.4.26], lines are the calculations, as described in the text).

where

A_f is the mass of a fissioning nucleus,
P_{LD} is the function describing the conversion of the asymmetric fragment mass distribution into a symmetric shape with increasing excitation energy of the fissioning nucleus:

$$P_{LD} = \left[1 + \exp\left(\frac{E' - E_{LD}}{\Delta E_{LD}}\right)\right]^{-1} \quad (4.4.24)$$

where

E^* is the excitation energy of a fissioning nucleus,
E_{LD} is the energy at which the asymmetric fragment mass distribution is converted into a symmetric fragment mass distribution,
ΔE_{LD} is the energy interval in which the conversion takes place.

The values of the remaining parameters included in Eqs (4.4.18)–(4.4.24) are listed in Table 4.4.1.

Comparisons of the experimental data for the fission fragment mass distributions from ^{239}Pu and ^{240}Pu fission with calculations using Eqs (4.4.18)–(4.4.24) are shown in Figs 4.4.10 and 4.4.11. One can see that the assumption made in the present work produces satisfactory agreement between the experimental data and calculations.

4.4.6. Fragment mass distribution for ^{238}U fission by neutrons

We have also performed an analysis of the experimental data of fragment mass distributions from ^{238}U fission by neutrons with energies ranging from 2 to 200 MeV [4.4.27]. The basic purpose of the work was to find the dependence of model parameters on the excitation energy and angular momentum.

Referring to the parameters contained in Eq. (4.4.5), the following equations were obtained from an analysis of the experimental data:

$$A^I_{L,H} = \begin{cases} A_f/2 \mp 17.18 & \ell \le \ell_{cr} \\ A_f/2 & \ell > \ell_{cr} \end{cases} \quad (4.4.25)$$

where

$\ell_{cr} = 7\hbar$ is the critical value of the angular momentum, above which the asymmetric standard I fission channel is converted into the symmetric super long channel,
$A_f = A_0 - \bar{\nu}_{pre}$ is the mass of the fissioning nucleus after emission of pre-fission neutrons,
A_0 is the mass of the compound nucleus.

$$\bar{\nu}_{pre} = 6.77\left(\frac{(0.02E^*)^2}{1+(0.02E^*)^2} + \exp\left[-\frac{(22.9 - E^*)^2}{2.625^2}\right]\right) \quad (4.4.26)$$

where E^* is the excitation energy of the compound nucleus,

$$A^{II}_{L,H} = A_f/2 \mp 20.56 \quad (4.4.27)$$

$$\sigma_{A_I} = 2.81 + (1 - P_{LD}) \times 7.25 \quad (4.4.28)$$

$$\sigma_{A_{II}} = 5.29 + (1 - P_{LD}) \times 5.14 \quad (4.4.29)$$

$$\sigma_{A_S} = 5.28 + (1 - P_{LD}) \times 13.07 \quad (4.4.30)$$

$$W_I = 100(1 - P_{LD}) \quad (4.4.31)$$

$$W_{II} = 100 \times P_{LD} \quad (4.4.32)$$

P_{LD} is the function describing the conversion of an asymmetric fragment mass distribution into a symmetric form with increasing excitation energy of the fissioning nucleus:

TABLE 4.4.1. PARAMETERS INCLUDED IN Eqs (4.4.18)–(4.4.24)

Nucleus	W^0_{II}	$\sigma^0_{A_I}$	$\Delta\sigma^0_{A_I}$	$\sigma^0_{A_{II}}$	$\Delta\sigma^0_{A_{II}}$	A^I_H	ΔA_{II}	ℓ_{cr}	E_{LD}	ΔE_{LD}
^{239}Pu	70.4	7.5	9.9	9.4	7.1	135.0	23.0	$7\hbar$	58.7	7.3
^{240}Pu	51.0	5.2	29.3	8.1	3.2	136.0	24.5	$9\hbar$	66.2	16.8

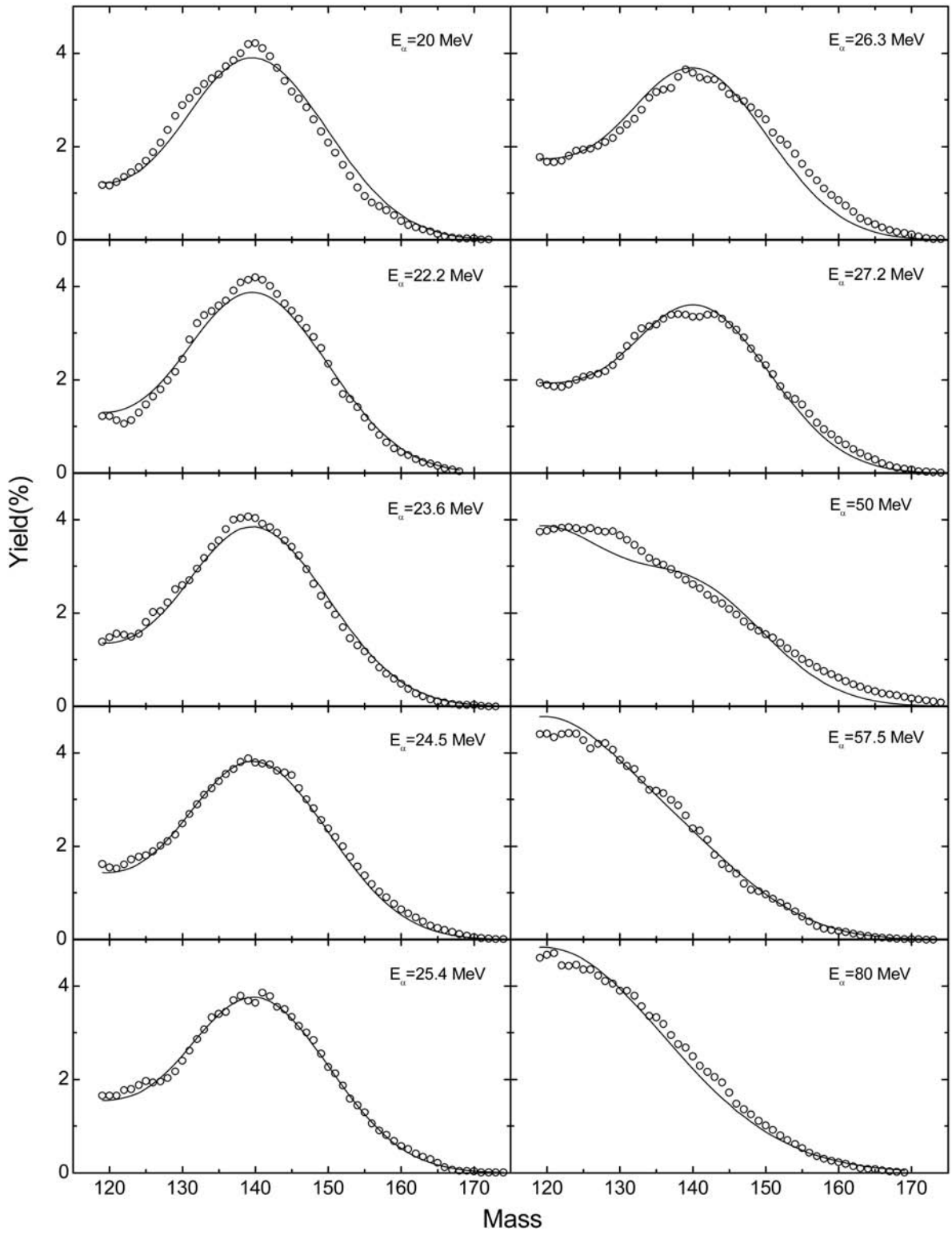

FIG. 4.4.10. Fragment mass distributions from fission of ^{239}Pu by α particles with energies of 20–80 MeV (points are the experimental data [4.4.7]; lines are the calculations, as described in the text).

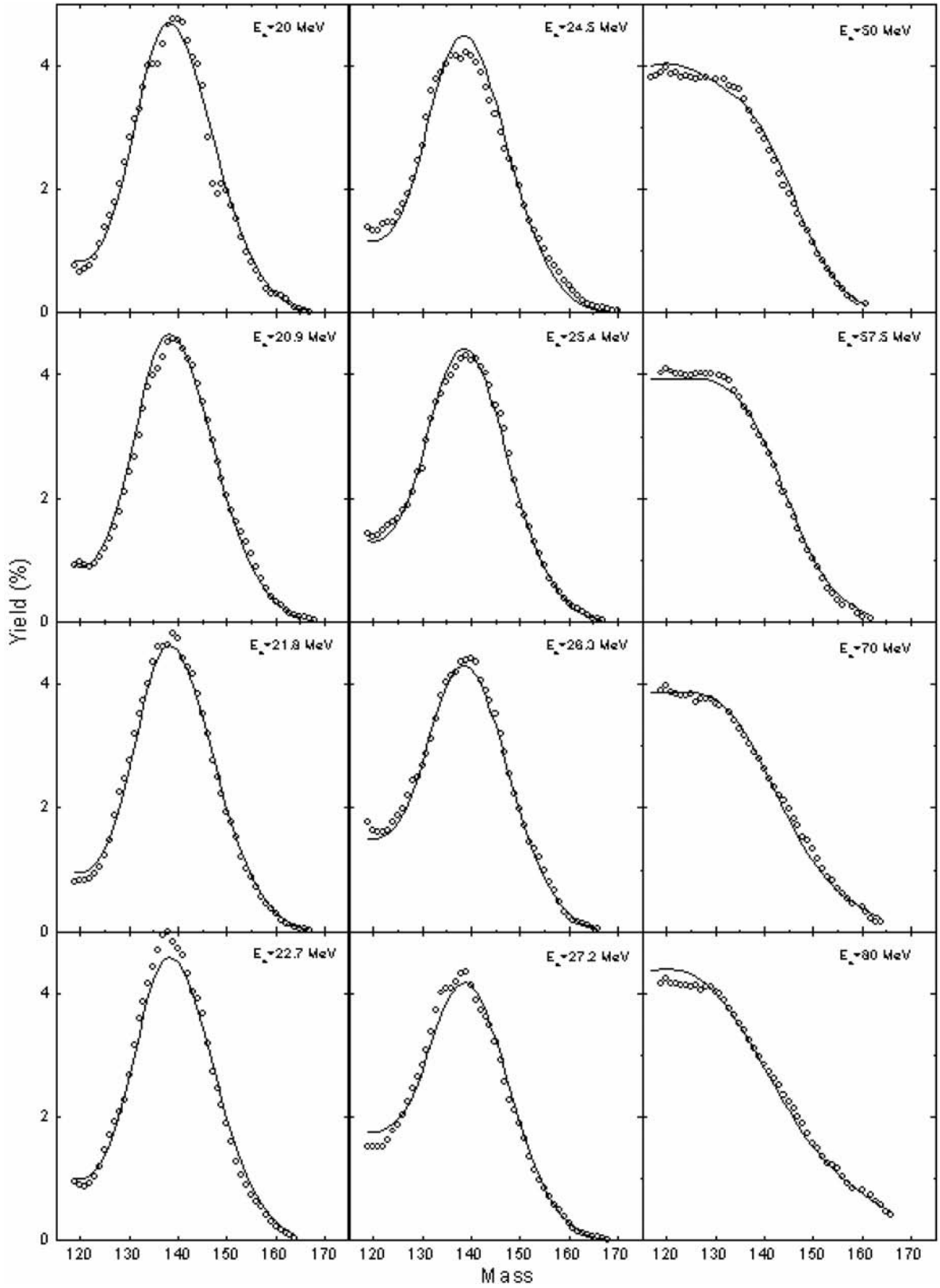

FIG. 4.4.11. Fragment mass distributions from fission of ^{240}Pu by α particles with energies of 20–80 MeV (points are the experimental data [4.4.7]; lines are the calculations, as described in the text).

$$P_{LD} = \left[1 + \exp\left(\frac{E^* - 44.7}{91.2}\right)\right]^{-1} \quad (4.4.33)$$

The data of Maslov were used for the transmission coefficients (T_l) [4.4.28]. These coefficients provide a good description of the cross-sections for the fission of ^{238}U by neutrons and take into account pre-fission neutron emission up to incident neutron energies of 200 MeV.

Zöller data [4.4.27] for pre-neutron emission fragment mass distributions from ^{238}U fission by neutrons with energies from 2 to 200 MeV are summarized in Figs 4.4.12–4.4.14. As can be seen from these figures, the assumption made in the present work results in satisfactory agreement between the experimental data and calculations over the whole energy range.

The following expressions were obtained from an analysis of Zöller data [4.4.27] to describe the post-neutron emission fragment mass distributions of ^{238}U fission by neutrons in this energy range:

$$A^I_{L,H} = \begin{cases} A_f/2 \mp 17.18 - \bar{\nu}^I_{L,H} & \ell \le \ell_{cr} \\ A_f/2 - \bar{\nu}_S & \ell > \ell_{cr} \end{cases} \quad (4.4.34)$$

$$A^{II}_{L,H} = A_f/2 \mp 20.56 - \bar{\nu}^{II}_{L,H} \quad (4.4.35)$$

where $\bar{\nu}^i_{L,H}$ are the average values of the neutrons emitted from fragments for the corresponding fission modes:

$$\begin{aligned} &\bar{\nu}^I_L = 3.26, \quad \bar{\nu}^I_H = 3.88, \\ &\bar{\nu}^{II}_L = 0.26, \quad \bar{\nu}^{II}_H = 3.6\ln(0.039E_n + 1.67), \\ &\bar{\nu}_S = 3.64 \end{aligned} \quad (4.4.36)$$

Descriptions of the post-neutron emission fragment mass distributions for ^{238}U fission by neutrons in the energy range from 2 to 200 MeV are summarized in Figs 4.4.15–4.4.17 and compared with the experimental data [4.4.27].

4.4.7. Fragment mass distribution for spontaneous fission

We have performed an analysis of the evaluated data on fragment mass distributions from spontaneous fission of nuclei [4.4.25] in order to determine the dependence of the model parameters on the mass and charge of the fissioning nuclei at zero excitation energy and angular momentum.

The following equations were obtained for the parameters appearing in Eq. (4.4.5):

$$A^I_H = 140, \quad A^I_L = A_f - A^I_H \quad (4.4.37)$$

$$A^{II}_H = 140, \quad A^{II}_L = A_f - A^{II}_H \quad (4.4.38)$$

$$A^{III}_H = 146, \quad A^{III}_L = A_f - A^{III}_H \quad (4.4.39)$$

$$\begin{aligned} &A_f = A_0 - \bar{\nu}, \\ &\bar{\nu} = 5.355 - 0.644(Z_0 - 96) + 0.386(A_0 - 252) \end{aligned} \quad (4.4.40)$$

$$\sigma_{A_I} = 2.472 + 0.005(A_0 - 252) \quad (4.4.41)$$

$$\sigma_{A_{II}} = 4.140 + 0.041(Z_0 - 96)^2 + 0.082(A_0 - 252) \quad (4.4.42)$$

$$\sigma_{A_{III}} = 6.166 + 0.027(Z_0 - 96)^2 + 0.150(A_0 - 252) \quad (4.4.43)$$

$$W_I = 14.0 - 2.993|Z_0 - 96| + 2.694|A_0 - 252| \quad (4.4.44)$$

$$W_{III} = 34.222 - 1.445|Z_0 - 96| + 2.427|A_0 - 252| \quad (4.4.45)$$

$$W_{II} = 100 - W_I - W_{III} \quad (4.4.46)$$

The fragment mass distributions for the spontaneous fission of ^{252}Cf nuclei are shown in Fig. 4.4.18, where our calculations are also compared with the evaluated data [4.4.25] and calculations of Wahl [4.4.29]. Figure 4.4.19 compares evaluated data [4.4.25] with our calculations of fragment mass distribution for the spontaneous fission of nuclei from ^{240}Pu up to ^{256}Fm.

Results of the analysis of the fragment mass distributions from spontaneous fission show the absence of the symmetric fission contribution, in agreement with the results of Wahl [4.4.29]. However, at least three asymmetric modes need to be taken into account for a satisfactory description of fragment mass distributions from the spontaneous fission of nuclei with Z > 94.

4.4.8. Description of fission fragment mass and charge distributions

A phenomenological approach has been developed in the present study to describe the

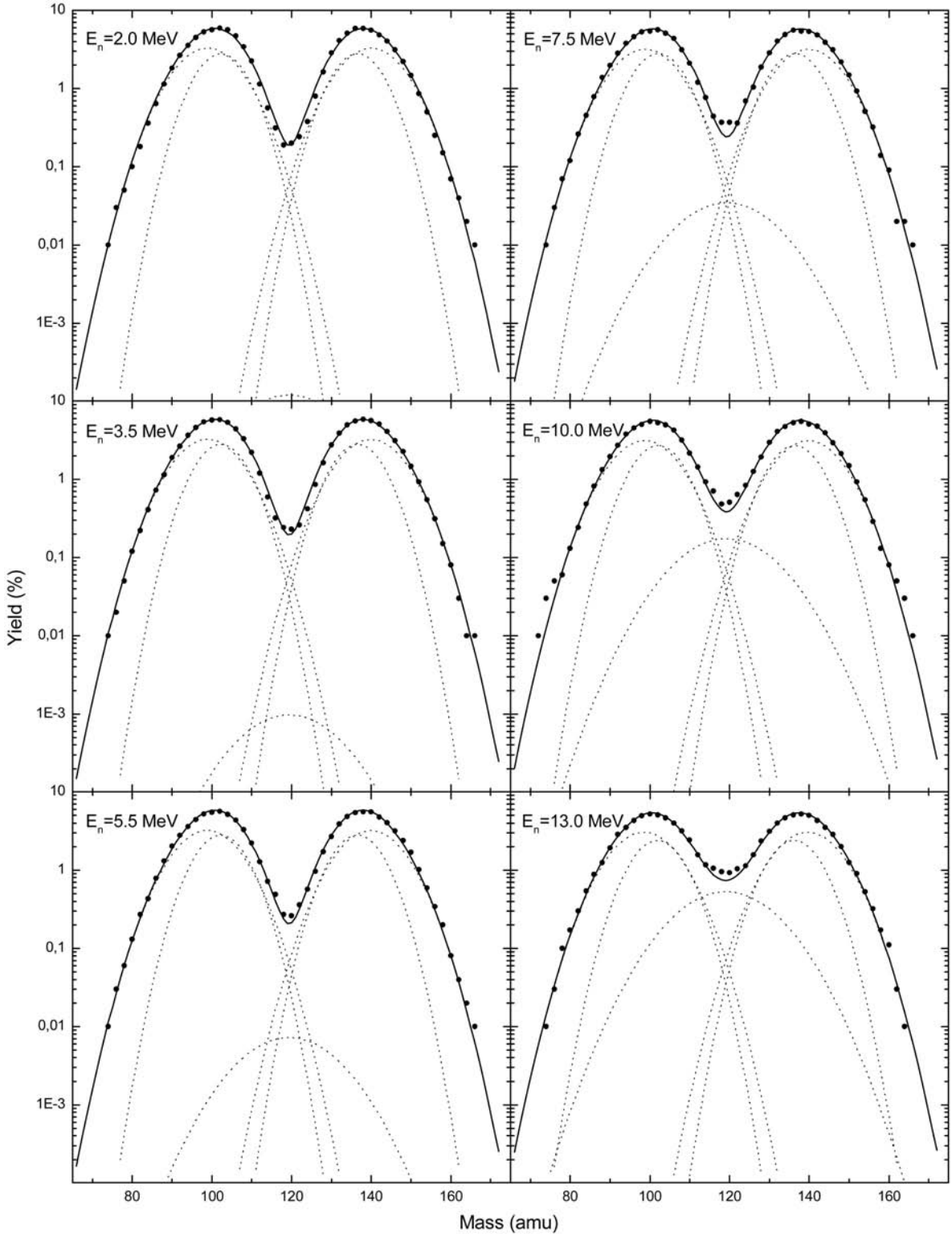

FIG. 4.4.12. Pre-neutron emission mass distributions from ^{238}U fission induced by neutrons (points are experimental data [4.4.27]; the lines are our calculations); neutron energies are given in the figure.

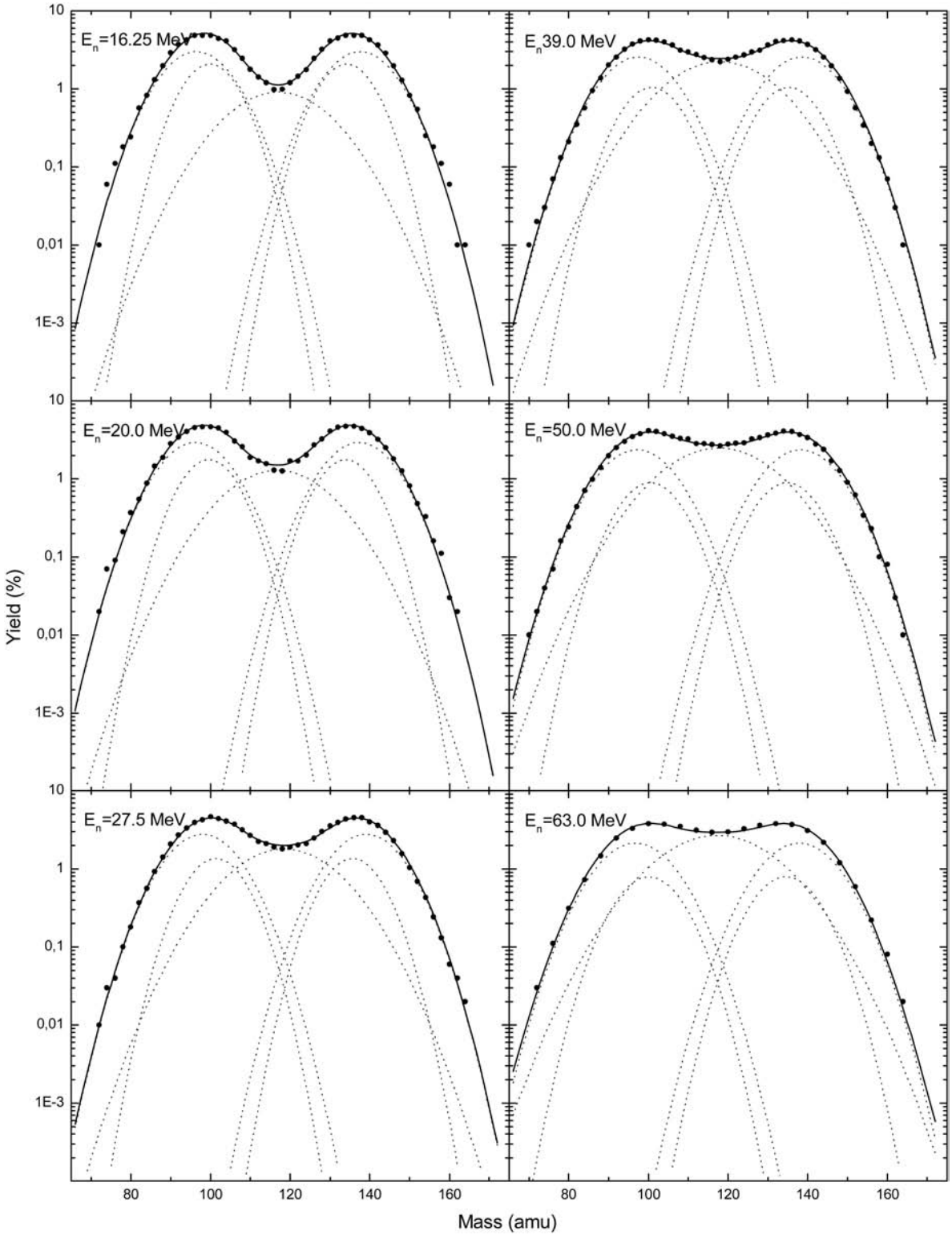

FIG. 4.4.13. Pre-neutron emission mass distributions from ^{238}U fission induced by neutrons (points are experimental data [4.4.27]; the lines are our calculations); neutron energies are given in the figure.

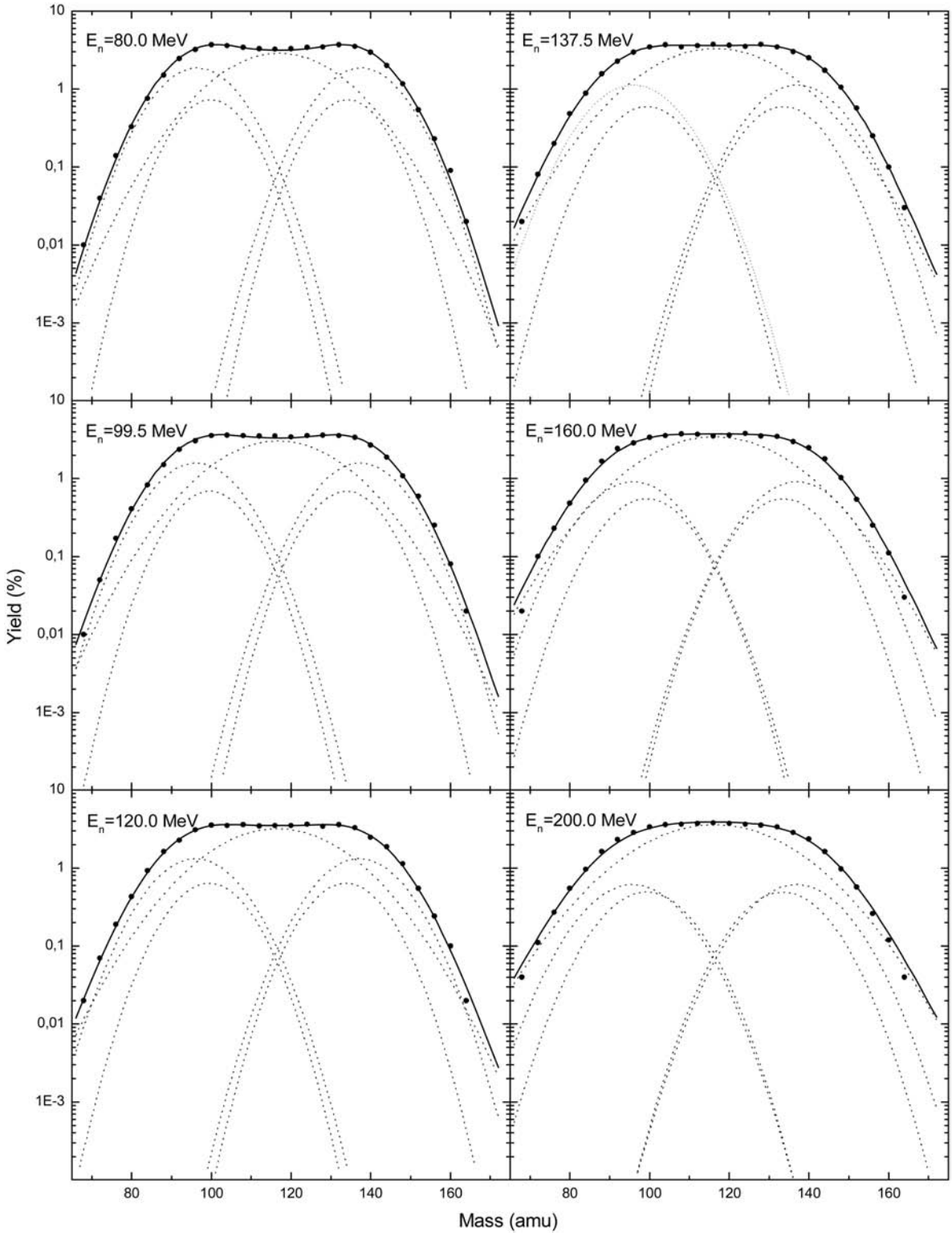

FIG. 4.4.14. Pre-neutron emission mass distributions from ^{238}U fission induced by neutrons (points are experimental data [4.4.27]; the lines are our calculations); neutron energies are given in the figure.

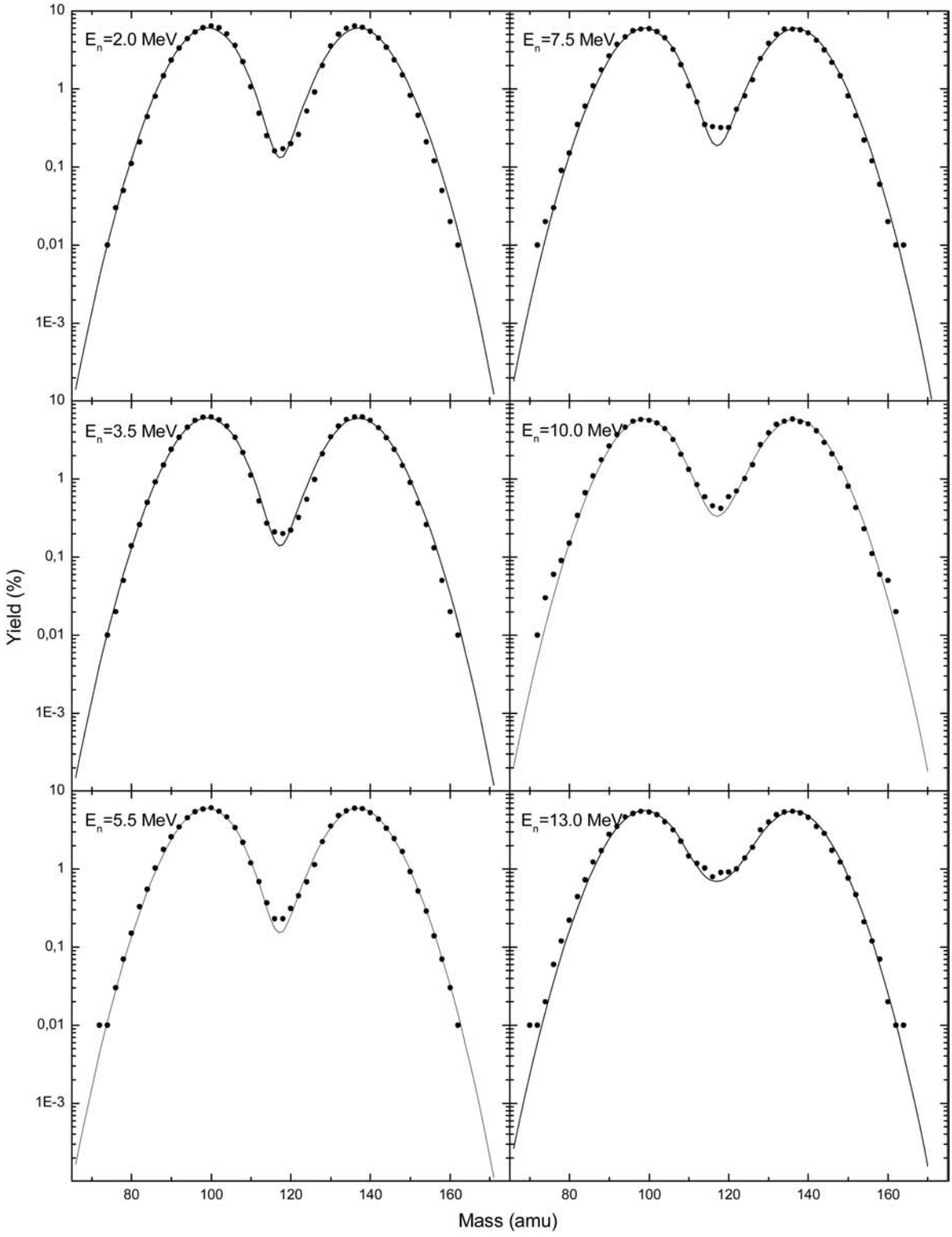

FIG. 4.4.15. Post-neutron emission mass distributions from ^{238}U fission induced by neutrons (points are experimental data [4.4.27]; the lines are our calculations); neutron energies are given in the figure.

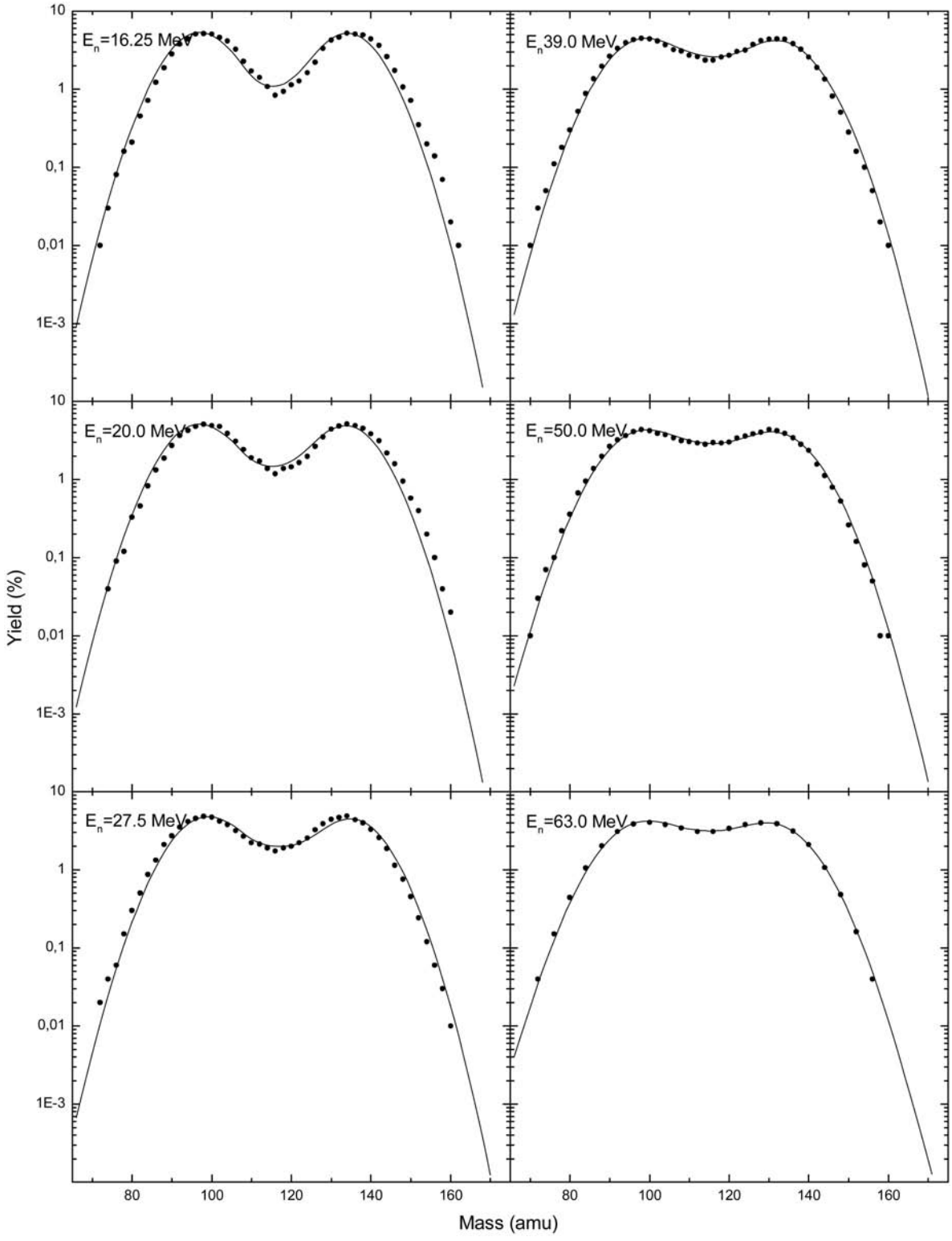

FIG. 4.4.16. Post-neutron emission mass distributions from ^{238}U fission induced by neutrons (points are experimental data [4.4.27]; the lines are our calculations); neutron energies are given in the figure.

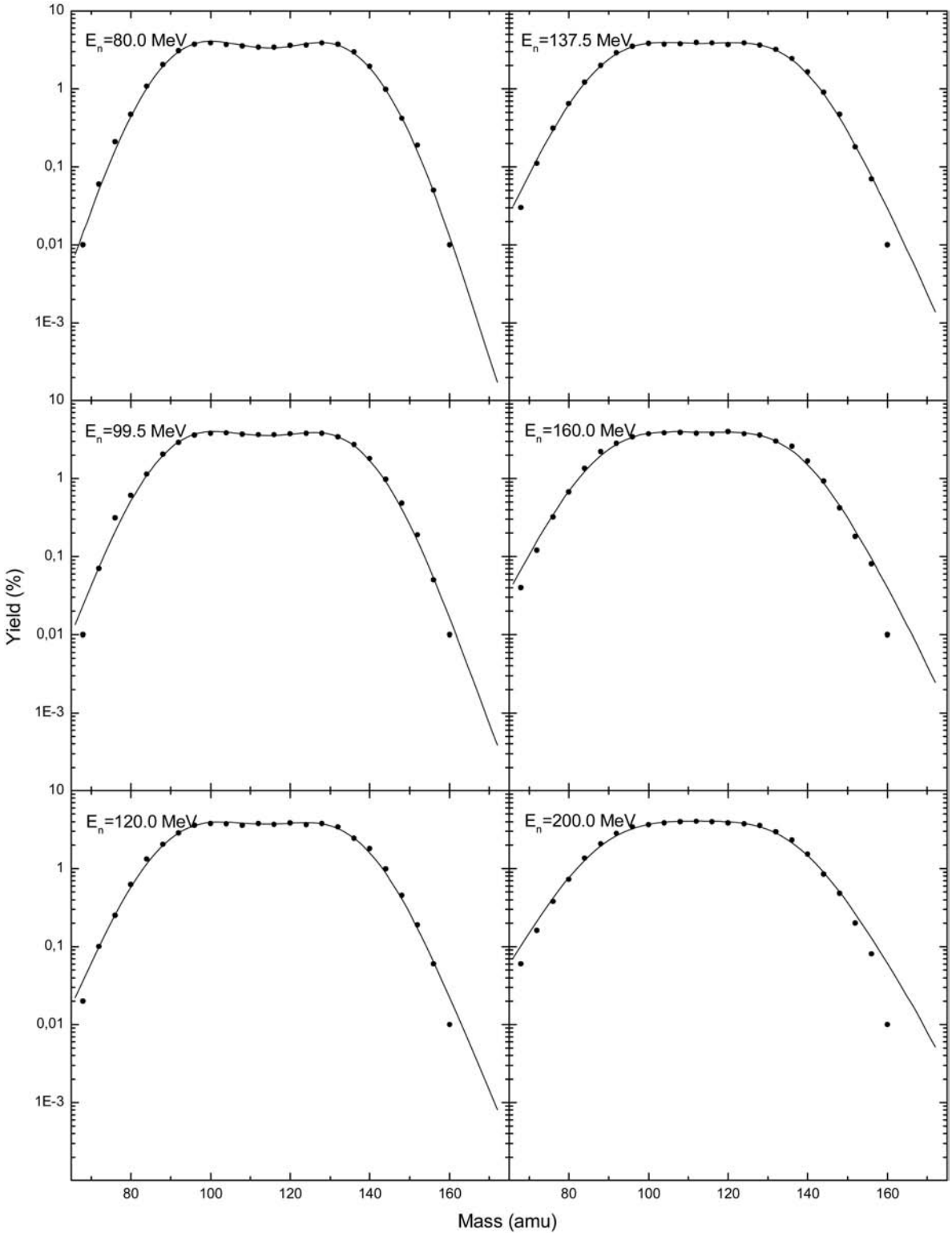

FIG. 4.4.17. Post-neutron emission mass distributions from ^{238}U fission induced by neutrons (points are experimental data [4.4.27]; the lines are our calculations); neutron energies are given in the figure.

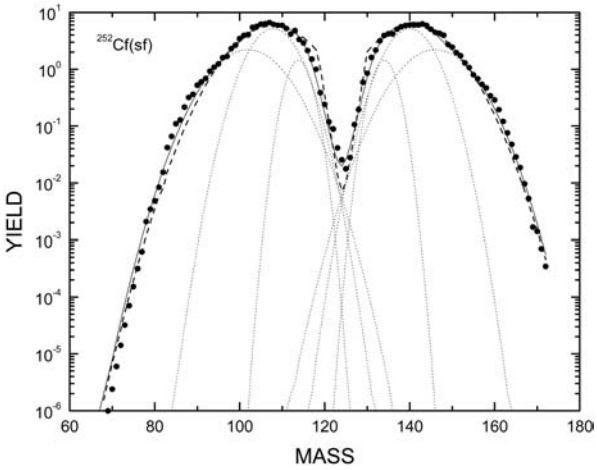

FIG. 4.4.18. Fragment mass distributions from spontaneous fission of ^{252}Cf (points are evaluated data [4.4.25]; the solid line is our calculations, as described in the text; the dashed line is the Wahl calculation [4.4.29]).

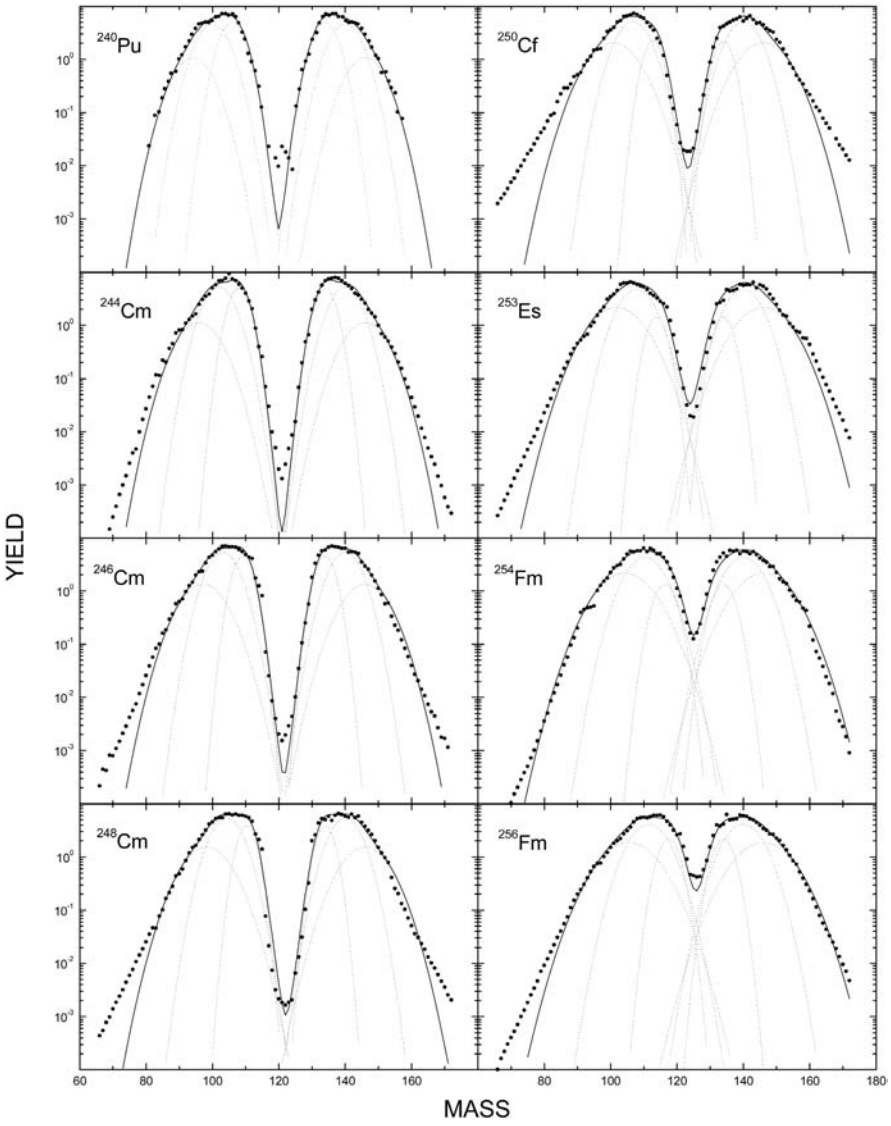

FIG. 4.4.19. Fragment mass distributions for spontaneous fission of nuclei (points are evaluated data [4.4.25]; lines are the calculations as described in the text).

fragment mass and charge distributions and account for quantum-mechanical transmission of the real fission barriers [4.4.30]. The fission barrier in the liquid drop model is determined by the interaction of nuclear forces that are modelled in terms of the surface tension of the liquid drop and the repulsive Coulomb forces of the nuclear charge. Hill and Wheeler [4.4.31] have developed the following expression to describe the penetration of the parabolic fission barrier:

$$P_f(E) = 1\Big/\left(1+\exp\left[\frac{E_f - E}{\hbar\omega_f/2\pi}\right]\right) \qquad (4.4.47)$$

where

E_f is the height of the fission barrier,
$\hbar\omega_f/2\pi$ is the width of the fission barrier expressed as the frequency of an inverted harmonic oscillator potential.

According to the concept of Bohr [4.4.32], above the fission barrier there are a number of transitive excited states with excitation energy ε_i (fission channels). The total fission width is the sum of the partial widths of these fission channels:

$$T_f^{J^\pi}(E) = \sum_i 1\Big/\left(1+\exp\left[\frac{E_f + \varepsilon_i - E}{\hbar\omega_f/2\pi}\right]\right) \qquad (4.4.48)$$

However, for the majority of actinides, the real form of the fission barrier is more complex [4.4.33] and consists of two barriers with a second minimum between them that arises from the shell effects in a highly deformed nucleus. The penetrability of the double humped fission barrier has an energy dependence based on the Lorentz function:

$$P_f(E) = \frac{\Gamma_A\Gamma_B}{(E_n - E)^2 + (\Gamma_A + \Gamma_B)^2/4}, \qquad \Gamma_x = \frac{\hbar\omega_{II}}{2\pi}P_x, \quad x = A, B, \ldots \qquad (4.4.49)$$

where

P_A and P_B are the penetrabilities of separate barriers,
Γ_A and Γ_B are the partial fission widths for separate barriers,
$\hbar\omega_{II}/2\pi$ is the characteristic frequency of the intermediate well.

Analysis of the experimental data on fragment mass and charge distributions from neutron fission [4.4.34] shows that the even–odd effects in charge distributions are more pronounced (~25–30%) than in neutron number distributions where the even–odd effects do not exceed 6%. Taking these facts into account, the formation of the proton and neutron structure of fragments can be assumed to occur at different stages of the deformation of a nucleus undergoing fission. From these results the fission process of heavy nuclei can be interpreted as follows: during the initial deformation of a nucleus undergoing fission, the nuclear charge is polarized and then separated when passing through the inner barrier. The formation of proton and inner neutron shells of fission fragments takes place in the second well, and the outer neutron shells are filled when passing through the outer barrier, followed by the descent of the nucleus to the scission point. After the passage through the inner barrier, a nucleus can either tunnel at once through the outer barrier or be reflected away. In the first case, fast symmetric fission is observed as the nucleus is axially symmetric after passage through the inner barrier and has essentially no time to change shape during passage through the outer barrier. In the second case, asymmetric fission dominates, with an ordering of the shell structure of fragments in the second well and passage through the second barrier.

Proceeding from the above mentioned assumptions, the following expression for the penetrability of barrier A can be written:

$$T_A = 1\Big/\left[1+\exp\left(\frac{|Z_0/2 - z| - \Delta z}{\sigma_z}\right)\right] \qquad (4.4.50)$$

Subsequent penetration of barrier B is defined by the ratio:

$$T_B = 1\Big/\left[1+\exp\left(\frac{\Delta n - |N_0/2 - n|}{\sigma_n}\right)\right] \qquad (4.4.51)$$

When describing the quasi-molecular states, all even–even states in the second well must be taken into account, and the following equation is obtained:

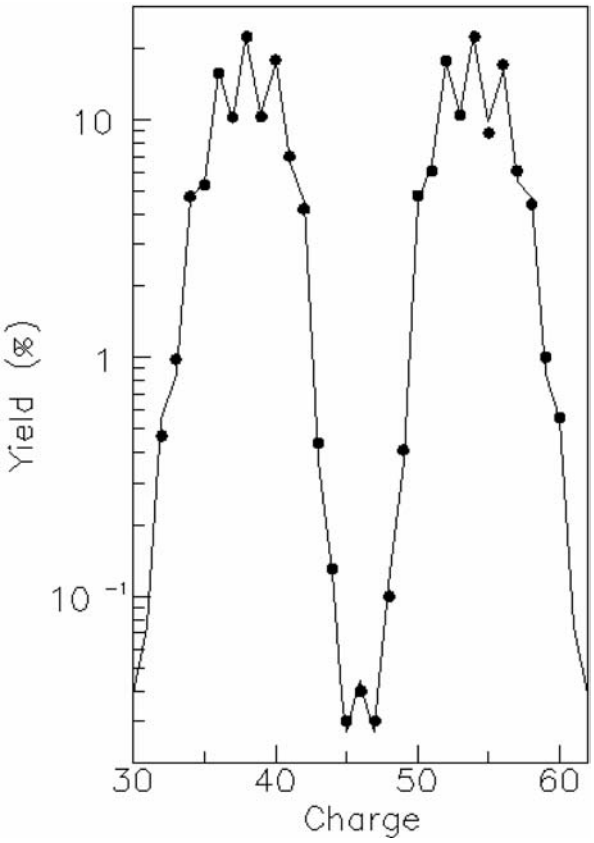

FIG. 4.4.20. Fragment charge distributions in ^{235}U fission induced by thermal neutrons (points are experimental data [4.4.35]; the line is our calculation).

$$G = \sum_{I,j} I \Big/ \left(q_z^2 - 2\rho q_z q_n + q_n^2 + \frac{\Gamma_{II}^2}{4} \right) \qquad (4.4.52)$$

where

$$\begin{aligned} q_z &= \left(\left| Z_0/2 - z \right| - 2j + \delta_p \right) \Big/ \sigma_z \\ q_n &= \left(\left| N_0/2 - n \right| - 2i + \delta_n \right) \Big/ \sigma_n \end{aligned} \qquad (4.4.53)$$

Combining Eqs (4.4.50)–(4.4.53), the following expression is obtained for the penetrability of the double humped fission barrier:

$$P_f(z,n) = \alpha T_A G \left[T_B + \beta \left(1 - T_B \right) \right] \qquad (4.4.54)$$

where α and β are normalization constants.

Calculations are compared in Fig. 4.4.20 with recommended experimental fragment charge distributions from ^{235}U fission by thermal neutrons [4.4.35]. Both the general shape of the charge distribution and the fine structure are well described by the calculations. The fragment mass distribution for

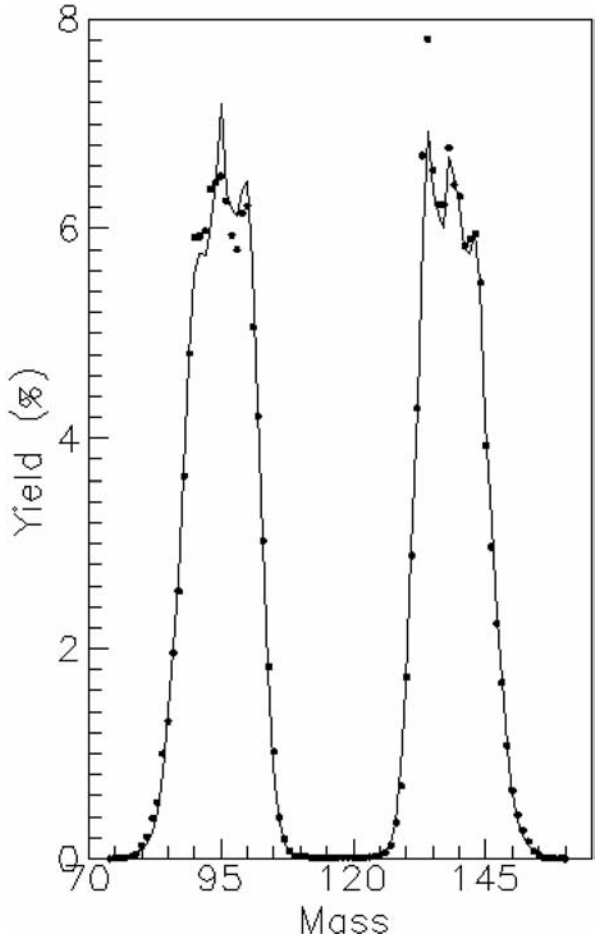

FIG. 4.4.21. Fragment mass distributions in ^{235}U fission induced by thermal neutrons (points are experimental data [4.4.35]; the line is our calculation).

the same reaction is presented in Fig. 4.4.21. Our approach also reproduces rather well the general shape and the fine structure of the distribution in this case. The phenomenological method offered in this work would appear to give a qualitatively new approach to the systematization of experimental data for investigating the systematics of fission fragment mass and charge distributions, and allows one to study the structure of a double humped fission barrier and the dependence on the characteristics of a fissioning nucleus.

4.4.9. Concluding remarks

An analysis of the total fission cross-sections has been carried out for the interaction of 20–140 MeV α particles with ^{232}Th, ^{235}U, ^{236}U and ^{238}U nuclei in order to study the cross-section dependence of the fissioning nucleus formation on excitation energy and transferred angular momentum. This approach leads to the derivation

of the energy dependence of the fusion radius and the critical value of the angular momentum leading to the formation of the fissioning system in the interaction of α particles with uranium nuclei in the energy range up to 140 MeV. The deduced dependences were used to analyse the experimental data for actinide fission by α particles.

Detailed analyses of experimental nuclei fission data show that the process of fission fragment formation depends not only on the temperature but also on the total angular momentum of the fissioning nucleus. Such studies were made of ^{236}U, ^{238}U, ^{239}Pu and ^{240}Pu nuclei formed in reactions with neutrons, γ quanta and α particles of excitation energies up to 200 MeV. The dependence of parameters from the Brosa model on the excitation energy and transferred angular momentum of a fissioning nucleus was noted.

A phenomenological description of the fission fragment mass and charge distributions has been developed that also accounts for the quantum-mechanical transmission of a real fission barrier [4.4.30]. This phenomenological method gives a qualitatively new approach to the systematization of experimental data, and the modelling of changes in the mass and charge fission fragment distributions; the structure of a double humped fission barrier and dependence on the characteristics of a fissioning nucleus can also be studied.

ACKNOWLEDGEMENTS

The author is indebted to M. Lammer for supporting the work and partial translations of Zöller's thesis, to A.A. Goverdovskii for help, and to V.M. Maslov for providing numerical data of transmission coefficients, as well as to N.I. Zaika, V.P. Tokarev and V.S. Semenov for many discussions concerning these calculations and their assistance during the work.

REFERENCES TO SECTION 4.4

[4.4.1] SWIATECKY, W.E., The dynamics of the fusion of two nuclei, Nucl. Phys. A **376** (1982) 275–291.

[4.4.2] CHUBARJAN, G.G., et al., Mass-energy distributions of fragments and angular momentum in fission of excited nuclei, Yad. Fiz. **56** (1993) 3–29.

[4.4.3] ZAIKA, N.I., et al., Dependence of fragment mass distributions on angular momentum of fissioning nucleus, Ukr. Phys. J. **45** (2000) 908–913.

[4.4.4] KIBKALO, Yu.V., Peculiarities of fission of actinide nuclei formed in reactions with light particles, Sci. Pap. Inst. Nucl. Res. Kiev **1** (2001) 52–62.

[4.4.5] THIERENS, H., et al., Kinetic energy and fragment mass distributions for ^{240}Pu (sf), ^{239}Pu ($n_{th,}$f), and ^{240}Pu (γ,f), Phys. Rev. C **23** (1981) 2104–2113.

[4.4.6] SURIN, V.M., et al., Yields and kinetic energies of fragments from fission of ^{233}U and ^{239}Pu by neutrons with energy 5.5 and 15 MeV, Sov. J. Nucl. Phys. **14** (1971) 935–938.

[4.4.7] ZAIKA, N.I., et al., Peculiarities of fragment mass and energy distributions from ^{235}U and ^{236}U fission by α particles of medium energies (<80 MeV), Sov. J. Nucl. Phys. **42** (1985) 304–311.

[4.4.8] GLASS, D., MOSEL, U., On the critical distance in fusion reactions, Nucl. Phys. A **237** (1975) 429–440.

[4.4.9] LEFORT, M., Various processes occurring in strong interactions between heavy ions: Compound nucleus formation, incomplete fusion and quasifission, Phys. Rev. C **12** (1975) 686–690.

[4.4.10] VANDENBOSH, R., Microscopic calculation of fission-fragment anisotropy for nuclei exhibiting a double barrier, Phys. Rev. C **7** (1973) 2092–2096.

[4.4.11] RAMAMURTHY, V.S., et al., Excitation dependence of shell effects on nuclear level densities and fission fragment anisotropy, Phys. Rev. Lett. **25** (1970) 386–390.

[4.4.12] KOLOMIEC, V.M., STRUTINSKY, V.M., Materials of the 8th winter school, LINP AS, USSR **2** (1973) 483–489.

[4.4.13] ZAIKA, N.I., et al., Variances of distributions of projections of an angular momentum for the interaction of nuclei with α-particles, Sov. J. Nucl. Phys. **41** (1985) 1454–1459.

[4.4.14] MURTHY, K.H.N., et al., Transmission coefficient for light projectiles, Z. Phys. A **305** (1982) 73–79; Z. Phys. A **307** (1982) 374–380.

[4.4.15] ZAIKA, N.I., et al., An energy dependence of an anisotropy for actinide nuclei fission by α-particles with energy 19–27 MeV, Sov. J. Nucl. Phys. **31** (1985) 43–46.

[4.4.16] VIOLA, V.R., Jr., et al., Linear momentum transfer in non-relativistic nucleus-nucleus collisions, Phys. Rev. C **26** (1982) 178–187.

[4.4.17] FOREMAN, B.M., Jr., WALTER, M., et al., Spallation-fission competition in heavy element reactions: Th^{232} + He^{4} and U^{233} + d, Phys. Rev. **116** (1959) 382–392.

[4.4.18] VANDENBOSCH, R., et al., Spallation-fission competition in heaviest elements; helium-ion-induced reactions in uranium isotopes, Phys. Rev. **111** (1958) 1358–1373.
[4.4.19] BROSA, U., et al., Nuclear scission, Phys. Rep. **197** (1990) 167–262.
[4.4.20] BROSA, U., et al., Nuclear scission, Nucl. Phys. A **502** (1989) 423c–442c.
[4.4.21] TIE-SHUAN FAN, et al., Study of multichannel theory for the neutron induced fission of actinide nuclei, Nucl. Phys. A **591** (1995) 161–181.
[4.4.22] STRAEDE, C., et al., ^{235}U (n,f) fragment mass, kinetic energy and angular distributions for incident neutron energies between thermal and 6 MeV, Nucl. Phys. A **462** (1987) 85–108.
[4.4.23] ZAIKA, N.I., et al., Fission fragment mass and energy distributions of ^{232}Th by α particles with energies 21–26.4 MeV, Ukr. Phys. J. **34** (1989) 493–498.
[4.4.24] KONDRATKO, M.Ga., et al., Product yields from photofission of ^{239}Pu, Sov. J. At. Energy **50** (1981) 41–43.
[4.4.25] ENGLAND, T.R., RIDER, B.F., Fission Product Yield Evaluation for the IAEA Co-ordinated Research Program and for the US Evaluated Nuclear Data Files, LA-UR-93-3106 (ENDF-349), IAEA, Vienna (1994).
[4.4.26] GUNTHER, W., et al., Symmetric and asymmetric yields in the photofission of ^{232}Th, ^{235}U, ^{238}U and ^{239}Pu, Z. Phys. A **295** (1980) 333–340.
[4.4.27] ZÖLLER, C.M., Untersuchung der neutroneninduzierten Spaltung von ^{238}U im Energiebereich von 1 MeV bis 500 MeV, PhD thesis, Technische Universität Darmstadt, Germany (1995).
[4.4.28] MASLOV, V.M., Belarus Academy of Sciences, personal communication, 2001.
[4.4.29] INTERNATIONAL ATOMIC ENERGY AGENCY, Compilation and Evaluation of Fission Yield Nuclear Data, IAEA-TECDOC-1168, Vienna (2000) 45–57.
[4.4.30] KIBKALO, Yu.V., Phenomenological Description of Fission Fragment Mass and Charge Distributions, Institute for Nuclear Research, Kiev (1997) 123–127.
[4.4.31] HILL, D.L., WHEELER, J.A., Nuclear constitution and the interpretation of fission phenomena, Phys. Rev. **89** (1953) 1102–1145.
[4.4.32] BOHR, A., Peaceful Uses of Atomic Energy (Proc. Int. Conf. Geneva, 1955), Vol. 2, Physics: Research Reactors, United Nations, New York (1956) 220.
[4.4.33] STRUTINSKY, V.M., Shell effects in nuclear masses and deformation energies, Nucl. Phys. A **95** (1967) 420–442.
[4.4.34] BOCQUET, J.P., BRISSOT, R., Mass, energy and nuclear charge distribution of fission fragments, Nucl. Phys. A **502** (1989) 213–232.
[4.4.35] GANGRSKY, Yu.P., et al., Fission fragments of nuclei, Energoatomizdat, Moscow (1986).

4.5. MODAL APPROACH TO THE DESCRIPTION OF FRAGMENT MASS YIELDS IN NEUTRON AND PROTON INDUCED FISSION OF ACTINIDES AT INCIDENT PARTICLE ENERGIES FROM 5 TO 200 MeV

D.M. Gorodisskiy, S.I. Mulgin, A.Ya. Rusanov, S.V. Zhdanov
National Nuclear Centre, Kazakhstan

Experimental and analytical work has been performed to obtain information on the relative yields, mean values and variances of masses and kinetic energies of fragments from the fission of actinide nuclei through independent fission modes. Regularities in the behaviour of these characteristics with respect to their dependence on the nucleonic composition of the fissile actinides and incident particle (proton and neutron) kinetic energies have been used to develop new systematics for fragment mass yields from the fission of target nuclei from Th to Bk at incident particle energies between 5 and 200 MeV.

4.5.1. Introduction

Numerous experimental investigations of the mass and energy distributions of fragments in the fission of nuclei from Pb to No [4.5.1] have confirmed the validity of a hypothesis concerning the existence of independent fission modes, as first stated by Turkevich and Niday [4.5.2]. This hypothesis has received physical substantiation in theoretical works by Pashkevich [4.5.3] and Brosa et al. [4.5.4]. These studies have shown that multimodality of the mass and energy distributions of fission fragments is caused by the valley structure of the deformation potential energy surface of a fissioning nucleus.

The experimental mass and energy distributions from the fission of actinide nuclei are usually assumed to consist of different mass and energy distributions for three independent fission modes: one symmetric (S) and two asymmetric — standard 1 (S1) and standard 2 (S2). Mode S is mainly conditioned by the liquid drop properties of nuclear matter, and therefore the most probable values of fragment masses M are close to $A_{CN}/2$, where A_{CN} is the compound nucleus mass. The asymmetric mode S1 with average masses of the heavy fragments $M_H \approx 134$ and high kinetic energies is due to the formation of spherical heavy fragments with Z_{FH} and N_{FH} (proton and neutron numbers of a heavy fragment) close to the magic numbers 50 and 82, respectively. The predominant asymmetric mode S2 is characterized by average masses of the heavy fragments $M_H \approx 140$, and kinetic energies are 10–12 MeV less than those of the S1 mode. Usually the origin of mode S2 is attributed to the deformed neutron shell closure $N \approx 88$ in the heavy fragments (see, e.g., Ref. [4.5.5]). Recently, the existence of an additional asymmetric mode S3, conditioned by the close to sphere shells formed in light fragments, has been experimentally revealed [4.5.6].

One of the most promising procedures for elaborating the mass and energy distribution calculation technique consists in obtaining quantitative information on the dependences of the basic characteristics of distinct fission modes (relative mass yields, average fragment masses and charges, kinetic energies of fragments, variations of masses, charges and energies, etc.) on the nucleon composition and the excitation energy of a fissioning nucleus. This method reveals the main regularities of their behaviour and permits reconstruction of the observed mass and energy distributions as a superposition of the mass and energy distributions of the distinct modes. In order to be successful in the realization of this approach, a rather large set of experimental data usable for a comparative quantitative analysis is needed, and an appropriate method to extract the characteristics of the modes from the experimental mass and energy distributions, since the distinct modes are rarely observed directly in the fission of actinides.

An analysis of literature data shows that investigators in different countries concentrated basically on the studies of spontaneous fission and low energy neutron induced fission of the actinides. In particular, there is only one study in which the same experimental technique has been employed to measure the mass and energy distributions of fragments from neutron induced fission of ^{238}U at neutron energies from 1 to 450 MeV [4.5.7].

Mass and energy distributions measured in reactions with protons can be included in the analysis to compensate partially for the lack of

available high energy neutron induced fission data on the basis of the following considerations. The heavy nucleus fission reaction passes through a stage of compound nucleus formation in which the mass and energy distributions of fragments from the fission of the nucleus with given nucleon composition, excitation energy and angular momentum do not depend on the mode of formation of the compound nucleus. Protons as well as neutrons introduce rather small angular momentum into the fissioning nucleus. Of course there are some features of direct and pre-equilibrium reactions with neutrons and protons, but they have no decisive influence on the majority of the basic characteristics of the distinct fission modes, as a preliminary analysis of the data has shown. These circumstances allow the expansion of the experimental database with respect to both (a) an increasing incident particle energy range and (b) possibilities to study the mass and energy distributions for important fissioning minor actinides from the Np and Am isotopes, where experiments with Np and Am target nuclei in neutron induced fission are rather difficult to perform due to the radiation safety requirements in handling highly radiotoxic target materials.

The mass and energy distributions in the proton induced fission have been spectroscopically measured in terms of the coincident fission fragments by means of surface barrier detectors for the following compound nuclei:

^{234,236,237,239}Np, ^{239,240,241,243}Am, ^{245}Bk at proton energy E_p = 10.3 MeV;

^{234,236,237,239}Np, ^{240,241,243}Am at proton energy E_p = 22.0 MeV;

^{233}Pa and ^{236}Np at proton energy E_p = 7.4–30.0 MeV.

Another problem to be solved in the multimodal approach is connected with the deconvolution of the experimental mass and energy distributions into the mass and energy distributions of distinct fission modes. For this purpose, a new method of multicomponent analysis has been developed free from any assumptions about the shapes of the mass distributions of distinct modes. This method was applied to the analysis of the available experimental information.

This analysis revealed regularities in the behaviour of the fission fragment mass yields that proved to be particularly useful in developing the predictive systematics of the yields. The systematics have been realized in the form of the PYF computer code (Program for Yields from Fission), which allows calculation of the pre- and post-neutron emission fragment mass yields in the proton and neutron induced fission of target nuclei ranging from Th to Bk for incident particle energies of 5–200 MeV.

4.5.2. Experiments

4.5.2.1. Experimental technique

Measurements have been carried out with external beams from the Almaty isochronous cyclotron U-150, which enables the protons to be accelerated in the energy range from 7.4 to 30.0 MeV within energy steps of about 2–3 MeV. A pair of Si–Au surface barrier detectors and eight targets are located in the vacuum area of a fission chamber. The targets of fissile isotopes were in the form of layers of thickness 20–40 μg/cm^2, made from chlorides of the corresponding elements by vacuum evaporation on 60 μg/cm^2 backings of Al_2O_3. The investigated isotope was enriched to ≥99.98% in all cases.

Mass and energy distributions (MEDs) have been measured by the fast spectrometry of coincident fragments, where background events have been identified by their characteristic flight time difference [4.5.8]. This version of the experimental technique differs from the commonly used method in that the short current signals with a pulse length of about 7×10^{-8} s and a front of about 5×10^{-9} s are used in the time and spectrometric channels. Thus the probability of 'false' events, such as random coincidences of pulses from fragments belonging to different fission events, and random overlapping of the pulses from a fragment and a beam particle scattered in the target, decreases by a factor of almost 10 in comparison with the traditional technique.

During the experiment, the following information has been recorded for every fission event:

Q_1, Q_2 — values of the charges induced by fragments in both detectors;

τ_1, τ_2 — rates of pulse rise;

δT_{exp} — difference in flight times of two fragments.

This information was used for the preliminary selection of fission events with the aim of decreasing the contribution of random coincidences, events distorted by overlapping pulses, and fission events accompanied by fission fragment energy losses by scattering on nuclei of targets or detectors. Q_1, Q_2 were used to calculate the kinetic energies E_k and masses M of both fragments on the basis of the conservation of mass, energy and linear momentum. Then these data and the data of the target detector flight lengths were used to determine the calculated differences in flight times, δT_{cal}. The experimental values of δT_{exp} were corrected, taking into account the time delays caused by the plasma effects in detectors [4.5.9]. The values of these corrections have been determined from the analysis of the data on τ_1, τ_2 according to Ref. [4.5.8]. The selection of the 'true' fission events was based on the condition $|\delta T_{exp} - \delta T_{cal}| \leq 2\sigma_{tot} \approx 4 \times 10^{-10}$ s, where σ_{tot} is the total resolution time of the method, defined by the experimental uncertainties and the uncertainties in the emission of pre- and post-fission neutrons.

The rather small 'dead' time and low sensitivity to the background of scattered charged particles allowed intensive proton beams (up to 2 μA) to be used to measure the mass and energy distributions in the vicinity and below the Coulomb barrier. The number of events accumulated in these experiments was limited by the incident proton energy and the thickness of a given target to $2–5 \times 10^5$.

The quality of the MED experimental data obtained by (E_1–E_2) spectrometry is determined by both the experimental uncertainties and the correctness of the detector calibration procedure. (E_1–E_2) spectrometry with surface barrier detectors requires consideration of the so-called pulse height defect caused by uncontrolled losses of the fragment kinetic energy (R) in the entrance window of the detectors and the recombination of ions in plasma. The value of R has a complicated dependence on E_k and M of the fragments. Moreover, the behaviour of R(M,E) changes, depending on the silicon characteristics and the detector operation conditions (bias voltage, radiation damage dose, temperature, etc.). As a consequence of the complexity and difficulty of taking into account the influence of all these factors, the dependence of R(M,E) is usually described by empirical equations, the parameters of which are determined experimentally for each individual detector.

In the majority of studies of nuclear fission that use the (E_1–E_2) method, the pulse height defect is taken into account by applying equations proposed in Ref. [4.5.10], but the values of parameters in these equations for R(M,E) do not reflect individual features inherent to different detectors. Another widespread method for describing the R(M,E) dependences by means of a simple one-parametric equation is outlined in Ref. [4.5.11], but sometimes the variation of a single parameter is not enough to reproduce the features of R(M,E) for each detector. Under these circumstances, we used a more universal calibration procedure proposed in our work [4.5.12], where the two parametric empirical equation for R(M,E) has been established on the basis of the analysis of a large set of literature data:

$$R(M,E) = \frac{0.55E}{1+13.9E/M} + \alpha ME + \beta \qquad (4.5.1)$$

where α and β are parameters that take into account the individual properties of a given detector at a fixed bias voltage.

The verification of the application limit for Eq. (4.5.1) has shown that such a definition of R(M,E) reproduces with good accuracy the experimental data obtained for detectors with a resistivity $\rho \approx 200–2000$ Ω cm at a bias voltage U ≈ 10–200 V in a mass range M ≈ 40–200 amu and energy range E ≈ 10–150 MeV.

The dependence of the pulse charge Q on the fragment mass M and energy E is calculated from:

$$Q(M,E) = B\left(E - \left(\frac{0.55E}{1 + 13.9\,E/M} + \alpha ME + \beta E\right)\right) + C \qquad (4.5.2)$$

where B is the scale coefficient and C is the zero shift value. The numerical values for B and C are easily obtained from a standard procedure, where a precision pulse generator and several alpha sources are used. The parameters α and β are derived from a ^{252}Cf spontaneous fission fragment energy spectrum according to the following equation:

$$\alpha = \left(2.997\,\frac{\langle P_L\rangle - C}{B} - 3.953\,\frac{\langle P_H\rangle - C}{B} - 7.593\right) \times 10^{-4},$$

$$\beta = 0.04266\,\frac{\langle P_L\rangle - C}{B} - 0.04355\,\frac{\langle P_H\rangle - C}{B} + 1.0445 \qquad (4.5.3)$$

where $\langle P_L \rangle$, $\langle P_H \rangle$ are the mean channel numbers for the light and heavy fragment groups in a measured Q distribution from the spontaneous fission of ^{252}Cf.

Transforming the charge matrix $N(Q_1, Q_2)$ into the matrix of the fragment masses and total kinetic energies $N(M,E_k)$ without taking into account the neutron emission effects, $N(M,E_k)$ must be symmetric with respect to mass M = A/2. Thus for any values M and E_k the condition $N(M,E_k) = N(A - M,E_k)$ for complementary fragments must be satisfied within the statistical uncertainties. The control check has shown that our experimental matrices meet this requirement.

Due to the low count rate from the ^{252}Cf source, the calibration procedure was performed only at the beginning and end of the experiments. During the experiments, the stability of the detector characteristics was monitored, taking the mean values and variances of the Q_1 and Q_2 spectra from reactions ^{235}U + p as reference.

The experimental technique described above was used to measure the MEDs of fragments in the proton induced fission of compound nuclei ^{234,236,237,239}Np, ^{239,240,241,243}Am, ^{245}Bk at a proton energy of E_p = 10.3 MeV, ^{234,236,237,239}Np, ^{240,241,243}Am at E_p = 22.0 MeV, and ^{233}Pa, ^{236}Np at E_p = 7.4–30.0 MeV.

4.5.2.2. Corrections and experimental uncertainties

The experimental MEDs measured by the method of $(E_1–E_2)$ spectrometry are distorted by several factors such as fragment energy losses in the target and the detector entrance window, as well as neutron effects such as neutron emission from a nucleus before fission (including the pre-equilibrium stage of the compound nucleus formation) and evaporation of prompt neutrons from fission fragments. These energy losses change the measured absolute value of the total kinetic energy E_k and the E_1/E_2 ratio, which influences the derived mass asymmetry M_2/M_1 of the fragments. The magnitude of these alterations depends on the charge, mass and kinetic energy of the fragments, as well as the charge and mass of the materials of the target backings, the working layers and the detector entrance window. Therefore the introduction of corrections for energy losses necessitates rather intricate calculations.

One consideration is that the influence of the energy losses on the experimental results depends on the location at which the losses take place. Losses in target working layers and detector entrance windows (if their parameters are similar) cause similar alterations in the energies of fragments recorded by both detectors, which leads to some broadening of the measured MEDs and to a decrease of the absolute value of E_k (but on average does not violate the condition $N(M,E_k) = N(A-M,E_k)$). These effects have been considered in detail in Ref. [4.5.13], where it was shown that they have a strong influence only in the vicinities of sharp peaks and narrow valleys, and are observed only at low energy neutron induced and spontaneous fission of actinides. The MEDs are rather smooth in our range of incident particle energies, and therefore the influence of these effects can be ignored.

The energy losses in target backings not only decrease the absolute values of E_k but also cause asymmetric alterations of the MEDs, thus violating the condition $N(M,E_k) = N(A-M,E_k)$, especially for large mass asymmetries of fragments. This factor could be taken into account effectively if during the experiment all targets are oriented in such a way that only one of the two detectors registers fragments passing through the backings, and if during the calibration a pure backing is placed between this detector and the calibration source. In the present work, the corrections for losses in target backings were introduced in the calibration procedure.

The experimental matrices $N(M,E_k)$ for the neutron emission effects can be corrected if information is available on the number of pre- and post-fission neutrons ν, their energies and emission direction for every fission event, or matrices $\nu_{pre}(M,E_k)$ and $\nu_{post}(M,E_k)$. As a rule, such information is not available, and therefore we carried out the multimodal analysis with uncorrected experimental MEDs. The consequences of this limitation on our results could be estimated from the following.

The emission of neutrons due to direct and pre-equilibrium reactions of light incident particles with target nuclei, as well as evaporation of neutrons from compound nuclei, leads to the formation of a whole range of fissioning nuclei with varying excitation energies. Therefore, each measured MED is composed of MEDs from the fission of the compound nuclei with masses A_{CN}, A_{CN-1}, A_{CN-2}, etc. The determination of the MED for the fission of a nucleus with a given mass and excitation energy is an important but rather complicated scientific task, which requires detailed information on the MEDs from fission of at least

two neighbouring isotopes at different excitation energies. However, from a practical point of view it is sufficient to know the composite mass and energy distributions and their dependence on incident particle energy, but not the dependence on the true excitation energy scale.

In addition, it should be noted that the emission of every pre-fission neutron decreases the mean value of the fragment mass distribution by 0.5 amu, so that in the case of fission contributions from a wide range of compound nuclei, dissymmetry is introduced into the true composite mass distribution. However, in the matrix $N(Q_1,Q_2)$ obtained from measurements with the $(E_1–E_2)$ method, all events with $M_1 = M_2$ are located along the main diagonal of the matrix, independent of the mass of the fissioning nucleus. Therefore, the measured mass and energy distributions are symmetric with respect to A/2, where $A = A_{CN} - \nu_{pre}$ is the mean mass of the fissioning compound nuclei. Whenever there is a large number and variance of emitted pre-fission neutrons, for example at high incident light particle kinetic energies, the $(E_1–E_2)$ method can only give information on the main features of the MDs. But in our case, the average number of pre-fission neutrons is $\nu_{pre} \leq 2$ with $(A/2 \leq A_{CN}/2–1)$, and therefore this effect is rather small.

In order to estimate the mass and energy yields for primary fragments (fragments before prompt neutron emission) when information on $\nu_{post}(M,E_k)$ is not available, a simplified procedure can be used for the adjustment of the experimental fragment yields, which is described in detail in Refs [4.5.14, 4.5.15]. Figure 4.5.1 shows the results of applying this procedure to relative mass yields Y(M), to average total kinetic energies of fragments, $E_k(M)$, and their variances, $\sigma^2_E(M)$, measured in the ^{235}U + p(12.5 MeV) reaction. The experimental data for the average post-fission neutron number $\nu(M)$ of the ^{235}U + p(12.7 MeV) reaction have been taken from Ref. [4.5.16]. The solid curve shows the smoothed $\nu(M)$ used for the adjustment. This adjustment for post-fission neutron emission has a strong influence on only the absolute values of E_k and does not cause significant changes in the M dependence of this quantity. In the case of Y(M) and $\sigma^2_E(M)$, the effect of the change is rather small.

One of the important features inherent to the correction procedure is that, if the number of neutrons evaporated from a fragment with mass M is proportional to M, the difference of primary and experimental (provisional) masses equals zero, independent of the absolute number of emitted neutrons. A similar situation is observed in fission at high excitation energies when the sawtooth structure in the dependence of $\nu(M)$ seen in Fig. 4.5.1 is smoothed out and can be approximated by a linear function. At thermal neutron induced and spontaneous fission, the sawtooth structure is more pronounced, and the effect of the adjustment Y(M) on the post-fission neutron emission increases.

Reassessing all features of the neutron effects mentioned above, it can be concluded that the effects due to pre-fission neutron emission increase with increasing incident particle energy, while the effects due to post-fission neutron emission decrease. Both types of neutron effect have a strong influence on the absolute values of the total kinetic energy of the fragments and a relatively small impact on the shapes of the mass and energy distributions.

We have performed seven independent control measurements in order to obtain an estimate of the relative uncertainties of the experimentally determined mass and energy distribution parameters, such as the average total kinetic energy (E_k), variances of the mass (σ^2_M), and energy (σ^2_E) yields. These measurements were carried out for the ^{235}U + p(10.3 MeV) reaction with different targets and detectors. The spread of values for the mass and energy distribution parameters derived from these control measurements were taken as an estimate of the experimental uncertainties; the values obtained are 0.4 MeV for ΔE_k (absolute) and about 2% (relative) for σ^2_M and σ^2_E.

In order to study the reproducibility of the experimental mass and energy distribution shapes, we undertook a linear transformation of the mass and energy distributions for these seven independent measurements to the values of Y(M), $E_k(M)$ and $\sigma^2_E(M)$, and compared these data (Fig. 4.5.2). There is practically no visible spread of data for Y(M) and $E_k(M)$; some spread in the data for $\sigma^2_E(M)$ can be seen in the areas of the peaks, valley and wings of the mass distribution. However, the variation of this quantity with fragment mass also exceeds the spread of experimental data. Therefore, we can hope that the relative accuracy of our experimental data is sufficient to study the behaviour of the basic characteristics of the distinct modes.

4.5.2.3. Experimental results

The experimental average total kinetic energies (E_k), the variances of total kinetic energy

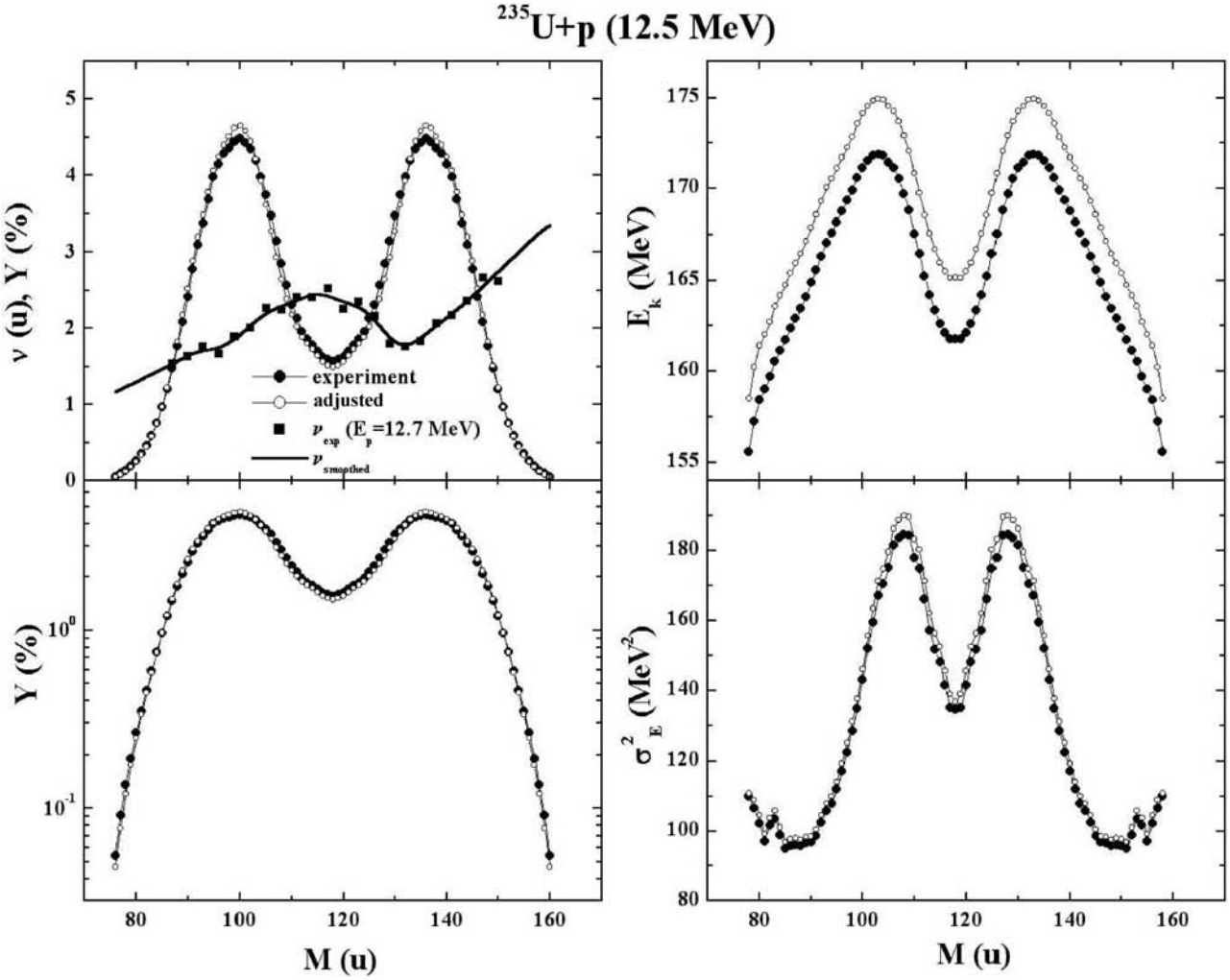

FIG. 4.5.1. Experimental and primary fragment relative mass yields Y(M), the average total kinetic energies of fragments E_k(M), and variances of the kinetic energy σ^2_E(M) for the ^{235}U + p(12.5 MeV) reaction. Experimental data for ν(M) are taken from Ref. [4.5.16].

(σ^2_E), and mass (σ^2_M) distributions as functions of the proton energy E_p and the nucleonic composition of the compound nuclei are listed in Tables 4.5.1–4.5.4. Adjustments for energy losses in the target working layers and the neutron effects were not introduced.

4.5.3. Multi-modal analysis of MEDs

4.5.3.1. Method of analysis

Any method of multi-component analysis is based on the assumption that experimental MEDs ($Y_{exp}(M,E_k) = 200\% \times N(M,E_k)/N_f$, where N_f is the number of recorded fission events) consist of the MEDs of independent fission modes [4.5.17–4.5.24]. Thus, for every element of the two dimensional matrix $Y_{exp}(M,E_k)$, the following relationship holds:

$$Y_{exp}(M,E_k) = Y_{exp}(M)Y_{exp,M}(E_k) = \sum_i Y_i(M)Y_{i,M}(E_k) \quad (4.5.4)$$

where $Y_{exp}(M)$ is the experimental relative yield of fragments with mass M, $Y_{exp,M}(E_k)$ is the normalized (to 1) distribution of the total kinetic energies for these fragments, the index i defines the fission mode, $Y_i(M)$ is the relative yield of mass M for the ith mode, and $Y_{i,M}(E_k)$ is the normalized (to 1) distribution of total kinetic energies for the fragments with mass M for the ith mode. The distributions $Y_i(M)$ and $Y_{i,M}(E_k)$ can be approximated by appropriate mathematical functions, the parameters of which are determined by a fit to the experimental MEDs, particularly with the least squares method.

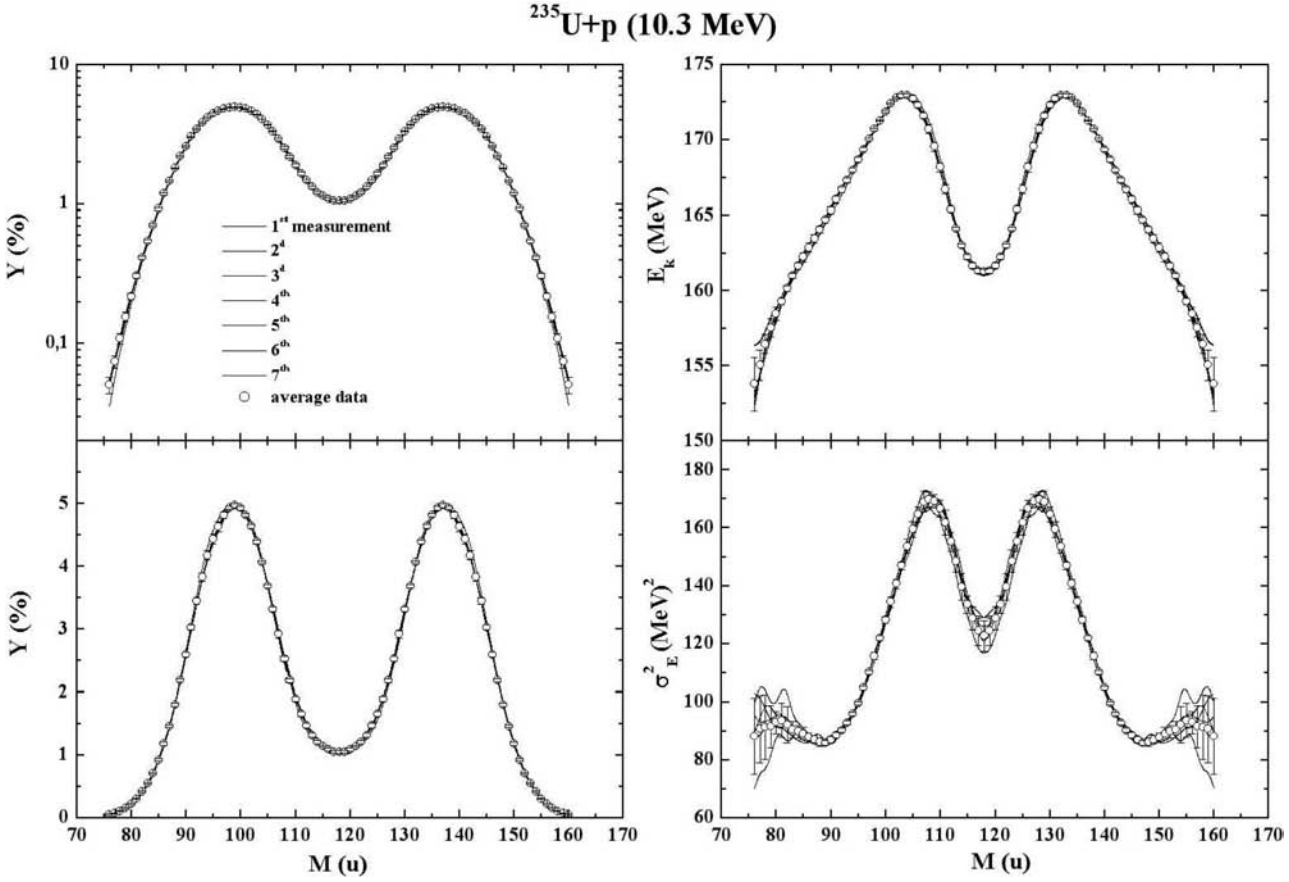

FIG.4.5.2. Experimental relative mass yield Y(M), average total kinetic energy of fragments $E_k(M)$, and variance of kinetic energy $\sigma^2_E(M)$ for seven independent measurements of the $^{235}U + p$ (10.3 MeV) reaction.

TABLE 4.5.1. AVERAGE TOTAL KINETIC ENERGY (E_k), TOTAL KINETIC ENERGY VARIANCE (σ^2_E), AND MASS DISTRIBUTION VARIANCE (σ^2_M) AT PROTON ENERGY E_p = 10.3 MeV

Compound nucleus	E_k (MeV)	σ^2_E (MeV)^2	σ^2_M (amu)^2
^{233}Pa	163.8	95	494
^{234}Np	169.8	128	391
^{236}Np	168.9	128	391
^{237}Np	170.8	122	411
^{239}Np	169.3	125	410
^{239}Am	174.0	141	371
^{240}Am	173.7	140	372
^{241}Am	174.3	140	377
^{243}Am	175.5	141	373
^{245}Bk	177.6	156	366

TABLE 4.5.2. AVERAGE TOTAL KINETIC ENERGY (E_k), TOTAL KINETIC ENERGY VARIANCE (σ_E^2), AND MASS DISTRIBUTION VARIANCE (σ_M^2) AT PROTON ENERGY E_p = 22.0 MeV

Compound nucleus	E_k (MeV)	σ_E^2 (MeV)^2	σ_M^2 (amu)^2
^{233}Pa	162.6	124	384
^{234}Np	167.2	157	318
^{236}Np	166.4	159	338
^{237}Np	166.8	147	342
^{239}Np	167.9	147	358
^{240}Am	173.6	169	322
^{241}Am	173.6	172	329
^{243}Am	173.7	174	334

TABLE 4.5.3. AVERAGED TOTAL KINETIC ENERGY (E_k), TOTAL KINETIC ENERGY VARIANCE (σ_E^2), AND MASS DISTRIBUTION VARIANCE (σ_M^2) FROM FISSION OF ^{233}Pa

Proton energy (MeV)	E_k (MeV)	σ_E^2 (MeV)^2	σ_M^2 (amu)^2
7.4	164.5	85	520
12.5	163.0	107	460
13.5	162.8	108	440
16.5	163.7	108	451
18.0	163.2	115	429
20.0	162.9	119	401
24.0	162.2	126	390
26.0	162.2	126	387
28.0	161.4	135	378
30.0	161.3	137	370

TABLE 4.5.4. AVERAGE TOTAL KINETIC ENERGY (E_k), TOTAL KINETIC ENERGY VARIANCE (σ_E^2), AND MASS DISTRIBUTION VARIANCE (σ_M^2) FROM FISSION OF ^{236}Np

Proton energy (MeV)	E_k (MeV)	σ_E^2 (MeV)^2	σ_M^2 (amu)^2
7.4	170.3	110	445
12.5	168.0	139	386
13.5	167.6	141	375
15.0	167.1	146	367
16.5	167.1	149	356
18.0	167.8	153	352
28.0	166.1	164	326
30.0	166.0	164	323

Frequently, the yields $Y_i(M)$ are approximated by Gaussians.

The adoption of either this function or any other to approximate $Y_i(M)$ is not necessary. The multi-component analysis of the mass and energy distributions can be fulfilled without any assumptions about the shapes of $Y_i(M)$, which could serve as an important source of information about the formation of distinct fission modes. As outlined below, we have proposed two versions of such an approach to analyse the mass and energy distributions on the basis of Eq. (4.5.4) from the following considerations:

The following equations:

$$Y_{exp}(M) = \sum_{Ek} Y_{exp}(M,E_k) = \sum_i Y_i(M) \sum_{Ek} Y_{i,M}(E_k) = \sum_i Y_i(M),$$

$$\left\langle E_k^n \right\rangle_{exp}(M) = \sum_{Ek} E_k^n Y_{exp}(M,E_k) / \sum_{Ek} Y_{exp}(M,E_k) = \sum_i Y_i(M) \left(\sum_{Ek} E_k^n Y_{i,M}(E_k) \right) / \sum_{Ek} Y_{exp}(M,E_k) = \sum_i \left\langle E_k^n \right\rangle_i Y_i(M) / Y_{exp}(M) \qquad (4.5.5)$$

depend linearly on $Y_i(M)$. Therefore, for every mass M and any total number L of independent modes one can build a system of L linear equations where the power n in the second relation has values from 1 to L-1.

In the three-modal case (S1, S2 and S), Eqs (4.5.5) reduce to the equation system outlined in Refs [4.5.6, 4.5.25]:

$$Y_{exp}(M) = \sum_i Y_i(M),$$

$$\bar{E}_{k,exp}(M) = \sum_i \frac{Y_i(M)}{Y_{exp}(M)} \bar{E}_{k,i}(M),$$

$$\sigma^2_{E,exp}(M) = \sum_i \left\{ \frac{Y_i(M)}{Y_{exp}(M)} \sigma^2_{E,i}(M) + \sum_j \frac{Y_i(M) Y_j(M)}{Y^2_{exp}(M)} \times \left[\bar{E}_{k,i}(M) - \bar{E}_{k,j}(M) \right]^2 \right\} \qquad (4.5.6)$$

$\bar{E}_{k,i}(M)$ and $\sigma^2_{E,i}(M)$ are the average total kinetic energy and variance as a function of fragment mass M, where the indices i and j define the modes S1, S2 or S.

Solutions to Eqs (4.5.5) or (4.5.6) require definitions of the expressions for $Y_{i,M}(E_k)$ that are proposed in our work [4.5.6] and described in detail below. However, it should be noted that any mathematical approximation of $Y_{i,M}(E_k)$ does not take into account the statistical scatter of the experimental MEDs, and if an approximate value is used for $Y_{i,M}(E_k)$, Eq. (4.5.4) also becomes an approximation:

$$Y_{exp}(M,E_k) \approx \sum_i Y_i(M) Y_{i,M}(E_k)$$

that can lead to undesired dependences of the analysis results on the statistical uncertainties of the experimental MEDs.

We have suggested a more general method to avoid this effect [4.5.25] that allows the yields $Y_i(M)$ to be determined with the experimental uncertainties of $Y_{exp,M}(E_k)$ taken into account. This approach is based on the least squares method, where

$$\left\{ Y_{exp}(M,E_k) - \sum_i Y_i(M) Y_{i,M}(E_k) \right\}^2$$

is minimized. The functional of $\chi^2(M)$ can be written as:

$$\chi^2(M) = \sum_{Ek} \left\{ \frac{1}{\delta^2(M,E_k)} \times \left[\sum_i Y_i(M) Y_{i,M}(E_k) - Y_{exp}(M,E_k) \right]^2 \right\} \qquad (4.5.7)$$

in which $\delta(M,E_k)$ is the experimental uncertainty of $Y_{exp,M}(E_k)$.

$\chi^2(M)$ is minimized if the conditions $\partial\chi^2(M)/\partial Y_i(M) = 0$ are fulfilled simultaneously for all i. Since the derivatives depend linearly on $Y_i(M)$, the determination of optimum values for $Y_i(M)$ is reduced to the solution of the following system of linear equations:

$$\frac{\partial\chi^2(M)}{\partial Y_i(M)} = 2\sum_{Ek}\left\{\frac{Y_{i,M}(E_k)}{\delta^2(M,E_k)}\times\left[\sum_j Y_j(M)Y_{j,M}(E_k) - Y_{exp}(M,E_k)\right]\right\} = 0 \tag{4.5.8}$$

As opposed to the initial approach of Eq. (4.5.5), the experimental uncertainties of the mass and energy distributions are taken into account in Eq. (4.5.8). Control calculations have shown that with sufficient statistical accuracy attached to the experimental data, Eqs (4.5.5) and (4.5.8) give practically the same results. However, on the whole, all solutions based on Eq. (4.5.8) are less sensitive to experimental uncertainties and can be used at lower statistics of the mass and energy distributions.

The equation systems (4.5.5) and (4.5.8) have been used in other studies for a three-modal analysis of the mass and energy distributions from the fission of a wide range of compound nuclei from ^{226}Th to ^{245}Bk [4.5.6, 4.5.25]. Some of the most interesting results have been obtained for shapes of the mass distributions for mode S1 that is characterized by high total kinetic energies of fragments. The mass distribution for ^{226}Th turned out to be anomalously broad, and for the remaining ten nuclides investigated the splitting of the $Y_{S1}(M)$ into two peaks with stable average masses $M_H \approx 134$ for the first peak and $M_L \approx 83$ for the second one has been observed. The appearance of the second peak, which is characteristic of a stable position in the light fragment group, has been interpreted as a manifestation of the S3 mode, which was predicted theoretically in Ref. [4.5.4] and conditioned by the formation of spherical shell closures in light fragments. As a result of this analysis we had to include the additional mode S3 in the multi-modal analysis, which required an increase of the number of equations in system (4.5.8) from 3 to 4, and we also used the four component version of the analysis.

As mentioned previously, the approximation function for $Y_{i,M}(E_k)$ must be defined in order to obtain information on $Y_i(M)$ [4.5.6, 4.5.25]. This problem was solved on the basis of a detailed study of the properties of the symmetric mode S for nuclei from ^{186}Os to ^{235}U outlined in Refs [4.5.26, 4.5.27], in which it was established that the dependences $\bar{E}_{k,i}(M)$ and $\sigma^2_{E,i}(M)$ could be described with good accuracy by the following equations:

$$\begin{aligned}&\bar{E}_k(M) = \bar{E}_k(A/2)(1-\mu^2)(1+\lambda\mu^2),\\ &\bar{E}_k^2(M)/\sigma_E^2(M) = \text{constant}\end{aligned} \tag{4.5.9}$$

$\mu = 1–2M/A$, and λ characterizes the deviation of $\bar{E}_{k,i}(M)$ from a simple parabolic dependence proposed in Ref. [4.5.28].

The distributions $Y_{S,M}(E_k)$ for the symmetric mode have been shown not to be Gaussian [4.5.25, 4.5.26], but are characterized by elongated low energy tails. The corresponding coefficients of dissymmetry $\gamma_1(M) = \langle(E_k - \bar{E}_k(M))^3\rangle/\sigma_E^3(M)$ and excess $\gamma_2(M) = \langle(E_k - \bar{E}_k(M))^4\rangle/\sigma_E^4(M) - 3$ were determined experimentally to be –0.1 and 0.0, respectively, independent of the fragment masses, excitation energy, and nucleonic composition of the fissioning nuclei.

When describing the distributions with small values of γ_1 and γ_2, it is convenient to use Charlier's distribution written as:

$$\begin{aligned}Y_M(E_k) &= \frac{f(u)}{\sigma_E(M)}\\ &\quad\times\left[1 - \frac{\gamma_1}{6}(3u - u^3) + \frac{\gamma_2}{24}(u^4 - 6u^2 + 3)\right],\\ u &= \frac{E_k - \bar{E}_k(M)}{\sigma_E(M)},\quad f(u) = \frac{1}{\sqrt{2\pi}}\exp\left(-\frac{u^2}{2}\right).\end{aligned} \tag{4.5.10}$$

When $\gamma_1 = \gamma_2 = 0$, Charlier's distribution is Gaussian.

We assume that all properties derived above for the symmetric mode can also be applied to the asymmetric modes. However, whilst experimental values for γ_1 and γ_2 are available for the symmetric mode, the optimum values of these coefficients for the asymmetric modes S1, S2 and S3 have been determined as $\gamma_1 = \gamma_2 = –0.2$ from a preliminary analysis of all available experimental mass and energy distributions. Parameter λ was the same for all fission modes.

The procedure for the multi-modal analysis was an iteration process performed with the standard code MINUIT [4.5.29]. When the initial values of $\bar{E}_{k,i}(M)$, $\sigma^2_{E,i}(M)$ and λ were adopted, the distributions $Y_{i,M}(E_k)$ were calculated according to Eqs (4.5.9) and (4.5.10), and the relative yields $Y_i(M)$ for all fragment masses were determined from solutions of Eq. (4.5.8) to build the approximation matrix $\sum_i Y_i(M)Y_{i,M}(E_k)$. Then the value of χ^2 was calculated as a measure of the convergence of $Y_{exp}(M,E_k)$ and $\sum_i Y_i(M)Y_{i,M}(E_k)$, and new values of $\bar{E}_{k,i}(M)$, $\sigma^2_{E,i}(M)$ and λ were determined. In all cases,

the nine optimum description parameters converged at χ^2 values less than 1 per degree of freedom.

The uncertainties of $Y_i(M)$, $\bar{E}_{k,i}(M)$ and $\sigma^2_{E,i}(M)$ as extracted from the analysis have been estimated by taking into account the convergence conditions, the influence of these quantities on the value of χ^2, and the statistical uncertainties of the experimental data. A control check has shown that the uncertainties estimated from the analysis for the ^{235}U + p (10.3 MeV) reaction are close to those derived from the scatter of the corresponding quantities extracted from the MEDs of the seven independent control measurements (described at the end of Section 4.5.2.2).

4.5.3.2. Results of the analysis

All available experimental data have been analysed by application of the method described above. The basic characteristics of the mass distribution for distinct fission modes are presented in Tables 4.5.5–4.5.8.

Typical results of decompositions of MEDs based on Eqs (4.5.4)–(4.5.6) are presented in Fig. 4.5.3, where the experimental data on the relative mass yield Y(M) and mass distributions of independent fission modes are shown for the proton induced fission of compound nuclei ^{233}Pa and ^{236}Np at E_p = 7.4, 18.0 and 30.0 MeV; and in Fig. 4.5.4, where the same distributions are shown for ^{233}Pa, ^{234,236,237,239}Np, ^{239,240,241,243}Am, and ^{245}Bk at E_p = 10.3 MeV.

4.5.4. Discussion

4.5.4.1. Energy dependences

The influence of the incident proton energy on the characteristics of the fission modes is shown for two compound nuclei ^{233}Pa and ^{236}Np in Figs 4.5.5 and 4.5.6.

The lines drawn in Figs 4.5.5 and 4.5.6 through the mean values of the corresponding characteristics act only as a guide for the eye. One can see that in both cases the values Y_i for the asymmetric modes decrease with increasing proton energy, in full accord with well known notions about the temperature rearrangement of shell effects. At the same time, the values $\langle M_{H,i} \rangle$ are practically independent of E_p.

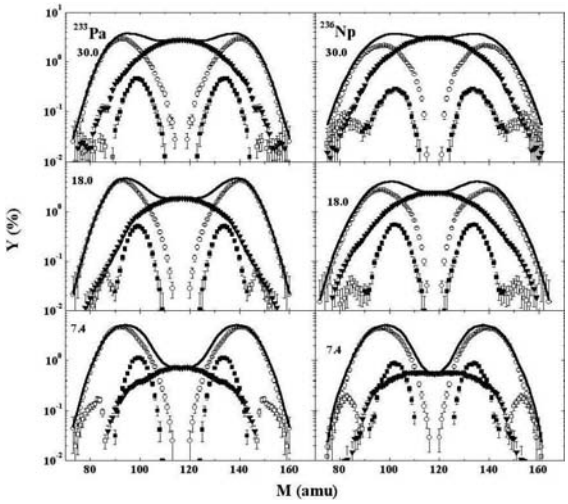

FIG. 4.5.3. Results of the decomposition of fragment mass distributions from the fission of nuclei ^{233}Pa and ^{236}Np at proton energies E_p = 7.4, 18.0 and 30.0 MeV. Lines — experiment; extracted mass yields: full square — S1, open circle — S2, open square — S3, full triangle — S.

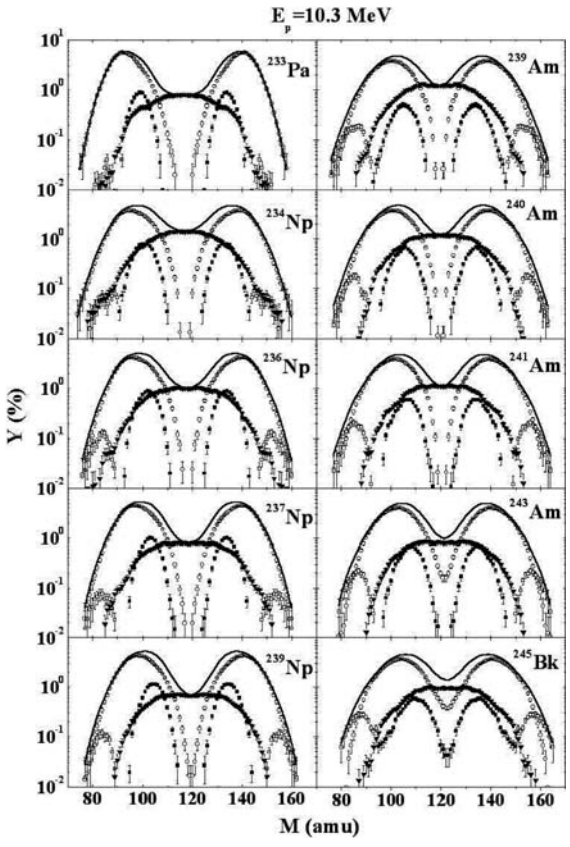

FIG. 4.5.4. Results of the decomposition of fragment mass distributions from the fission of nuclei ^{233}Pa, ^{234,236,237,239}Np, ^{239,240,241,243}Am and ^{245}Bk at proton energy E_p = 10.3 MeV. Symbols are the same as in Fig. 4.5.3.

TABLE 4.5.5. RELATIVE CONTRIBUTIONS OF MODE i (Y_i), AVERAGE MASSES OF HEAVY FRAGMENTS ($\overline{M}_{H,i}$) AND MASS DISTRIBUTION VARIANCES ($\sigma^2_{M,i}$) FOR DISTINCT FISSION MODES AT A PROTON ENERGY OF E_p = 10.3 MeV

Compound nucleus	Mode	Y_i (%)	$\overline{M}_{H,i}$ (amu)	$\sigma^2_{M,i}$ (amu^2)
^{233}Pa	S1	6.6	133.8	9.5
	S2	79.3	139.5	34
	S3	0.3	148.1	4
	S	13.8		154
^{234}Np	S1	8.0	133.2	14
	S2	65.9	137.9	47
	S3	0.8	147.9	11
	S	25.3		164
^{236}Np	S1	8.3	133.9	13
	S2	71.3	138.8	43
	S3	1.0	152.3	14
	S	19.4		167
^{237}Np	S1	8.7	133.9	11
	S2	74.7	139.3	43
	S3	0.6	153.4	9
	S	16		173
^{239}Np	S1	11.1	134.6	13
	S2	73.9	140.1	44
	S3	1.0	155.1	9
	S	14.0		169
^{239}Am	S1	5.4	134.0	18
	S2	69.5	139.0	49
	S3	1.9	154.1	15
	S	23.2		161
^{240}Am	S1	7.0	134.4	17
	S2	69.4	139.6	50
	S3	1.4	155.5	10
	S	22.2		156
^{241}Am	S1	6.3	134.7	16
	S2	71.3	140.0	50
	S3	1.8	155.9	12
	S	20.6		154
^{243}Am	S1	7.3	135.2	18
	S2	74.1	140.5	51
	S3	1.9	156.8	11
	S	16.7		169
^{245}Bk	S1	7.8	135.5	29
	S2	70.2	141.0	55
	S3	3.1	157.6	18
	S	18.9		174

TABLE 4.5.6. RELATIVE CONTRIBUTIONS OF MODE i (Y_i), AVERAGE MASSES OF HEAVY FRAGMENTS ($\overline{M}_{H,i}$) AND MASS DISTRIBUTION VARIANCES ($\sigma^2_{M,i}$) FOR DISTINCT FISSION MODES AT A PROTON ENERGY OF E_p = 22.0 MeV

Compound nucleus	Mode	Y_i (%)	$\overline{M}_{H,i}$ (amu)	$\sigma^2_{M,i}$ (amu^2)
^{233}Pa	S1	4.8	133.9	13
	S2	54.2	139.1	41
	S3	0.1	149.1	3
	S	40.9		169
^{234}Np	S1	5.3	134.3	23
	S2	39.5	137.6	56
	S3	1.1	150.4	12
	S	54.1		179
^{236}Np	S1	4.4	133.6	16
	S2	44.1	138.8	52
	S3	0.9	152.9	12
	S	50.6		195
^{237}Np	S1	6.1	134.5	19
	S2	51.8	139.0	53
	S3	0.9	152.7	13
	S	41.2		168
^{239}Np	S1	5.0	135.1	14
	S2	55.3	140.0	49
	S3	1.7	154.5	12
	S	38		170
^{240}Am	S1	2.5	133.6	16
	S2	51.1	138.5	60
	S3	2.7	155.5	15
	S	43.7		169
^{241}Am	S1	3.5	134.6	17
	S2	51.3	139.4	64
	S3	1.6	156.2	16
	S	43.6		194
^{243}Am	S1	3.4	134.6	16
	S2	56.3	140.4	60
	S3	1.9	157.8	17
	S	38.4		172

TABLE 4.5.7. RELATIVE CONTRIBUTIONS OF MODE i (Y_i), AVERAGE MASSES OF HEAVY FRAGMENTS ($\overline{M}_{H,i}$) AND MASS DISTRIBUTION VARIANCES ($\sigma^2_{M,i}$) FOR DISTINCT FISSION MODES OF ^{233}Pa AT DIFFERENT PROTON ENERGIES

Proton energy (MeV)	Mode	Y_i (%)	$\overline{M}_{H,i}$ (amu)	$\sigma^2_{M,i}$ (amu^2)
7.4	S1	10.3	133.8	12
	S2	75.8	140.0	42
	S3	0.6	151.7	9
	S	13.3		169
12.5	S1	8.5	133.9	12
	S2	69.7	139.5	38
	S3	0.5	148.2	7
	S	21.3		153
13.5	S1	6.1	133.4	12
	S2	69.1	139.2	39
	S3	0.3	147.6	6
	S	24.5		147
16.5	S1	4.2	134.0	11
	S2	68.7	139.7	38
	S3	0.2	148.5	5
	S	26.9		152
18.0	S1	4.5	133.8	13
	S2	64.8	139.4	40
	S3	0.3	147.6	5
	S	30.4		151
20.0	S1	4.4	133.5	11
	S2	59.7	139.1	42
	S3	0.3	148.2	7
	S	35.6		150
24.0	S1	4.7	134.1	12
	S2	56.0	139.1	44
	S3	0.2	147.7	7
	S	39.1		155
26.0	S1	4.0	133.7	12
	S2	55.7	139.2	43
	S3	0.2	147.2	5
	S	40.1		155
28.0	S1	5.0	133.8	17
	S2	50.6	139.4	46
	S3	0.1	149.4	3
	S	44.3		161
30.0	S1	4.8	133.8	16
	S2	49.2	139.4	46
	S3	0.2	148.7	4
	S	45.8		158

TABLE 4.5.8. RELATIVE CONTRIBUTIONS OF MODE i (Y_i), AVERAGE MASSES OF HEAVY FRAGMENTS ($\overline{M}_{H,i}$) AND MASS DISTRIBUTION VARIANCES ($\sigma^2_{M,i}$) FOR DISTINCT FISSION MODES OF ^{236}Np AT DIFFERENT PROTON ENERGIES

Proton energy (MeV)	Mode	Y_i (%)	$\overline{M}_{H,i}$ (amu)	$\sigma^2_{M,i}$ (amu^2)
7.4	S1	8.5	134.1	14
	S2	77.4	139.1	43
	S3	1.6	153.2	11
	S	12.5		197
12.5	S1	9.0	133.7	19
	S2	61.4	139.0	50
	S3	0.6	152.2	13
	S	29.0		175
13.5	S1	7.5	133.3	15
	S2	59.0	139.1	50
	S3	0.3	152.5	6
	S	33.2		178
15.0	S1	6.2	133.6	17
	S2	58.1	138.8	50
	S3	0.4	152.6	12
	S	35.3		174
16.5	S1	5.4	133.5	16
	S2	53.4	139.0	52
	S3	0.4	152.0	13
	S	40.8		180
18.0	S1	5.7	133.7	17
	S2	50.2	139.2	52
	S3	0.3	151.1	13
	S	43.8		184
28.0	S1	2.8	133.6	16
	S2	46.4	139.0	54
	S3	0.6	153.6	12
	S	50.2		156
30.0	S1	3.6	134.8	24
	S2	41.3	139.1	53
	S3	0.8	153.8	13
	S	54.3		170

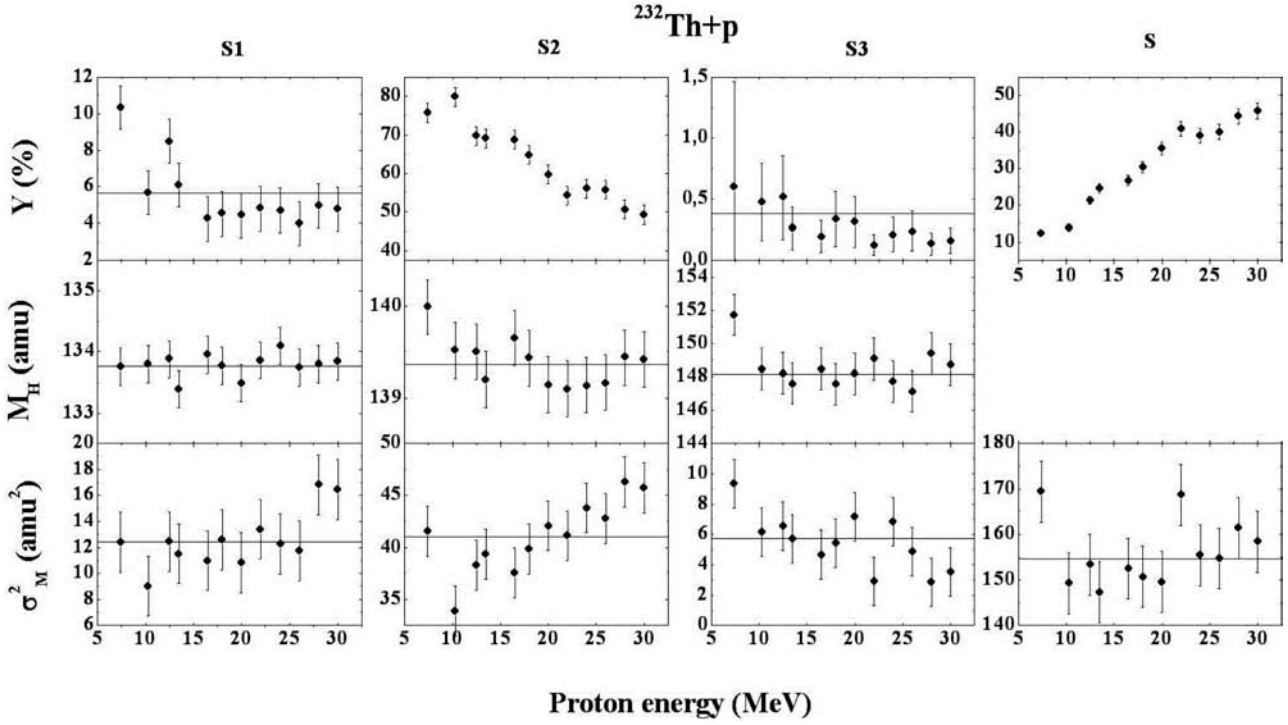

FIG.4.5.5. Relative contributions (Y), average masses of heavy fragments (M_H) and mass variances (σ^2_M) of the independent modes from fission of target nuclide ^{232}Th as a function of the incident proton energy.

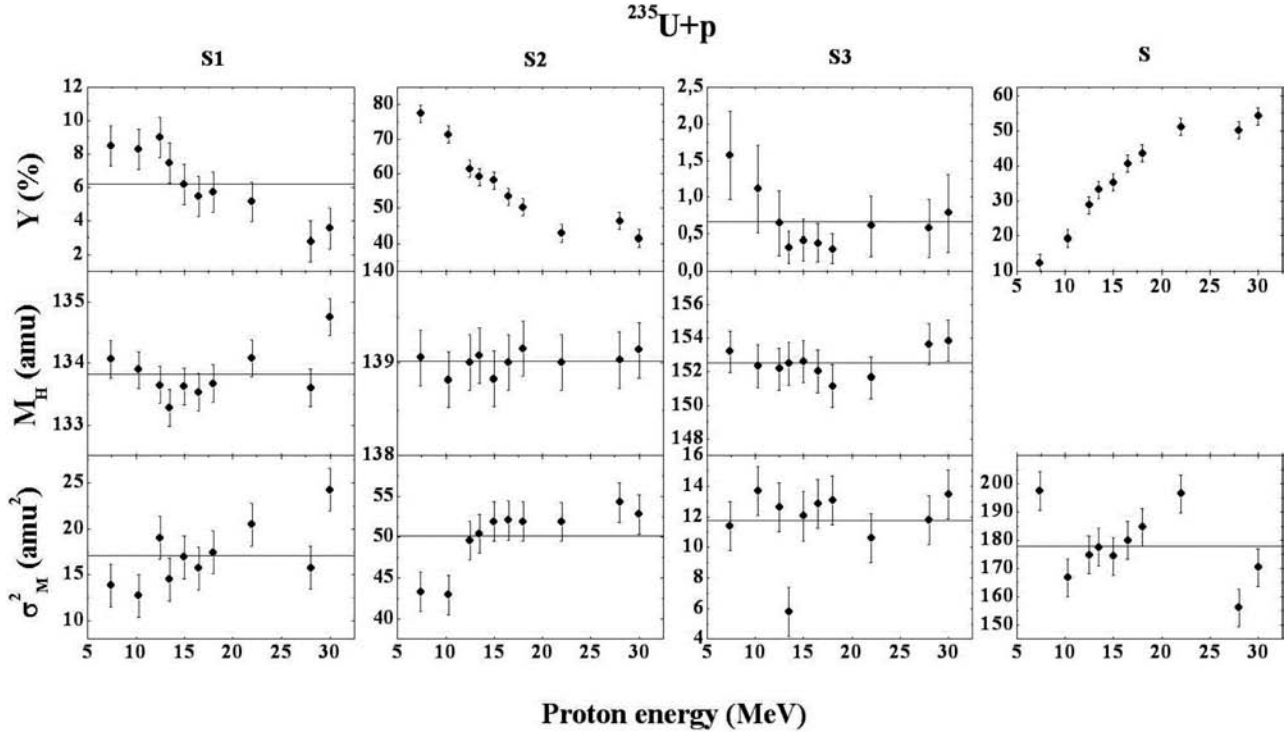

FIG. 4.5.6. Relative contributions (Y), average masses of heavy fragments (M_H) and mass variances (σ^2_M) of the independent modes from fission of target nuclide ^{235}U as a function of the incident proton energy.

Extracted values of $\sigma^2_{M,S}$ demonstrate rather complicated dependences and could possibly be explained by the influence of shell effects arising from strongly deformed shell closures that cause flattening of the symmetric mass distributions in the vicinity of masses close to A/2 (seen in Figs 4.5.3 and 4.5.4). On the other hand, the uncertainties of the extracted $Y_S(M)$ on the wings of these distributions are rather large, which could cause additional data scatter. The contribution of mode S3 is very small and the uncertainties of the extracted values of $\sigma^2_{M,S3}$ are rather large, which does not permit reliable quantification of the dependence of this value on proton energy. The values of $\sigma^2_{M,i}$ for the main asymmetric modes S1 and S2 increase slowly with increasing proton energy, in accord with notions about the influence of the fissile nucleus temperature on the width of the mass yield.

The observed regularities, such as the independence of $\langle M_{H,i} \rangle$ of the incident particle energy and the rather slow growth of $\sigma^2_{M,i}$ for modes S1 and S2, offer favourable opportunities for developing simple systematics for the fission yields of actinide nuclei.

4.5.4.2. Nucleon composition dependences

The contributions Y_i, average heavy fragment masses $M_{H,i}$ and variances of mass yields $\sigma^2_{M,i}$ of the most intensive fission modes S1, S2 and S for all compound nuclei studied in the reactions with protons at E_p = 10.3 MeV are displayed in Fig. 4.5.7.

The behaviour of the asymmetric modes S1 and S2 for Np and Am isotopes is shown against a background of the general trends in the A dependences. The isotopic dependences increase, whereas the general trend displays a constant value for Y_{S1} and a weak decrease of Y_{S2} with increasing A of the fissioning nuclide. For the values M_H of these asymmetric modes, the general and the isotopic trends demonstrate the increase with increasing A, but with a distinct difference in slopes. The values for $\sigma^2_{M,S1}$ and $\sigma^2_{M,S2}$ are practically independent of A within isotopes of an element, but exhibit an overall general increase.

The observed difference between the isotopic and general trends in A dependences of both predominant modes S1 and S2 could indicate the different roles played by the proton and neutron components of the nucleon composition in the fission fragment mass distribution formation for

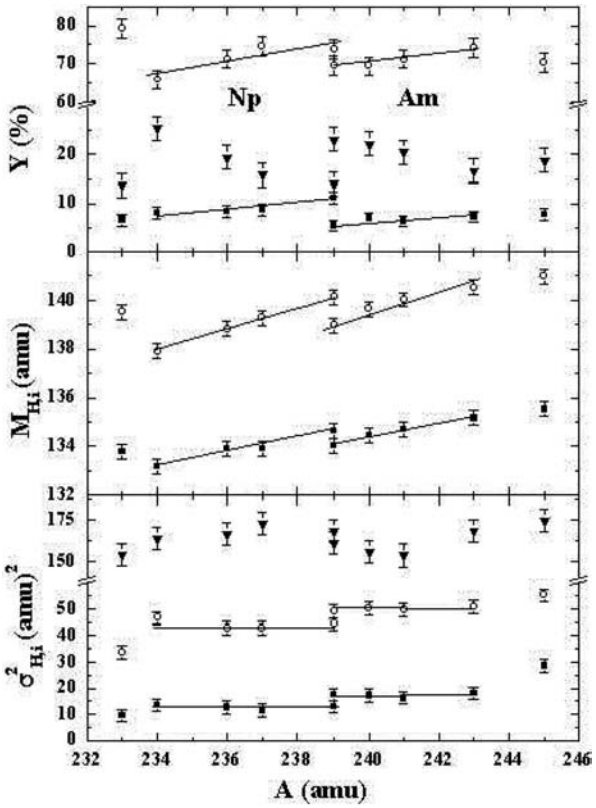

FIG. 4.5.7. Contributions (Y_i), average heavy fragment masses ($M_{H,i}$) and dispersions of mass yields ($\sigma^2_{M,i}$) for modes S1, S2 and S versus compound masses A at E_p = 10.3 MeV. Symbols are the same as in Fig. 4.5.3; lines show the mean values as a guide for the eye.

actinide nuclides. This difference is more clearly visible in Fig. 4.5.8, where the average proton (Z_F) and neutron (N_F) numbers of the light fragment group are presented for the modes S1 and S2 as a function of A of the fissioning nuclide. These numbers were calculated assuming the unchanged charge density (UCD), defined as $Z_F = M^*(Z_{CN}/A)$ and $N_F = M^*(N_{CN}/A)$.

The lines in the upper part of Fig. 4.5.8 show the proton numbers averaged over the Np and Am isotopes. For isotopes of one element, $\langle Z_L \rangle_{S1}$ and $\langle Z_L \rangle_{S2}$ are practically constant. In the lower part of Fig. 4.5.8, the lines represent the results of a linear fit to the complete set of data. Significant deviations of the isotopic dependences from these lines are not evident. The standard deviations of $\langle N_L \rangle_i$ from these lines do not exceed ~0.2. The general picture for the nucleon composition of the heavy fragment group is equivalent to that of the light group. Therefore, Fig. 4.5.8 shows for the isotopes of one element that the average proton numbers of heavy fragments of

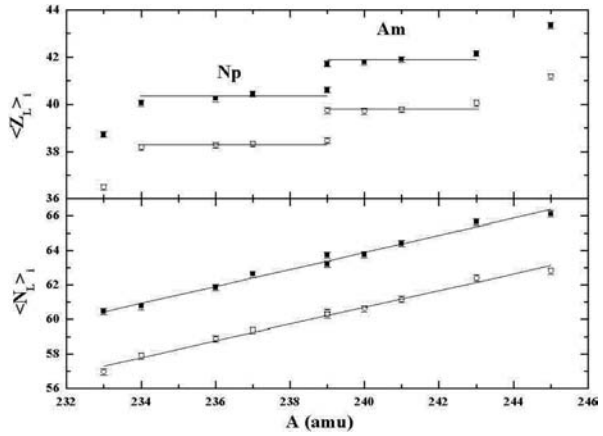

FIG. 4.5.8. Average proton $\langle Z_L \rangle_i$ and neutron $\langle N_L \rangle_i$ numbers of the light fragment group for modes S1 and S2 for E_p = 10.3 MeV. Full squares: S1, open circles: S2.

the modes S1 and S2 are more stable against variations of A than the average neutron numbers.

As the peak positions $\langle Z_{peak} \rangle$ for the two main asymmetric fission modes are conserved within the isotopes of an element, and the width of the peaks is practically independent of A, the composite asymmetric distribution can be expected to be $Y_A(Z) = \Sigma Y_i(Z)$ (i = S1, S2 and S3) for isotopes of the same element. Since the total contribution of asymmetric fission at E_p = 10.3 MeV exceeds 80%, the grouping effect for Y(Z) from the fission of isotopes of the same element can be observed directly in experimental distributions without any preliminary decomposition.

Figure 4.5.9 shows the dependence of the experimental relative fragment yields at E_p = 10.3 MeV on M, N_F and Z_F of the fragments. As known for the asymmetric fission of actinides, the positions of the heavy fragment peaks of the mass yields stay practically constant for all A, making it difficult to observe the details of the isotopic dependences in this part of the distributions. On the other hand, for the light fragments the peak positions exhibit a clear dependence on the fissioning actinide, and there is a distinct grouping of yield distributions for Np and Am isotopes for Y(M) and $Y(Z_F)$ that is not evident for $Y(N_F)$. Visible differences of the $Y(Z_F)$ curves inside the Np and Am isotopes are observed only in the limited regions close to the tops of the peaks and in the valleys of these distributions, which could be conditional on the competition between symmetric and asymmetric fission modes.

The observation of the strong grouping in the $Y(Z_F)$ distributions for isotopes of the same

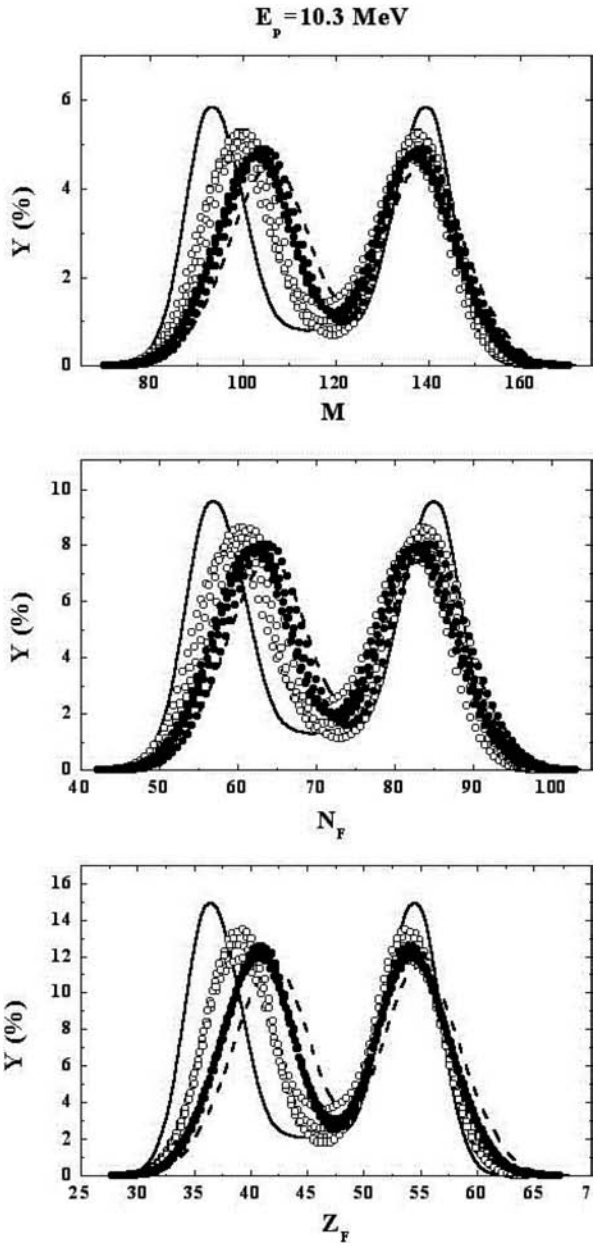

FIG. 4.5.9. Fragment mass (Y(M)), neutron number ($Y(N_F)$) and charge ($Y(Z_F)$) yields from fission of compound nuclei ^{233}Pa to ^{245}Bk at E_p = 10.3 MeV. Solid lines: ^{233}Pa, open circles: ^{234,236,237,239}Np, full squares: ^{239,240,241,243}Am, dashed lines: ^{245}Bk.

element is supported by measurements of the charge distributions of the Pa isotopes by electromagnetic excitation of relativistic nuclei on a Pb target [4.5.30, 4.5.31]. The results are shown in Fig. 4.5.10 for the four heaviest Pa isotopes (which have the least contribution of symmetric fission). This grouping of yields is evident in the coincidence of all distributions over the whole charge range, with differences only in the heights of the peaks and

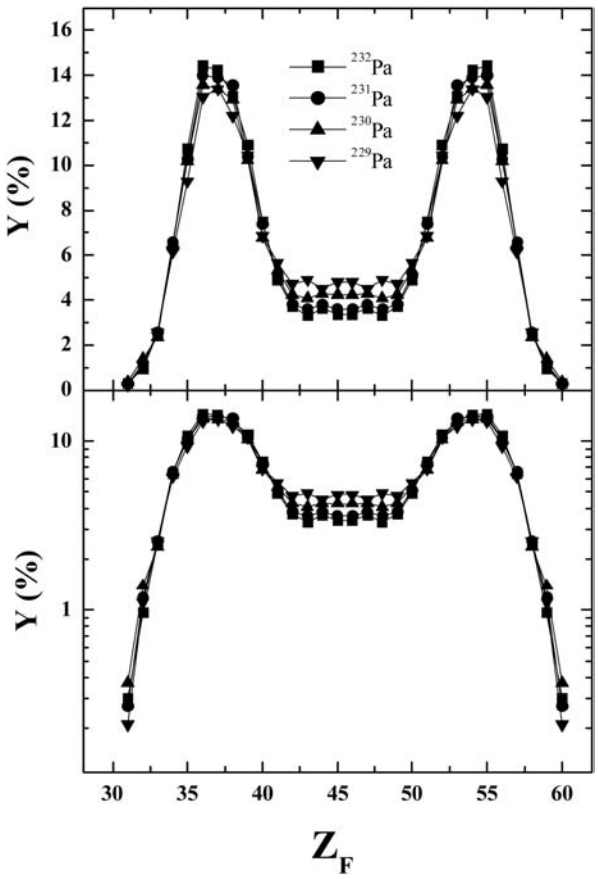

FIG. 4.5.10. Fission fragment charge distributions $Y(Z_F)$ for nuclei $^{229, 230, 231, 232}$Pa from Refs [4.5.30, 4.5.31].

the valley, as also observed in the $Y(Z_F)$ distributions for Np and Am isotopes (Fig. 4.5.9).

It can be seen that the main features of the UCD charge distributions in Fig. 4.5.9 and the measured fragment charge yields presented in Fig. 4.5.10 (such as coincidence of the curves for different isotopes at the sides of peaks) look similar. This result supports the validity of the approximations used (non-emissive fission and UCD). The decomposition of the experimental fragment charge yields into symmetric and asymmetric fission components [4.5.30, 4.5.31] showed that the positions of the heavy fragment (asymmetric) peaks stay constant ($Z_{FH} \approx 54$) not only for all Pa isotopes, but also for the isotopes of U and Th, and more or less for all actinides with predominantly asymmetric fission.

Features of the shapes of the asymmetric fission yields are presented in detail in Figs 4.5.11 and 4.5.12, where the symmetric mode yields are subtracted and the asymmetric fission yields $Y_a(Z_F)$ and $Y_a(N_F)$ at E_p = 10.3 and 22.0 MeV are displayed in linear and logarithmic scales. Clearly, the $Y_a(Z_F)$ curves for all the nuclides studied coincide for both light fragments ($Z_F \approx 30$) close to the magic number N = 28 and for heavy fragments with $Z_F \approx 50$ (see arrows). The mass distributions for the actinide nuclei are concentrated between fragments with $Z_{FL} \approx 28$ and $Z_{FH} \approx 50$, and therefore the widths of these distributions are mainly defined by $\Delta Z \sim Z_{CN} - 50 - 28$, and are almost independent of N_{CN}. Recently, a similar global grouping effect in fission fragment yields was revealed in Refs [4.5.32, 4.5.33] for Y(M) in the thermal neutron induced fission of actinides. This effect was interpreted as evidence that spherical closed shells in asymmetric fission fragment formation determine the position and slopes of the peaks in the fragment mass distributions.

Figures 4.5.11 and 4.5.12 show even more clearly the coincidence of the $Y_a(Z_F)$ curves from the fission of isotopes of the same element (Np and Am), whereas the $Y_a(N_F)$ curves do not exhibit any visible coincidence, not even in the vicinity of the magic neutron numbers 50 and 82 that are marked by arrows.

The different effects of fragment proton and neutron numbers on the shapes of $Y_a(Z_F)$ and $Y_a(N_F)$ are shown in more detail in Fig. 4.5.13, where the distributions are presented for the fission of ^{237,239}Np and ^{239,241}Am at E_p = 10.3 MeV. This set of compound nuclei consists of two isotopic (Z_{CN} = 93, 95) and two isotonic (N_{CN} = 144, 146) pairs. Whereas the charge yields within both isotopic pairs coincide practically over the whole range of fragment proton numbers, the curves $Y_a(N_F)$ for both these isotonic pairs coincide only in a narrow range in the vicinities of neutron numbers 52 and 82. For other ranges of fragment neutron numbers, the difference of the yields is also rather significant in the vicinity of N = 88 (arrows). As mentioned above, the deformed neutron shell 88 is normally used to explain the properties of S2 as the predominant asymmetric fission mode. Under these circumstances, some stabilizing influence of this shell on the positions and/or shapes of the heavy fragment asymmetric distributions would be observed, at least for nuclei with equal N_{CN}. Instead, very strong stabilizing effects can be detected in $Y_a(Z_F)$ for nuclei with equal Z_{CN}.

4.5.5. Systematics of fragment mass yields

Studies of the asymmetric fission modes have shown that the unchanged charge density distributions for asymmetric fission $Y_a(Z_F) = \Sigma Y_i(Z_F)$ (i = S1, S2, S3) practically coincide for all isotopes of one element. Therefore, the relative

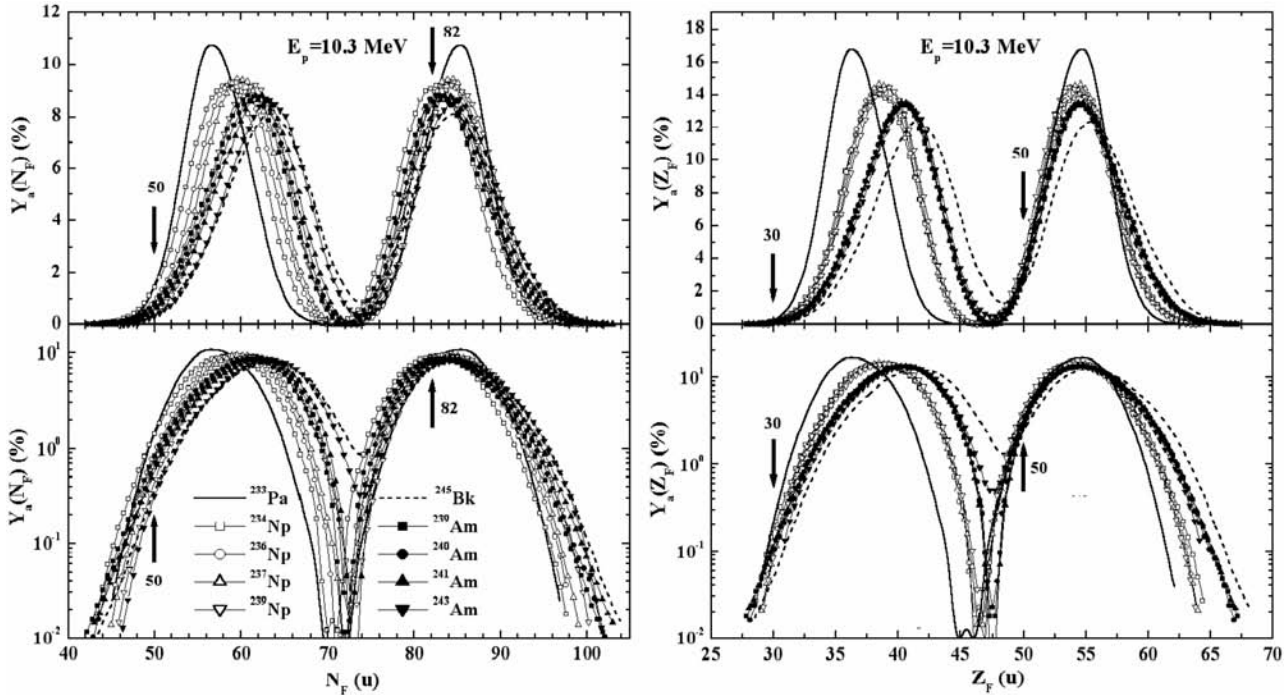

FIG. 4.5.11. Unchanged charge density $Y(Z_F)$ and neutron number $Y(N_F)$ distributions from the asymmetric fission component only for compound nuclei from ^{233}Pa to ^{245}Bk at E_p = 10.3 MeV.

fragment mass yields can be described in terms of a two-modal (symmetric and asymmetric) approximation, and consequently the required systematics can be significantly simplified by reducing the number of necessary descriptive parameters.

Figures 4.5.3 and 4.5.4 show that the shapes of $Y_S(M)$ and $Y_a(M)$ are not Gaussian and that the Charlier's peak function could be used to describe both modes. However, the deviations of the $Y_S(M)$ from Gaussian shapes are only observed at relatively low energies of incident protons when the total contribution Y_S is rather small. As mentioned above, these deviations may be due to either the influence of strongly deformed shells on the mode S (analogous to the effect observed in Ref. [4.5.34]) or the uncertainties of the modal decomposition. At higher particle energies, when Y_S increases, the deviations decrease and the shape of $Y_S(M)$ becomes close to Gaussian. This observation has led us to use the Charlier's peak function for $Y_a(M)$ only and to describe $Y_S(M)$ with a Gaussian distribution in the whole range of incident particle energies.

So, at M ≥ A/2, the fragment mass yields can be described as:

$$Y(M) = (2\pi)^{-1/2}((Y_S/\sigma_S)\exp(-u_S^2/2) + (Y_a/\sigma_a) \times \exp(-u_a^2/2)(1 - \gamma_1(3u_a - u_a^3)/6 + \gamma_2(u_a^4 - 6u_a^2 + 3)/24)) \quad (4.5.11)$$

$u_S = (M - A/2)/\sigma_S$ and $u_a = (M - M_a)/\sigma_a$

where Y_S and Y_a are the total contributions of the symmetric and asymmetric modes, respectively, M_a is the average mass of the asymmetric modes, σ_S and σ_a are the variances for the symmetric and asymmetric modes, and γ_1 and γ_2 are the coefficients of dissymmetry and of excess for the asymmetric mode, respectively. At M < A/2, Y(M) = Y(A – M) that avoids any overlap of the asymmetric peaks in the vicinity of A/2.

The applicability of the two-modal description is shown in Fig. 4.5.14 by the experimental Y(M) at E_p = 10.3 and 22.0 MeV, results of the modal decomposition $Y_S(M)$ and $Y_a(M)$ (Eq. (4.5.8)), and their description according to Eq. (4.5.11). Irrespective of the deviations of $Y_S(M)$ from a Gaussian shape, this approximation in the $Y_S(M)$ parameterization does not significantly decrease the quality of the description of the experimental Y(M). Charlier's parameterization of $Y_a(M)$ is able to reproduce all the main features of the mass yields for asymmetric fission. Some deviations of $Y_{a,des}(M)$ extracted from $Y_a(M)$ in the vicinity of the peaks at the lower proton energy compensate for the shortage of $Y_{S,des}(M)$.

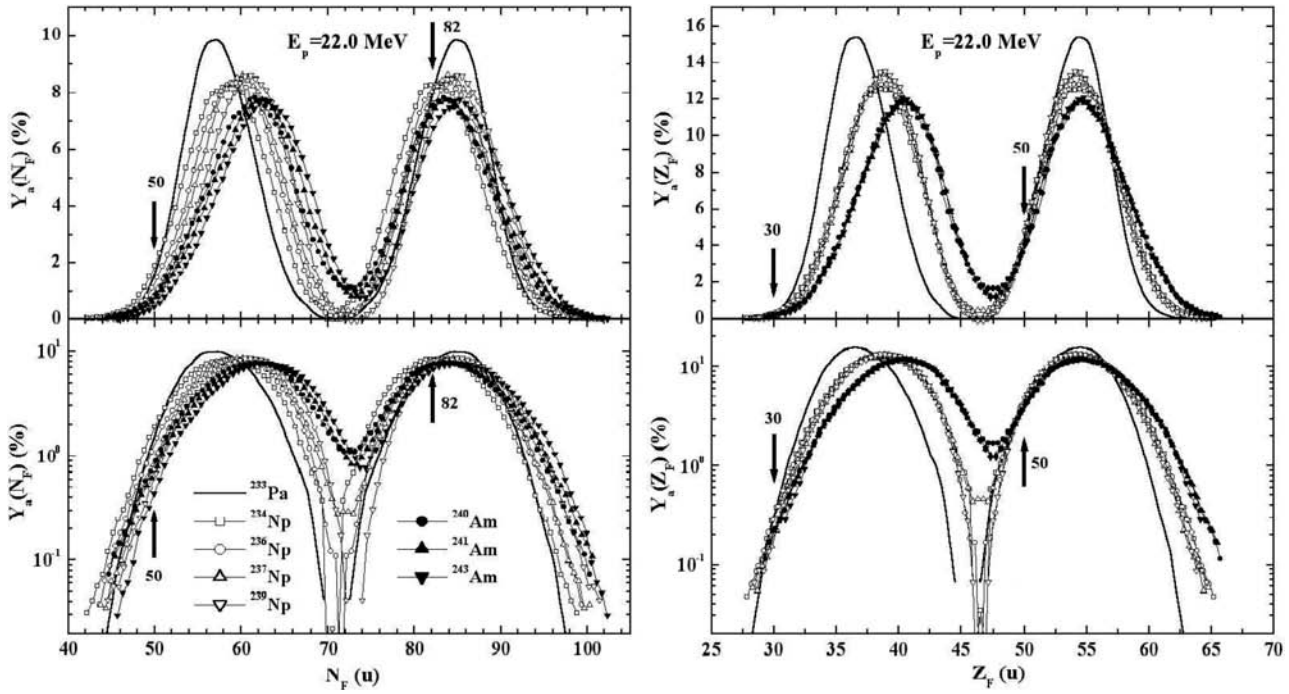

FIG. 4.5.12. Unchanged charge density $Y(Z_F)$ and neutron number $Y(N_F)$ distributions from the asymmetric fission component only for compound nuclei from ^{233}Pa to ^{243}Am at E_p = 22.0 MeV.

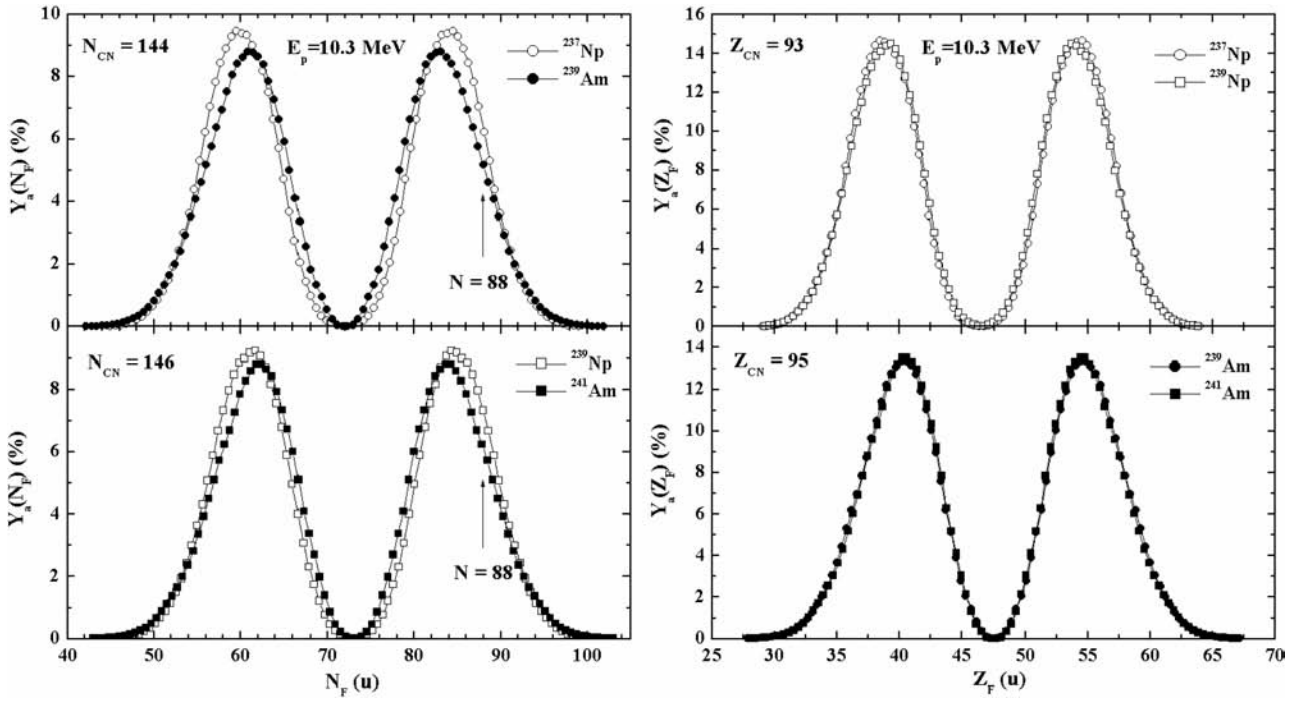

FIG. 4.5.13. Unchanged charge density asymmetric fission yields $Y(Z_F)$ and $Y(N_F)$ for $^{237,239}Np$ and $^{239,241}Am$.

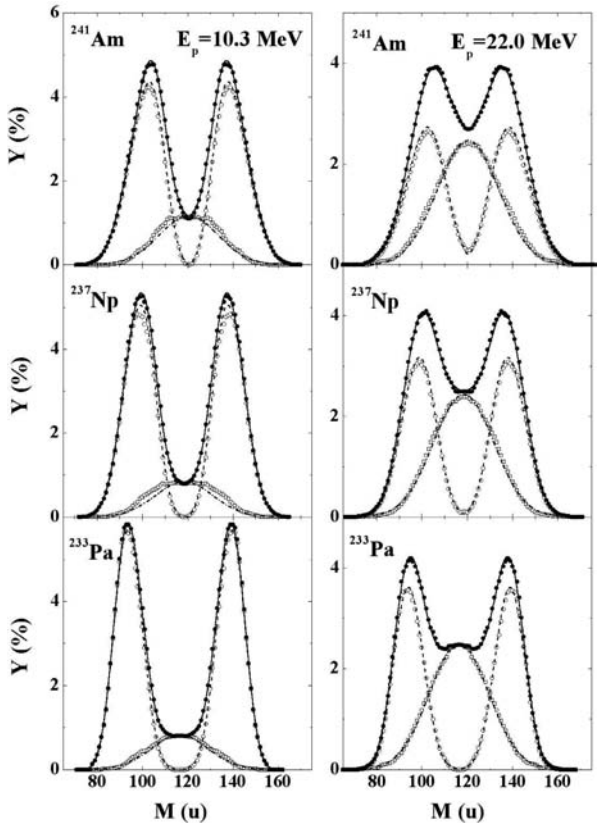

FIG. 4.5.14. Experimental Y(M) (full circles), Y_a(M) (open circles) and Y_S(M) (open squares) from the modal decomposition, and their description Y_{des}(M) (solid lines), $Y_{a,des}$(M) (dashed lines) and $Y_{S,des}$(M) (dash–dotted lines).

Therefore, the proposed two-modal parameterization can be applied in the development of fragment mass yield systematics based on six descriptive parameters: Y_a/Y_S, M_a, σ_a, σ_S, γ_1 and γ_2, the values of which depend on the nucleon composition of the compound nuclei and incident particle energy.

4.5.5.1. Description parameters

The calculation of M_a values for a given compound nucleus and particle energy is based on the following consideration. As noted above, this value is practically independent of proton energy, so $M_a = M_a(Z_{CN},A)$. $M_{H,a}/Z_{CN}$ at E_p = 10.3 (full circles) and 22.0 MeV (open circles) are shown in Fig. 4.5.15 as functions of $(Z_{CN})^2/A$ of the compound nuclei: the experimental points lie on a straight line, which can be approximated by the linear function:

$$M_{H,a} = a_M A/Z_{CN} + b_M Z_{CN} \qquad (4.5.12)$$

where a_M and b_M are parameters of the systematics.

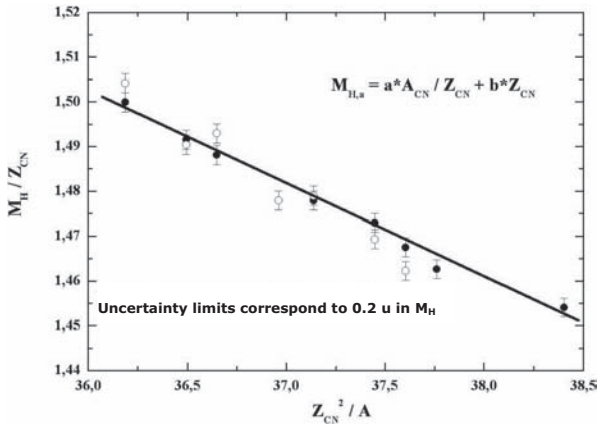

FIG. 4.5.15. Ratios of average masses of heavy fragments from asymmetric fission to atomic numbers of compound nuclei M_H/Z_{CN} as a function of Z_{CN}/A of the compound nuclei at E_p = 10.3 MeV (full circles) and 22 MeV (open circles).

The mass yield variance for asymmetric fission (σ_a) is shown in Fig. 4.5.16 as a function of A (left hand side) and Z_{CN} (right hand side) of different compound nuclei for E_p = 10.3 and 22 MeV. At both proton energies, σ_a is linearly dependent on Z_{CN}; but within one element, σ_a is practically independent of the isotope, reflecting the previous observation that the $Y_a(Z_F)$ curves for isotopes of one element coincide. The difference in the average σ_a for isotopes of neighbouring elements (lines on left hand side of Fig. 4.5.16) increases with increasing proton energy. We conclude that σ_a is mainly dependent on Z_{CN} and on $E^* = Q_R + E_{part}A_t/A$ (where A_t is the target nucleus mass), and can be described by the following equation:

$$\sigma_a = A/Z_{CN}(Z_{CN} - a_a)(b_a + c_a(E^*)^{0.25}) \qquad (4.5.13)$$

where a_a, b_a and c_a are parameters of the systematics.

Unfortunately we were unable to define a simple parameterization function for γ_1 and γ_2. However, since these values depend mainly on Z_{CN} and the range of interest of Z_{CN} for practical applications is rather narrow (90–98), we have determined these parameters separately for every Z_{CN} (see Table 4.5.9).

σ_S was parameterized on the basis of the well known equation: $\sigma_S^2 = \theta/C$, where θ is the fissioning nuclei temperature, and C is the stiffness with respect to mass asymmetric deformations.

Figure 4.5.17 presents the dependence of the experimental values C on Z_{CN}^2/A — from Th to Bk, C can be approximated by the linear function:

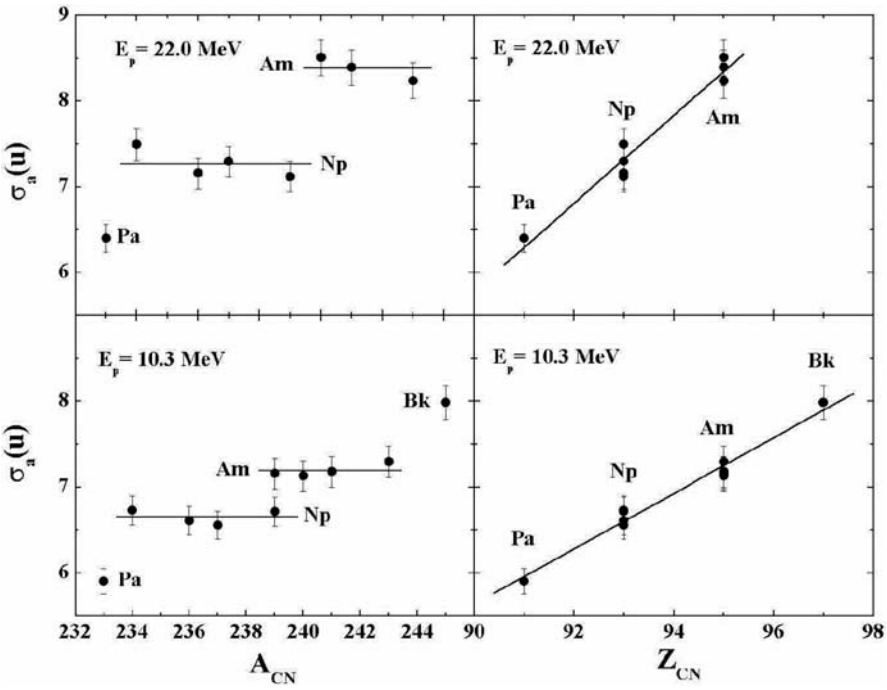

FIG. 4.5.16. Mass yield variance for asymmetric fission, σ_a versus A and Z_{CN} at E_p = 10.3 and 22.0 MeV.

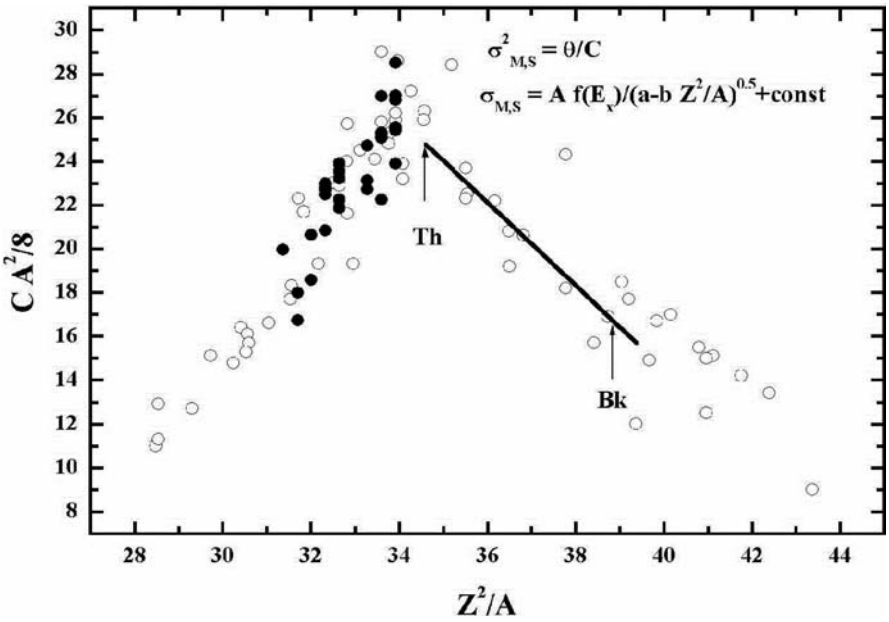

FIG. 4.5.17. Experimental values $CA^2/8$ and their linear parameterization from Th to Bk; closed circles: Ref. [4.5.34], open circles: Ref. [4.5.35].

TABLE 4.5.9. VALUES OF γ_1 AND γ_2 FOR DIFFERENT Z_{CN}

	Z_{CN}								
	90	91	92	93	94	95	96	97	98
γ_1	0	–0.08	0.36	0.23	0.3	0.38	0.34	0.29	0.0
γ_2	–0.36	–0.07	–0.34	–0.27	–0.3	–0.34	–0.25	–0.15	0.0

$$\sigma_S = A\, f(E^*)/(a_a - b_a\, Z_{CN}^2/A) + c_a \qquad (4.5.14)$$

where a_a, b_a and c_a are parameters of the systematics.

The systematics parameters from Eqs (4.5.12)–(4.5.14) and dependences of Y_S/Y_a on Z_{CN}, A and E* for proton and neutron induced fission have been determined by systematically fitting experimental data from the present work and from Refs [4.5.37–4.5.44]. One conclusion of this procedure is that the functions Y_S/Y_a for protons and neutrons differ, and the final equations are as follows:

$M_{H,a} = 28.6(A/Z_{CN}) + 0.708\, Z_{CN}$ for $Z_{CN} \geq 92$;

$M_{H,a} = 54A/Z_{CN}$ for $Z_{CN} = 90, 91$;

$\sigma_a = (A/Z_{CN})(Z_{CN} - 73)(0.074 + 0.0296(E^*)^{0.25})$;

$\sigma_S = 0.031A(E^*)^{0.25}/(90.54 - 1.9(Z_{CN}^2/A))^{0.5} + 9.64$;

γ_1 and γ_2 from Table 4.5.9;

$$Y_S/Y_a = 1.244(E^*)^{0.25}(1 - \exp(-0.0027(E^* - 5.7)^{1.5})) \times (1 + 100/(E^*)^{0.5}(Z_{CN}/A - 0.4))$$

for neutrons with E_n = 5–200 MeV;

$$Y_S/Y_a = 1.18((E^*-5.7)^{0.25}(1 - \exp(-0.011(E^* - 5.7)^{1.5})) - 0.101)(1 + 2500/E^*(Z_{CN}/A - 0.393))$$

for protons with E_p = 5–200 MeV;

$Y_a = 200/(Y_S/Y_a + 2)$; $Y_S = 200 - 2Y_a$

Mass distributions Y(M) calculated from the systematics are compared to the experimental data in Figs 4.5.18–4.5.20.

These figures show that this systematics reproduces the main features of the experimental data and could be used as the basis for predicting fission product yields from 5 to 200 MeV neutron reactions of interest for the transmutation of minor actinides.

4.5.6. PYF code

The systematics has been encompassed within the PYF computer code [4.5.45] in order to calculate the pre- and post-neutron emission fragment mass yields for the fission of target nuclei from Th to Bk in reactions with protons and neutrons at incident energies from 5 to 200 MeV. The numbers of emitted prompt neutrons are

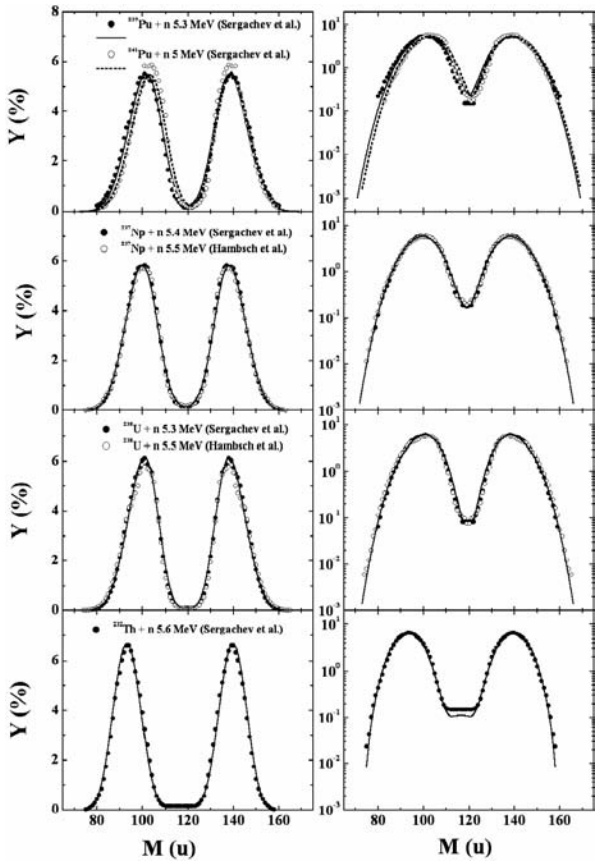

FIG. 4.5.18. Experimental mass yields (circles) from neutron induced fission at $E_n \approx 5$ MeV [4.5.36, 4.5.38–4.5.41]; their systematic descriptions are also shown in linear and logarithmic scales (lines).

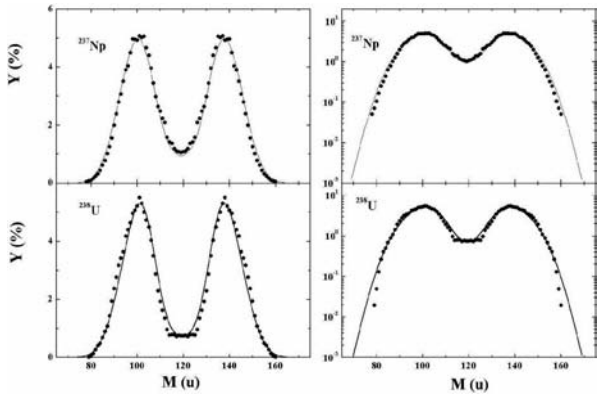

FIG. 4.5.19. Experimental mass yields from neutron induced fission at E_n =16.5 MeV [4.5.43] (circles) and their systematic descriptions (lines) are shown in linear and logarithmic scales.

calculated with the post-fission neutron number systematics from Ref. [4.5.46].

Figure 4.5.21 depicts the user's window to the code, in which the initial input data for the desired reaction, the calculated results and the name of the

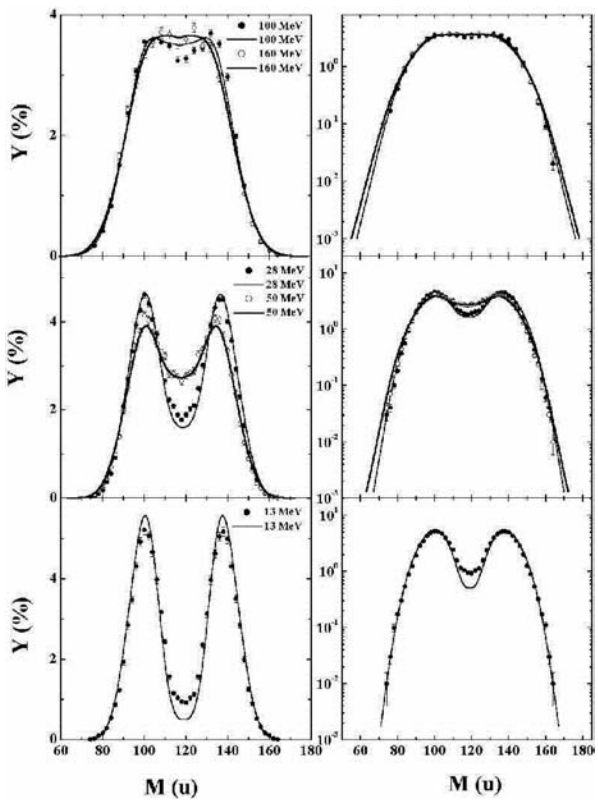

FIG. 4.5.20. Experimental mass yields from neutron induced fission at E_n = 13–160 MeV [4.5.44] (circles) and their calculation from systematics (lines) in linear and logarithmic scales.

output file are shown. The target element and type of incident particle are chosen by clicks in the corresponding circles. Target nucleus mass and particle energy are entered in the corresponding input fields.

The number of pre-fission neutrons is calculated automatically as:

$$\nu_{pre} = INT(0.3(E^* - 6 - B_n)^{0.6} + 0.5)$$

where INT is the FORTRAN integer value process operator and B_n is the neutron emission barrier. The user also has the option to input a value of ν_{pre} selected from any other source (the only program limitation on ν_{pre} is that the value must be an integer). Calculated results are given in the scrollable part of the window, and in the graphics which appear automatically on the screen when the 'OK' button is pressed (Fig. 4.5.22). An output file containing these results is written, the name of which is formulated automatically when the required reaction parameters are defined.

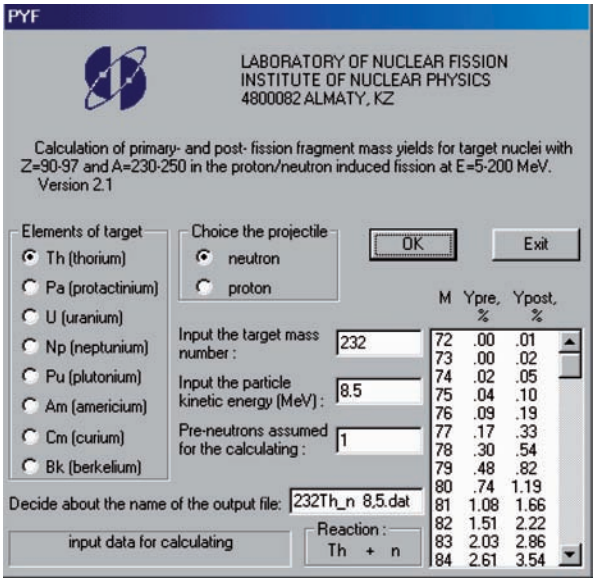

FIG. 4.5.21. User's window for PYF.

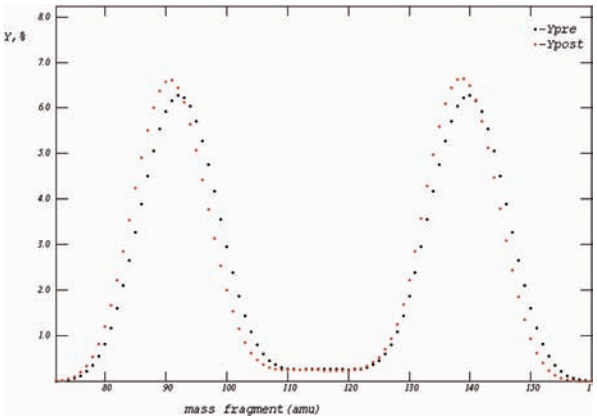

FIG. 4.5.22. Example of the calculated results for the reaction defined in Fig. 4.5.21.

4.5.7. Conclusions

The MEDs in the proton induced fission of compound nuclei ^{234,236,237,239}Np, ^{239,240,241,243}Am, ^{245}Bk at proton energy E_p = 10.3 MeV; ^{234,236,237,239}Np, ^{240,241,243}Am at proton energy E_p = 22.0 MeV; ^{233}Pa and ^{236}Np at E_p = 7.4–30.0 MeV have been measured by means of surface barrier spectrometric studies of the coincident fission fragments. All of the resulting experimental data have been analysed in terms of a newly developed method of multi-component analysis, which is free from any assumptions about the shapes of the mass distributions of distinct modes. These analyses generated information on the basic characteristics of the distinct fission modes and their dependence

on the incident particle kinetic energy and nucleonic composition of the fissioning systems.

Characteristic regularities were revealed in the behaviour of the fission modes, and these phenomena were used to develop new systematics for the pre- and post-neutron emission fragment mass yields from Th to Bk target nuclei in reactions with protons and neutrons at kinetic energies ranging from 5 to 200 MeV. These systematics have been used to formulate the PYF computer code. This approach reproduces the main features of the experimental data and can be used as a basis for the calculation of fission product yields in reactions with neutrons over the energy range 5–200 MeV of interest for the transmutation of minor actinides.

REFERENCES TO SECTION 4.5

[4.5.1] GÖNNENWEIN, F., "Mass, charge and kinetic energy of fission fragments", The Nuclear Fission Process (WAGEMANS, C., Ed.), CRC Press, Boca Raton, USA (1991) 287–473.

[4.5.2] TURKEVICH, A., NIDAY, J.B., Radiochemical studies on the fission of Th^{232} with pile neutrons, Phys. Rev. **84** (1951) 52–60.

[4.5.3] PASHKEVICH, V.V., On the asymmetric deformation of fissioning nuclei, Nucl. Phys. A **169** (1971) 175–293.

[4.5.4] BROSA, U., et al., Nuclear scission, Phys. Rep. **197** (1990) 167–262.

[4.5.5] WILKINS, B.D., et al., Scission-point model of nuclear fission based on deformed-shell effects, Phys. Rev. C **14** (1976) 1832–1863.

[4.5.6] MULGIN, S.I., et al., Observation of new channel in the proton-induced low-energy fission of nuclei from ^{233}Pa to ^{245}Bk, Phys. Lett. **462B** (1999) 29–33.

[4.5.7] ZÖLLER, C.M., "Fission fragment properties in the ^{238}U(n,f) reaction at incident neutron energies from 1 MeV to 500 MeV", Pont d'Oye III (Proc. Sem. Habay-la-Neuve, Belgium, 1995), Rep. IKDA-95/25, Technische Hochschule Darmstadt, Germany (1995).

[4.5.8] KONDRATIEV, N.A., et al., Method of fast spectrometry of pair fission fragments from fission with time-of-flight selection of events, Prib. Tekh. Ehksp. **2** (1990) 62–66 (in Russian).

[4.5.9] HENSHEL, H., et al., The influence of plasma effects on the timing of fission fragments with semiconductor detectors, Nucl. Instrum. Methods **125** (1975) 365–372.

[4.5.10] SCHMITT, H.W., et al., Precision measurements of correlated energies and velocities of ^{252}Cf fission fragments, Phys. Rev. **4** (1965) B837–B847.

[4.5.11] KAUFMAN, S.B., et al., A calibration procedure for the response of silicon surface-barrier detectors to heavy ions, Nucl. Instrum. Methods **115** (1974) 47–55.

[4.5.12] MULGIN, S.I., et al., Two-parametric method for silicon detector calibration in heavy ion and fission fragment spectrometry, Nucl. Instrum. Methods Phys. Res. A **388** (1997) 254–259.

[4.5.13] GAVRON, A., Correction of experimental results in fission experiments, Nucl. Instrum. Methods **115** (1974) 93–98.

[4.5.14] SCHMITT, H.W., et al., Fragment energy correlation measurements for ^{252}Cf spontaneous fission and ^{235}U thermal-neutron fission, Phys. Rev. **141** (1966) 1146–1160.

[4.5.15] PLASIL, F., et al., Kinetic energy-mass distributions from the fission of nuclei lighter than Radium, Phys. Rev. **142** (1966) 696–715.

[4.5.16] STRECKER, M., et al., Pre-scission and post-scission neutrons from the reactions $p+^{235,236,238}$U with $E_p \leq 25.6$ MeV, Phys. Rev. C **41** (1990) 2172–2187.

[4.5.17] STRAEDE, C., et al., ^{235}U(n,f) fragment mass-, kinetic energy- and angular distributions for incident neutron energies between thermal and 6 MeV, Nucl. Phys. A **462** (1987) 85–108.

[4.5.18] PIESSENS, M., et al., Mass and kinetic energy distributions for the photofission of ^{232}Th with 6.44 to 13.15 MeV Bremsstrahlung, Nucl. Phys. A **556** (1993) 88–106.

[4.5.19] BEIZIN, S.D., et al., Study of the trimodal structure of the mass and energy distributions of fission fragments of transactinide nuclei, Sov. J. Nucl. Phys. **53** (1991) 411–414.

[4.5.20] STEIPER, E., et al., Mass dependence of fragment angular distributions in the fission of ^{232}Th and ^{236}U induced by polarized photons, Nucl. Phys. A **563** (1993) 282–300.

[4.5.21] WAGEMANS, C., et al., Investigation of neutron shell effects and fission channels in the spontaneous fission of the Pu-isotopes, Nucl. Phys. A **502** (1989) 287–296.

[4.5.22] SCHILLEBEECKX, P., et al., Comparative study of the fragments' mass and energy characteristics in the spontaneous fission of ^{238}Pu, ^{240}Pu and ^{242}Pu and in the thermal-neutron-induced fission of ^{239}Pu, Nucl. Phys. A **545** (1992) 623–645.

[4.5.23] DEMATTE, L., et al., Fragments' mass and energy characteristics in the spontaneous fission of ^{236}Pu, ^{238}Pu, ^{240}Pu, ^{242}Pu, and ^{244}Pu, Nucl. Phys. A **617** (1997) 331–346.

[4.5.24] GOVERDOVSKII, A.A., MITROFANOV, V.F., Standard modes of thorium fission, Phys. At. Nucl. **60** (1997) 1787–1793.
[4.5.25] POKROVSKY, I.V., et al., Fission modes in the reaction ^{208}Pb(^{18}O,f), Phys. Rev. C **62** (2000) 014615–014625.
[4.5.26] ZHDANOV, S.V., et al., Higher moments of energy distributions of fragments of symmetric fission, Sov. J. Nucl. Phys. **55** (1992) 1766–1771.
[4.5.27] ZHDANOV, S.V., et al., Fragment energy distributions and fission dynamics of heated nuclei, Phys. At. Nucl. **56** (1993) 175–181.
[4.5.28] NIX, J.R., SWIATECKI, W.J., Studies in the liquid-drop theory of nuclear fission, Nucl. Phys. **71** (1965) 1–94.
[4.5.29] CERN Computer 6600 Series Program Library Long-Write-Up MINUIT.
[4.5.30] SCHMIDT, K.-H., et al., Relativistic radioactive beams: A new access to nuclear-fission studies, Nucl. Phys. A **665** (2000) 221–267.
[4.5.31] BÖCKSTIEGEL, C., Bestimmung der totalen kinetischen Energien in der Niederenergiespaltung neutronenarmer radioaktiver Isotope, PhD Thesis 98-05, Technische Universität Darmstadt, Germany (1998).
[4.5.32] GÖNNENWEIN, F., "Nuclear shells in low energy fission", Nuclear Physics Nuclear Shells — 50 Years (Proc. Int. Conf. Dubna, Russian Federation, 1999), World Scientific, Singapore (1999) 64.
[4.5.33] TSEKHANOVICH, I., et al., Mass and charge distributions in the very asymmetric mass region of the neutron induced fission of ^{238}Np, Nucl. Phys. A **688** (2001) 633–658.
[4.5.34] MULGIN, S.I., et al., Shell effects in the symmetric-modal fission of pre-actinide nuclei, Nucl Phys. A **640** (1998) 375–388.
[4.5.35] RUSANOV, A.Ya., et al., Features of mass distributions of hot rotating nuclei, Phys. At. Nucl. **60** (1997) 683–712.
[4.5.36] HAMBSCH, F.-J., et al., Study of the ^{237} Np(n,f)-reaction at MeV neutron energies, Nucl. Phys. A **679** (2000) 3–24.
[4.5.37] GORODISSKIY, D.M., et al., Isotopic and isotonic effects in fission-fragment mass yields of actinide nuclei, Phys. Lett. **548B** (2002) 45–51.
[4.5.38] SERGACHEV, A.I., et al., Influence of intermediate states of fissioning Th^{233} nucleus on the mass and kinetic energy distributins of the fragments, Yad. Fiz. **7** (1968) 778–784.
[4.5.39] VOROBIEVA, V.G., et al., Influence of uranium-232 fission nucleus excitation energy on the yields and kinetic energy distribution of fission fragments, Preprint IPPE-108, Obninsk (1967) 3–16.
[4.5.40] KUZMINOV, B.D., et al., Mass and energy distribution of fragments at the fission of Np-237 by neutrons, Yad. Fiz. **11** (1970) 297–303.
[4.5.41] SERGACHEV, A.I., Influence of the Fission Nuclei Excitation Energy on the Mass and Kinetic Energy Distributions of the Fragments, PhD Thesis, IPPE, Obninsk (1974).
[4.5.42] VIVÈS, F., et al., Investigation of the fission fragment properties of the reaction ^{238}U(n,f) at incident neutron energies up to 5.8 MeV, Nucl. Phys. A **662** (2000) 63–92.
[4.5.43] GOVERDOVSKII, A.A., MITROFANOV, V.F., Shaping of the mass-energy spectra of ^{238}Np fission fragments near the barrier, Yad. Fiz. **56** (1992) 43.
[4.5.44] ZÖLLER, C.M., Untersuchung der neutroneninduzierten Spaltung von ^{238}U im Energiebereich von 1 MeV bis 500 MeV, PhD Thesis, Technische Universität Darmstadt, Germany (1995).
[4.5.45] http://www.inp.kz/laboratoryrus/lpdpyf.php
[4.5.46] WAHL, A.C., Systematics of Fission-Product Yields, Rep. LA-13928, Los Alamos National Laboratory, NM (2002).

4.6. FISSION YIELDS IN NUCLEON INDUCED REACTIONS AT INTERMEDIATE ENERGIES

M.C. Duijvestijn, A.J. Koning
Nuclear Research and Consultancy Group, Netherlands

Results are presented of an activation experiment on proton induced fission of ^{nat}W, ^{197}Au, ^{nat}Pb, ^{208}Pb and ^{232}Th at 190 MeV. Fission product yields have been measured and an attempt has been made to reconstruct the charge and mass yield curves. This is followed by the description of a new theoretical approach to predict fission fragment mass yields for both actinides and sub-actinides in the incident energy range between 10 and 200 MeV. Temperature dependent fission barriers and pre-scission shapes are determined within a temperature dependent version of the Brosa model. These quantities combined with the original random neck rupture model and the existing nuclear reaction code ALICE-91 provide a new way of calculating fission fragment and product yields. The predictive power of this method is tested against a set of experimental data.

4.6.1. Introduction

The absence of a satisfactory theoretical description to predict isotope yields as well as the need for experimental fragment mass and charge distributions at intermediate energies form the motivation of this contribution. The work performed in the framework of the CRP consists of four separate topics:

(1) Compilation of proton induced fission product and fission fragment mass distributions from literature;
(2) Experimental efforts aimed at measuring proton induced fission product yields at 190 MeV of ^{232}Th and several sub-actinide targets;
(3) Development of a new computational method to predict intermediate energy nucleon induced fission product mass yields using a combination of the existing nuclear reaction code ALICE-91 and the Brosa model extended with a temperature dependence;
(4) Theoretical predictions of fission fragment and fission product mass yield curves for all reactions specified by the CRP benchmark.

Several parts of this research have already been published in journals and conference proceedings [4.6.1–4.6.8]. A more detailed description of the experimental as well as the theoretical work can be found in Ref. [4.6.9].

4.6.2. Compilation of proton induced fission product isotope yields

Fission product isotope yield and mass yield data have been gathered for proton induced reactions on actinide targets. The search has been limited to the intermediate energy region (i.e. proton energies ranging from 15 to 200 MeV). The data are taken from 14 references. The reaction specification is found in Table 4.6.1, as are the incident proton energies, the type of compiled data (mass yields/isotope yields), the compilation form (read from figures or tables) and the reference. In the case of data read from figures, an extra uncertainty has been added to the published one because of the inevitable amount of arbitrariness linked to estimating data from figures. The files containing the compiled experimental data can be downloaded from web site: http://ndsalpha.iaea.org/fycrp/

All data taken from a single reference are collected in one file. Each entry starts with a title revealing the necessary information regarding the target and the incident proton energy, which is followed by the reference, comments and the data points. The comments concern the given uncertainties, whether data are taken from tables or figures, and a description of the contents of the columns containing the data points. In case of more incoming proton energies or target nuclides, entries are concatenated.

4.6.3. Activation experiment on proton induced fission of ^{nat}W, ^{197}Au, ^{nat}Pb, ^{208}Pb and ^{232}Th at 190 MeV

Several sub-actinide targets and a ^{232}Th target have been irradiated with a 190 MeV proton beam from the AGOR cyclotron at the KVI, Groningen.

TABLE 4.6.1. FISSION PRODUCT YIELD DATA SETS COMPILED FOR THE CRP
Data sets marked with an asterisk correspond to fission fragment yields (as opposed to fission product yields)

Reaction	Incident proton energy (MeV)	Comments	Reference
p + ^{232}Th	8.0, 9.3, 13.3, 17.8, 21.1	Mass yields taken from table	[4.6.10]
p + ^{232}Th	13.0, 20.0, 27.0, 35.0, 40.0, 45.0, 53,0	Mass yields read from figures	[4.6.11]*
p + ^{232}Th	8.6, 9.9, 11.9, 13.0, 13.9, 14.8, 16.0, 17.0, 18.4, 20.2, 21.9	Isotope yields taken from table	[4.6.12]
p + ^{nat}U	75.0, 100.0, 170.0, 250.0, 340.0	Mass yields read from figures	[4.6.13]
p + ^{238}U	10.0, 32.0, 70.0, 100.0 150.0, 200.0, 250.0, 300.0, 340.0	Isotope yields taken from table	[4.6.14]
p + ^{nat}U	170.0	Isotope yields taken from table	[4.6.15]
p + ^{nat}U	170.0	Isotope yields taken from table	[4.6.16]
p + ^{238}U	13.0, 15.7, 18.1, 21.8, 25.0 30.0, 35.0, 40.0, 44.9, 50.1, 55.0	Mass/isotope yields taken from table	[4.6.17]
p + ^{238}U	13.0, 14.0, 15.0, 16.0	Mass/isotope yields taken from table	[4.6.18]
p + ^{238}U	20.0, 25.0, 30.0, 35.0, 40.0, 45.0, 50.0, 55.0, 60.0, 65.0, 70.0, 77.0, 85.0	Isotope yields taken from table	[4.6.19]
p+ ^{238}U	14.8, 17.9	Mass/isotope yields taken from table	[4.6.20]
p + ^{238}U	24.0	Fractional chain yields taken from table	[4.6.21]
p + ^{238}U	20.0, 60.0	Mass yields read from figures	[4.6.22]*
p + ^{233}U	9.8, 11.2, 13.9, 15.5	Isotope yields taken from table	[4.6.23]
p + ^{235}U	10.2, 12.0, 13.6, 15.6, 18.0	Isotope yields taken from table	[4.6.23]
p + ^{236}U	10.2, 12.1, 14.0, 15.6	Isotope yields taken from table	[4.6.23]
p + ^{237}Np	10.2, 11.9, 13.2, 14.2, 15.5, 19.5, 20.5, 21.6, 22.5, 23.6, 24.6, 25.5, 26.5, 27.5, 28.8, 31.7	Isotope yields taken from table	[4.6.23]
p + ^{239}Pu	11.2, 12.2, 13.9, 15.5	Isotope yield taken from table	[4.6.23]
p + ^{242}Pu	12.0, 18.0	Isotope yield taken from table	[4.6.23]
p + ^{244}Pu	11.7, 13.1, 15.5, 18.0	Isotope yield taken from table	[4.6.23]
p + ^{241}Am	10.0, 12.0, 14.0, 15.0, 16.0	Isotope yield taken from table	[4.6.23]
p + ^{243}Am	10.4, 12.0, 14.0, 15.6	Isotope yield taken from table	[4.6.23]

An advanced target stacking technique is employed to separate the fission products from the evaporation residues. The fission products in the irradiated samples have been measured by off-line γ ray spectroscopy. A detailed description of the experimental set-up as well as the data analysis can be found in Refs [4.6.2, 4.6.7, 4.6.9]. The final results of relevance to the CRP are emphasized in this report.

4.6.3.1. Fission product isotopic yields

At the incident energy considered in this experiment, fission fragments are produced in the vicinity of, or even in, the valley of stability. This is not surprising because the fission event is preceded by pre-equilibrium emission and evaporation. For the heavy targets studied here, this emission will mainly involve neutrons. Consequently the neutron-rich fission products associated with low energy fission of actinides will be less prominent in these results. Instead, a high yield of stable or extremely long lived isotopes among the fission products is expected. These nuclei escape the detection method utilized here — just like nuclei that do not emit detectable γ rays — leading to incompletely measured yields in many mass bins. On the other

hand, the on average longer half-lives of the less neutron rich fission products also give rise to an advantage. Part of the primary fission products, which remain after post-scission neutron evaporation by the fragments, occur with longer half-lives and hence are easier to observe. They can now be measured directly, instead of only through their beta decay products.

4.6.3.2. Sub-actinide fission

4.6.3.2.1. Mass distributions

For each sub-actinide target, the mass distribution is extracted from the measured cumulative and independent isotope yields by fitting simultaneously the mass and charge distribution. The fission process is assumed to be symmetric for the sub-actinide targets. Therefore, the mass and the charge distribution for a given mass are each described by a single Gaussian in the fit. Moreover, the assumption is made that the most probable charge, as well as the width of the charge distribution, vary linearly with the mass of the fission fragment. The following parameterization of the production cross-section as a function of the mass and charge of the fission fragment is adopted:

$$\sigma_{\mathrm{prod}}(A,Z) = \lambda_A e^{-\frac{(A-M_A)^2}{\Gamma_A^2}} \frac{1}{\sqrt{\pi}\Gamma_Z} \sum_i e^{\frac{(Z-i-Z_p)^2}{\Gamma_Z^2}} \qquad (4.6.1)$$

with $Z_p = \mu_1 + \mu_2 A$ and $\Gamma_Z = \gamma_1 + \gamma_2 A$. The first Gaussian represents the symmetric mass distribution defined by the height λ_A, mean M_A and width Γ_A. The rest of the formula reflects the charge distribution. In the case of an independent yield, only one term in the sum of the normalized Gaussian charge distribution (i.e., i = 0) contributes. A cumulative yield is described by summing the contributions of neighbouring isobars. The index i is equal to 0, 1,…5 for neutron rich cumulative yields, and equal to 0, –1,…–5 for neutron deficient cumulative yields. The number of terms (six) in the summation for cumulative yields is rather arbitrary, but in these investigations has turned out to be sufficient. A more elaborate description of the functional form can be found in the work by Hagebø and Lund [4.6.24].

The values of the fit parameters obtained for all sub-actinide targets are tabulated in Table 4.6.2. The mean value as well as the height of the mass distribution clearly increases with increasing target mass, as expected. From the mean of the mass distributions it can be concluded that, on average, nine mass units are emitted before and after fission. With the charge distribution known from the fit of Eq. (4.6.1), it is straightforward to determine the fractional independent or cumulative yields represented by each of the observed independent or cumulative isotope yields in their mass chains. Subsequently, the measured yields are divided by their corresponding fractional yields to derive the experimental mass yields. In the case of ^{nat}Pb, the spread in the adjusted yields is rather large. Therefore, the final mass distribution has been obtained after fitting to the measured yields, which represent at least 50% of the complete mass distribution. The total mass yields are plotted in Fig. 4.6.1, together with the mass distribution obtained in the fit for ^{nat}W, ^{197}Au, ^{nat}Pb and ^{208}Pb. The results agree with the assumption of a symmetric mass and charge distribution.

4.6.3.2.2. Charge distributions

Integrating over the Gaussian and multiplying by a factor 1/2, because of the two fission fragments in each fission event, gives an estimate for the fission cross-section. The values for the fission cross-sections determined in this way are also given in Table 4.6.2. The assumption is made that the uncertainties in the independent and cumulative yields that have been used in the fit are uncorrelated, since they stem from many different spectra. Therefore the only uncertainty remaining in the deduced fission cross-sections is the systematic uncertainty due to the overall normalization determined from the proton flux. Eismont et al. [4.6.25] have made a data compilation for the fission cross-section as a function of incident proton energy for some of these target materials. The values from the Eismont et al. fit are also shown in Table 4.6.2 for comparison and are in fairly good agreement with the results from this work.

By fitting Eq. (4.6.1) to the available experimental independent and cumulative yields, information on the charge distribution is obtained. The charge distributions in three fission fragment mass regions of ^{208}Pb are shown in Fig. 4.6.2 as an example. The fitted charge distributions are evaluated for the indicated masses. Since the charge yield curves vary only slowly as a function of mass, the fits should give a good representation of the

TABLE 4.6.2. FIT PARAMETER VALUES OBTAINED FOR A SINGLE GAUSSIAN FOR THE DIFFERENT SUBACTINIDE TARGETS (Eq. (4.6.1)).

The mass distribution is described by a Gaussian with the parameters λ_A for the height, M_A for the mean, and Γ_A for the width. The charge distribution is also given by a Gaussian, with the width given as $\Gamma_Z = \gamma_1 + \gamma_2 A$ and the most probable charge as $Z_p = \mu_1 + \mu_2 A$. Fission cross-sections are deduced from the fitted mass distributions and compared with values obtained from Ref. [4.6.25]. The uncertainties in the fit parameters indicate the sensitivity of the fit. The uncertainties in the fission cross-sections include the 10% systematic uncertainty that arises from the uncertainty in the proton flux.

	^{nat}W	^{197}Au	^{nat}Pb	^{208}Pb
λ_A	0.2323 ± 0.0022	2.085 ± 0.011	5.88 ± 0.26	5.0 ± 0.7
M_A	87.1 ± 0.2	92.9 ± 0.1	99.5 ± 0.4	100.7 ± 0.8
Γ_A	22.1 ± 0.3	17.7 ± 0.1	18.1 ± 0.3	19.8 ± 0.6
γ_1	0.801 ± 0.010	0.850 ± 0.005	0.74 ± 0.10	0.5 ± 0.3
γ_2	0.0051 ± 0.0004	0.00395 ± 0.00022	0.0046 ± 0.0014	0.008 ± 0.004
μ_1	1.619 ± 0.007	1.642 ± 0.005	1.18 ± 0.08	0.97 ± 0.18
μ_2	0.4147 ± 0.0002	0.41193 ± 0.00010	0.4137 ± 0.0009	0.413 ± 0.002
χ^2	3.0	3.2	11.7	1.14
σ_f^{exp}	4.5 ± 0.5	32.8 ± 3.3	94 ± 9	88 ± 9
$\sigma_f^{Eismont}$	3.7	–	88	74

behaviour of the charge yields in a certain mass range. Experimental yields found in the neighbourhood of the indicated mass are drawn as a function of the distance to the most probable charge Z_p and compared to the fitted charge distributions. The experimental values are normalized to filter out the dependence on the total mass yields in the considered bins and make this comparison possible. The plot contains both the independent and the cumulative yields. The fits agree nicely with the experimental data. When going to heavier fission products, the width of the charge distribution increases slightly.

Two approaches are commonly used to describe the most probable charge of a fission product: the uniform charge distribution (UCD) and the equal charge displacement (ECD). The uniform charge distribution approach assumes that the proton over neutron ratio in the fissioning system, characterized by Z_{tot}/A_{tot}, is conserved by the fission process. In this case the charge of a fission fragment is given by Z_{tot}/A_{tot} multiplied by its mass. The equal charge displacement model proposes that the fission fragments with masses A_1 and A_2 are formed at equal distance to the line of stability:

$$Z_p = Z_s(A_1) + \tfrac{1}{2}(Z_{tot} - Z_s(A_1) - Z_s(A_2)) \quad (4.6.2)$$

with the most probable stable charge Z_s as a function of mass (i.e. line of stability) taken from an empirical relation [4.6.26]:

$$Z_s(A) = \frac{A}{1.98 + 0.0155A^{2/3}} \quad (4.6.3)$$

Both approaches are compared to the fit results for ^{208}Pb in Fig. 4.6.3. Three possible average fissioning systems are tried as input: ^{200}Pb, ^{200}Bi and ^{198}Bi, accounting for the evaporation of around ten nucleons before fission. In reality, Z_p comes about as a superposition of contributions of many fissioning nuclides. The calculated lines correspond to fission fragments, whereas the experimental line originates from a fit to fission products. All the attempts result in an underestimation of the experimental line, which agrees well with the expectation that fission fragments will also evaporate neutrons. In general, the heavier fragments will evaporate more neutrons than the light fragments. This will change the slope of the calculated lines. The slope of the UCD lines that provide the best description for the slope of the most probable charge as a function of mass in Fig. 4.6.3 will become too steep after the inclusion of post-scission neutron emission. The

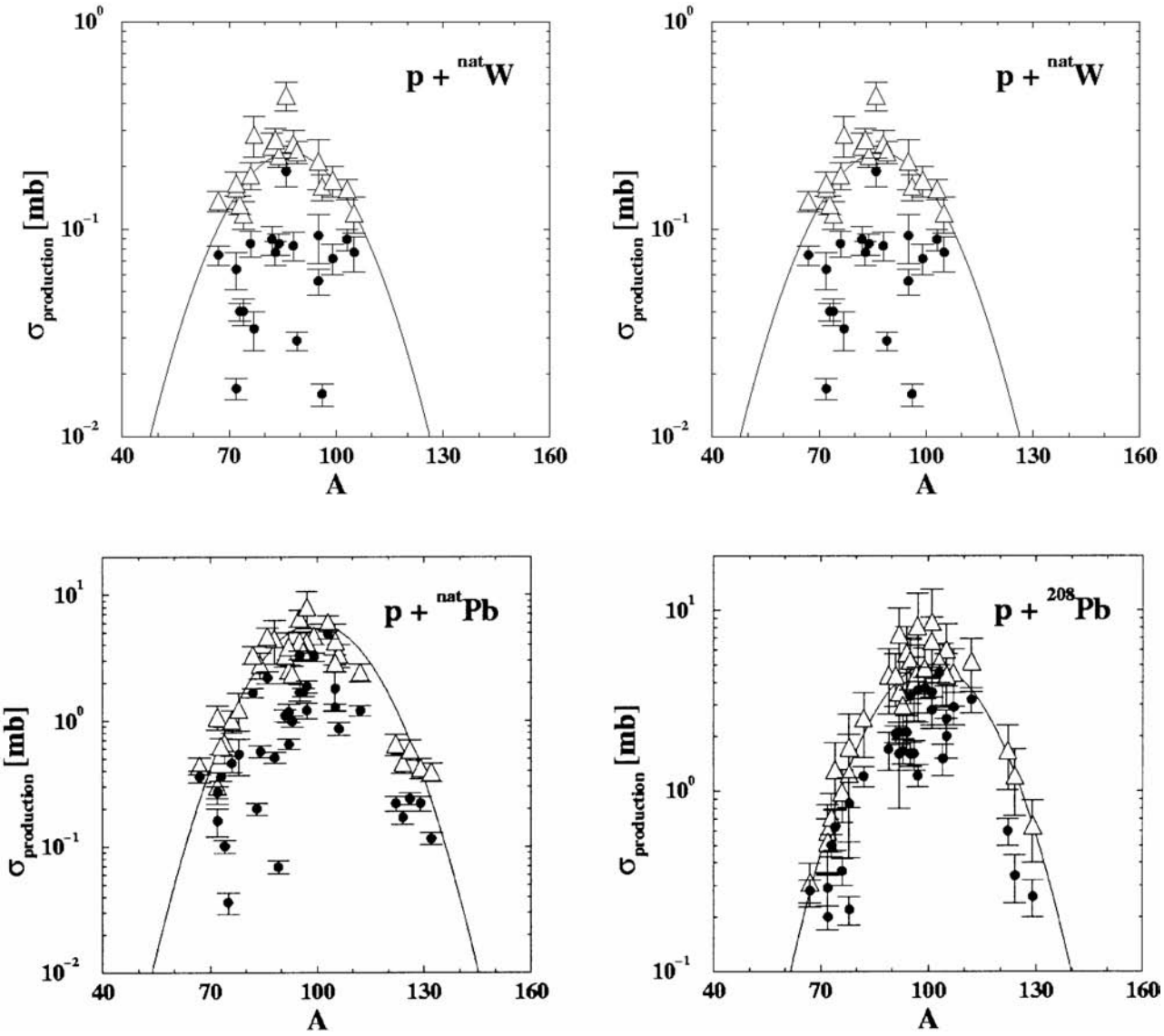

FIG. 4.6.1. Fission product mass yields from 190 MeV proton induced fission of ^{nat}W, ^{197}Au, ^{nat}Pb and ^{208}Pb. The lines indicate the fitted Gaussian mass distributions; the filled circles denote the independent and cumulative yields used in the fit; triangles correspond to the experimental mass yields deduced from these measured independent and cumulative yields.

slope of the ECD lines will probably attain a value closer to the fitted slope. It is impossible to draw a conclusion as to which model gives the best predictions on the most probable charges of the fission fragments.

4.6.3.3. Fission in thorium

4.6.3.3.1. Symmetric and asymmetric fission contributions

Fitting Eq. (4.6.1) to the measured yields of ^{232}Th produces the mass yields and the mass distribution, as shown in Fig. 4.6.4. The result is certainly not a Gaussian, as is the case for the sub-actinide targets. Furthermore, the fission cross-section obtained in this manner is 630 ± 60 mb, which is much lower than the value by Eismont et al. of 1236 mb from systematics [4.6.25]. The values of the fit parameters can be found in Table 4.6.3. Looking carefully at the ^{232}Th mass yields, one notices a dip around fragment mass 125. Therefore, the suggestion is that the fragment mass distribution for ^{232}Th cannot be properly described by a single Gaussian, but rather is a superposition of a wide flattened distribution and a narrower Gaussian.

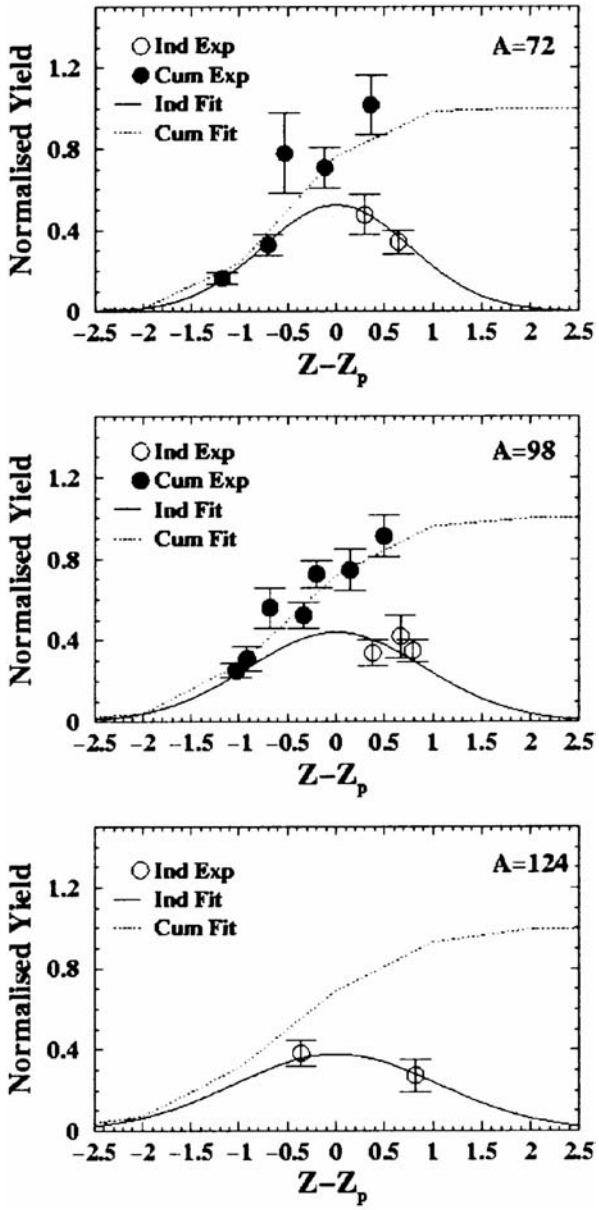

FIG. 4.6.2. Charge distributions for three mass regions in 190 MeV proton induced fission of ^{208}Pb — normalized yields are drawn as a function of the distance to the most probable charge. Open and filled circles correspond to the experimental independent and cumulative yields, respectively, which are observed in a region around the denoted mass; solid and dotted lines represent the independent and cumulative yields, respectively, which result from the fit.

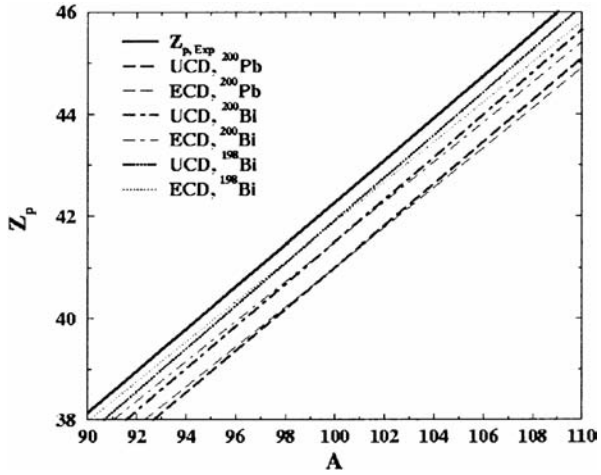

FIG. 4.6.3. Most probable charge Z_p for ^{208}Pb as a function of fission product (or fission fragment) mass A. The upper bold solid line stems from the fit to the experimental data; other bold lines belong to the uniform charge distribution approach, and the normal lines to equal charge displacement; dashed lines correspond to ^{200}Pb, dot–dashed lines to ^{200}Bi, and dotted lines to ^{198}Bi as the average fissioning systems assumed in the calculation of Z_p.

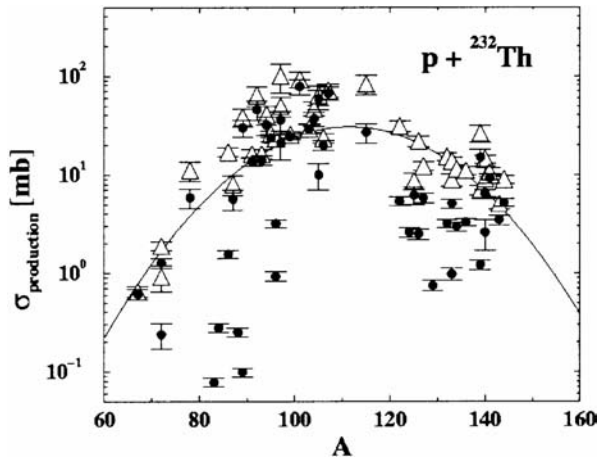

FIG. 4.6.4. Same as Fig. 4.6.1, but for ^{232}Th. Experimental mass yields obtained from the parameterization of Eq. (4.6.1) are not described in a satisfactory way by the Gaussian.

This more complicated form of the mass distribution can stem from contributions by different fissioning mechanisms in the many fissioning intermediate nuclides.

Due to the particle evaporation process that takes place before fission, a set of various fissioning nuclides exists. Each of them has its own fission characteristics and excitation energy and angular momentum distributions. Chung and Hogan [4.6.27, 4.6.28] have collected data on the mass yield curves for fissioning nuclei with atomic numbers ranging from Z = 80 to Z = 105. They propose that nuclides with a fissility parameter Z^2/A greater than a critical value $(Z^2/A)_C$ are situated in the region of symmetrical fission, while nuclides with Z^2/A smaller than that value fission only asymmetrically. Their approach is based on the observation that the

TABLE 4.6.3. FIT PARAMETER VALUES FOR THE ^{232}Th MASS YIELD CURVES

The first two columns contain the values of the fit parameters for the single Gaussian mass and charge distribution fit, see Eq. (4.6.1) (referred to as symmetric). In the third and fourth column the parameter values that describe the decomposition of the mass distribution can be found, see Eq. (4.6.5) (referred to as decomposed). The meaning of the parameters is explained in the text. The fission cross-sections as obtained from the fit parameters are given as well as the value of Ref. [4.6.25]. The uncertainties in the fit parameters indicate the sensitivity of the fit. The uncertainties in the fission cross-sections include a 10% systematic uncertainty that arises from the uncertainty in the proton flux.

Symmetric fit parameters	Value	Decomposed fit parameters	Value
λ_A	30.7 ± 0.5	s_1	52 ± 4
M_A	111.5 ± 0.2	s_2	107.3 ± 0.4
Γ_A	23.15 ± 0.14	s_3	14.7 ± 0.6
—	—	m_1	5.3 ± 1.0
—	—	m_2	110.0 ± 0.3
—	—	m_3	30.2 ± 2.2
—	—	m_4	11.2 ± 0.7
—	—	m_5	27.7 ± 0.3
—	—	m_6	6.5 ± 0.4
γ_1	0.820 ± 0.012	γ_1	0.345 ± 0.012
γ_2	0.00786 ± 0.00013	γ_2	0.0129 ± 0.0002
μ_1	1.92 ± 0.02	μ_1	2.07 ± 0.02
μ_2	0.3910 ± 0.0002	μ_2	0.38953 ± 0.0004
χ^2	12.8	χ^2	5.9
σ_f^{exp} [mb]	630 ± 60	σ_f^{exp} [mb]	950 ± 95
$\sigma_f^{Eismont}$ [mb]	1236	$\sigma_f^{Eismont}$ [mb]	1236

symmetric component increases with excitation energy, which is coupled to an increase of neutron evaporation resulting in a larger contribution of the neutron deficient nuclides with a higher fissility parameter. The excitation energy for which symmetric fission starts to contribute gives rise to a number of evaporated nucleons, corresponding to a certain neutron deficient nucleus. This nucleus is held responsible for the symmetric contribution and, hence, marks the position of the critical fissility parameter. From the data they have extracted an expression for this critical value as a function of nuclide charge:

$$(Z^2/A)_C = 35.5 + 0.4(Z - 90). \quad (4.6.4)$$

This criterion is compared to theoretical results in Section 4.6.4.

When compared to other experimental data, this criterion turns out to contradict these results. Measurements of proton induced fission of Th between 8 and 22 MeV have been performed by Kudo et al. [4.6.12]. According to the assumption made by Chung and Hogan, the mass distributions in their experiment should be purely asymmetric, since all the fissioning systems that contribute have a Z^2/A smaller than the critical value. However, the mass distributions in their experiment reveal a symmetric component as well. Another experiment by Schmidt et al. [4.6.29] on fission of neutron deficient actinides shows a clear transition of mixed symmetrical and asymmetrical charge distributions towards purely symmetrical charge distributions with decreasing neutron number.

Several attempts other than the one by Chung and Hogan have been made in the past to describe and understand the varying fission characteristics of nuclides with excitation energy (e.g. Refs [4.6.30–4.6.34]). An overview can be found in Ref. [4.6.35]. Moreover, Brosa et al. [4.6.36] have developed a

model which is elucidated elsewhere in this report. In summary, the competition between symmetric and asymmetric fission is thought to be connected to shell effects in the deformed nucleus. The presence of these shell structures leads to the existence of symmetric and asymmetric fission modes or channels, which a nucleus can choose to follow on its way to fission. It is the contribution of each fission mode that changes with excitation energy. In addition, shell effects fade with higher excitation energy, leaving behind a nucleus which possesses merely a symmetric fission mode. As a result of these properties, actinides near the valley of stability prefer asymmetric fission at low energies but are subject to an increasing contribution of symmetric fission at increasing energies. Further away in the neutron deficient region, the nuclides tend to fission symmetrically even at lower excitation energies [4.6.29, 4.6.31]. This understanding, together with the experimental observations, suggests that Chung and Hogan have only elucidated half of the story: the largest contribution to symmetric fission at high energies seems to originate from the very neutron deficient nuclides plus the target-like fissioning systems at higher excitation energies.

In the light of these ideas, the following two assumptions are made in the analysis of the experimental data presented in this work. Firstly, the fissioning nuclides like ^{232}Th and adjacent isotopes are thought to be responsible for a mass yield curve which is wide and to some extent flattened, due to the mixed contributions from asymmetric and symmetric fission modes (referred to as mixed fission). Secondly, it is proposed that the very neutron deficient lighter isotopes of Th and of the neighbouring lower Z elements produce a narrower Gaussian mass distribution belonging to a symmetric fission mode only (referred to as purely symmetric fission). This idea is consistent with the observation that the narrower Gaussian in the experimental mass distribution seems to be shifted to lower masses in comparison to the wide and flattened part of the mass distribution. The image of the neutron deficient nuclides possessing merely a symmetric fission mode is too simplistic. Nevertheless, regarding the fact that symmetric fission dominates at both low and high energies, it may serve to give a schematic description of the observed mass yields together with the mixed fission contribution.

It is possible to decompose the mass yield curve observed for ^{232}Th, following the assumptions described above, by splitting the dependence on the fission fragment mass of the production cross-section into a part for purely symmetric and into a part for mixed fission:

$$\sigma_{\mathrm{prod}}(A,Z) = \left[\underbrace{s_1 e^{-\frac{(A-s_2)^2}{s_3^2}}}_{\text{symmetric}} + \underbrace{m_1 e^{-\frac{(A-m_2)^2}{m_3^2}} + m_4 e^{-\frac{(A-(m_2-m_5))^2}{m_6^2}} + m_4 e^{-\frac{(A-(m_2+m_5))^2}{m_6^2}}}_{\text{mixed}}\right] \cdot \frac{1}{\sqrt{\pi}\Gamma} \sum_i e^{\frac{(Z-i-Z_p)^2}{\Gamma_Z^2}}, \quad (4.6.5)$$

with A and Z being the fragment mass and charge, $s_{1...3}$ the fit parameters of the purely symmetric fission contribution and $m_{1...6}$ the fit parameters of the mixed fission contribution. The mixed fission parameterization consists of three Gaussians, the first Gaussian describing the symmetric and the other two describing the asymmetric fission contribution. Although the fission process is assumed to be a sum of symmetric and mixed contributions, the charge dependence taken is the same as in Eq. (4.6.1). An attempt to take a more general form of the charge distribution into account, consisting of a sum of two Gaussians, failed because the experimental data are not sufficiently descriptive to reconstruct a more complicated form. The values of the fit parameters can be found in Table 4.6.3.

The result for the mass distribution is given in Fig. 4.6.5. The triangles denote the mass yields that were obtained by dividing the experimental independent or cumulative yields by the corresponding fractional yields, which were determined with the charge distribution from the fit. Those mass yields, which were derived from observed yields that correspond to less than 10% of the total mass chain yield, are not considered in the final fit. The spread in the complete mass yields may be due to the use of the simplified parameterization of the charge distribution. Adding the mixed and the purely symmetric contributions results in a mass yield curve that resembles the measured form of the mass distribution better than the single Gaussian fit of Eq. (4.6.1). The purely symmetric Gaussian has a smaller mean value than the Gaussian that represents the symmetric component of mixed

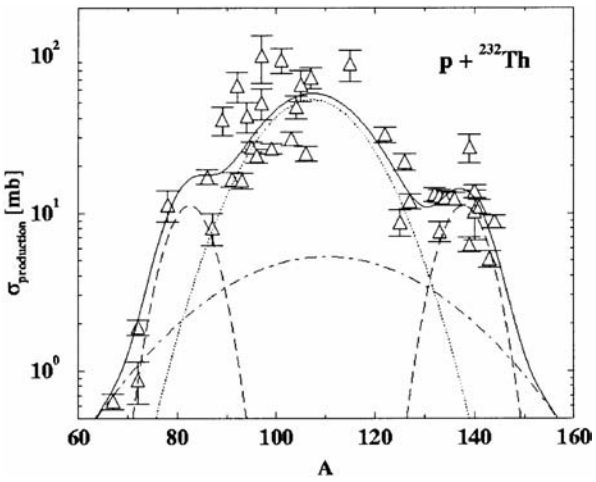

FIG. 4.6.5. Decomposition of the ^{232}Th mass yield curve into one Gaussian (dotted line) coming from purely symmetric fission of lighter nuclides, and three Gaussians representing the mixed symmetric (dot-dashed line) and asymmetric (dashed line) fission modes of heavier nuclides. The solid line indicates the sum of the symmetric and the mixed contributions; triangles represent the experimental mass yields resulting from dividing the measured yields by the fractional yields obtained with Eq. (4.6.5).

fission. This is in agreement with the idea that the purely symmetric Gaussian comes from the fissioning nuclides that have lost more pre-fission neutrons. The four Gaussians give only a schematic description of reality, but enable one to estimate the part of the fission cross-section originating from purely symmetric and from mixed fission. A disentanglement of the contributions of the different fission modes in all the fissioning nuclides is far more complicated. From this decomposition the cross-section is estimated to be 680 ± 70 mb for purely symmetric and 271 ± 27 mb for mixed fission. The new total fission cross-section thus becomes 950 ± 100 mb, which is in better agreement with the Eismont et al. [4.6.25] value of 1236 mb than the value originating from the single Gaussian fit. The result from the Eismont fit is based on experimental data points ranging from 1050 mb to 1250 mb. Therefore the conclusion is that a decomposition of the ^{232}Th fission fragment mass distribution into a mixed fission and a purely symmetric fission component gives a better description of the data than a single Gaussian.

The previously mentioned experiment by Schmidt et al. [4.6.29] supports the assumptions on the mixed and purely symmetric fission components. Other experimental evidence for the particular form of the fission product mass distribution can be found in the work by Pappas and Hagebø [4.6.16] and by Lee et al. [4.6.37]. Pappas and Hagebø arrived at similar findings when inducing fission of ^{238}U with 170 MeV protons. They have proposed a decomposition of the mass yield curve into a symmetric contribution caused by high deposition energy events, and two asymmetric contributions connected to low and high deposition energy events. Lee et al. have studied fission in the bombardment of ^{238}U with 240 MeV C ions. They have interpreted the mass distribution as a superposition of three components: asymmetric low energy fission, symmetric high energy fission (combination of fusion fission and fast fission) and symmetric sequential fission (i.e. fission preceded by multiple nucleon emission). What both these approaches have in common with this work is the symmetric component linked with the more neutron deficient fissioning systems. The treatment of the less neutron poor nuclides differs. Here both symmetric and asymmetric fission modes are thought to play a role in this part of the chart of nuclides, while Pappas and Hagebø omit the symmetric fission contribution completely and Lee et al. neglect the asymmetric fission contribution for excitation energies above 35 MeV (although, according to theoretical calculations, the shell effects responsible for asymmetric fission have not yet vanished at these energies, see, e.g., Ref. [4.6.38]).

4.6.3.3.2. Charge distributions

In Fig. 4.6.6 the charge distributions as they result from the fit of Eq. (4.6.5) are compared to the measured independent and cumulative yields in three different mass regions. Due to the various asymmetric and symmetric contributions, the charge distribution is expected to be much broader than for ^{208}Pb in Fig. 4.6.2. However, in the region around the maximum of the mass yield curve (A ~ 110), the dominant contribution is purely symmetric (as can be concluded from Fig. 4.6.5). Therefore, the corresponding charge distribution should be narrower in this region. The charge distribution fit with a single Gaussian is obviously not able to take into account these changes of the width throughout the different regions. Moreover, the sum of different contributing fission modes may result in a shape for the charge distribution which is no longer a well defined Gaussian. In the upper graph, the experimental yields around mass 103 are not properly described by the fit. The fitted width seems to be overestimated, whereas in the other two plots

the agreement is better. The observed discrepancies of a factor of two between the fitted and the measured independent and cumulative yields give rise to the spread in the constructed experimental mass yields that have been discussed in the previous section. This reveals a clear disadvantage of the experimental technique.

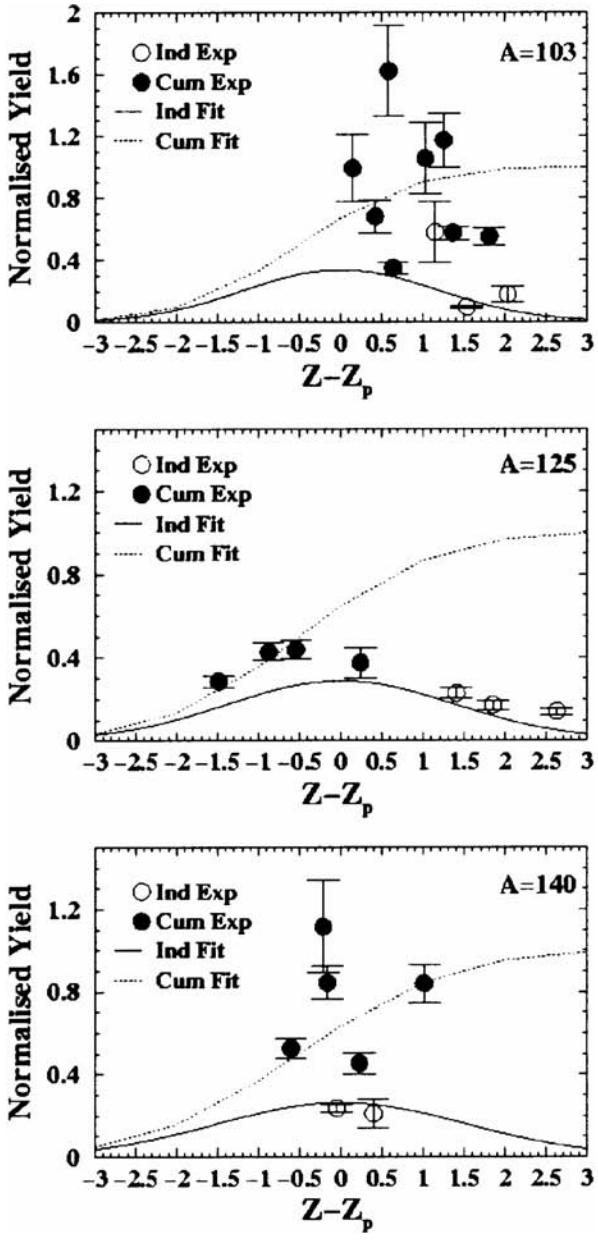

FIG. 4.6.6. Charge distributions for three mass regions in 190 MeV proton induced fission of ^{232}Th. Normalized yields are drawn as a function of the distance to the most probable charge. Open and filled circles correspond to the experimental independent and cumulative yields, respectively, which are observed in a region around the denoted mass; solid and dotted lines represent the independent and cumulative yields, respectively, which result from the fit.

4.6.4. Predictions of fission yields at intermediate energies

In fission at intermediate energies, two factors emerge that complicate the description in comparison with low energy fission: multi-chance fission and the varying fission characteristics with excitation energy. Hence, in the approach of intermediate energy fission presented here, two main ingredients can be distinguished:

(1) A model to determine the fission cross-sections for all fissioning systems (FS) contributing to a specific fission reaction as a function of their excitation energies $\sigma_F(A_{FS},Z_{FS},E^*)$, thus coping with multi-chance fission;
(2) A model to predict the fission fragment and fission product yields for each set of (A_{FS},Z_{FS},E^*), incorporating the variation of the fission characteristics with excitation energy.

To obtain an improved description of nucleon induced fission up to 200 MeV, temperature dependent fission barriers and fission fragment mass distributions are calculated in the framework of a new version of the multi-modal random neck rupture model of Brosa et al. [4.6.36]. Linking this result with the fission cross-section contributions by all possible fissioning systems (A_{FS},Z_{FS},E^*) as computed by the nuclear reaction code ALICE-91 [4.6.39], the total pre-neutron emission mass yields as well as the post-neutron emission mass yields may be determined for any imaginable light particle induced fission reaction from 15 up to roughly 200 MeV. A more detailed description of this work can be found in Ref. [4.6.1].

4.6.4.1. Revised Brosa model

The random neck rupture model, as originally developed by Brosa et al. [4.6.36], is able to calculate properties of the fission fragments at zero temperature (i.e. for spontaneous fission). This model has now been extended for use at temperatures between 0 and 3 MeV (corresponding to 250 MeV excitation energy).

The major adjustment to the original model consists of including temperature dependent shell and pairing effects and combining these with the energy of a heated liquid drop [4.6.40] in the Strutinsky approach [4.6.41] to determine the deformation energy of the excited nucleus. For the shell correction as well as the liquid drop energy, the

isothermal free energy has been employed. A search for the fission channels in deformation space subsequently yields the super long, standard I (ST-1), and standard II (ST-2) fission barriers and the pre-scission shapes as a function of temperature. In this manner, the incorporated melting of shell effects naturally gives rise to the vanishing of the asymmetric fission modes with increasing excitation energies. The super long fission mode results in symmetric fission, whereas the ST-1 and ST-2 fission modes lead to asymmetric fission.

The obtained temperature dependent fission barrier and pre-scission shape parameters serve as input for the fragment mass distribution computations. Each mass distribution is a sum over contributions of the three dominant fission modes (FM):

$$Y(A_{FF};A_{FS},Z_{FS},E^*) = \sum_{FM=SL,STI,STII} W_{FM}(A_{FS},Z_{FS},E^*) \times Y_{FM}(A_{FF};A_{FS},Z_{FS},E^*) \quad (4.6.6)$$

$W_{FM}(A_{FS}, Z_{FS}, E^*)$ denotes the weight of a fission mode, and $Y_{FM}(A_{FF}; A_{FS}, Z_{FS}, E^*)$ is the corresponding fission fragment (FF) mass distribution. An analogous expression can be written down for the fission product (FP) mass yield $Y(A_{FP}; A_{FS}, Z_{FS}, E^*)$. The relative contributions of the different fission modes are evaluated with the Hill–Wheeler penetrability [4.6.42] through inverted parabolic barriers using ground state level densities and temperature dependent barrier parameters. The classic random neck rupture model subsequently translates the rupture probability as a function of the position at the neck of the scissioning nucleus into the pre-neutron emission mass yield curve. In this last step the pre-scission shape of the fissioning nucleus enters the calculation.

4.6.4.1.1. Temperature dependent fission barriers

The ^{238}U barriers for the super long, ST-1 and ST-I modes are depicted in Fig. 4.6.7 as a function of the distance between the fragment centres (d) for several temperatures. At low temperatures, all three fission modes are present. Their inner barriers seem to coincide. The modes subsequently bifurcate in the second minimum. The outer barrier is lowest and narrowest for ST-1, making this the dominant mode. The super long and ST-2 outer barriers have a comparable height, but the super long width is larger. For sub-barrier excitation energies, therefore,

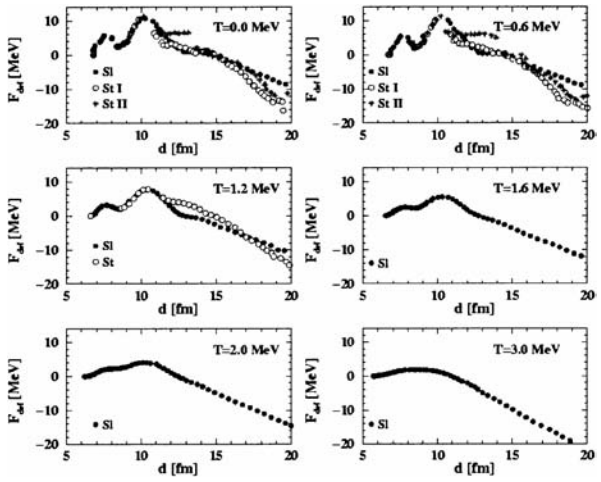

FIG. 4.6.7. Super long (Sl), ST-1 and ST-2 fission channels at varying temperatures for ^{238}U.

the transmission through the ST-2 barrier is higher than through the super long barrier. With an increase in temperature, the shell effects melt away. First the distinction between the two asymmetric standard modes disappears, before at even higher temperatures the standard mode and the double humped structure vanish altogether. Above τ = 2.0 MeV (or E^* ~ 100 MeV) only the liquid drop fission barriers remain, resulting in symmetric fission.

The barrier height and width are obtained by fitting a parabola to the points found in the channel search. Ground state masses are used to determine the barrier width from the fit. Using the penetrability through a parabolic barrier by Hill and Wheeler [4.6.42], with the barrier height B_f and curvature $\hbar\omega$ computed as a function of temperature, the expression for the transmission coefficient at excitation energy E becomes:

$$T_{f,FM}(A_{FS},Z_{FS},E^*) = \int_0^{E^*} d\varepsilon\, \rho_{gs}(A_{FS},Z_{FS},\varepsilon) \times \frac{1}{1+\exp\left[\frac{2\pi(B_{f,FM}(A_{FS},Z_{FS},T(\varepsilon))+\varepsilon-E^*)}{\hbar\omega_{f,FM}(A_{FS},Z_{FS},T(\varepsilon))}\right]} \quad (4.6.7)$$

In this formula, $\rho_{gs}(A_{FS}, Z_{FS}, \varepsilon)$ is the ground state level density for which we use the expression of Gilbert and Cameron [4.6.43] evaluated with the level density parameter by Ignatyuk et al. [4.6.44]. All actinides encounter a double humped barrier on their way to fission. However, since the theoretical

inner barrier is much lower than the outer barrier, the relative contribution of the three fission modes may simply be expressed in terms of the transmission probability through the three outer parallel barriers:

$$W_{SL}(A_{FS}, Z_{FS}, E^*) = \frac{T_{f,SL}}{T_{f,SL} + T_{f,STI} + T_{f,STII}} \quad (4.6.8)$$

Equivalent formulas hold for $W_{ST\text{-}1}$ (A_{FS}, Z_{FS}, E^*) and $W_{ST\text{-}2}$ (A_{FS}, Z_{FS}, E^*).

In the case of sub-actinides it is not possible to calculate the competition between symmetric and asymmetric fission modes, since the computed fission channels exhibit rather broad and strangely shaped outer barriers, which makes a parabola fit to these barriers impossible. Hence the Hill–Wheeler approach cannot be applied. Fortunately, the super long barriers are much lower than the ST barriers. Therefore in all these calculations the asymmetric fission modes are simply discarded and the dominant symmetric super long mode is solely taken into account for sub-actinides.

4.6.4.1.2. Temperature dependent pre-scission shapes

The fission channels end when the neck of the fissioning nucleus becomes smaller than ~2 nucleon radii and is determined by applying the same recipe to all nuclei [4.6.1]. The parameters that determine the pre-scission shapes emerging at the end of the fission paths are input for the random neck rupture model, which gives the mass distributions and the post-scission neutron multiplicities for the various fission modes. These input parameters are the average heavy fragment mass A_h, the half-length of the necked nucleus *l* and its temperature. The loss and gain of excitation energy in crossing the barrier is taken into account in a new temperature of the nucleus at scission. The super long and standard mass distributions are weighted with their relative contributions and added to produce the total mass distribution.

In Fig. 4.6.8 the pre-scission shape parameters A_h and *l* are given as a function of temperature for ^{226}U and ^{238}U. The decline in the fission modes is clearly visible. In both isotopes a fission mode with average heavy fragment mass around 140 exists. The ST-2 mode remains around the same position in fragment mass in going from ^{238}U to ^{226}U, while the ST-1 mode shifts to lighter masses. The super long fission mode results in a more compact configuration, with a smaller value, in the neutron deficient nuclides.

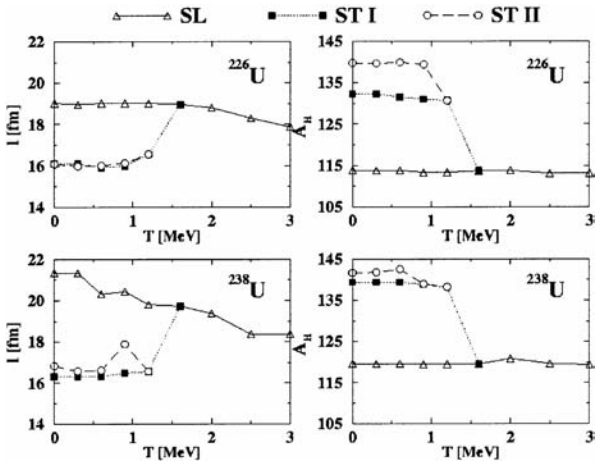

FIG. 4.6.8. The pre-scission shape half-length l and the average heavy fragment mass A_h as a function of temperature for ^{226}U and ^{238}U.

4.6.4.1.3. Random neck rupture model

The random neck rupture model is employed to calculate the mass distribution per fission mode. An elaborative description of the random neck rupture model may be found in Ref. [4.6.36]. Only the main ideas are communicated below. In this model, the fission process is regarded as a series of instabilities. After the passage over the barriers, a neck starts to form. If this neck becomes flat, rupture may happen anywhere, which means that the point of future constriction can shift over the neck. This motion of the dent is called the shift instability. In the instant that the Rayleigh instability starts to deepen the dent, the position of the asymmetry is frozen and rupture is taking place. The random neck rupture model translates the effect of both mechanisms into measurable quantities.

In order for the shift instability to do its work, a perfectly flat neck is required. Hence the so-called flat neck parameterization is introduced (see Fig. 4.6.9):

$$\rho(\zeta) = \begin{cases} (r_1^2 - \zeta^2)^{\frac{1}{2}} & -r_1 \le \zeta \le \zeta_1 \\ r + a^2 c(\mathrm{Cosh}(\dfrac{\zeta - z + l - r_1}{a}) - 1) & \zeta_1 \le \zeta \le \zeta_2 \\ (r_2^2 - (2l - r_1 - r_2 - \zeta)^2)^{\frac{1}{2}} & \zeta_2 \le \zeta \le 2l - r_1. \end{cases} \quad (4.6.9)$$

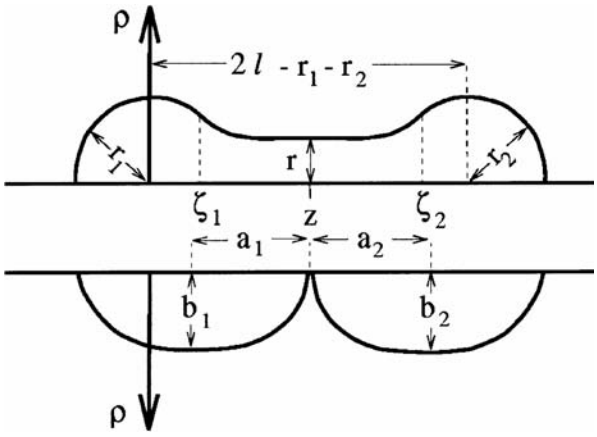

FIG. 4.6.9. The upper part illustrates the flat neck representation; the lower part contains the embedded spheroids parameterization.

The radius of the nucleus is given by ρ as a function of a parameter ζ in terms of several parameters: the semi-length l, the neck radius r, the position z of the dent, the curvature c, the extension of the neck a, the radii of the spherical heads r_1 and r_2, and the transitional points ζ_1 and ζ_2. By requiring continuity and differentiability of the shape, volume conservation and a minimal value of c for a really flat neck, only (l, r, z) remain as independent parameters. Subsequently, the neck radius is eliminated by the Rayleigh criterion, which relates the total length $2l$ of the pre-scission shape to the neck radius r by $2l = 11r$. The value of z can be transformed into the heavy fragment mass A_h by:

$$A_h = \frac{3A_{FS}}{4r_{cn}^3}\int_{-l}^{z}\rho^2(\zeta)\,d\zeta \qquad (4.6.10)$$

where r_{cn} is the compound nucleus radius. The actual values of A_h and l originate from the channel searches and are called the pre-scission shape parameters. They are input to the random neck rupture model calculations.

One last ingredient is missing for the computation of the mass distribution, namely, the surface tension:

$$\gamma_0 = 0.9517\left(1 - 1.7828\left(\frac{N_{FS}-Z_{FS}}{A_{FS}}\right)^2\right)\text{MeV fm}^{-2} \qquad (4.6.11)$$

This is taken from the liquid droplet model by Myers and Swiatecki [4.6.45].

Fluctuations amplified by the shift instability alter the shape slightly and enable the rupture of the nucleus to take place at another point than the most probable point z. In order to determine the fission fragment mass distribution, the probability of cutting the neck at an arbitrary position z_r has to be calculated. This probability is given by the change in potential energy from z_r to z: $E(z_r) - E(z)$. This is replaced by the energy to cut the nucleus at the two positions: $E_{cut}(z_r) - E_{cut}(z)$, with $E_{cut}(z_r) = 2\pi\gamma_0\rho^2(z_r)$. The rupture probability is now proportional to the Boltzmann factor:

$$y(A_{FF}) \propto \exp\left(\frac{2\pi\gamma_0(\rho^2(z_r)-\rho^2(z))}{T}\right) \qquad (4.6.12)$$

The fragment mass number A_{FF} can be computed according to the analogue of Eq. (4.6.10):

$$A_{FF}(z_r) = \frac{3A_{FS}}{4r_{cn}^3}\int_{-l}^{z_r}\rho^2(\zeta)\,d\zeta \qquad (4.6.13)$$

The theoretical yield is finally determined with the following relation in which $y(A_{FF})$ stands for the normalized fission fragment mass yield:

$$Y_{FM}(A_{FF};A_{FS},Z_{FS},E^*) = y(A_{FF}) + y(A_{FS}-A_{FF}) \qquad (4.6.14)$$

In Eq. (4.6.12) the temperature of the scissioning nucleus must be provided. All calculations of the potential energy surface and the crossing of the fission barriers have been isothermal. However, for the random neck rupture model the loss and gain of excitation energy in crossing the barrier is taken into account in a new excitation energy and temperature at scission:

$$E^*_{scission} = E^*_{groundstate} + F_{def,scission} \qquad (4.6.15)$$

The new excitation energy has two components: the original excitation energy in the ground state $E^*_{groundstate}$ and the deformation energy at scission $F_{def,scission}$. $F_{def,scission}$ is positive for actinides and becomes negative in the sub-actinide region. The new excitation energy is related to a new temperature $T_{scission}$. However, a new pre-scission temperature corresponds to a different pre-scission shape with a somewhat different value for $F_{def,scission}$. Therefore, the temperature $T_{scission}$ has to

be determined in a self-consistent manner together with the final pre-scission shape. If a pre-scission shape has a high temperature or a very long neck, the mass distribution will be broad. Low temperatures and short necks result in a narrow mass distribution.

4.6.4.1.4. Post-scission neutron multiplicities

The mass distribution calculated above belongs to the primary fission fragments. However, most fragments are highly excited directly after their creation. They take their share of total excitation energy available at scission (Eq. (4.6.15)). Moreover, they are strongly deformed, which manifests itself in an extra amount of excitation energy set free when this deformation relaxes towards the ground state deformation of the fragments by the strong surface tension. The superfluous excitation energy is released during the process of post-scission neutron and gamma emission. The neutron emission is responsible for a shift of the pre-neutron emission mass distribution to somewhat smaller masses.

The total excitation energy in a newly created fragment with mass A_{FF} results from:

$$E^*_{fragment}(A_{FF}) = E_{def,fragment}(A_{FF}) + \frac{A_{FF}}{A_{FS}} E^*_{scission}. \tag{4.6.16}$$

$E_{def,fragment}(A_{FF})$ denotes the deformation energy of the fragment, and the second term contains the portion of the thermal energy at scission of the whole fissioning system picked up by the fragment. The assumption is that the fragment receives a share proportional to its mass.

For the calculation of $E_{def,fragment}(A_{FF})$, another shape parameterization is employed: embedded spheroids (see Fig. 4.6.9). The newborn fragments are modelled as two contacting spheroids with major axes a_1 and a_2, which are linked to $2l$ and z_r by:

$$a_1 = \frac{1}{2}(r_1 + z_r), \qquad a_2 = l - \frac{1}{2}(r_1 + z_r) \tag{4.6.17}$$

The minor axes b_1 and b_2 follow from volume conservation:

$$b_1^2 = \frac{3}{4a_1}\int_{-r_1}^{z_r} \rho^2(\zeta)d\zeta, \quad b_2^2 = \frac{3}{4a_2}\int_{z_r}^{2l-r_1} \rho^2(\zeta)d\zeta \tag{4.6.18}$$

The energy difference of the spheroidally deformed and the spherical fragment $E_{def,fragment}(A_{FF})$ is given by:

$$E_{def,fragment}(A_{FF},\varepsilon_i) = E^{sph}_{surf}(A_{FF})\left(\frac{\arcsin(\varepsilon_i)+\varepsilon_i(1-\varepsilon_i{}^2)^{1/2}}{2\varepsilon_i(1-\varepsilon_i{}^2)^{1/6}} - 1\right) + E^{sph}_{coul}(A_{FF})\left(\frac{(1-\varepsilon_i{}^2)^{1/3}}{2\varepsilon_i}\ln\left(\frac{1+\varepsilon_i}{1-\varepsilon_i}\right) - 1\right) \tag{4.6.19}$$

The eccentricity is defined as:

$$\varepsilon_i = \left(1 - \left(\frac{b_i}{a_i}\right)^2\right)^{1/2} \tag{4.6.20}$$

and $E^{sph}_{surf}(A_{FF})$ and $E^{sph}_{Coul}(A_{FF})$ represent the liquid droplet model surface and the Coulomb energy of a spherical nucleus obtained from Ref. [4.6.46].

The neutron multiplicity $\nu_{FM}(A_{FF})$ for a fragment with mass A_{FF} is now derived by finding the root of the following relationship:

$$E^*_{fragment}(A_{FF}) = \sum_{n=1}^{\nu_{FM}(A_{FF})} (S_n + \eta_n) + E_\gamma \tag{4.6.21}$$

The separation energy S_n is calculated from the mass formula [4.6.46]. The average kinetic energy of the neutrons is taken to be 3/2 times the fragment temperature, and the energy carried off by γ rays E_γ is approximately half the separation energy of the first non-evaporated neutron.

The final fission product mass yield per fission mode is given by:

$$Y_{FM}(A_{FP};A_{FS},Z_{FS},E^*) = Y_{FM}(A_{FF} - \nu_{FM}(A_{FF});A_{FS},Z_{FS},E^*) + Y_{FM}(A_{FS} - A_{FF} - \nu_{FM}(A_{FS} - A_{FF});A_{FS},Z_{FS},E^*) \tag{4.6.22}$$

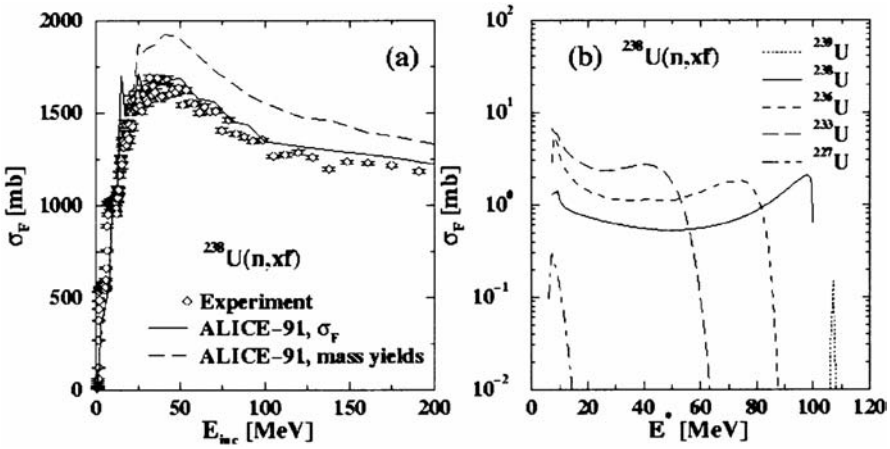

FIG. 4.6.10. (a): ALICE-91 predictions for the fission cross-section compared to experimental data [4.6.48]. The solid line corresponds to calculations tuned to experimental fission cross-sections, while the dashed line is obtained with level density ratios reproducing at best the experimental mass distributions in Section 4.6.4.3. (b): Results of ALICE-91 calculations on the excitation energy dependence of the fission cross-section for several fissioning nuclides in 100 MeV neutron induced fission on ^{238}U.

4.6.4.2. Multi-chance fission in ALICE-91

The fission cross-section calculations are performed with the pre-compound plus compound nucleus decay code ALICE-91 developed by Blann [4.6.39]. The geometry dependent hybrid model is employed in the pre-equilibrium part of the reaction. The compound part of the reaction is computed using Weisskopf–Ewing evaporation with fission competition via the Bohr–Wheeler approach, in which the fission process is described by a passage probability of the nucleus over the classical fission saddle point. Single humped fission barriers and ground state energies are supplied by a conventional rotating liquid drop model [4.6.47]. A simple Fermi gas description of the level density with a constant level density parameter is used. The fission cross-section computed with ALICE-91 is dependent on the choice for a_f/a_n, the ratio of saddle point to ground state level density parameters. Because of the stronger deformation at the saddle point, this ratio is expected to be larger than 1.0. The use of this ratio accounts, in an effective way, for a change in the intrinsic level density parameter as well as in the rotational enhancement.

Figure 4.6.10(a) contains the calculated and experimental total fission cross-section [4.6.48] as a function of incoming neutron energy on ^{238}U. By adjusting the level density ratio to the experimental fission cross-section, an overall agreement of 10% or better can be achieved (except for low energy fission in the sub-actinide region where deviations as large as 50% may occur). A second prediction is included, which is obtained by fitting the level density ratio to reproduce the shape of the mass distribution at best instead of the fission cross-section. In most cases the outcome of these other calculations still lies within 10% of the experimental data, but may lead to differences of 15–20%. In Fig. 4.6.10(b) a calculation of the fission cross-section as a function of excitation energy for several fissioning systems in the reaction of 100 MeV neutrons on ^{238}U is pictured. Both high and low excitation energies are contributing. In reaching the more neutron deficient nuclides, fission takes place at lower excitation energies due to the preceding neutron evaporation.

4.6.4.3. Coupling of the temperature dependent Brosa model with ALICE

A combination of the temperature dependent Brosa model from Section 4.6.4.1 and the nuclear reaction code ALICE-91 as described in Section 4.6.4.2 enables the prediction of pre-neutron emission mass yields as well as post-neutron emission mass yields in intermediate energy light particle induced fission reactions. After the determination in ALICE-91 of all contributions to the fission cross-section by excited evaporation residues, which are characterized by $\sigma_F(A_{FS}, Z_{FS}, E^*)$, the temperature dependent Brosa model computes (A_{FS}, Z_{FS}, E^*) the corresponding fission fragment mass yield curve for each configuration. All these curves are summed with their proper weight given by $\sigma_F(A_{FS}, Z_{FS}, E^*)$.

Figure 4.6.11 illustrates the coupling between the temperature dependent Brosa model and

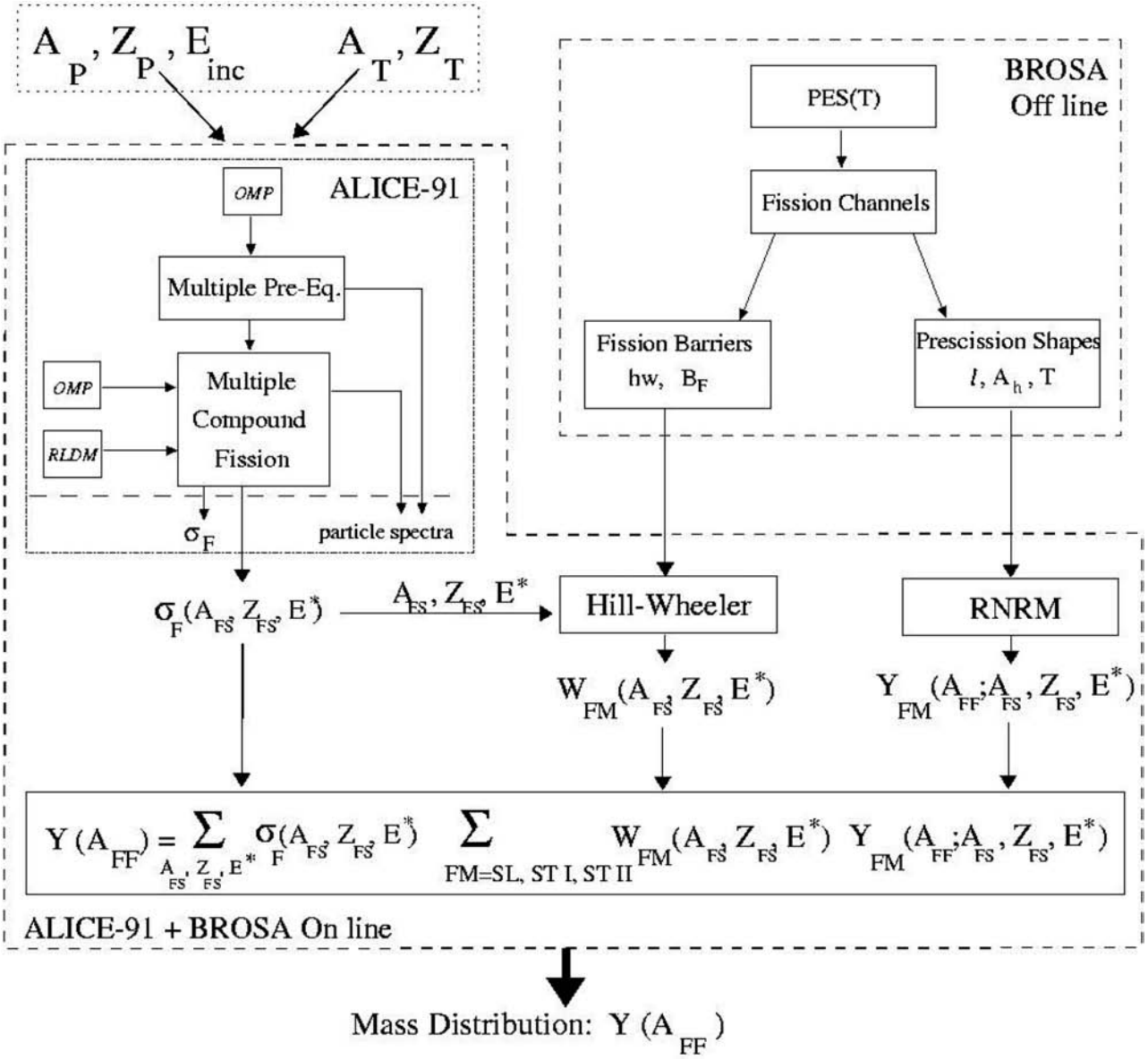

FIG. 4.6.11. Overview of the coupling of ALICE-91 and the temperature dependent Brosa model. The subscript FM denotes the three dominant fission modes super long (SL), ST-1 and ST-2; Y_{FM} is the mass yield curve and W_{FM} the relative contribution of a specific fission mode.

ALICE-91. Part of the contents from Section 4.6.4.1 is grouped in a dashed box situated in the upper right corner of the figure. These fission mode calculations are performed only once to construct files containing the fission barrier parameters and prescission shapes of the investigated nuclides. This information serves as input for the on-line mass distribution calculations.

Projectile, incoming energy and target specifications form the main input (dotted box in the top left corner) of these on-line calculations together with the ALICE-91 level density input parameters a_n and a_f/a_n, the role of which has been already highlighted in the previous section. The calculation starts with an ALICE-91 run, which is indicated in the picture inside the dot–dashed frame. ALICE-91 keeps track of the flux going into fission for each individual isotope per excitation energy bin encountered in the Weisskopf–Ewing evaporation stage. Besides the normal output of the particle spectra and the total fission cross-section, the fission cross-section per fissioning isotope and excitation energy bin $\sigma_F(A_{FS}, Z_{FS}, E^*)$ is listed at the end.

For each configuration (A_{FS}, Z_{FS}, E^*) the programme subsequently calls a subroutine which performs two tasks. First of all, the relative

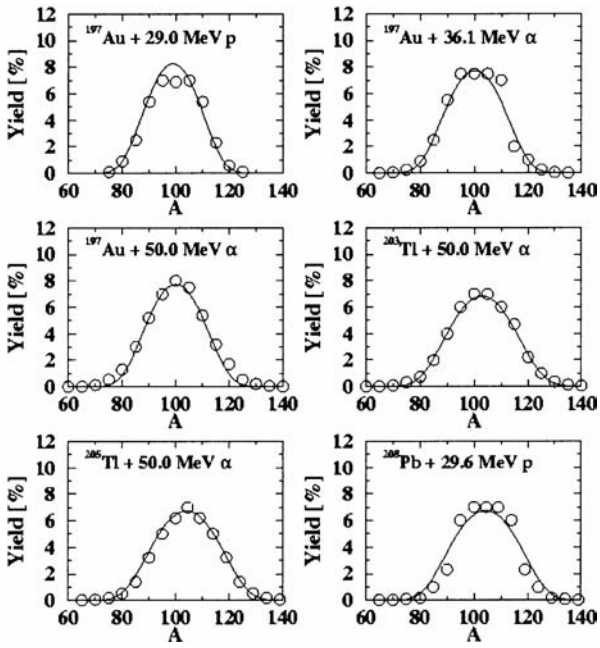

FIG. 4.6.12. Normalized pre-neutron emission mass yields for the reactions specified in each graph. Experimental data are taken from Refs [4.6.49] and [4.6.50]; the lines correspond to the calculations.

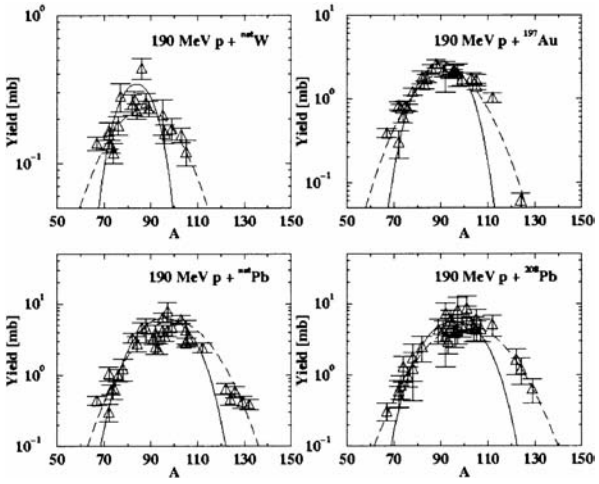

FIG. 4.6.13. Post-neutron emission mass yields in proton induced fission of ^{nat}W, ^{197}Au, ^{nat}Pb and ^{208}Pb at 190 MeV, obtained from Ref. [4.6.2]. Triangles denote the experimental data; the dashed line originates from the fit of a single Gaussian made by the original authors, and the solid line belongs to our calculation.

contributions $W_{FM}(A_{FS}, Z_{FS}, E^*)$ of the three predominant fission modes super long, ST-1 and ST-2 are determined. This happens inside the box which carries the label Hill–Wheeler and uses the fission barrier parameters as input. The second task comprises the calculation of the mass yield curve $Y_{FM}(A_{FF}; A_{FS}, Z_{FS}, E^*)$ with the help of the random neck rupture model based on the fission mode, the configuration (A_{FS}, Z_{FS}, E^*) and the pre-scission shape parameters. The computed pre-neutron emission mass distribution is subsequently corrected for the post-scission neutron multiplicities. In this manner the post-neutron emission mass yields are constructed. The final fission fragment mass distribution $Y(A_{FF})$ is simply obtained by adding all separate pre-neutron emission mass yields $Y_{FM}(A_{FF}; A_{FS}, Z_{FS}, E^*)$ with the relative contributions $W_{FM}(A_{FS}, Z_{FS}, E^*)$ and the fission cross-sections $\sigma_F(A_{FS}, Z_{FS}, E^*)$ as weights. Obviously, a completely equivalent approach gives rise to the final fission product mass distribution $Y(A_{FP})$.

Predicted mass yields are compared in the following sections to experimental data for sub-actinide and actinide fission between 15 and 200 MeV. Moreover, an investigation is included regarding the transition between asymmetric and symmetric fission when going from the line of stability towards neutron deficient nuclides in the actinide region.

4.6.4.3.1. Mass yields in sub-actinide fission

The results from the ALICE-91 plus temperature dependent Brosa model calculations for light particle induced fission reactions in sub-actinide targets are shown in Figs 4.6.12 and 4.6.13. In the case of sub-actinide targets it is not possible to calculate the competition between symmetric and asymmetric fission modes. Results of the fission channel search in ^{208}Pb exhibit rather broad and strangely shaped outer barriers, which makes a fit of these barriers with a parabola impossible. Hence the Hill–Wheeler approach cannot be applied. In all calculations in this section, the asymmetric fission modes are discarded. Only the symmetric super long mode is taken into account for sub-actinides.

The experimental data included in Fig. 4.6.12 are taken from the extensive work on sub-actinide fission of Itkis et al. [4.6.49, 4.6.50]. Examples of proton and alpha induced fission between 29 and 50 MeV are given. In general the agreement with the calculations is very good, both for the position of the most probable mass and for the width of the distribution. In the case of the 29 MeV proton induced reactions, the calculations deviate 15% at most from the experimental values, but on average the agreement is much better. The assumption that for these nuclides asymmetric fission can be neglected seems valid for these energies.

The yields are normalized. Therefore, the uncertainty in the prediction of the overall fission

cross-section also has to be incorporated. The calculations are performed with the level density parameters stemming from a fit to experimental neutron and proton induced fission cross-sections for ^{209}Bi and ^{197}Au.

The basic assumption made is that the saddle point to ground state ratios a_f/a_n vary smoothly over the isotopes and hence that the ratios for ^{208}Pb and ^{203,205}Tl lie in between those of ^{209}Bi and ^{197}Au. The fission cross-sections in this region of the chart of nuclides can be predicted with an accuracy of 10%. This has to be added to the uncertainty in the prediction of the normalized yields.

The predictions in Fig. 4.6.13 for the production cross-sections of fission product masses in 190 MeV proton induced fission of ^{nat}W, ^{197}Au, ^{nat}Pb and ^{208}Pb are less satisfactory. The experimental data have been obtained from Ref. [4.6.2]. Figure 4.6.13 also contains, apart from the experimental data and the calculation (solid line), a Gaussian (dashed line) that originates from a fit to the data and is given by the original authors. The calculation does a fairly good job in the description of the left wings and of the top, but the experimental yields are underestimated by one order of magnitude in the right wings. The huge discrepancy for heavier masses is mainly due to the prediction of a too small width. In addition, the predicted mean mass is shifted to lighter masses compared to the measured value. A lighter mean mass is related to an overestimation of the total number of evaporated mass units. This may indicate an underprediction of the energy carried away by the emitted particles prior to or after scission. A possible explanation of the first effect lies in the calculation of the post-scission neutron multiplicities. With the temperature dependent Brosa model as described in Section 4.6.4.1, the neutron evaporation between the saddle and scission points is neglected. This results in an excitation energy of the fragments that is too high. Since the division of the excitation energy available at scission between the two fragments is proportional to the fragment mass, the heavy fragment will have a relatively higher post-scission neutron multiplicity. Therefore it will shift more towards lower masses than the light fragment, thereby reducing the width of the mass distribution. A similar situation of a higher scission temperature occurs if the energy carried away by the pre-scission neutrons is too small. An overestimation of the post-scission neutron multiplicity can also be caused by an under-prediction of the energy required for the emission of neutrons by the fragments. The last two assumptions would

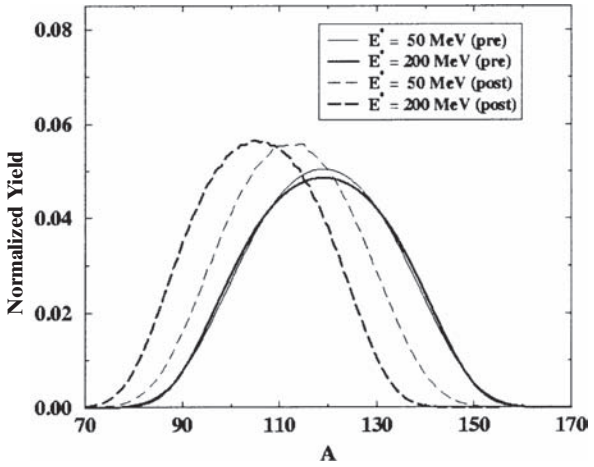

FIG. 4.6.14. Pre-neutron emission and post-neutron emission mass yield curves for the super long mode in a ^{238}U nucleus with excitation energies at scission of 50 and 200 MeV.

simultaneously explain the smaller predicted mean mass, as already mentioned above.

A higher excitation energy at scission is linked to a higher scission temperature, and this also influences the width. The pre-scission shape half-length is smaller at higher temperatures (see Fig. 4.6.8). A more compact shape results in a narrower mass distribution. On the other hand, an increase of the temperature enlarges the width (see Eq. (4.6.12)). A comparison of the two effects shows that the latter is stronger. Figure 4.6.14 contains the pre-neutron emission and post-neutron emission mass yield curves of the super long mode for a ^{238}U nucleus with an excitation energy of 50 and 200 MeV at scission. The pre-neutron emission yield curve at 200 MeV is broader than the pre-neutron emission yield curve at 50 MeV, although the pre-scission shape is shorter around 200 MeV. The post-neutron emission yield distribution at 200 MeV becomes slightly narrower than the one around 50 MeV. This observation supports the explanation given above that the inclusion of post-scission neutron emission in its present form reduces the width of the mass distribution. Whether the overprediction of the post-scission neutron multiplicity is connected to an overestimation of the temperature at scission or to an underestimation of the energy required for the emission of a neutron by the fragments cannot be concluded from these data. The next section will shed more light on this question.

Table 4.6.4 shows the fission cross-sections resulting from the experiment, the calculations and the Eismont et al. data compilation [4.6.25].

TABLE 4.6.4. PROTON INDUCED SUB-ACTINIDE FISSION CROSS-SECTIONS OBTAINED FROM EXPERIMENT AND FROM ALICE-91 CALCULATIONS; VALUES FROM THE DATA COMPILATION BY EISMONT ET AL. [4.6.25] ARE ALSO INCLUDED FOR COMPARISON

	^{nat}W	^{197}Au	^{nat}Pb	^{208}Pb
σ_f^{exp} [mb]	4.5 ± 0.5	32.8 ± 3.3	94 ± 9	88 ± 8
$\sigma_f^{ALICE\text{-}91}$ [mb]	3.7	31.2	83.6	76.4
$\sigma_f^{Eismont}$ [mb]	3.7	–	88	74

ALICE-91 tends to underestimate the fission cross-section by 10–15%.

4.6.4.3.2. Mass yields in actinide fission

The full competition between the symmetric and asymmetric fission modes is taken into account in the case of actinide fission. With these modes a variety of shapes can be described that are needed to cover the whole range of intermediate energy fission between several and 200 MeV. Pre-neutron emission mass yields in neutron induced fission of ^{238}U are plotted in Fig. 4.6.15 for various different projectile energies. The experimental data come from the work by Zöller et al. [4.6.51]. At an average incident neutron energy of approximately 13 MeV the mass distribution exhibits pronounced asymmetric behaviour. This asymmetric character persists up to an average neutron incident energy of roughly 100 MeV. Above this energy a broad mass yield curve remains, which still suggests some asymmetric components through the appearance of a broad and flat top. With increasing excitation energy the symmetric valley from low energy fission fills up due to a stronger symmetric contribution. This forms the main contribution. Another much smaller effect is the widening of the asymmetric contributions.

The calculations of Fig. 4.6.15 show that the agreement is within 10% or even better almost everywhere. Figure 4.6.16 contains the same data and calculation results but on a logarithmic scale. This is done to enable a better comparison of the experimental data and the calculations in the tails of the distributions. At very high energies (around 200 MeV), the predictions and data start to deviate at extremely asymmetric yields by one order of magnitude. This is a similar effect to the sub-actinide post-neutron emission yields at 190 MeV of the previous section, but is less strong. A possible explanation is that the predicted pre-scission shapes are too compact. The fact that the mean mass, the

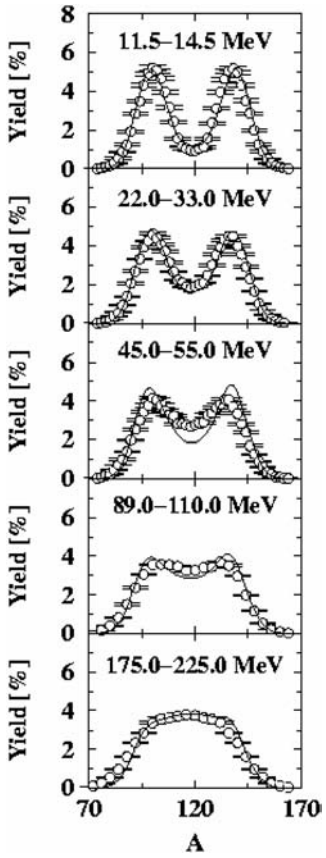

FIG. 4.6.15. Pre-neutron emission mass yields in neutron induced fission reactions on ^{238}U with the neutron incoming energy range specified in the graphs. The saddle point to ground state level density ratios are fitted to reproduce the shape of the mass yield curve. Data taken from Ref. [4.6.51].

width, and the relative asymmetric and symmetric contributions come so close to the results found experimentally indicates that neither the calculated temperature at scission can be much too high nor the calculated pre-scission neutron multiplicity can be much too low. This observation agrees with the supposition that the calculated post-scission neutron multiplicity may be too high due to a wrong estimation of the energy required for the emission

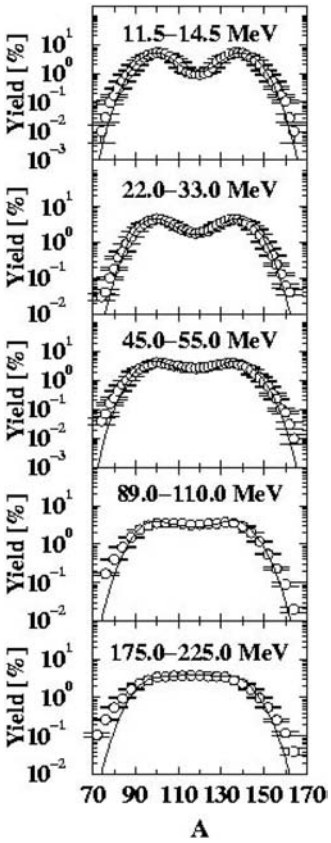

FIG. 4.6.16. Same as Fig. 4.6.15, but on a logarithmic scale. Data taken from Ref. [4.6.51].

of neutrons by the fragments and not due to a scission temperature that is too high.

The predictions for these normalized yields are obtained by adjusting the saddle point to ground state level density ratios to reproduce the experimental mass yields. The influence on the prediction of the total fission cross-section has already been examined in Section 4.6.4.2. It turns out that the fission cross-section in the reactions under study is overestimated by approximately 15%. The influence of this level density ratio is rather profound, as can be concluded from Fig. 4.6.17. This figure shows the results of the mass yield calculations based on the level density ratios, which perfectly describe the fission cross-section. These ratios are lower than the ones used in Fig. 4.6.15. For low energies (up to 30 MeV) the difference is rather small, but at higher energies the asymmetric contributions are overestimated. This is understandable, since with a smaller value of the ratio fission is preceded by more evaporation and takes place at lower excitation energies. The discrepancies with the experimental mass yield curves amount to 30%.

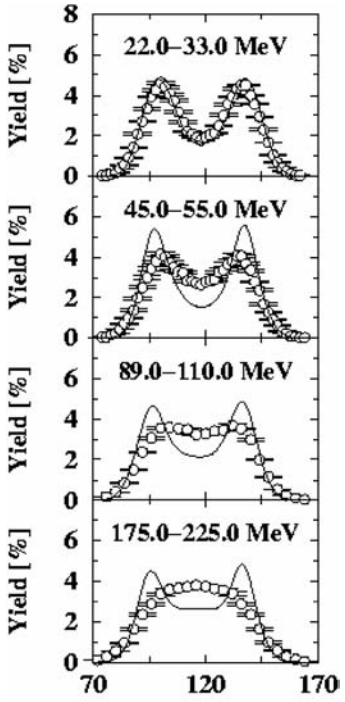

FIG. 4.6.17. Pre-neutron emission mass yields in neutron induced fission reactions on ^{238}U. The saddle point to ground state level density ratios are fitted to reproduce the total fission cross-section. Data taken from Ref. [4.6.51].

Figure 4.6.18 is included to illustrate the effect of taking a different pre-scission shape in the calculation. According to Brosa, the neck becomes unstable against rupture at the Rayleigh criterion. The results in Fig. 4.6.18 are obtained by assuming that scission already takes place at the Rayleigh criterion. This corresponds to more compact pre-scission shapes and hence to shorter necks. The consequence is obvious: the neck can break at fewer locations with equal probability. This causes the peaks to be narrower, and the widths of the distributions differ significantly from the measurements.

Besides neutron induced reactions, proton induced fission has also been investigated. In Fig. 4.6.19 the results are plotted for pre-neutron emission mass yields in proton induced fission of ^{232}Th at three different energies. The experimental data are taken from Ref. [4.6.11]. Agreement is again quite good (within 10%) for 13 and 20 MeV. The reaction at an incident energy of 53 MeV shows an incorrect relative contribution of asymmetric and symmetric fission. As will be further explained, thorium lies on the edge of the actinide region and is subject to a transition to symmetric fission which occurs much earlier than in the case of uranium. Apparently, the ALICE-91 plus temperature

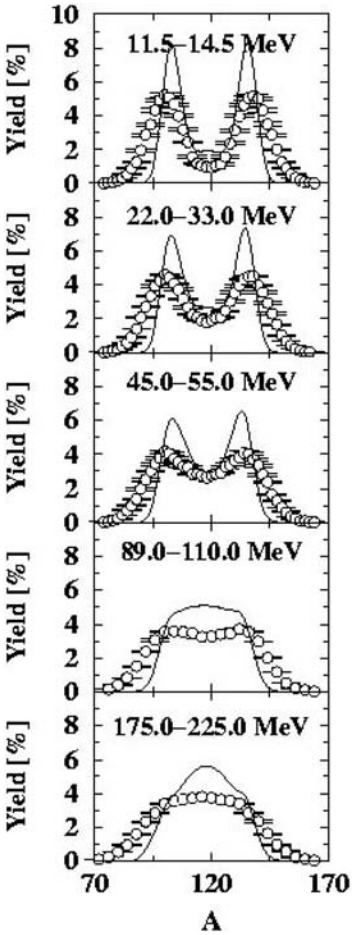

FIG. 4.6.18. Pre-neutron emission mass yields in neutron induced fission reactions on ^{238}U with the pre-scission shapes taken at the Rayleigh criterion. Data taken from Ref. [4.6.51].

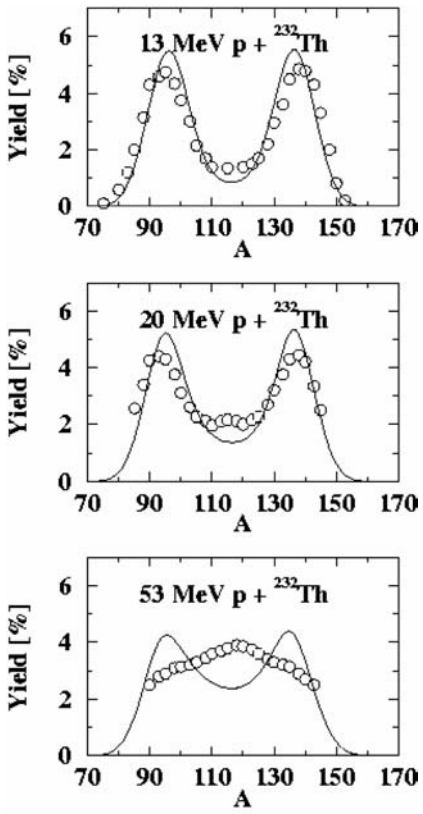

FIG. 4.6.19. Pre-neutron emission mass yields in proton induced fission reactions on ^{232}Th for the incoming energies given in the graphs. Data taken from Ref. [4.6.11].

dependent Brosa model is not able to predict this transition accurately. Up to 50 MeV the prediction of the fission cross-section ends up within 10% of the experimental values.

Figure 4.6.20 shows pre-neutron emission mass yields in proton induced fission of ^{226}Ra and ^{238}U [4.6.22, 4.6.52]. In the case of 13 MeV protons on ^{226}Ra, the prediction gives a triple humped distribution in accordance with experimental observations. Unfortunately, the relative contributions of the fission modes are incorrect. Furthermore, the position of the asymmetric peak does not agree with the experimental data. This is due to the fact that the ST-1 mode is predominant in the calculation, while from the experimental data the peak around mass 140 indicates a strong contribution of the ST-2 mode. The first problem resembles the underprediction of symmetric fission in 53 MeV proton induced reactions in ^{232}Th as mentioned in the previous paragraph. The outcome of the calculations for ^{238}U at 20 and 60 MeV incident energies is acceptable. On top of the 10% uncertainty in the normalized mass yields, an additional uncertainty of 15% also occurs in the total fission cross-section.

Post-neutron emission mass yields can be found in Figs 4.6.21 and 4.6.22. Figure 4.6.21 displays post-neutron emission mass yields in neutron induced fission of ^{238}U [4.6.51]. The same incident energy ranges are chosen as for the pre-neutron emission yields. The agreement for the 13 and 28 MeV incident energies is excellent. At higher energies, the effect from the excessive post-scission neutron evaporation is present. The underprediction of the width of the pre-neutron emission mass yield curve is enhanced by the post-scission neutron evaporation. This has already been encountered and explained in the previous section and further elucidated at the beginning of this section. The heavy fragments lose too many neutrons, which leads to an underprediction in the right wing of the distribution and to an overprediction on the left hand side. Especially the mass yield curve around 200 MeV suffers from this effect

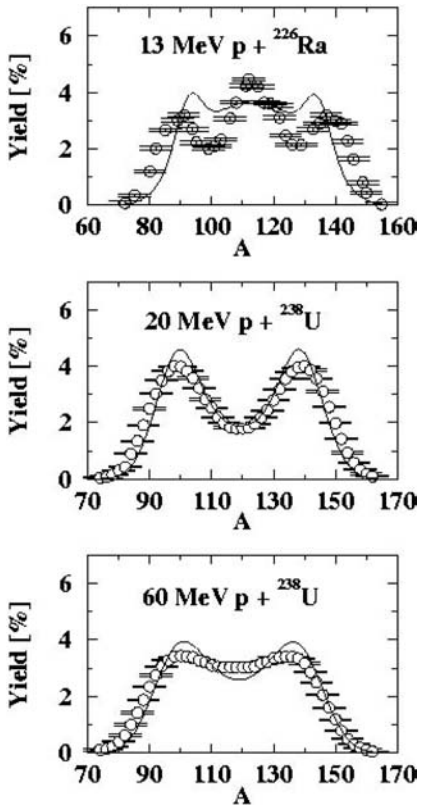

FIG. 4.6.20. Pre-neutron emission mass yields in proton induced fission reactions on ^{226}Ra and ^{238}U for the incident energies given in the graphs. Data taken from Refs [4.6.22, 4.6.52].

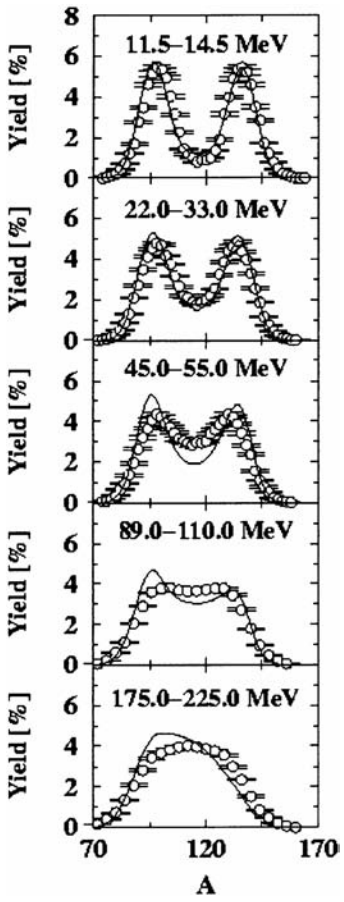

FIG. 4.6.21. Post-neutron emission mass yields in neutron induced fission reactions on ^{238}U. The neutron incident energy ranges are denoted in the graphs. Data taken from Ref. [4.6.51].

to the same extent as the sub-actinides in proton induced reactions at 190 MeV (Fig. 4.6.13).

Unfortunately, the experimental data for other nuclides are limited to neutron energies around 14 MeV. Figure 4.6.22 shows data for four different nuclides: ^{232}Th, ^{233}U, ^{242}Pu and ^{241}Am [4.6.53–4.6.56]. At the corresponding excitation energies the post-scission neutron evaporation does not yet spoil the outcomes. The predictions in the wings of the mass distributions deviate from experiment to a maximum of 30% for ^{232}Th, ^{242}Pu and ^{241}Am. However, in the case of ^{233}U the right tail is underpredicted by a factor of 10. On the top of the distribution and in the symmetric valley, the agreement is within 20%, except in some mass regions of ^{232}Th where the calculated yields lack the small symmetric hump.

4.6.4.3.3. Transition from symmetric to asymmetric fission

From all mass yield curves seen so far in the previous two sections, somewhere at the edge of the actinide region a transition takes place between symmetric and mixed (symmetric plus asymmetric) fission. Moreover, observations by Schmidt et al. [4.6.35] suggest a change towards symmetric fission in the neutron deficient part of the actinide region. In addition, an increase in symmetric fission is observed with increasing excitation energy. The question arises whether this last effect is mainly due to the vanishing of asymmetric fission modes with increasing excitation energy or to the contributions of more and more neutron poor isotopes with an intrinsic symmetric behaviour.

Figure 4.6.23 shows mass distributions of various isotopes between actinium and uranium labelled by the element name and neutron number. The calculations are carried out for nuclides with an excitation energy of 10 MeV. The gradual change from asymmetric and mixed to symmetric fission is clearly visible. Near the valley of stability, at the right hand side of the plot, fissioning isotopes tend to produce mass distributions with a strong asymmetric signature. At the left hand side the

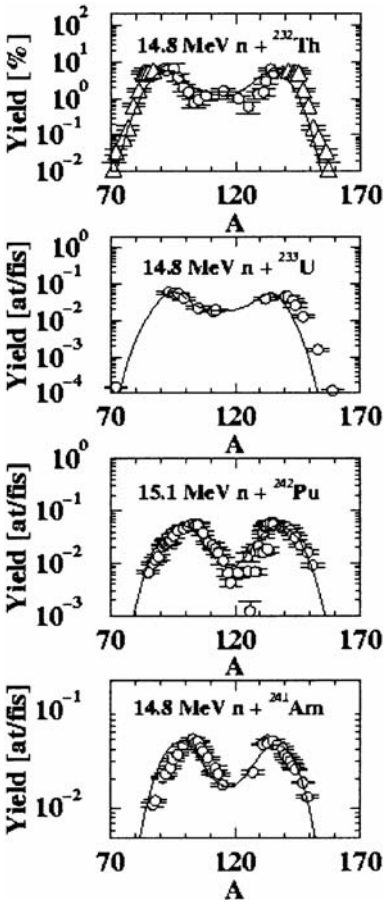

FIG. 4.6.22. Post-neutron emission mass yields in neutron induced fission reactions as specified in the graphs. Data taken from Refs [4.6.53–4.6.56]. The triangles in the upper graph correspond to data taken from a table, whereas the circles were read from a figure.

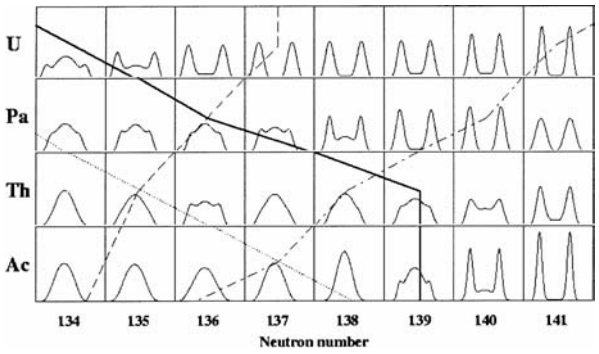

FIG. 4.6.23. Mass distributions of various isotopes labelled by the element name and neutron number — calculations are performed at a fixed excitation energy of 10 MeV. The thick solid line connects isotopes for which the symmetric hump exceeds the asymmetric humps for the first time, starting from stability and going towards neutron poor nuclides; the dotted line is obtained in an equivalent manner from charge distributions measured by Schmidt et al. [4.6.35]; the dot–dashed line represents a condition defined by Chung and Hogan [4.6.27, 4.6.28], and the dashed line corresponds to a calculation by Möller [4.6.57].

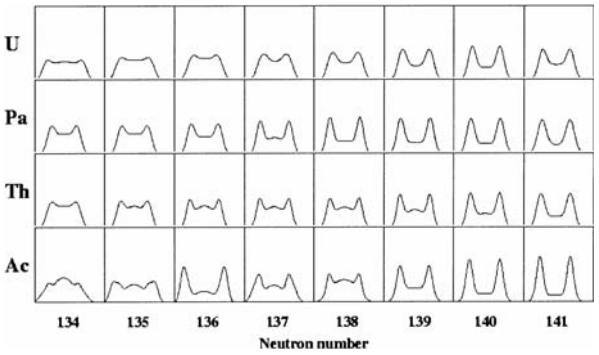

FIG. 4.6.24. Same as Fig. 4.6.23, but for an excitation energy of 20 MeV.

resulting mass yields are entirely symmetric or possess at least a large symmetric share. A solid line connects the isotopes for which the symmetric hump exceeds the asymmetric humps for the first time in going towards neutron poor nuclides starting from stability. This is taken as a crude measure for the transition. The dot–dashed line represents a condition defined by Chung and Hogan [4.6.27, 4.6.28], which also marks the transition from symmetric to asymmetric (mixed) fissioning isotopes. The dashed line corresponds to a calculation by Möller [4.6.57], who determined the stability of the saddle point configuration against asymmetric deformations. Both lines belonging to Chung–Hogan and Möller run more or less parallel to the line of stability. However, the line originating from the ALICE-91 plus temperature dependent Brosa model calculations is perpendicular to these lines. This completely different behaviour is also observed by Schmidt et al. [4.6.35] in the charge distributions of the same fissioning isotopes at excitation energies peaked around 11 MeV. Here the transition marked by the dotted line also tends to occur along a line perpendicular to the Möller line. Therefore, the prediction by the ALICE-91 plus temperature dependent Brosa model exhibits the same tendency as experimentally observed. In conclusion, at low energies the transition seems to take place at less neutron poor nuclides for thorium and actinium than for uranium.

The preportions of symmetric and asymmetric fission depend on the excitation energy. Therefore, similar calculations are carried out for an excitation energy of 20 MeV (Fig. 4.6.24). Because the excitation energy lies well above the barriers, all fission modes

present have a reasonable contribution. This explains the mixed mass yields visible in all graphs. Apparently, only at quite low energies, symmetric fission is preferred by the neutron deficient isotopes as well as by most actinium isotopes at the edge of the actinide region. Since the melting away of fission modes happens in beta stable and very neutron deficient nuclides at a comparable rate, the situation of Fig. 4.6.24 persists up to a certain excitation energy, above which an overall and gradual transition to symmetry occurs simultaneously for all isotopes. Hence, in the calculations presented here the increase of symmetric fission at high energies is fed more by the disappearance of the asymmetric fission modes due to the vanishing of shell effects and less by a larger contribution of neutron deficient nuclides due to the preceding neutron evaporation.

In the previous section a systematic underprediction of the symmetric component in the description of intermediate energy fission of thorium and radium has been observed. Two effects may be responsible: the increase of the symmetric component in these elements may be too slow with excitation energy or the asymmetric fission modes do not vanish in time. The alternative possibility is a lack of symmetric fission in neutron poor nuclides due to wrong barrier parameters resulting in an overestimation of asymmetric fission at higher energies, or due to an overprediction of the excitation energy in these nuclides. Based on the comparisons between calculations and experimental results shown here it is not possible to draw a final conclusion. Perhaps in future, experiments can be designed to investigate mass distributions in a systematic way (similar to the calculated results presented in Figs 4.6.23 and 4.6.24, but also at higher excitation energies), so that the results will help to solve the question of how the transition between symmetric and asymmetric fission takes place.

4.6.5. Summary and outlook

4.6.5.1. Summary

This work focused on nucleon induced fission at intermediate energies between roughly 10 and 200 MeV. Some effort has been invested in the compilation of existing proton induced fission yield data in the desired energy range. In order to supplement the limited experimental data available, especially regarding the fission product isotopes, an experiment for 190 MeV proton induced fission has been performed. However, the major contribution of this work comprises the development of a new theoretical approach to calculate the fission product mass yields in competition with all other reaction channels for light particle induced nuclear reactions up to about 200 MeV. This new method is based on the extension of the original Brosa model, with a temperature dependence and the coupling of the resulting model with a nuclear reaction code that provides the connection between fission and other reaction mechanisms such as pre-equilibrium and compound emission.

4.6.5.1.1. Experiment

An activation experiment has been carried out that aims at the measurement of independent and cumulative fission product yields originating from 190 MeV proton induced reactions on ^{nat}W, ^{197}Au, ^{nat}Pb, ^{208}Pb and ^{232}Th. By placing catchers on both sides of each target during the irradiation, the fission products have been separated from the enormous amounts of evaporation products. In this manner, rather clean spectra with fission product γrays have been obtained. With separate experimental set-ups for a short irradiation (catcher cylinder) and a long irradiation (catcher foil) it is possible to observe both short lived and long lived fission products.

The mass yields of ^{nat}W, ^{197}Au, ^{nat}Pb and ^{208}Pb are well described by a single Gaussian for both the mass and the charge distribution. Fission cross-sections extracted from the single Gaussian fits are comparable with the values obtained from a data compilation made by Eismont et al. [4.6.25]. Sub-actinide fission at this energy is purely symmetric.

A careful look at the mass yields for ^{232}Th shows that the mass yield curve has a more complicated form than that of a single Gaussian. This indicates the contribution of other asymmetric fission modes besides the symmetric mode already encountered in sub-actinide fission. The origin of this particular form of the mass distribution resides in the process of multi-chance fission. Particle evaporation prior to fission results in a wide variety of fissioning nuclides, each contributing to the mass distribution with its own fission characteristics. The suggestion made is that the observed strong symmetric component in the ^{232}Th mass distribution is only partly caused by an enhanced crossing of the symmetric fission barrier in the fissioning nuclides near the valley of stability, which possess both symmetric and asymmetric fission

modes and thus give rise to a mixed fission contribution. A large share of the symmetric contribution is proposed to be related to purely symmetric fission in the neutron poor region. This last assumption is too simplistic, but together with the mixed fission contribution it serves to give a schematic description of the experimentally observed mass yields. The measured mass yield curve is decomposed into a single Gaussian belonging to the purely symmetric fission mode and a contribution of three Gaussians, together describing mixed fission. The fission cross-section resulting from this decomposition is slightly smaller than the value of Eismont et al. The fission cross-section resulting from the single Gaussian description for ^{232}Th underestimates the value of Eismont et al. by a factor of 2.

From a comparison between the measured independent and cumulative yields with the fitted charge distribution it becomes clear that the assumption of a single Gaussian for the ^{232}Th charge distribution is not good enough. The fitted and measured values differ by a factor of 2, which consequently also shows up in the constructed mass yields. This reveals the main disadvantage of this experimental method. The reconstruction of the mass and charge distributions from the measured independent and cumulative yields rests fully on a suitable parameterization of these respective distributions. In the case of the sub-actinides, the shapes of these distributions are Gaussian-like and everything works well. In the case of actinide fission, however, the contributions of asymmetric fission make a good description by a single Gaussian impossible. Taking a more complicated shape to fit the charge distribution would mean introducing more fit parameters. The quality of the experimental data set is insufficient for this purpose.

4.6.5.1.2. Theory

In intermediate energy fission studies the key concept is multi-chance fission. The evolution of an entirely equilibrated nucleus from its ground state shape to the scission point is thought to proceed at a pace comparable to the emission of light particles. The process of sequential particle evaporation populates many intermediate nuclides characterized by (A_{FS}, Z_{FS}, E^*). Each nuclide in each excitation energy bin fissions or evaporates further. Hence, in the description of fission two main ingredients can be distinguished: a model to determine the fission cross-sections for all fissioning systems as a function of their excitation energies $\sigma_F(A_{FS}, Z_{FS}, E^*)$, and a model to predict the fission fragment and fission product yields for each set of (A_{FS}, Z_{FS}, E^*).

The original Brosa model [4.6.36] has been extended in various ways. First of all, the temperature is added to the calculation of the potential energy landscape of the nucleus. In this manner, the incorporated melting away of the shell effects naturally gives rise to the vanishing of asymmetric fission modes ST-1 and ST-2 with increasing excitation energies. Secondly, the relative contributions of the different fission modes are evaluated with the Hill–Wheeler penetrability through inverted parabolic barriers using ground state level densities and temperature dependent barrier parameters. The classic random neck rupture model subsequently translates the rupture probability as a function of the position at the neck of the scissioning nucleus into pre-neutron and post-neutron emission mass yield curves. Linking this result with the fission cross-section contributions by all possible fissioning systems as computed by ALICE-91 [4.6.39], the total pre-neutron emission and post-neutron emission mass yields may be determined for any imaginable light particle induced fission reaction from 15 up to roughly 200 MeV. In this way, the competition with all other outgoing channels is automatically taken into account. By separating the calculation of the fission cross-section from the fission fragment properties, the final uncertainty in the prediction is a superposition of the uncertainties stemming from both steps.

Actinide nuclides turn out to have three dominant fission modes: the symmetric super long mode, and the asymmetric modes standard I (ST-1) and standard II (ST-2), whereas sub-actinides possess only one asymmetric mode ST in addition to the super long mode. For sub-actinides, asymmetric fission is completely neglected in the present calculations. The outer barrier is not described well by a parabola, which prevents the determination of the relative fission mode weights by the Hill–Wheeler approach. Although the fission barrier heights resulting from the channel searches in the potential energy surface agree very well with experimental values for the inner barriers, the outer barriers are much too high. Nevertheless, from the final mass distributions it can be concluded that these outer barriers suffice to determine correctly the relative weights of the fission modes in most cases.

TABLE 4.6.5. ACCURACIES OBTAINED FROM COMPARING THE PREDICTIONS WITH EXPERIMENTAL DATA FOR INCIDENT ENERGIES BETWEEN 15 AND 200 MeV AND SEVERAL ISOTOPES.

Uncertainties in the proton and neutron induced fission cross-sections, as well as in the pre-neutron and post-neutron emission mass yields, are given, and are expressed as percentages.

	Sub-actinide region		Actinide region	
	Z < 84	Z < 91	Uranium	Z > 93
$\sigma_F(p,f)$	10–100%	10–20%	10%	—
$\sigma_F(n,f)$	10–15%	10–20%	10–15%	20%
$Y_{pre}(A)$	10–15%	10–50%	10%	—
$Y_{post}(A)$	50–1000%	—	10–1000%	30%

Mass yields can be predicted with a proper choice of both the ground state to saddle point level density parameter ratio and the pre-scission shapes. The pre-scission shapes are fixed by applying the same recipe to all nuclei. This leaves a_f/a_n as the only parameter which is tuned to reproduce at best both the fission cross-section and the mass yield curve for a given reaction. The obtainable accuracy depends in general on the incident energy, as well as on the isotope investigated. Table 4.6.5 contains a summary of the uncertainties. They are extracted from comparing the predictions for the total fission cross-sections, as well as for the pre-neutron and post-neutron emission mass yields with experimental data. The incident nucleon energies range from 15 to 200 MeV and the isotopes are either sub-actinides or actinides. In Table 4.6.5 the actinide region is subdivided into (a) the nuclides on the edge marking the transition to low energy symmetric fission, (b) uranium for which a large amount of data is available, and (c) the heavier actinides. The predictive power changes drastically with observable nuclide and excitation energy.

The prediction of the total fission cross-section is fairly accurate. Deviations of up to 100% can occur only in the case of the sub-actinides, for which the probabilities become very small. The determination of pre-neutron emission mass yields is satisfactory. The good agreement for uranium at energies as high as 200 MeV suggests that the temperature dependent liquid droplet model does not break down above a temperature of 2.0 MeV [4.6.40]. This value has been given as the validity boundary. Only in the fission of ^{226}Ra and ^{232}Th can the model not correctly describe the experimentally observed transition to symmetric fission. Asymmetric fission persists up to incident energies that are too high. This leads to deviations between 10% at low energies and 50% at high energies in the fission fragment mass yields. Whether this stems from asymmetric fission that vanishes too slowly with increasing excitation energies or from a lack of symmetric fission contributions from neutron deficient nuclides could not be determined from the results of this work. In general, the calculated post-neutron emission mass yields are too narrow: the light wing and the top are reproduced within 50% or better, whereas the heavy wing is underestimated by one order of magnitude. This is probably related to an overestimation of the post-scission neutron multiplicity. The model neglects the neutron evaporation between the saddle point and the scission point, leaving too much excitation energy in the fission fragments. Consequently the heavier fragment, which receives a larger portion of the excitation energy of the fissioning system, evaporates more neutrons than the lighter fragment and reduces the width of the final mass distribution. However, since the calculated mean mass of the pre-neutron emission mass yield curves agrees very well with the experimental values, the pre-scission neutron multiplicity, which momentarily excludes neutron evaporation between the saddle point and the scission point, cannot be completely wrong. Furthermore, the temperature of the fissioning system cannot be far too high because of the correctly reproduced relative contributions of the different fission modes in the calculated pre-neutron emission mass yield distributions. Therefore, a more likely explanation is provided by the supposition that the fragments evaporate too many neutrons because of an underestimation of the energy required for the emission of particles.

4.6.5.2. Outlook

Future developments in the theory may contribute to a better prediction of either the multi-chance fission process or the fission fragment properties. Three major extensions possible in the calculation of the fission fragment properties consist of including the charge distribution, the total kinetic energy, and the neutron emission between the saddle point and scission point. The addition of the total kinetic energy requires only minor effort, since this is already computed by the random neck rupture model and can be easily implemented by coupling with ALICE-91. The calculation of the charge distribution does not follow from the random neck rupture model. Here another model, possibly the scission point model by Wilkins et al. [4.6.30], has to be introduced. The neutron emission from saddle point to scission point may be taken into account in some effective way by assuming that part of the available excitation energy is transformed into neutrons emitted from the fissioning system before scission takes place.

Ingredients in the temperature dependent Brosa model also might lead to further refinements. The parameterization of the deforming nucleus may require more than the five parameters which are currently used. The addition of some extra parameters will allow the nucleus more freedom in the choice of shapes and, hence, in the fission channel. This may result in a better agreement between the experimentally determined outer barrier heights and the calculated values. Moreover, the fact that only the shell effects of the complete fissioning nucleus are computed can possibly account for deviations observed in the predicted average heavy fragment mass. The inclusion of shell effects in the fragments may turn out to be indispensable for an even more reliable prediction of this quantity. Another refinement may originate from the inclusion of the collective enhancement in the calculation of the transmission through the different outer barriers in order to determine the relative weights of the fission modes. For this purpose a calculation of the moments of inertia at each of the saddle points will be necessary. In this work the ground state level density is used in combination with temperature dependent barriers disregarding the change in collective effects between the ground state and the various outer saddles.

Improvements are also achievable in the description of the multi-chance fission process. This may be connected either to the replacement of the Bohr–Wheeler approach for a single humped barrier, as used in ALICE-91, by a more sophisticated treatment, or to a better understanding of the other reaction channels which indirectly influence the fission outcomes through their competition with the fission process.

The research work presented in this section merely forms a start in the process of acquiring a deeper understanding of the fission process at intermediate energies. The combination of future refinements in the calculations and the appropriate additional experiments might in the end provide an answer to the still open question about the true nature of the observed energy and mass dependent transition between asymmetric and symmetric fission.

REFERENCES TO SECTION 4.6

[4.6.1] DUIJVESTIJN, M.C., et al., Mass distributions in nucleon-induced fission at intermediate energies, Phys. Rev. C **64** (2001) 014607–014643.

[4.6.2] DUIJVESTIJN, M.C., et al., Proton-induced fission at 190 MeV of ^{nat}W, ^{197}Au, ^{nat}Pb, ^{208}Pb, and ^{232}Th, Phys. Rev. C **59** (1999) 776–788.

[4.6.3] DUIJVESTIJN, M.C., et al., "Fission in proton-induced reactions on Pb: Cross-sections and fragment yields", Nuclear Data for Science and Technology (Proc. Int. Conf. Trieste, 1997) (REFFO, G., VENTURA, A., GRANDI, C., Eds), Vol. 59, Part I, Italian Physical Soc., Bologna (1997) 455–457.

[4.6.4] DUIJVESTIJN, M.C., et al., "Proton induced fission at 190 MeV: Mass distributions and fission cross sections", Fission and Properties of Neutron-rich Nuclei (Proc. Int. Conf. Sanibal Island, FL, 1997) (HAMILTON, J.H., RAMAYA, A.V., Eds), World Scientific, Singapore (1997) 291–295.

[4.6.5] DUIJVESTIJN, M.C., HAMBSCH, F.-J., "Temperature-dependent fission barriers and mass distributions for ^{239}U", Fission and Properties of Neutron-rich Nuclei (Proc. 2nd Int. Conf., St. Andrews, 1999) 149.

[4.6.6] DUIJVESTIJN, M.C., et al., "Experimental and theoretical high-energy fission studies", in Proc. 4th Sem. on Fission, Pont d'Oye, Belgium, 1999 (WAGEMANS, C., SEROT, O., D'HONDT, P., Eds), World Scientific, Singapore (1999) 247–255.

[4.6.7] BEIJERS, J.P.M., et al., Separation of proton-induced fission isotopes from dominant evaporation residues by adapted target stacking, Nucl. Instrum. Methods Phys. Res. B **159** (1999) 176–182.

[4.6.8] DUIJVESTIJN, M.C., et al., "Nucleon-induced fission at intermediate energies", Nuclear Data for Science and Technology (Proc. Int. Conf. Tsukuba, Japan, 2002), J. Nucl. Sci. Technol. **1** Suppl. 2 (2002) 754–757.

[4.6.9] DUIJVESTIJN, M.C., Nucleon-induced Fission at Intermediate Energies, PhD thesis, Rijksuniversiteit Groningen, Netherlands (2000).

[4.6.10] TEWES, H.A., JAMES, R.A., Proton induced reactions of thorium–fission yield curves, Phys. Rev. **88** (1952) 860–867.

[4.6.11] CROALL, I., CUNINGHAME, J.G., Fragment distributions in the fission of ^{232}Th by protons of energies 13 to 53 MeV, Nucl. Phys. A **125** (1969) 402–416.

[4.6.12] KUDO, H., et al., Fission fragment yields in the fission of ^{232}Th by protons of energies 8 to 22 MeV, Phys. Rev. C **25** (1982) 3011–3023.

[4.6.13] HICKS, H.G., GILBERT, R.S., Radiochemical studies of the high-energy fission process, Phys. Rev. **100** (1955) 1286–1293.

[4.6.14] STEVENSON, P.C., et al., Further radiochemical studies of the high-energy fission products, Phys. Rev. **111** (1958) 886–891.

[4.6.15] HAGEBØ, E., et al., Radiochemical studies of charge and mass distribution in the light fragment region in fission of uranium induced by 170 MeV protons, J. Inorg. Nucl. Chem. **26** (1964) 1639–1652.

[4.6.16] PAPPAS, A.C., HAGEBØ, E., The charge and mass distributions in fission of uranium induced by 170 MeV protons, J. Inorg. Nucl. Chem. **28** (1966) 1769–1785.

[4.6.17] BABA, S., et al., Mass distribution and the total fission cross section in the fission of ^{238}U with protons of energies ranging between 13 and 55 MeV, Nucl. Phys. A **175** (1971) 177–198.

[4.6.18] KANDIL, A.T., Proton induced fission of ^{238}U, J. Inorg. Nucl. Chem. **38** (1976) 37–39.

[4.6.19] GALINIER, J.L., YAFFE, L., Nuclear charge distribution in the region of asymmetric fission of ^{238}U by protons of energy 20–85 MeV, J. Inorg. Nucl. Chem. **39** (1977) 1497–1508.

[4.6.20] BABA, H., et al., Abrupt changes of the characteristics of the proton-induced fission of ^{238}U around 14-MeV excitation, Z. Phys. A **356** (1996) 61–70.

[4.6.21] KUDO, H., et al., Most probable charge of fission products in 24 MeV proton induced fission of ^{238}U, Phys. Rev. C **57** (1998) 178–188.

[4.6.22] ÄYSTÖ, J., et al., "New results on superasymmetric fission at intermediate energy", Fission and Properties of Neutron-rich Nuclei (Proc. Int. Conf. Sanibal Island, FL, 1997) (HAMILTON, J.H., RAMAYA, A.V., Eds), World Scientific, Singapore (1997) 457–466.

[4.6.23] OHTSUKI, T., et al., Mass yield curves in low-energy proton-induced fission of ^{233}U, ^{235}U, ^{236}U, ^{237}Np, ^{239}Pu, ^{242}Pu, ^{244}Pu, ^{241}Am, and ^{243}Am, Phys. Rev. C **44** (1991) 1405–1423.

[4.6.24] HAGEBØ, E., LUND, T., Fission of lead induced by 600-MeV protons, J. Inorg. Nucl. Chem. **37** (1975) 1569–1582.

[4.6.25] EISMONT, V.P., et al., in Accelerator Driven Transmutation Technologies and Applications (Proc. 2nd Int. Conf. Sweden, 1996) Vol. II (CONDÉ, H., KALMAR, H., Eds), (1996) 592.

[4.6.26] MARMIER, P., SHELDON, E., Physics of Nuclei and Particles, Academic Press, New York and London (1969).

[4.6.27] CHUNG, C., HOGAN, J.J., Fission of ^{232}Th at energies up to 90 MeV, Phys. Rev. C **24** (1981) 180–191.

[4.6.28] CHUNG, C., HOGAN, J.J., ^{238}U fission at energies up to 100 MeV, Phys. Rev. C **25** (1982) 899–908.

[4.6.29] SCHMIDT, K.-H., et al., Low-energy fission studies of neutron-deficient projectile fragments of ^{238}U, Phys. Lett. **325B** (1994) 313–316.

[4.6.30] WILKINS, B.D., et al., Scission-point model of nuclear fission based on deformed-shell effects, Phys. Rev. C **14** (1976) 1832–1863.

[4.6.31] SPECHT, H.J., Experimental observables and the fission barrier, Phys. Scr. **10A** (1974) 21.

[4.6.32] KUDYAEV, G.A., et al., Thresholds and saddle shapes in symmetric and asymmetric fission in the vicinity of Ra, Sov. J. Nucl. Phys. **45** (1987) 951–958.

[4.6.33] KUDYAEV, G.A., et al., Fissility of nuclei and damping of the contribution of rotational modes to the level density, Sov. J. Nucl. Phys. **47** (1988) 976–980.

[4.6.34] BENLLIURE, J., et al., Calculated nuclide production yields in relativistic collisions of fissile nuclei, Nucl. Phys. A **628** (1998) 458–478.

[4.6.35] SCHMIDT, K.-H., et al., GSI-Preprint-99-30 (1999).

[4.6.36] BROSA, U., et al., Nuclear scission, Phys. Rep. **197** (1990) 167–262.

[4.6.37] LEE, C.H., et al., Charge and mass distributions from the reaction of 240 MeV ^{12}C ions with ^{238}U, Phys. Rev. C **38** (1988) 1757–1764.

[4.6.38] JENSEN, A.S., DAMGAARD, J., Shell effects in a paired nucleus for finite excitation energies, Nucl. Phys. A **203** (1973) 578–596.

[4.6.39] BLANN, M., "Recent progress and current status of pre-equilibrium reaction theories and computer code ALICE", Computation and Analysis of Nuclear Data Relevant to Nuclear Energy and Safety (Proc. Workshop Trieste, 1992) (MEHTA, M.K., SCHMIDT, J.J., Eds), World Scientific, Singapore (1993) 517–586.

[4.6.40] DIEBEL, M., et al., Microscopic calculations of fission barriers and critical angular momenta for excited heavy nuclear systems, Nucl. Phys. A **355** (1981) 66–92.

[4.6.41] STRUTINSKY, V.M., Shell effects in nuclear masses and deformation energies, Sov. J. Nucl. Phys. **3** (1966) 449–471.

[4.6.42] HILL, D.L., WHEELER, J.A., Nuclear constitution and the interpretation of fission phenomena, Phys. Rev. **89** (1953) 1102–1145.

[4.6.43] GILBERT, A., CAMERON, A.G.W., A composite nuclear-level density formula with shell corrections, Can. J. Phys. **43** (1965) 1446–1496.

[4.6.44] IGNATYUK, A.V., et al., Phenomenological description of the energy dependence of the level density parameter, Sov. J. Nucl. Phys. **21** (1975) 255–257.

[4.6.45] MYERS, W.D., SWIATECKI, W.J., Nuclear masses and deformations, Nucl. Phys. **81** (1966) 1–60.

[4.6.46] MYERS, W.D., SWIATECKI, W.S., Anomalies in nuclear masses, Ark. Fysik **36** (1967) 343–352.

[4.6.47] COHEN, S., et al., Equilibrium configurations of rotating charged or gravitating liquid masses with surface tension, Ann. Phys. **82** (1974) 557–596.

[4.6.48] DONETS, A.Yu., et al., Rep. E3-98-212, JINR, Dubna, Russian Federation (1999) 357.

[4.6.49] ITKIS, M.G., et al., Experimental investigation of the region of existence of asymmetric fission in light nuclei, Sov. J. Nucl. Phys. **41** (1985) 544–553.

[4.6.50] ITKIS, M.G., et al., Low-energy fission of gold nuclei by protons and α particles, Sov. J. Nucl. Phys. **47** (1988) 4–8.

[4.6.51] ZÖLLER, C.M., Untersuchung der Neutroneninduzierten Spaltung von ^{238}U im Energiebereich von 1 MeV bis 500 MeV, PhD Thesis, Technische Hochule Darmstadt, Germany (1995).

[4.6.52] PERRY, D.G., FAIRHALL, F.W., Mass-yield curve of first-chance fission from proton- and deuteron-induced fission of ^{226}Ra, Phys. Rev. C **4** (1971) 977–989.

[4.6.53] THEIN, M., et al., Mass distribution in 14.8 MeV neutron-induced fission of ^{232}Th, J. Inorg. Nucl. Chem. **30** (1968) 1145–1150.

[4.6.54] NETHAWAY, D.R., MENDOZA, B., Fission of ^{233}U with 14.8-MeV neutrons, Phys. Rev. C **2** (1970) 2289–2296.

[4.6.55] WINKELMANN, I., AUMANN, D.C., Fission of ^{242}Pu with 15.1-MeV neutrons, Phys. Rev. C **30** (1984) 934–940.

[4.6.56] PRINDLE, A.L., et al., Fission of ^{241}Am with 14.8-MeV neutrons, Phys. Rev. C **20** (1979) 1824–1830.

[4.6.57] MÖLLER, P., Odd-multipole shape distortions and the fission barriers of elements in the region $84 \leq Z \leq 120$, Nucl. Phys. A **192** (1972) 529–580.

[4.6.58] KONING, A.J., HILAIRE, S., DUIJVESTIJN, M.C., Nuclear Research and Consultancy Group, Netherlands, personal communication, 2003.

[4.6.59] SIEREK, A.J., Macroscopic model of rotating nuclei, Phys. Rev. C **33** (1986) 2039–2053.

5. NEW MODELS AND SYSTEMATICS: DEFINITIONS AND TESTING

M. Lammer
International Atomic Energy Agency

5.1. OUTPUT AND PRODUCTS

Brief descriptions of the most important features of the systematics and models used in the benchmark calculations are given in Section 5.1.3 for a better understanding of the results and analyses. Participants have also provided full accounts of their work in their individual contributions to this report, along with more detailed descriptions of the benchmark exercise and results. All participants contributed to the developments achieved during this CRP through fruitful discussions at project meetings, constructive critiques and the formulation of useful ideas towards the solutions of problems.

5.1.1. Data files

A bibliographic database of experimental yield data from neutron, photon and light charged particle induced fission has been assembled. The data are published in this final report, and also as a computer file in the Appendix of the CD-ROM, to enable direct access to the desired references.

Experimental yield data from neutron and light charged particle induced fission have been collected and compiled in different data files. All of these fission yield data have been converted to the well known EXFOR format and have been incorporated into the EXFOR database [5.1]. The attached CD-ROM also includes these experimental data to allow rapid computer searches.

Sets of reference fission yields have been assembled through an evaluation effort. These fission yields have been derived with higher accuracy than those recommended for complete yield sets in evaluated data files through careful evaluation of individual reference fission products. Full use was also made of correlations and covariance information by means of careful analysis and adjustment of the experimental data and assessment of uncertainties. No final overall adjustment has been applied to these fission yield data, as is normally done for complete yield sets to comply with physical constraints, a procedure that reduces the overall uncertainty of complete yield sets but increases the uncertainty of individual yields. Reference fission yield sets are presented as two individual sections in this report. Section 3.2 contains the data for U235T, U235F and U235H, and for U238F and U238H, while Section 3.3 is devoted to the spontaneous fission of ^{252}Cf.

5.1.2. Dedicated studies

Several of these studies have been performed by more than one participant, and the individual results are presented in the various contributions to this final report.

5.1.2.1. Measurements

Measurements (initiated by Duijvestijn, Ethvignot, Goverdovski and Zhdanov) have been performed to support the investigations of the CRP. The results have been used for the development of systematics, derivation of model parameters, and to check the validity of the fission yield predictions.

5.1.2.2. Differences between neutron induced and other fission reactions

Studies have been performed to determine the validity of using both neutron and non-neutron induced fission yields in systematics, with the following results:

(a) General conclusions drawn from model analyses of fission yields with different projectiles are also valid for neutron induced fission;
(b) Trends observed in systematic studies of yield distributions for non-neutron induced fission are also valid for neutron induced fission.

However, not all functional dependences, values for model parameters and numerical results can be used (e.g. transfer of angular momentum; see Section 5.1.3.4).

5.1.2.3. Multi-chance fission contributions

Maslov has performed a theoretical study of the fission mechanisms and the emissive fission contributions to the total fission cross-section in order to obtain the contributions of the fissioning nuclides to the total fission yield distributions. Fission cross-sections for neutron and proton induced reactions have been analysed and compared with different model calculations to obtain the best descriptions (Section 3.1). The statistical model was found to be the most adequate for this purpose. Also, the emissive fission contribution to the observed fission cross-section is dependent on target fissility and fission probability for high excitation energies. A method of partitioning the observed neutron induced fission cross-section into emissive and non-emissive fission has been validated for all neutron energies up to 200 MeV on Th, U, Np and Pu target nuclides. Emissive fission contributions (also for symmetric and asymmetric fission separately) have been calculated for several target nuclides.

5.1.2.4. Systematics derived from experimental data

The systematic behaviour of the energy dependence of the experimental fission yields has been studied for several fissioning nuclides:

(a) Global systematics of the dependences of fission product mass distributions on fissioning nuclide and excitation energy have been derived from experimental data for neutron, photon and charged particle induced fission;
(b) Experimental data are insufficient to derive global systematics for fission product charge distributions, and theoretical models do not provide adequate descriptions — therefore the empirical Z_p model as developed from low energy fission data was used, and parameter values were determined by the least squares method from fractional independent and cumulative yield values derived from the few available experimental data.

5.1.2.5. Phenomenological models for the fission yield distributions derived from experimental data

Two new phenomenological models have been developed for the analysis of experimental yield distributions from neutron, proton and alpha particle induced fission (see Sections 5.1.3.4 and 5.1.3.5). Detailed studies of the dependences of model parameters on target nuclide, projectile and incident particle energy have revealed regularities in their behaviour that can be used for systematics. Thus the models and computer programs have been successfully adapted during the course of the CRP to allow predictive calculations of mass distributions.

5.1.2.6. Theoretical prediction of fission yields at intermediate incident particle energies

A new theoretical approach has been developed to predict fission yields at intermediate energies and solve the problems of emissive fission, as well as the changing fission characteristics with excitation energy (Section 5.1.3.6). This approach is based on a newly developed version of the Brosa model for the calculation of fission yield distributions [5.2], coupled to a nuclear reaction code for the calculation of fission cross-sections and emissive fission contributions.

5.1.2.7. Progress towards computer programs for evaluations

Models and systematics have been developed that can in principle be used for an evaluation of energy dependent fission yields. However, the results of the benchmark exercise are not conclusive enough to recommend one analytical method at the present time, and the same is true for the computer programs. CYF (Section 5.1.3.3) and PYF (Section 5.1.3.5; also available on the Internet [5.3]) are designed to be user friendly.

5.1.3. Models and systematics

5.1.3.1. Fission yield systematics and covariance study of ^{238}U (Liu Tingjin)

The work of Liu Tingjin was restricted to ^{238}U fission yields, and no attempt was made to derive parameters for global systematics in order to predict fission yields for other fissioning nuclides. Mass distribution data from only one experiment (Zöller [5.4] over the energy range from 2 to 200 MeV) were used, adjusted for mass resolution and fitted with five (or three at higher energies) Gaussian functions. Gaussian parameters and their energy dependence were obtained from a non-linear least squares fit over the whole energy range, and uncertainties and correlations in the systematics were also studied. Liu adjusted for mass resolution, and

therefore his benchmark calculations do not agree in the intercomparison with the unadjusted experimental data, nor with the other calculations.

5.1.3.2. *Five Gaussian systematics for fission product mass yields (J. Katakura)*

Prior to the CRP, Moriyama–Ohnishi systematics [5.5] was used in Japan to calculate fission yields. However, as originally formulated, this approach failed to reproduce more recent measurements, especially for high energy neutron and proton induced fission. Using the basic structure of the systematics, the parameters were adapted to more recent data.

Mass distributions are described by five Gaussians in the newly developed systematics. Heavy asymmetric components are assumed to be related to the light components by reflection about a symmetry axis chosen as $(AF - (\bar{\nu}))/2$, where AF is the mass of the target plus projectile system, and $\bar{\nu}$ is the average number of post-scission neutron emissions This relationship reduces the number of independent Gaussians to three. However, the assumption of reflection symmetry is incorrect at higher energies (see Section 1.3.4.2).

The five Gaussians were fitted to the experimental data to obtain global systematics, and the functional dependences of the parameters on fissioning nuclides and incident particle energy were derived. An expression developed by Wahl for this CRP (see below) was used to determine the energy dependent $\bar{\nu}$ values. Only post-neutron emission mass distributions were calculated.

5.1.3.3. *Systematics of fission product yields (A.C. Wahl)*

Systematics of fission product yields were derived in two successive stages:

(1) Gaussian functions were fitted by least squares methods to experimental data for each fission reaction;
(2) Resulting Gaussian parameters were fitted to the corresponding values for U-235T by equations containing differences between the fissioning nuclides and excitation energies.

Two energy ranges were defined:

(1) Low energy fission of ≤8 MeV;
(2) High energy fission of ≥20 MeV;

and both ranges from 8 to 20 MeV to obtain a smooth transition.

Fission yields were assumed to be independent of composite nuclei formation. Emissive fission was accounted for by determination of an 'average loss' of mass number and atomic number from yield calculations, but the excitation energy of the composite nucleus had to be maintained as a parameter.

Experimental mass distributions were fitted with either three (above 20 MeV), five (at low energies) or even seven (for some targets at very low energies and for spontaneous fission) Gaussian functions. As with the systematics of Katakura, reflection symmetry in the shape of the distribution was assumed and the symmetry point was calculated in the same way; only $\bar{\nu}$ was replaced by NT, the 'average' total number of neutrons before and after fission, to account for emissive fission. NT was derived as a model parameter in the fitting procedure. The Gaussian parameters determined for each fission reaction were then fitted by mathematical functions of the average charge and mass of the fissioning nuclide and the composite nucleus excitation energy. These studies also resulted in the development of a charge distribution, as outlined briefly at the end of Section 5.1.2.4.

Wahl also evaluated the average numbers of total neutrons and neutrons emitted by fragments, and developed a model and systematics for the energy dependence. These data have been used by other CRP participants for their systematics.

5.1.3.4. *Phenomenological model for fragment mass and charge distribution in actinide nuclei fission (Yu.V. Kibkalo et al.)*

The phenomenological model of Kibkalo et al. was originally developed to study the dependence of the fissioning nucleus formation cross-section and the fission fragment mass and energy distributions on the excitation energy and total angular momentum. A detailed analysis of the dependence of experimental yield distributions on actinide nuclei fission has shown, at the time of formation of the angular mass and energy distributions of fission fragments, that an essential role is played by the spectrum of transition states above the fission barrier, as characterized by their excitation energy and the total angular momentum. This work was conducted because only a few studies were devoted to the influence of the total angular momentum on fission fragment

distributions. Some results of these investigations are summarized below.

The angular momentum transferred by the projectile and hence the total angular momentum of the fissioning nucleus increase with the mass of the projectile. Thus the characteristics of a compound nucleus are not independent of formation, even for the same excitation energy. There is a critical value for the angular momentum of some projectiles, below which compound nucleus formation occurs. However, fission can take place without compound nucleus formation if the projectile transfers sufficient energy. Thus the parameters of fragment distributions at particular excitation energies can be correctly extracted from experimental data only if the reaction mechanism leading to the formation of a fissioning nucleus is known. It is not sufficient to consider only the system projectile plus target nucleus and ignore the details of the formation process.

There is another critical value of the angular momentum for each type of projectile, above which the asymmetric fission channel ST-1 is converted into the super long symmetric channel over the whole excitation energy range. This change, as well as the complete disappearance of asymmetric fission due to the disappearance of shell effects, has solely been ascribed to the increasing excitation energy.

The Brosa model [5.2] was used for the parameterization of total and partial mass distributions in certain studies, and the dependence of the model parameters on the excitation energy was deduced. However, the functional dependence of all parameters on the total angular momentum could not be derived. Only parameter values below and above critical values of the angular momentum have been determined for different target–projectile combinations. Up to about 30 MeV, mass distributions can be satisfactorily fitted with four Gaussians, corresponding to two each for ST-1 and ST-2 with identical shapes.

5.1.3.5. Modal approach to the description of fragment mass yields (S.V. Zhdanov et al.)

The aim of this work was to obtain quantitative information on the dependences of the basic characteristics of the distinct fission modes (fragment mass, charge and energy distributions, their average values and variances, etc.) as a function of the nuclear composition and the excitation energy of the fissioning nucleus. A new method of multi-component analysis free from any assumption about the shapes of mass distributions of distinct fission modes was developed in order to deconvolute experimental mass and energy distribution into mass and energy distributions for distinct fission modes.

Experimental mass and energy distributions are expressed as sums of the contributions of individual fission modes for multi-modal analysis. Two versions of such an approach have been proposed:

(1) Experimental mass and energy distributions are described as the sum of the mass and energy distributions for each mode — but a drawback to this analysis is that the mathematical expressions for the modal contributions do not take into account the experimental uncertainties, and this omission can lead to undesired dependences of the results on the accuracy of the measurements;
(2) Minimization of the differences between the experimental mass and energy distributions and their descriptions in terms of modal contributions in an iterative process — experimental uncertainties are taken into account.

The two methods give practically the same results when analysing data with sufficient statistical accuracy, but method (2) is less sensitive to experimental uncertainties and judged to be more appropriate.

Results of the analysis include the following observations:

(i) An additional mode (Standard 3) had to be included in the multi-modal analysis that was attributed to spherical shell closures in the light fragments around mass 83;
(ii) The shapes of the peaks show low energy tails that can be best described by Charlier's distribution (accounting for deviations from Gaussian);
(iii) Yield distributions as a function of fragment charge exhibit little dependence on the isotope of a fissioning nuclide with a given charge, but strong dependence on the charge of the fissioning nuclide (i.e. yield distribution from ^{238}U fission is close to that of ^{233}U, but distinctly different to that of ^{238}Np). Thus the fragment charge distributions coincide almost exactly for fissioning isotopes of the same element; this effect is less pronounced for

mass distributions and practically undetectable for distributions as a function of fragment neutron number.

Functional dependences of modal distribution parameters on fissioning nuclides and excitation energy have been derived that have been used to develop systematics for modal yields. The mass distributions can be represented by a single Gaussian symmetric mode and one asymmetric mode described by Charlier's peak function. These findings have been incorporated into the PYF computer code [5.3] for the prediction of fission yields from Th to Bk target nuclides in reactions with protons and neutrons at incident energies of 5 to 200 MeV.

5.1.3.6. Fission yields from nucleon induced reactions at intermediate energies (M.C. Duijvestijn and A.J. Koning)

An experiment has been conducted to study the 190 MeV proton induced fission of several subactinides and ^{232}Th, and the resulting mass distributions were fitted with Gaussians. An interesting result was obtained for ^{232}Th: the mass distribution could not be fitted by a single Gaussian because of the asymmetric shape. A probable explanation involves the effect of emissive fission, as described in Section 1.3.4.2(1): at 190 MeV excitation energy, only the symmetric fission mode is present, but is superimposed by (a) mixed fission modes from even lower mass fissioning nuclei that have lost excitation energy, and furthermore (b) lower intensity contributions of predominantly symmetric fission modes located at different positions that arise from lower mass even neutron deficient isotopes. Attempts to decompose the experimental data into a purely symmetric and a mixed fission mode at lower masses gave a much better fit that supports the above explanation, as derived from the Brosa model [5.2].

The theoretical approach to the prediction of fission yields combines two concepts:

(1) A model to determine the fission cross-section for all fissioning systems contributing to a specific fission reaction as a function of their excitation energies (and therefore accommodating emissive fission);
(2) A model to predict the fission fragment and fission product yields for each set of fissioning nuclides that also incorporates the variation of the fission characteristics with excitation energy.

The original multi-modal random neck rupture model by Brosa et al. [5.2] has been extended in various ways in order to obtain an improved description of nucleon induced fission up to 200 MeV. Temperature is added to the calculation of the potential energy landscape of the nucleus, and the melting of the shell effect gives rise to the vanishing of asymmetric fission modes (first ST-1 and then ST-2) with increasing excitation energy. Relative contributions of the different fission modes are evaluated with Hill–Wheeler penetrability through inverted parabolic barriers using ground state level densities and temperature dependent barrier parameters. Subsequently, the classical multi-modal random neck rupture model translates the rupture probability as a function of the position at the neck of the scissioning nucleus into the pre-neutron and post-neutron emission mass yield curve. Linking this result with the fission cross-section contributions by all fissioning systems as computed by ALICE-91 [5.6], the total pre-neutron and post-neutron emission mass yields may be determined for any imaginable light particle induced fission reaction from 15 up to 200 MeV, and competition with all other outgoing channels is automatically taken into account. By separating the calculation of the fission cross-section from the fission fragment properties, the final uncertainty in the prediction is a superposition of the uncertainties arising from both steps.

ALICE-91 produces sound results only above 10 MeV because the Bohr–Wheeler model used to determine the fission probability forbids tunnelling through the fission barrier at low excitation energies. This form of tunnelling is allowed in the newly developed TALYS code [5.7], which has several other improvements over ALICE-91, but fails at excitation energies above approximately 30 MeV.

Conclusions from the intercomparison between model predictions and experiments can be summarized as follows:

(a) Pre-neutron emission mass yields — agreement is satisfactory and good for ^{238}U at energies as high as 200 MeV, which implies that the temperature dependent liquid drop model does not break down above 2 MeV (corresponding to an excitation energy of about 100 MeV, where only the liquid drop

fission barrier remains). Only in the fission of ^{226}Ra and ^{232}Th does asymmetric fission persist in predictions up to higher energies than found in experiments — possibly caused by the rather slow disappearance of the asymmetric fission with increasing excitation energy or from a lack of symmetric fission contributions from neutron deficient nuclides.

(b) Post-neutron emission mass yields — generally too narrow, with the heavy wing underestimated by an order of magnitude that may be related to an overestimation of the post-scission neutron multiplicity. The model neglects the neutron evaporation between saddle and scission points, which leaves too much excitation energy within the fission fragments. Consequently, the heavier fragment, which receives a larger portion of the excitation energy of the fissioning system, evaporates more neutrons than the light fragment, reducing the width of the final mass distribution. However, there is evidence from a comparison with experiments that the pre-scission neutron multiplicity is not completely incorrect and the calculated temperature of the fissioning system is not excessively high. A more likely explanation is that the fragments evaporate too many neutrons because of an underestimation of the energy required for the emission of particles.

5.1.3.7. Summary of the essential features of the new models and systematics

The five systematic approaches are derived from fitting functions representing the different fission modes to the experimental data. Parameters were then fitted by expressions that describe the dependences of these parameters on the system target plus projectile and excitation energy. One model was also explored in which the fission yields are calculated from nuclear fission theory to derive fission mechanisms and yield distributions.

Liu developed systematics solely for post-neutron emission yields from neutron induced ^{238}U fission by means of a non-linear least squares analysis and correlation study of the experimental data. This systematics approach is based on experimental data adjusted for mass resolution.

Katakura and Wahl have fitted the experimental data for actinide nuclei with 3 to 7 Gaussians. They used neutron and proton induced fission reactions, assuming reflection symmetry in the shape of the mass distribution around a point of symmetry calculated from the compound nucleus mass minus the average total number of emitted post (Katakura) or pre + post (Wahl) scission neutrons. Katakura can only predict post-neutron emission mass distributions. Wahl has not included the extensive measurements of Zöller [5.4], and this omission may be responsible for the discrepancies of his predictions compared with others at higher energies (50–160 MeV).

Kibkalo's phenomenological model was originally designed to study mass distribution dependences on transferred angular momentum for different projectiles, and was later adapted for predictions of fission yields. The systematics are similar to Katakura and Wahl, but without the prior calculation of a point of mass symmetry in the mass distribution.

The approach of Zhdanov et al. differs from others in several respects:

(a) Experimental mass and energy distributions of fragments are analysed;
(b) Expressions for the different fission modes do not include assumptions concerning the shapes of the distributions;
(c) Parameter values for the systematics were derived by minimizing the differences between experimental and calculated mass distributions;
(d) Charlier's peak functions were used in the systematics to describe the shapes of the asymmetric components.

Duijvestijn's predictions are based entirely on theoretical models for the fission mechanisms and yield distributions. The fission cross-sections and emissive fission contributions are calculated by means of a modelling code to obtain the contributions from different fissioning systems. A revised version of the Brosa model [5.2] includes the temperature dependence in the potential energy landscape of the nucleus to derive the probabilities for different fission modes. This approach is coupled with a model for the neck rupture to obtain the mass and charge split for calculating the fission fragment and product mass and charge distributions. ALICE-91 [5.6], as well as the newly developed TALYS code [5.7], were used in the benchmark exercise.

5.2. BENCHMARK EXERCISE

5.2.1. Benchmark exercise — general remarks

Only a brief summary of the benchmark exercise and calculation results are presented in this section. A more detailed description, together with figures and tables, is given in Section 6, which is devoted to the benchmark exercise. All calculations and intercomparison plots can be found in the Appendix on the CD. This summary is followed by a discussion of the analysis, which forms the basis for the conclusions and recommendations of the CRP. Since models are also used in systematics (for descriptions of mass distributions), the term 'model' is used generally to simplify the discussion.

The models developed during the course of the CRP are described in the relevant sections contained in this report. Comparisons were also made between the calculated and experimental yield distributions, and satisfactory agreement was found. However, these comparisons were only undertaken for selected targets and excitation energies, often in the lower energy range where the problem of emissive fission is negligible or small. The real predicting capability of the models and their accuracy were tested by conducting a benchmark exercise in which calculations were performed with all models for selected sets of fissioning systems (combination of target, projectile and excitation energy). An intercomparison and analysis of the results should help shed some light on possible sources of error in the models, and on the validity and quantitative influence of the various assumptions, simplifications and parameterizations. The benchmark exercise was designed to serve two purposes:

(1) To help reveal errors and/or wrong assumptions of any kind in the models;
(2) To give some kind of quantitative information about the accuracy of the model predictions that can be presented as recommendations to potential users.

The benchmark exercise was subdivided into two parts:

Part A: an intercomparison with the extensive experimental data for neutron induced ^{238}U fission; some other fissioning systems were also chosen for comparison.

Part B: predictions for fissioning systems with no experimental data that avoids an improved quality of predictions and/or good agreement between calculations arising from model parameters deduced from fits to experimental data; 'true' predictive capabilities should be revealed as a consequence of the choice of model parameters.

Pre- and post-neutron emission mass distributions should be calculated for all fissioning systems.

Several of the model calculations were only performed for selected sets of fissioning systems:

Liu:	Only part A: for ^{238}U + n, and post-neutron emission only;
Kibkalo:	Only part A: for ^{238}U + n (pre- and post-neutron emission) only;
Katakura:	Parts A and B: for neutron induced fission, post-neutron emission (all targets) only;
Zhdanov:	Parts A and B: from 5.5 MeV upwards (all targets and projectiles);
Wahl:	Parts A and B: all fissioning systems;
Duijvestijn:	Parts A and B: all fissioning systems: ALICE-91: 8–160 MeV; TALYS: 1–28 MeV (loses validity above about 30 MeV); ALICE-91 and TALYS are coupled to the modified Brosa model [5.2].

When discussing the applicability of model predictions for applied purposes, we consider discrepancies in terms of absolute fission yields (% per fission) as relevant, and use them throughout the analysis of the intercomparisons. With this understanding, large discrepancies in the low yield ranges of the mass distribution become unimportant for applications, although they may be important in finding the reasons for the discrepancies within the models themselves.

5.2.2. Summary of results and intercomparisons

We have restricted the analysis of part A to neutron induced fission of ^{238}U because this particular intercomparison covers by far the widest range of incident particle energy values. This system allows a more meaningful analysis of the characteristic features of model predictions with varying excitation energy. The intercomparison with the other fissioning systems does not give any additional insight, but is of theoretical interest to the authors of the models.

5.2.2.1. Pre- and post-neutron emission results

Calculations were performed for several incident neutron energies up to 28 MeV, and then for 50, 100 and 160 MeV. The most significant overall result of the intercomparison is that up to a neutron energy of 28 MeV there is reasonable agreement among the calculations (although some discrepancies do occur), but above that energy the calculated shapes of the mass distributions diverge.

Energies up to 28 MeV:

The largest relative differences between calculations are in the wing regions of the mass distributions, where they reach several orders of magnitude in the far wings around mass numbers 65–80 and 160–175. This observation can be explained by differences in the widths of the Gaussians used for the descriptions of the mass distributions. Fortunately, the yields are too low to have any impact on applied calculations, and hence the discrepancies are insignificant in terms of absolute yields. The same is true for the yields in the valley region, which differ up to a factor of two.

Yields in the peak regions that include the slopes from the peaks to the wings and the valley down to about 1.5–2% absolute yield are significant when comparing discrepancies with accuracy requirements. The calculated peak heights are normally within (tolerable) 1–1.5% absolute yield. However, the discrepancies between yields increase to 2–2.5% absolute due to differences in the peak positions, where the peak maxima of some calculations coincide with the slopes of other calculations.

Special observations:

(a) Only the peaks calculated by Wahl and Katakura show fine structure up to about 10 MeV, corresponding to the fission modes ST-1 and ST-2. This structure is not visible in other calculations due to the use of broader Gaussians or only one peak function.
(b) Some models show irregular deviations from the smooth trend in peak position and height that cannot be explained by the authors. The reason for this observation should be explored further.
(c) The agreement among calculations is slightly better (by about 0.5% absolute yield) for pre- than for post-neutron emission yields. This observation can be attributed to the additional differences introduced by the choice of the multiplicity distribution of neutrons emitted by fragments.

5.2.2.2. Energy region from 50 to 160 MeV

Best agreement with the experimental data of Zöller [5.4] was achieved by Liu and Kibkalo (whose systematics are based on these data) and by Zhdanov. For the pre-neutron emission case the results of Kibkalo (which agree completely with the experimental data) and Zhdanov almost coincide.

The symmetric peak within the systematics of Wahl rises more rapidly at lower energies than all other calculations, and dominates at 100 and 160 MeV. This behaviour can probably be attributed to the parameterization of Wahl's global systematics, which is entirely based on proton induced reactions at these energies. Apparently, this dominant central peak is only present in the distribution calculated from his global systematics, whereas the distribution derived from the original least squares analysis (of ^{238}U yields only) has a shape much closer to those calculated with the other models in the benchmark exercise. This is evident from Fig. 4.2.7 in Section 4.2.2, where the results of the global systematics and least squares analysis are compared for ^{238}U at 100 MeV.

Three distinct peaks visible in the predictions of Wahl at 50 MeV and Katakura at 160 MeV (as opposed to the flatter distributions calculated by others) are probably due to narrower Gaussians (as found for the 'fine structure'). The two peaks derived by Liu at 160 MeV are the result of his adjustment for incomplete mass resolution.

The pre-neutron emission mass distribution calculated by Duijvestijn with ALICE-91 possesses a taller heavy mass peak than the light mass peak. This difference in height can be explained by the effect of multi-chance fission: the position of the heavy mass peak remains stable for all fissioning nuclides, whereas the light mass peak is broadened and flattened. The calculated post-neutron emission mass distribution is skewed: the heavy mass peak is lower than the light mass peak and completely disappears at 160 MeV. This observation is attributed by Duijvestijn to incorrectly derived multiplicities for the neutrons emitted from the fission fragments (too many neutrons emitted, particularly by the heavy fragments). Such behaviour shows the strong influence of the assumed neutron emission distributions on predictions, and illustrates the importance of a

thorough and detailed analysis of the observed discrepancies.

5.2.2.3. Part B benchmark exercise

The results of part B of the benchmark exercise have not been analysed in detail because of the serious inability to explain the various discrepancies in part A. Explanations for the observed discrepancies and inconsistencies can only be given after a thorough study of the models themselves and different treatments of fission modes, multi-chance fission, neutron emission, etc. The results of part B of the benchmark are probably valuable for such a study, and are included on the CD-ROM.

Qualitatively, the shapes of the mass distributions, their changes with excitation energy and the discrepancies at higher energies are similar to the observations for ^{238}U(n,f). However, the discrepancies are larger below 50 MeV, and increase with the mass and charge of the fissioning nucleus. All predictions are worse than for ^{238}U, and the models cannot be recommended for use in applications or evaluations without further analyses and improvements.

5.2.3. Discussion

Systematics are only able to reproduce the experimental data on which they are based. Certain assumptions are made about the fitted model parameters, the correctness of which have to be investigated with the aid of a theoretical model. This approach is the only way one can study in detail certain features of mass distribution curves and all associated contributions (e.g. multi-chance fission and fission modes) and the reasons for the observed discrepancies. However, for predictions and detailed analyses that are quantitatively exact, models with valid assumptions and parameters are required. Unfortunately, the theoretical model developed by Duijvestijn is not yet able to reproduce the experimental data (that are also not particularly reliable). Duijvestijn attributes the modelling difficulties to incorrect values for particular parameters (e.g. post-scission neutron emission) and inappropriate assumptions concerning the contributions of the dominant fission modes. Despite these problems, the theoretical model is able to show the predicted trends. Therefore, a qualitative discussion is given below in the light of these predictions and is based on the intercomparison for the ^{238}U (n,f) reaction.

5.2.3.1. Comparison with experimental data

Overall, the calculations of Wahl and Duijvestijn, and at higher energies Katakura, fail to reproduce the experimental data. The other models are in agreement with the physical measurements of the fission fragments, but not with the γ ray spectrometric measurements of the fission products. The latter are in many cases too discrepant to allow conclusions to be made concerning the shapes of the peaks. All of the physical measurements have not been adjusted for mass resolution, which can cause quite significant changes in the mass distribution as shown by Liu. Altogether, the present comparison exercise has not been conclusive in the study of model predictions, and many more exact experiments are required at intermediate energies.

5.2.3.2. Symmetric and asymmetric fission modes

The distinction between the two asymmetric fission modes ST-1 and ST-2 is only visible in the predicted mass distributions of Wahl and Katakura in which narrower Gaussians are used. This fine structure is 'washed out' in the other model predictions that use broader peak functions. However, the structure predicted by Wahl and Katakura does not coincide with the measured observations.

The disappearance of the asymmetric fission modes with increasing excitation energy goes hand in hand with an increase of the symmetric fission mode, and is accounted for in all models (although the change in the dominating fission mode is calculated to occur at different excitation energies). Models with narrower peak functions show three distinct peaks, while models with broader peak functions exhibit broad flat plateaus. The latter is supported by the experimental data, which suffer from incomplete mass resolution, and the attempted adjustment for this effect by Liu resulted in two small peaks emerging from the plateau. While only the predictions, of Wahl exhibit a dominant symmetric peak (at 160 MeV), this phenomenon is also expected to occur in other model calculations, but at higher energies beyond the range of the present study.

5.2.3.3. Influence of multi-chance fission

The previous discussion of fission modes is valid only for the fissioning nucleus. While the

predicted effects of multi-chance fission have been described in Section 1.3.4.2, the impact of this phenomenon on the observed shape of the composite mass distribution is briefly outlined below.

(a) Superposition of preferred fission modes

At 100 MeV, the asymmetric and symmetric fission modes are about equal in the observed mass distribution. Asymmetric fission is likely to dominate below 100 MeV, and expected contributions from multi-chance fission are probably not sufficient to change the shape of the mass distribution significantly. Above 100 MeV, symmetric fission starts to dominate, contributions from higher-chance fission are more significant, and therefore the composite mass distribution is no longer symmetric in shape.

(b) Change in peak positions and mass symmetry point in asymmetric fission

The expected effect of the contributions from lower mass fissioning nuclides — a stable position for heavy mass peak, and a broadened and lower light mass peak — are only observed in the predictions of Duijvestijn with ALICE-91. There are several possible reasons:

(1) This possible effect is not included in most systematics, and reflection symmetry is assumed in the modelling of the mass distributions;
(2) As above, the predicted effect is too small below 100 MeV to cause a noticeable change in the mass distribution;
(3) When the chosen peak functions are too broad, any such visible effect at 100 MeV and above would be washed out, resulting in a flat plateau (even if reflection symmetry in the peak functions is not assumed).

At higher excitation energies, when symmetric fission becomes significant, the composite symmetric mass peak is expected to broaden towards lower masses. Similarly, the point of symmetry in the mass distribution, defined originally as the point where both fragments have equal mass (symmetric fission), changes from the position of first chance fission towards lower masses (broader valleys or symmetric peaks) with decreasing mass of the fissioning nucleus. When the composite mass distribution is considered, the symmetry point becomes the point above and below which the sums of the mass yields are equal and total 100%. However, this new point of mass symmetry is not defined solely by the mass of the target, plus projectile, and minus the total number of neutrons emitted, as assumed in some systematics.

(c) Multiplicity distribution of neutrons emitted from fission fragments

The observed multiplicity distribution of neutrons emitted from fission fragments is the sum of the contributions from different fissioning nuclides. Systematics and models have to include this effect when calculating the unmeasured neutron distributions derived for target nuclei only. Since there are hardly any measurements at intermediate energies, the neutron multiplicity distributions used in these models to calculate fission yields are based on crude assumptions.

5.2.3.4. Consequences for model predictions at higher energies

The following considerations have to be taken into account in systematics when modelling fission product mass distributions at higher energies:

(a) Mass distributions are not symmetric in shape;
(b) Light and heavy mass peaks cannot be described by peak functions that are identical in shape;
(c) Peak heights and widths are not equal — the shapes, particularly that of the light mass peak, cannot be described by symmetric functions like single Gaussians;
(d) When the asymmetric and symmetric fission contributions are both significant, the distribution could be broad and flat;
(e) At still higher energies, symmetric fission dominates, and the mass distribution should broaden and not have the shape of a single Gaussian;
(f) Mass distributions cannot be described by single Gaussians with identical parameters for each fission mode, but either by a superposition of Gaussians accounting for multi-chance fission or by using 'effective' peak functions that describe the actual peak shapes;
(g) If necessary, an effective point of symmetry has to be calculated from an effective mass of

the fissioning nucleus and the number of neutrons emitted by fragments at symmetry;

(h) The multiplicity distribution of neutrons emitted from fragments is crucial for the correct calculation of pre- and post-neutron emission mass distributions — this quantity should be carefully investigated and evaluated, and more measurements are needed to derive more reliable systematics;

(i) Assumptions made about neutron distributions in calculations could be checked against measured pre- and post-neutron emission mass distributions and adjusted accordingly.

If the effects of multi-chance fission are part of the calculations (purely theoretical approaches), the following parameters need to be chosen with care:

(1) Parameters and penetrability of the fission barrier;
(2) Contributions of multi-chance fission components as functions of incident energies;
(3) Energies at which the asymmetric fission modes disappear;
(4) Preferred fission modes of different fissioning nuclides as a function of excitation energy;
(5) The number of neutrons emitted before and after scission, but also between saddle and scission;
(6) Neutron multiplicity distributions from fragments.

5.2.3.5. Remarks on systematics and theoretical models

Our present knowledge of the expected impacts on the observed mass distribution is insufficient to predict the real shapes. There are neither sufficiently reliable experimental data nor confident predictions by systematics and theoretical models. Hence, we can only say that the assumptions associated with shape symmetry and the calculation of the point of mass symmetry are incorrect, but we cannot tell whether and at what energies the error is significant.

At lower energies up to 30 MeV, the deviations from Gaussian and shape symmetry are probably so small that the uncertainty is negligible compared with all other uncertainties. Discrepancies up to 2.5% absolute yield around the peaks and in the slopes of the valley are mainly due to differences in the positions of peak maxima, the peak shapes and the widths of valleys, while the peak heights are less discrepant. At still lower energies up to 10 MeV, structure in the peaks should be visible due to the two fission modes ST-1 and ST-2, but in several models this effect cannot be detected because the peak functions are too broad. Furthermore, the experimental results are not conclusive because of differences in the observed structure. A detailed analysis should clarify the shape and position of the structure and the energy at which ST-1 starts to become insignificant.

The survey plots of the mass distribution parameters between 13 and 20 MeV have revealed deviations from the smooth energy dependences for some calculations. The nature of these 'irregularities' could not really be explained, although they may arise from the onset of a new fission chance. Further investigations are strongly recommended.

At energies above 30 MeV, the predicted shapes are discrepant. At the present time there is little indication of what the correct shapes should be and which model gives the best predictions. All that can be noted is that the calculations of Wahl, Katakura and the theoretical model predictions seem to be far from reality, even considering the probable necessary adjustments to the experimental data. The following questions need to be clarified in a detailed analysis, particularly for this high energy region:

(a) How significant is the expected broadening of the peaks?
(b) At what energy does the symmetric peak start to become significant and dominate?
(c) Are three peaks visible at a certain energy, or does the broadening of the peaks due to multi-chance fission result in a broad and flat plateau?

5.3. CONCLUSIONS AND RECOMMENDATIONS

Accuracy requirements for fission yields in waste transmutation studies are ill defined. We assume that only fission yields ≥2% are important, and should be known to about 25% relative accuracy, amounting to roughly 1.5% absolute yield uncertainty for peak fission yields of 6–7%. At low energies for ^{238}U, where agreement is better, the discrepancies among calculations are 2.5% in many cases. Clearly for those nuclides included in part B of the benchmark exercise the agreement is worse, even without detailed analyses. Therefore, the

target of 25% relative accuracy for the important fission yields has not been met to date. Furthermore, since the comparisons of experiments are also inconclusive, we are not in a position to recommend any of the models or computer programs for use in applied calculations.

On the other hand, models for fission yield predictions at intermediate energies have been developed for the first time, and contributions to mass distributions due to different fission modes and emissive fission have been calculated. These models have the potential to give reliable predictions after additional improvements involving detailed analyses of their contents and parameters, results and reasons for discrepancies. Proposals for further developments and improvements should be based on more reliable quantitative theoretical predictions of the influence of multi-chance fission and of the shapes of the mass distribution and associated components. The inclusion of higher energies above 100 MeV in such studies is equally important, as the present limit of 150 MeV has only been set as the first step in the evaluation of nuclear data for transmutation.

We recommend the following studies to achieve the required improvements.
More accurate measurements:

(a) Up to about 20 MeV incident neutron energy to investigate the exact structure within the peak shape and their disappearance;
(b) Up to about 100 MeV incident neutron energy to determine the exact peak positions;
(c) Above about 20 MeV incident neutron energy for the accurate determination of the peak shapes to reveal possible broadening;
(d) Above about 30 MeV incident neutron energy to assist in the study of different methods for the determination of the real shape of the mass distributions;
(e) Systematic measurements for ^{238}U, as well as several measurements for other fissioning nuclides.

Adjustment for mass resolution:

An expert familiar with the experimental methods used to determine physical fission fragment mass and energy distributions should study the details of the measurements concerned and the proposed data handling methods, with the aim of finding a valid and acceptable form of subsequent adjustment.

Theoretical models:

Study systematically the important quantities listed in Section 5.2.3.4 (e.g. vary the values of parameters and investigate the impact on the calculated mass distribution; study the effect of assumed neutron emission distributions).

Neutron emissions:

(1) Study the number of pre-scission neutrons (particularly those neutrons emitted between saddle and scission), and multiplicity distributions of neutrons emitted from fragments;
(2) More measurements are required up to an incident neutron energy of 150 MeV;
(3) Detailed and systematic theoretical analysis to develop more reliable models (neutron distributions have a significant influence on calculated mass distributions);
(4) Systematic measurements for ^{238}U and other fissioning nuclides.

Systematics and their models for mass distribution shapes:

Current models should be analysed to address the following questions.

(i) What are the reasons for the observed irregularities?
(ii) Why are there such large differences in the predicted shapes of mass distributions?
(iii) Can asymmetric peak shapes be introduced for composite peaks, and do they give better results?

Improvements will depend on the results of the recommended theoretical analysis and further experiments. How can theoretically predicted distribution shapes and deviations from symmetric Gaussian components be described in terms of peak functions? Is the introduction of an effective mass for the fissioning nucleus or an effective point of mass symmetry sufficient?

Ancillary comments:

— Measurements recommended by CRP participants should be published in order to reach a wide audience;
— Detailed analysis of the present models and systematics and of the benchmark calculations

should be undertaken — such a study should be performed in close contact with the authors of the models and will impact significantly on efforts to improve systematics and theoretical models;
— Analyses should include a detailed assessment of the problem of the need to adjust the experimental data for mass resolution.

REFERENCES TO SECTION 5

[5.1] McLANE, V., EXFOR basics, a short guide to the nuclear reaction data exchange format, http://www-nds.iaea.org/reports/nds-206.pdf

[5.2] BROSA, U., et al., Nuclear scission, Phys. Rep. **197** (1990) 167–262.

[5.3] http://www.inp.kz/laboratoryrus/lpdpyf.php

[5.4] ZÖLLER, C.M., Untersuchung der neutronen-induzierten Spaltung von ^{238}U im Energiebereich von 1 MeV bis 500 MeV, PhD Thesis, Technische Universität Darmstadt, Germany (1995).

[5.5] MORIYAMA, H., OHNISHI, T., Systematics of fission fragment mass yield curves, Rep. 166, Kyoto University (1974).

[5.6] BLANN, M., "Recent progress and current status of pre-equilibrium reaction theories and computer code ALICE", Computation and Analysis of Nuclear Data Relevant to Nuclear Energy and Safety (Proc. Workshop Trieste, 1992) (MEHTA, M.K., SCHMIDT, J.J., Eds), World Scientific, Singapore (1993) 517–586.

[5.7] KONING, A.J., et al., "TALYS: Comprehensive nuclear reaction modelling", Nuclear Data for Science and Technology (Proc. Int. Conf. Santa Fe, NM) (HAIGHT, R.C., et al., Eds), AIP Conf. Proc. 769, Melville, New York (2005) 1154–1159.

6. BENCHMARK EXERCISE

M. Lammer
International Atomic Energy Agency

The motivation to conduct this benchmark exercise, a summary of the results, and a discussion of and conclusions from the intercomparison are given in Section 5.2. This section contains further details of the results of the calculations and intercomparisons, illustrated by tables and figures, but avoiding repetition of Section 5.2 as far as possible.

6.1. CHOICE OF FISSIONING SYSTEMS

Part A: Only fissioning systems (combination of target, projectile and incident energy) were selected for which measurements exist. The most extensive set of data was available for neutron induced ^{238}U fission; some other fissioning systems were also chosen for comparison.

Part B: Predictions for fissioning systems with no experimental data.

The fissioning systems included in the benchmark exercise were as follows:

Part A: ^{233}U, ^{237}Np, ^{245}Cm + thermal neutrons
^{233}U + n at 1 MeV
^{238}U + n at 1.6–2.0, 5.5, 8, 10–11, 13, 14–15, 21, 27–28, 50, 100, 160 MeV
^{238}U + p at 20, 60 MeV
^{237}Np + n at 5.0, 5.5, 16.5 MeV
^{239}Pu + n at 0.17, 7.9, 14.5 MeV
^{242}Pu + n at 15.1 MeV.

Part B: ^{237}Np, ^{241}Am, ^{244}Cm + n at 13, 27–28, 50, 100, 160 MeV.

Pre- and post-neutron emission mass distributions should be calculated for all fissioning systems.

Several of the model calculations were only performed for selected sets of fissioning systems:

Liu: Only part A: for ^{238}U + n, and post-neutron emission only;

Kibkalo: Only part A: for ^{238}U + n (pre- and post-neutron emission) only;

Katakura: Parts A and B: for neutron induced fission, post-neutron emission (all targets) only;

Zhdanov: Parts A and B: from 5.5 MeV upwards (all targets and projectiles);

Wahl: Parts A and B: all fissioning systems;

Duijvestijn: Parts A and B: all fissioning systems:
ALICE-91: 8–160 MeV;
TALYS: 1–28 MeV (loses validity above about 30 MeV);
ALICE-91 and TALYS are coupled to the modified Brosa model [6.1].

6.2. PART A BENCHMARK EXERCISE

6.2.1. General remarks

6.2.1.1. Adjustment for mass resolution

Liu evaluated all experimental ^{238}U, ^{239}Pu and ^{242}Pu fission yields included in part A of the benchmark exercise. Results from physical measurements were adjusted for mass resolution (see Section 6.2.3), using the method proposed by Schmitt et al. [6.2]. These modifications were discussed at a Research Coordination Meeting and rejected as there were believed to be too many uncertainties associated with incomplete mass resolution and any proposed adjustments. The applicability of the adjustment procedure to other measurements was also called into doubt. Although the need for adjustments for incomplete mass resolution was recognized, the conclusion of the CRP participants was that the published unadjusted data should be used in the intercomparison. All model parameters except those of Liu were derived from unadjusted data, and Zöller [6.3] has not given an adjustment function for his fission yield data (which are the basis of the comparisons with experiments). The experimental details should be thoroughly studied by an expert familiar with the

experimental method in order to derive an appropriate and valid adjustment procedure.

6.2.1.2. Presentation of the analyses

Intercomparison plots for part A of the benchmark exercise were prepared for $^{238}U + n$, $^{238}U + p$, $^{239}Pu + n$ and $^{242}Pu + n$, including mass distributions and various ratios. For reasons given in Section 5 we present here only the intercomparison for $^{238}U + n$. Figures comparing measured and calculated mass distributions provide the best picture of differences in terms of absolute yields, and they are presented for energy values at which the shapes of the mass distributions and/or the agreement among data change significantly. Some parameters of the mass distributions are tabulated and plotted as a function of the incident neutron energy.

6.2.2. Post-neutron emission

There are more experimental data and more calculated results for post-neutron emission than for the pre-neutron emission yields. A survey of measured and calculated asymmetric mass peak positions and heights, valley heights at symmetry and peak to valley ratios as a function of incident neutron energy is presented in Table 6.2.1 and Figs 6.2.1–6.2.4. Intercomparisons of actual mass distributions are plotted in Figs 6.2.5–6.2.11 for E_n = 1.5, 8, 14–15, 27–28, 50, 100 and 160 MeV. A more detailed discussion of the intercomparison is restricted to energies up to 28 (sometimes 50) MeV because above that value the shapes of the mass distributions are too divergent (e.g. the same plot shows distributions that contain 1, 2 or 3 peaks or are broad and flat, so that terms like asymmetric peak or valley lose their meaning). The energy range 50–160 MeV is discussed in a separate analysis.

6.2.2.1. Experimental data

The experimental data can be subdivided into two groups:

(1) Yields determined either by γ ray spectroscopy of unseparated fission products, or by β-γ spectrometry of individual fission products after chemical separation, E_n = 1.5, 5.5, 8.1 + 8.3, 11.3, 14.4 + 14.9 and 22 MeV;

(2) Directly recorded mass distributions of Zöller [6.3] at 13, 20, 27–28, 50, 100 and 160 MeV.

Yields determined by method (1) exhibit large fluctuations and fine structure in the peak regions, not all of which are necessarily real and reproduced by model calculations. Furthermore, the experimental peak maxima are always closer to symmetry than the calculated profiles, and lead to narrower valleys. However, low yield products in the valley and wing regions are generally not included in these measurements because the intensities of the emitted radiations are too low.

Mass distributions from Zöller [6.3] are much smoother because of the poor and unadjusted mass and energy resolutions. For example, at an energy quoted to be 27.5 MeV, the actual energy range is 22–33 MeV and the given fragment mass number covers 3 mass units. Similarly, for '100 MeV', the energy range is 89–110 MeV and the mass range is 5 mass units. The better agreement with model calculations can be attributed to most of the systematics being based on Zöller's data. At higher energies (50–160 MeV) these data favour the results of Kibkalo and Zhdanov, and also Liu's systematic calculations without any adjustment for mass resolution. Finally, a striking observation is that the agreement between the measurements of Zöller and the experimental data from method (1) is worse than between Zöller and the calculated results.

6.2.2.2. Model calculations

(a) Discrepant results

ALICE-91 (8–160 MeV):

The distribution is in most cases narrower, the valley higher, and the wings and peaks lower than in other calculations. While the heavy mass peak becomes lower than the light mass peak with increasing neutron energy and disappears completely at 160 MeV, the light mass peak starts to rise above all others at 50 MeV. The position of the light mass peak is consistently two mass units lower than all other calculations, whereas there is agreement for the position of the heavy mass peak.

TALYS (1.6–28 MeV):

Similar to ALICE-91, but fails above about 30 MeV.

TABLE 6.2.1. ^{238}U POST-NEUTRON EMISSION MASS DISTRIBUTIONS: SURVEY OF DISTRIBUTION PARAMETERS

Peak positions

E_n (MeV)	1.6–2		5.5		7–8		10–11		13		14–16		21		27–28		50		100		160	
Peak	Light	Heavy	Light	Heavy	Light	Heavy	Light	Heavy	Light	Heavy	Light	Heavy	Light	Heavy	Light	Heavy	Light	Heavy	Light	Heavy	Light	Heavy
Experiment	101	135	100	136	100	135	99.5	134	99	135	100	134	97	134	98	134	98.5	130.5	103	126	107	120
ALICE	—	—	—	—	96.8	136.8	96.5	135.8	96.8	135.8	96.7	135.6	96.4	135.0	96.5	134.4	95.8	134.0	96.3	131.8	98.0	—
TALYS	96.9	137.7	97.3	136.8	96.8	136.1	97.3	135.7	97.5	135.4	97.2	135.6	97.3	134.8	97.0	134.4	95.6	134.7	—	—	—	—
Katakura	99.6	136.7	99.5	136.6	99.3	136.3	99.2	136.3	99.1	136.2	99.0*	136.1*	98.8	136.1	98.4	135.3	97.7	134.0	96.8	131.7	96.8	129.3
Kibkalo	99.0	137.0	98.9	137.0	98.8	136.7	98.7	136.7	98.9	136.3	96.8	134.2	96.9	133.7	99.2	134.8	99.3	130.7	101.0	125.9	—	—
Liu	99.5	137.0	99.5	136.3	99.5	136.0	99.0	135.5	99	135	98.8	134.9	99	134	98	133	98.5	130.5	101	128.5	101	124
Wahl	99.6	136.9	99.8	136.2	99.8	136.2	99.5	136.3	97.2	138.2	96.7	138.6	96.5	138.1	97.0	137.0	98.7	133.4	—	—	—	—
Zhdanov	—	—	98.8	137.1	98.9	136.8	98.3	136.3	98.4	136.3	98.5*	136.3*	98.3	135.3	98.5	134.7	99.3	132.7	99.5	129.5	—	—

* Average of data for 14 and 15 MeV.

Peak heights

E_n (MeV)	1.6–2		5.5		7–8		10–11		13		14–16		21		27–28		50		100		160	
Peak	Light	Heavy	Light	Heavy	Light	Heavy	Light	Heavy	Light	Heavy	Light	Heavy	Light	Heavy	Light	Heavy	Light	Heavy	Light	Heavy	Light	Heavy
Experiment	7	8	6.5	7.0	6.2	7.0	5.8	6.6	5.5	5.5	5.85	6.20	6.6	6.6	4.9	4.9	4.4	4.36	3.82	3.78	3.9	4.0
ALICE	—	—	—	—	5.95	5.75	5.75	5.50	5.65	5.35	5.65	5.35	5.58	5.26	5.26	4.88	5.37	4.84	4.68	3.66	4.6	—
TALYS	6.75	6.61	6.00	5.85	5.84	5.70	5.82	5.56	5.60	5.28	5.95	5.73	5.44	5.10	5.36	4.92	6.80	6.56	—	—	—	—
Katakura	6.95	6.95	6.52	6.52	6.36	6.36	6.25	6.25	6.10	6.10	6.01*	6.01*	5.74	5.74	5.51	5.51	4.98	4.98	4.28	4.28	3.88	3.88
Kibkalo	6.07	6.03	6.02	6.00	6.00	5.98	5.88	5.84	5.62	5.55	5.37	5.23	5.12	4.90	4.78	4.50	4.33	4.07	4.00	3.89	—	—
Liu	7.10	7.00	6.85	6.85	6.84	6.82	6.7	6.7	6.5	6.5	6.35	6.35	6.04	6.12	5.82	5.78	4.83	4.81	4.25	4.25	4.16	4.18
Wahl	7.46	7.46	7.05	7.05	6.60	6.60	6.20	6.20	5.73	5.73	5.66	5.66	5.18	5.18	4.57	4.57	3.60	3.60	—	—	—	—
Zhdanov	—	—	6.45	6.55	6.24	6.34	6.10	6.18	5.87	5.89	5.74*	5.76*	5.26	5.28	4.86	4.88	4.14	4.14	3.64	3.64	—	—

* Average of data for 14 and 15 MeV; Katakura — both peaks 6.03 resp. 5.99; Zhdanov — light peak 5.78 resp. 5.70, heavy peak 5.80 resp. 5.72.

Valley heights and peak-to-valley ratios (P/V)

E_n (MeV)	1.6–2		5.5		7–8		10–11		13		14–16		21		27–28		50		100		160	
Peak	Valley	P/V	Valley	P/V	Valley	P/V	Valley	P/V	Valley	P/V	Valley	P/V	Valley	P/V	Valley	P/V	Valley	P/V	Valley	P/V	Valley	P/V
Experiment	—	—	—	—	0.17	40	0.4	16	0.8	7	0.8	7.6	1.3	5.1	1.7	2.9	2.8	1.6	3.6	1.06	3.75	1.05
ALICE	—	—	—	—	0.866	6.8	1.12	5.0	1.25	4.4	1.15	4.8	1.45	3.7	1.75	2.9	1.93	2.6	3.08	1.35	—	—
TALYS	0.0274	244	0.45	13	0.632	9.1	1.16	4.9	1.48	3.7	0.93	6.3	1.70	3.1	1.96	2.6	0.94	7.1	—	—	—	—
Katakura	0.088	79	0.278	23.5	0.393	16.2	0.48	13	0.61	10	0.67*	9.0*	0.92	6.2	1.16	4.75	1.78	2.8	2.75	1.56	3.58	1.08
Kibkalo	0.132	46	0.152	39.5	0.185	32	0.33	18	0.70	8	1.09	4.9	1.48	3.4	1.99	2.33	2.89	1.45	3.56	1.11	—	—
Liu	0.120	59	0.195	35	0.26	26	0.39	17	0.56	12	0.80	7.9	1.10	5.5	1.70	3.4	2.57	1.88	3.40	1.25	3.82	1.09
Wahl	0.012	620	0.082	86	0.232	28	0.36	17	0.57	10	0.68	8.3	1.21	4.3	1.82	2.5	3.40	1.06	—	—	—	—
Zhdanov	—	—	0.085	76	0.184	34	0.30	20	0.49	12	0.59*	9.8*	1.08	4.9	1.57	3.1	2.68	1.55	3.49	1.04	—	—

* Average of data for 14 and 15 MeV; Katakura — valley 0.65 and 0.69, P/V 9.2 and 8.8; Zhdanov — valley 0.55 resp. 0.62, P/V 10.5 resp. 9.2.

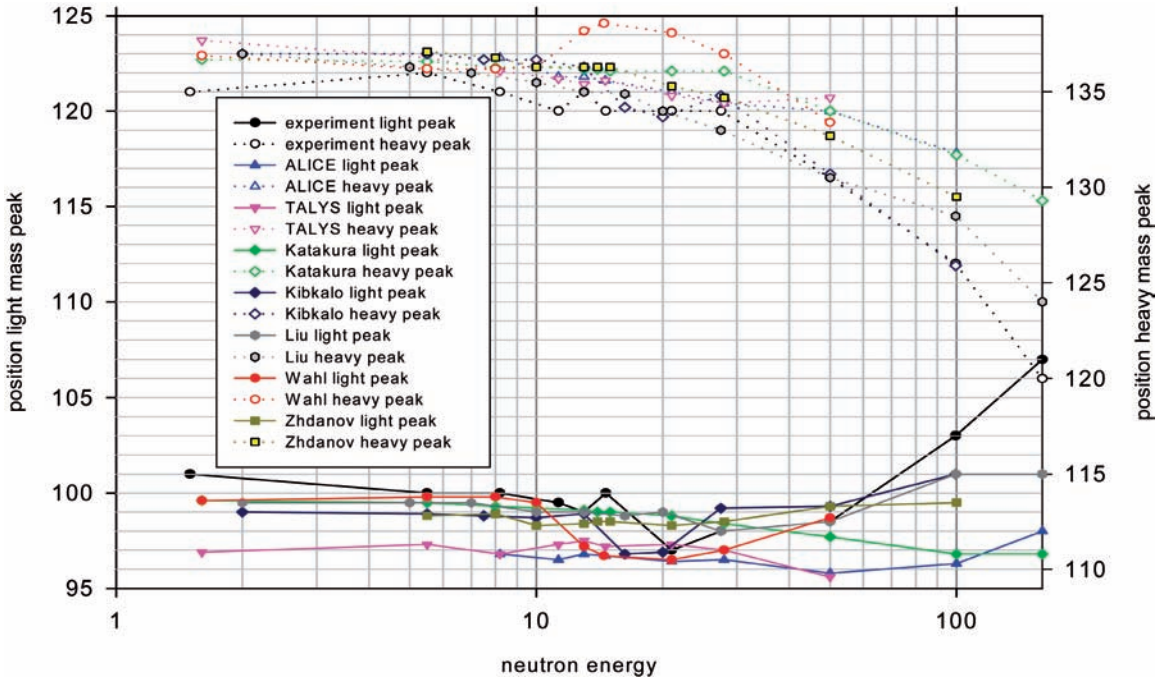

FIG. 6.2.1. Benchmark exercise, part A: ^{238}U post-neutron emission mass distribution, positions of mass peaks versus neutron energy.

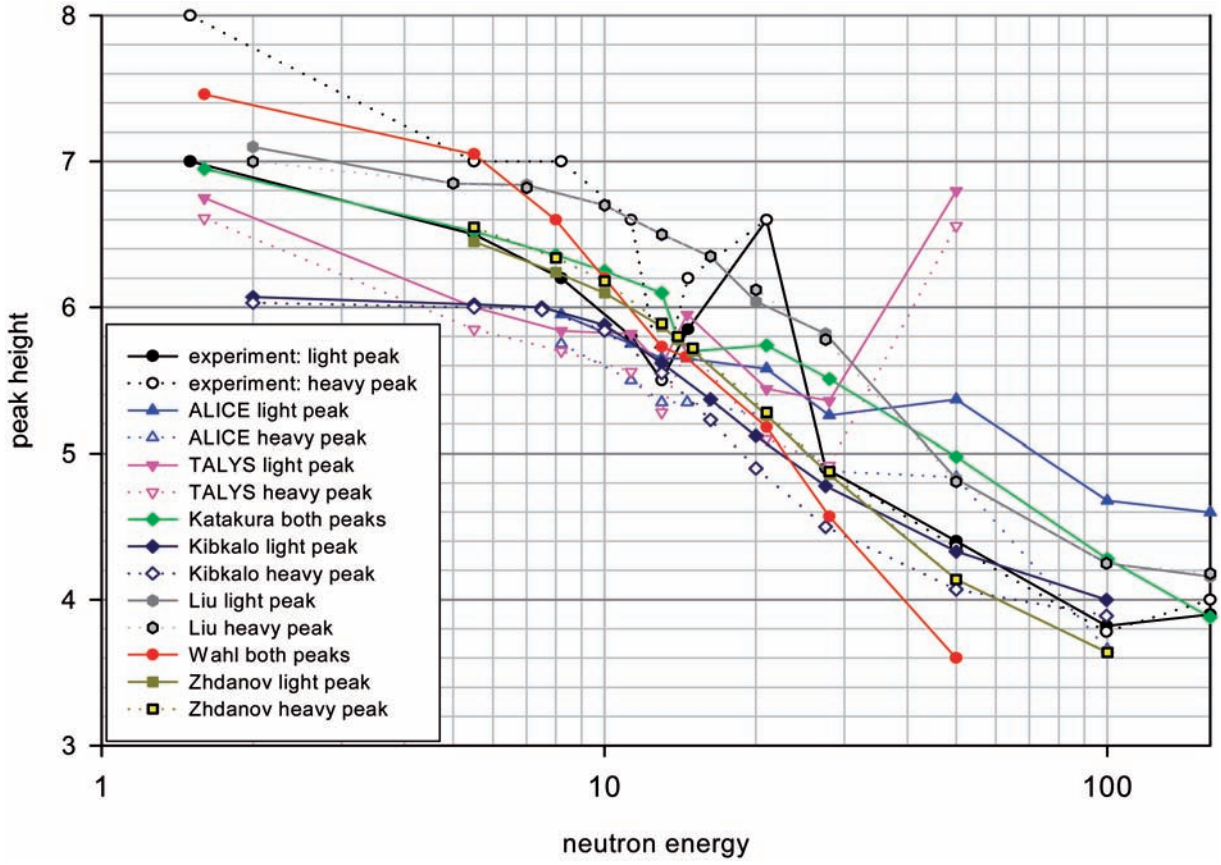

FIG. 6.2.2. Benchmark exercise, part A: ^{238}U post-neutron emission mass distribution, heights of mass peaks versus neutron energy.

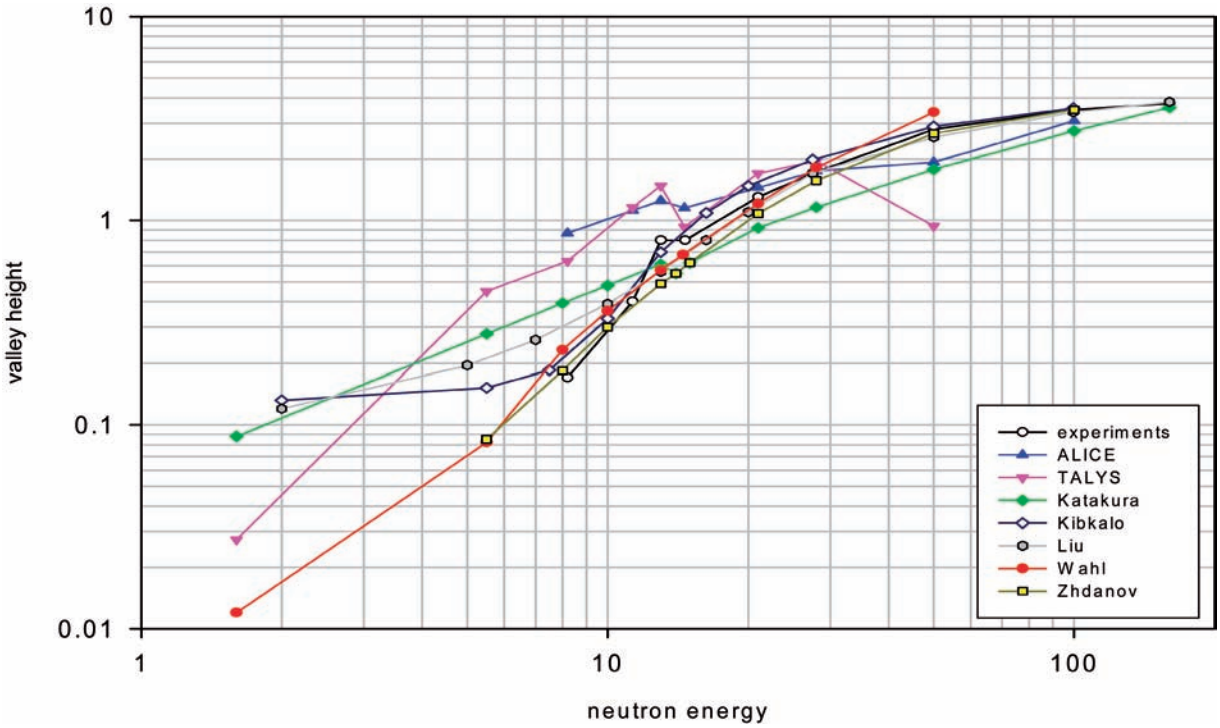

FIG. 6.2.3. Benchmark exercise, part A: ^{238}U post-neutron emission mass distribution survey: heights of valley versus neutron energy.

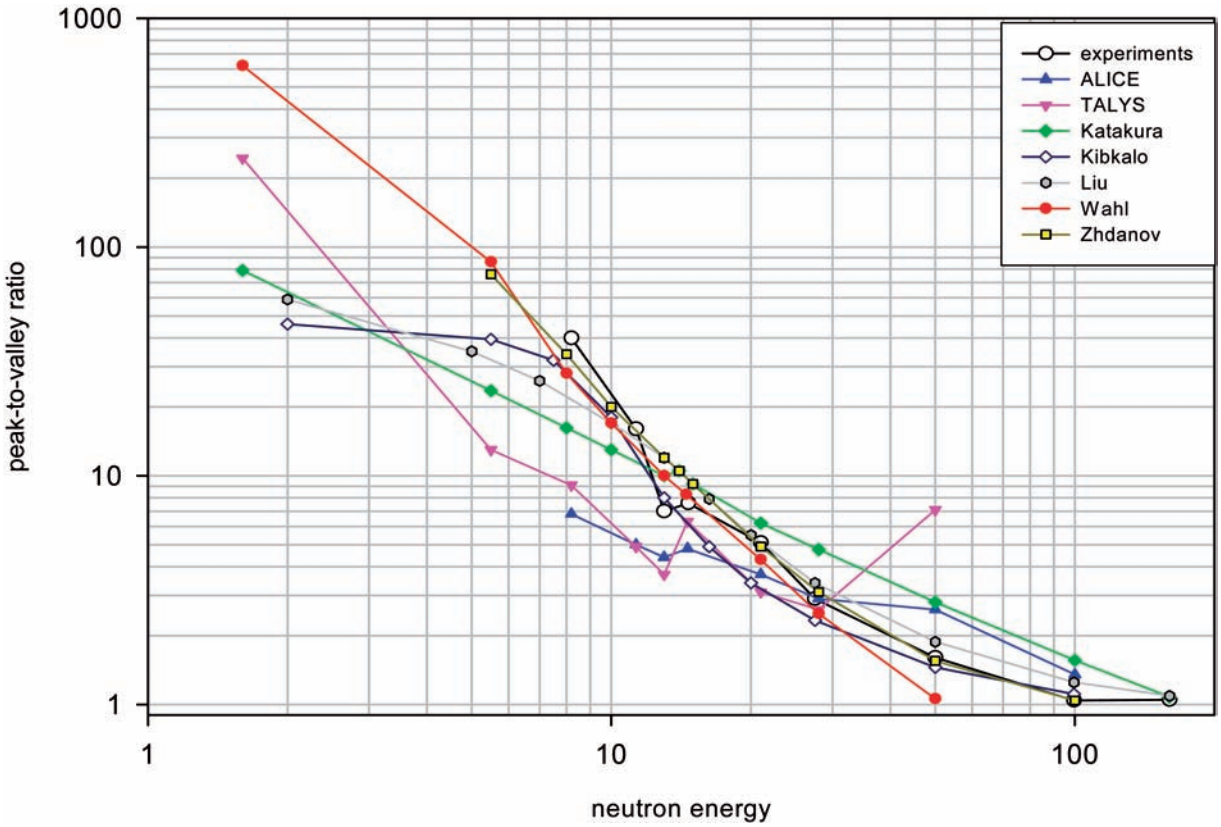

FIG. 6.2.4. Benchmark exercise, part A: ^{238}U post-neutron emission mass distribution survey: peak to valley ratio versus neutron energy.

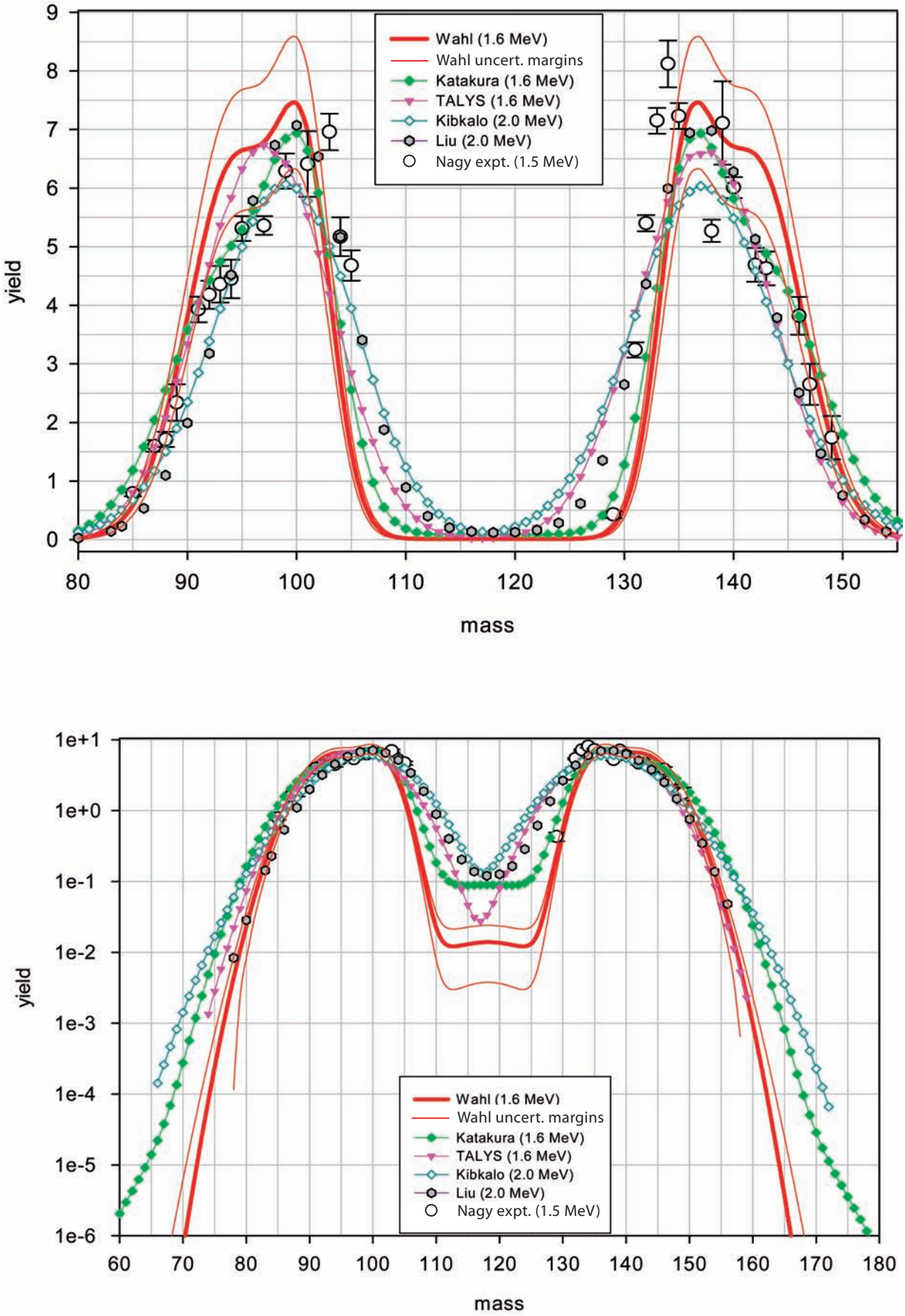

FIG. 6.2.5. Benchmark exercise, part A: ^{238}U at 1.5–2 MeV, post-neutron emission yields.

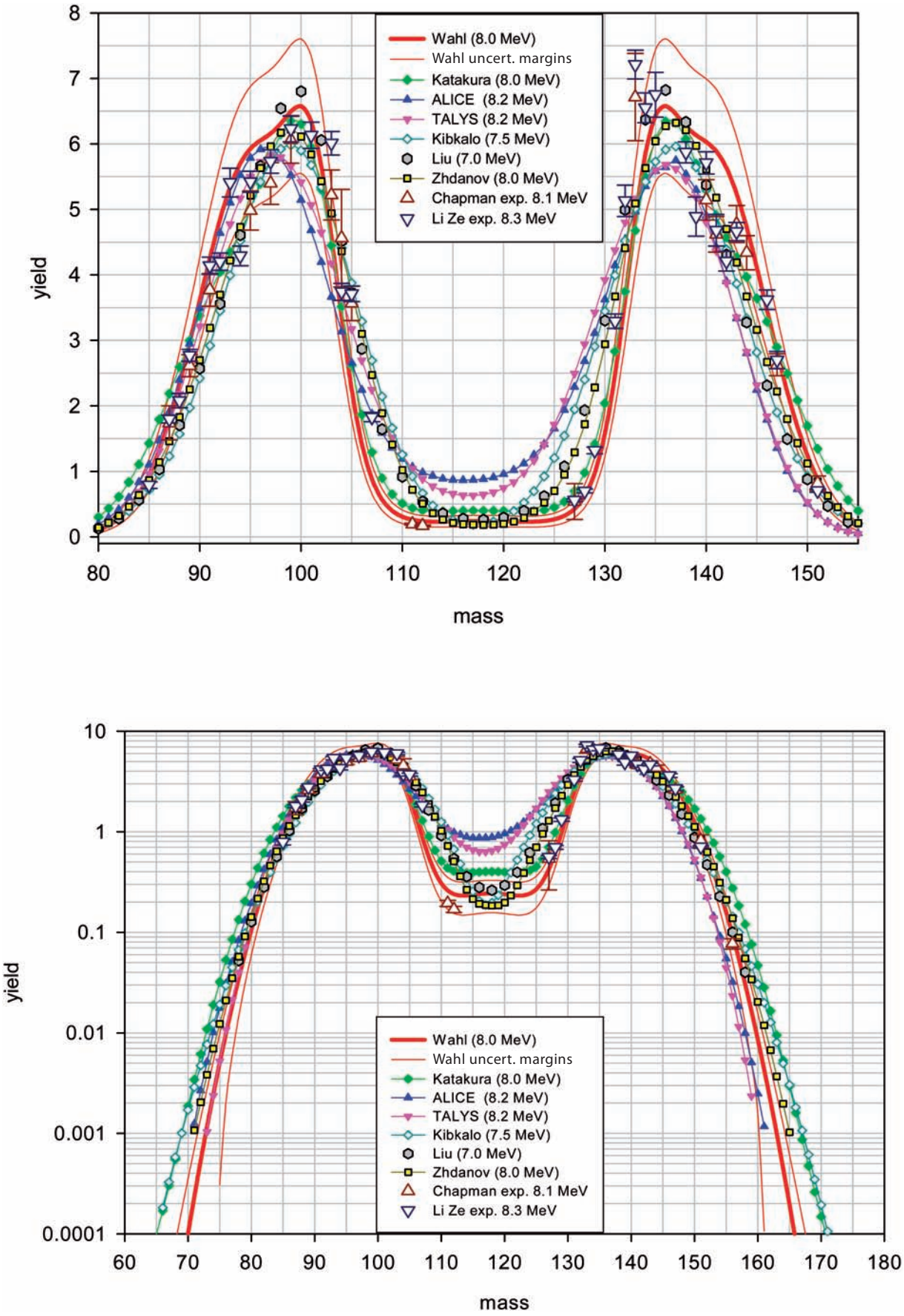

FIG. 6.2.6. Benchmark exercise, part A: ^{238}U at 7.0–8.3 MeV, post-neutron emission yields.

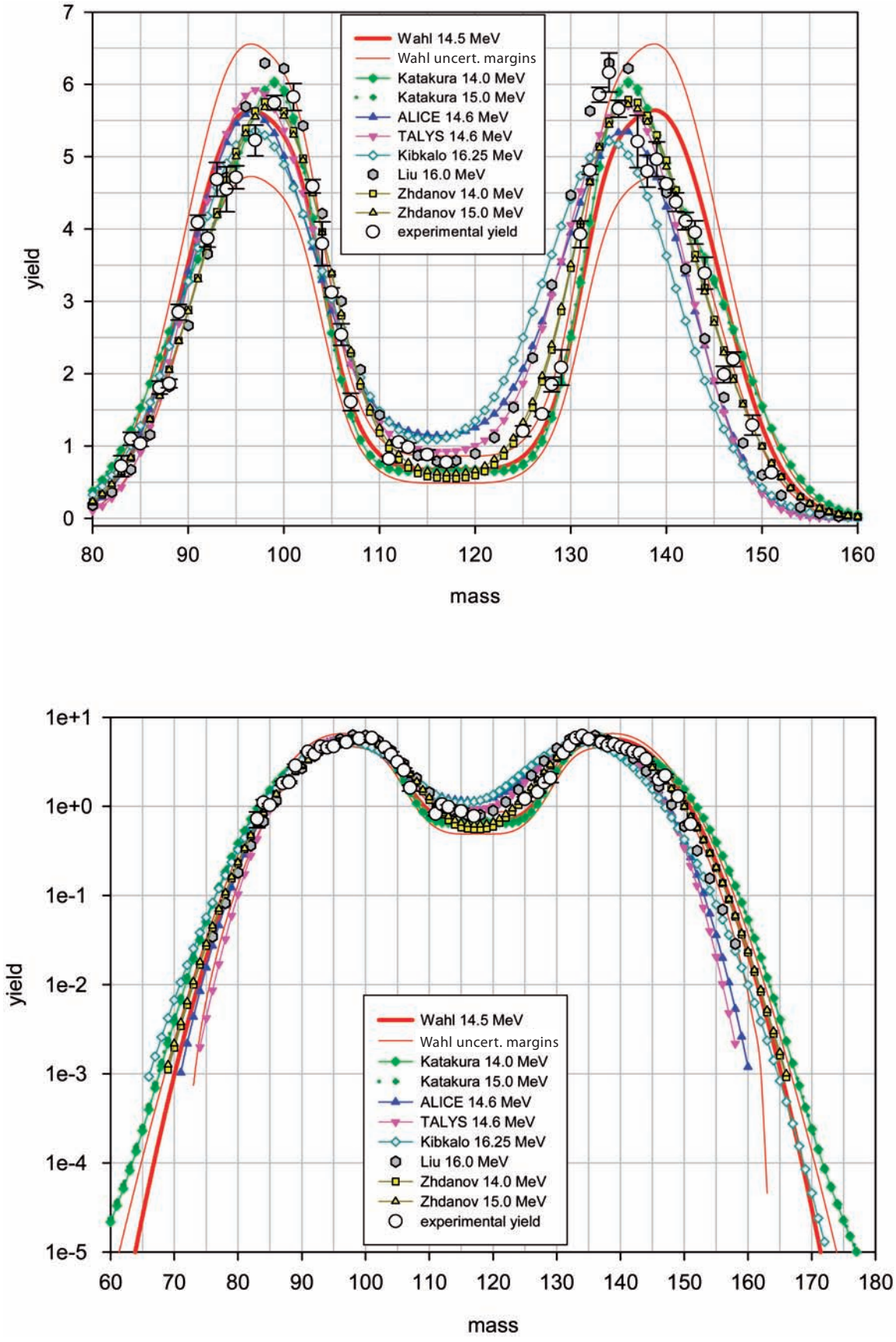

FIG. 6.2.7. Benchmark exercise, part A: ^{238}U at 14–15 MeV, post-neutron emission yields.

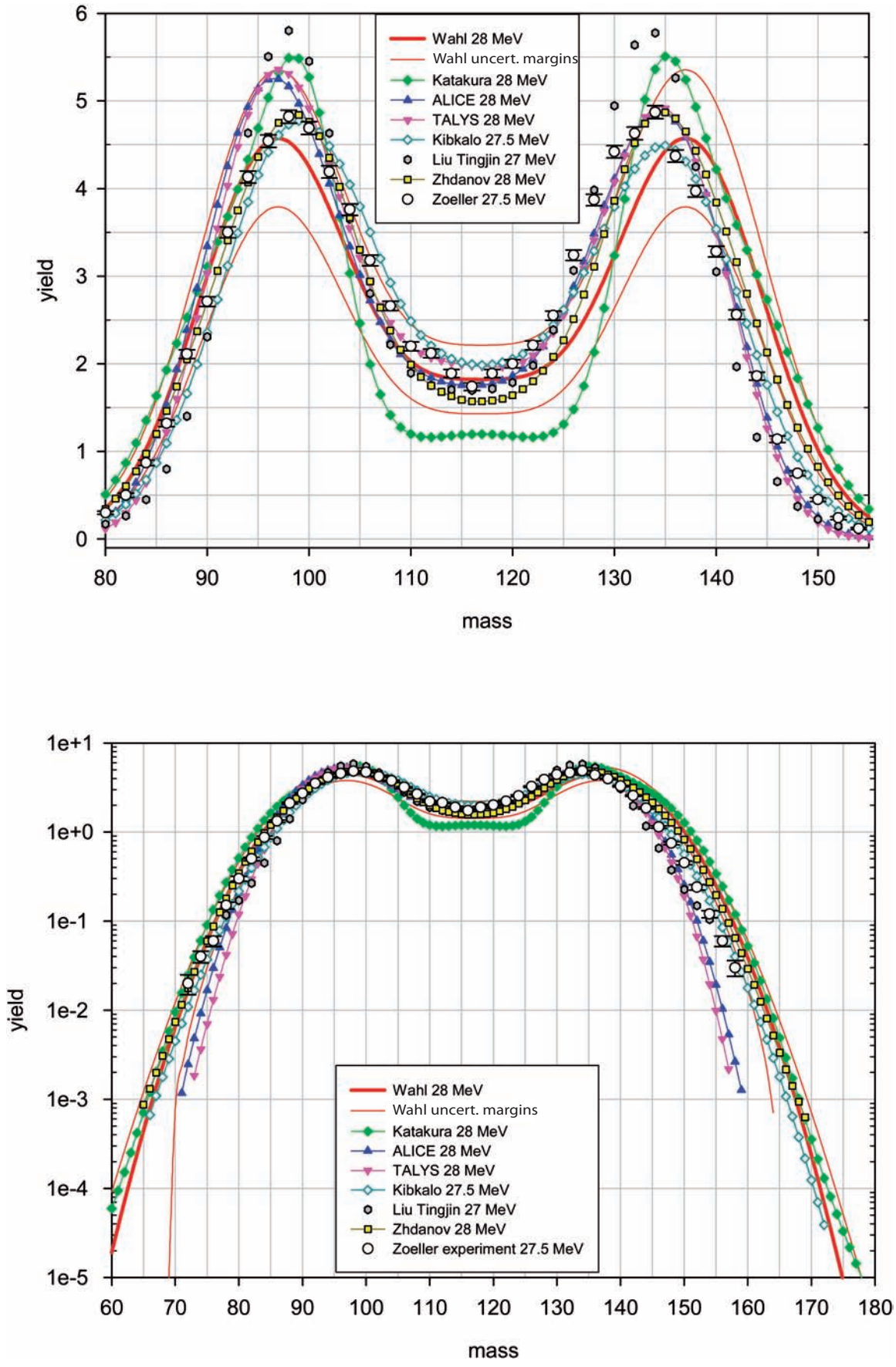

FIG. 6.2.8. Benchmark exercise, part A: ^{238}U at 27–28 MeV, post-neutron emission yields.

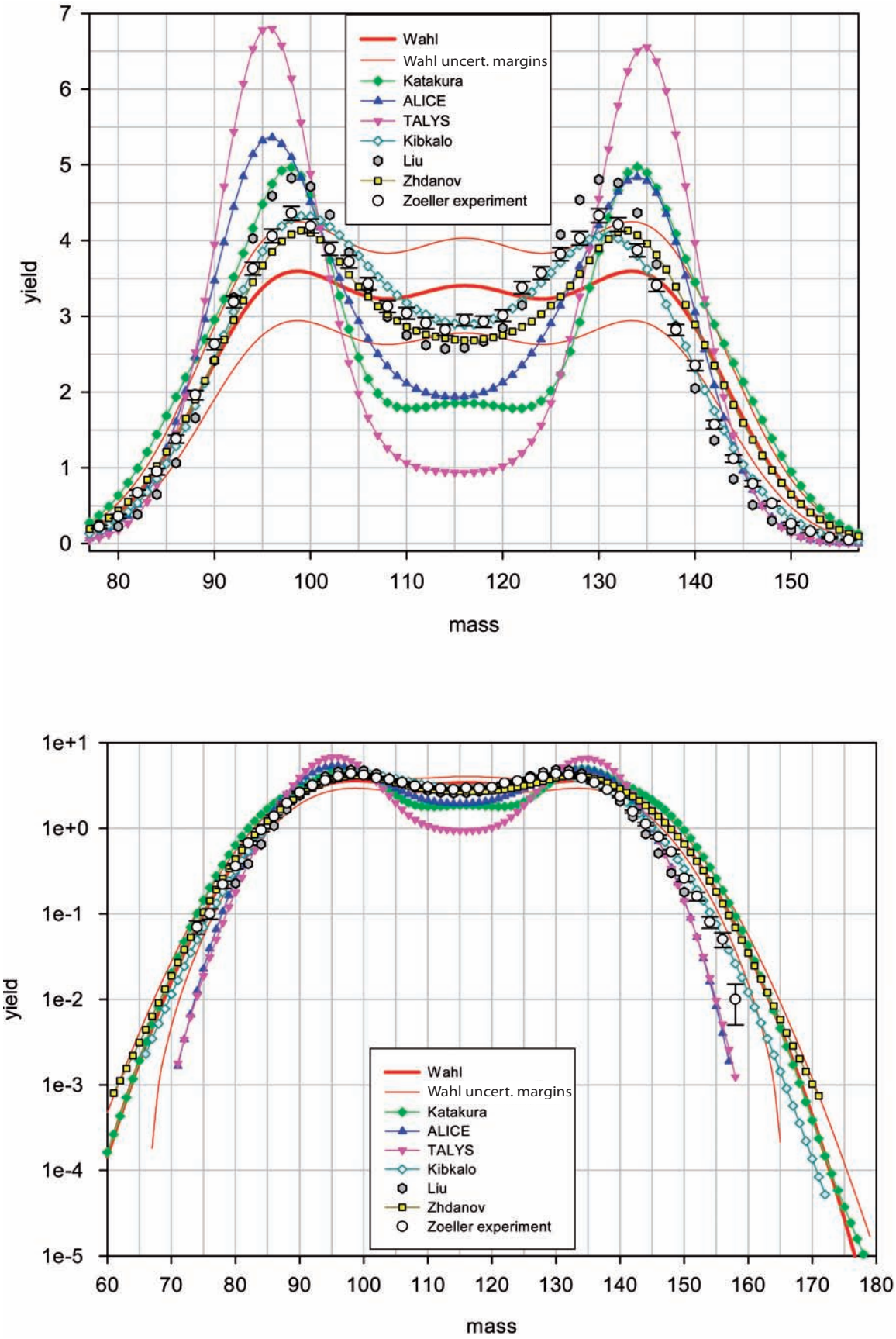

FIG. 6.2.9. Benchmark exercise, part A: ^{238}U at 50 MeV, post-neutron emission yields.

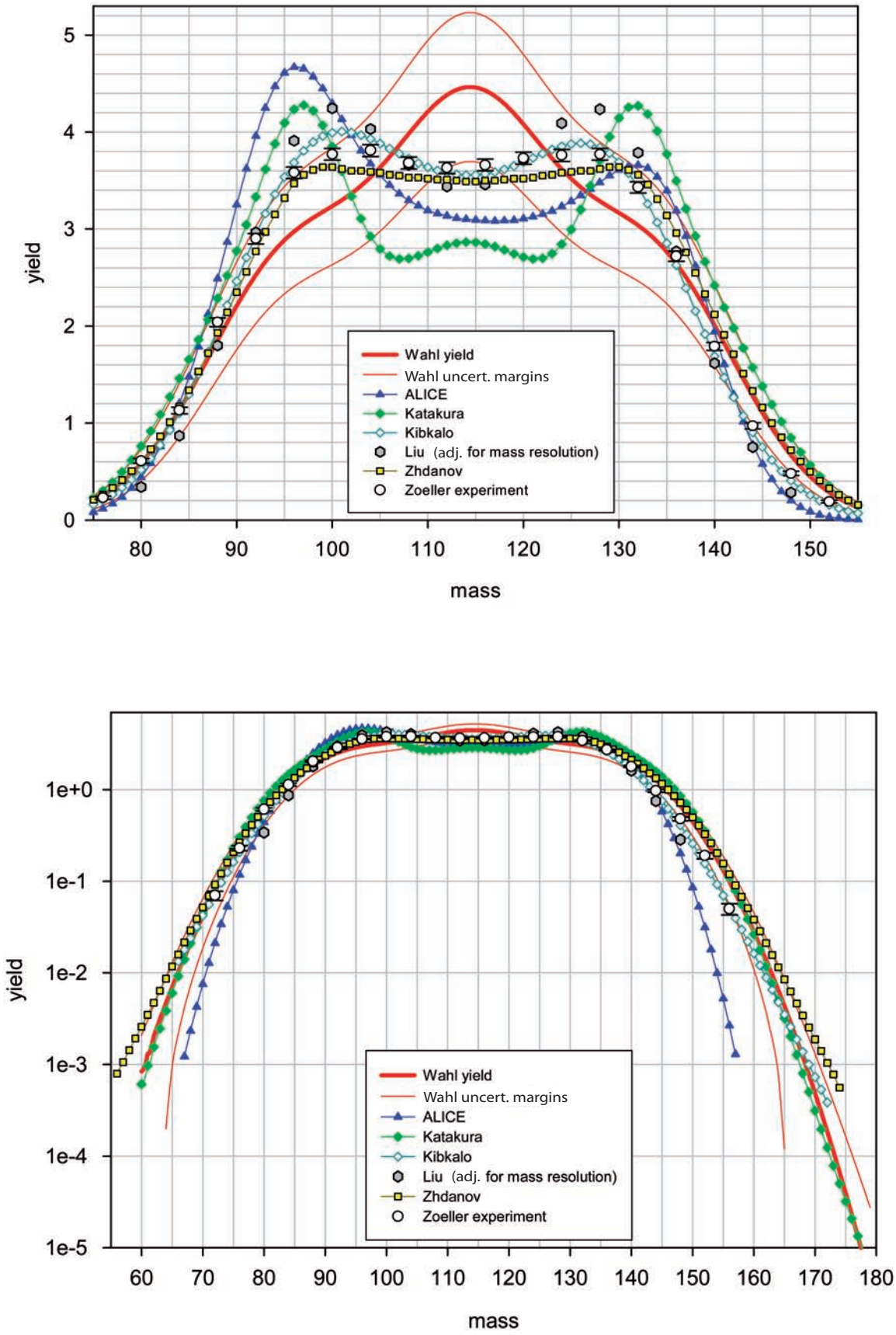

FIG. 6.2.10. Benchmark exercise, part A: ^{238}U at 100 MeV, post-neutron emission yields.

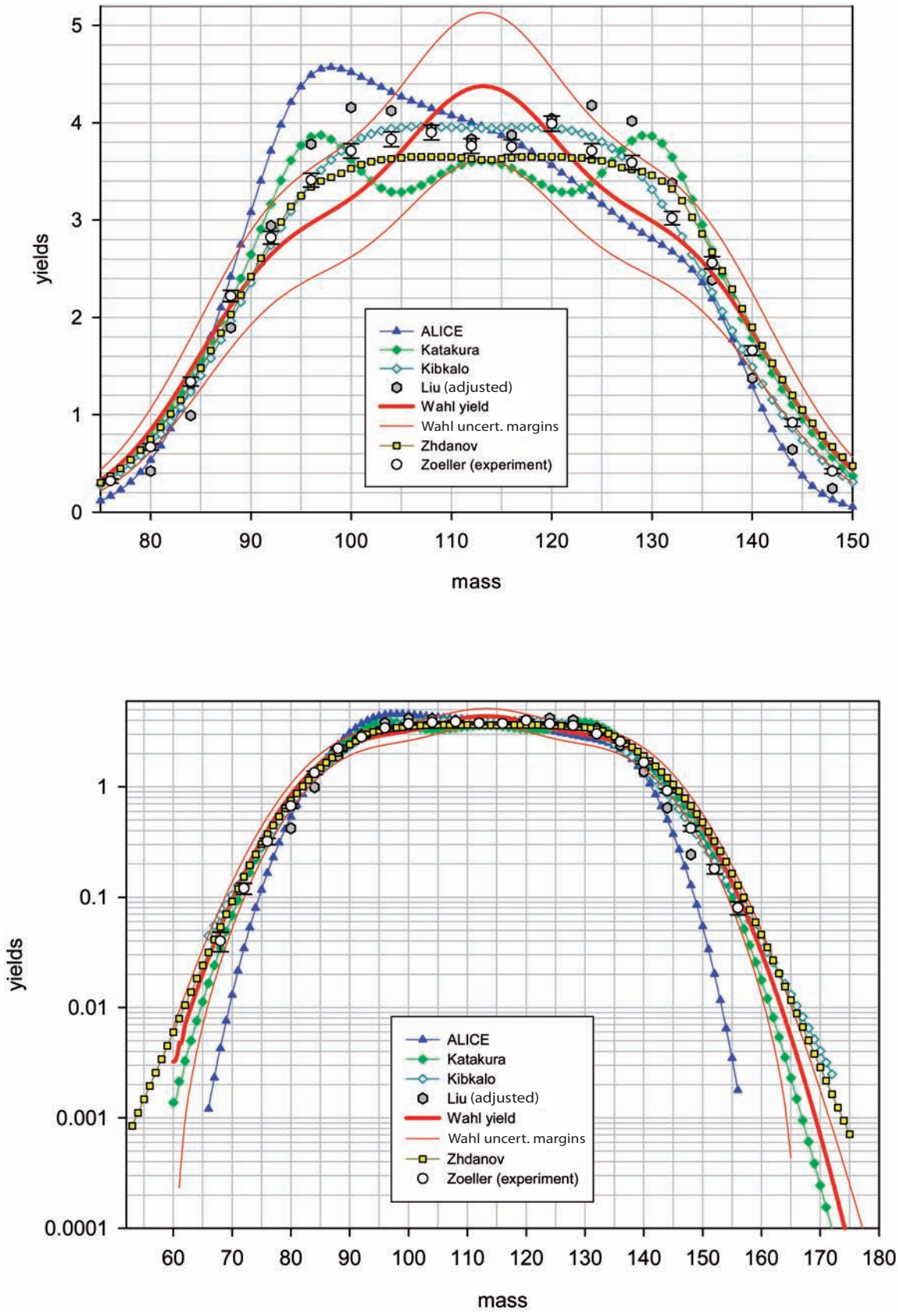

FIG. 6.2.11. Benchmark exercise, part A: ^{238}U at 160 MeV, post-neutron emission yields.

Wahl (1.6–160 MeV):

Distributions are narrower and the wings are lower than most of the other calculations. The valley is lower and broader with a small central bump that develops into a third symmetric peak at higher energies and becomes the only peak at 100 MeV. Asymmetric peaks are higher than other calculations and show 'fine structure' (from two Gaussians corresponding to ST-1 and ST-2) at lower energies (Figs 6.2.5 and 6.2.6) that begins to disappear at 13 MeV (when calculations of the positions of the peaks start to disagree).

(b) Fair or good agreement

Katakura (1.6–160 MeV):

The distribution is broader and has higher wings than most of the other calculations. A broader valley with a small central bump (similar to the calculations of Wahl) develops into a symmetric peak at 160 MeV. Both the heights and positions of the asymmetric peaks are always within the range of other calculations and are of equal height with fine structure. This model also produces two pronounced peaks at 100 MeV and three small distinct peaks at 160 MeV, unlike the other calculations.

Kibkalo (2–160 MeV):

The calculated mass distribution is generally within the range of other results at most energies; only at a few energy points is the valley higher and narrower, the wings higher, and the peaks lower and closer together than in other studies. At 100 and 160 MeV incident neutron energy the distribution was found to be broad and flat. Special features included the observation that the heavy mass peak was always slightly lower than the light peak, and that the positions of the mass peaks drop by two mass units at 16 and 20 MeV and fall below all others (Table 6.2.1 and Fig. 6.2.1).

Liu (2–160 MeV):

The distribution is average at most energies, except for the peaks which are higher than other calculations up to 28 MeV. Small peaks are still found in the distributions at 50–160 MeV that arise from the adjustment for mass resolution. Furthermore, this systematics is the only one based directly on experimental ^{238}U post-neutron emission yields only, whereas the results of the other calculations are derived from global systematics and/or from pre-neutron emission yields involving assumptions about the neutron emission distributions from fission fragments.

Zhdanov (8–160 MeV):

The shape of the distributions and the peaks are within the range of the equivalent observations from the other calculations. Up to 28 MeV the valley is lower than for other calculations and the wings are relatively high. The heavy mass peak is always a little higher than the light mass peak, and the mass distributions at 100 and 160 MeV are broad and flat (similar to Kibkalo systematics).

6.2.2.3. Mass distributions

Shapes:

Overall the shapes are reasonably similar up to 28 MeV.
1.5–5.5 MeV: most noticeable differences are in the slopes on both sides of the peaks;
8–28 MeV: increasingly better agreement — in terms of absolute yields, all models are within 2% (per fission), and better.
The peak heights decrease and the heights of valley and wings increase with excitation energy in all calculations. This observation is consistent with the predicted increase of the symmetric fission contribution, which is represented by a broad Gaussian that extends to the wings of the distribution.

Peaks:

With a few exceptions, the peak positions agreed within three mass units, and the heights at peak maximum are within 1–1.4% absolute yield (in some cases ≥1.5% compared to experimental yields). These differences increase to 1.5–2.5% absolute in the regions on both sides of the maxima, particularly when there are larger differences in the peak positions and distributions of Wahl show 'fine structure' (compare Figs 6.2.5, 6.2.6 and 6.2.8 — agreement is best for 10–21 MeV). Some models show irregular deviations from the smooth trend in peak position and height (Table 6.2.1, Figs 6.2.1 and 6.2.2), the origin of which cannot be explained by the authors.

Up to 10 MeV the peaks by Wahl, and to a lesser extent by Katakura, show 'fine structure'

(two Gaussians corresponding to the ST-1 and ST-2 asymmetric fission modes) that changes into a broader feature at 13–15 MeV (ST-1 and ST-2 contributions are equally prominent) and adopts a regular single Gaussian shape above these energies (after the disappearance of ST-1). This structure arises from the two Gaussians representing the ST-1 and ST-2 asymmetric fission modes: at low energies ST-1 determines the peak maximum, until this mode decreases with increasing energy and disappears around 20 MeV (single Gaussian representing only ST-2), in accordance with the predictions of the temperature dependent Brosa model [6.1] (see also Section 1.2). The fine structure is not visible in other calculations due to their broader Gaussians (Duijvestijn and Kibkalo), only one asymmetric peak function (Zhdanov), or inconsistencies in the experimental data (Liu).

The positions of the light mass peaks as determined by ALICE-91 and TALYS are consistently 2 or 3 mass units lower than all other calculations, whereas there is agreement over the position of the heavy mass peak. Since this is not the case for the pre-neutron emission yields the reason for this observation was attributed to the estimated multiplicity distribution of the neutrons emitted by the fission fragments (probably incorrect).

Valleys:

The calculated valleys are very narrow at low energies (1.5–5.5 MeV), except those of Wahl and Katakura that are broad with a 'bump' at the point of symmetry (Fig. 6.2.5). These differences vanish gradually with increasing excitation energy. Differences in the heights of the valley bottoms are within 1% absolute yield at all energies, although the relative yields are discrepant, particularly at low energies (up to a factor of 10). Larger differences are observed within the slopes of the peaks down towards the valley.

Wings:

Fission yields at the wings further away from the peaks are very low and therefore insignificant for applied purposes, although the data are very discrepant (up to a factor of 10^{10} around masses 60 and 180). The differences are probably due to the widths of the symmetric mass peaks in the models. Since there are hardly any experimental data beyond mass 150 it is difficult to draw a conclusion as to which model gives the best representation. The most striking observation is that the theoretical predictions of Duijvestijn are well below all other data, including the experimental results.

6.2.2.4. Energy region from 50 to 160 MeV

There are considerable differences in the shapes of the mass distributions, as shown in Figs 6.2.9–6.2.11. Best agreement with the experimental data of Zöller [6.3] was achieved by Liu and Kibkalo (whose systematics are based on these data) and by Zhdanov.

The symmetric peak within the systematics of Wahl rises more rapidly at lower energies than all other calculations, and dominates at 100 and 160 MeV. This behaviour can probably be attributed to the parameterization of Wahl's global systematics, which is entirely based on proton induced reactions in this energy range. Apparently, this dominant central peak is only present in the distribution calculated from his global systematics, whereas the distribution derived from the original least squares analysis (of ^{238}U yields only) has a shape much closer to those calculated with the other models in the benchmark exercise. This is evident from Fig. 4.2.7 (Wahl), where the results of the global systematics and of the least squares analysis are compared for ^{238}U at 100 MeV.

Three distinct peaks visible in the predictions of Wahl at 50 MeV and Katakura at 160 MeV (as opposed to the flatter distributions calculated by others) are probably (like the 'fine structure') due to narrower Gaussians. The two peaks derived by Liu at 160 MeV are the result of his adjustment for incomplete mass resolution.

ALICE-91 calculates a skewed distribution that is attributed by Duijvestijn to incorrectly derived multiplicities for the neutrons emitted from the fission fragments (too many neutrons emitted, particularly by the heavy fragments), because such skewness is absent in the pre-neutron emission mass distribution (Fig. 6.2.19). This behaviour shows the strong influence of the assumed neutron emission distributions on predictions, and illustrates the importance of a thorough and detailed analysis of the observed discrepancies.

6.2.3. Pre-neutron emission mass distributions

The survey of mass distribution parameters can be found in Table 6.2.2 and Figs 6.2.12–6.2.15. Comparisons of mass distributions are only plotted for 14–16, 27–28, 100 and 160 MeV in Figs 6.2.16–6.2.19,

TABLE 6.2.2. ^{238}U PRE-NEUTRON EMISSION MASS DISTRIBUTIONS: SURVEY OF DISTRIBUTION PARAMETERS

Peak positions

E_n (MeV)	1.6		5.5		8		10–11		13		14–16*		21		27–28		50		100		160	
Peak	Light	Heavy	Light	Heavy	Light	Heavy	Light	Heavy	Light	Heavy	Light	Heavy	Light	Heavy	Light	Heavy	Light	Heavy	Light	Heavy	Light	Heavy
Experiment	102	137	101.5	137.5	—	—	—	—	—	—	—	—	—	—	101.5	137.5	100.5	134.5	104	133	109	125
ALICE	—	—	—	—	99.3	139.7	99.6	138.9	99.4	138.8	99.3	138.3	99.3	138.3	99.5	137.8	98.5	137.2	99.4	135.5	99.5	133.4
TALYS	99	140	99.4	139.6	99.5	138.8	99.5	138.5	99.6	138.3	99.2	138.3	99.3	137.6	99.2	137.1	97.1	136.7	—	—	—	—
Kibkalo	100.8	138.2	100.7	138.3	100.6	137.7	100.7	137.7	100.6	137.7	100.2 98.6	137.2 135.5	99.3	136.2	100.3	136.7	100.4	135.0	102.5	131	—	—
Wahl	100.9	138.1	101.2	137.8	101.3	137.5	101.2	137.6	98.7	138.2	98.3	140.2	98.2	139.8	98.8	138.8	100.7	135.5	99	135	—	—
Zhdanov	—	—	100.9	138.1	100.9	138.1	101	138	100.3	137.3	101.2 101.2	137.8 137.8	100.5	137.5	100.5	136.5	100.8	134.2	104.5	129.5	—	—

Peak heights

E_n (MeV)	1.6		5.5		8		10–11		13		14–16*		21		27–28		50		100		160	
Peak	Light	Heavy	Light	Heavy	Light	Heavy	Light	Heavy	Light	Heavy	Light	Heavy	Light	Heavy	Light	Heavy	Light	Heavy	Light	Heavy	Light	Heavy
Experiment	6.3	6.3	6.0	6.0	—	—	—	—	—	—	—	—	—	—	4.7	4.6	4.2	4.1	3.6	3.7	3.7	3.8
ALICE	—	—	—	—	5.95	5.75	5.75	5.50	5.65	5.35	5.65	5.35	5.58	5.26	5.26	4.88	5.37	4.84	4.68	3.66	4.6	—
TALYS	6.11	6.11	5.40	5.40	5.28	5.30	5.27	5.27	5.04	5.04	5.37	5.39	4.90	4.92	4.84	4.84	6.22	6.22	—	—	—	—
Kibkalo	5.87	5.87	5.85	5.85	5.78	5.78	5.68	5.68	5.40	5.40	5.29 5.12	5.29 5.12	4.80	4.80	4.48	4.48	3.97	3.97	3.64	3.64	—	—
Wahl	7.47	7.47	7.04	7.04	6.57	6.57	6.17	6.17	5.73	5.73	5.65	5.65	5.18	5.18	4.58	4.58	3.60	3.60	3.0	3.0	—	—
Zhdanov	—	—	6.14	6.14	5.93	5.93	5.77	5.77	5.57	5.57	5.49 5.42	5.49 5.42	5.02	5.02	4.65	4.65	3.91	3.91	3.61	3.61	—	—

Valley heights and peak-to-valley ratios (P/V)

E_n (MeV)	1.6		5.5		8		10–11		13		14–16*		21		27–28		50		100		160	
Peak	Valley	P/V	Valley	P/V	Valley	P/V	Valley	P/V	Valley	P/V	Valley	P/V	Valley	P/V	Valley	P/V	Valley	P/V	Valley	P/V	Valley	P/V
Experiment	0.0071	887	0.080	75	—	—	—	—	—	—	—	—	—	—	1.8	2.6	2.6	1.6	3.2	1.13	3.5	1.06
ALICE	—	—	—	—	0.842	6.4	1.07	4.83	1.19	4.26	1.10	4.6	1.37	3.67	1.66	2.85	1.83	2.6	2.88	1.40	3.63	0.99
TALYS	0.053	115	0.46	12	0.632	8.4	1.09	4.83	1.39	3.63	0.88	6.1	1.59	3.09	1.84	2.6	0.88	7.1	—	—	—	—
Kibkalo	0.18	33	0.205	28.5	0.255	22.7	0.38	15.0	0.74	7.30	0.91 1.12	5.81 4.57	1.58	3.04	2.03	2.21	2.72	1.46	3.33	1.09	—	—
Wahl	0.0138	540	0.087	81	0.232	28.3	0.36	17.1	0.57	10	0.676	8.36	1.21	4.28	1.82	2.5	3.2	1.12	4.47	0.67	—	—
Zhdanov	—	—	0.098	72	0.207	28.6	0.315	18.3	0.51	10.9	0.572 0.640	9.60 8.47	1.07	4.9	1.60	2.9	2.73	1.43	3.48	1.04	—	—

* ALICE and TALYS: 14.6 MeV; Wahl: 14.5 MeV; Kibkalo: 14.5 MeV (upper value) and 16.5 MeV (lower value); Zhdanov: 14 MeV (upper value) and 15 MeV (lower value).

as most features are very similar to the post-neutron emission mass distributions. Comparisons between pre- and post-neutron emission mass distributions are made in terms of the 'pre-case' and 'post-case' in the following discussion, and the energy range 50–160 MeV is again treated separately. Experimental data are only available from measurements by Zöller [6.3] and Vivès et al. [6.4].

6.2.3.1. Model calculation results

ALICE-91 (8–160 MeV) and TALYS (1.6–28 MeV)

Statements made for the post-case are also valid for the pre-case, but the agreement with other calculations is better. The peaks are equally high except at 160 MeV, where the slightly higher heavy mass peak is attributed to the influence of emissive fission. The asymmetric peaks are further apart than in all other models (except for the systematics of Wahl above 11 MeV).

Wahl (1.6–160 MeV)

The description and overall agreement is similar to the post-case. Coincident with the disappearance of the fine structure from 13 MeV upwards, the peak maxima are further apart than in all other calculations. Only in these predictions are the shapes and peak heights the same as in the post-case, where the whole distribution has shifted to lower masses compared with the pre-case.

Kibkalo (2–160 MeV)

Similar to the post-case, including the discontinuity around 16.5 MeV. The equally high peaks are lower than in the post-case, but agree better with other models, while the peak positions fall within the range of the other calculations.

Zhdanov (8–160 MeV)

All the comments made with respect to the post-case apply to the pre-case (most data are within the range of other calculations). The only significant difference is that the asymmetric peaks have the same height in the pre-case.

6.2.3.2. Mass distributions

Shapes:

The most noticeable differences in the calculated distributions are at low energies and involve the shapes from the peaks to the valley (>2% absolute at 1.6 MeV) and the peak heights. With increasing energy, the agreement in this mass range improves gradually (generally to within 2% absolute), but the peak positions continue to vary. Overall, agreement is the same or slightly better than in the post-case.

Peaks:

As in the post-case the peak positions for the pre-case generally fall within three mass units. Up to 13 MeV, the ALICE-91 and TALYS peak positions do not match the other calculations (light mass peak is lower and heavy mass peak is higher), and the peak positions of Wahl are more discrepant from 14 MeV onwards. The peak heights are within 1% absolute above 8 MeV, and up to 1.5% at 1.6 MeV; however, the positions of the maxima do not coincide and therefore the differences in fission yields around the peak maxima are larger at about 2.5% for 1.6 MeV, 1.5% for 5.5–8 MeV, and all within 1% at higher energies.

Valley and wings:

Pre-case observations are very similar (sometimes identical) to the post-case.

Energy dependence:

The pre-case variation of parameters with energy is again similar to the post-case, including irregularities in the energy dependence of peak positions and heights. This observation indicates that the irregularities are not introduced by the choice of neutron emission functions.

6.2.3.3. Energy region from 50 to 160 MeV

Overall, the shapes of the mass distributions (and the discrepancies) for the pre-case are almost the same as for the post-case. The most striking exception is that the ALICE-91 mass distribution is not skewed and the peaks are of almost equal height.

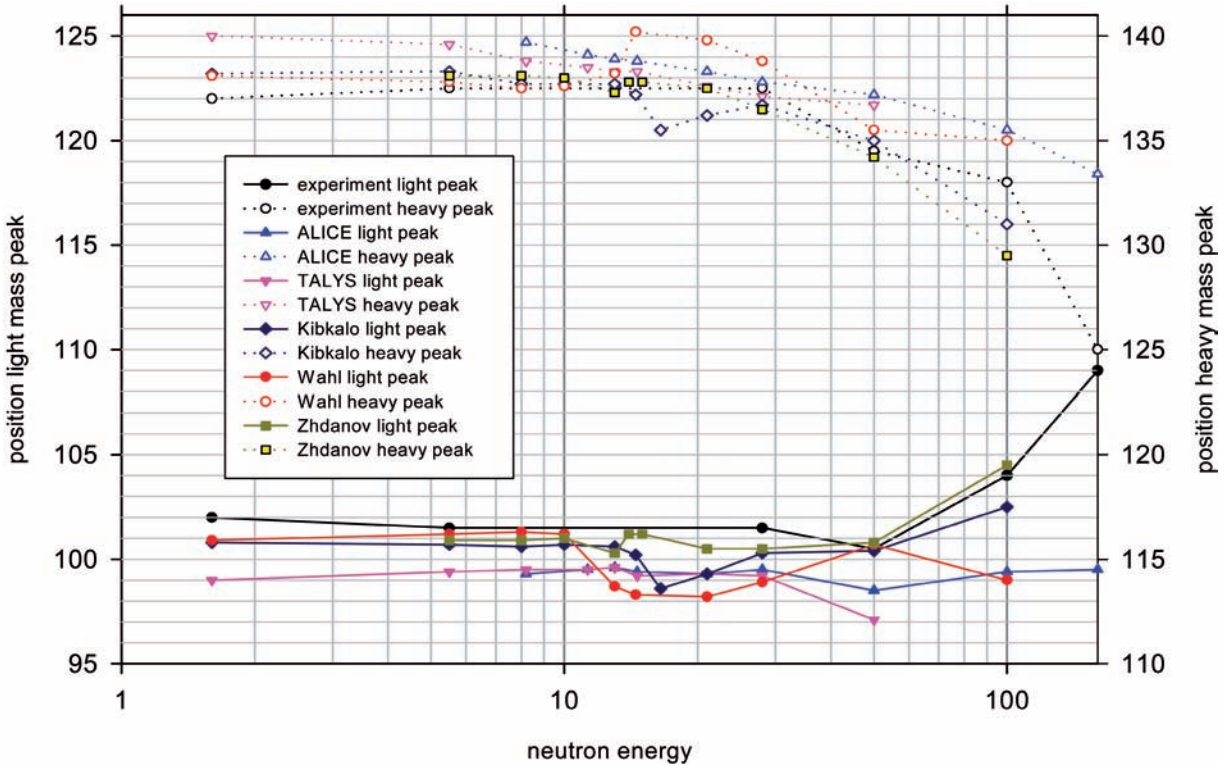

FIG. 6.2.12. Benchmark exercise, part A: ^{238}U pre-neutron emission mass distribution, positions of mass peaks versus neutron energy.

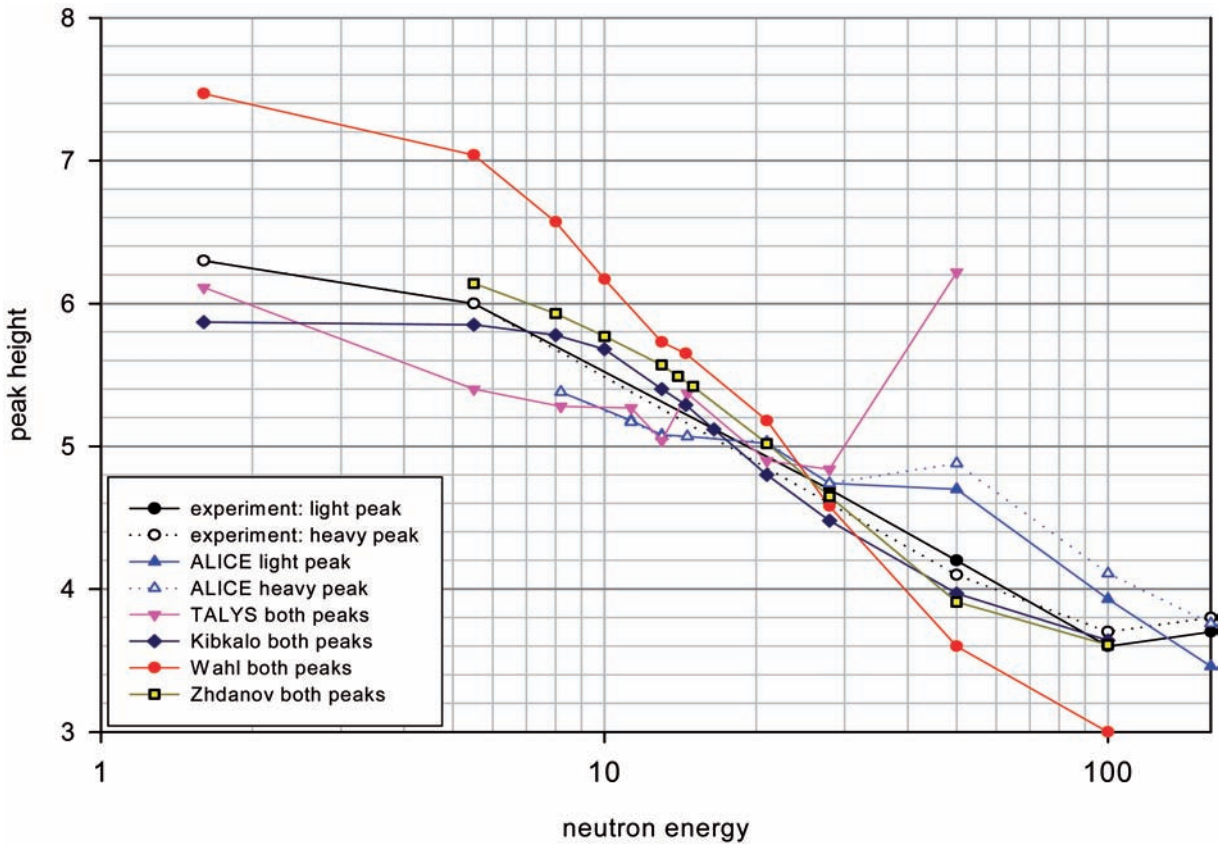

FIG. 6.2.13. Benchmark exercise, part A: ^{238}U pre-neutron emission mass distribution, heights of mass peaks versus neutron energy.

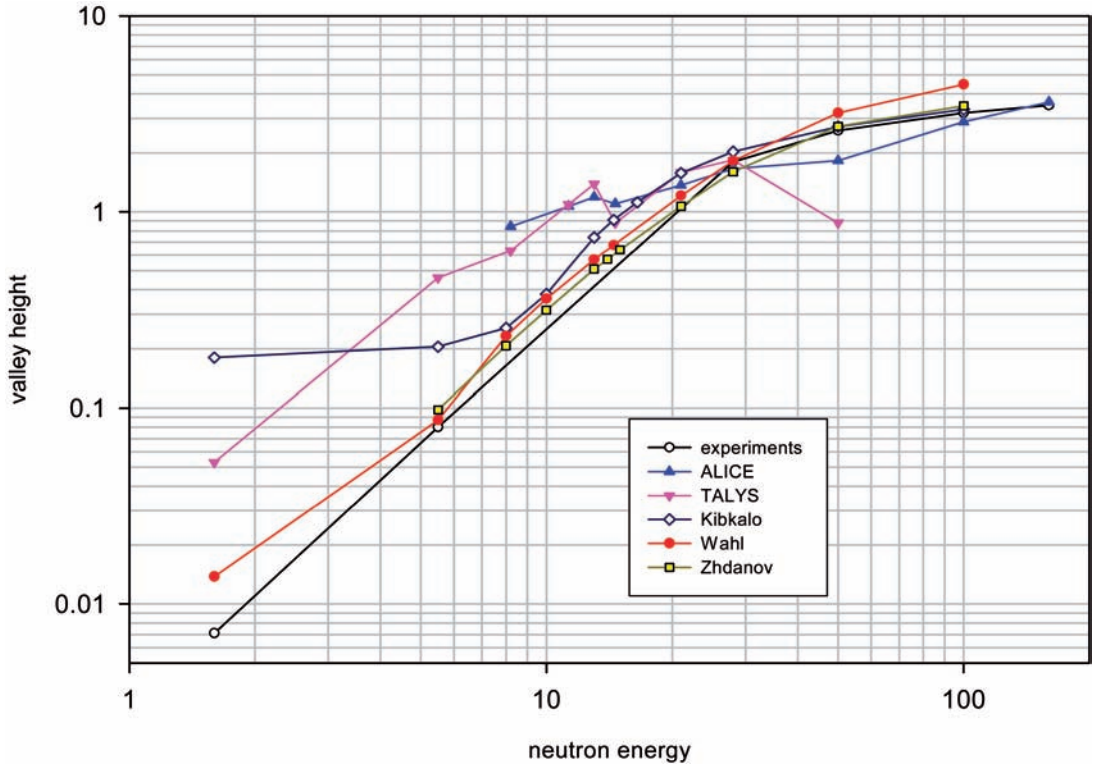

FIG. 6.2.14. Benchmark exercise, part A: ^{238}U pre-neutron emission mass distribution survey: heights of valley versus neutron energy.

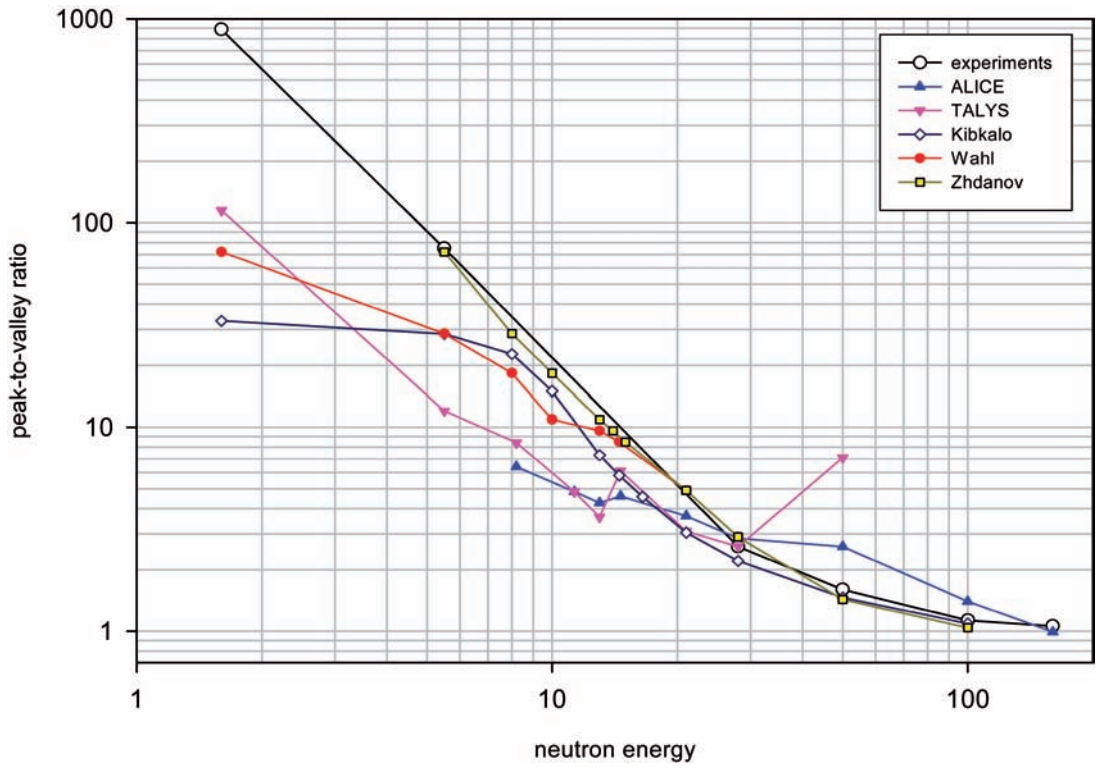

FIG. 6.2.15. Benchmark exercise, part A: ^{238}U pre-neutron emission mass distribution survey: peak to valley ratio versus neutron energy.

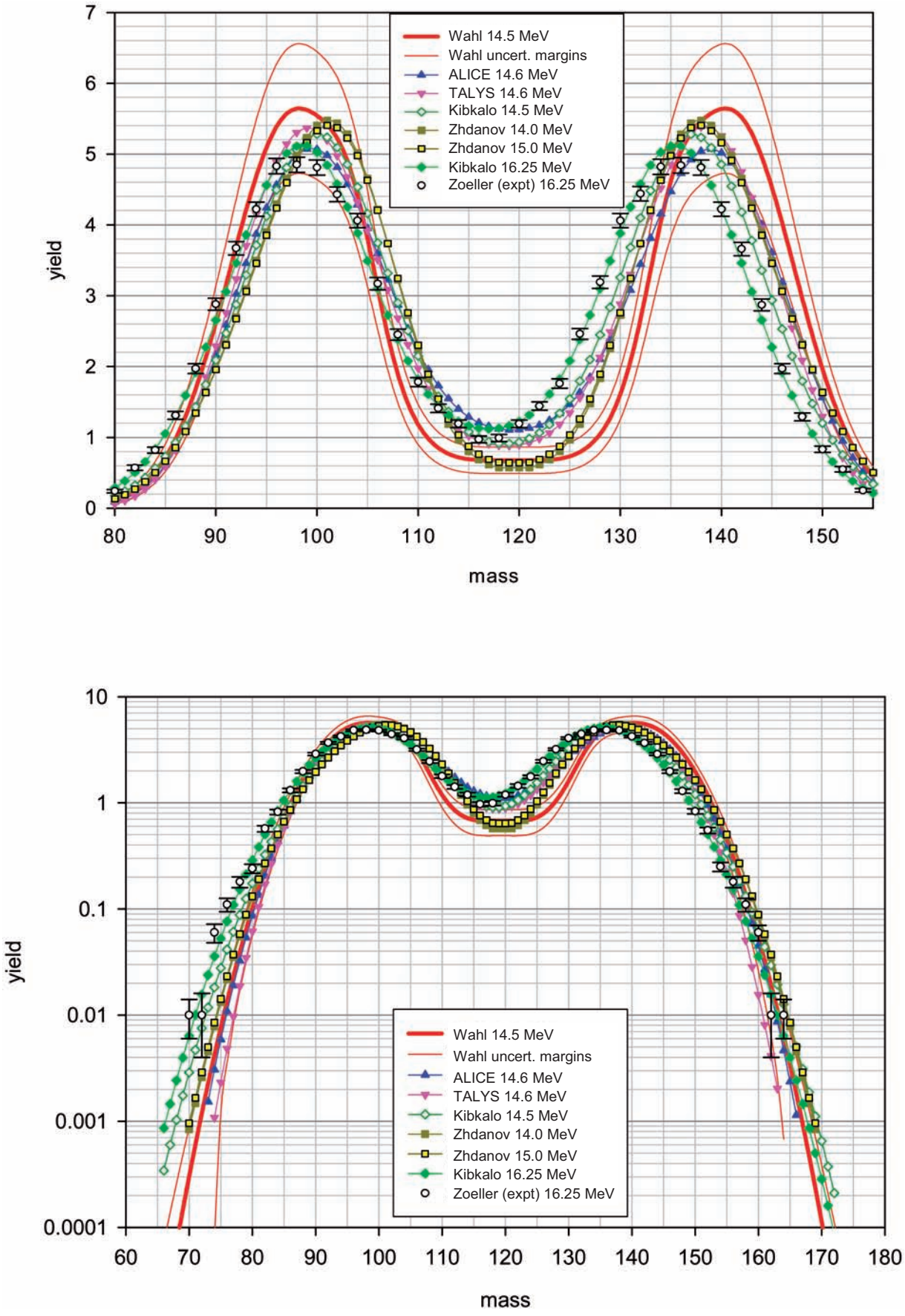

FIG. 6.2.16. Benchmark exercise part A: ^{238}U at 14–16 MeV, pre-neutron emission yields.

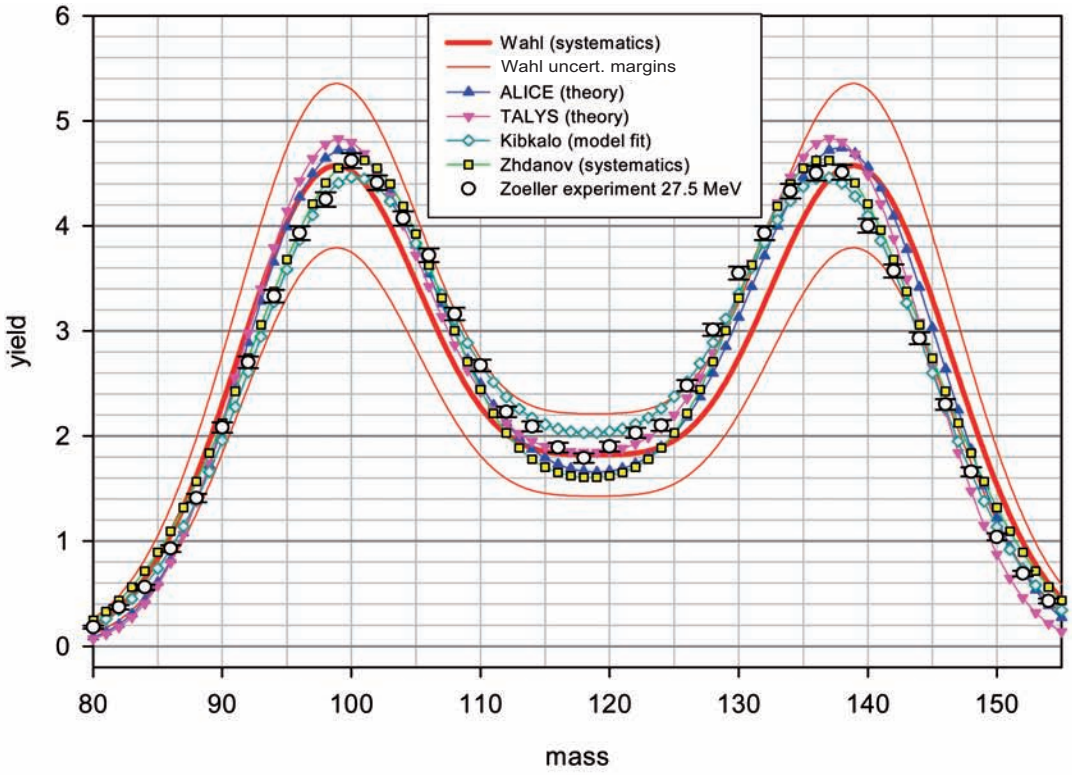

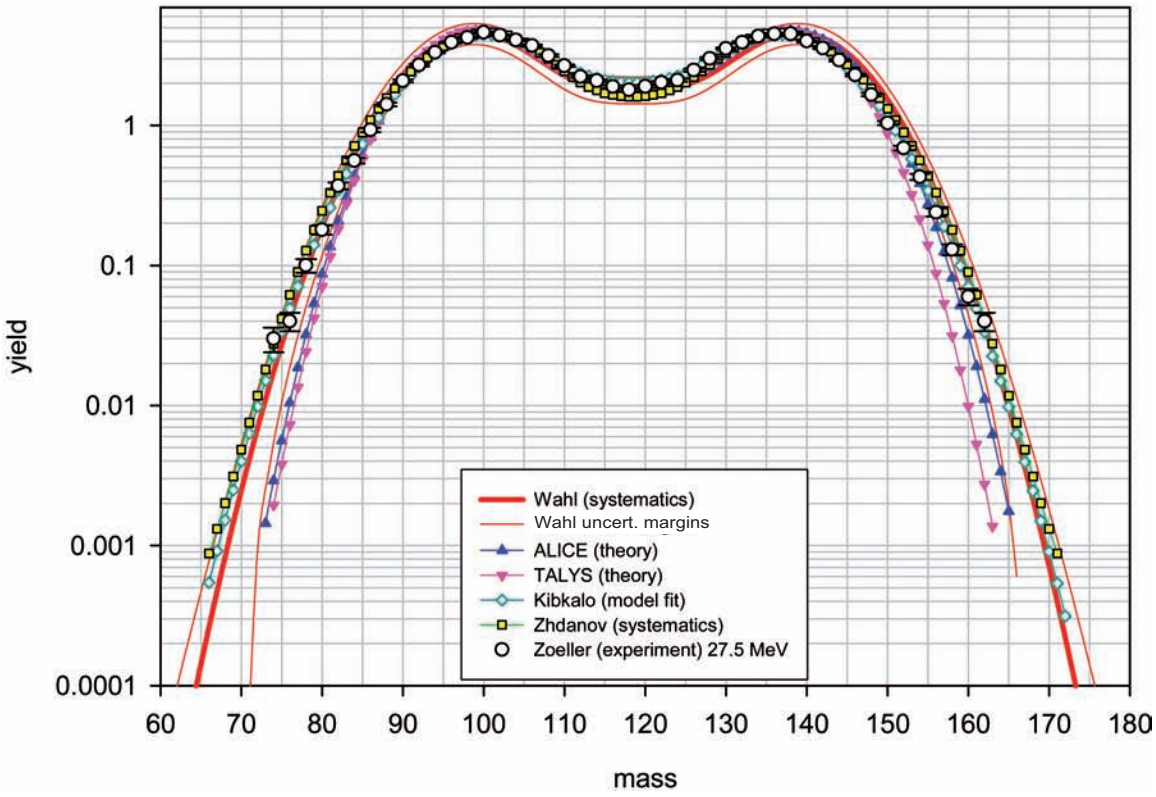

FIG. 6.2.17. Benchmark exercise, part A: ^{238}U at 27–28 MeV, pre-neutron emission yields.

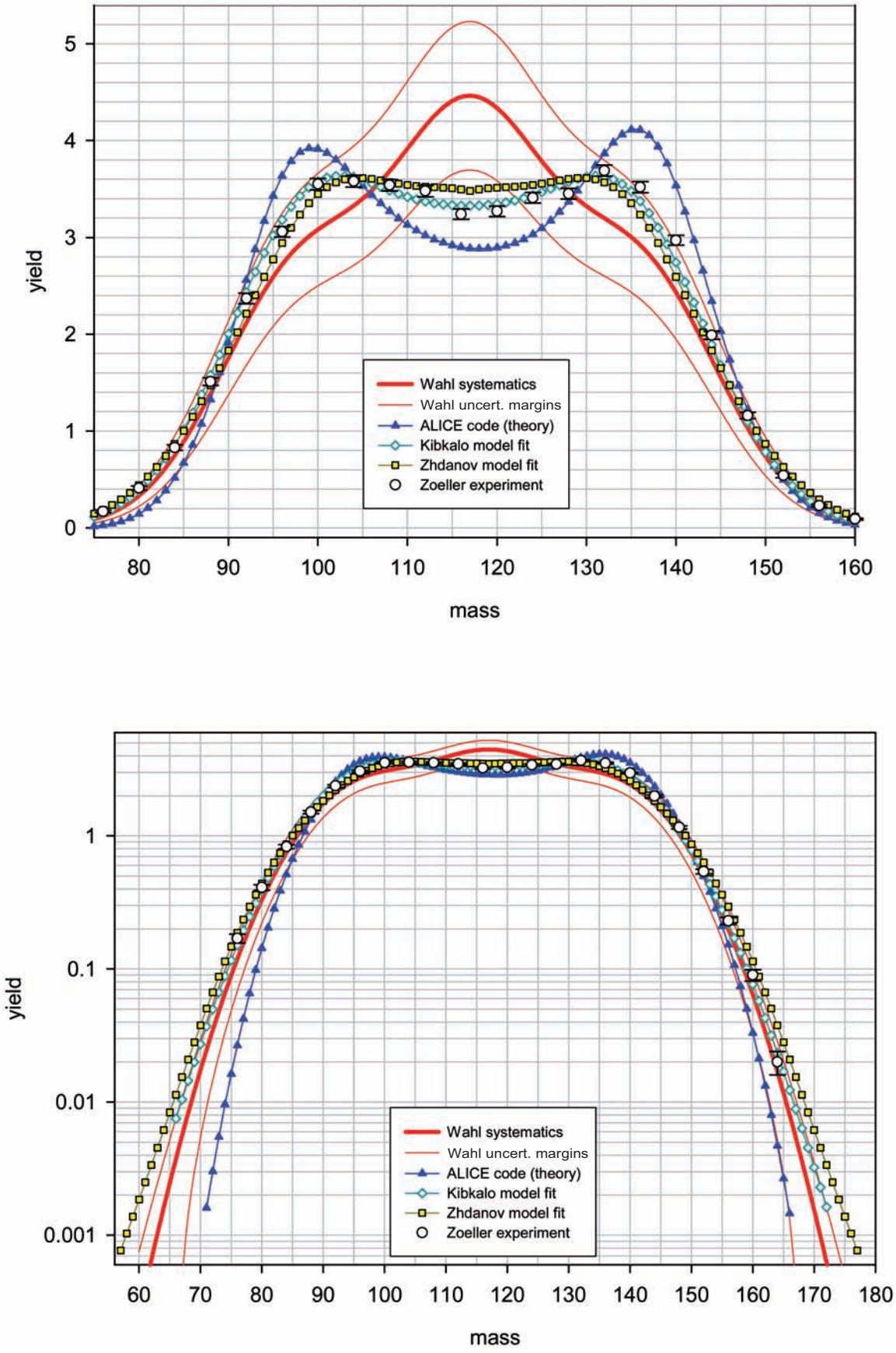

FIG. 6.2.18. Benchmark exercise part A: ^{238}U at 100 MeV, pre-neutron emission yields.

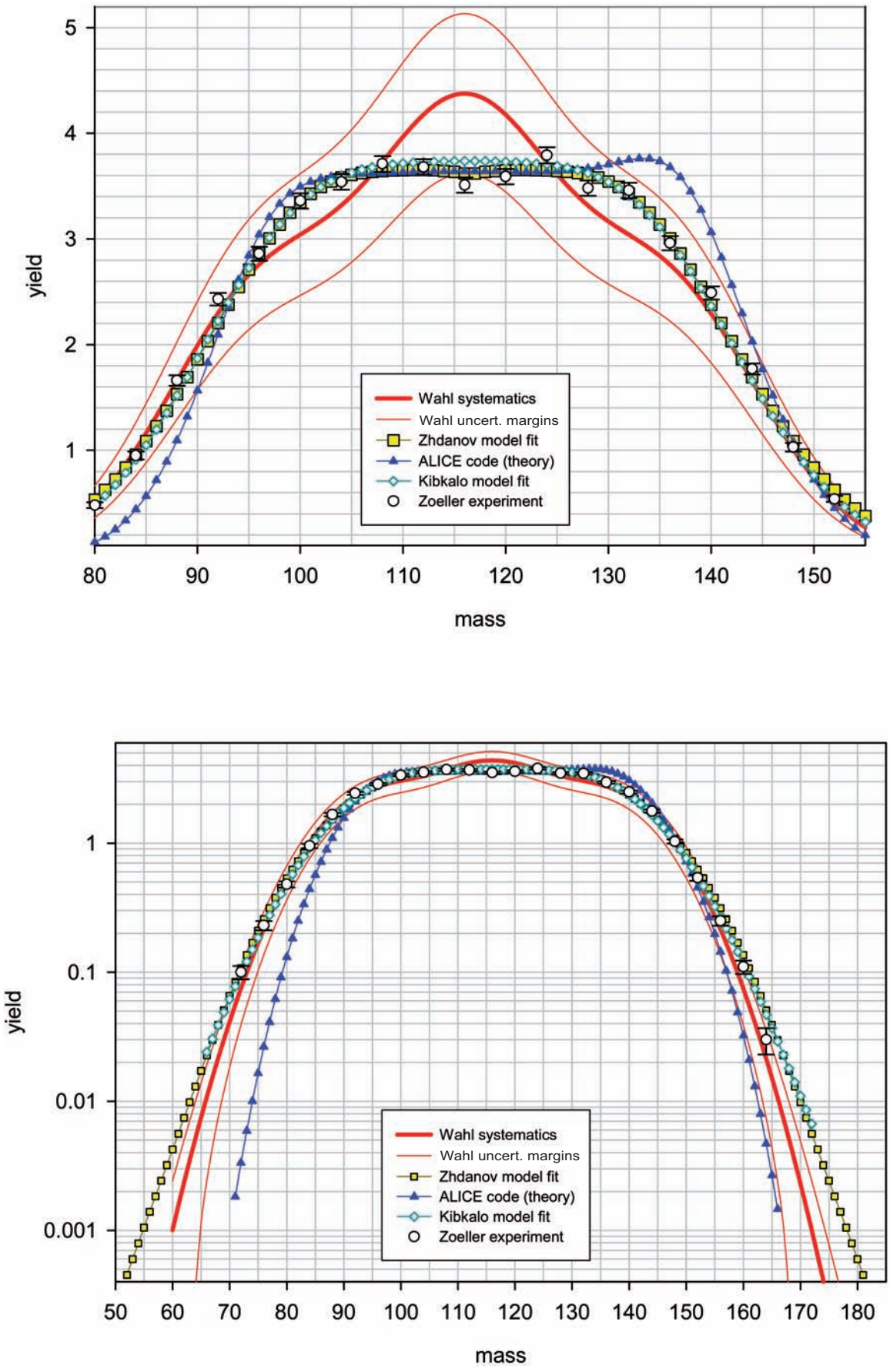

FIG. 6.2.19. Benchmark exercise part A: ^{238}U at 160 MeV, pre-neutron emission yields.

The results of Kibkalo agree completely with the experimental data, and the calculations of Zhdanov are very close; both sets of calculations almost coincide for the pre-case, whereas the mass distributions of Zhdanov are always below that of Kibkalo in the post-case. ALICE-91 produces a flat distribution at 160 MeV that agrees with the other calculations, except for a 'bump' in the fragment mass range of 130–145 that indicates the presence of a peak around A = 138.

6.3. PART B BENCHMARK EXERCISE

The results of part B of the benchmark exercise have not been analysed in detail because of the serious inability to explain the various discrepancies in part A. Explanations for the observed discrepancies and inconsistencies can only be given after a thorough study of the models themselves and the different treatments of fission modes, multi-chance fission, neutron emission, etc. The results of part B of the benchmark are probably valuable for such a study and are included on the CD-ROM.

6.4. INFLUENCE OF MULTI-CHANCE FISSION

Most of the discussion of the benchmark intercomparisons are included in Section 5.2. Here we present only some additional details on the effect of multi-chance fission as reflected in the benchmark calculations.

6.4.1. Superposition of preferred fission modes

The reduction of the mass and excitation energy of the fissioning nucleus as compared with the composite nucleus could cause a change in the preferred fission mode, leading to a superposition of fission modes that may become noticeable in the mass distributions at higher energies. At 100 MeV (Fig. 6.2.10), the asymmetric and symmetric fission modes are about equal in the observed mass distribution. Maslov has calculated significant contributions up to 11th chance fission at this energy (see Fig. 3.1.1 of Section 3.1). Asymmetric fission is likely to dominate below 100 MeV, and according to Maslov's calculations we can expect significant contributions from fissioning nuclides down to ^{231}U (9th chance fission) with a possible preference for the symmetric fission mode. However, the expected contribution is probably not sufficient to change the shape of the mass distribution significantly. At energies above 100 MeV, symmetric fission starts to dominate and the contributions from higher chance fission are more significant. The symmetric distribution from lower chance fission is superimposed by asymmetric distributions centred at lower fragment masses, as observed by Duijvestijn (Section 5.1.3.6), and the composite mass distribution is no longer symmetric in shape.

6.4.2. Change in peak positions and mass symmetry point in asymmetric fission

The observed mass distribution is composed of contributions from lower mass isotopes of the target nucleus. Consequently, the mass of fission fragments from these contributions is also reduced. Since the position of the heavy mass peak also remains stable for the lower mass isotopes of the target nucleus due to shell effects, the position of the light mass peak changes to lighter masses and the valley becomes broader. Thus the heavy mass peak remains more or less unchanged in height and position, whereas the light mass peak becomes smaller and broader with a slope towards the light mass wing. As a consequence, the whole distribution should become broader and asymmetric in shape.

The point of symmetry in the mass distribution, defined originally as the point where both fragments have equal mass (symmetric fission), changes from the position of first chance fission towards lower masses (broader valleys), with decreasing mass of the fissioning nucleus. When the composite mass distribution is considered, the symmetry point becomes the point above and below which the sums of the mass yields are equal and total 100%. However, this new point of mass symmetry is not defined solely by the mass of the target plus projectile, minus the total number of neutrons emitted.

At higher excitation energies, symmetric fission becomes significant and the position of the composite symmetric peak will also be broadened towards lower masses with increasing energy. This behaviour should lead to a broad flattened plateau instead of a Gaussian shaped peak, particularly in those energy regions in which asymmetric fission has a noticeable contribution.

REFERENCES TO SECTION 6

[6.1] BROSA, U., et al., Nuclear scission, Phys. Rep. **197** (1990) 167–262.

[6.2] SCHMITT, H.W., et al., Precision measurements of correlated energies and velocities of ^{252}Cf fission fragments, Phys. Rev. **137** (1965) B837.

[6.3] ZÖLLER, C.M., Untersuchung der neutroneninduzierten Spaltung von ^{238}U im Energiebereich von 1 MeV bis 500 MeV, PhD Thesis, Technische Universität Darmstadt, Germany (1995).

[6.4] VIVÈS, F., et al., Investigation of the fission fragment properties of the reaction ^{238}U(n, f) at incident neutron energies up to 5.8 MeV, Nucl. Phys. A **662** (2000) 63–92.

Appendix I

EVALUATION OF THE MASS DISTRIBUTION DATA FOR ^{238}U, ^{239}PU AND ^{242}PU FISSION

Liu Tingjin
China Institute of Atomic Energy, China

Mass distribution data from the fission of ^{238}U at E_n = 1.5, 5.5, 8.3, 11.3, 14.9, 22.0, 27.5, 50.0, 99.5 and 160.0 MeV, and at E_p = 20.0 and 60.0 MeV, of ^{239}Pu at E_n = 0.17, 7.9 and 14.5 MeV, and of ^{242}Pu at E_n = 15.1 MeV were evaluated and recommended on the basis of the experimental data. These data were analysed and adjusted where necessary, taking into account the essential differences between the two experimental methods involved, i.e. the kinetic energy method and the radiochemical method. The adjusted data have been plotted and tabulated as the experimental database for the CRP benchmark exercise.

I.1. INTRODUCTION

Over the past four years, progress has been made in the development of calculational methods and corresponding computer codes for fission product yield data, including microscopic theoretical models, phenomenological models and systematics for the incident particle energy range 1–200 MeV. In order to test the prediction capability and reliability of these models and codes, and to enable realistic uncertainty estimates for the calculated yields, a benchmark exercise was designed in November 2001. Calculations of fission yields will be performed for defined sets of fission reactions where many experimental data are available, and the results will be compared with evaluated experimental yield data from the present evaluation, which has been conducted as part of the benchmark exercise in order to test the models.

The fission yield data were evaluated according to the requirement of the benchmark exercise defined at the final RCM. In fact they comprise all of the main available sets of measured mass distribution data for ^{238}U, ^{239,242}Pu neutron induced fission in the energy range up to 200 MeV.

For the mass distribution, the following fission yield definitions are relevant, as agreed at the previous CRP on the compilation and evaluation of fission yield nuclear data: cumulative yield is the total number of atoms of a specific nuclide produced (directly and via decay of precursors) in 100 fission reactions; chain yield is the (sum of) cumulative yield(s) of the last stable or long lived chain member(s); mass (number) yield is the sum of all independent yields of a given mass chain. 'Independent yield' is the number of atoms of a specific nuclide produced directly — without decay of precursors — in 100 fission reactions. The difference between chain yield and mass yield for a mass chain is that the former is defined after and the latter before delayed neutron emission. In measurements of mass distributions by quantification of prompt fission fragments, a distinction has to be made between pre- and post-neutron emission data — in this case prompt neutrons emitted from the compound nucleus and moving fragments by evaporation of neutrons before and after scission.

Mass distribution data for ^{238}U at E_n = 1.5, 5.5, 8.3, 11.3, 14.9, 22.0, 27.5, 50.0, 99.5 and 160.0 MeV, E_p = 20.0 and 60.0 MeV, for ^{239}Pu at E_n = 0.17, 7.9 and 14.5 MeV, and for ^{242}Pu at E_n = 15.1 MeV were evaluated on the basis of the available experimental data.

I.2. DATA COLLECTION AND SELECTION

The sources of experimental data were CRP participants, the EXFOR library and the open literature. Valuable data were received from members of the CRP that had not yet been published or compiled into the EXFOR library, including the data of Vivès, Zöller, Äystö and Winkelman for ^{238}U and ^{242}Pu.

As mentioned above, the mass distribution data may be classified as 'chain yields', 'cumulative yields' and 'fragment mass yields'. At the start of the evaluation, all types of yield data, even 'pre-neutron emission yields', were collected for analysis. More than 200 sub-entries were retrieved from the EXFOR master library. Also, some important data not yet compiled into the EXFOR library were collected from publications, including the data of Liu Conggui and Liu Yonghui (see Section I.3.2.).

The data were selected for evaluation according to the following criteria:

(a) As the aim of this work is to produce evaluated 'mass distributions', measurements were primarily selected which cover a greater part of the mass distributions. Measurements that included smaller numbers of fission products were used only in cases where more extensive data sets were not available.
(b) According to the yield definitions, only chain yield or mass yield data should be used for the evaluation of mass distributions. If no such data were available, cumulative yields were used. In this case, only such cumulative yields were considered, where the differences to the corresponding chain yields are within the experimental uncertainty limits.
(c) More recent data obtained with more reliable measurement methods were given higher weight. If several data sets are available, older data from measurements employing outdated methods were not considered.
(d) If not enough experimental data are available, some primary yield data (marked 'PRE, FY' in the EXFOR library) were also considered, and their use in the evaluation process was decided after an analysis and comparison with other data.

I.3. DATA ANALYSES AND EVALUATION

I.3.1. Measurement types

We distinguish between two types of measurements:

Type 1 measurements — prompt fission fragments are recorded simultaneously and directly, and cover almost the complete range of the mass distribution. There is no difference in the systematic uncertainty among the measured fragments, the main uncertainty being statistical. Due to the limited mass resolution, the measured fragment mass yield has a Gaussian distribution (with a width of several mass units) that extends over several 'mass bins'. In other words, each mass bin contains contributions from the Gaussians of several fragment masses. Measurements of this type are numbers (1), (2) and (9), as described below.

Type 2 measurements — radiation emitted by fission products (after prompt and generally also after delayed neutron emission) is measured individually at given times after irradiation of the fissioning sample to deduce the fission yields. Adjustments for decay in these measurements have to be applied for the measured fission products and their precursors. Only cumulative yields can be considered for type 2 measurements. The significant differences compared with type 1 measurements are: (1) due to half-life limitations and/or the absence of measurable radiation, only a limited part of the mass distribution can be measured; (2) there is no mass resolution problem; (3) as the fission products are measured individually and adjustments of varying accuracy are made, the possible systematic uncertainties are different in nature and magnitude. All other experiments described below are of this type.

I.3.2. Experimental data

Information is given below concerning the data that fulfil the criteria listed in Section I.2 and were selected for the final evaluation. For each data set, a brief description of the measurement is given in the first paragraph, followed by the treatment of the data in the evaluation.

I.3.2.1. Vivès et al. [I.1]

Measurement type 1: The pre-neutron emission fission fragment mass, kinetic energy and angular distributions were measured with a double Frisch gridded ionization chamber. ^{238}U samples were mounted in the centre of the common cathode, and information about the fission fragment properties was obtained from the anode and the sum of the anode and grid signals of the ionization chamber. The kinetic energy of the fission fragments was obtained from the anode signal, whereas the emission angle was provided by the sum signal. The mass resolution of the chamber was about 2 mass units. Mono-energetic neutrons were produced by a van de Graaff accelerator in the energy range from 1.2 to 5.8 MeV through different

neutron source reactions. The data were adjusted for prompt neutron emission to obtain the pre-neutron emission mass distribution.

The numerical data not given in the publication were provided by Duijvestijn [I.2]. The pre-neutron emission fragment mass distribution data at E_n = 1.6 and 5.5 MeV were selected for the evaluation. Data were renormalized to 200% (originally they were normalized to 100%). As the authors give no uncertainties, they were assigned according to the method used and an estimation was made from the figure in the paper (Fig. 9) as: 2% for yields ≥4%, 6% for yields <4% and ≥1%, and 8% for yields <1%.

I.3.2.2. Zöller [I.3]

Measurement type 1: The measurements were performed with the LANL spallation neutron source WNR, fed by 800 MeV protons from the LAMPF accelerator. The fragments were identified by a double energy measurement using 38 silicon PIN diodes assembled to two detector arrays of 171 cm^2 area each. Adjustments were made for detector pulse height defect, energy losses in the target material and backing, and for linear momentum transferred to the compound nucleus. Adjustments were also made to take into account the average mass losses of both the compound nucleus and the fragments by evaporation of neutrons prior to and after scission to get pre-neutron emission mass distributions. The mass resolution is 3.5 mass units at 13 MeV neutron energy and 4 mass units at 22 MeV. The fragment mass and kinetic energy distributions for ^{238}U were measured in the energy range from 2.0 to 450 MeV.

This is the same kind of measurement and has the same advantage and disadvantage as that of Vivès et al. [I.1]. In addition, this measurement was performed with a white neutron source (not mono-energetic neutrons), so the data were averaged over given energy bins and weighted with the corresponding neutron spectra in the bins.

The pre- and post-neutron emission fragment mass distributions at 13 (11.5–14.5), 20 (18–22), 27.5 (22–33), 50 (45–55), 99.5 (89–110) and 160 (145–175) MeV neutron energy were selected. The numerical values were provided by Duijvestijn [I.2]. The data at 5.0 (4.5–6.5) MeV (taken from Zöller [I.3]) were not used in the evaluation but included in the comparison of yield data.

I.3.2.3. Nagy et al. [I.4]

Measurement type 2: The chain yields for 44 mass chains were determined by direct γ ray spectrometry with a Ge(Li) detector, or by radiochemical separation of the fission products followed by β counting and/or γ ray spectrometry. The data were measured absolutely by recording the fission rates and normalizing the yield curve to 200%. The mono-energy neutrons at 1.5, 2.0, 3.9, 5.5, 6.9 and 7.7 MeV were produced by means of $^7Li(p,n)$ and D(d,n) reactions with the ANL fast neutron generator.

The data at neutron energies 1.5 and 5.5 MeV were used. The yield of mass number 107 at E_n = 1.5 MeV was discarded because the value is too small and not consistent with the others.

I.3.2.4. Chapman [I.5]

Measurement type 2: Cumulative yields from $^{235,238}U$ fission at 6.0, 7.1, 8.1 and 9.1 MeV neutron energy were determined by the radiochemical separation method followed by β counting and γ ray spectrometry with a Ge(Li) detector. The neutrons were produced by the D(d,n) reaction by means of a van de Graaff accelerator.

The data at E_n = 8.1 MeV were selected. As cumulative yields were measured, the yields of seven fission products, whose difference to the corresponding chain yields are larger than the experimental uncertainties, were not used. The data for mass 137 (believed to be incorrect) and 142 (uncertainty too large) were also discarded.

I.3.2.5. Li Ze et al. [I.6, I.7]

Measurement type 2: Over 30 chain yields for ^{238}U fission were determined by direct γ ray spectrometry with a HPGe detector, or by radiochemical separation of the fission products followed by β counting and/or γ ray spectrometry. Absolute yields were obtained by recording the fission rates. The measurements were performed at neutron energies of 8.3 [I.6] and 11.3 [I.7] MeV at the CIAE cyclotron and tandem accelerator, respectively. Adjustments were made for the recorded β or γ ray spectra and for the difference between the measured cumulative yield and corresponding chain yield.

Both sets of data were used. The yields of 5 mass numbers were determined by both methods, and a weighted average was taken.

I.3.2.6. Liu Conggui et al. [I.8]

Measurement type 2: The mass distribution for 14.9 MeV neutron induced fission of ^{238}U was determined by direct γ ray spectrometry with a Ge(Li) detector. Absolute yields were obtained by recording the fission rates with a double ionization chamber. 39 chain yields and 1 cumulative yield were determined in the mass region A = 84–151. Among them, 13 yields were measured relative to the yields of ^{132}Te or ^{140}Ba. Fine structure was observed in the vicinity of mass number 134.

The data were taken from the paper. However, since the yield for ^{130}Sb is cumulative and not equal to the corresponding chain yield, this particular value was not used in the evaluation.

I.3.2.7. Daroczy et al. [I.9]

Measurement type 2: Cumulative yields for 14.5 MeV neutron induced fission of ^{238}U (relative to ^{27}Al(n,α) and ^{62}Cu(n,2n) reactions) were determined by means of direct γ ray spectrometry with a Ge(Li) detector. Three sets of separately measured data are given, and weighted averages were taken. To deduce chain yields, the averaged data were adjusted using charge distribution data and branching ratios for the formation of the measured nuclides from β decay of their precursors. The resulting chain yield data were used in the evaluation.

I.3.2.8. Liu Yonghui et al. [I.10]

Measurement type 2: 32 chain yields were determined for ^{238}U fission induced by 22 MeV neutrons, which were produced by the T(d,n) reaction by means of the CIAE HI-13 tandem accelerator. Product activities were determined by direct γ ray spectrometry with a HPGe detector, and the absolute fission rate was monitored with a double-fission chamber. Yields at this neutron energy were measured for the first time.

The data were used, but the yield of mass number 128 was discarded because the associated uncertainty was too large (checked with the author).

I.3.2.9. Äystö et al. [I.11]

Measurement type 1: The pre-neutron emission fragment mass distribution from ^{238}U proton induced fission was measured at E_p = 20.0 and 60.0 MeV by recording prompt fission fragments. The mass resolution for the recording of fragments is about 4 mass units. The main uncertainty is statistical, although an estimate was not given by the author.

The relative uncertainties were assigned as: 1% for yields ≥4%, 3% for yields <4% and ≥1%, and 5% for yields <1%. Numerical data were provided by Duijvestijn [I.2] and were adopted.

I.3.2.10. Gindler et al. [I.12]

Measurement type 2: Absolute cumulative yields for ^{239}Pu fission at 0.17, 1.0, 2.0, 3.4, 4.5, 6.1 and 7.9 MeV neutron energy were determined by direct γ ray spectrometry by means of a Ge(Li) detector, and by radiochemical separation of the fission products followed by β counting with a proportional counter. Neutrons were produced with the ANL fast neutron generator through the ^{7}Li(p,n) reaction for neutron energies less than 5 MeV, and the D(d,n) reaction for E_n greater than 5 MeV. The nuclides measured were fewer, but they are the only data available in this energy range.

The data at neutron energy E_n = 0.17 and 7.9 MeV were selected. Yields were only used in the evaluation when differences with the corresponding chain yields were smaller than the experimental uncertainty. As a result, the yields of four nuclides at E_n = 0.17 MeV and three at E_n = 7.9 MeV were discarded. The data table was processed to the required format.

I.3.2.11. Ford [I.13]

Measurement type 2: Relative cumulative yields from the 14 MeV neutron induced fission of ^{239}Pu were measured using the radiochemistry method. The ^{99}Mo cumulative yield from ^{239}Pu fission or the corresponding cumulative yield from ^{235}U fission were used as reference yields. The 14 MeV neutrons were produced by the T(d,n) reaction by means of a Cockcroft–Walton machine.

Two sets of data are given in Ref. [I.13], measured by the same method and at the same neutron energy but for different product nuclides (except ^{111}Ag) that are compiled as different EXFOR entries. The two sets of data were combined, and the data for ^{111}Ag were arithmetically averaged. No uncertainties are given by the author. Considering the radiochemical method employed and the age of the measurement (1976), and taking into account the uncertainty given by the author for the R values, the relative uncertainties were assigned values of 10% for

all product nuclides. The data tables were processed to generate the data in the required format.

I.3.2.12. Laurec et al. [I.14]

Measurement type 2: The cumulative yields from ^{233,235,238}U and ^{239}Pu fission induced by fission spectrum and 14.7 MeV neutrons were measured by the radiochemical method. The γ ray spectra were measured with a Ge(Li) detector and the number of fissions was determined with a plane ionization chamber.

The data for ^{239}Pu fission at 14.9 MeV were used. Although the measured yields are cumulative, the differences between these values and the chain yields are all within the experimental uncertainties. So all data were used except for ^{136}Xe, whose yield is small and possibly incorrect.

I.3.2.13. Winkelmann et al. [I.15]

Measurement type 2: The cumulative yields from ^{242}Pu fission induced by 15.1 MeV neutrons were measured for 65 fission products from ^{85}Kr to ^{151}Pm. The fission product activities were measured by direct γ ray spectrometry with a Ge(Li) detector, as well as chemical separation of the fission product elements Pd, Ag, Cd, Sn, Sb and Ce, followed by β counting or γ ray spectrometry. The chain yields of 43 mass chains were obtained by dividing the measured cumulative yields by an adjustment factor, which is the ratio of the cumulative yield of the measured product nuclide to the corresponding chain yield.

The data were used after the following procedures had been applied:

(a) Some chain yields were obtained from two or more cumulative yields — the recommended chain yield was taken as their weighted average.
(b) Two fission yields were not used: that of ^{126g}Sb because the value is an independent yield, and that of ^{111m}Pm because the datum is only a partial isomeric yield.
(c) The data of product nuclides ^{130g}Sb, ^{131}Sb and ^{131m}Te were also discarded. The chain yields deduced from the cumulative yields of these nuclides are too small. The fractions of the measured cumulative yields to the corresponding chain yields are too small, which could introduce large uncertainties into the resulting chain yields. In addition, there are large differences for the adjustment factors of these nuclides between the values given in the paper and those calculated with the data from ENDF/B-VI.

I.4. RESULTS, RECOMMENDATIONS AND DISCUSSION

Based on the data selected from the available experimental data, and after their evaluation and processing as described above, the recommended mass distribution data for ^{238}U, ^{239,242}Pu fission are listed in Table I.1. All recommended data are given in the annex to this section, and plotted in Figs I.1–I.16.

As mentioned above, there are two types of measurements for mass distributions:

(a) Data are obtained by recording prompt fission fragments (data type 1 in Table I.1) with a double Frisch gridded ionization chamber, silicon PIN diode detector arrays, etc., as described by Vivès et al., Zöller and Äystö et al.
(b) Data are obtained by recording the radioactivity of fission product nuclides (data type 2 in Table I.1) by means of γ ray spectrometry with a Ge(Li) or HPGe detector, either directly from the fission sample or after radiochemical separation, as undertaken by Nagy et al., Chapman, Li Ze et al., Liu Conggui et al., Daroczy et al., Liu Yonghui et al., Gindler et al., Ford, Laurec et al. and Winkelmann et al.

From the comparisons in Figs I.17–I.19, the data measured by different laboratories but obtained with the same type of method (data type 1 or 2) are generally found to be in good agreement within the experimental uncertainty. But there is a systematic difference between the two types of data. The reason lies (a) in the physical nature of the measured yield and (b) in differences in the measurement techniques. The essential difference between the two types of method is that for type 2 there is some delay time (days, hours seconds, etc.) between fragment formation and measurement, during which the radioactive products decay (although this effect can be accounted for), whereas for data type 1 the measurement is 'prompt'. Nevertheless, even in the type 1 method the fragments are generally measured

TABLE I.1. RECOMMENDED MASS DISTRIBUTION DATA

Fissile nuclide	Energy (MeV)	Author (energy (MeV))	Reference	Data type
^{238}U	E_n around 1.5	Vivès (1.6)	I.1	1
		Nagy (1.5)	I.4	2
	E_n = 5.5	Vivès	I.1	1
		Nagy	I.4	2
	E_n around 8.2	Li Ze (8.3)	I.6	2
		Chapman (8.1)	I.5	2
	E_n around 11.3	Li Ze (11.3)	I.7	2
		Zöller (11.5–14.5)	I.3	1
	E_n around 14.5	Liu Conggui (14.9)	I.8	2
		Daroczy (14.5)	I.9	2
		Zöller (11.5–14.5)	I.3	1
	E_n around 22.0	Liu Yonghui (22)	I.10	2
		Zöller (18–22)	I.3	1
	E_n around 27.5	Zöller (22–33)	I.3	1
	E_n around 50.0	Zöller (45–55)	I.3	1
	E_n around 100	Zöller (89–110)	I.3	1
	E_n around 160	Zöller (145–175)	I.3	1
	E_p = 20.0	Äystö	I.11	1
	E_p = 60.0	Äystö	I.11	1
^{239}Pu	E_n = 0.17	Gindler	I.12	2
	E_n = 7.9	Gindler	I.12	2
	E_n around 14.5	Ford (14.0)	I.13	2
		Laurec (14.7)	I.14	2
^{242}Pu	E_n = 15.1	Winkelmann	I.15	2

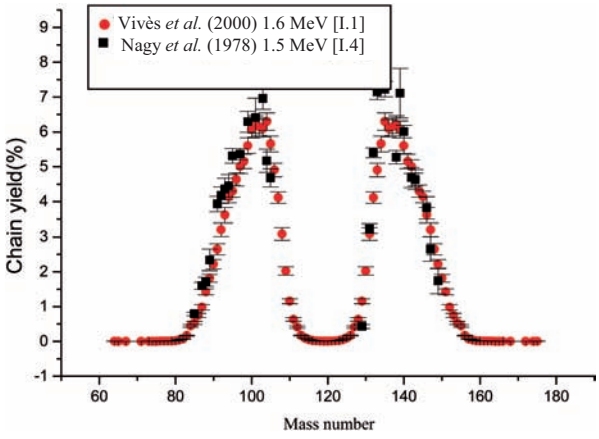

FIG. I.1. Mass distribution from ^{238}U fission at E_n of around 1.5 MeV.

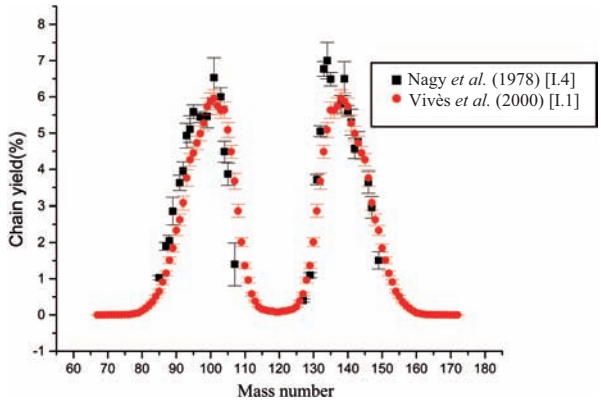

FIG. I.2. Mass distribution from ^{238}U fission at E_n = 5.5 MeV.

after prompt-neutron emission, and are labelled as post-neutron emissions. Fragment data before prompt emission, (pre-neutron emission data) are obtained after adjustment, as described by Vivès et al. and Zöller [I.1, I.3]. So in the data file (figures and annex), 'post' and 'pre' refer to the prompt neutrons for type 1. However, all type 2 data are not only post-neutron emission, but also after delayed neutron emission.

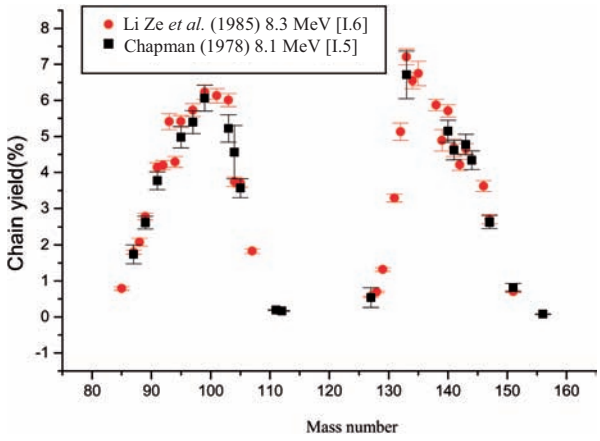

FIG. I.3. Mass distribution from ^{238}U fission at E_n of around 8.2 MeV.

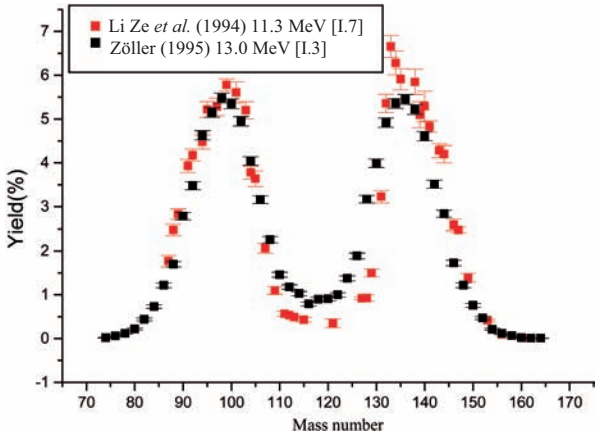

FIG. I.4. Mass distribution from ^{238}U fission at E_n of around 11.3 MeV.

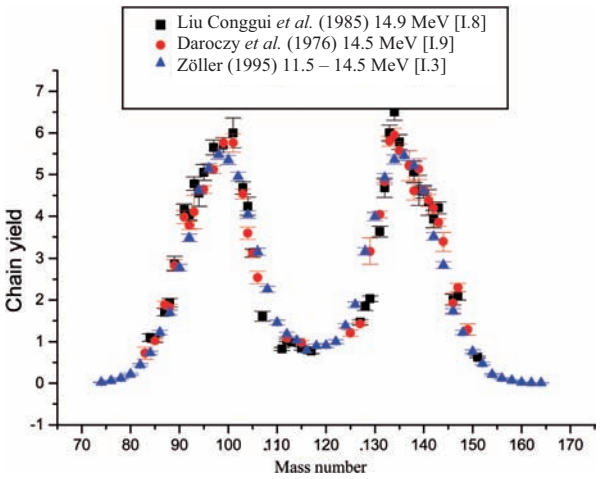

FIG. I.5. Mass distribution from ^{238}U fission at E_n of around 14.5 MeV.

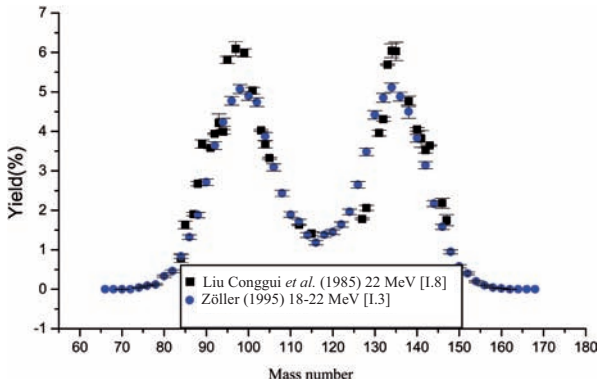

FIG. I.6. Mass distribution from ^{238}U fission at E_n of around 22 MeV.

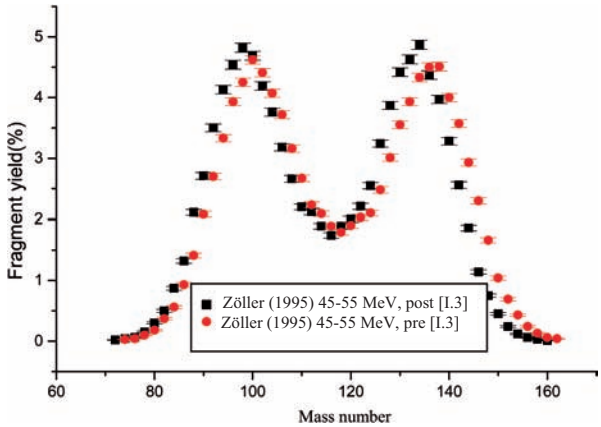

FIG. I.7. Fragment mass distribution from ^{238}U fission at E_n of around 27.5 MeV.

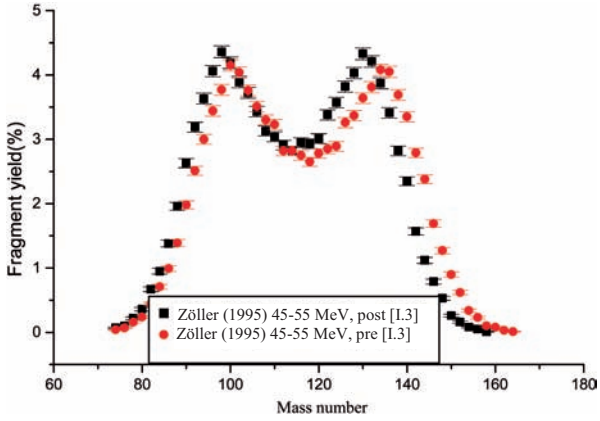

FIG. I.8. Fragment mass distribution from ^{238}U at E_n of around 50 MeV.

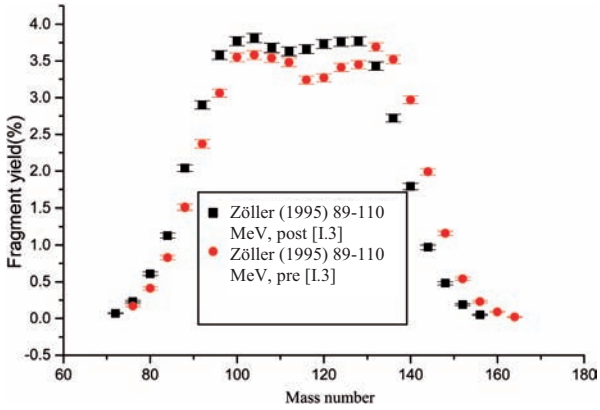

FIG. I.9. Fragment mass distribution from ^{238}U fission at E_n of around 160 MeV.

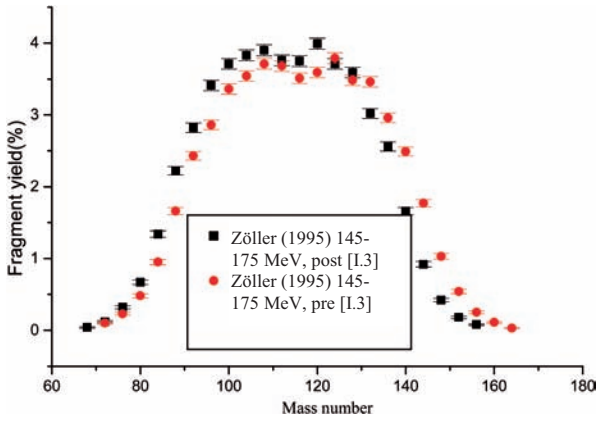

FIG. I.10. Fragment mass distribution from ^{238}U fission at E_n of around 160 MeV.

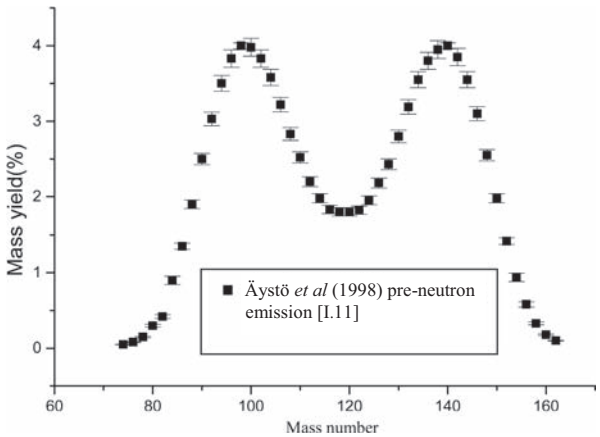

FIG. I.11. Mass distribution from ^{238}U at E_p = 20 MeV.

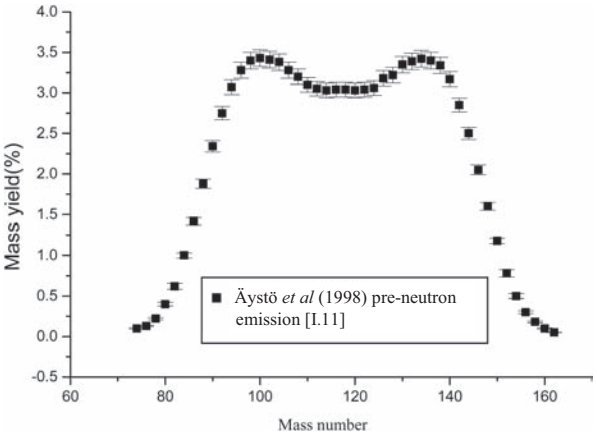

FIG. I.12. Mass distribution from ^{238}U at E_p = 60 MeV.

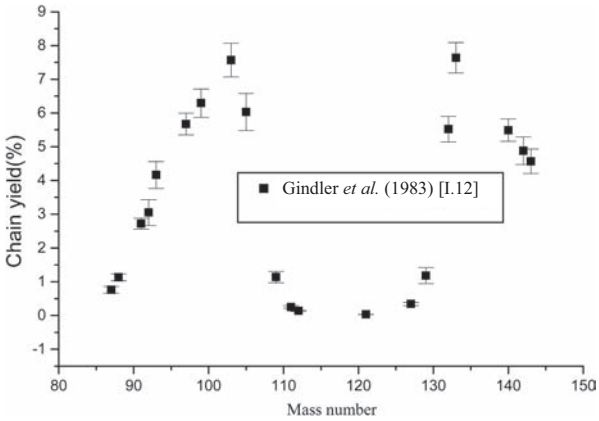

FIG. I.13. Mass distribution from ^{239}Pu fission at E_n = 0.17 MeV.

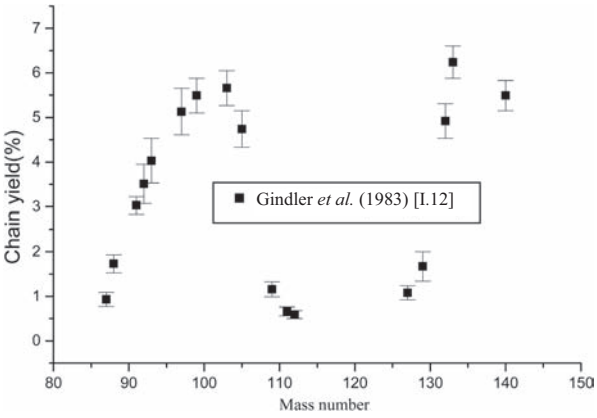

FIG. I.14. Mass distribution from ^{239}Pu fission at E_n = 7.9 MeV.

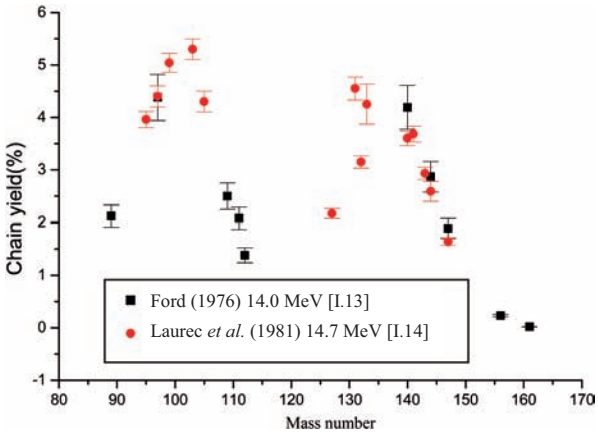

FIG. I.15. Mass distribution from ^{239}Pu fission at E_n of around 14.5 MeV.

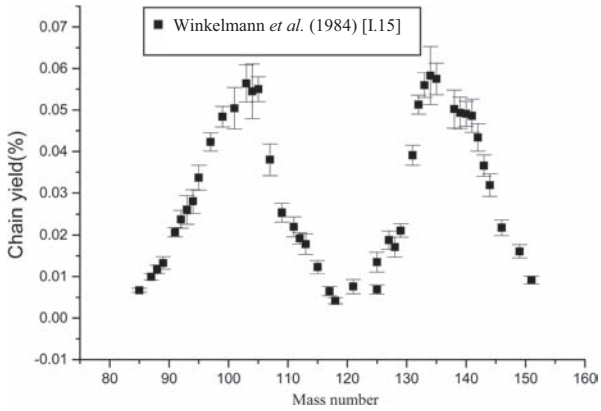

FIG. I.16. Mass distribution from ^{242}Pu fission at E_n = 15.1 MeV.

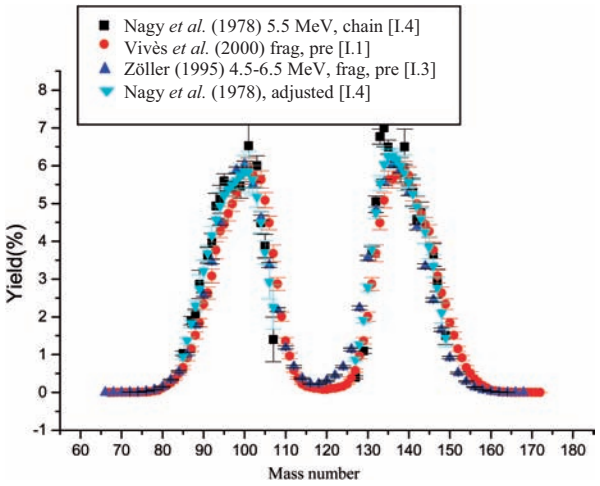

FIG. I.17. Comparison of mass distribution from ^{238}U fission of around 5.5 MeV measured with different methods.

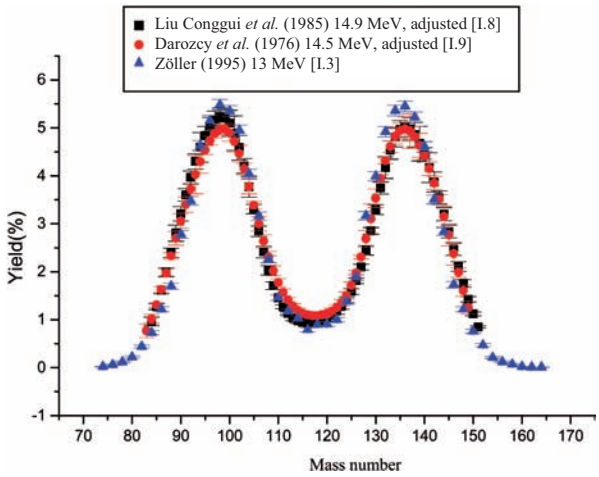

FIG. I.18. Comparison of mass distribution from ^{238}U fission at E_n of around 14 MeV measured with different methods.

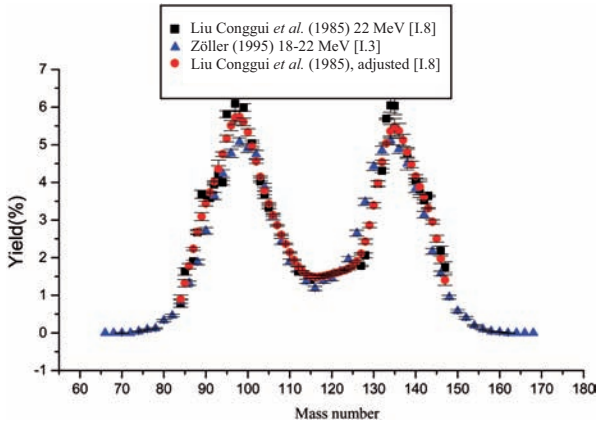

FIG. I.19. Comparison of mass distribution from ^{238}U fission of around 22 MeV measured with different methods.

An important difference between the two types of data is delayed neutron emission. Thus, in addition to β decay, some of the radioactive fission product nuclides also decay by emitting delayed neutrons. Type 2 data are applicable after emission of delayed neutrons, unlike data type 1, even though the data are post-neutron emission with respect to prompt neutrons. Another difference is the mass resolution, which is more important when using the data to compare with calculated values. Mass resolution is not a problem for type 2 data; but for type 1 data, as mentioned above, the measured mass distribution is not real but is a superposition of Gaussian distributions with the mass resolution defined as the width for each mass number. The second type of data were 'adjusted' by the following steps to illustrate this point:

(1) Data were linearly interpolated for mass numbers when there were no measured data, so that there are yields for all masses in the mass range measured.
(2) For the yields of each mass A, the data were folded with Gaussians of width 3 or 4 mass units, corresponding to the mass resolution of the measurements of Vivès et al. or Zöller at the given energies.
(3) All yields were summed over all mass numbers in the measured mass range.

The results are shown in Figs I.17–I.19 (marked 'adjusted') and indicate that the adjusted second type of data are consistent with the first type of data, e.g. adjusted Nagy et al., with Vives et al. and Zöller in Fig. I.17; adjusted Liu Conggui et al. and adjusted Daroczy et al., with Zöller in Fig. I.18; adjusted Liu Conggui et al. data, with Zöller in Fig. I.19.

I.5. CONCLUSIONS

The recommended mass distribution data were evaluated on the basis of the available experimental data at energies E_n = 1.5, 5.5, 8.2, 11.3, 14.5, 22, 27.5, 50, 100 and 160 MeV and E_p = 20 and 60 MeV for ^{238}U fission, E_n = 0.17, 7.9 and 14.5 MeV for ^{239}Pu fission, and E_n = 15.1 MeV for ^{242}Pu fission. The data measured at different laboratories by the same kind of method (either data type 1 or 2) are in good agreement within the experimental uncertainty. Considering the differences between the two types of data in their physics and measurement techniques, they are consistent with each other after corresponding adjustments. The data are recommended for use in the benchmark exercise of the CRP to test and improve the model calculations.

Differences between the two types of data must be taken into account in these comparisons. The calculated data should be folded with Gaussian distributions, with the widths corresponding to the experimental mass resolutions when comparing them with type 1 data. There is no problem in comparisons with type 2 data.

ACKNOWLEDGEMENTS

The author is indebted to M.C. Duijvestijn and M. Mutterer for providing papers and numerical experimental data, and to M. Lammer for supporting the work and partial translations of Zöller's thesis.

REFERENCES TO APPENDIX I

[I.1] VIVÈS, F., et al., Investigation of the fission fragment properties of the reaction ^{238}U(n,f) at incident neutron energies up to 5.8 MeV, Nucl. Phys. A **662** (2000) 63–92.

[I.2] DUIJVESTIJN, M.C., Nuclear Research and Consultancy Group, Petten, Netherlands, personal communication, 2002.

[I.3] ZÖLLER, C.M., Untersuchung der neutronen-induzierten Spaltung von ^{238}U im Energiebereich von 1 MeV bis 500 MeV, PhD thesis, Technische Universität Darmstadt, Germany (1995).

[I.4] NAGY, S., et al., Mass distributions in monoenergetic-neutron-induced fission of ^{238}U, Phys. Rev. C **17** (1978) 163–171.

[I.5] CHAPMAN, T.C., Fission product yields from 6–9 MeV neutron-induced fission of ^{235}U and ^{238}U, Phys. Rev. C **17** (1978) 1089–1097.

[I.6] LI ZE, et al., Mass distribution in 8.3 MeV neutron-induced fission of ^{238}U, Chin. J. Nucl. Phys. **7** (1985) 97–105.

[I.7] LI ZE, et al., Fission product yields from 11.3-MeV neutron-induced fission of ^{238}U, Radiochim. Acta **64** (1994) 95–97.

[I.8] LIU CONGGUI, et al., The mass distribution in 14.9-MeV neutron-induced fission of ^{238}U, Chin. J. Nucl. Phys. **7** (1985) 235–241.

[I.9] DAROCZY, S., et al., Experimental results on mass distribution of ^{238}U fission induced by 14 MeV neutrons, Atomki Koezl. **18** (1976) 317–329.

[I.10] LIU YONGHUI, et al., Mass distribution of 22.0 MeV neutron-induced fission of ^{238}U, Comm. Nucl. Data Prog. No. 26, INDC (CPR)-056 (2001) 2–4.

[I.11] ÄYSTÖ, J., et al., New results on superasymmetric fission at intermediate energy, Fission and Properties of Neutron-rich Nuclei (Proc. Int. Conf. Sanibel Island, FL, 1997) (HAMILTON, J.H., RAMAYYA, I.V., Eds), World Scientific, Singapore (1998) 457–466.

[I.12] GINDLER, J.E., et al., Mass distribution in monoenergetic-neutron-induced fission of ^{239}Pu, Phys. Rev. C **27** (1983) 2058–2062.

[I.13] FORD, G.P., A Compilation of Yields from Neutron-induced Fission of ^{232}Th, ^{235}U, ^{236}U, ^{237}Np, ^{238}U and ^{239}Pu Measured Radiochemically at Los Alamos, Rep. LA-6129, Los Alamos National Lab., NM (1976).

[I.14] LAUREC, J., et al., Détermination des Rendements de Fissions Induites par un Spectre de Neutrons de Fission et des Neutrons de 14.7 MeV dans ^{233}U, ^{235}U, ^{238}U, ^{239}P, Rep. CEA-R–5147 (1981).

[I.15] WINKELMANN, I., et al., Fission of ^{242}Pu with 15.1-MeV neutrons, Phys. Rev. C **30** (1984) 934–940.

Annex to Appendix I

RECOMMENDED EVALUATED MASS DISTRIBUTION DATA FOR ^{238}U, ^{239}Pu, ^{242}Pu

1. ^{238}U NEUTRON INDUCED FISSION

1.1. $E_n \approx 1.5$ MeV

Nagy et al. (1978) [I.4] E_n = 1.5 MeV Post-neutron emission chain yield			Vivès et al. (2000) [I.1] E_n = 1.6 MeV Pre-neutron emission mass yield		
Mass	Yield (%)	Uncertainty	Mass	Yield (%)	Uncertainty
85.0	0.79	0.05	64	3.5522E–03	2.8418E–04
87.0	1.60	0.10	65	1.7761E–03	1.4209E–04
88.0	1.71	0.13	67	1.7761E–03	1.4209E–04
89.0	2.34	0.31	71	1.7761E–03	1.4209E–04
91.0	3.93	0.22	73	5.3283E–03	4.2627E–04
92.0	4.18	0.24	74	1.7761E–03	1.4209E–04
93.0	4.36	0.31	75	1.7761E–03	1.4209E–04
94.0	4.45	0.33	76	8.8805E–03	7.1044E–04
95.0	5.31	0.21	77	8.8805E–03	7.1044E–04
97.0	5.36	0.16	78	8.8805E–03	7.1044E–04
99.0	6.29	0.30	79	1.4209E–02	1.1367E–03
101.0	6.41	0.56	80	1.9537E–02	1.5630E–03
103.0	6.96	0.31	81	4.4403E–02	3.5522E–03
104.0	5.17	0.33	82	7.2820E–02	5.8256E–03
105.0	4.68	0.26	83	1.6873E–01	1.3498E–02
129.0	0.43	0.06	84	4.4580E–01	3.5664E–02
131.0	3.24	0.13	85	5.3106E–01	4.2484E–02
132.0	5.40	0.14	86	7.4952E–01	5.9961E–02
133.0	7.15	0.22	87	9.8219E–01	7.8575E–02
134.0	8.12	0.40	88	1.4262E+00	8.5573E–02
135.0	7.23	0.22	89	1.8134E+00	1.0880E–01
138.0	5.27	0.19	90	2.2148E+00	1.3289E–01
139.0	7.11	0.71	91	2.6464E+00	1.5878E–01
140.0	6.01	0.18	92	3.2059E+00	1.9235E–01
142.0	4.69	0.29	93	3.6108E+00	2.1665E–01
143.0	4.63	0.29	94	4.1330E+00	1.6532E–01
146.0	3.82	0.32	95	4.2982E+00	1.7193E–01
147.0	2.65	0.35	96	4.6321E+00	1.8528E–01
149.0	1.74	0.37	97	5.0033E+00	2.0013E–01

Vivès et al. (2000) [I.1] E_n = 1.6 MeV Pre-neutron emission mass yield			Vivès et al. (2000) [I.1] E_n = 1.6 MeV Pre-neutron emission mass yield		
Mass	Yield (%)	Uncertainty	Mass	Yield (%)	Uncertainty
98	5.1507E+00	2.0603E–01	135	6.2963E+00	2.5185E–01
99	5.6036E+00	2.2414E–01	136	6.1009E+00	2.4404E–01
100	6.0707E+00	2.4283E–01	137	6.1435E+00	2.4574E–01
101	6.2164E+00	2.4865E–01	138	6.2164E+00	2.4865E–01
102	6.1435E+00	2.4574E–01	139	6.0707E+00	2.4283E–01
103	6.1009E+00	2.4404E–01	140	5.6036E+00	2.2414E–01
104	6.2963E+00	2.5185E–01	141	5.1507E+00	2.0603E–01
105	5.6551E+00	2.2620E–01	142	5.0033E+00	2.0013E–01
106	4.9038E+00	1.9615E–01	143	4.6321E+00	1.8528E–01
107	4.1135E+00	1.6454E–01	144	4.2982E+00	1.7193E–01
108	3.0851E+00	1.8511E–01	145	4.1330E+00	1.6532E–01
109	2.0230E+00	1.2138E–01	146	3.6108E+00	2.1665E–01
110	1.1545E+00	6.9268E–02	147	3.2059E+00	1.9235E–01
111	6.3229E–0	5.0583E–02	148	2.6464E+00	1.5878E–01
112	4.1206E–01	3.2964E–02	149	2.2148E+00	1.3289E–01
113	1.7228E–01	1.3783E–02	150	1.8134E+00	1.0880E–01
114	9.7686E–02	7.8149E–03	151	1.4262E+00	8.5573E–02
115	5.1507E–02	4.1206E–03	152	9.8219E–01	7.8575E–02
116	2.6642E–02	2.1313E–03	153	7.4952E–01	5.9961E–02
117	1.5985E–02	1.2788E–03	154	5.3106E–01	4.2484E–02
118	1.0657E–02	8.5253E–04	155	4.4580E–01	3.5664E–02
119	7.1044E–03	5.6835E–04	156	1.6873E–01	1.3498E–02
120	7.1044E–03	5.6835E–04	157	7.2820E–02	5.8256E–03
121	1.0657E–02	8.5253E–04	158	4.4403E–02	3.5522E–03
122	1.5985E–02	1.2788E–03	159	1.9537E–02	1.5630E–03
123	2.6642E–02	2.1313E–03	160	1.4209E–02	1.1367E–03
124	5.1507E–02	4.1206E–03	161	8.8805E–03	7.1044E–04
125	9.7686E–02	7.8149E–03	162	8.8805E–03	7.1044E–04
126	1.7228E–01	1.3783E–02	163	8.8805E–03	7.1044E–04
127	4.1206E–01	3.2964E–02	164	1.7761E–03	1.4209E–04
128	6.3229E–01	5.0583E–02	165	1.7761E–03	1.4209E–04
129	1.1545E+00	6.9268E–02	166	5.3283E–03	4.2627E–04
130	2.0230E+00	1.2138E–01	168	1.7761E–03	1.4209E–04
131	3.0851E+00	1.8511E–01	172	1.7761E–03	1.4209E–04
132	4.1135E+00	1.6454E–01	174	1.7761E–03	1.4209E–04
133	4.9038E+00	1.9615E–01	175	3.5522E–03	2.8418E–04
134	5.6551E+00	2.2620E–01			

1.2. E_n = 5.5 MeV

Nagy et al. (1978) [I.4] E_n = 5.5 MeV Post-neutron emission chain yield			Vivès et al. (2000) [I.1] E_n = 5.5 MeV Pre-neutron emission mass yield		
Mass	Yield (%)	Uncertainty	Mass	Yield (%)	Uncertainty
85	1.03	0.06	67	6.9231E–04	5.5385E–05
87	1.90	0.11	68	6.9231E–04	5.5385E–05
88	2.05	0.15	69	1.3846E–03	1.1077E–04
89	2.86	0.37	70	2.7692E–03	2.2154E–04
91	3.63	0.21	71	3.4615E–03	2.7692E–04
92	3.96	0.25	72	4.1539E–03	3.3231E–04
93	4.93	0.34	73	4.1539E–03	3.3231E–04
94	5.11	0.37	74	6.2308E–03	4.9846E–04
95	5.59	0.19	75	8.3077E–03	6.6462E–04
97	5.44	0.15	76	1.2462E–02	9.9693E–04
99	5.46	0.32	77	2.0077E–02	1.6062E–03
101	6.53	0.55	78	4.2231E–02	3.3785E–03
103	6.00	0.26	79	5.6769E–02	4.5416E–03
104	4.49	0.29	80	1.1908E–01	9.5262E–03
105	3.87	0.31	81	1.7239E–01	1.3791E–02
107	1.40	0.59	82	2.6031E–01	2.0825E–02
127	0.40	0.04	83	3.5654E–01	2.8523E–02
129	1.10	0.07	84	5.0746E–01	4.0597E–02
131	3.72	0.14	85	6.5839E–01	5.2671E–02
132	5.05	0.15	86	9.1316E–01	7.3053E–02
133	6.77	0.20	87	1.1534E+00	6.9203E–02
134	7.00	0.50	88	0.5092E+00	9.0554E–02
135	6.49	0.19	89	1.8471E+00	1.1082E–01
138	5.80	0.24	90	2.3338E+00	1.4003E–01
139	6.50	0.47	91	2.6301E+00	1.5781E–01
140	5.61	0.15	92	3.0808E+00	1.8485E–01
141	5.30	0.36	93	3.7634E+00	2.2580E–01
142	4.58	0.28	94	4.2639E+00	1.7056E–01
143	4.75	0.29	95	4.4543E+00	1.7817E–01
146	3.64	0.30	96	4.7299E+00	1.8919E–01
147	2.96	0.29	97	4.9888E+00	1.9955E–01
149	1.51	0.24	98	5.2761E+00	2.1104E–01

Vivès et al. (2000) [I.1] E_n = 5.5 MeV Pre-neutron emission mass yield			Vivès et al. (2000) [I.1] E_n = 5.5 MeV Pre-neutron emission mass yield		
Mass	Yield (%)	Uncertainty	Mass	Yield (%)	Uncertainty
99	5.7365E+00	2.2946E–01	136	5.6333E+00	2.2533E–01
100	5.8756E+00	2.3503E–01	137	5.7503E+00	2.3001E–01
101	5.9649E+00	2.3860E–01	138	5.9649E+00	2.3860E–01
102	5.7503E+00	2.3001E–01	139	5.8756E+00	2.3503E–01
103	5.6333E+00	2.2533E–01	140	5.7365E+00	2.2946E–01
104	5.6326E+00	2.2531E–01	141	5.2761E+00	2.1104E–01
105	5.0864E+00	2.0346E–01	142	4.9888E+00	1.9955E–01
106	4.4862E+00	1.7945E–01	143	4.7299E+00	1.8919E–01
107	3.6776E+00	2.2065E–01	144	4.4543E+00	1.7817E–01
108	2.8696E+00	1.7218E–01	145	4.2639E+00	1.7056E–01
109	2.0077E+00	1.2046E–01	146	3.7634E+00	2.2580E–01
110	1.3645E+00	8.1873E–02	147	3.0808E+00	1.8485E–01
111	9.6370E–01	7.7096E–02	148	2.6301E+00	1.5781E–01
112	5.7946E–01	4.6357E–02	149	2.3338E+00	1.4003E–01
113	3.7869E–01	3.0295E–02	150	1.8471E+00	1.1082E–01
114	2.2500E–01	1.8000E–02	151	1.5092E+00	9.0554E–02
115	1.5992E–01	1.2794E–02	152	1.1534E+00	6.9203E–02
116	1.3154E–01	1.0523E–02	153	9.1316E–01	7.3053E–02
117	1.1008E–01	8.8062E–03	154	6.5839E–01	5.2671E–02
118	1.0454E–01	8.3631E–03	155	5.0746E–01	4.0597E–02
119	8.0308E–02	6.4246E–03	156	3.5654E–01	2.8523E–02
120	8.0308E–02	6.4246E–03	157	2.6031E–01	2.0825E–02
121	1.0454E–01	8.3631E–03	158	1.7239E–01	1.3791E–02
122	1.1008E–01	8.8062E–03	159	1.1908E–01	9.5262E–03
123	1.3154E–01	1.0523E–02	160	5.6769E–02	4.5416E–03
124	1.5992E–01	1.2794E–02	161	4.2231E–02	3.3785E–03
125	2.2500E–01	1.8000E–02	162	2.0077E–02	1.6062E–03
126	3.7869E–01	3.0295E–02	163	1.2462E–02	9.9693E–04
127	5.7946E–01	4.6357E–02	164	8.3077E–03	6.6462E–04
128	9.6370E–01	7.7096E–02	165	6.2308E–03	4.9846E–04
129	1.3645E+00	8.1873E–02	166	4.1539E–03	3.3231E–04
130	2.0077E+00	1.2046E–01	167	4.1539E–03	3.3231E–04
131	2.8696E+00	1.7218E–01	168	3.4615E–03	2.7692E–04
132	3.6776E+00	2.2065E–01	169	2.7692E–03	2.2154E–04
133	4.4862E+00	1.7945E–01	170	1.3846E–03	1.1077E–04
134	5.0864E+00	2.0346E–01	171	6.9231E–04	5.5385E–05
135	5.6326E+00	2.2531E–01	172	6.9231E–04	5.5385E–05

1.3. $E_n \approx 8$ MeV

Chapman (1978) [I.5] E_n = 8.1 MeV Post-neutron emission chain yield			Li Ze et al. (1985) [I.6] E_n = 8.3 MeV Post-neutron emission chain yield		
Mass	Yield (%)	Uncertainty	Mass	Yield (%)	Uncertainty
87	1.7395E+00	2.6092E–01	85	0.79	0.05
89	2.6125E+00	1.6720E–01	87	1.80	0.06
91	3.7717E+00	2.4893E–01	88	2.08	0.11
95	4.9810E+00	2.9886E–01	89	2.77	0.09
97	5.3968E+00	3.1841E–01	91	4.14	0.13
99	6.0623E+00	3.5768E–01	92	4.20	0.13
103	5.2195E+00	3.8102E–01	93	5.41	0.22
104	4.5611E+00	7.4346E–01	94	4.29	0.15
105	3.5643E+00	2.6376E–01	95	5.42	0.16
111	1.9450E–01	1.3420E–02	97	5.73	0.18
112	1.6880E–01	1.1647E–02	99	6.23	0.20
127	5.3900E–01	2.7543E–01	101	6.13	0.20
133	6.7132E+00	6.6461E–01	103	6.01	0.18
140	5.1455E+00	3.0873E–01	104	3.74	0.13
141	4.6197E+00	2.7256E–01	105	3.71	0.12
143	4.7749E+00	2.8172E–01	107	1.83	0.07
144	4.3396E+00	2.6038E–01	127	0.56	0.02
147	2.6285E+00	1.6822E–01	128	0.70	0.03
151	8.2080E–01	1.1081E–01	129	1.32	0.05
156	7.7000E–02	9.0860E–03	131	3.29	0.11
			132	5.13	0.24
			133	7.21	0.22
			134	6.55	0.23
			135	6.75	0.34
			138	5.87	0.16
			139	4.89	0.30
			140	5.71	0.17
			141	4.68	0.24
			142	4.21	0.15
			143	4.66	0.14
			146	3.62	0.15
			147	2.70	0.13
			151	0.707	0.024

1.4. $E_n \approx 11–13$ MeV

Li Ze et al. (1985) [I.7] E_n = 11.3 MeV Post-neutron emission chain yield			Zöller (1995) [I.3] E_n = 13.0 (11.5–14.5) MeV Post-neutron emission mass yield		
Mass	Yield (%)	Uncertainty	Mass	Yield (%)	Uncertainty
87	1.77	0.13	74.0	0.02	0.006
88	2.48	0.13	76.0	0.06	0.012
89	2.83	0.12	78.0	0.12	0.017
91	3.93	0.15	80.0	0.22	0.023
92	4.18	0.14	82.0	0.44	0.032
94	4.48	0.16	84.0	0.73	0.041
95	5.22	0.18	86.0	1.22	0.053
97	5.28	0.20	88.0	1.70	0.063
99	5.78	0.14	90.0	2.78	0.081
101	5.61	0.24	92.0	3.48	0.090
103	5.20	0.20	94.0	4.63	0.104
104	3.78	0.15	96.0	5.15	0.110
105	3.64	0.18	98.0	5.48	0.113
107	2.06	0.11	100.0	5.35	0.112
109	1.10	0.09	102.0	4.95	0.108
111	0.57	0.06	104.0	4.04	0.097
112	0.53	0.03	106.0	3.16	0.086
113	0.49	0.03	108.0	2.26	0.073
115	0.43	0.05	110.0	1.46	0.058
121	0.35	0.10	112.0	1.18	0.053
127	0.92	0.03	114.0	1.03	0.049
128	0.927	0.074	116.0	0.79	0.043
129	1.50	0.09	118.0	0.90	0.046
131	3.23	0.14	120.0	0.91	0.046
132	5.36	0.21	122.0	1.00	0.048
133	6.66	0.25	124.0	1.38	0.057
134	6.28	0.27	126.0	1.89	0.067
135	5.91	0.24	128.0	3.17	0.086
138	5.85	0.29	130.0	3.99	0.097
139	5.10	0.30	132.0	4.92	0.107
140	5.29	0.35	134.0	5.36	0.112
141	4.83	0.13	136.0	5.45	0.113
143	4.28	0.16	138.0	5.22	0.111
144	4.20	0.20	140.0	4.61	0.104
146	2.59	0.13	142.0	3.51	0.091
147	2.48	0.07	144.0	2.84	0.082
149	1.39	0.10	146.0	1.73	0.064
153	0.415	0.025	148.0	1.22	0.053
156	0.0954	0.0054	150.0	0.76	0.042
161	0.0094	0.0009	152.0	0.47	0.033
			154.0	0.21	0.022
			156.0	0.12	0.017
			158.0	0.07	0.013
			160.0	0.02	0.006
			162.0	0.01	0.003
			164.0	0.01	0.004

1.5. E_n = 14–15 MeV

Daroczy et al. (1976) [I.9] E_n = 14.4 MeV Post-neutron emission chain yield			Liu Conggui et al. (1985) [I.8] E_n = 14.9 MeV Post-neutron emission mass yield		
Mass	Yield (%)	Uncertainty	Mass	Yield (%)	Uncertainty
8.3000E+01	7.2200E–01	1.4400E–01	84	1.10	0.09
8.5000E+01	1.0230E+00	4.6000E–02	85	1.05	0.06
8.7000E+01	1.8910E+00	8.3000E–02	87	1.71	0.09
8.8000E+01	1.8290E+00	7.0000E–02	88	1.94	0.10
8.9000E+01	2.8300E+00	1.4000E–01	89	2.88	0.17
9.1000E+01	3.9800E+00	1.6000E–01	91	4.16	0.13
9.2000E+01	3.7800E+00	1.0000E–01	92	4.03	0.13
9.3000E+01	4.1000E+00	4.0000E–01	93	4.78	0.16
9.5000E+01	4.6400E+00	9.0000E–02	94	4.55	0.31
9.7000E+01	5.1200E+00	9.0000E–02	95	5.05	0.19
9.9000E+01	5.7600E+00	1.2000E–01	97	5.65	0.18
1.0100E+02	5.7600E+00	2.2000E–01	99	5.71	0.18
1.0300E+02	4.5300E+00	1.2000E–01	101	6.00	0.36
1.0400E+02	3.5900E+00	1.5000E–01	103	4.68	0.15
1.0500E+02	3.1200E+00	8.0000E–02	104	4.24	0.22
1.0600E+02	2.5400E+00	1.5000E–01	105	3.13	0.10
1.1200E+02	1.0770E+00	5.2000E–02	107	1.61	0.12
1.1500E+02	9.7500E–01	5.5000E–02	111	0.823	0.037
1.2500E+02	1.2050E+00	7.3000E–02	112	1.04	0.04
1.2700E+02	1.4310E+00	3.8000E–02	113	0.985	0.058
1.2900E+02	3.1700E+00	3.1000E–01	115	0.834	0.039
1.3100E+02	4.0400E+00	8.0000E–02	117	0.775	0.062
1.3200E+02	4.8200E+00	6.0000E–02	127	1.47	0.06
1.3300E+02	5.8000E+00	1.2000E–01	128	1.85	0.10
1.3400E+02	5.9500E+00	1.6000E–01	129	2.03	0.07
1.3500E+02	5.5800E+00	1.5000E–01	131	3.63	0.13
1.3700E+02	5.2100E+00	3.6000E–01	132	4.68	0.23
1.3800E+02	4.6100E+00	2.2000E–01	133	6.00	0.19
1.3900E+02	5.1300E+00	2.5000E–01	134	6.50	0.20
1.4000E+02	4.6300E+00	7.0000E–02	135	5.78	0.18
1.4100E+02	4.3800E+00	1.4000E–01	138	5.06	0.26
1.4200E+02	4.1900E+00	1.4000E–01	139	4.62	0.36
1.4300E+02	3.8500E+00	9.0000E–02	140	4.59	0.15
1.4400E+02	3.3900E+00	2.2000E–01	141	4.33	0.31
1.4600E+02	1.9250E+00	2.3500E–01	142	3.93	0.21
1.4700E+02	2.3000E+00	1.0000E–01	143	4.20	0.14
1.4900E+02	1.2900E+00	1.3700E–01	146	2.01	0.13
			147	2.10	0.10
			151	0.631	0.022

1.6. E_n = 20–22 MeV

Zöller (1995) [I.3] E_n = 20.0 (18–22) MeV Post-neutron emission mass yield			Liu Yonghui et al. (2001) [I.10] E_n = 22 MeV Post-neutron emission chain yield		
Mass	Yield (%)	Uncertainty	Mass	Yield (%)	Uncertainty
66	0.0	0.0	84	0.79	0.108
68	0.0	0.0	85	1.63	0.096
70	0.0	0.003	87	1.90	0.041
72	0.0	0.000	88	2.67	0.052
74	0.04	0.01	89	3.68	0.107
76	0.09	0.015	91	3.58	0.019
78	0.12	0.018	92	3.94	0.017
80	0.33	0.029	93	4.21	0.237
82	0.46	0.034	94	3.99	0.058
84	0.83	0.046	95	5.81	0.089
86	1.32	0.058	97	6.09	0.180
88	1.88	0.069	99	5.99	0.103
90	2.71	0.083	101	5.03	0.083
92	3.64	0.096	103	4.02	0.024
94	4.23	0.104	104	3.67	0.093
96	4.77	0.110	105	3.32	0.025
98	5.07	0.114	112	1.63	0.016
100	4.90	0.112	115	1.41	0.040
102	4.74	0.110	127	1.78	0.024
104	3.87	0.099	128	2.06	0.065
106	3.09	0.089	131	3.96	0.073
108	2.43	0.079	132	4.31	0.053
110	1.89	0.069	133	5.69	0.021
112	1.71	0.066	134	6.04	0.178
114	1.37	0.059	135	6.03	0.232
116	1.18	0.055	138	4.76	0.126
118	1.38	0.059	140	4.05	0.044
120	1.45	0.061	141	3.81	0.213
122	1.64	0.065	142	3.52	0.070
124	1.96	0.070	143	3.64	0.019
126	2.65	0.082	146	2.18	0.129
128	3.48	0.094	147	1.75	0.140
130	4.42	0.106			
132	4.85	0.111			
134	5.11	0.114			
136	4.88	0.111			
138	4.50	0.170			
140	3.83	0.099			
142	3.14	0.089			
144	2.17	0.074			
146	1.58	0.063			
148	0.95	0.049			
150	0.58	0.038			
152	0.40	0.032			
154	0.20	0.022			
156	0.10	0.016			
158	0.04	0.01			
160	0.02	0.006			
162	0.00	0.003			
164	0.00	0.00			
166	0.00	0.00			
168	0.00	0.00			

1.7. E_n = 27.5 (22–33) MeV, Zöller (1995) [I.3]

Pre-neutron emission mass yield			Post-neutron emission mass yield		
Mass	Yield (%)	Uncertainty	Mass	Yield (%)	Uncertainty
			72.0	0.02	0.005
74.0	0.03	0.006	74.0	0.04	0.006
76.0	0.04	0.006	76.0	0.06	0.008
78.0	0.10	0.011	78.0	0.15	0.013
80.0	0.18	0.014	80.0	0.30	0.018
82.0	0.37	0.020	82.0	0.50	0.024
84.0	0.56	0.025	84.0	0.87	0.031
86.0	0.93	0.032	86.0	1.32	0.038
88.0	1.41	0.040	88.0	2.11	0.049
90.0	2.08	0.048	90.0	2.71	0.055
92.0	2.70	0.055	92.0	3.50	0.063
94.0	3.33	0.061	94.0	4.13	0.068
96.0	3.93	0.066	96.0	4.54	0.071
98.0	4.25	0.069	98.0	4.82	0.074
100.0	4.62	0.072	100.0	4.69	0.072
102.0	4.41	0.070	102.0	4.19	0.069
104.0	4.07	0.068	104.0	3.76	0.065
106.0	3.72	0.065	106.0	3.18	0.060
108.0	3.16	0.059	108.0	2.66	0.055
110.0	2.67	0.055	110.0	2.20	0.050
112.0	2.23	0.050	112.0	2.12	0.049
114.0	2.09	0.048	114.0	1.89	0.046
116.0	1.89	0.046	116.0	1.74	0.044
118.0	1.79	0.045	118.0	1.89	0.046
120.0	1.90	0.046	120.0	2.00	0.047
122.0	2.03	0.048	122.0	2.21	0.050
124.0	2.10	0.049	124.0	2.55	0.053
126.0	2.48	0.053	126.0	3.24	0.060
128.0	3.01	0.058	128.0	3.87	0.066
130.0	3.55	0.063	130.0	4.42	0.070
132.0	3.93	0.066	132.0	4.63	0.072
134.0	4.33	0.070	134.0	4.87	0.074
136.0	4.50	0.071	136.0	4.37	0.070
138.0	4.51	0.071	138.0	3.97	0.067
140.0	4.00	0.067	140.0	3.28	0.061
142.0	3.57	0.063	142.0	2.56	0.054
144.0	2.93	0.057	144.0	1.86	0.046
146.0	2.30	0.051	146.0	1.14	0.036
148.0	1.66	0.043	148.0	0.75	0.029
150.0	1.04	0.034	150.0	0.45	0.022
152.0	0.69	0.028	152.0	0.24	0.016
154.0	0.43	0.022	154.0	0.12	0.011
156.0	0.24	0.016	156.0	0.06	0.008
158.0	0.13	0.012	158.0	0.03	0.006
160.0	0.06	0.008	160.0	0.01	0.004
162.0	0.04	0.006			

1.8. E_n = 50 (45–55) MeV, Zöller (1995) [I.3]

Pre-neutron emission mass yield			Post-neutron emission mass yield		
Mass	Yield (%)	Uncertainty	Mass	Yield (%)	Uncertainty
74.0	0.04	0.009	74.0	0.07	0.012
76.0	0.07	0.012	76.0	0.10	0.014
78.0	0.16	0.017	78.0	0.22	0.021
80.0	0.24	0.021	80.0	0.36	0.026
82.0	0.44	0.029	82.0	0.67	0.036
84.0	0.71	0.037	84.0	0.95	0.043
86.0	0.99	0.044	86.0	1.38	0.052
88.0	1.39	0.052	88.0	1.96	0.061
90.0	1.98	0.062	90.0	2.63	0.071
92.0	2.51	0.070	92.0	3.19	0.078
94.0	3.00	0.076	94.0	3.63	0.084
96.0	3.44	0.081	96.0	4.06	0.089
98.0	3.77	0.085	98.0	4.36	0.092
100.0	4.15	0.089	100.0	4.19	0.090
102.0	4.04	0.088	102.0	3.89	0.087
104.0	3.76	0.085	104.0	3.72	0.085
106.0	3.51	0.082	106.0	3.43	0.081
108.0	3.30	0.080	108.0	3.13	0.078
110.0	3.23	0.079	110.0	3.04	0.077
112.0	2.82	0.074	112.0	2.91	0.075
114.0	2.82	0.074	114.0	2.82	0.074
116.0	2.75	0.073	116.0	2.95	0.075
118.0	2.65	0.072	118.0	2.93	0.075
120.0	2.78	0.073	120.0	3.01	0.076
122.0	2.85	0.074	122.0	3.38	0.081
124.0	2.89	0.075	124.0	3.57	0.083
126.0	3.26	0.079	126.0	3.82	0.086
128.0	3.37	0.081	128.0	4.03	0.088
130.0	3.64	0.084	130.0	4.33	0.091
132.0	3.81	0.086	132.0	4.21	0.091
134.0	4.08	0.089	134.0	3.87	0.086
136.0	4.05	0.088	136.0	3.41	0.081
138.0	3.69	0.084	138.0	2.82	0.074
140.0	3.35	0.080	140.0	2.35	0.067
142.0	2.79	0.073	142.0	1.57	0.055
144.0	2.38	0.068	144.0	1.12	0.046
146.0	1.69	0.057	146.0	0.79	0.039
148.0	1.27	0.049	148.0	0.53	0.032
150.0	0.90	0.042	150.0	0.26	0.022
152.0	0.62	0.035	152.0	0.16	0.018
154.0	0.34	0.026	154.0	0.08	0.012
156.0	0.23	0.021	156.0	0.05	0.010
158.0	0.10	0.014	158.0	0.01	0.005

1.9. E_n = 99.5 (89–110) MeV, Zöller (1995) [I.3]

Pre-neutron emission mass yield			Post-neutron emission mass yield		
Mass	Yield (%)	Uncertainty	Mass	Yield (%)	Uncertainty
			72.0	0.07	0.008
76.0	0.17	0.013	76.0	0.23	0.015
80.0	0.41	0.020	80.0	0.61	0.025
84.0	0.83	0.029	84.0	1.13	0.034
88.0	1.51	0.039	88.0	2.04	0.045
92.0	2.37	0.056	92.0	2.90	0.054
96.0	3.06	0.055	96.0	3.58	0.060
100.0	3.55	0.059	100.0	3.77	0.061
104.0	3.58	0.060	104.0	3.81	0.062
108.0	3.54	0.059	108.0	3.68	0.061
112.0	3.48	0.059	112.0	3.63	0.060
116.0	3.24	0.054	116.0	3.66	0.060
120.0	3.27	0.054	120.0	3.73	0.061
124.0	3.41	0.055	124.0	3.76	0.061
128.0	3.45	0.055	128.0	3.77	0.061
132.0	3.69	0.057	132.0	3.43	0.058
136.0	3.52	0.056	136.0	2.72	0.052
140.0	2.97	0.051	140.0	1.79	0.042
144.0	1.99	0.042	144.0	0.97	0.031
148.0	1.16	0.032	148.0	0.48	0.022
152.0	0.54	0.022	152.0	0.19	0.014
156.0	0.23	0.014	156.0	0.05	0.007
160.0	0.09	0.009			
164.0	0.02	0.004			

1.10. E_n = 160 (145–175) MeV, Zöller (1995) [I.3]

Pre-neutron emission mass yield			Post-neutron emission mass yield		
Mass	Yield (%)	Uncertainty	Mass	Yield (%)	Uncertainty
			68.0	0.04	0.008
72.0	0.10	0.012	72.0	0.12	0.014
76.0	0.23	0.019	76.0	0.32	0.022
80.0	0.48	0.027	80.0	0.67	0.032
84.0	0.95	0.038	84.0	1.34	0.045
88.0	1.66	0.050	88.0	2.22	0.058
92.0	2.43	0.061	92.0	2.82	0.066
96.0	2.86	0.066	96.0	3.41	0.072
100.0	3.36	0.072	100.0	3.71	0.075
104.0	3.54	0.074	104.0	3.83	0.076
108.0	3.71	0.075	108.0	3.90	0.077
112.0	3.68	0.075	112.0	3.76	0.076
116.0	3.51	0.073	116.0	3.75	0.076
120.0	3.59	0.074	120.0	3.99	0.078
124.0	3.79	0.076	124.0	3.71	0.075
128.0	3.48	0.073	128.0	3.59	0.074
132.0	3.46	0.073	132.0	3.02	0.068
136.0	2.96	0.067	136.0	2.56	0.063
140.0	2.49	0.062	140.0	1.66	0.050
144.0	1.77	0.052	144.0	0.92	0.038
148.0	1.03	0.040	148.0	0.42	0.025
152.0	0.54	0.029	152.0	0.18	0.017
156.0	0.25	0.020	156.0	0.08	0.011
160.0	0.11	0.013			
164.0	0.03	0.007			

2. ^{238}U PROTON INDUCED FISSION

Äystö et al. (1998) [I.11]

E_p = 20 MeV Pre-neutron emission mass yield			E_p = 60 MeV Pre-neutron emission mass yield		
Mass	Yield (%)	Uncertainty	Mass	Yield (%)	Uncertainty
74	5.0000E–02	3.0000E–03	74	1.0000E–01	6.0000E–03
76	8.0000E–02	4.8000E–03	76	1.3000E–01	7.8000E–03
78	1.5000E–01	9.0000E–03	78	2.2000E–01	1.3200E–02
80	3.0000E–01	1.8000E–02	80	4.0000E–01	2.4000E–02
82	4.2000E–01	2.5200E–02	82	6.2000E–01	3.7200E–02
84	9.0000E–01	5.4000E–02	84	1.0000E+00	3.0000E–02
86	1.3500E+00	4.0500E–02	86	1.4200E+00	4.2600E–02
88	1.9000E+00	5.7000E–02	88	1.8800E+00	5.6400E–02
90	2.5000E+00	7.5000E–02	90	2.3400E+00	7.0200E–02
92	3.0300E+00	9.0900E–02	92	2.7500E+00	8.2500E–02
94	3.5000E+00	1.0500E–01	94	3.0700E+00	9.2100E–02
96	3.8300E+00	1.1490E–01	96	3.2800E+00	9.8400E–02
98	4.0000E+00	4.0000E–02	98	3.4000E+00	1.0200E–01
100	3.9800E+00	1.1940E–01	100	3.4300E+00	1.0290E–01
102	3.8300E+00	1.1490E–01	102	3.4100E+00	1.0230E–01
104	3.5800E+00	1.0740E–01	104	3.3800E+00	1.0140E–01
106	3.2200E+00	9.6600E–02	106	3.2800E+00	9.8400E–02
108	2.8300E+00	8.4900E–02	108	3.2000E+00	9.6000E–02
110	2.5200E+00	7.5600E–02	110	3.1000E+00	9.3000E–02
112	2.2000E+00	6.6000E–02	112	3.0500E+00	9.1500E–02
114	1.9800E+00	5.9400E–02	114	3.0300E+00	9.0900E–02
116	1.8300E+00	5.4900E–02	116	3.0400E+00	9.1200E–02
118	1.8000E+00	5.4000E–02	118	3.0400E+00	9.1200E–02
120	1.8000E+00	5.4000E–02	120	3.0300E+00	9.0900E–02
122	1.8200E+00	5.4600E–02	122	3.0400E+00	9.1200E–02
124	1.9500E+00	5.8500E–02	124	3.0600E+00	9.1800E–02
126	2.1800E+00	6.5400E–02	126	3.1800E+00	9.5400E–02
128	2.4300E+00	7.2900E–02	128	3.2200E+00	9.6600E–02
130	2.8000E+00	8.4000E–02	130	3.3500E+00	1.0050E–01
132	3.1900E+00	9.5700E–02	132	3.3900E+00	1.0170E–01
134	3.5500E+00	1.0650E–01	134	3.4200E+00	1.0260E–01
136	3.8000E+00	1.1400E–01	136	3.4000E+00	1.0200E–01
138	3.9500E+00	1.1850E–01	138	3.3400E+00	1.0020E–01
140	4.0000E+00	4.0000E–02	140	3.1700E+00	9.5100E–02
142	3.8500E+00	1.1550E–01	142	2.8500E+00	8.5500E–02
144	3.5500E+00	1.0650E–01	144	2.5000E+00	7.5000E–02
146	3.1000E+00	9.3000E–02	146	2.0500E+00	6.1500E–02
148	2.5500E+00	7.6500E–02	148	1.6000E+00	4.8000E–02
150	1.9800E+00	5.9400E–02	150	1.1800E+00	3.5400E–02
152	1.4200E+00	4.2600E–02	152	7.8000E–01	4.6800E–02
154	9.4000E–01	5.6400E–02	154	5.0000E–01	3.0000E–02
156	5.8000E–01	3.4800E–02	156	3.0000E–01	1.8000E–02
158	3.3000E–01	1.9800E–02	158	1.8000E–01	1.0800E–02
160	1.8000E–01	1.0800E–02	160	1.0000E–01	6.0000E–03
162	1.0000E–01	6.0000E–03	162	5.0000E–02	3.0000E–03

Gindler et al. (1983) [I.12]
E_n = 0.17 MeV
Post-neutron emission chain yield

Mass	Yield (%)	Uncertainty
87	0.76	0.10
88	1.13	0.10
91	2.72	0.16
92	3.05	0.38
93	4.16	0.40
97	5.67	0.32
99	6.29	0.42
103	7.57	0.50
105	6.03	0.55
109	1.14	0.17
111	0.25	0.04
112	0.14	0.02
121	0.032	0.005
127	0.34	0.05
129	1.18	0.24
132	5.52	0.38
133	7.64	0.45
140	5.49	0.33
142	4.88	0.41
143	4.57	0.36

Gindler et al. (1983) [I.12]
E_n = 7.9 MeV
Post-neutron emission chain yield

Mass	Yield (%)	Uncertainty
87	0.93	0.16
88	1.73	0.20
91	3.03	0.19
92	3.51	0.44
93	4.03	0.50
97	5.13	0.52
99	5.49	0.39
103	5.66	0.39
105	4.74	0.41
109	1.16	0.17
111	0.66	0.10
112	0.59	0.09
127	1.08	0.16
129	1.67	0.33
132	4.92	0.39
133	6.24	0.36
140	5.49	0.34

Ford (1976) [I.13]
E_n = 14.0 MeV
Post-neutron emission chain yield

Mass	Yield (%)	Uncertainty
89	2.12	0.21
97	4.38	0.44
109	2.50	0.25
111	2.078	0.21
112	1.380	0.14
140	4.19	0.42
144	2.87	0.29
147	1.89	0.19
156	0.230	0.023
161	0.0196	0.002

Laurec et al. (1981) [I.14]
E_n = 14.7 MeV
Post-neutron emission chain yield

Mass	Yield (%)	Uncertainty
95	3.9600E+00	1.5444E–01
97	4.4000E+00	1.9800E–01
99	5.0400E+00	1.8144E–01
103	5.3000E+00	1.9610E–01
105	4.3000E+00	1.9780E–01
127	2.1700E+00	9.5480E–02
132	3.1500E+00	1.1655E–01
131	4.5500E+00	2.1840E–01
133	4.2500E+00	3.8250E–01
140	3.6000E+00	1.3680E–01
141	3.6800E+00	1.5088E–01
143	2.9300E+00	1.1720E–01
144	2.5900E+00	1.8907E–01
147	1.6400E+00	6.8880E–02

4. ^{242}Pu NEUTRON INDUCED FISSION

Winkelmann et al. (1984) [I.15] E_n = 15.1 MeV Post-neutron emission chain yield			Winkelmann et al. (1984) [I.15] E_n = 15.1 MeV Post-neutron emission chain yield		
Mass	Yield (%)	Uncertainty	Mass	Yield (%)	Uncertainty
85	0.00672	0.00048	118	0.0042	0.0007
87	0.00995	0.00076	121	0.0076	0.0017
88	0.0118	0.0010	125	0.0135	0.0024
89	0.0133	0.0015	127	0.0188	0.0022
91	0.0207	0.0011	128	0.0171	0.0024
92	0.0238	0.0021	129	0.0211	0.0016
93	0.0260	0.0034	131	0.0391	0.0024
94	0.0280	0.0028	132	0.0513	0.0023
95	0.0337	0.0030	133	0.0560	0.0030
97	0.0423	0.0022	134	0.0583	0.0070
99	0.0484	0.0025	135	0.0575	0.0038
101	0.0504	0.0050	138	0.0502	0.0046
103	0.0564	0.0045	139	0.0493	0.0038
104	0.0545	0.0066	140	0.0491	0.0030
105	0.0550	0.0030	141	0.0486	0.0040
107	0.0380	0.0038	142	0.0434	0.0033
109	0.0253	0.0022	143	0.0366	0.0026
111	0.0220	0.0024	144	0.0319	0.0027
112	0.0192	0.0014	146	0.0218	0.0019
113	0.0178	0.0025	149	0.0161	0.0016
115	0.0123	0.0016	151	0.0092	0.0009
117	0.0065	0.0011			

Appendix II

DATA ADJUSTMENT FOR MASS RESOLUTION

Liu Tingjin
China Institute of Atomic Energy, China

A method and code have been developed for mass resolution adjustment of mass distribution data measured by means of the kinetic energy method. Data were smoothed before adjustment with a second order function for 7 or 9 adjacent points, and the investigation shows that taking too few or too many data points in the smoothing procedure could lead to unreasonable results. The code was tested by folding the adjusted data with a Gaussian distribution and a resolution width the same as the one used in the adjustment procedure. Results were practically identical to the original unadjusted input data. The data uncertainties were also adjusted by the code. This code has subsequently been applied to re-define the mass distribution data measurements of Zöller, Vivès and Äystö by the kinetic energy method.

II.1. INTRODUCTION

The fission yield for each product nuclide measured by the kinetic energy or double time-of-flight method is not a true mass yield but, due to incomplete mass resolution, the sum of contributions from several adjacent masses, the yields of which are each folded by a Gaussian distribution function. They must be adjusted for mass resolution in order to obtain the true yield.

II.2. ADJUSTMENT METHOD AND CODE

According to Schmitt [II.1], the adjustment can be done using the following formula:

$$Y_C(A) = Y_U(A) - \frac{\sigma^2}{2}\frac{d^2 Y_C(A)}{dA^2} \qquad \text{(II.1)}$$

where Y_C, Y_U are the corrected/adjusted and uncorrected/unadjusted yields respectively, and σ is the mass resolution, defined as half-width at half-maximum (σ is erroneously called the full width in Ref. [II.1]).

To avoid the effect of statistical fluctuation, the data were smoothed before adjustment by fitting with a second order function for every 5 adjacent data points,

$$Y(A) = a + bA + cA^2 \qquad \text{(II.2)}$$

and the yield of the central mass was taken as the new yield at that mass. For the first and last two data points at the ends of the measured mass distributions, the results of the respective complete 5 point fits for the corresponding third points from the ends were used as the adjusted yields.

The coefficients *a, b, c* were obtained from the following group of equations, which were deduced by the least squares method for each group of 5 data points:

$$\left(\sum_{i=n}^{N} w_i\right)a + \left(\sum_{i=n}^{N} w_i A_i\right)b + \left(\sum_{Ii=n}^{N} w_i A_i^2\right)c = \sum_{i=n}^{N} w_i Y_i$$

$$\left(\sum_{i=n}^{N} w_i A_i\right)a + \left(\sum_{i=n}^{N} w_i A_i^2\right)b + \left(\sum_{Ii=n}^{N} w_i A_i^3\right)c = \sum_{i=n}^{N} w_i Y_i A_i$$

$$\left(\sum_{i=n}^{N} w_i A_i^2\right)a + \left(\sum_{i=n}^{N} w_i A_i^3\right)b + \left(\sum_{Ii=n}^{N} w_i A_i^4\right)c = \sum_{i=n}^{N} w_i Y_i A_i^2 \qquad \text{(II.3)}$$

where $N = n + 5$, $n = 1, 2, \ldots\ldots(M - 4)$, and M is the total number of data points to be fitted.

The double differential of Eq. (II.2) with respect to A is $2c$, so Eq. (II.1) becomes

$$Y_C(A) = Y_U(A) - c\,\sigma^2 \qquad \text{(II.4)}$$

The data were adjusted using Eq. (II.4). σ reflects the uncertainty due to the experimental conditions and is usually given by the author in the publication.

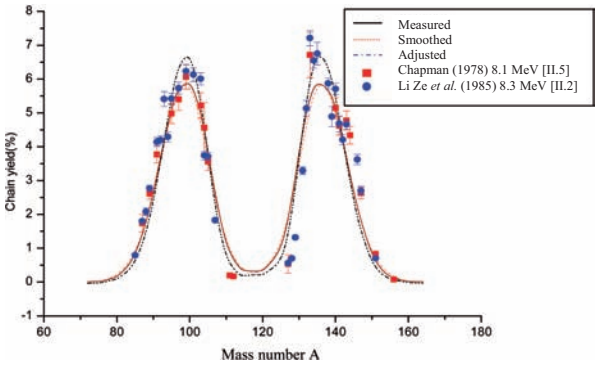

FIG. II.1. Comparison of adjusted Zöller data at 7 MeV [II.7] with data measured by the radiochemical method.

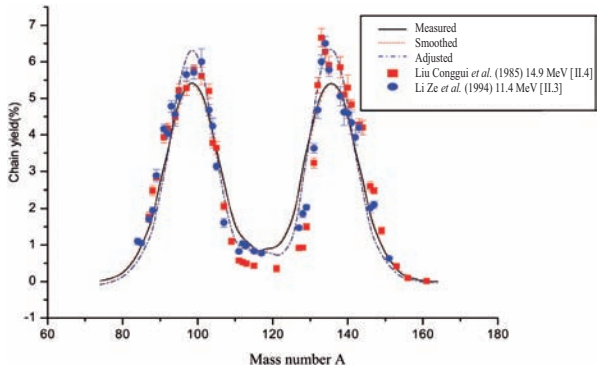

FIG. II.2. Comparison of adjusted Zöller data at 13 MeV [II.7] with data measured by the radiochemical method.

A code was developed with the following features: instead of $Y_C(A)$, $Y_U(A)$ was used as 0 rank approximation in the double differential, because $Y_C(A)$ was unknown. $Y_U(A)$ was smoothed and a_0, b_0, c_0 were obtained from group Eq. (II.3). By using coefficient c_0, $Y_{C1}(A)$ was calculated from Eq. (II.4′)

$$Y_{C1}(A) = Y_U(A) - c_0\,\sigma^2 \qquad \text{(II.4′)}$$

Smoothing $Y_{C1}(A)$, coefficients a_1, b_1, c_1 were obtained from Eq. (II.3); and using c_1, $Y_{C2}(A)$ was calculated from Eq. (II.4′), and so on. Iteration was continued until convergence. The following convergence criterion was used in the code: $\varepsilon = (Y_{Cn+1}(A) - Y_{Cn}(A))/\,Y_{Cn}(A) < 0.000001$ for all mass numbers A, which means that $Y_{Cn+1}(A)$ and $Y_{Cn}(A)$ agree within 5 significant figures.

II.3. TESTING THE CODE

The method and code were tested. Figures II.1 and II.2 show Zöller data [II.7] in original, smoothed and adjusted form at 7 and 13 MeV respectively, compared with the data of Li Ze [II.2, II.3], Liu Conggui [II.4] and Chapman [II.5] measured at similar energies by the radiochemical method. The σ values used in the adjustments are 3.3 and 3.675 for 7 and 13 MeV, respectively, as given by the author. The adjusted data are basically in agreement within the uncertainty limits with the data measured by the radiochemical method, in which the mass resolution problem does not exist.

Using the INTERP code [II.6], the adjusted data (smoothed over 7 points) at 13 MeV were folded on the basis of a Gaussian resolution function with $\sigma = 3.675$, which is the value given in

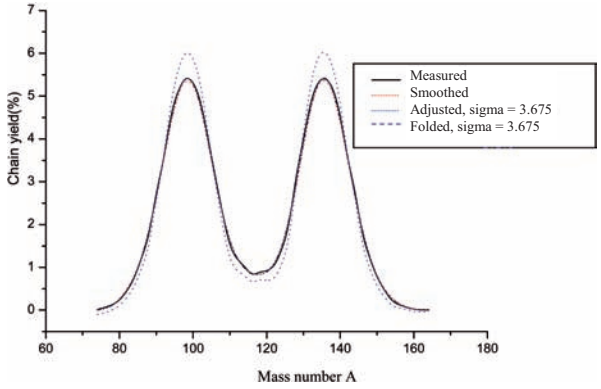

FIG. II.3. Comparison of folded adjusted data with measured data at 13 MeV.

Ref. [II.7] for the mass resolution in the measurement. The results should reproduce the originally measured data. As shown in Fig. II.3, the folded data agree well with the original data, which proves the reliability of the method and code.

II.4. PRACTICAL ADJUSTMENTS

When smoothing the measured data, the adoption of 5 adjacent points (as shown in the equations) was not enough to obtain good results: the iterations did not converge, there were some unreasonable fluctuations in the adjusted data, and incorrect results appeared with increasing iteration times. An attempt was made to solve the problem by smoothing the data twice, but this approach did not always work. It turned out to be more efficient to smooth the data over 7 points, so that $\boldsymbol{N} = n + 7$, and $n = 1, 2, \ldots\ldots (M - 6)$ in Eq. (II.3); investigations showed that the iterations were convergent and gave more reasonable results for the adjustments (see Figs II.1 and II.2) of the data measured by

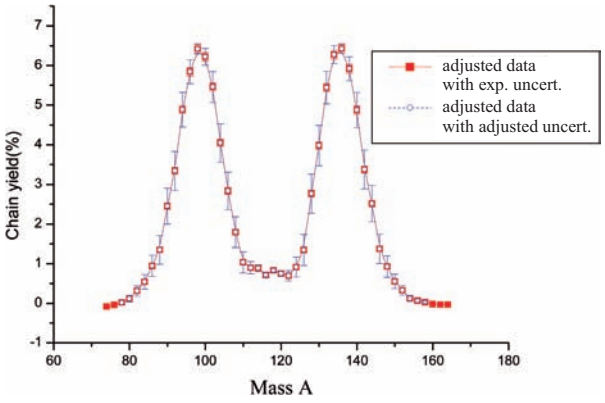

FIG. II.4. Intercomparison between adjusted uncertainty and original experimental uncertainty at E_n = 13 MeV.

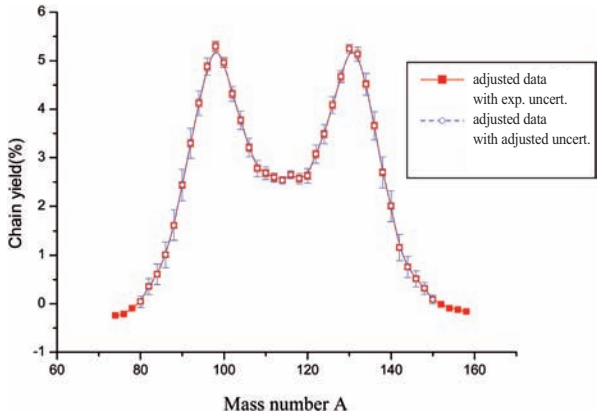

FIG. II.5. Intercomparison between adjusted uncertainty and original experimental uncertainty at E_n = 50 MeV.

Vivès [II.8], Zöller [II.7] and Äystö [II.9], except for Zöller data at 50 MeV (both post- and pre-neutron emission). When Zöller data at 50 MeV were smoothed over 9 data points, the iteration was convergent and reasonable results were obtained. The data were adjusted in the following way: first smoothed over 7 (or 9) data points according to Eq. (II.3), and then modified according to Eq. (II.4).

A crucial criterion for the success of the adjustment is the choice of the number of data points in a group used in the smoothing procedure. If too few data points are used in Eq. (II.3) to smooth out the statistical fluctuations, the iterations do not converge and there would be unreasonable structures in the adjusted data. If too many data points are used in Eq. (II.3), the true structures in the mass distribution may be smoothed out. Best results were obtained with 7 data points for most of the measured data, and with 9 data points for data with larger fluctuations. The adjusted data with original experimental uncertainties are listed in Annex 1.

II.5. ADJUSTMENT OF DATA UNCERTAINTIES

For the fission yield data measured by the kinetic energy or the double time-of-flight method, the uncertainty of the mass calibration (by energy measurement or the time-of-flight method) could make a contribution to the total uncertainty of a yield. At the peak, valley and wings (Figs II.1 and II.2) the uncertainties due to mass calibration are smaller, but on the slopes of the light and heavy peak (where the yields vary rapidly with mass A) they could be larger. In comparison with the data measured by the radiochemical method (where this kind of problem does not exist), the uncertainty of the mass calibration could be ±1 mass unit.

The data were smoothed with the function $Y = a + bA + cA^2$, and the first differential is

$$\frac{dY}{dA} = b + 2cA$$

and the uncertainty due to the mass calibration is

$$\Delta Y = (b + 2cA)\,\Delta A \qquad \text{(II.5)}$$

Total uncertainty ΔY composed of the yield measurement ΔY_1 (mainly counting statistics) and the mass calibration uncertainty ΔY_2 is given by the expression:

$$\Delta Y = (\Delta Y_1^2 + \Delta Y_2^2)^{1/2} \qquad \text{(II.6)}$$

By using Eq. (II.5) and taking ΔA = 1, the uncertainties ΔY_2 from the mass calibration were calculated, and ΔY_1 were taken as given by the authors. The total uncertainties ΔY were calculated from Eq. (II.6). Adjusted data with adjusted uncertainties are given in Annex 2, and the comparison of the adjusted uncertainty with the original data is given in Figs II.4 and II.5 as examples.

REFERENCES TO APPENDIX II

[II.1] SCHMITT, H.W., et al., Precision measurements of correlated energies and velocities of ^{252}Cf fission fragments, Phys. Rev. **137** (1965) B837–B847 (EXFOR 13081002).

[II.2] LI ZE, et al., Mass distribution in 8.3 MeV neutron-induced fission of ^{238}U, Chin. J. Nucl. Phys. **7** (1985) 97–105.

[II.3] LI ZE, et al., Fission product yields from 11.3 MeV neutron-induced fission of ^{238}U, Radiochim. Acta **64** (1994) 95–97.

[II.4] LIU CONGGUI, et al., The mass distribution in 14.9 MeV of ^{238}U neutron-induced fission, Chin. J. Nucl. Phys. **7** (1985) 235–241.

[II.5] CHAPMAN, T.C., Fission product yields from 6–9 MeV neutron-induced fission of ^{235}U and ^{238}U, Phys. Rev. C **17** (1978) 1089–1097.

[II.6] LIU TINGJIN, internal document, China Nuclear Data Centre, China Institute of Atomic Energy, Beijing (2002).

[II.7] ZÖLLER, C.M., Untersuchung der neutronen-induzierten Spaltung von ^{238}U im Energiebereich von 1 MeV bis 500 MeV, PhD Thesis, Technische Universität Darmstadt, Germany (1995).

[II.8] VIVÈS, F., et al., Investigation of the fission fragment properties of the reaction ^{238}U(n,f) at incident neutron energies up to 5.8 MeV, Nucl. Phys. A **662** (2000) 63–92.

[II.9] ÄYSTÖ, J., et al., "New results on superasymmetric fission at intermediate energy", Fission and Properties of Neutron-rich Nuclei (Proc. Int. Conf. Sanibel Island, FL, 1997) (HAMILTON, J.H., RAMAYYA, A.V., Eds), World Scientific, Singapore (1998) 457–466.

Annex 1 to Appendix II

ADJUSTED DATA MEASURED BY VIVÈS, ZÖLLER AND ÄYSTÖ

Vivès et al. (2000) [II.8]

E_n = 1.60 MeV Pre-neutron emission			E_n = 5.5 MeV Pre-neutron emission		
Mass A	Yield (%)	Uncertainty	Mass A	Yield (%)	Uncertainty
			6.7000E+01	2.7711E–04	5.5385E–05
			6.8000E+01	2.7711E–04	5.5385E–05
			6.9000E+01	9.6940E–04	1.1077E–04
			7.0000E+01	2.3540E–03	2.2154E–04
			7.1000E+01	3.2430E–03	2.7692E–04
			7.2000E+01	4.2099E–03	3.3231E–04
			7.3000E+01	4.1060E–03	3.3231E–04
			7.4000E+01	5.3387E–03	4.9846E–04
7.5000E+01	–4.3656E–03	1.4209E–04	7.5000E+01	6.0832E–03	6.6462E–04
			7.6000E+01	7.8019E–03	9.9693E–04
			7.7000E+01	1.1983E–02	1.6062E–03
7.8000E+01	2.7388E–03	7.1044E–04	7.8000E+01	2.9070E–02	3.3785E–03
7.9000E+01	8.0673E–03	1.1367E–03	7.9000E+01	3.5724E–02	4.5416E–03
8.0000E+01	1.3395E–02	1.5630E–03	8.0000E+01	8.9406E–02	9.5262E–03
8.1000E+01	2.8005E–02	3.5522E–03	8.1000E+01	1.3484E–01	1.3791E–02
8.2000E+01	3.8401E–02	5.8256E–03	8.2000E+01	2.1427E–01	2.0825E–02
8.3000E+01	9.8707E–02	1.3498E–02	8.3000E+01	3.0298E–01	2.8523E–02
8.4000E+01	3.5164E–01	3.5664E–02	8.4000E+01	4.4530E–01	4.0597E–02
8.5000E+01	4.2392E–01	4.2484E–02	8.5000E+01	5.7356E–01	5.2671E–02
8.6000E+01	6.4248E–01	5.9961E–02	8.6000E+01	8.1798E–01	7.3053E–02
8.7000E+01	8.7907E–01	7.8575E–02	8.7000E+01	1.0490E+00	6.9203E–02
8.8000E+01	1.3097E+00	8.5573E–02	8.8000E+01	1.4099E+00	9.0554E–02
8.9000E+01	1.6787E+00	1.0880E–01	8.9000E+01	1.7439E+00	1.1082E–01
9.0000E+01	2.1215E+00	1.3289E–01	9.0000E+01	2.2224E+00	1.4003E–01
9.1000E+01	2.5971E+00	1.5878E–01	9.1000E+01	2.5176E+00	1.5781E–01
9.2000E+01	3.2447E+00	1.9235E–01	9.2000E+01	3.0491E+00	1.8485E–01
9.3000E+01	3.7560E+00	2.1665E–01	9.3000E+01	3.8910E+00	2.2580E–01
9.4000E+01	4.3424E+00	1.6532E–01	9.4000E+01	4.4983E+00	1.7056E–01
9.5000E+01	4.4360E+00	1.7193E–01	9.5000E+01	4.6434E+00	1.7817E–01
9.6000E+01	4.6361E+00	1.8528E–01	9.6000E+01	4.7660E+00	1.8919E–01
9.7000E+01	4.9172E+00	2.0013E–01	9.7000E+01	4.9223E+00	1.9955E–01
9.8000E+01	5.0394E+00	2.0603E–01	9.8000E+01	5.2338E+00	2.1104E–01
9.9000E+01	5.5539E+00	2.2414E–01	9.9000E+01	5.8253E+00	2.2946E–01
1.0000E+02	6.1263E+00	2.4283E–01	1.0000E+02	6.0551E+00	2.3503E–01
1.0100E+02	6.3753E+00	2.4865E–01	1.0100E+02	6.1702E+00	2.3860E–01
1.0200E+02	6.4716E+00	2.4574E–01	1.0200E+02	5.9899E+00	2.3001E–01
1.0300E+02	6.6572E+00	2.4404E–01	1.0300E+02	5.9916E+00	2.2533E–01
1.0400E+02	7.0271E+00	2.5185E–01	1.0400E+02	6.1456E+00	2.2531E–01
1.0500E+02	6.3598E+00	2.2620E–01	1.0500E+02	5.6174E+00	2.0346E–01
1.0600E+02	5.2813E+00	1.9615E–01	1.0600E+02	4.7795E+00	1.7945E–01
1.0700E+02	3.9937E+00	1.6454E–01	1.0700E+02	3.6097E+00	2.2065E–01
1.0800E+02	2.6459E+00	1.8511E–01	1.0800E+02	2.5537E+00	1.7218E–01
1.0900E+02	1.5191E+00	1.2138E–01	1.0900E+02	1.6316E+00	1.2046E–01
1.1000E+02	7.4444E–01	6.9268E–02	1.1000E+02	1.0536E+00	8.1873E–02
1.1100E+02	3.9131E–01	5.0583E–02	1.1100E+02	7.3045E–01	7.7096E–02
1.1200E+02	2.6189E–01	3.2964E–02	1.1200E+02	4.0852E–01	4.6357E–02
1.1300E+02	8.7609E–02	1.3783E–02	1.1300E+02	2.5812E–01	3.0295E–02
1.1400E+02	5.8556E–02	7.8149E–03	1.1400E+02	1.5572E–01	1.8000E–02

E_n = 1.60 MeV Pre-neutron emission			E_n = 5.5 MeV Pre-neutron emission		
Mass A	Yield (%)	Uncertainty	Mass A	Yield (%)	Uncertainty
1.1500E+02	3.1986E–02	4.1206E–03	1.1500E+02	1.2397E–01	1.2794E–02
1.1600E+02	1.5134E–02	2.1313E–03	1.1600E+02	1.1322E–01	1.0523E–02
1.1700E+02	8.7290E–03	1.2788E–03	1.1700E+02	9.7121E–02	8.8062E–03
1.1800E+02	4.9015E–03	8.5253E–04	1.1800E+02	9.1891E–02	8.3631E–03
1.1900E+02	1.8036E–03	5.6835E–04	1.1900E+02	6.3970E–02	6.4246E–03
1.2000E+02	1.8036E–03	5.6835E–04	1.2000E+02	6.3970E–02	6.4246E–03
1.2100E+02	4.9015E–03	8.5253E–04	1.2100E+02	9.1891E–02	8.3631E–03
1.2200E+02	8.7290E–03	1.2788E–03	1.2200E+02	9.7121E–02	8.8062E–03
1.2300E+02	1.5134E–02	2.1313E–03	1.2300E+02	1.1322E–01	1.0523E–02
1.2400E+02	3.1986E–02	4.1206E–03	1.2400E+02	1.2397E–01	1.2794E–02
1.2500E+02	5.8556E–02	7.8149E–03	1.2500E+02	1.5572E–01	1.8000E–02
1.2600E+02	8.7609E–02	1.3783E–02	1.2600E+02	2.5812E–01	3.0295E–02
1.2700E+02	2.6189E–01	3.2964E–02	1.2700E+02	4.0852E–01	4.6357E–02
1.2800E+02	3.9131E–01	5.0583E–02	1.2800E+02	7.3045E–01	7.7096E–02
1.2900E+02	7.4444E–01	6.9268E–02	1.2900E+02	1.0536E+00	8.1873E–02
1.3000E+02	1.5191E+00	1.2138E–01	1.3000E+02	1.6316E+00	1.2046E–01
1.3100E+02	2.6459E+00	1.8511E–01	1.3100E+02	2.5537E+00	1.7218E–01
1.3200E+02	3.9937E+00	1.6454E–01	1.3200E+02	3.6097E+00	2.2065E–01
1.3300E+02	5.2813E+00	1.9615E–01	1.3300E+02	4.7795E+00	1.7945E–01
1.3400E+02	6.3598E+00	2.2620E–01	1.3400E+02	5.6174E+00	2.0346E–01
1.3500E+02	7.0271E+00	2.5185E–01	1.3500E+02	6.1456E+00	2.2531E–01
1.3600E+02	6.6572E+00	2.4404E–01	1.3600E+02	5.9916E+00	2.2533E–01
1.3700E+02	6.4716E+00	2.4574E–01	1.3700E+02	5.9899E+00	2.3001E–01
1.3800E+02	6.3753E+00	2.4865E–01	1.3800E+02	6.1702E+00	2.3860E–01
1.3900E+02	6.1263E+00	2.4283E–01	1.3900E+02	6.0551E+00	2.3503E–01
1.4000E+02	5.5539E+00	2.2414E–01	1.4000E+02	5.8253E+00	2.2946E–01
1.4100E+02	5.0394E+00	2.0603E–01	1.4100E+02	5.2338E+00	2.1104E–01
1.4200E+02	4.9172E+00	2.0013E–01	1.4200E+02	4.9223E+00	1.9955E–01
1.4300E+02	4.6361E+00	1.8528E–01	1.4300E+02	4.7660E+00	1.8919E–01
1.4400E+02	4.4360E+00	1.7193E–01	1.4400E+02	4.6434E+00	1.7817E–01
1.4500E+02	4.3424E+00	1.6532E–01	1.4500E+02	4.4983E+00	1.7056E–01
1.4600E+02	3.7560E+00	2.1665E–01	1.4600E+02	3.8910E+00	2.2580E–01
1.4700E+02	3.2447E+00	1.9235E–01	1.4700E+02	3.0491E+00	1.8485E–01
1.4800E+02	2.5971E+00	1.5878E–01	1.4800E+02	2.5176E+00	1.5781E–01
1.4900E+02	2.1215E+00	1.3289E–01	1.4900E+02	2.2224E+00	1.4003E–01
1.5000E+02	1.6787E+00	1.0880E–01	1.5000E+02	1.7439E+00	1.1082E–01
1.5100E+02	1.3097E+00	8.5573E–02	1.5100E+02	1.4099E+00	9.0554E–02
1.5200E+02	8.7907E–01	7.8575E–02	1.5200E+02	1.0490E+00	6.9203E–02
1.5300E+02	6.4248E–01	5.9961E–02	1.5300E+02	8.1798E–01	7.3053E–02
1.5400E+02	4.2392E–01	4.2484E–02	1.5400E+02	5.7356E–01	5.2671E–02
1.5500E+02	3.5164E–01	3.5664E–02	1.5500E+02	4.4530E–01	4.0597E–02
1.5600E+02	9.8707E–02	1.3498E–02	1.5600E+02	3.0298E–01	2.8523E–02
1.5700E+02	3.8401E–02	5.8256E–03	1.5700E+02	2.1427E–01	2.0825E–02
1.5800E+02	2.8005E–02	3.5522E–03	1.5800E+02	1.3484E–01	1.3791E–02
1.5900E+02	1.3395E–02	1.5630E–03	1.5900E+02	8.9406E–02	9.5262E–03
1.6000E+02	8.0673E–03	1.1367E–03	1.6000E+02	3.5724E–02	4.5416E–03
1.6100E+02	2.7388E–03	7.1044E–04	1.6100E+02	2.9070E–02	3.3785E–03
			1.6200E+02	1.1983E–02	1.6062E–03
			1.6300E+02	7.8019E–03	9.9693E–04
1.6400E+02	–4.3656E–03	1.4209E–04	1.6400E+02	6.0832E–03	6.6462E–04
			1.6500E+02	5.3387E–03	4.9846E–04
			1.6600E+02	4.1060E–03	3.3231E–04
			1.6700E+02	4.2099E–03	3.3231E–04
			1.6800E+02	3.2430E–03	2.7692E–04
			1.6900E+02	2.3540E–03	2.2154E–04
			1.7000E+02	9.6940E–04	1.1077E–04
			1.7100E+02	2.7711E–04	5.5385E–05
			1.7200E+02	2.7711E–04	5.5385E–05

Zöller (1995) [II.7]

E_n = 13 (11.5–14.5) MeV Post-neutron emission			E_n = 20 (18–2–22) MeV Post-neutron emission		
Mass A	Yield (%)	Uncertainty	Mass A	Yield (%)	Uncertainty
7.4000E+01	–8.1187E–02	6.0000E–03	7.4000E+01	–8.8686E–02	1.0000E–02
7.6000E+01	–4.1187E–02	1.2000E–02	7.6000E+01	–3.8686E–02	1.5000E–02
7.8000E+01	1.8813E–02	1.7000E–02	7.8000E+01	–8.6862E–03	1.8000E–02
8.0000E+01	1.1881E–01	2.3000E–02	8.0000E+01	2.0131E–01	2.9000E–02
8.2000E+01	3.0957E–01	3.2000E–02	8.2000E+01	2.9589E–01	3.4000E–02
8.4000E+01	5.4075E–01	4.1000E–02	8.4000E+01	6.0174E–01	4.6000E–02
8.6000E+01	9.4186E–01	5.3000E–02	8.6000E+01	1.0079E+00	5.8000E–02
8.8000E+01	1.3488E+00	6.3000E–02	8.8000E+01	1.5159E+00	6.9000E–02
9.0000E+01	2.4527E+00	8.1000E–02	9.0000E+01	2.4023E+00	8.3000E–02
9.2000E+01	3.3420E+00	9.0000E–02	9.2000E+01	3.5812E+00	9.6000E–02
9.4000E+01	4.8841E+00	1.0400E–01	9.4000E+01	4.5505E+00	1.0400E–01
9.6000E+01	5.8441E+00	1.1000E–01	9.6000E+01	5.5173E+00	1.1000E–01
9.8000E+01	6.4219E+00	1.1300E–01	9.8000E+01	6.0553E+00	1.1400E–01
1.0000E+02	6.2181E+00	1.1200E–01	1.0000E+02	5.7786E+00	1.1200E–01
1.0200E+02	5.4582E+00	1.0800E–01	1.0200E+02	5.2153E+00	1.1000E–01
1.0400E+02	4.0475E+00	9.7000E–02	1.0400E+02	3.8440E+00	9.9000E–02
1.0600E+02	2.8362E+00	8.6000E–02	1.0600E+02	2.7515E+00	8.9000E–02
1.0800E+02	1.7950E+00	7.3000E–02	1.0800E+02	1.9950E+00	7.9000E–02
1.1000E+02	1.0332E+00	5.8000E–02	1.1000E+02	1.5075E+00	6.9000E–02
1.1200E+02	8.9544E–01	5.3000E–02	1.1200E+02	1.4368E+00	6.6000E–02
1.1400E+02	8.8351E–01	4.9000E–02	1.1400E+02	1.1806E+00	5.9000E–02
1.1600E+02	7.1250E–01	4.3000E–02	1.1600E+02	1.0338E+00	5.5000E–02
1.1800E+02	8.3191E–01	4.6000E–02	1.1800E+02	1.2503E+00	5.9000E–02
1.2000E+02	7.5065E–01	4.6000E–02	1.2000E+02	1.2416E+00	6.1000E–02
1.2200E+02	6.9458E–01	4.8000E–02	1.2200E+02	1.2858E+00	6.5000E–02
1.2400E+02	9.1531E–01	5.7000E–02	1.2400E+02	1.4537E+00	7.0000E–02
1.2600E+02	1.3478E+00	6.7000E–02	1.2600E+02	2.1264E+00	8.2000E–02
1.2800E+02	2.7680E+00	8.6000E–02	1.2800E+02	3.2068E+00	9.4000E–02
1.3000E+02	3.9817E+00	9.7000E–02	1.3000E+02	4.6837E+00	1.0600E–01
1.3200E+02	5.4409E+00	1.0700E–01	1.3200E+02	5.6061E+00	1.1100E–01
1.3400E+02	6.2736E+00	1.1200E–01	1.3400E+02	6.1981E+00	1.1400E–01
1.3600E+02	6.4255E+00	1.1300E–01	1.3600E+02	5.8150E+00	1.1100E–01
1.3800E+02	5.9191E+00	1.1100E–01	1.3800E+02	4.9785E+00	1.7000E–01
1.4000E+02	4.8756E+00	1.0400E–01	1.4000E+02	3.8589E+00	9.9000E–02
1.4200E+02	3.3774E+00	9.1000E–02	1.4200E+02	2.8917E+00	8.9000E–02
1.4400E+02	2.5176E+00	8.2000E–02	1.4400E+02	1.7922E+00	7.4000E–02
1.4600E+02	1.3749E+00	6.4000E–02	1.4600E+02	1.2367E+00	6.3000E–02
1.4800E+02	9.2647E–01	5.3000E–02	1.4800E+02	6.8348E–01	4.9000E–02
1.5000E+02	5.5202E–01	4.2000E–02	1.5000E+02	3.9955E–01	3.8000E–02
1.5200E+02	3.2973E–01	3.3000E–02	1.5200E+02	2.8095E–01	3.2000E–02
1.5400E+02	1.2060E–01	2.2000E–02	1.5400E+02	1.0621E–01	2.2000E–02
1.5600E+02	6.6397E–02	1.7000E–02	1.5600E+02	6.2059E–03	1.6000E–02
1.5800E+02	2.9809E–02	1.3000E–02	1.5800E+02	–5.3794E–02	1.0000E–02
1.6000E+02	–2.0191E–02	6.0000E–03	1.6000E+02	–7.3794E–02	6.0000E–03
1.6200E+02	–3.0191E–02	3.0000E–03			
1.6400E+02	–3.0191E–02	4.0000E–03			

E_n = 27.5 (22–33) MeV Post-neutron emission			E_n = 27.5 (22–33) MeV Pre-neutron emission		
Mass A	Yield (%)	Uncertainty	Mass A	Yield (%)	Uncertainty
7.2000E+01	–8.5067E–02	5.0000E–03			
7.4000E+01	–6.5067E–02	6.0000E–03	7.4000E+01	–8.2944E–02	6.0000E–03
7.6000E+01	–4.5067E–02	8.0000E–03	7.6000E+01	–7.2944E–02	6.0000E–03
7.8000E+01	4.4933E–02	1.3000E–02	7.8000E+01	–1.2944E–02	1.1000E–02
8.0000E+01	1.6800E–01	1.8000E–02	8.0000E+01	6.7056E–02	1.4000E–02
8.2000E+01	3.0940E–01	2.4000E–02	8.2000E+01	2.3382E–01	2.0000E–02
8.4000E+01	5.8619E–01	3.1000E–02	8.4000E+01	3.6967E–01	2.5000E–02
8.6000E+01	9.4302E–01	3.8000E–02	8.6000E+01	6.6278E–01	3.2000E–02
8.8000E+01	1.6845E+00	4.9000E–02	8.8000E+01	1.0760E+00	4.0000E–02
9.0000E+01	2.3728E+00	5.5000E–02	9.0000E+01	1.7408E+00	4.8000E–02
9.2000E+01	3.4702E+00	6.3000E–02	9.2000E+01	2.4637E+00	5.5000E–02
9.4000E+01	4.6021E+00	6.8000E–02	9.4000E+01	3.3561E+00	6.1000E–02
9.6000E+01	5.4842E+00	7.1000E–02	9.6000E+01	4.3293E+00	6.6000E–02
9.8000E+01	5.9471E+00	7.4000E–02	9.8000E+01	5.0102E+00	6.9000E–02
1.0000E+02	5.5870E+00	7.2000E–02	1.0000E+02	5.5580E+00	7.2000E–02
1.0200E+02	4.5363E+00	6.9000E–02	1.0200E+02	5.2116E+00	7.0000E–02
1.0400E+02	3.5806E+00	6.5000E–02	1.0400E+02	4.4781E+00	6.8000E–02
1.0600E+02	2.7268E+00	6.0000E–02	1.0600E+02	3.6849E+00	6.5000E–02
1.0800E+02	2.1787E+00	5.5000E–02	1.0800E+02	2.8284E+00	5.9000E–02
1.1000E+02	1.8433E+00	5.0000E–02	1.1000E+02	2.2327E+00	5.5000E–02
1.1200E+02	1.9328E+00	4.9000E–02	1.1200E+02	1.8397E+00	5.0000E–02
1.1400E+02	1.8091E+00	4.6000E–02	1.1400E+02	1.8321E+00	4.8000E–02
1.1600E+02	1.6767E+00	4.4000E–02	1.1600E+02	1.7552E+00	4.6000E–02
1.1800E+02	1.7591E+00	4.6000E–02	1.1800E+02	1.7178E+00	4.5000E–02
1.2000E+02	1.7005E+00	4.7000E–02	1.2000E+02	1.8074E+00	4.6000E–02
1.2200E+02	1.7104E+00	5.0000E–02	1.2200E+02	1.8275E+00	4.8000E–02
1.2400E+02	1.9321E+00	5.3000E–02	1.2400E+02	1.7375E+00	4.9000E–02
1.2600E+02	2.7520E+00	6.0000E–02	1.2600E+02	2.0311E+00	5.3000E–02
1.2800E+02	3.8176E+00	6.6000E–02	1.2800E+02	2.6095E+00	5.8000E–02
1.3000E+02	5.0083E+00	7.0000E–02	1.3000E+02	3.4002E+00	6.3000E–02
1.3200E+02	5.7124E+00	7.2000E–02	1.3200E+02	4.1910E+00	6.6000E–02
1.3400E+02	6.0344E+00	7.4000E–02	1.3400E+02	5.0172E+00	7.0000E–02
1.3600E+02	5.1890E+00	7.0000E–02	1.3600E+02	5.4132E+00	7.1000E–02
1.3800E+02	4.2780E+00	6.7000E–02	1.3800E+02	5.3581E+00	7.1000E–02
1.4000E+02	3.1285E+00	6.1000E–02	1.4000E+02	4.5395E+00	6.7000E–02
1.4200E+02	2.1739E+00	5.4000E–02	1.4200E+02	3.7280E+00	6.3000E–02
1.4400E+02	1.4309E+00	4.6000E–02	1.4400E+02	2.7698E+00	5.7000E–02
1.4600E+02	7.8122E–01	3.6000E–02	1.4600E+02	1.9795E+00	5.1000E–02
1.4800E+02	4.9249E–01	2.9000E–02	1.4800E+02	1.3106E+00	4.3000E–02
1.5000E+02	2.8354E–01	2.2000E–02	1.5000E+02	7.4535E–01	3.4000E–02
1.5200E+02	1.2776E–01	1.6000E–02	1.5200E+02	4.7688E–01	2.8000E–02
1.5400E+02	3.5269E–02	1.1000E–02	1.5400E+02	2.7803E–01	2.2000E–02
1.5600E+02	–2.4731E–02	8.0000E–03	1.5600E+02	1.1742E–01	1.6000E–02
1.5800E+02	–5.4731E–02	6.0000E–03	1.5800E+02	7.4197E–03	1.2000E–02
1.6000E+02	–7.4731E–02	4.0000E–03	1.6000E+02	–6.2580E–02	8.0000E–03
			1.6200E+02	–8.2580E–02	6.0000E–03

E_n = 50 (45–55) MeV Post-neutron emission			E_n = 50 (45–55) MeV Pre-neutron emission		
Mass A	Yield (%)	Uncertainty	Mass A	Yield (%)	Uncertainty
7.4000E+01	–2.4347E–01	1.2000E–02	7.4000E+01	–1.7328E–01	9.0000E–03
7.6000E+01	–2.1347E–01	1.4000E–02	7.6000E+01	–1.4328E–01	1.2000E–02
7.8000E+01	–9.3469E–02	2.1000E–02	7.8000E+01	–5.3282E–02	1.7000E–02
8.0000E+01	4.6531E–02	2.6000E–02	8.0000E+01	2.6718E–02	2.1000E–02
8.2000E+01	3.5653E–01	3.6000E–02	8.2000E+01	2.2672E–01	2.9000E–02
8.4000E+01	6.0887E–01	4.3000E–02	8.4000E+01	4.6984E–01	3.7000E–02
8.6000E+01	1.0098E+00	5.2000E–02	8.6000E+01	7.0275E–01	4.4000E–02
8.8000E+01	1.6168E+00	6.1000E–02	8.8000E+01	1.0610E+00	5.2000E–02
9.0000E+01	2.4363E+00	7.1000E–02	9.0000E+01	1.6680E+00	6.2000E–02
9.2000E+01	3.2980E+00	7.8000E–02	9.2000E+01	2.3321E+00	7.0000E–02
9.4000E+01	4.1272E+00	8.4000E–02	9.4000E+01	3.0929E+00	7.6000E–02
9.6000E+01	4.8790E+00	8.9000E–02	9.6000E+01	3.8640E+00	8.1000E–02
9.8000E+01	5.2961E+00	9.2000E–02	9.8000E+01	4.4885E+00	8.5000E–02
1.0000E+02	4.9618E+00	9.0000E–02	1.0000E+02	4.9864E+00	8.9000E–02
1.0200E+02	4.3165E+00	8.7000E–02	1.0200E+02	4.7515E+00	8.8000E–02
1.0400E+02	3.7725E+00	8.5000E–02	1.0400E+02	4.1770E+00	8.5000E–02
1.0600E+02	3.2085E+00	8.1000E–02	1.0600E+02	3.6036E+00	8.2000E–02
1.0800E+02	2.7786E+00	7.8000E–02	1.0800E+02	3.1305E+00	8.0000E–02
1.1000E+02	2.6809E+00	7.7000E–02	1.1000E+02	2.9357E+00	7.9000E–02
1.1200E+02	2.5927E+00	7.5000E–02	1.1200E+02	2.5005E+00	7.4000E–02
1.1400E+02	2.5328E+00	7.4000E–02	1.1400E+02	2.5540E+00	7.4000E–02
1.1600E+02	2.6474E+00	7.5000E–02	1.1600E+02	2.5407E+00	7.3000E–02
1.1800E+02	2.5715E+00	7.5000E–02	1.1800E+02	2.4543E+00	7.2000E–02
1.2000E+02	2.6272E+00	7.6000E–02	1.2000E+02	2.5572E+00	7.3000E–02
1.2200E+02	3.0752E+00	8.1000E–02	1.2200E+02	2.5678E+00	7.4000E–02
1.2400E+02	3.4876E+00	8.3000E–02	1.2400E+02	2.5716E+00	7.5000E–02
1.2600E+02	4.0858E+00	8.6000E–02	1.2600E+02	2.9936E+00	7.9000E–02
1.2800E+02	4.6720E+00	8.8000E–02	1.2800E+02	3.2714E+00	8.1000E–02
1.3000E+02	5.2460E+00	9.1000E–02	1.3000E+02	3.8318E+00	8.4000E–02
1.3200E+02	5.1351E+00	9.1000E–02	1.3200E+02	4.3261E+00	8.6000E–02
1.3400E+02	4.5155E+00	8.6000E–02	1.3400E+02	4.8502E+00	8.9000E–02
1.3600E+02	3.6568E+00	8.1000E–02	1.3600E+02	4.8721E+00	8.8000E–02
1.3800E+02	2.6974E+00	7.4000E–02	1.3800E+02	4.3244E+00	8.4000E–02
1.4000E+02	2.0058E+00	6.7000E–02	1.4000E+02	3.6796E+00	8.0000E–02
1.4200E+02	1.1594E+00	5.5000E–02	1.4200E+02	2.7988E+00	7.3000E–02
1.4400E+02	7.5863E–01	4.6000E–02	1.4400E+02	2.1717E+00	6.8000E–02
1.4600E+02	5.1537E–01	3.9000E–02	1.4600E+02	1.3850E+00	5.7000E–02
1.4800E+02	3.1952E–01	3.2000E–02	1.4800E+02	9.5207E–01	4.9000E–02
1.5000E+02	8.7507E–02	2.2000E–02	1.5000E+02	5.9871E–01	4.2000E–02
1.5200E+02	–1.2493E–02	1.8000E–02	1.5200E+02	3.1871E–01	3.5000E–02
1.5400E+02	–9.2493E–02	1.2000E–02	1.5400E+02	3.8708E–02	2.6000E–02
1.5600E+02	–1.2249E–01	1.0000E–02	1.5600E+02	–7.1292E–02	2.1000E–02
1.5800E+02	–1.6249E–01	5.0000E–03	1.5800E+02	–2.0129E–01	1.4000E–02

E_n = 99.5 (89–1105) MeV Post-neutron emission			E_n = 99.5 (89–1105) MeV Pre-neutron emission		
Mass A	Yield (%)	Uncertainty	Mass A	Yield (%)	Uncertainty
7.2000E+01	–2.0552E–01	8.0000E–03			
7.6000E+01	–4.5517E–02	1.5000E–02	7.6000E+01	–2.8248E–02	1.3000E–02
8.0000E+01	3.3448E–01	2.5000E–02	8.0000E+01	2.1175E–01	2.0000E–02
8.4000E+01	8.5448E–01	3.4000E–02	8.4000E+01	6.3175E–01	2.9000E–02
8.8000E+01	1.8984E+00	4.5000E–02	8.8000E+01	1.3118E+00	3.9000E–02
9.2000E+01	3.0114E+00	5.4000E–02	9.2000E+01	2.3326E+00	5.6000E–02
9.6000E+01	3.9480E+00	6.0000E–02	9.6000E+01	3.2846E+00	5.5000E–02
1.0000E+02	4.2092E+00	6.1000E–02	1.0000E+02	3.9707E+00	5.9000E–02
1.0400E+02	4.0797E+00	6.2000E–02	1.0400E+02	3.9677E+00	6.0000E–02
1.0800E+02	3.6745E+00	6.1000E–02	1.0800E+02	3.7210E+00	5.9000E–02
1.1200E+02	3.4607E+00	6.0000E–02	1.1200E+02	3.4096E+00	5.9000E–02
1.1600E+02	3.5163E+00	6.0000E–02	1.1600E+02	3.0072E+00	5.4000E–02
1.2000E+02	3.7913E+00	6.1000E–02	1.2000E+02	3.0421E+00	5.4000E–02
1.2400E+02	4.0852E+00	6.1000E–02	1.2400E+02	3.3736E+00	5.5000E–02
1.2800E+02	4.2197E+00	6.1000E–02	1.2800E+02	3.6973E+00	5.5000E–02
1.3200E+02	3.7421E+00	5.8000E–02	1.3200E+02	4.1599E+00	5.7000E–02
1.3600E+02	2.7628E+00	5.2000E–02	1.3600E+02	3.9426E+00	5.6000E–02
1.4000E+02	1.6053E+00	4.2000E–02	1.4000E+02	3.1060E+00	5.1000E–02
1.4400E+02	6.8261E–01	3.1000E–02	1.4400E+02	1.8613E+00	4.2000E–02
1.4800E+02	1.9261E–01	2.2000E–02	1.4800E+02	9.0736E–01	3.2000E–02
1.5200E+02	–9.7387E–02	1.4000E–02	1.5200E+02	2.6474E–01	2.2000E–02
1.5600E+02	–2.3739E–01	7.0000E–03	1.5600E+02	–4.5258E–02	1.4000E–02
			1.6000E+02	–1.8526E–01	9.0000E–03
			1.6400E+02	–2.5526E–01	4.0000E–03

E_n = 160 (145–175) MeV Post-neutron emission			E_n = 160 (145–175) MeV Pre-neutron emission		
Mass A	Yield (%)	Uncertainty	Mass A	Yield (%)	Uncertainty
6.8000E+01	–3.0476E–01	8.0000E–03	7.2000E+01	–2.0709E–01	1.2000E–02
7.2000E+01	–2.2476E–01	1.4000E–02	7.6000E+01	–7.7090E–02	1.9000E–02
7.6000E+01	–2.4760E–02	2.2000E–02	8.0000E+01	1.7291E–01	2.7000E–02
8.0000E+01	3.2524E–01	3.2000E–02	8.4000E+01	6.4291E–01	3.8000E–02
8.4000E+01	1.0449E+00	4.5000E–02	8.8000E+01	1.4476E+00	5.0000E–02
8.8000E+01	2.0899E+00	5.8000E–02	9.2000E+01	2.4261E+00	6.1000E–02
9.2000E+01	2.9734E+00	6.6000E–02	9.6000E+01	3.1215E+00	6.6000E–02
9.6000E+01	3.8538E+00	7.2000E–02	1.0000E+02	3.8070E+00	7.2000E–02
1.0000E+02	4.2049E+00	7.5000E–02	1.0400E+02	3.9391E+00	7.4000E–02
1.0400E+02	4.1260E+00	7.6000E–02	1.0800E+02	3.9100E+00	7.5000E–02
1.0800E+02	3.9231E+00	7.7000E–02	1.1200E+02	3.6483E+00	7.5000E–02
1.1200E+02	3.6277E+00	7.6000E–02	1.1600E+02	3.3601E+00	7.3000E–02
1.1600E+02	3.6762E+00	7.6000E–02	1.2000E+02	3.5156E+00	7.4000E–02
1.2000E+02	4.1773E+00	7.8000E–02	1.2400E+02	3.9487E+00	7.6000E–02
1.2400E+02	4.1455E+00	7.5000E–02	1.2800E+02	3.8529E+00	7.3000E–02
1.2800E+02	4.0944E+00	7.4000E–02	1.3200E+02	3.9153E+00	7.3000E–02
1.3200E+02	3.3158E+00	6.8000E–02	1.3600E+02	3.2602E+00	6.7000E–02
1.3600E+02	2.5413E+00	6.3000E–02	1.4000E+02	2.5113E+00	6.2000E–02
1.4000E+02	1.3981E+00	5.0000E–02	1.4400E+02	1.5848E+00	5.2000E–02
1.4400E+02	5.5866E–01	3.8000E–02	1.4800E+02	7.6064E–01	4.0000E–02
1.4800E+02	5.8658E–02	2.5000E–02	1.5200E+02	2.5773E–01	2.9000E–02
1.5200E+02	–1.8134E–01	1.7000E–02	1.5600E+02	–3.2273E–02	2.0000E–02
1.5600E+02	–2.8134E–01	1.1000E–02	1.6000E+02	–1.7227E–01	1.3000E–02
			1.6400E+02	–2.5227E–01	7.0000E–03

Äystö et al. (1998) [II.9]

E_p = 20.0 MeV Pre-neutron emission			E_p = 60.0 MeV Pre-neutron emission		
Mass A	Yield (%)	Uncertainty	Mass A	Yield (%)	Uncertainty
7.4000E+01	1.3213E–02	3.0000E–03	7.4000E+01	3.8586E–02	6.0000E–03
7.6000E+01	4.3213E–02	4.8000E–03	7.6000E+01	6.8586E–02	7.8000E–03
7.8000E+01	1.1321E–01	9.0000E–03	7.8000E+01	1.5859E–01	1.3200E–02
8.0000E+01	2.6321E–01	1.8000E–02	8.0000E+01	3.3859E–01	2.4000E–02
8.2000E+01	3.7720E–01	2.5200E–02	8.2000E+01	5.5845E–01	3.7200E–02
8.4000E+01	8.5018E–01	5.4000E–02	8.4000E+01	9.4303E–01	3.0000E–02
8.6000E+01	1.3005E+00	4.0500E–02	8.6000E+01	1.3767E+00	4.2600E–02
8.8000E+01	1.8684E+00	5.7000E–02	8.8000E+01	1.8655E+00	5.6400E–02
9.0000E+01	2.5026E+00	7.5000E–02	9.0000E+01	2.3591E+00	7.0200E–02
9.2000E+01	3.0692E+00	9.0900E–02	9.2000E+01	2.8059E+00	8.2500E–02
9.4000E+01	3.5568E+00	1.0500E–01	9.4000E+01	3.1470E+00	9.2100E–02
9.6000E+01	3.9114E+00	1.1490E–01	9.6000E+01	3.3615E+00	9.8400E–02
9.8000E+01	4.0863E+00	4.0000E–02	9.8000E+01	3.4681E+00	1.0200E–01
1.0000E+02	4.0584E+00	1.1940E–01	1.0000E+02	3.4790E+00	1.0290E–01
1.0200E+02	3.8858E+00	1.1490E–01	1.0200E+02	3.4418E+00	1.0230E–01
1.0400E+02	3.6153E+00	1.0740E–01	1.0400E+02	3.3978E+00	1.0140E–01
1.0600E+02	3.2262E+00	9.6600E–02	1.0600E+02	3.2833E+00	9.8400E–02
1.0800E+02	2.8163E+00	8.4900E–02	1.0800E+02	3.1902E+00	9.6000E–02
1.1000E+02	2.4921E+00	7.5600E–02	1.1000E+02	3.0813E+00	9.3000E–02
1.1200E+02	2.1642E+00	6.6000E–02	1.1200E+02	3.0302E+00	9.1500E–02
1.1400E+02	1.9428E+00	5.9400E–02	1.1400E+02	3.0167E+00	9.0900E–02
1.1600E+02	1.7945E+00	5.4900E–02	1.1600E+02	3.0332E+00	9.1200E–02
1.1800E+02	1.7675E+00	5.4000E–02	1.1800E+02	3.0345E+00	9.1200E–02
1.2000E+02	1.7681E+00	5.4000E–02	1.2000E+02	3.0193E+00	9.0900E–02
1.2200E+02	1.7855E+00	5.4600E–02	1.2200E+02	3.0221E+00	9.1200E–02
1.2400E+02	1.9128E+00	5.8500E–02	1.2400E+02	3.0398E+00	9.1800E–02
1.2600E+02	2.1431E+00	6.5400E–02	1.2600E+02	3.1670E+00	9.5400E–02
1.2800E+02	2.3986E+00	7.2900E–02	1.2800E+02	3.2177E+00	9.6600E–02
1.3000E+02	2.7831E+00	8.4000E–02	1.3000E+02	3.3614E+00	1.0050E–01
1.3200E+02	3.1944E+00	9.5700E–02	1.3200E+02	3.4156E+00	1.0170E–01
1.3400E+02	3.5841E+00	1.0650E–01	1.3400E+02	3.4622E+00	1.0260E–01
1.3600E+02	3.8545E+00	1.1400E–01	1.3600E+02	3.4617E+00	1.0200E–01
1.3800E+02	4.0264E+00	1.1850E–01	1.3800E+02	3.4187E+00	1.0020E–01
1.4000E+02	4.0841E+00	4.0000E–02	1.4000E+02	3.2488E+00	9.5100E–02
1.4200E+02	3.9308E+00	1.1550E–01	1.4200E+02	2.9121E+00	8.5500E–02
1.4400E+02	3.6108E+00	1.0650E–01	1.4400E+02	2.5314E+00	7.5000E–02
1.4600E+02	3.1379E+00	9.3000E–02	1.4600E+02	2.0499E+00	6.1500E–02
1.4800E+02	2.5541E+00	7.6500E–02	1.4800E+02	1.5674E+00	4.8000E–02
1.5000E+02	1.9560E+00	5.9400E–02	1.5000E+02	1.1270E+00	3.5400E–02
1.5200E+02	1.3805E+00	4.2600E–02	1.5200E+02	7.2412E–01	4.6800E–02
1.5400E+02	8.9311E–01	5.6400E–02	1.5400E+02	4.4995E–01	3.0000E–02
1.5600E+02	5.3157E–01	3.4800E–02	1.5600E+02	2.5472E–01	1.8000E–02
1.5800E+02	2.8157E–01	1.9800E–02	1.5800E+02	1.3472E–01	1.0800E–02
1.6000E+02	1.3157E–01	1.0800E–02	1.6000E+02	5.4722E–02	6.0000E–03
1.6200E+02	5.1569E–02	6.0000E–03	1.6200E+02	4.7218E–03	3.0000E–03

Annex 2 to Appendix II

ADJUSTED DATA WITH ADJUSTED UNCERTAINTY

Vivès et al. (2000) [II.8]

E_n = 1.60 MeV Pre-neutron emission			E_n = 5.5 MeV Pre-neutron emission		
Mass A	Yield (%)	Uncertainty	Mass A	Yield (%)	Uncertainty
			67.000	2.7711E–04	1.8881E–04
			68.000	2.7711E–04	3.9204E–04
			69.000	9.6940E–04	6.0592E–04
			70.000	2.3540E–03	8.3330E–04
			71.000	3.2430E–03	9.3584E–04
			72.000	4.2099E–03	9.6907E–04
			73.000	4.1060E–03	1.0853E–03
			74.000	5.3387E–03	1.5877E–03
75.000	–4.3656E–03	2.8176E–03	75.000	6.0832E–03	2.7429E–03
			76.000	7.8019E–03	5.5764E–03
			77.000	1.1983E–02	1.0235E–02
78.000	2.7388E–03	6.4378E–03	78.000	2.9070E–02	1.8139E–02
79.000	8.0673E–03	9.5373E–03	79.000	3.5724E–02	3.0553E–02
80.000	1.3395E–02	1.2637E–02	80.000	8.9406E–02	4.7665E–02
81.000	2.8005E–02	2.4160E–02	81.000	1.3484E–01	6.7734E–02
82.000	3.8401E–02	4.7866E–02	82.000	2.1427E–01	9.2463E–02
83.000	9.8707E–02	9.6615E–02	83.000	3.0298E–01	1.2096E–01
84.000	3.5164E–01	1.5110E–01	84.000	4.4530E–01	1.5611E–01
85.000	4.2392E–01	2.0549E–01	85.000	5.7356E–01	1.9856E–01
86.000	6.4248E–01	2.6242E–01	86.000	8.1798E–01	2.4900E–01
87.000	8.7907E–01	3.2172E–01	87.000	1.0490E+00	2.9564E–01
88.000	1.3097E+00	3.7598E–01	88.000	1.4099E+00	3.4797E–01
89.000	1.6787E+00	4.3974E–01	89.000	1.7439E+00	4.0598E–01
90.000	2.1215E+00	4.9996E–01	90.000	2.2224E+00	4.7023E–01
91.000	2.5971E+00	5.2460E–01	91.000	2.5176E+00	5.2122E–01
92.000	3.2447E+00	5.2547E–01	92.000	3.0491E+00	5.4232E–01
93.000	3.7560E+00	4.9028E–01	93.000	3.8910E+00	5.2344E–01
94.000	4.3424E+00	4.0316E–01	94.000	4.4983E+00	4.3647E–01
95.000	4.4360E+00	3.4669E–01	95.000	4.6434E+00	3.7329E–01
96.000	4.6361E+00	3.2422E–01	96.000	4.7660E+00	3.3354E–01
97.000	4.9172E+00	3.4553E–01	97.000	4.9223E+00	3.3390E–01
98.000	5.0394E+00	3.7463E–01	98.000	5.2338E+00	3.3729E–01
99.000	5.5539E+00	4.0886E–01	99.000	5.8253E+00	3.3562E–01
100.000	6.1263E+00	4.1947E–01	100.000	6.0551E+00	3.0549E–01
101.000	6.3753E+00	3.7575E–01	101.000	6.1702E+00	2.6205E–01
102.000	6.4716E+00	2.8362E–01	102.000	5.9899E+00	2.3069E–01
103.000	6.6572E+00	2.5881E–01	103.000	5.9916E+00	2.9124E–01
104.000	7.0271E+00	4.5861E–01	104.000	6.1456E+00	4.4976E–01
105.000	6.3598E+00	7.4180E–01	105.000	5.6174E+00	6.4812E–01
106.000	5.2813E+00	9.6442E–01	106.000	4.7795E+00	8.0488E–01
107.000	3.9937E+00	1.0722E+00	107.000	3.6097E+00	9.0297E–01
108.000	2.6459E+00	1.0319E+00	108.000	2.5537E+00	8.5961E–01
109.000	1.5191E+00	8.3792E–01	109.000	1.6316E+00	7.1911E–01
110.000	7.4444E–01	5.9326E–01	110.000	1.0536E+00	5.2990E–01
111.000	3.9131E–01	3.5047E–01	111.000	7.3045E–01	3.7068E–01
112.000	2.6189E–01	2.0773E–01	112.000	4.0852E–01	2.4651E–01
113.000	8.7609E–02	1.1291E–01	113.000	2.5812E–01	1.5444E–01
114.000	5.8556E–02	5.3899E–02	114.000	1.5572E–01	8.6253E–02

E_n = 1.60 MeV Pre-neutron emission			E_n = 5.5 MeV Pre-neutron emission		
Mass A	Yield (%)	Uncertainty	Mass A	Yield (%)	Uncertainty
115.000	3.1986E–02	2.7494E–02	115.000	1.2397E–01	4.9173E–02
116.000	1.5134E–02	1.5342E–02	116.000	1.1322E–01	2.9974E–02
117.000	8.7290E–03	8.3316E–03	117.000	9.7121E–02	1.9775E–02
118.000	4.9015E–03	4.3950E–03	118.000	9.1891E–02	1.3402E–02
119.000	1.8036E–03	1.4785E–03	119.000	6.3970E–02	7.4131E–03
120.000	1.8036E–03	1.4785E–03	120.000	6.3970E–02	7.4131E–03
121.000	4.9015E–03	4.3950E–03	121.000	9.1891E–02	1.3402E–02
122.000	8.7290E–03	8.3316E–03	122.000	9.7121E–02	1.9775E–02
123.000	1.5134E–02	1.5342E–02	123.000	1.1322E–01	2.9974E–02
124.000	3.1986E–02	2.7494E–02	124.000	1.2397E–01	4.9173E–02
125.000	5.8556E–02	5.3899E–02	125.000	1.5572E–01	8.6253E–02
126.000	8.7609E–02	1.1291E–01	126.000	2.5812E–01	1.5444E–01
127.000	2.6189E–01	2.0773E–01	127.000‘	4.0852E–01	2.4651E–01
128.000	3.9131E–01	3.5047E–01	128.000	7.3045E–01	3.7068E–01
129.000	7.4444E–01	5.9326E–01	129.000	1.0536E+00	5.2990E–01
130.000	1.5191E+00	8.3792E–01	130.000	1.6316E+00	7.1911E–01
131.000	2.6459E+00	1.0319E+00	131.000	2.5537E+00	8.5961E–01
132.000	3.9937E+00	1.0722E+00	132.000	3.6097E+00	9.0297E–01
133.000	5.2813E+00	9.6442E–01	133.000	4.7795E+00	8.0488E–01
134.000	6.3598E+00	7.4180E–01	134.000	5.6174E+00	6.4812E–01
135.000	7.0271E+00	4.5861E–01	135.000	6.1456E+00	4.4976E–01
136.000	6.6572E+00	2.5881E–01	136.000	5.9916E+00	2.9124E–01
137.000	6.4716E+00	2.8362E–01	137.000	5.9899E+00	2.3069E–01
138.000	6.3753E+00	3.7575E–01	138.000	6.1702E+00	2.6205E–01
139.000	6.1263E+00	4.1947E–01	139.000	6.0551E+00	3.0549E–01
140.000	5.5539E+00	4.0886E–01	140.000	5.8253E+00	3.3562E–01
141.000	5.0394E+00	3.7463E–01	141.000	5.2338E+00	3.3729E–01
142.000	4.9172E+00	3.4553E–01	142.000	4.9223E+00	3.3390E–01
143.000	4.6361E+00	3.2422E–01	143.000	4.7660E+00	3.3354E–01
144.000	4.4360E+00	3.4669E–01	144.000	4.6434E+00	3.7329E–01
145.000	4.3424E+00	4.0316E–01	145.000	4.4983E+00	4.3647E–01
146.000	3.7560E+00	4.9028E–01	146.000	3.8910E+00	5.2344E–01
147.000	3.2447E+00	5.2547E–01	147.000	3.0491E+00	5.4232E–01
148.000	2.5971E+00	5.2460E–01	148.000	2.5176E+00	5.2122E–01
149.000	2.1215E+00	4.9996E–01	149.000	2.2224E+00	4.7023E–01
150.000	1.6787E+00	4.3974E–01	150.000	1.7439E+00	4.0598E–01
151.000	1.3097E+00	3.7598E–01	151.000	1.4099E+00	3.4797E–01
152.000	8.7907E–01	3.2172E–01	152.000	1.0490E+00	2.9564E–01
153.000	6.4248E–01	2.6242E–01	153.000	8.1798E–01	2.4900E–01
154.000	4.2392E–01	2.0549E–01	154.000	5.7356E–01	1.9856E–01
155.000	3.5164E–01	1.5110E–01	155.000	4.4530E–01	1.5611E–01
156.000	9.8707E–02	9.6615E–02	156.000	3.0298E–01	1.2096E–01
157.000	3.8401E–02	4.7866E–02	157.000	2.1427E–01	9.2463E–02
158.000	2.8005E–02	2.4160E–02	158.000	1.3484E–01	6.7734E–02
159.000	1.3395E–02	1.2637E–02	159.000	8.9406E–02	4.7665E–02
160.000	8.0673E–03	9.5373E–03	160.000	3.5724E–02	3.0553E–02
161.000	2.7388E–03	6.4378E–03	161.000	2.9070E–02	1.8139E–02
			162.000	1.1983E–02	1.0235E–02
			163.000	7.8019E–03	5.5764E–03
164.000	–4.3656E–03	2.8176E–03	164.000	6.0832E–03	2.7429E–03
			165.000	5.3387E–03	1.5877E–03
			166.000	4.1060E–03	1.0853E–03
			167.000	4.2099E–03	9.6907E–04
			168.000	3.2430E–03	9.3584E–04
			169.000	2.3540E–03	8.3330E–04
			170.000	9.6940E–04	6.0592E–04
			171.000	2.7711E–04	3.9204E–04
			172.000	2.7711E–04	1.8881E–04

Zöller (1995) [II.7]

E_n = 13 (11.5–14.5) MeV Post-neutron emission			E_n = 20 (18–22) MeV Post-neutron emission		
Mass A	Yield (%)	Uncertainty	Mass A	Yield (%)	Uncertainty
74.000	–8.1187E–02	9.7831E–03	74.000	–8.8686E–02	1.3363E–02
76.000	–4.1187E–02	2.5272E–02	76.000	–3.8686E–02	2.7853E–02
78.000	1.8813E–02	5.4909E–02	78.000	–8.6862E–03	5.8634E–02
80.000	1.1881E–01	8.5338E–02	80.000	2.0131E–01	9.2784E–02
82.000	3.0957E–01	1.2717E–01	82.000	2.9589E–01	1.3616E–01
84.000	5.4075E–01	1.8509E–01	84.000	6.0174E–01	1.9596E–01
86.000	9.4186E–01	2.6724E–01	86.000	1.0079E+00	2.7155E–01
88.000	1.3488E+00	3.6605E–01	88.000	1.5159E+00	3.5804E–01
90.000	2.4527E+00	4.5211E–01	90.000	2.4023E+00	4.2620E–01
92.000	3.3420E+00	4.9006E–01	92.000	3.5812E+00	4.4891E–01
94.000	4.8841E+00	4.3961E–01	94.000	4.5505E+00	3.9401E–01
96.000	5.8441E+00	3.0039E–01	96.000	5.5173E+00	2.6444E–01
98.000	6.4219E+00	1.2748E–01	98.000	6.0553E+00	1.2127E–01
100.000	6.2181E+00	2.1323E–01	100.000	5.7786E+00	2.0104E–01
102.000	5.4582E+00	3.8810E–01	102.000	5.2153E+00	3.4242E–01
104.000	4.0475E+00	4.8150E–01	104.000	3.8440E+00	4.1241E–01
106.000	2.8362E+00	4.7340E–01	106.000	2.7515E+00	4.0054E–01
108.000	1.7950E+00	3.8640E–01	108.000	1.9950E+00	3.2400E–01
110.000	1.0332E+00	2.6429E–01	110.000	1.5075E+00	2.2583E–01
112.000	8.9544E–01	1.5467E–01	112.000	1.4368E+00	1.4314E–01
114.000	8.8351E–01	8.7111E–02	114.000	1.1806E+00	8.7544E–02
116.000	7.1249E–01	5.3308E–02	116.000	1.0338E+00	5.8521E–02
118.000	8.3191E–01	4.6001E–02	118.000	1.2503E+00	6.2128E–02
120.000	7.5065E–01	6.2527E–02	120.000	1.2416E+00	9.3157E–02
122.000	6.9458E–01	1.3042E–01	122.000	1.2858E+00	1.6484E–01
124.000	9.1531E–01	2.5012E–01	124.000	1.4537E+00	2.7231E–01
126.000	1.3478E+00	3.9096E–01	126.000	2.1264E+00	3.8263E–01
128.000	2.7680E+00	4.9337E–01	128.000	3.2068E+00	4.4508E–01
130.000	3.9817E+00	5.1094E–01	130.000	4.6837E+00	4.1343E–01
132.000	5.4409E+00	4.1082E–01	132.000	5.6061E+00	2.9824E–01
134.000	6.2736E+00	2.3063E–01	134.000	6.1981E+00	1.2692E–01
136.000	6.4255E+00	1.2237E–01	136.000	5.8150E+00	1.9969E–01
138.000	5.9191E+00	2.9995E–01	138.000	4.9785E+00	3.8162E–01
140.000	4.8756E+00	4.3982E–01	140.000	3.8589E+00	4.4374E–01
142.000	3.3774E+00	4.9184E–01	142.000	2.8917E+00	4.4127E–01
144.000	2.5176E+00	4.5559E–01	144.000	1.7922E+00	3.8758E–01
146.000	1.3749E+00	3.7023E–01	146.000	1.2367E+00	2.9866E–01
148.000	9.2647E–01	2.6977E–01	148.000	6.8348E–01	2.1799E–01
150.000	5.5202E–01	1.8301E–01	150.000	3.9955E–01	1.5092E–01
152.000	3.2973E–01	1.2114E–01	152.000	2.8095E–01	1.0331E–01
154.000	1.2060E–01	7.7488E–02	154.000	1.0621E–01	7.0177E–02
156.000	6.6397E–02	4.7788E–02	156.000	6.2059E–03	4.5948E–02
158.000	2.9809E–02	2.9641E–02	158.000	–5.3794E–02	2.1920E–02
160.000	–2.0191E–02	1.5910E–02	160.000	–7.3794E–02	7.2444E–03
162.000	–3.0191E–02	4.1250E–03			
164.000	–3.0191E–02	9.9150E–03			

E_n = 27.5 (22–33) MeV Post-neutron emission			E_n = 27.5 (22–33) MeV Pre-neutron emission		
Mass A	Yield (%)	Uncertainty	Mass A	Yield (%)	Uncertainty
72.000	–8.5067E–02	1.2955E–02	74.000	–8.2944E–02	1.1124E–02
74.000	–6.5067E–02	1.2107E–02	76.000	–7.2944E–02	1.5956E–02
76.000	–4.5067E–02	3.3939E–02	78.000	–1.2944E–02	4.0461E–02
78.000	4.4933E–02	5.6954E–02	80.000	6.7056E–02	6.4624E–02
80.000	1.6800E–01	8.7373E–02	82.000	2.3382E–01	9.5804E–02
82.000	3.0940E–01	1.3061E–01	84.000	3.6967E–01	1.3805E–01
84.000	5.8619E–01	1.9201E–01	86.000	6.6278E–01	1.9507E–01
86.000	9.4303E–01	2.7016E–01	88.000	1.0760E+00	2.6207E–01
88.000	1.6845E+00	3.5333E–01	90.000	1.7408E+00	3.2939E–01
90.000	2.3728E+00	4.2014E–01	92.000	2.4637E+00	3.7808E–01
92.000	3.4702E+00	4.3148E–01	94.000	3.3561E+00	3.8230E–01
94.000	4.6021E+00	3.6154E–01	96.000	4.3293E+00	3.2116E–01
96.000	5.4842E+00	2.1604E–01	98.000	5.0102E+00	2.0206E–01
98.000	5.9471E+00	7.4600E–02	100.000	5.5580E+00	7.6380E–02
100.000	5.5870E+00	1.9361E–01	102.000	5.2116E+00	1.5584E–01
102.000	4.5363E+00	3.1788E–01	104.000	4.4781E+00	2.7097E–01
104.000	3.5806E+00	3.5678E–01	106.000	3.6849E+00	3.2189E–01
106.000	2.7268E+00	3.1716E–01	108.000	2.8284E+00	3.0318E–01
108.000	2.1787E+00	2.3369E–01	110.000	2.2327E+00	2.3762E–01
110.000	1.8433E+00	1.4766E–01	112.000	1.8397E+00	1.5584E–01
112.000	1.9328E+00	8.9211E–02	114.000	1.8321E+00	9.1875E–02
114.000	1.8091E+00	6.1260E–02	116.000	1.7552E+00	5.6595E–02
116.000	1.6767E+00	4.7695E–02	118.000	1.7178E+00	4.5271E–02
118.000	1.7591E+00	4.6982E–02	120.000	1.8074E+00	5.0147E–02
120.000	1.7005E+00	7.8267E–02	122.000	1.8275E+00	7.4920E–02
122.000	1.7104E+00	1.5993E–01	124.000	1.7375E+00	1.3032E–01
124.000	1.9321E+00	2.7080E–01	126.000	2.0311E+00	2.0949E–01
126.000	2.7520E+00	3.6212E–01	128.000	2.6095E+00	2.8568E–01
128.000	3.8176E+00	3.8695E–01	130.000	3.4002E+00	3.2385E–01
130.000	5.0083E+00	3.1263E–01	132.000	4.1910E+00	2.9835E–01
132.000	5.7124E+00	1.6005E–01	134.000	5.0172E+00	2.0145E–01
134.000	6.0344E+00	9.7997E–02	136.000	5.4132E+00	7.8568E–02
136.000	5.1890E+00	2.6986E–01	138.000	5.3581E+00	1.5125E–01
138.000	4.2780E+00	3.9572E–01	140.000	4.5395E+00	2.8464E–01
140.000	3.1285E+00	4.3841E–01	142.000	3.7280E+00	3.6758E–01
142.000	2.1739E+00	4.0499E–01	144.000	2.7698E+00	3.8620E–01
144.000	1.4309E+00	3.2994E–01	146.000	1.9795E+00	3.5063E–01
146.000	7.8122E–01	2.4441E–01	148.000	1.3106E+00	2.8725E–01
148.000	4.9249E–01	1.6895E–01	150.000	7.4535E–01	2.1815E–01
150.000	2.8354E–01	1.1230E–01	152.000	4.7688E–01	1.5646E–01
152.000	1.2776E–01	7.4513E–02	154.000	2.7803E–01	1.0943E–01
154.000	3.5269E–02	4.8229E–02	156.000	1.1742E–01	7.4956E–02
156.000	–2.4731E–02	2.9928E–02	158.000	7.4197E–03	4.8524E–02
158.000	–5.4731E–02	1.2285E–02	160.000	–6.2580E–02	2.2289E–02
160.000	–7.4731E–02	8.4106E–03	162.000	–8.2580E–02	8.0779E–03

E_n = 50 (45–55) MeV Post-neutron emission			E_n = 50 (45–55) MeV Pre-neutron emission		
Mass A	Yield (%)	Uncertainty	Mass A	Yield (%)	Uncertainty
74.000	–2.4347E–01	2.1724E–02	74.000	–1.7328E–01	1.3348E–02
76.000	–2.1347E–01	2.9554E–02	76.000	–1.4328E–01	2.3472E–02
78.000	–9.3469E–02	7.3240E–02	78.000	–5.3281E–02	5.3003E–02
80.000	4.6531E–02	1.1722E–01	80.000	2.6719E–02	8.2935E–02
82.000	3.5653E–01	1.6248E–01	82.000	2.2672E–01	1.1401E–01
84.000	6.0887E–01	2.1332E–01	84.000	4.6984E–01	1.5086E–01
86.000	1.0098E+00	2.6579E–01	86.000	7.0275E–01	1.9383E–01
88.000	1.6168E+00	3.0806E–01	88.000	1.0610E+00	2.3974E–01
90.000	2.4363E+00	3.2623E–01	90.000	1.6680E+00	2.7791E–01
92.000	3.2980E+00	3.0801E–01	92.000	2.3321E+00	2.9615E–01
94.000	4.1272E+00	2.5427E–01	94.000	3.0929E+00	2.8191E–01
96.000	4.8790E+00	1.7685E–01	96.000	3.8640E+00	2.3640E–01
98.000	5.2961E+00	1.0535E–01	98.000	4.4885E+00	1.6971E–01
100.000	4.9618E+00	1.0242E–01	100.000	4.9864E+00	1.0460E–01
102.000	4.3165E+00	1.5400E–01	102.000	4.7515E+00	9.5147E–02
104.000	3.7725E+00	1.8977E–01	104.000	4.1770E+00	1.3706E–01
106.000	3.2085E+00	1.9286E–01	106.000	3.6036E+00	1.7062E–01
108.000	2.7786E+00	1.6829E–01	108.000	3.1305E+00	1.7729E–01
110.000	2.6809E+00	1.3111E–01	110.000	2.9357E+00	1.5978E–01
112.000	2.5927E+00	9.4759E–02	112.000	2.5005E+00	1.2714E–01
114.000	2.5328E+00	7.4839E–02	114.000	2.5540E+00	9.7646E–02
116.000	2.6474E+00	8.2767E–02	116.000	2.5407E+00	7.7818E–02
118.000	2.5715E+00	1.1236E–01	118.000	2.4543E+00	7.2209E–02
120.000	2.6272E+00	1.5215E–01	120.000	2.5572E+00	8.2605E–02
122.000	3.0752E+00	1.8693E–01	122.000	2.5678E+00	1.0613E–01
124.000	3.4876E+00	1.9702E–01	124.000	2.5716E+00	1.3745E–01
126.000	4.0858E+00	1.7448E–01	126.000	2.9936E+00	1.6706E–01
128.000	4.6720E+00	1.2322E–01	128.000	3.2714E+00	1.7764E–01
130.000	5.2460E+00	9.1308E–02	130.000	3.8318E+00	1.6300E–01
132.000	5.1351E+00	1.4526E–01	132.000	4.3261E+00	1.2252E–01
134.000	4.5155E+00	2.2502E–01	134.000	4.8502E+00	8.9369E–02
136.000	3.6568E+00	2.8932E–01	136.000	4.8721E+00	1.2192E–01
138.000	2.6974E+00	3.2052E–01	138.000	4.3244E+00	1.9144E–01
140.000	2.0058E+00	3.1294E–01	140.000	3.6796E+00	2.5502E–01
142.000	1.1594E+00	2.7363E–01	142.000	2.7988E+00	2.9231E–01
144.000	7.5863E–01	2.1907E–01	144.000	2.1717E+00	2.9798E–01
146.000	5.1537E–01	1.6598E–01	146.000	1.3850E+00	2.7466E–01
148.000	3.1952E–01	1.2272E–01	148.000	9.5207E–01	2.3457E–01
150.000	8.7507E–02	8.8877E–02	150.000	5.9871E–01	1.8894E–01
152.000	–1.2493E–02	6.4391E–02	152.000	3.1871E–01	1.4605E–01
154.000	–9.2493E–02	3.9408E–02	154.000	3.8708E–02	1.0271E–01
156.000	–1.2249E–01	1.6600E–02	156.000	–7.1292E–02	6.0694E–02
158.000	–1.6249E–01	1.2117E–02	158.000	–2.0129E–01	2.0172E–02

E_n = 99.5 (89–110) MeV Post-neutron emission			E_n = 99.5 (89–110) MeV Pre-neutron emission		
Mass A	Yield (%)	Uncertainty	Mass A	Yield (%)	Uncertainty
72.000	–2.0552E–01	2.1421E–02			
76.000	–4.5517E–02	7.1751E–02	76.000	–2.8248E–02	6.1240E–02
80.000	3.3448E–01	1.2303E–01	80.000	2.1175E–01	9.8095E–02
84.000	8.5448E–01	1.7411E–01	84.000	6.3175E–01	1.3537E–01
88.000	1.8984E+00	1.9486E–01	88.000	1.3118E+00	1.7287E–01
92.000	3.0114E+00	1.8098E–01	92.000	2.3326E+00	1.7998E–01
96.000	3.9480E+00	1.3925E–01	96.000	3.2846E+00	1.5116E–01
100.000	4.2092E+00	9.0770E–02	100.000	3.9707E+00	1.0573E–01
104.000	4.0797E+00	6.3584E–02	104.000	3.9677E+00	6.6536E–02
108.000	3.6745E+00	6.2389E–02	108.000	3.7210E+00	6.1718E–02
112.000	3.4607E+00	6.0388E–02	112.000	3.4096E+00	6.7446E–02
116.000	3.5163E+00	6.0854E–02	116.000	3.0072E+00	5.5642E–02
120.000	3.7913E+00	6.1715E–02	120.000	3.0421E+00	5.7131E–02
124.000	4.0852E+00	6.6118E–02	124.000	3.3736E+00	6.4361E–02
128.000	4.2197E+00	1.0232E–01	128.000	3.6973E+00	5.5674E–02
132.000	3.7421E+00	1.5086E–01	132.000	4.1599E+00	7.3555E–02
136.000	2.7628E+00	1.8744E–01	136.000	3.9426E+00	1.2362E–01
140.000	1.6053E+00	1.9367E–01	140.000	3.1060E+00	1.6883E–01
144.000	6.8261E–01	1.6463E–01	144.000	1.8613E+00	1.8991E–01
148.000	1.9261E–01	1.1142E–01	148.000	9.0736E–01	1.7332E–01
152.000	–9.7387E–02	5.8468E–02	152.000	2.6474E–01	1.2894E–01
156.000	–2.3739E–01	8.2179E–03	156.000	–4.5258E–02	7.8071E–02
			160.000	–1.8526E–01	2.8041E–02
			164.000	–2.5526E–01	2.4025E–02

E_n = 160 (145–175) MeV Post-neutron emission			E_n = 160 (145–175) MeV Pre-neutron emission		
Mass A	Yield (%)	Uncertainty	Mass A	Yield (%)	Uncertainty
68.000	–3.0476E–01	1.6743E–02	76.000	–2.8248E–02	6.1240E–02
72.000	–2.2476E–01	3.7558E–02	80.000	2.1175E–01	9.8095E–02
76.000	–2.4760E–02	8.7231E–02	84.000	6.3175E–01	1.3537E–01
80.000	3.2524E–01	1.3774E–01	88.000	1.3118E+00	1.7287E–01
84.000	1.0449E+00	1.7859E–01	92.000	2.3326E+00	1.7998E–01
88.000	2.0899E+00	1.9549E–01	96.000	3.2846E+00	1.5116E–01
92.000	2.9734E+00	1.8200E–01	100.000	3.9707E+00	1.0573E–01
96.000	3.8538E+00	1.4554E–01	104.000	3.9677E+00	6.6536E–02
100.000	4.2049E+00	1.0387E–01	108.000	3.7210E+00	6.1718E–02
104.000	4.1260E+00	7.9606E–02	112.000	3.4096E+00	6.7446E–02
108.000	3.9231E+00	7.7000E–02	116.000	3.0072E+00	5.5642E–02
112.000	3.6277E+00	7.6012E–02	120.000	3.0421E+00	5.7131E–02
116.000	3.6762E+00	7.6035E–02	124.000	3.3736E+00	6.4361E–02
120.000	4.1773E+00	7.8690E–02	128.000	3.6973E+00	5.5674E–02
124.000	4.1455E+00	9.0216E–02	132.000	4.1599E+00	7.3555E–02
128.000	4.0944E+00	1.2864E–01	136.000	3.9426E+00	1.2362E–01
132.000	3.3158E+00	1.7022E–01	140.000	3.1060E+00	1.6883E–01
136.000	2.5413E+00	1.9555E–01	144.000	1.8613E+00	1.8991E–01
140.000	1.3981E+00	1.9112E–01	148.000	9.0736E–01	1.7332E–01
144.000	5.5866E–01	1.5638E–01	152.000	2.6474E–01	1.2894E–01
148.000	5.8658E–02	1.0283E–01	156.000	–4.5258E–02	7.8071E–02
152.000	–1.8134E–01	5.0738E–02	160.000	–1.8526E–01	2.8041E–02
156.000	–2.8134E–01	1.1753E–02	164.000	–2.5526E–01	2.4025E–02

Äystö et al (1998) [II.9]

E_p = 20.0 MeV Pre-neutron emission			E_p = 60.0 MeV Pre-neutron emission		
Mass A	Yield (%)	Uncertainty	Mass A	Yield (%)	Uncertainty
74.000	1.3213E–02	1.1667E–02	74.000	3.8586E–02	1.0617E–02
76.000	4.3213E–02	2.5960E–02	76.000	6.8586E–02	3.1526E–02
78.000	1.1321E–01	6.2946E–02	78.000	1.5859E–01	7.1086E–02
80.000	2.6321E–01	1.0071E–01	80.000	3.3859E–01	1.1176E–01
82.000	3.7720E–01	1.4731E–01	82.000	5.5845E–01	1.5306E–01
84.000	8.5018E–01	2.0107E–01	84.000	9.4303E–01	1.8601E–01
86.000	1.3005E+00	2.4172E–01	86.000	1.3767E+00	2.1398E–01
88.000	1.8684E+00	2.7285E–01	88.000	1.8655E+00	2.2852E–01
90.000	2.5026E+00	2.8426E–01	90.000	2.3591E+00	2.2180E–01
92.000	3.0692E+00	2.5574E–01	92.000	2.8059E+00	1.9925E–01
94.000	3.5568E+00	2.2160E–01	94.000	3.1470E+00	1.6682E–01
96.000	3.9114E+00	1.7016E–01	96.000	3.3615E+00	1.3477E–01
98.000	4.0863E+00	6.0106E–02	98.000	3.4681E+00	1.1217E–01
100.000	4.0584E+00	1.2402E–01	100.000	3.4790E+00	1.0332E–01
102.000	3.8858E+00	1.5245E–01	102.000	3.4418E+00	1.0378E–01
104.000	3.6153E+00	1.7520E–01	104.000	3.3978E+00	1.0686E–01
106.000	3.2262E+00	1.9325E–01	106.000	3.2833E+00	1.0639E–01
108.000	2.8163E+00	1.8887E–01	108.000	3.1902E+00	1.0357E–01
110.000	2.4921E+00	1.6982E–01	110.000	3.0813E+00	9.8144E–02
112.000	2.1642E+00	1.4047E–01	112.000	3.0302E+00	9.3871E–02
114.000	1.9428E+00	1.0756E–01	114.000	3.0167E+00	9.1630E–02
116.000	1.7945E+00	7.6802E–02	116.000	3.0332E+00	9.1291E–02
118.000	1.7675E+00	5.7285E–02	118.000	3.0345E+00	9.1211E–02
120.000	1.7681E+00	5.5817E–02	120.000	3.0193E+00	9.1240E–02
122.000	1.7855E+00	7.2987E–02	122.000	3.0221E+00	9.2694E–02
124.000	1.9128E+00	1.0256E–01	124.000	3.0398E+00	9.5693E–02
126.000	2.1431E+00	1.3628E–01	126.000	3.1670E+00	1.0187E–01
128.000	2.3986E+00	1.6686E–01	128.000	3.2177E+00	1.0451E–01
130.000	2.7831E+00	1.8881E–01	130.000	3.3614E+00	1.0712E–01
132.000	3.1944E+00	1.9488E–01	132.000	3.4156E+00	1.0466E–01
134.000	3.5841E+00	1.7786E–01	134.000	3.4622E+00	1.0262E–01
136.000	3.8545E+00	1.5547E–01	136.000	3.4617E+00	1.0682E–01
138.000	4.0264E+00	1.2527E–01	138.000	3.4187E+00	1.2482E–01
140.000	4.0841E+00	5.4421E–02	140.000	3.2488E+00	1.5407E–01
142.000	3.9308E+00	1.6338E–01	142.000	2.9121E+00	1.8575E–01
144.000	3.6108E+00	2.1485E–01	144.000	2.5314E+00	2.1182E–01
146.000	3.1379E+00	2.4709E–01	146.000	2.0499E+00	2.2444E–01
148.000	2.5541E+00	2.7643E–01	148.000	1.5674E+00	2.1558E–01
150.000	1.9560E+00	2.6959E–01	150.000	1.1270E+00	1.9219E–01
152.000	1.3805E+00	2.4352E–01	152.000	7.2412E–01	1.6459E–01
154.000	8.9311E–01	2.0976E–01	154.000	4.4995E–01	1.2686E–01
156.000	5.3157E–01	1.5975E–01	156.000	2.5472E–01	9.2153E–02
158.000	2.8157E–01	1.0929E–01	158.000	1.3472E–01	6.2342E–02
160.000	1.3157E–01	6.0032E–02	160.000	5.4722E–02	3.2972E–02
162.000	5.1569E–02	1.2199E–02	162.000	4.7218E–03	4.5672E–03

Appendix III

FISSION YIELD SYSTEMATICS AND COVARIANCE STUDY FOR ^{238}U

Liu Tingjin, Sun Zhengjun
China Institute of Atomic Energy, China

Mass distribution data measured up to 200 MeV by the kinetic energy method by Zöller were adjusted for mass resolution and used to study the systematics of the chain yield dependence on incident neutron energy. The energy dependence for each fission fragment mass number was represented by linear and quadric functions. Furthermore, the systematics of the whole mass distribution and representation by a 5 (or 3) Gaussian model as a function of the incident neutron energy was also investigated. A code was developed to deduce the model parameters by a non-linear least squares fit of the experimental data. The mass distributions calculated with these parameters were subsequently compared with the experimental data. However, comparisons with radiochemically measured yields revealed systematic differences between the data obtained by the two methods. The uncertainties and correlations in the systematics were also studied: uncertainties in the mass distributions can be reduced by 20–80% (about 50% on average) when calculated from the systematics, and greater reductions can be achieved when the initial uncertainty is higher. These studies have also shown that there is a strong but rather complicated correlation between the yields calculated from the systematics and the parameters of the systematics.

III.1. INTRODUCTION

There are three approaches to determining the energy dependence of fission yields: experimental measurement, theoretical calculation and systematics. Systematics is the most simple and promising approach so long as there is a sufficiently large experimental database. In recent years, Zöller and others have systematically measured mass distributions in the energy range from 2 to 600 MeV for ^{238}U fission by means of the fragment kinetic energy method and using a white neutron source. This experimental work has provided a good basis for the study of systematics.

III.2. DATABASE

The mass distribution data measured by Zöller [III.1] at 2, 3, 5, 7, 10, 13, 16.25, 20, 27.5, 39, 50, 63, 80, 99.5, 120, 137.5, 160 and 200 MeV were used as the basis of our studies. Data measured by Nagy et al. [III.2], Chapman [III.3], Daroczy et al. [III.4], Liu Conggui et al. [III.5], Li Ze et al. [III.6, III.7] and Liu Yonghui et al. [III.8] following radiochemical separation were also used as reference and for comparative purposes. Zöller's data and their uncertainties were first adjusted to correct for mass resolution [III.9].

III.3. SYSTEMATICS FOR THE DEPENDENCE OF CHAIN YIELDS ON ENERGY FOR EACH FISSION PRODUCT MASS NUMBER

The systematic behaviour of the dependence of chain yields on incident neutron energy can be seen qualitatively in Fig. III.1. Yields in the valley increase, while yields at the two peaks decrease with increasing incident neutron energy (Figs III.2–III.6); these increases or decreases are non-linear, even in the energy range 0–20 MeV. The neutron energy dependence of the yields at the wings tends to be quite complicated, increasing at first with increasing energy and then decreasing.

The dependence of chain yields on neutron energy in the range 0–20 MeV was fitted quantitatively with a linear-linear and a log-linear function (coefficients a, b), as shown in Tables III.1 and III.2 and in Fig. III.7, or better with a quadratic function (coefficients a, b, c), as shown in Table III.3 and Fig. III.8.

III.4. SYSTEMATICS OF MASS DISTRIBUTIONS

(1) The mass distribution data of Zöller were adjusted for mass resolution, and fitted with 5

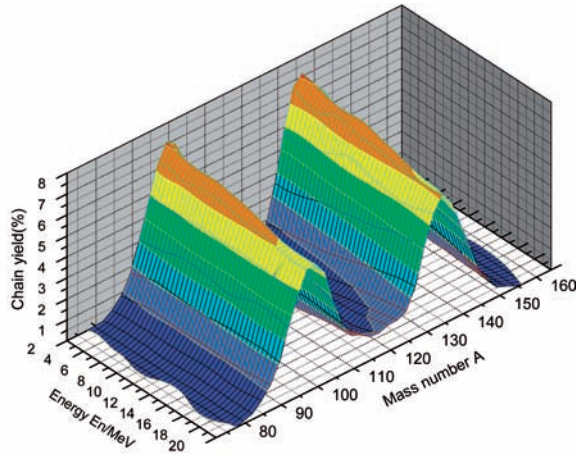

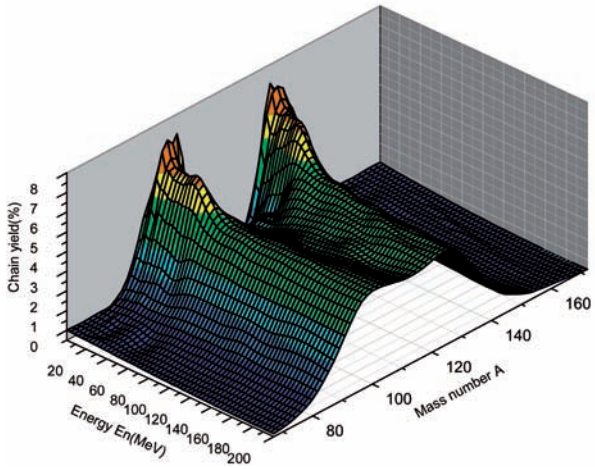

FIG.III.1. Systematic behaviour of the dependence of chain yield on energy.

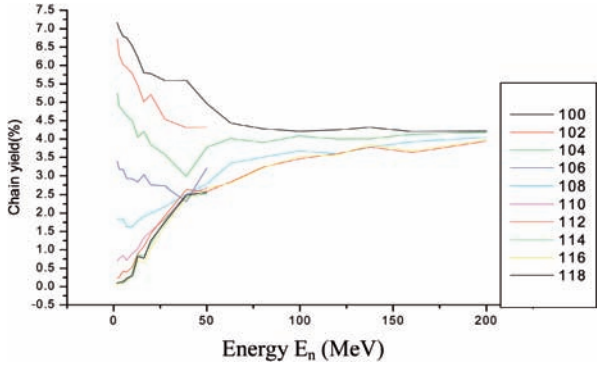

FIG. III.3. Dependence of the chain yield on energy for the right hand side of the light peak.

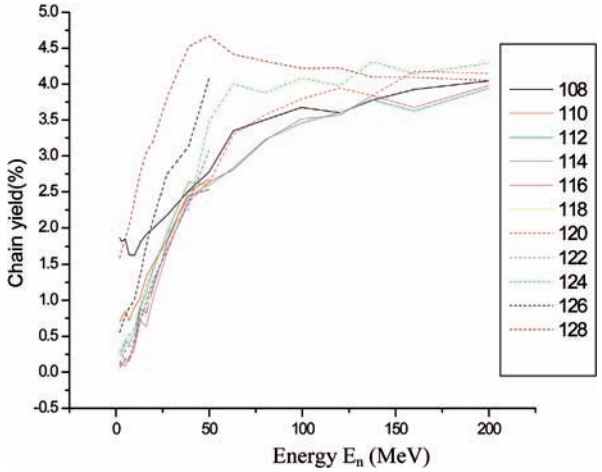

FIG. III.4. Dependence of the chain yield on energy in the valley range.

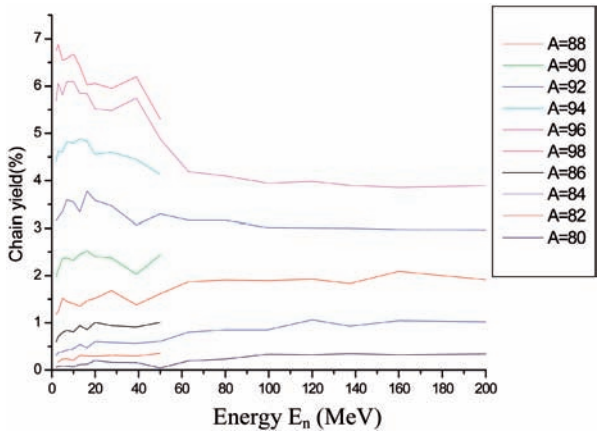

FIG. III.2. Dependence of the chain yield on energy for the left hand side of the light peak.

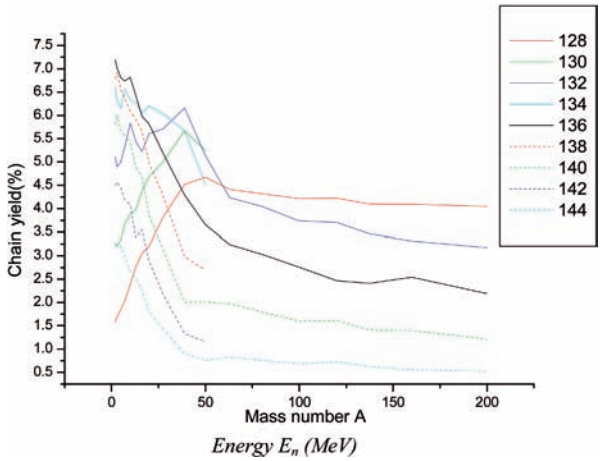

FIG. III.5. Dependence of chain yield on energy for both sides of the heavy peak.

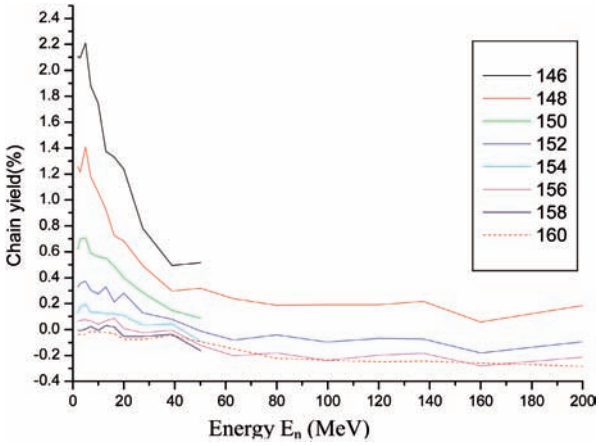

FIG. III.6. Dependence of chain yield on energy for the right hand side of the heavy peak.

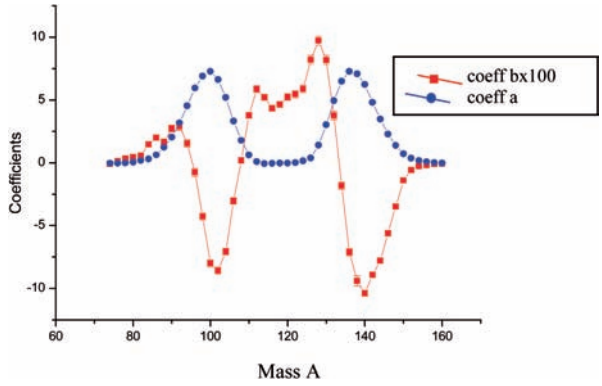

FIG. III.7. Dependence of linear fit coefficients on mass A.

(for $E_n \leq 20$ MeV) or 3 (for $E_n \geq 20$ MeV) Gaussian functions:

$$Y(A) = \frac{\sum_{i=1}^{I} y_i}{\sqrt{2\pi\sigma_i}} \exp - \frac{(A - \bar{A} + \Delta_i)^2}{2\sigma_i^2}$$

where $I = 5$ ($E_n \leq 20$ MeV) or 3 ($E_n \geq 20$ MeV) and $\bar{A} = (A_F - \bar{\nu})/2$ (A_F is the mass of the fissioning nucleus). Due to the symmetry of the distribution, there are altogether 9 (for 5 Gaussians) or 6 (for 3 Gaussians) adjusted parameters: Δ_1, (Δ_2), γ_1, (γ_2), γ_3, σ_1, (σ_2), σ_3, $\bar{A}$.

The optimum parameters were obtained from a non-linear least squares fit using iteration procedures:

$$\bar{C} = C^{(k+1)}$$
$$= C^k + (F^{(k)T} V_Y^{-1} F^{(k)})^{-1} F^{(k)T} V_Y^{-1} (Y - Y^{(k)})$$
$$V_{\bar{C}} = (F^{(k)T} V_Y^{-1} F^{(k)})^{-1}$$
$$\bar{Y} = Y^{(k+1)} = F^{(k)} C^{(k)} + Y^{(k)}$$
$$V_{\bar{Y}} = F^{(k)} V_{\bar{C}} F^{(k)T}$$

where F is the sensitivity matrix of yield Y to parameters C. The initial values $Y^{(0)}$ were calculated according to the Wahl equations [III.10]. Although the iteration should proceed until convergence is reached, this point of termination was not always achieved. Experimental data have to be normally smoothed over several data points. Zöller data were generally smoothed over 7 points (in special cases over 9 points) in order to obtain convergence. Since the search for optimal multi-parameter values is a complex process, the solution is not always unique. The parameters must be chosen from several possible solutions to maintain the systematic behaviour for each parameter at different energy points and require extensive and sometimes complicated calculations. Reduced χ^2 for the final fit is smaller than 1.0 for all energy points.

(2) Each parameter was fitted at different energy points by the least squares method with a second order function $y = a + bx^{s1} + x^{s2}$, where s can be either '+' or '–', to reduce χ^2. The 9 parameters were fitted in the energy region from 0 to 20 MeV, and 6 parameters from 20 to 200 MeV. Results are given in Figs III.9–III.17 for 0–20 MeV, and in Figs III.18–III.23 for 20–200 MeV.

(3) Experimental mass distribution data measured by means of the kinetic energy method (on which our systematics is based) have been compared with the data calculated using adjusted and systematics parameters, and are given in Figs III.24–III.39. The latter can generally reproduce the former, except for some differences at 50 and 63 MeV.

(4) Comparisons of various experimental mass distribution data measured with the radiochemical method and the data calculated with adjusted and systematics parameters are given in Figs III.40–III.47.

Some systematic differences can be seen to occur. Mass distributions calculated with systematics at the two wings are normally narrower, especially the right side of the heavy mass peak, that can be attributed to a systematic difference between

TABLE III.1. LINEAR–LINEAR FIT COEFFICIENTS a, Δa AND b, Δb AND χ^2, y = a + bE

Mass *A*	Coeff *b* × 100	Uncertainty of *b* × 100	Coeff *a*	Uncertainty of *a*	χ^2
80	4.4132E–01	1.0115E–01	5.6516E–02	6.5807E–03	1.65
82	5.6911E–01	6.3240E–02	1.7571E–01	1.4361E–02	2.02
84	1.4603E+00	1.7245E–01	3.0392E–01	1.4381E–02	1.44
86	1.9988E+00	2.0858E–01	6.2864E–01	2.0406E–02	3.47
88	1.6561E+00	2.3028E–01	1.2312E+00	2.8319E–02	6.27
90	2.7170E+00	2.7671E–01	2.0500E+00	3.5437E–02	5.18
92	2.9007E+00	3.0633E–01	3.1690E+00	4.2809E–02	4.23
94	1.5419E+00	3.1440E–01	4.5368E+00	5.0596E–02	4.19
96	–7.7440E–01	3.1551E–01	5.9457E+00	5.7003E–02	6.85
98	–4.2976E+00	3.0693E–01	6.9091E+00	6.0986E–02	2.52
100	–8.0050E+00	2.9082E–01	7.2704E+00	6.2008E–02	0.98
102	–8.5889E+00	2.8456E–01	6.6210E+00	5.9408E–02	5.92
104	–7.0673E+00	2.6536E–01	5.1893E+00	5.4007E–02	3.67
106	–3.0285E+00	2.4897E–01	3.3087E+00	4.5019E–02	4.08
108	1.9644E–01	2.3865E–01	1.7823E+00	3.4151E–02	5.19
110	3.7744E+00	2.4096E–01	6.0791E–01	2.2114E–02	5.51
112	5.8563E+00	2.7011E–01	8.1563E–02	1.1849E–02	6.57
114	5.2108E+00	2.5001E–01	–6.4665E–02	6.8609E–03	18.17
116	4.3468E+00	2.3856E–01	–5.0020E–02	4.7802E–03	14.28
118	4.6524E+00	2.4572E–01	–3.5454E–02	4.4867E–03	25.48
120	5.2324E+00	2.6143E–01	–3.0769E–02	5.1275E–03	14.33
122	5.4493E+00	2.8323E–01	9.0936E–03	7.0759E–03	4.86
124	5.8781E+00	2.9366E–01	1.4210E–01	1.2195E–02	3.62
126	8.1932E+00	3.4988E–01	3.7731E–01	1.7625E–02	1.23
128	9.7178E+00	3.5540E–01	1.3911E+00	2.9412E–02	0.90
130	8.1890E+00	3.5279E–01	3.0181E+00	4.2131E–02	1.55
132	3.7598E+00	3.3305E–01	4.9461E+00	5.2346E–02	10.81
134	–1.8240E+00	3.1795E–01	6.4860E+00	5.8729E–02	4.39
136	–7.1292E+00	2.9066E–01	7.2812E+00	6.2137E–02	2.19
138	–9.4191E+00	4.0504E–01	7.0728E+00	5.5668E–02	1.79
140	–1.0385E+01	2.5022E–01	6.2269E+00	5.9467E–02	5.48
142	–8.9264E+00	2.2096E–01	4.8041E+00	5.3829E–02	4.51
144	–7.7906E+00	1.7982E–01	3.4683E+00	4.6910E–02	1.78
146	–5.6127E+00	1.4270E–01	2.2820E+00	3.9816E–02	4.58
148	–3.4833E+00	1.1200E–01	1.3802E+00	3.2122E–02	5.46
150	–1.3995E+00	9.5925E–02	7.0814E–01	2.3825E–02	2.34
152	–5.9363E–01	8.0314E–02	3.6077E–01	1.7377E–02	2.26
154	–2.7922E–01	5.8022E–02	1.6458E–01	1.2399E–02	2.51

Note: Average χ^2 for all mass A is 5.32.

TABLE III.2. Ln(y)-LINEAR(E) FIT COEFFICIENTS a, Δa AND b, Δb AND χ^2, n(y) = a + bE OR $y = y_0$*exp(bE)

Mass A	Coeff $b \times 100$	Uncertainty of $b \times 100$	Coeff a	Uncertainty of a	χ^2
80	5.2890E+00	1.8857E–01	–2.8120E+00	1.3649E–01	1.35
82	2.0653E+00	3.0792E–02	–1.6577E+00	8.6161E–02	2.40
84	3.2342E+00	1.6620E–01	–1.1366E+00	5.1523E–02	1.77
86	2.3102E+00	1.4229E–01	–4.2482E–01	3.4417E–02	3.97
88	1.1005E+00	1.2636E–01	2.2716E–01	2.3654E–02	6.52
90	1.1300E+00	9.1777E–02	7.2920E–01	1.7728E–02	5.51
92	8.4233E–01	7.2014E–02	1.1573E+00	1.3824E–02	4.39
94	3.3401E–01	6.3048E–02	1.5134E+00	1.1157E–02	4.24
96	–1.2881E–01	5.7237E–02	1.7840E+00	9.4241E–03	6.88
98	–6.5760E–01	5.7316E–02	1.9342E+00	8.5645E–03	2.57
100	–1.2361E+00	6.2861E–02	1.9881E+00	8.0902E–03	0.95
102	–1.5081E+00	7.1615E–02	1.8986E+00	8.4552E–03	5.24
104	–1.5944E+00	8.7519E–02	1.6554E+00	9.7136E–03	3.25
106	–1.0187E+00	1.0428E–01	1.2021E+00	1.3150E–02	3.90
108	1.6368E–01	1.2159E–01	5.7900E–01	1.9679E–02	5.23
110	4.1054E+00	5.5630E–02	–4.4053E–01	3.9769E–02	3.80
112	9.9016E+00	–1.6864E–01	–1.5499E+00	8.0199E–02	3.81
114	1.3494E+01	–4.7475E–01	–2.3433E+00	1.3594E–01	16.67
116	1.3577E+01	–4.2746E–01	–2.5396E+00	1.3303E–01	13.56
118	1.4081E+01	–3.4903E–01	–2.4676E+00	1.1421E–01	12.17
120	1.3173E+01	–2.8728E–01	–2.2571E+00	1.0247E–01	8.69
122	1.1416E+01	–2.0995E–01	–1.9420E+00	9.2085E–02	5.27
124	9.0375E+00	–9.5683E–02	–1.3542E+00	6.8872E–02	1.91
126	7.2996E+00	–2.4642E–02	–6.6246E–01	4.6532E–02	1.00
128	4.1835E+00	3.9631E–02	4.0902E–01	2.2899E–02	2.89
130	2.1463E+00	4.8577E–02	1.1219E+00	1.4880E–02	1.54
132	7.1471E–01	5.1714E–02	1.6024E+00	1.0778E–02	11.02
134	–2.9459E–01	5.4467E–02	1.8711E+00	8.9683E–03	4.39
136	–1.0757E+00	6.0169E–02	1.9883E+00	8.1305E–03	2.34
138	–1.5125E+00	8.6961E–02	1.9618E+00	7.3172E–03	1.91
140	–1.9307E+00	8.4137E–02	1.8362E+00	8.5500E–03	7.08
142	–2.2177E+00	1.0425E–01	1.5803E+00	9.9006E–03	5.52
144	–2.8115E+00	1.4470E–01	1.2599E+00	1.1366E–02	3.31
146	–3.2429E+00	1.9355E–01	8.5283E–01	1.4434E–02	4.97
148	–3.2497E+00	2.6941E–01	3.5032E–01	1.8642E–02	6.69
150	–2.4366E+00	3.3583E–01	–3.2442E–01	2.8702E–02	2.62
152	–1.7574E+00	4.2496E–01	–1.0089E+00	4.4075E–02	2.32
154	–2.3624E+00	7.5126E–01	–1.7356E+00	6.3303E–02	2.74

Note: Average χ^2 for all mass A is 4.85.

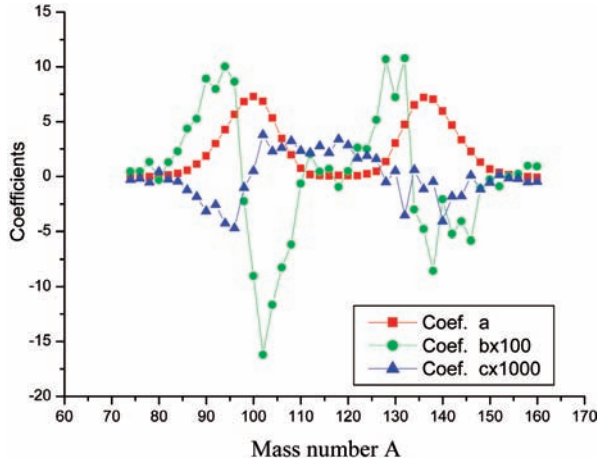

FIG. III.8. Coefficients of second order fit $y = a + bx + cx^2$.

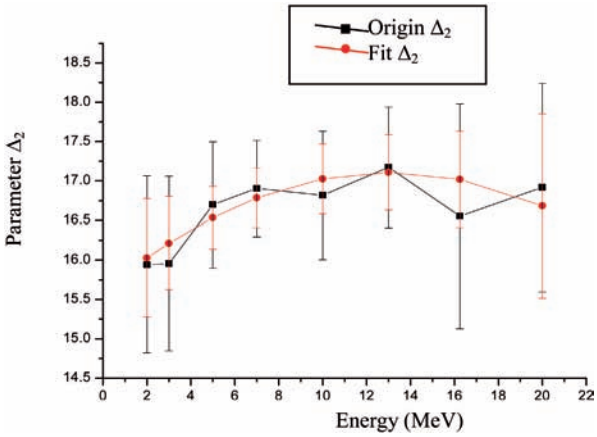

FIG. III.11. Dependence of parameter Δ_2 on energy.

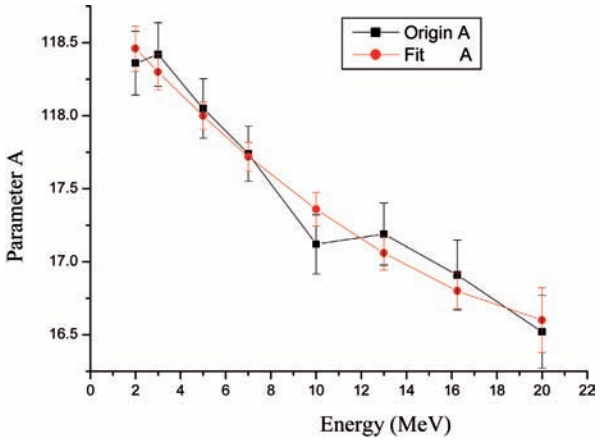

FIG. III.9 Dependence of parameter A on energy.

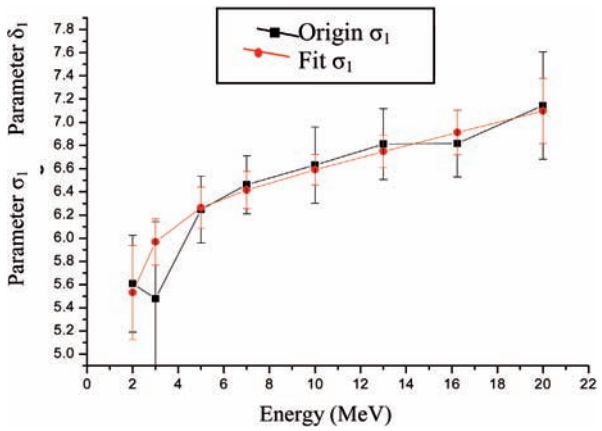

FIG. III.12. Dependence of parameter σ_1 on energy.

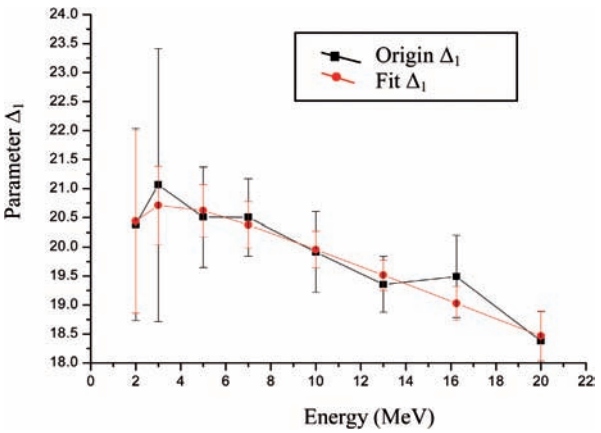

FIG. III.10. Dependence of parameter Δ_1 on energy.

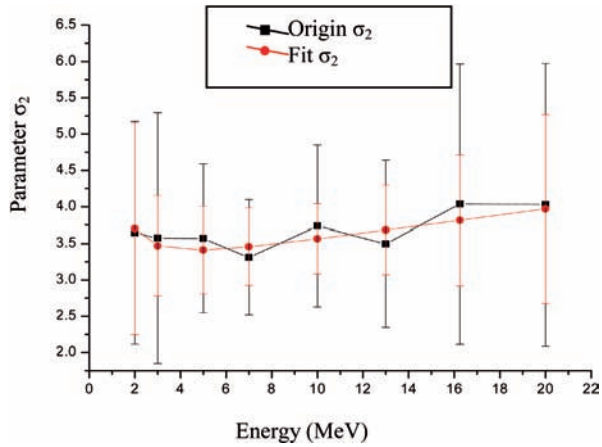

FIG. III.13. Dependence of parameter σ_2 on energy.

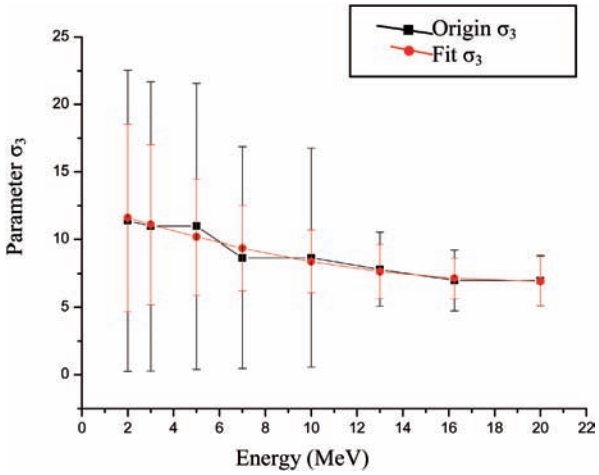

FIG. III.14. Dependence of parameter σ_3 on energy.

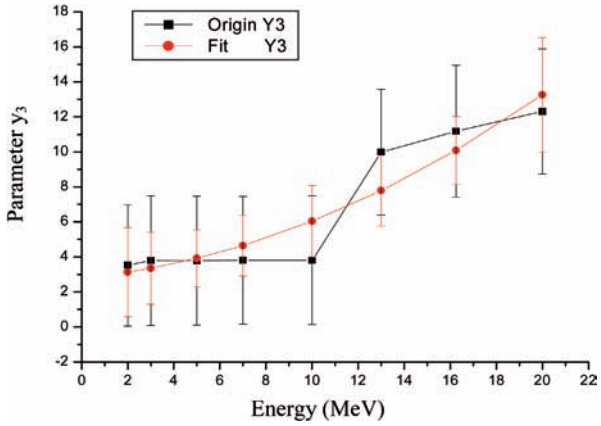

FIG. III.17. Dependence of parameter $\boldsymbol{y}_3$ on energy.

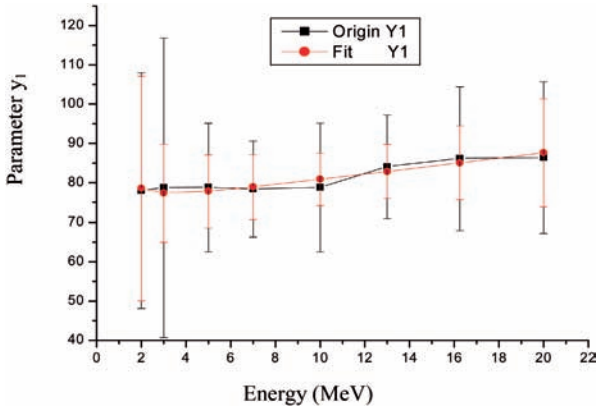

FIG. III.15. Dependence of parameter y_1 on energy.

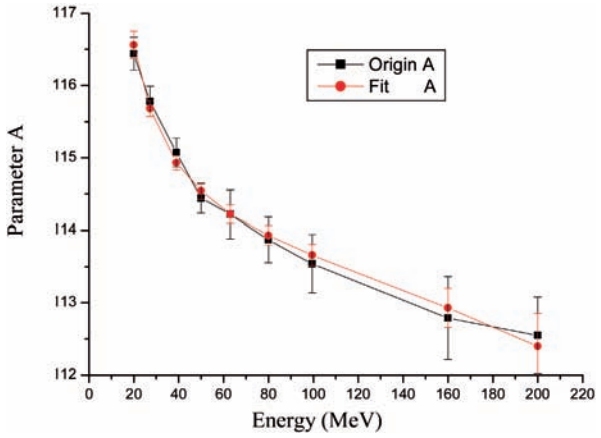

FIG. III.18. Dependence of parameter A on energy.

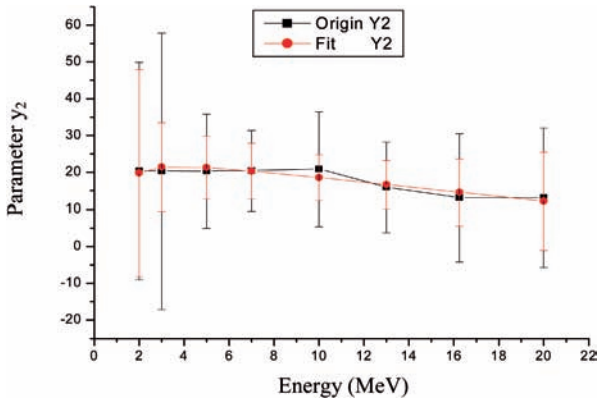

FIG. III.16. Dependence of parameter $\boldsymbol{y}_2$ on energy.

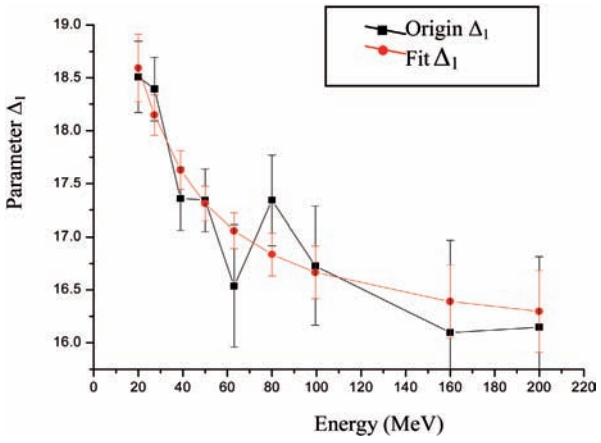

FIG. III.19. Dependence of parameter Δ_1 on energy.

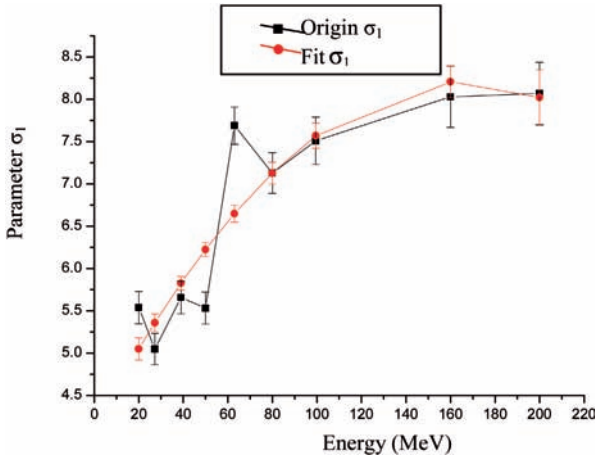

FIG. III.20. Dependence of parameter σ_1 on energy.

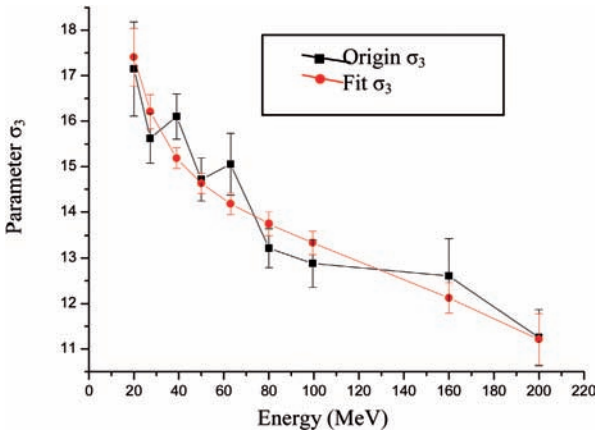

FIG. III.21. Dependence of parameter σ_3 on energy.

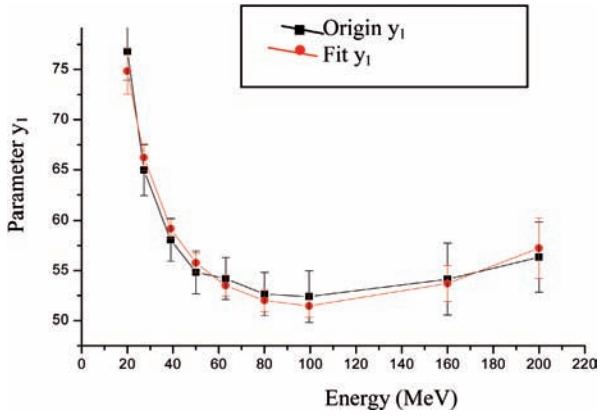

FIG. III.22. Dependence of parameter γ_1 on energy.

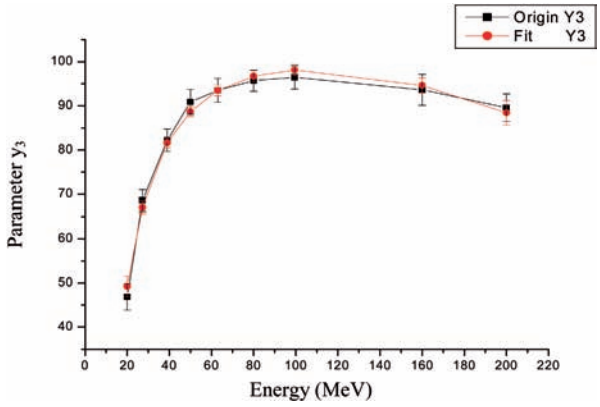

FIG. III.23. Dependence of parameter γ_3 on energy.

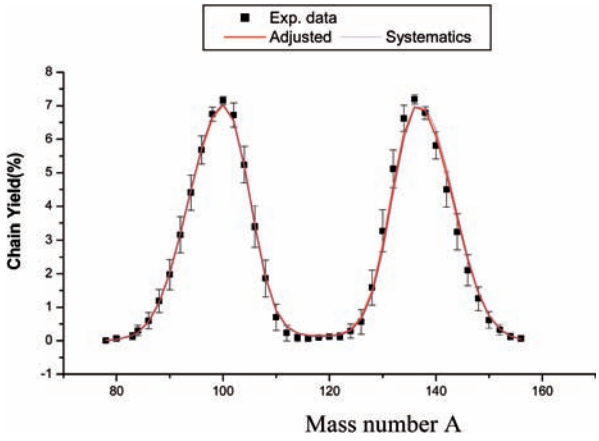

FIG. III.24. Comparison of the mass distribution ^{238}U fission calculated with adjusted and systematics parameters at 2.0 MeV.

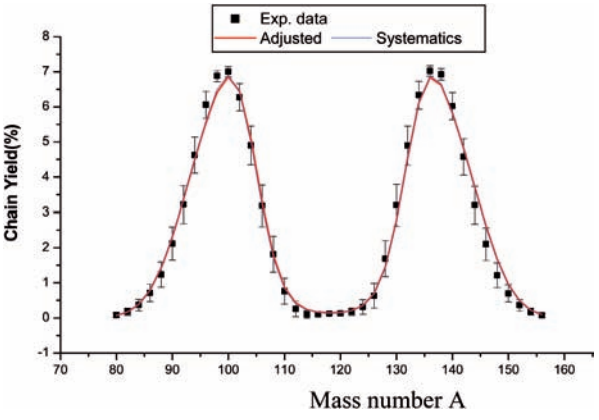

FIG. III.25. Comparison of the mass distribution ^{238}U fission calculated with adjusted and systematics parameters at 3.0 MeV.

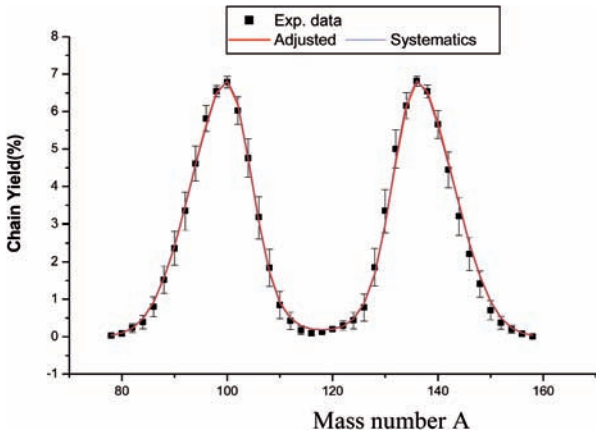

FIG. III.26. Comparison of the mass distribution ^{238}U fission calculated with adjusted and systematics parameters at 5.0 MeV.

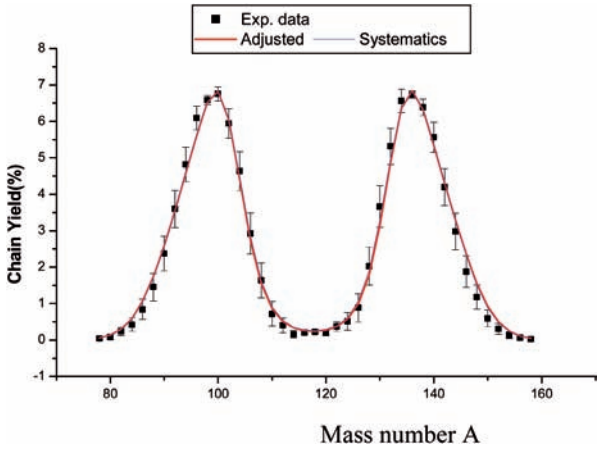

FIG. III.27. Comparison of the mass distribution ^{238}U fission calculated with adjusted and systematics parameters at 7.0 MeV.

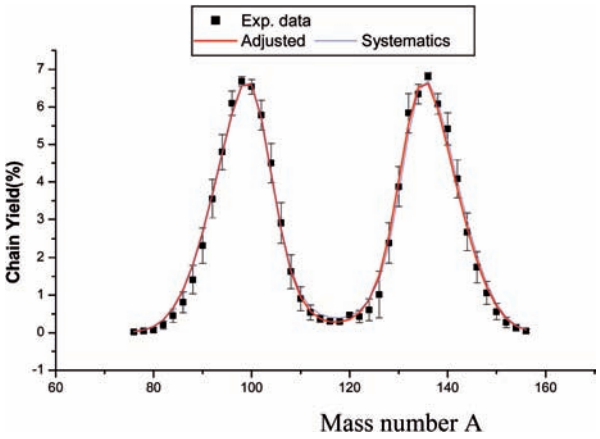

FIG. III.28. Comparison of the mass distribution ^{238}U fission calculated with adjusted and systematics parameters at 10.0 MeV.

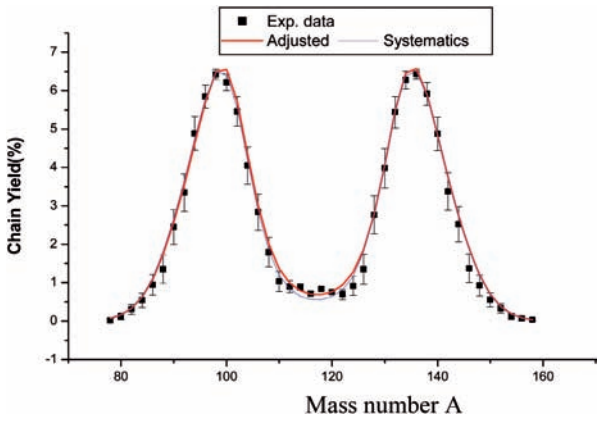

FIG. III.29. Comparison of the mass distribution ^{238}U fission calculated with adjusted and systematics parameters at 13.0 MeV.

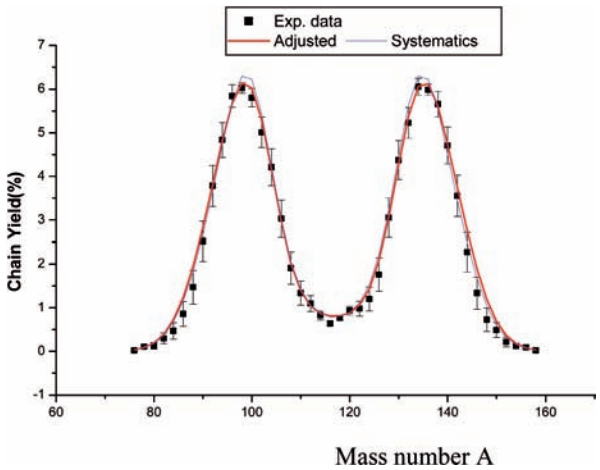

FIG. III.30. Comparison of the mass distribution ^{238}U fission calculated with adjusted and systematics parameters at 16.25 MeV.

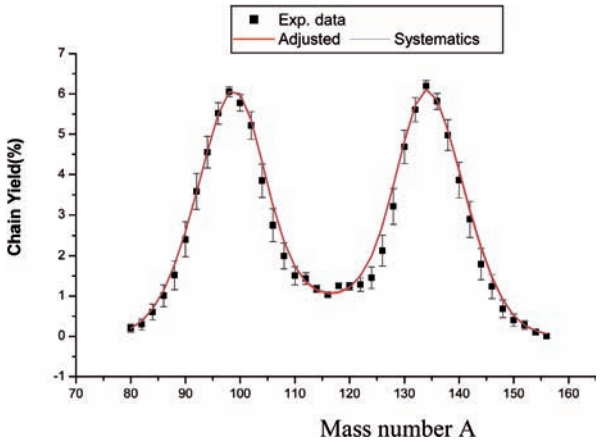

FIG. III.31. Comparison of the mass distribution ^{238}U fission calculated with adjusted and systematics parameters at 20.0 MeV.

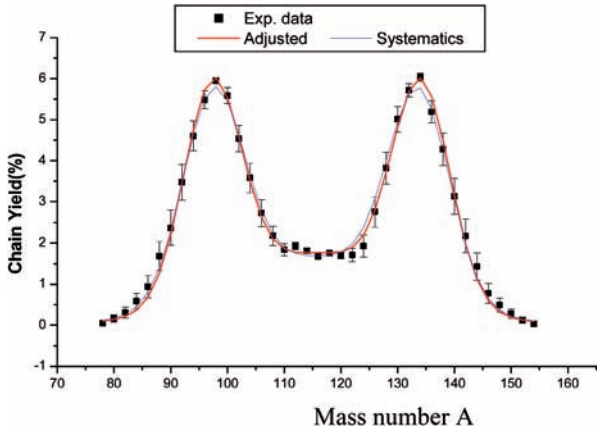

FIG. III.32. Comparison of the mass distribution ^{238}U fission calculated with adjusted and systematics parameters at 27.5 MeV.

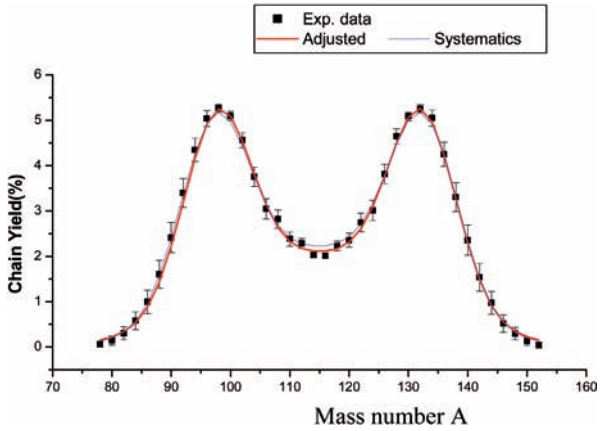

FIG. III.33. Comparison of the mass distribution ^{238}U fission calculated with adjusted and systematics parameters at 39.0 MeV.

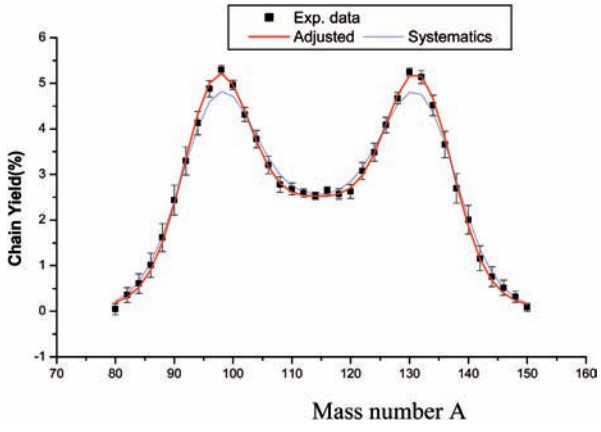

FIG. III.34. Comparison of the mass distribution ^{238}U fission calculated with adjusted and systematics parameters at 50.0 MeV.

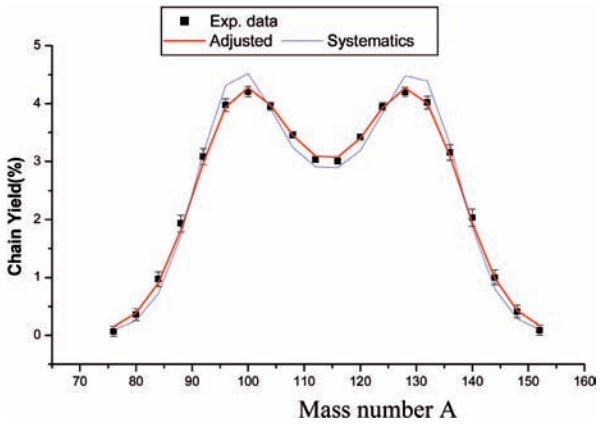

FIG. III.35. Comparison of the mass distribution ^{238}U fission calculated with adjusted and systematics parameters at 63.0 MeV.

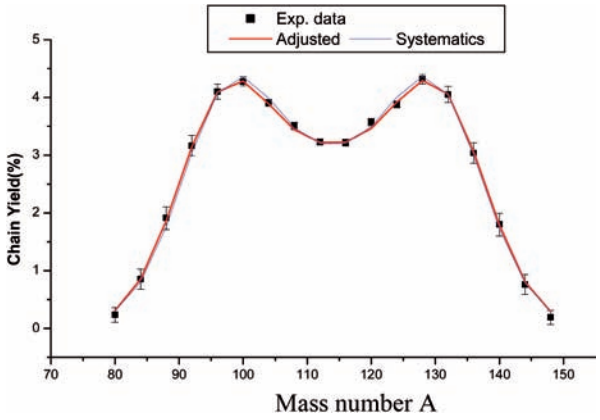

FIG. III.36. Comparison of the mass distribution ^{238}U fission calculated with adjusted and systematics parameters at 80.0 MeV.

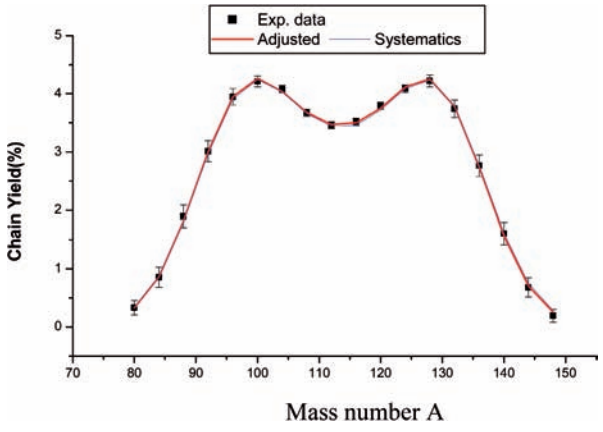

FIG. III.37. Comparison of the mass distribution ^{238}U fission calculated with adjusted and systematics parameters at 99.5 MeV.

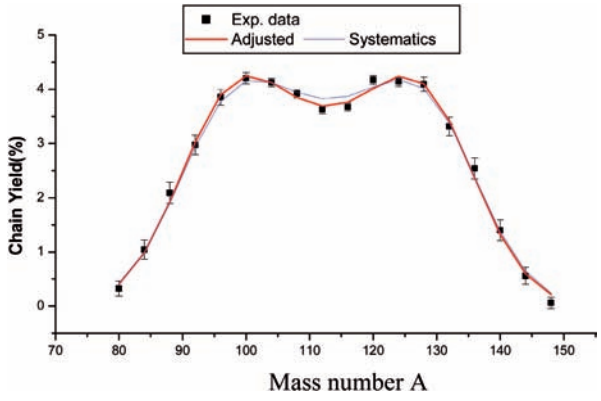

FIG. III.38. Comparison of the mass distribution ^{238}U fission calculated with adjusted and systematics parameters at 160.0 MeV.

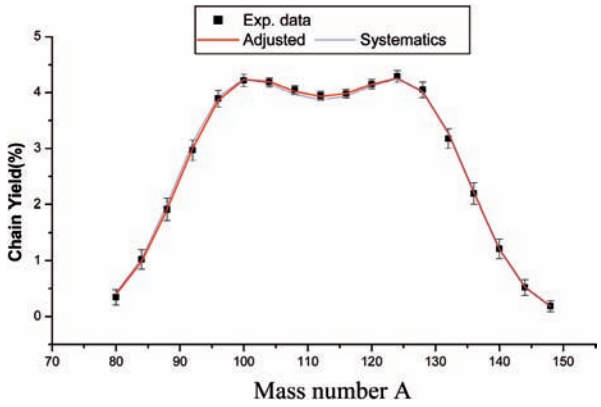

FIG. III.39. Comparison of the mass distribution ^{238}U fission calculated with adjusted and systematics parameters at 200.0 MeV.

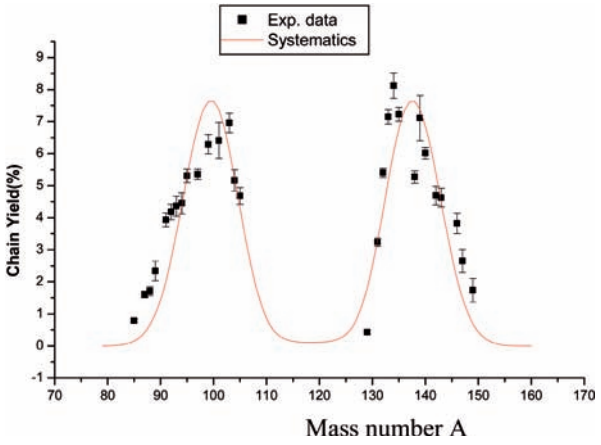

FIG. III.40. Comparison of the experimental mass distribution for ^{238}U fission with equivalent data from calculated systematics parameters at 1.5 MeV.

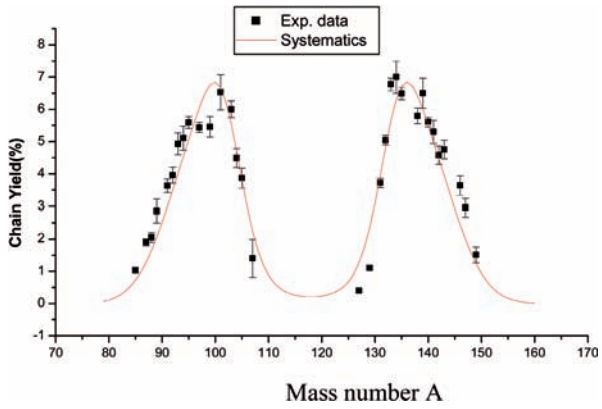

FIG. III.41. Comparison of the experimental mass distribution for ^{238}U fission with equivalent data from calculated systematics parameters at 5.5 MeV.

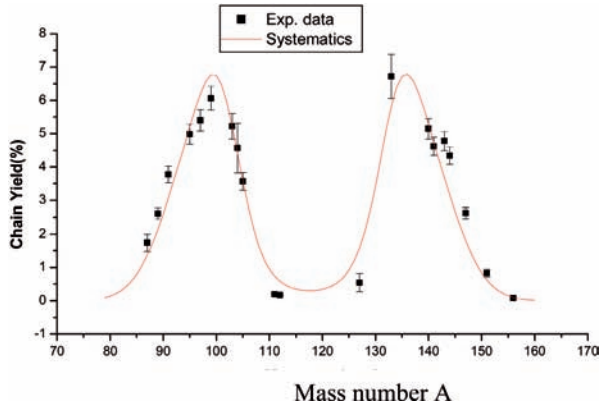

FIG. III.42. Comparison of the experimental mass distribution for ^{238}U fission with equivalent data from calculated systematics parameters at 8.1 MeV.

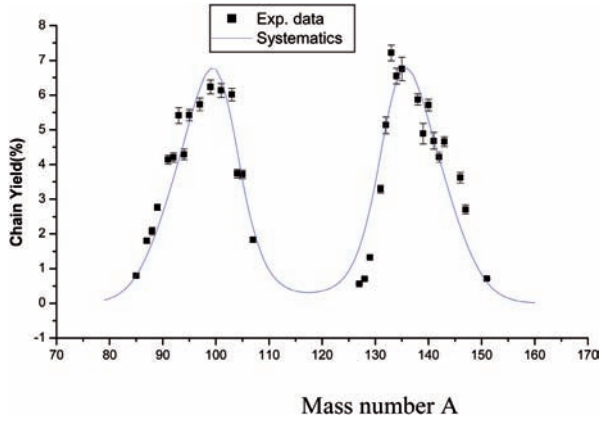

FIG. III.C.43. Comparison of the experimental mass distribution for ^{238}U fission with equivalent data from calculated systematics parameters at 8.3 MeV.

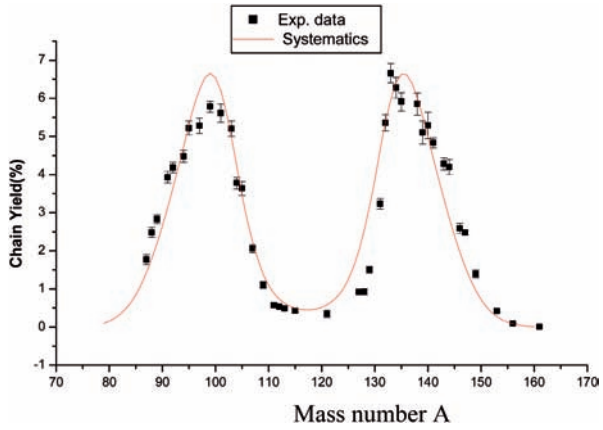

FIG. III.44. Comparison of the experimental mass distribution for ^{238}U fission with equivalent data from calculated systematics parameters at 11.3 MeV.

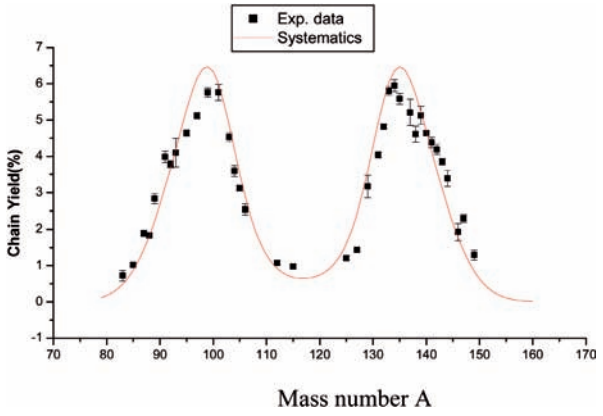

FIG. III.45. Comparison of the experimental mass distribution for ^{238}U fission with equivalent data from calculated systematics parameters at 14.4 MeV.

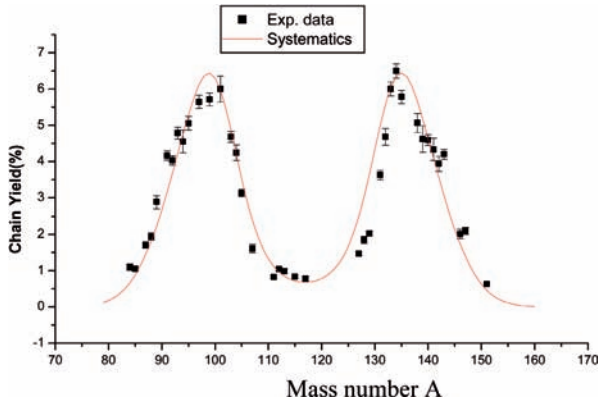

FIG. III.46. Comparison of the experimental mass distribution for ^{238}U fission with equivalent data from calculated systematics parameters at 14.9 MeV.

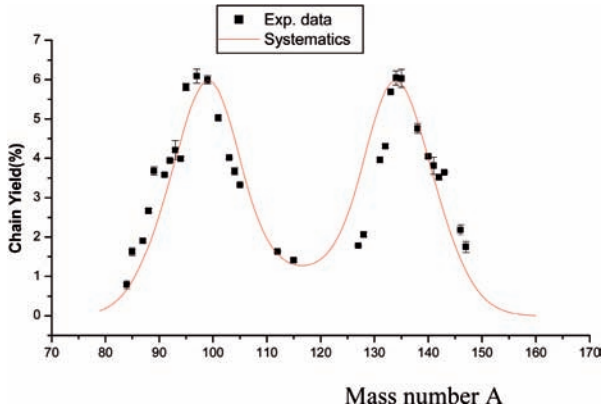

FIG. III.47. Comparison of the experimental mass distribution for ^{238}U fission with equivalent data from calculated systematics parameters at 22.0 MeV.

the data measured by Zöller using the kinetic method [III.1] with the data measured by radiochemistry [III.2–III.8].

The χ^2 for fitting the measured data with adjusted and systematics parameters are listed in Table III.4. These data are all smaller than 1.0 for all energy points with adjusted parameters and for most cases with systematics parameters, except at 13, 20 and 63 MeV, where they are 1.683, 1.800 and 5.820, respectively. All of these data and figures showing the dependence of parameters σ_1 and Δ_1 on energy indicate that there is some systematic difference for the data at 63.0 MeV compared with others.

III.5. UNCERTAINTY STUDIES IN THE SYSTEMATICS

The covariance of the data to be fitted is transferred according to the following equations:

$$C = (F^T V_Y^{-1} F)^{-1} F^T V_Y^{-1} Y$$

$$V_C = (F^T V_Y^{-1} F)^{-1}$$

$$Y = FC$$

$$V_Y = F V_C F^T$$

where Y is the data vector to be fitted, V_Y is its covariance matrix, C is the fitting coefficient vector, V_C is its covariance matrix, and F is the sensitivity matrix.

The following transformations are included:

(a) From experimental data covariance V_Y to Gaussian fit coefficients (c1) via model fitting of 5 or 3 Gaussians;

TABLE III.3. QUADRATIC FUNCTION FIT COEFFICIENTS a, b, c AND χ^2, $y = a + bx + cx^2$

Mass A	Coeff a	Coeff b	Coeff c	χ^2
74	–5.5832E–02	4.5560E–03	–2.9637E–04	12.47
76	–3.7930E–02	4.5910E–03	–1.8179E–04	6.62
78	–3.2065E–02	1.3211E–02	–5.3969E–04	3.61
80	7.7263E–02	–3.1322E–03	4.1843E–04	0.69
82	1.4521E–01	1.2959E–02	–2.5443E–04	1.10
84	2.8035E–01	2.2982E–02	–4.4357E–04	0.90
86	5.6116E–01	4.3607E–02	–1.2353E–03	1.79
88	1.1254E+00	5.2672E–02	–1.8603E–03	3.52
90	1.8670E+00	8.9142E–02	–3.1701E–03	1.58
92	3.0174E+00	7.9697E–02	–2.5824E–03	2.06
94	4.2804E+00	1.0022E–01	–4.2774E–03	0.68
96	5.6586E+00	8.6396E–02	–4.7207E–03	2.56
98	6.8460E+00	–2.2571E–02	–1.0199E–03	1.78
100	7.3016E+00	–9.0110E–02	5.0137E–04	0.71
102	6.8586E+00	–1.6203E–01	3.8011E–03	2.78
104	5.3316E+00	–1.1644E–01	2.2814E–03	2.03
106	3.4708E+00	–8.2544E–02	2.6269E–03	1.79
108	1.9755E+00	–6.1499E–02	3.2506E–03	1.09
110	7.3690E–01	–6.4558E–03	2.3442E–03	1.80
112	1.8442E–01	2.0261E–02	2.1504E–03	2.09
114	6.0826E–02	4.3419E–03	2.7862E–03	6.33
116	4.3015E–02	6.8381E–03	2.1707E–03	5.20
118	1.0593E–01	–9.5232E–03	3.3891E–03	6.35
120	8.9536E–02	4.8903E–03	2.8484E–03	2.71
122	8.0482E–02	2.6234E–02	1.6501E–03	1.59
124	2.3236E–01	2.5132E–02	1.8839E–03	0.80
126	4.5923E–01	5.1546E–02	1.5958E–03	0.20
128	1.3635E+00	1.0682E–01	–5.0838E–04	0.62
130	3.0462E+00	7.2385E–02	4.9034E–04	1.13
132	4.7335E+00	1.0778E–01	–3.5508E–03	6.58
134	6.5228E+00	–3.0164E–02	5.9816E–04	3.25
136	7.2085E+00	–4.7920E–02	–1.1615E–03	1.50
138	7.0470E+00	–8.5530E–02	–4.6389E–04	1.33
140	5.9680E+00	–2.0860E–02	–4.0919E–03	1.97
142	4.6889E+00	–5.2417E–02	–1.8171E–03	2.86
144	3.3524E+00	–4.0944E–02	–1.8107E–03	0.62
146	2.2882E+00	–5.8095E–02	9.6883E–05	3.43
148	1.3052E+00	–1.0769E–02	–1.1785E–03	3.42
150	6.7315E–01	–2.6816E–03	–5.5572E–04	1.50
152	3.7000E–01	–8.9287E–03	1.4980E–04	1.67
154	1.5561E–01	1.5237E–04	–1.4710E–04	1.82
156	6.2581E–02	2.1905E–03	–2.0514E–04	1.42
160	–5.9279E–02	9.0189E–03	–4.7674E–04	1.26
158	–2.8688E–02	9.8028E–03	–5.2810E–04	2.37

Note: Average χ^2 for all mass A is 2.54.

TABLE III.4. FITTED χ^2 WITH ADJUSTED AND SYSTEMATICS PARAMETERS

0–20 MeV			20–200 MeV		
E_n (MeV)	Adjusted	Systematics	E_n(MeV)	Adjusted	Systematics
2.0	0.888	0.725	20.0	0.589	1.847
3.0	0.803	0.891	27.5	0.674	0.921
5.0	0.619	0.841	39.0	0.508	0.975
7.0	0.676	0.672	50.0	0.314	2.055
10.0	0.751	0.975	63.0	0.460	5.820
13.0	0.883	1.683	80.0	0.349	0.738
16.25	0.896	0.971	99.5	0.135	0.267
20.0	0.830	0.857	160.0	0.805	1.395
			200.0	0.0592	0.265

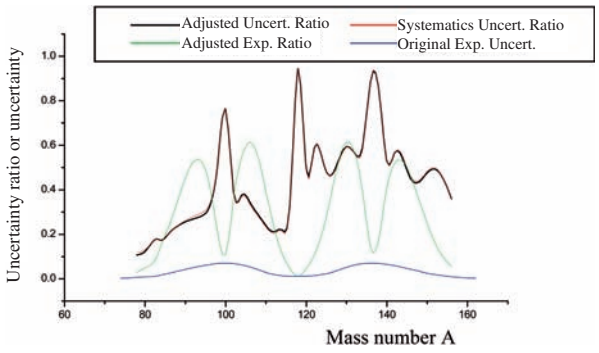

FIG. III.48. Ratio of adjusted (systematics) and experimental uncertainties at 2 MeV for ^{238}U fission mass distribution.

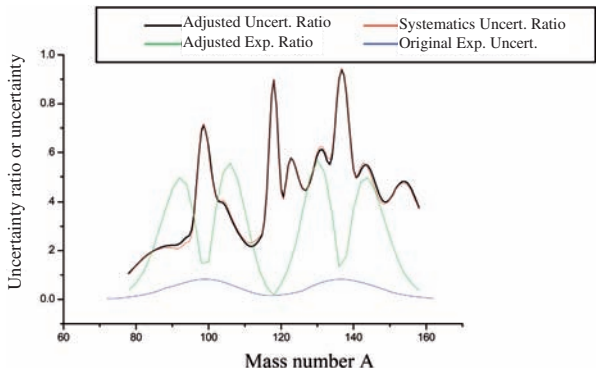

FIG. III.49. Ratio of adjusted (systematics) and experimental uncertainties at 5 MeV for ^{238}U fission mass distribution.

(b) From Gaussian fit coefficient covariance V_{C1} to systematic fit coefficients (c2) via second order function fitting;
(c) From systematic fit coefficient covariance V_{C2} to yields calculated with systematics via the corresponding 5 or 3 Gaussian model using coefficients from systematics.

All input covariance matrices for these three steps are supposed to be diagonal (although they are not) in order to prevent the processing from becoming too complicated. Nevertheless, there should be a reasonably strong correlation for the experimental yield data because they were measured simultaneously at each energy point by means of the kinetic energy method. As examples, Figs III.48–III.55 show comparisons between the original uncertainties given by the author, uncertainties adjusted for mass resolution, and uncertainties calculated with the adjusted coefficients from systematics.

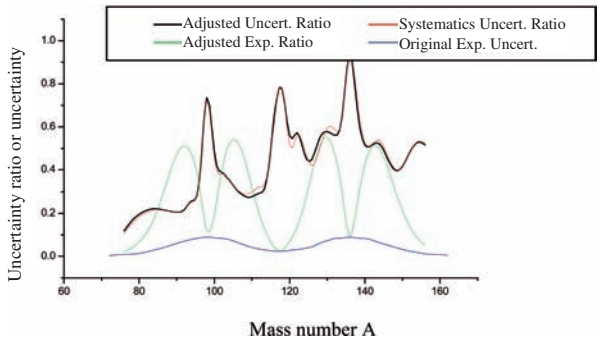

FIG. III.50. Ratio of adjusted (systematics) and experimental uncertainties at 10 MeV for ^{238}U fission mass distribution.

The following observations can be made from the figures:

(1) The uncertainties from the data adjusted for mass resolution are much larger than the original values given by the author. In fact, the

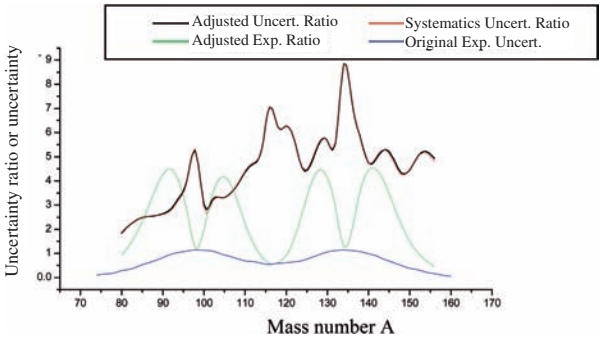

FIG. III.51. Ratio of adjusted (systematics) and experimental uncertainties at 20 MeV for ^{238}U fission mass distribution.

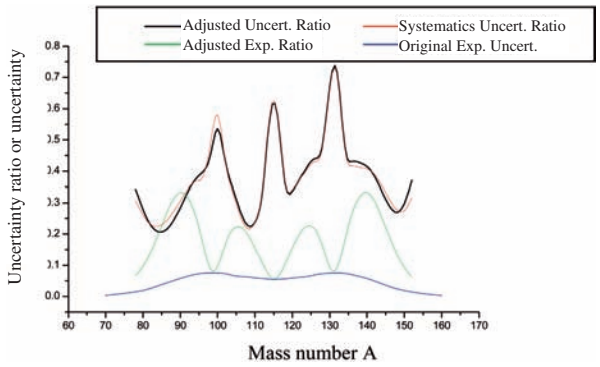

FIG. III.52. Ratio of adjusted (systematics) and experimental uncertainties at 39 MeV for ^{238}U fission mass distribution.

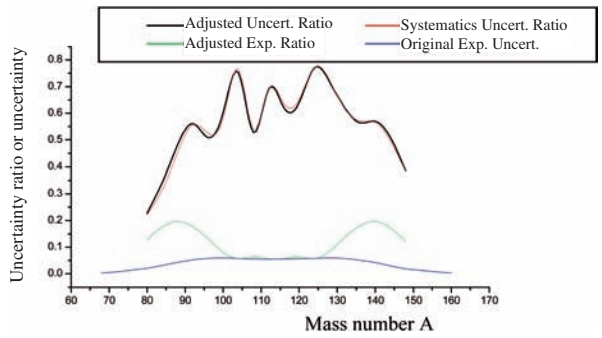

FIG. III.53. Ratio of adjusted (systematics) and experimental uncertainties at 80 MeV for ^{238}U fission mass distribution.

uncertainties given by the author are only the counting statistics, while the main source of uncertainty from the mass calibration was not taken into account. Since the effect is greater at the wings of the fission yield peaks, the changes in the uncertainties after adjustment are much larger. On the other hand, the effect is smaller for the yields in the valley and at the bottom of the left side of the light mass peak and the right side of the heavy mass peak, so the changes in the uncertainties after these adjustments are relatively small.

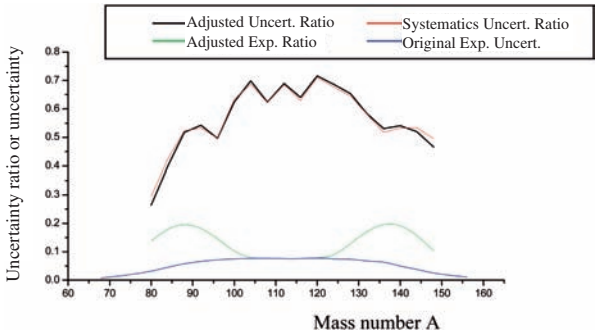

FIG. III.54. Ratio of adjusted (systematics) and experimental uncertainties at 160 MeV for ^{238}U fission mass distribution.

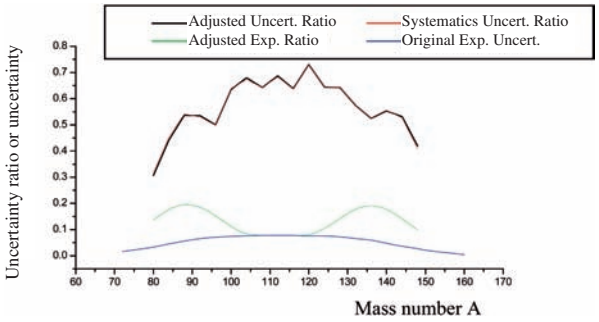

FIG. III.55. Ratio of adjusted (systematics) and experimental uncertainties at 200 MeV for ^{238}U fission mass distribution.

(2) The uncertainties calculated with adjusted and systematics parameters are almost the same at all energy points, which means that the uncertainty is not sensitive to these parameters.
(3) When compared with the experimental uncertainty, the uncertainties calculated with systematics are reduced to 20–80% (about 50% on average). This improvement can be understood in terms of the increased amount of available data.
(4) The reduced uncertainty calculated by means of systematics differs due to the strong correlation between the calculated yields (that makes the uncertainty flat).

III.6. CORRELATION STUDY IN THE SYSTEMATICS

The covariance matrices V_C were calculated for the fitting coefficients of the Gaussians of the mass distribution and of the systematics (V_S), and for the mass distributions from systematics (V_Y) in each step, as mentioned above. The correlations in matrices V_C, V_S and V_Y are rather complicated and strong, and stem from the imposed fitting conditions.

The matrix V_C gives the correlation among the 9 (E_n = 0–20 MeV) or 5 (20–200 MeV) parameters used to fit the mass distribution with 5 or 3 Gaussians. The calculated results show that in the lower energy region, parameter A (midpoint of the mass distribution) has a lower correlation with the other parameters. Also, the parameters Y_3, σ_3 (representing the height and width of the third Gaussian) have less correlation with others, but a strong correlation among themselves. Also, the correlation among the parameters Y_1, σ_1, Y_2, σ_2 (heights and widths of the first and second Gaussian) is quite strong. This latter finding is reasonable since the two peaks are well separated and the contribution from the third Gaussian distribution is relatively small. With increasing energy, the yields in the valley increase and the correlation among the parameters of the third Gaussian and the first and second Gaussians become stronger.

The matrix V_Y gives the correlation among yields calculated with the systematics parameters. Not unreasonably, the correlations of a yield with neighbourhood yields are generally strong (correlation coefficient ρ = 0.8–1.0), but become very weak (ρ < 0.1) with yields that are significantly separated.

REFERENCES TO APPENDIX III

[III.1] ZÖLLER, C.M., Untersuchung der neutroneninduzierten Spaltung von ^{238}U im Energiebereich von 1 MeV bis 500 MeV, PhD Thesis, Technische Universität Darmstadt, Germany (1995).

[III.2] NAGY, S., et al., Mass distribution in monoenergetic-neutron-induced fission of ^{238}U, Phys. Rev. C **17** (1978) 163–171.

[III.3] CHAPMAN, T.C., Fission product yields from 6–9 MeV neutron-induced fission of ^{235}U and ^{238}U, Phys. Rev. C **17** (1978) 1089–1097.

[III.4] DAROCZY, S., et al., Experimental results on mass distribution of ^{238}U fission induced by 14 MeV neutrons, Atomki Koezl. **18** (1976) 317–329.

[III.5] LIU CONGGUI, et al., The mass distribution in 14.9 MeV neutron-induced fission of ^{238}U, Chin. Nucl. Phys. **7** (1985) 235–241.

[III.6] LI ZE, et al., Mass distribution in 8.3 MeV neutron-induced fission of ^{238}U, Chin. Nucl. Phys. **7** (1985) 97–105.

[III.7] LI ZE, et al., Fission product yields from 11.3 MeV neutron-induced fission of ^{238}U, Radiochim. Acta **64** (1994) 95–97.

[III.8] LIU YONGHUI, et al., Mass distribution of 22.0 MeV neutron-induced fission of ^{238}U, Commun. Nucl. Data Prog. No. 26 (2001) 2–4.

[III.9] LIU TINGJIN, Data correction to mass resolution, Commun. Nucl. Data Prog. No. 28 (2002) 52–54.

[III.10] WAHL, A.C., Los Alamos National Laboratory, NM, personal communication, 2001.

CONTENTS OF THE CD-ROM

The attached CD-ROM contains products of the CRP comprising additional valuable information: compilations of experimental data, unedited contributed papers, tables considered too bulky for inclusion in the printed book, and detailed results of the benchmark exercise.

APPENDIX A: Compilations of experimental data

J.-O. Denschlag: Measurements of product yields from fission reactions induced by high energy neutrons, protons, deuterons, alpha particles, other charged particles and photons: Collection of references
M.C. Duijvestijn: Compilation of proton induced fission yield data
Liu Tingjin: EXFOR entries of neutron induced fission yield data
R.W. Mills: References collected for consideration of the CRP

APPENDIX B: Papers and tables for the benchmark exercise

V.M. Maslov: Emissive fission contributions to total fission cross-sections up to 200 MeV
V.M. Maslov: Symmetric/asymmetric fission cross-sections for ^{235}U and ^{238}U up to 200 MeV
Yu.V. Kibkalo: Fragment mass distribution for ^{238}U fission by neutrons of 2 to 200 MeV.

APPENDIX C: Individual results of the benchmark calculations

M.C. Duijvestijn
J. Katakura
Yu.V. Kibkalo
Liu Tingjin
A.C. Wahl
S.V. Zhdanov

APPENDIX D: Detailed plots of the benchmark results

LIST OF PARTICIPANTS IN THE COORDINATED RESEARCH PROJECT

Denschlag, J.-O.	Johannes-Gutenberg-Universität Mainz, Germany
Duijvestijn, M.C.	Nuclear Research and Consultancy Group, Netherlands
Ethvignot, Th.	Service de Physique Nucléaire, Commissariat à l'Énergie Atomique, France
Goverdovskii, A.A.	Institute of Physics and Power Engineering, Russian Federation
Hambsch, F.-J.	EC Joint Research Centre, Institute for Reference Materials and Measurements, Belgium
Katakura, J.	Japan Atomic Energy Agency, Japan
Kibkalo, Yu.V.	SC Institute for Nuclear Research, Ukraine
Lammer, M.	International Atomic Energy Agency
Tingjin, Liu	China Institute of Atomic Energy, China
Maslov, V.M.	Belarus Academy of Sciences, Belarus
Mills, R.W.	Nexia Solutions, British Nuclear Fuels plc, United Kingdom
Storrer, F.	Commissariat à l'Énergie Atomique, Cadarache, France
Wahl, A.C.	Los Alamos National Laboratory, United States of America
Zhdanov, S.V.	National Nuclear Centre, Kazakhstan

This publication reports on a coordinated research project devoted to the development of methodologies designed to derive recommended fission yields for direct application in studies of the transmutation of nuclear waste. Emphasis is placed on the derivation of adequate systematics and models for the calculation of energy dependent fission yields up to 150 MeV incident neutron energy. A benchmark exercise revealed the worth and predictive capabilities of the proposed systematics and theoretical models. These methods of analysis have the potential to give reliable predictions after implementation of further improvements suggested in this report. A brief introduction and the various studies undertaken by individual participants are given at the beginning of this publication, followed by a detailed description of the resulting overall achievements, conclusions and recommendations of the coordinated research project, and a summary of the benchmark exercise and results. Additional material is contained on a CD-ROM, including various compilations of the fission product yields, unedited papers and full details of the benchmark exercise.

INTERNATIONAL ATOMIC ENERGY AGENCY
VIENNA
ISBN 92–0–115306–6